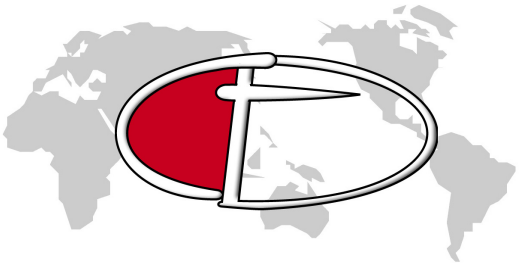

Third International Symposium on Acoustic Wave Devices for Future Mobile Communication Systems

Tuesday, 6th - Thursday, 8th March, 2007
Keyaki Hall, Chiba University

Sponsored by
Chiba University

Welcome to Chiba Symposium!

The organising committee is very grateful to you for joining this Third International Symposium on Acoustic Wave Devices for Future Mobile Communication Systems in Chiba. We really take your participation as a great honor.

The symposium was initially planned to return university academic fruits to worldwide society by offering researchers and engineers a platform of this sort to discuss the most recent developments, common interests and future trends in acoustic wave device technologies and their related fields. Thinking back to the last two symposia held in 2001 and 2004, we are convinced that both of them were a complete success with nearly 200 participants each, a quarter of which being from overseas. In addition to a significant impact and academic importance provided, human relationships fostered throughout the symposia should have been most valuable for the researchers and engineers participated, which may be everlasting and contribute a great deal to their future work.

Acoustic wave devices have established their present status, in particular, as indispensable ingredients in "mobile phones". Entering ubiquitous society, however, we need the creation of new concepts of acoustic wave devices as well as further evolution and breakthroughs to maximise their performance with minimised physical size and weight, should they become real indispensable ingredients in "mobile information communications". This may be dealt only by true cooperation amongst researchers and engineers all over the world.

Because of the success of the last two symposia and changes in circumstances surrounding the acoustic wave device technologies, the university headquarters is happy to hold and support this symposium, which also meets the university policy of expanding international academic exchanges.

We trust that this symposium will provide an opportunity to expand human relationships and mutual cooperation as well as a useful source for research and development of acoustic wave device technologies.

The organising committee deeply indebted to Chiba University and Venture Business Laboratory of Chiba University for their sponsorship, and to the Murata Science Foundation and NTT DoCoMo, Inc. for their financial support.

6th March 2007

M. Yamaguchi

Masatsune Yamaguchi
Chairman of the Organising Committee
Professor EEE, Chiba University

Tuesday, 6th March

Opening Remarks

Wednesday, 7th March

2A Recent RF BAW Technologies (Chair: M.A. Dubois)

2B Integration of RF BAW Devices (Chair: R. Aigner)

2C Thin Films and Processes for High Performance BAW Filters (Chair: M. Yamaguchi)

2D Modern SAW Duplexers (Chair: G. Kovacs)

Thursday, 8th March

3A New Structure and Packaging Technologies for SAW Devices (Chair: M. Solal)

3B Integrated Functional SAW Modules (Chair: O. Ikata)

Closing Address

12:30 K.Hashimoto, Chiba University

Transmitter System Using Polar Modulation for Mobile Applications

Earl McCune

Panasonic Emerging Advanced RF Laboratory
Santa Clara, California USA
emccune@research.panasonic.com

Abstract – **As multimode becomes a more common product requirement, cost and efficiency are also becoming much more important. Starting from a maximum efficiency circuit, we derive that polar modulation is the natural transmitter structure to realize multimode signalling. Measurements of prototype polar transmitters are provided to validate the predictions.**

I. Introduction

For many reasons, mobile wireless devices must now operate using multiple signal types. These reasons include the use of different services (voice and/or data) at different times, and having the cellular infrastructure environment change in a new location. These signal types include both constant-envelope (e.g. GSM, Bluetooth, etc.), and envelope-varying (e.g. EDGE, (W)CDMA, OFDM, QAM, etc.) characteristics. Because the envelope-varying signals conventionally require linear RF circuitry to properly generate them, they are often called 'linear signals'.

It is very well known that a conventional linear amplifier will exhibit good linearity at low efficiency (DC in to RF out), or good efficiency at compression where linearity is very poor. Much of radio engineering for the last several decades has been spent trying to reconcile these opposing characteristics, intent on realizing good circuit linearity while simultaneously exhibiting good efficiency.

In addition, the cost of this reconciliation must be very low because modern GSM mobiles have set the size, weight, cost, operating temperature, and battery life expectations of over one billion (10^9) consumers. Consumers are not interested in the radio technology used within their mobile device. But compared to the compressed (and therefore efficient) RF transmitter in GSM mobiles, the linear RF transmitter needed for higher bandwidth-efficient signals are much more expensive to design and produce. The challenge to the RF engineering community is very clear.

Traditonal RF engineering begins with linear circuitry, and then modifications are worked on to improve efficiency. This paper presents an opposite approach – begin with efficient, compressed RF circuitry, and work out designs to improve linear performance. The result is a change to polar coordinate signal processing, while keeping all RF circuitry fully compressed. Even though some aspects of polar modulation date back to before 1920 [1], the technique is gaining popularity as more engineering teams tackle this 'linear and also efficient' problem. [2] [3] [4] [5] [6] [7]

This paper is structured as follows. Following this introduction, section II derives the polar signal processing conversion of the efficiency-based transmitter. Section III presents Performance measurements from this transmitter. Finally, conclusions are drawn.

II. Efficiency Based Architecture Derivation

To begin, we review some important characteristics of linear amplifiers when operated toward compression. The first concept that must be re-examined is the concept of gain.

In a linear amplifier, the transfer function is simply

$$y = a_1 \cdot x \quad . \tag{1}$$

There are two ways to interpret gain from this transfer function. The first is to take the first derivative of the output with respect to the input, referred to as the differential gain [8]

$$g_d(x) = \frac{d}{dx} y(x) = a_1 \quad . \tag{2}$$

A second way to interpret gain is to take the ratio of the output over the input, referred to as the ratiometric gain

$$g_r(x) = \frac{a_1 x}{x} = a_1 \quad . \tag{3}$$

Clearly, both the differential (2) and ratiometric gain (3) evaluate to the same value in this linear case. But they differ greatly when nonlinear operation is encountered. This difference is shown in Figure 1.

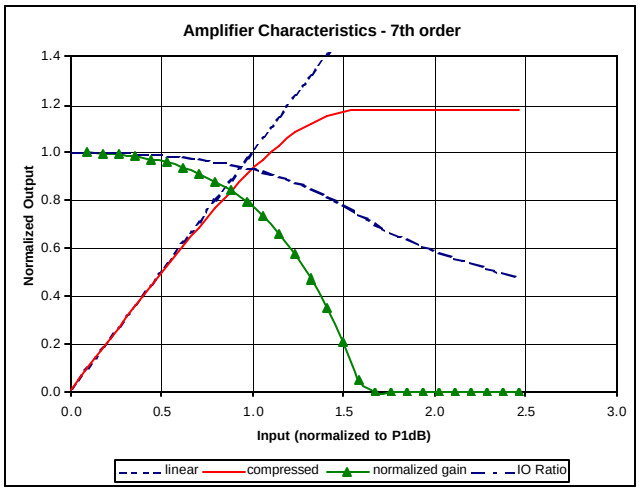

Figure 1. Amplifier transfer function, with corresponding normalized differential and ratiometric gains.

Reviewing Figure 1, it is seen that the differential gain goes to zero when the amplifier enters clipping. However, the ratiometric gain never goes to zero because the output signal is never zero. Ratiometric gain does drop when the input signal continues to grow after the output reaches compression.

It is important to keep these gain definitions clearly separated because they represent very different effects. Differential gain represents the waveform distortion of the amplifier, and therefore its effective linearity

$$y(x)=\begin{cases}\sum_{k=0}^{\infty}a_k x^k = a_0+a_1x+D & x<x_c \\ y_{MAX} & x\ge x_c\end{cases} \quad . \qquad (4a)$$

$$\text{gain}=\begin{cases}a_1+\sum_{k=2}^{\infty}k a_k x^{k-1} & x<x_c \\ 0 & x\ge x_c\end{cases} . \qquad (4b)$$

This is not equivalent to the usual gain measurement performed in an RF laboratory, where gain is often taken as the difference of output power and input power measured in dBm

$$G_R = P_{out} - P_{in} = 10\log(p_{out}) - 10\log(p_{in})$$
$$= 10\log\left(\frac{p_{out}}{p_{in}}\right) \qquad (5)$$
$$= 10\log\left(\frac{V_{out}^2/R}{V_{in}^2/R}\right) = 20\log\left(\frac{V_{out}}{V_{in}}\right)$$

which we see is a ratiometric gain.

When the transmitter design starting point is the maximum efficiency operating condition of the amplifier, we get the condition shown in Figure 2. The amplifier is operating just into the output clipping region.

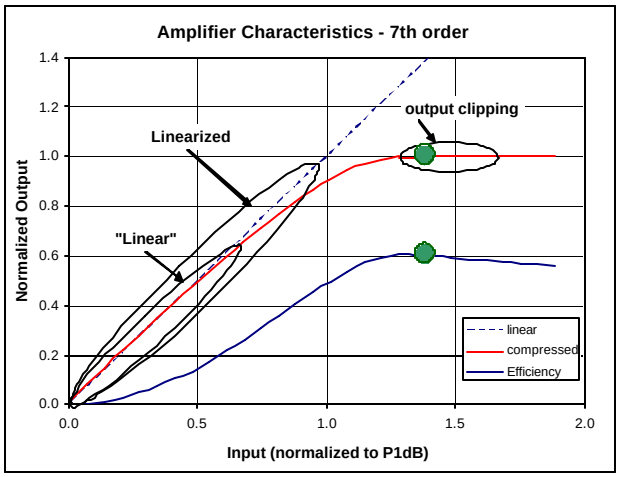

Figure 2. Amplifier maximum efficiency operating condition

Operating in this condition, the differential gain is equal to zero. The amplifier is no longer acting as a controlled current source, but rather as a switch. This shift is modeled as shown in Figure 3.

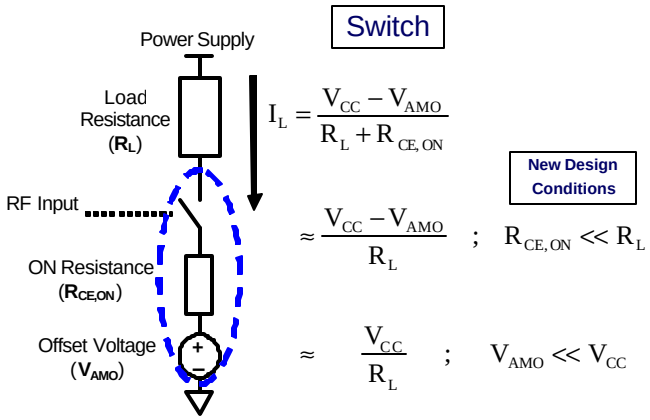

Figure 3. When the differential gain is zero, the RF circuit model transforms from a controlled current source to a switch.

Current through the load is governed by four terms. Two relate to the circuitry external to the transistor, the load resistance R_L, and the power supply V_{CC}. The remaining two parameters are transistor related, which are the conducting ON resistance $R_{CE,ON}$, and the device DC offset voltage (if any) V_{AMO}. When the design conditions of this amplifier meet the criteria $R_{CE,ON} << R_L$ and $V_{AMO} << V_{CC}$, then we see that the load current is independent (to first order) of the transistor characteristics. This directly implies very stable operation over manufacturing, temperature, and aging, which is confirmed by extensive measurements.

But how do we use such a circuit? Clearly the differential gain is zero, so it is essentially a limiter and has no linearity. It is seen though that there are still two degrees of freedom in the signal processing of this circuit, which are sufficient to realize all of the desired signals.

If we postulate that time can be manipulated, then we can write

$$\cos(w(t+\Delta(t))) = \cos(wt + w\cdot\Delta(t)) \qquad (6)$$

It is then observed that time manipulation is equivalent to phase modulation when

$$f(t) = w\cdot\Delta(t) \qquad (7)$$

Time manipulation is the variation of the opening and closing times of the switch in Figure 3. Thus, phase modulation passes through this circuit without change.

The second degree of freedom relates to the current that flows through the switch. Assuming for simplicity a aero transition time for the switch between OFF and ON states in each direction we can write the load current as

$$I_L(t) = \frac{V_{CC}(t)}{R_L}\cdot\frac{1}{2}[\text{sgn}(\cos(w(t+\Delta(t))))+1] \qquad (8)$$

Following bandpass or lowpass filtering to remove the carrier harmonics from the switch and using (7) this becomes the standard signal equation

$$I_L(t) = \frac{V_{CC}(t)}{R_L} \cdot \cos(wt + f(t)) = a(t) \cdot \cos(wt + f(t)) \quad (9)$$

which is in polar coordinates. The magnitude coordinate is controlled by varying the power supply to the switch, and the phase component is controlled by varying the time that the switch acts by closing and opening.

Basing a transmitter on switching circuits lends itself naturally to CMOS implementation, since a CMOS gate is one of the best switch circuits ever devised. One block diagram of such a transmitter is shown in Figure 4. Much of the transmitter is transformed from linear RF CMOS circuit designs to a digital logic state machine.

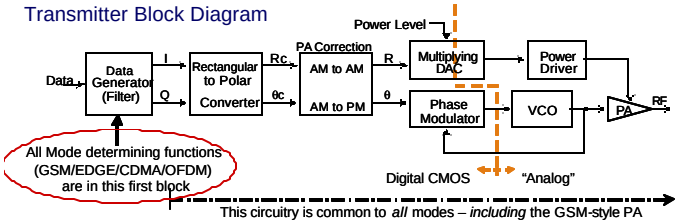

Figure 4. Polar transmitter based on switch circuits

Besides being manufacturable in low cost digital CMOS, having the transmitter implemented as a state machine also naturally lends itself to multimode operation. This is a direct consequence from the fact that a state machine does not care what the numbers are that it is manipulating. If the input signal coordinates represent GSM, then a GSM signal will be generated. Similarly, if the input signal coordinates represent OFDM, then the output signal will be OFDM.

Performance Measurements

Several polar transmitters following the block diagram of Figure 4 have been built and tested. One set of tests is the actual multimode capability, meaning how many signal types can be generated using this one design. To date, over 10 different signal types have been realized with this one design. A subset of six of these signals is shown in Figure 5.

These six signals represent a bandwidth ratio of nearly 400:1. At the narrowband end is the π/4-DQPSK signal used in the North American TDMA cellular network. This signal has a bandwidth of 30 kHz. At the wideband end is the OFDM signal used in IEEE 802.11a/g wireless LAN, which has an 18 MHz bandwidth. In between are GSM GMSK and EDGE 3π/8-8PSK, both at 200 kHz bandwidth, cdma2000 at 1.25 MHz bandwidth, and WCDMA at 3.84 MHz bandwidth.

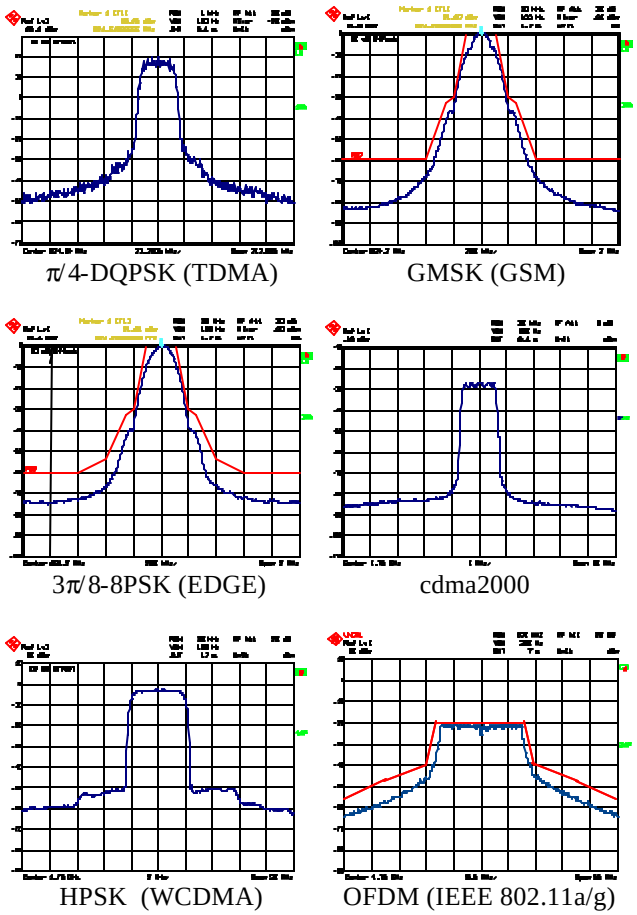

Figure 5. Multimode operation measurements from the Polar transmitter

Other characteristics are also important. In particular for a transmitter, RF output power is very important. A very important property of the polar transmitter is that there is no output backoff in the transmitter final stage like is necessary for a linear transmitter. With the final transistor operating as a switch, it is operating at saturated power at all times (the mose efficient condition). Peak envelope power (PEP) of an envelope varying signal can rise all the way to the fully saturated power (PSAT) as shown in Figure 6.

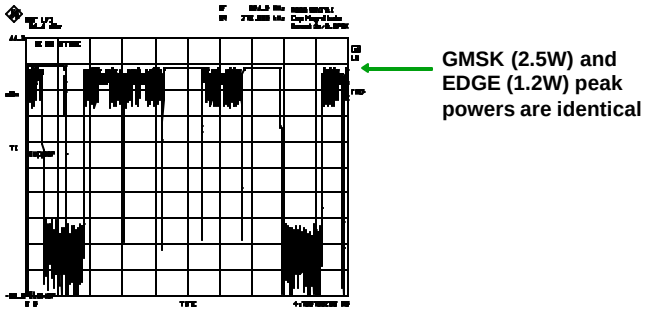

Figure 6. No output backoff (OBO): peak envelope power can easily equal saturated output power

The next characteristic of major interest is realizable efficiency from this transmitter. Taking the EDGE signal for an example, using a standard compressed power amplifier designed for GSM and achieving an efficiency of 60% at 2.5 watts (+34.0 dBm) PA output power, the same device produced an EDGE output power of 1.2 watts (+30.8 dBm) with 40% efficiency. The difference in output powers is 3.2dB, which is exactly equal to the EDGE signal peak to average power ratio (PAR), confirming that there is no PA output backoff. Compared to a linear transmitter using the same size output transistor, this performance is 2 to 3 dB more output power at nearly twice the efficiency [9] – a significant improvement.

Figure 7 shows some comparative power consumption measurements between EDGE mobile device designs using linear and polar transmitters. For any output power, the polar transmitter consistently draws less current than the two linear approaches. Indeed, as output power increases the difference between the two approaches increases. This is taken advantage of two ways in the cellular system. First, the lower power consumption improves mobile device battery life and lowers operating temperature to more closely match the widespread GSM mobile consumer experience. Second, the ability to produce higher power is used by the system operators to improve coverage and / or on-air signal to noise ratio, all of which improves the data rate experienced by the user.

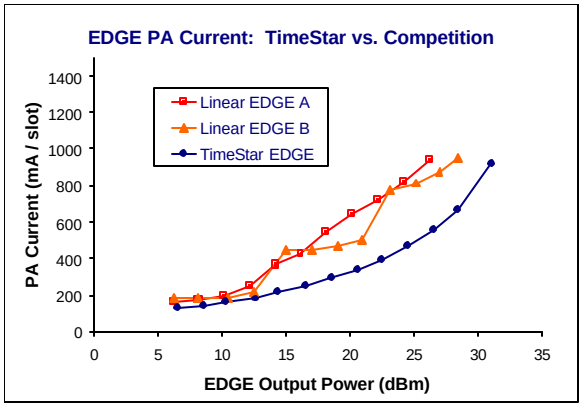

Figure 7. At equal output powers the polar transmitter draws about one-half the current – or for the same current the output power is 5 to 7 dB higher

After validating multimode performance, output power availability, and transmitter efficiency, the next validation is for dynamic modulation agility. Specifically, does the digital state machine nature of the modulator actually provide the ability to rapidly switch between different modulation types available to it? The measurement in Figure 8 validates that this capability is real. In this measurement, one 8-slot GSM frame interleaves both the GMSK and $3\pi/8$-8PSK EDGE modulations, at differing powers, among all slots. This measurement corresponds to GPRS class-29 mobile operation.

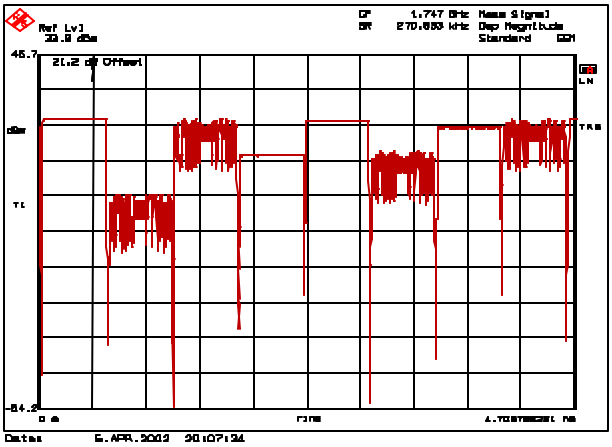

Figure 8. Dynamic modulation from the digital state machine between GSM and EDGE across a full GSM frame

One final check for the polar transmitter is on the prediction from Figure 3, where the variations of transistor characteristics can be eliminated from first-order concern. One easy way to do this test is to cycle temperature of the transmitter before any temperature compensation is added. In this way the inherent temperature stability of the polar transmitter can be evaluated.

In Figure 9, an overlay of nine EDGE signal spectra measurements is shown, taken over the temperature cycle set of {+30C, 40C, 50C, 60C, 70C, 60C, 50C, 40C, 30C}. It is seen that the overlay is extremely good, not only at the peak representing consistent output power, but also along the signal skirts 70dB abd 80dB below the peak. It is concluded that the inherent temperature stability of the polar transmitter is excellent, and that no further thermal compensation needs to be designed.

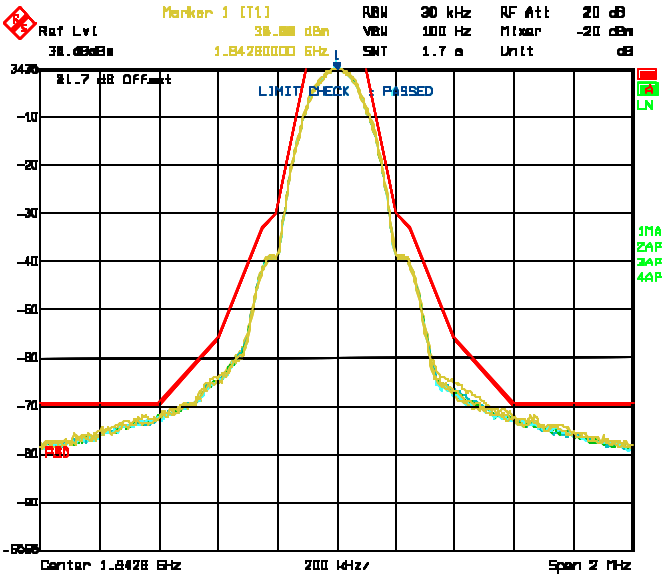

Figure 9. Output signal stability as operating temperature is cycled from +30C to +70C and back again.

Conclusions

Designing a transmitter beginning from maximum efficiency conditions naturally leads to a shift to polar modulation. The resulting transmitter is realized predominantly using switch circuits, which readily map onto a digital CMOS implementation. This not only lowers cost, but it also provides a design that readily operates in multiple modes. These modes are shown to span very wide bandwidth ratios, and are dynamically agile if the application requires fast switching among one or more of them.

The final power stage also acts as a switch, which requires a new set of design criteria to properly take advantage of. When these criteria are met, it is seen that not only is higher output power available compared to a linear amplifier using the same transistor size, but also there is excellent inherent thermal stability that eliminates the need for further temperature compensation design. It is expected that the growing popularity of polar modulation will continue.

References

[1] R. A. Heising, "Modulation Methods," *Proceedings of the IEEE*, May 1962, pp. 896-901

[2] W. Sander, "Polar Modulator for Multi-mode Cell Phones," *Proceedings of the 2003 IEEE Custom Integrated Circuits Conference* (CICC 2003), invited paper

[3] T. Sowlati, et. al., "Quad Band GSM/GPRS/EDGE Polar Loop Transmitter," *IEEE Intl Solid State Circuits Conference*, San Francisco, Feb. 2004

[4] A. Hadjichristos, "Transmit Architectures and Power Control Schemes for Low Cost Highly Integrated Transceivers for GSM/EDGE Applications," *IEEE Intl Symposium on Circuits and Systems*, Bangkok, May 2003

[5] S. V. Schell, "EDGE Systems and Linearization Requirements," IEEE MTT-S Intl Microwave Symposium Workshop on Linearization for 3G Systems, Phoenix, 21 May 2001

[6] R. Staszewski, et.al. "All-Digital PLL and GSM/EDGE Transmitter in 90nm CMOS," *Proceedings of the 2005 IEEE Int'l Solid-State Circuits Conference* (ISSCC 2005)

[7] M. Elliott, T. Montalvo, B. Jeffries, F. Murden, J. Strange, A. Hill, S. Nandipaku, and J. Harrebek, "A polar modulator transmitter for EDGE," in *ISSCC Tech. Dig.*, Feb. 2004, pp. 190-191

[8] E. McCune, "Gain in Compressed Amplifiers," *Microwave Journal*, May 2002.

[9] RF3158 data sheet, www.rfmd.com .

Mixed Analog and Digital Calibration Techniques in RF ICs

Satoshi Tanaka, Yukinori Akamine, Koji Maeda, Manabu Kawabe, Taizo Yamawaki
Hitachi, Ltd. Central Research Laboratory
1-280 Higashi-Koigakubo Kokubunji Tokyo 185-8601 Japan
satoshi.tanaka.xm@hitachi.com

1. Introduction

The wireless mobile communication systems grow in wide area, such as mobile phone, W-LAN, Bluetooth, Zigbee and UWBs. Future mobile terminal systems will be required to cover those different many applications with single terminal. In addition, it will also support many broadcasting service such as DTV or radio.

To adopt those applications and systems, the high integration of RF solutions will become a first priority. The rapid progress of device technology also pushes to increase integration level. In this case those solutions must be robust for large process, temperature and power supply voltage variations.

Table 1 shows RX and TX circuit architectures which are applied in various kind of wireless communication systems. For the receivers, in many systems, direct conversion receiver [1-11] and low-IF receiver [12-18] are applied. For the transmitter, direct conversion transmitters [19-24] and PLL based transmitters such as offset PLL [25-27], ΔΣ transmitters [28-32] are applied. Each of those circuits has some sensitivity to process, temperature and power supply voltage variations. The key techniques of highly integrated RF circuits are calibration techniques for canceling above variations. This paper reviews those calibration techniques [36] for high integrated receivers and transmitters.

Table 1 RX,TX systems in mobile wireless applications

	GSM	EDGE	Bluetooth	WCDMA	CDMA	W-LAN	UWB
RX	Direct Conv. Low-IF Sampling		Low-IF Sampling	Direct Conv.	Direct Conv.	Direct Conv. Sliding IF	Direct Conv.
TX	O-PLL ΔΣ Direct Conv. DCO	Polar (closed) Polar (open) Direct Conv.	ΔΣ DCO Direct Mod. Low-IF	Direct Conv. 2-Step Conv.	Direct onv.	Direct Conv. Sliding IF	Direct Conv.

2. Direct conversion receiver

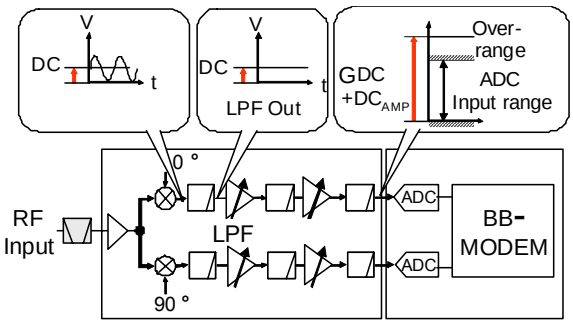

Figure1 Direct Conversion Receiver

Figure 1 shows direct conversion receiver

block diagram. It consist of low-noise amplifier (LNA) and quadrature demodulator, low-pass channel filters (LPF), programmable gain control amplifiers. The feature of direct conversion receiver is demodulator has function of both RF down converter and demodulator. Output signals of demodulator are *I* and *Q* baseband signals. Because the RF signal is converted base band signal directly, no High-Q off-chip IF filter is required. The integrated low pass channel filer can take part of IF filter. The direct conversion receiver is suitable for high integration system, because it can avoid applying off-chip IF filter. However it also has essential issue of DC offset.

Figure 2-5 shows typical sources of DC offset from direct conversion receiver [4,5].

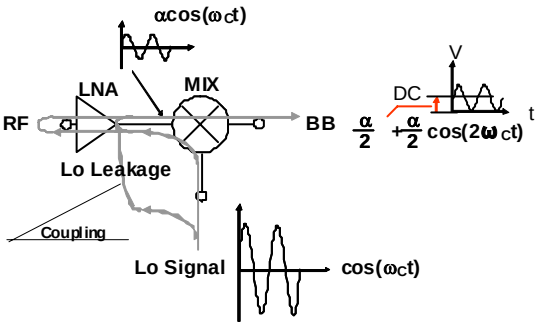

Figure 2 Local Signal Self Mixing Effect

Figure 2 shows self-mixing effect in mixers. If there is a leakage from the local signal input to the RF input, the local signal leaks out to the RF signal path and return to the mixer. The returned signal is downconverted to DC level. This signal becomes DC offset. As shown in Fig.2, leakage path is not always through mixer, there is a case that local path has direct coupling.

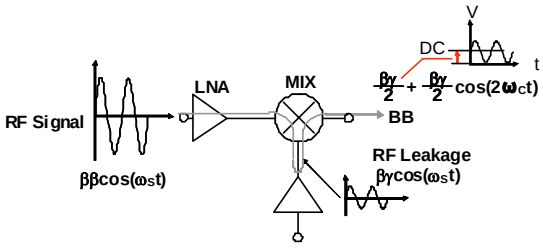

Figure 3 RF Signal Self Mixing Effect

Figure 3 shows another type of self mixing. In this case, the leakage path is from RF signal input to the local signal input of mixer. When large RF signal is received, returned RF signal is downconvered by RF signal itself. This signal also becomes DC offset.

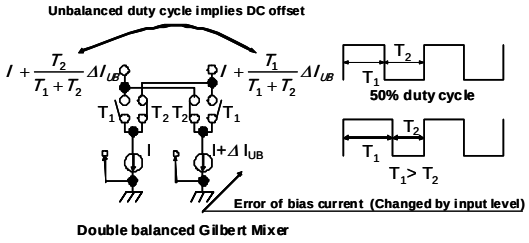

Figure 4 Impact of Local Duty Cycle on DC Offset

Figure 4 shows the impact of local-signal duty cycle on DC offset. The mixer is balanced type mixer and local signal assumed as square waveform. When duty cycle is 50% (T_1=T_2), DC currents of mixer output are same. In case it becomes non 50%, if driving current sources *I* are matched, output DC current are still same. However, if driving current sources have mismatch factor, ΔI_{UB}, output DC currents become unbalanced and DC offset is generated.

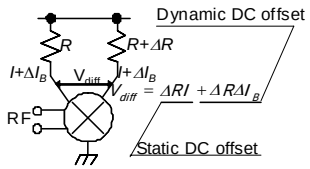

Figure 5 Impact of Relative Deviation of Resistor on DC Offset

Figure 5 shows the impact of the relative deviation of the resistor on DC offset. Here, R is load resistor, ΔR is relative deviation of resistor, I is driving current of mixer, ΔI_B is current deviation which depend on the input signal level. ΔR generates DC offset. ΔI_B adds input signal level dependence on the DC offset. The DC offsets those are presented above can divide into two categories whether dependence of input signal level exist or not. One is static DC offset that does not depend on the input signal level. The other is dynamic DC offset that depends on the input signal level. The example of Fig. 2 is static DC offset. In case of Fig.3, it is categorized as dynamic DC offset. If current source mismatch ΔI_{UB} depends on the input signal level, the example of Fig. 4 is dynamic DC offset. In following two sections, calibration methods for static DC offset and dynamic DC offset are presented.

3. Static DC offset canceling schemes

To solve static DC offset issue, many kinds of solutions are applied. Those solutions are summarized in Fig. 6. Total gain of base band amplifier chain is depending on the system and ADC performance; however, it may approximately from 40 dB to 60 dB. With this high gain, small DC offset at the output of mixer become large at the output of the amplifier chain. And it degrades dynamic range of ADC.

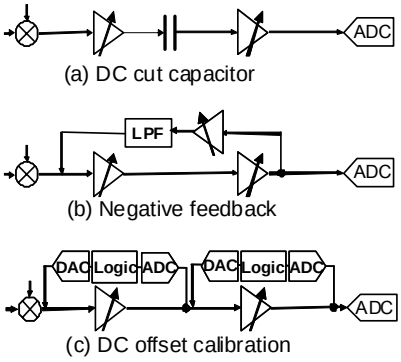

Figure 6 Static DC offset Cancellation methods

Figure 6 (a) [22] shows one of the simplest solution for avoiding this phenomenon. The DC components of the each amplifiers is eliminated by bypass capacitors. This method can apply in case that signal bandwidth is rather high such as W -CDMA and the cut off frequency of DC cut circuit can be negligible. Another example [7] is shown in Fig. 6 (b). In this example, DC offset is suppressed by negative feedback chain. This circuit has same transfer function as high pass filter. So this circuit is also rather suitable for wide band applications. For narrow band applications, direct DC connected configuration is required. Fig. 6 (c) [4,5] shows DC offset calibration method with DC offset collection circuits which consist of ADC, control logics and DAC. This example is for TDMA (Time Domain Multiple Access) system such as GSM (Global System for Mobile Communications), which

has intermittent transmitting and receiving burst. DC offset calibration is executed just before every receiving burst for suppressing temperature variation and voltage supply variation. ADC detects DC offset and DAC generates DC voltage to compensate the DC offset. This calibration is done from the first stage to following stage sequentially. With this sequence, the calibration error of the stage is calibrated by following stage.

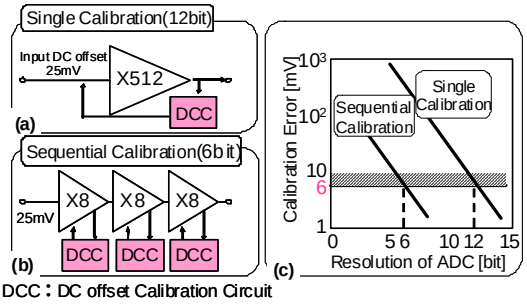

DCC : DC offset Calibration Circuit

Figure 7 Comparison between Single Calibration and Sequential Calibration

Figure 7 shows the comparison of two cases. First one has single calibration circuit, let's say "single calibration scheme" and next one has three calibration circuits which is operated in sequentially "sequential calibration scheme". Followings are assumed for comparison; 25mV of input DC offset, 54dB (x512) of total gain and 6mV of target output DC offset. In case of single calibration scheme, 12 bit ADC is required. On the other hand, sequential calibration scheme required ADC resolution is only 6 bit. The 6 bit ADC does not require fine resolution circuit technique. Therefore, it is much robust and easy to implement on the real system.

4. Dynamic DC offset and canceling schemes

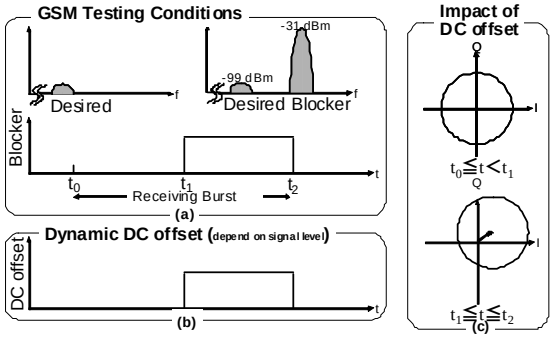

Figure 8 DC offset impact on Direct Conversion Receiver

Figure 8 summarizes AM suppression characteristic of GSM [34]. This might be a typical example of dynamic DC offset. The measurement conditions are shown in fig. 8 (a). The wanted signal level is -99 dBm. When that small-level signal is received, A 6 MHz-offset -31 dBm-level blocking signal is injected during later half of receiving burst ($t_1<t<t_2$). Under this condition, total receiver performance is observed whether the blocking signal degrades error rate or not. If mixer has dynamic DC offset, output signal contains time domain DC shift as shown in fig. 8 (b). This DC shift has an impact on the demodulated *IQ* trajectory as shown in fig. 8 (c), and degrades error rate.

As discussing in the previous section, unbalance of circuits especially mixer is main cause of dynamic DC offset. To reduce the dynamic DC offset, unbalance factor of mixer should be calibrated.

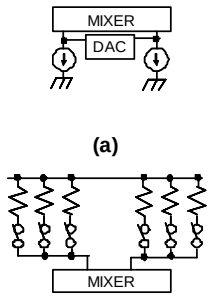

Figure 9 Balance calibration methods

Figure 9 shows examples of unbalanced calibration method for mixers. One major reason of unbalance factor is bias current mismatch.. Figure 9 (a) [8] shows a method to calibrate the bias current mismatch. A differential current DAC is connected in parallel with a pair of bias current source. The output of mixer is monitored and minimized DC offset by controlling DAC. Figure 9 (b) shows an example of load resistors calibration [9]. This example reduces DC offset by controlling load resistor value by switching resistor arrays.

The unbalanced characteristic is equivalent with existence of a 2^{nd}-order distortion characteristic. Two examples calibrating 2^{nd} order distortion are shown in Fig. 10. The first example shown in Fig. 10 (a) [10] has a 2^{nd} order distortion generator, which is connected in parallel with mixer. The output of the distortion generator is connected to the output of the mixer through waited control circuit.

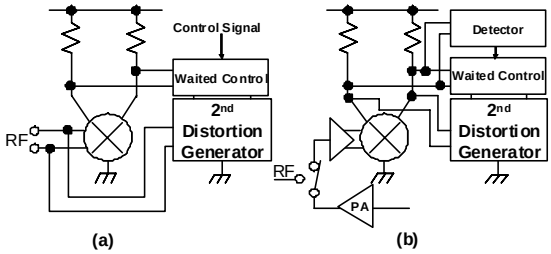

Figure 10 2^{nd} order distortion cancellation technique

By controlling the wait of output signal from the distortion generator, the output DC offset is minimized. The mixer and distortion generator have different circuit topology, therefore there might be some mismatch if temperature, power supply voltage or input level conditions are changed. The key of this kind of technique is calibration sequence for avoiding above variations.

The second example (Fig. 10 (b) [11]) is for GSM system and it calibrates 2^{nd} order distortion before every receiving burst to adapting temperature and voltage variation during handset operation. The distortion generator is connected at the output of the mixer. Before receiving burst, the transmitter is connected to the receiver and generates test signal. Based on the test signal, a waited coefficient is optimized to cancel out the DC offset.

5. Low- IF Receiver and calibration methods

The low-IF receiver is another receiver architecture which is suitable for high integration. As shown in Fig. 11, the difference from the direct conversion receiver

is, even its frequency is low, existence of IF signal. Therefore both static and dynamic DC offset can be set out of receiving band width. Compared with conventional super heterodyne receiver, the IF signal is low, so image signal cannot be removed by RF filter. The key of the low-IF receiver is image rejection technology.

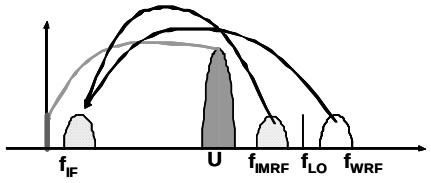

Figure 11 Frequency Plan of Low-IF Receiver

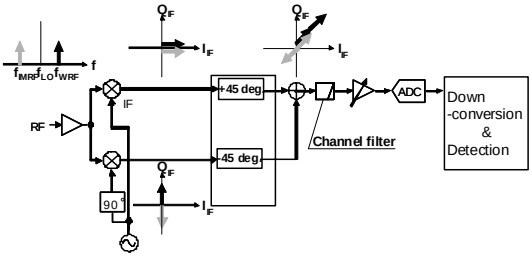

Figure 12 Analog Domain Image rejection Low-IF Receiver

Figure 12 shows an example of analog domain image rejection type low-IF receiver. The system consists of a LNA, pair of Mixers, pair of +/-45 deg. phase shifter, channel filter, variable gain amplifier, ADC and digital demodulator. Through LNA and mixers, the input signal is converted *I* and *Q* low-IF signal. As shown in Fig. 11, the wanted signal and image signal are converted to same IF frequency. The difference of the wanted IF signal and image IF signal is sign of *I* and *Q* signals as shown in Fig. 12. The *I* signal is shifted +45 deg and Q signal is shifted -45 deg through phase shifter, and those signals are added each other. The wanted signals are in the same phase and the image signals are in opposite phase at the output of phase shifter. Therefore only wanted signal is selected. The wanted IF signal passes channel filter. After being amplified, it is converted to digital signal and demodulated. The image rejection ratio of this system is dominated by phase-shift accuracy.

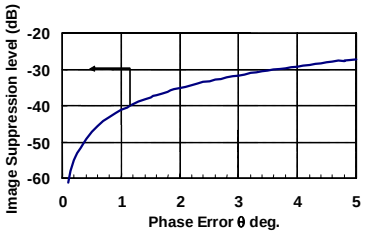

Figure 13 Phase imbalance effect on image rejection level

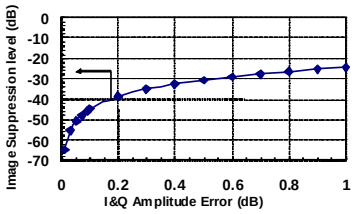

Figure 14 Amplitude imbalance effect on image rejection level

Figure 13 and 14 show the impact of phase and amplitude IF-signal error on image rejection ratio [35]. For example, for achieving -40 dBc of image rejection ratio, less than -1.2 degree of phase error or 0.18dB of amplitude error is required. This type of low-IF receiver has been widely applied for Bluetooth applications [12-13].

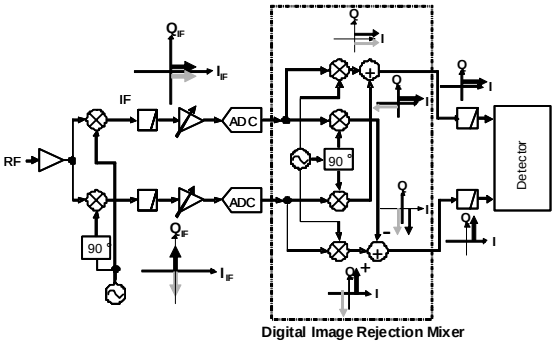

Figure 15 Digital Domain Image rejection Low-IF Receiver

Figure 15 shows an example of digital domain image rejection type low-IF receiver. It consists of LNA, mixers, pair of channel filters, variable gain amplifiers, ADCs and digital domain image rejection mixer. A pair of quadrature digital demodulator cancels out image signal as shown in Fig. 15. The circuits operate digitally; therefore there is no variation for temperature, voltage supply, and process variation. In this system, the image signal exists in analog IF signal, therefore wide dynamic range of ADC is required. This example is applied for GSM cellular phone application [14].

Even if digital image rejection mixer operates accurately, image rejection ratio is degraded by the amplitude and phase mismatches of RF mixers and *I*,*Q* analog signal path. These mismatch errors should be detected and optimized.

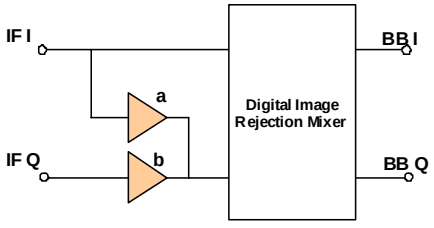

Figure 16 Principal of IQ Calibration

Figure 16 shows the fundamental calibration method for those errors. For simple explanation, only phase error θ_{ERROR} is assumed to exist. In this case, image signal IF_{IMI} and IF_{IMQ} are described as follows;

$$\begin{pmatrix} IF_{IMI} \\ IF_{IMQ} \end{pmatrix} = \begin{pmatrix} 1 & 0 \\ \sin(\theta_{ERROR}) & -\cos(\theta_{ERROR}) \end{pmatrix} \begin{pmatrix} \cos(\omega_{IF} t) \\ \sin(\omega_{IF} t) \end{pmatrix}$$

Here ω_{IF} is angular frequency of IF signal. For canceling error, following matrix is multiplied to *I* and *Q* signal vector.

$$\begin{pmatrix} 1 & 0 \\ -\tan(\theta_{ERROR}) & \dfrac{1}{\cos(\theta_{ERROR})} \end{pmatrix} = \begin{pmatrix} 1 & 0 \\ a & b \end{pmatrix}$$

Here *a* and *b* are coefficients in Fig. 16. This calibration scheme can be implemented in both analog an digital domain. This calibration system is applied for TV tuners, [15,16] and GSM receivers [17,18].

6. Direct Conversion Transmitter

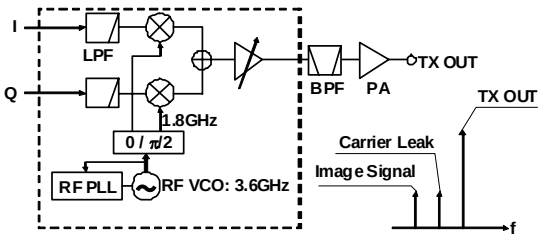

Figure 17 Direct Conversion Transmitter

Figure 17 shows direct conversion transmitter block diagram. It consists of LPF, quadrature modulator, 90-degree phase-shift local generator (including PLL) and RF variable gain control amplifiers. It also consists of RF BPF (band pass filter) and a power amplifier. The feature of direct conversion transmitter is that a modulator has functions of both RF up converter and modulator. The architecture is quite simple; however it is sensitive, to DC offset, amplitude and phase mismatch. If there is DC offset in *I,Q* baseband signal path, carrier leakage signal appears. If there is phase or amplitude mismatch, image signal is generated.

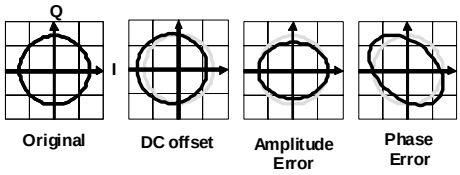

Figure 18 Impact of DC offset, Amplitude and phase error on modulation signal

Figure 18 shows impact of those errors on modulation signal. The *I* and *Q* signal are assumed as cosine and sine wave form. With DC offset, the origin of *I* and *Q* signal is shifted. If amplitude error or phase error exists, the signal is distorted and modulation error becomes large. Calibration methods for those errors are the key for the implementation of direct conversion transmitter.

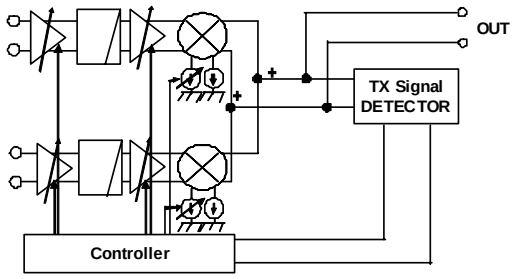

Figure 19 An example of DC offset collection system of transmitter

Figure 19 shows an example of W-CDMA applications [23]. In this example, gain control is carried out in baseband signal, therefore DC offset become relatively significant when output signal level becomes low. Therefore DC offset calibration is indispensable for this system. The carrier leakage signal is detected and the error is retuned bias control circuits.

Figure 20 shows another example of DC offset and I,Q mismatch calibration [20]. This example is for Bluetooth low-IF transmitter. This example is not direct up conversion, however basic operation is same as

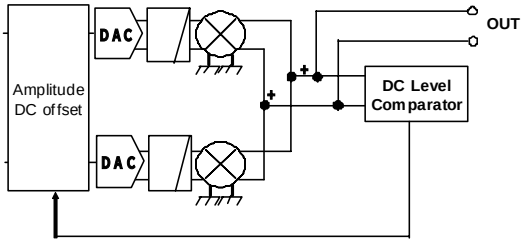

Figure 20 A example of amplitude and DC offset collection system

direct conversion transmitter except image signal becomes not inband noise but adjacent channel noise. Both carrier leakage and image signal become critical for this system. The quadrature modulator consists of two Gilbert type balanced mixers. In this example,

instead of detecting RF signal level, DC offset and DC gain mismatch of mixer are detected by comparator. Based on the sign of the detected error, DC offset and gain are calibrated in digital part.

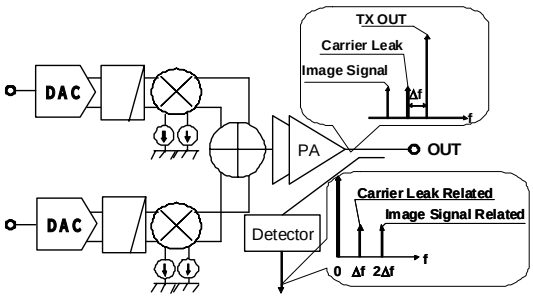

Figure 21 Detecting method for carrier leak and image signal

Figure 21 shows an example for detecting carrier leakage and image signal level [33]. If testing tone signal is injected to the modulator, the single tone TX signal, carrier leakage signal, and image signal are observed as shown in Fig. 21. There are 3 components at the output of detector as followings; (1) DC component which is mainly generated by square of TX signal, (2) Δf tone signal which is generated by multiplication of TX signal and carrier leakage signal, and (3) $2\Delta f$ tone signal which is generated by multiplication of TX signal and image signal. By monitoring these components, carrier leakage signal and image signal can be minimize to calibrate DC offset, amplitude mismatch and phase mismatch of baseband signals in digital domain. The image signal is dominated by both amplitude mismatch and phase mismatch. Therefore, simple negative feedback algorism is not applicable. The linear programming method is required to find a image minimized condition.

7. ΔΣ Transmitter

Direct conversion is applied for various applications (See Table1). In case of constant envelope modulation, for example, GMSK (Gaussian filtered Minimum Shift Keying), other transmitter architectures are applied such as offset PLL [25-26], ΔΣ Transmitter [28-32] and DCO (Digitally Controlled Oscillator). In this section, operation of ΔΣ Transmitter is briefly reviewed and a method to calibrate loop gain of PLL is introduced [32].

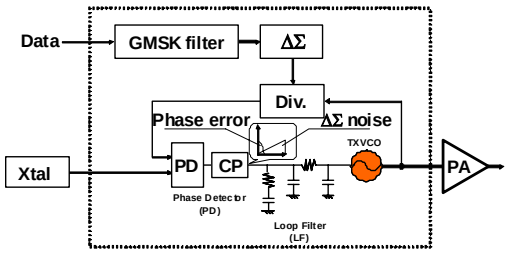

Figure 22 ΔΣ transmitter

Figure 22 shows a ΔΣ Transmitter. It consists of VCO, programmable divider, ΔΣ modulator, Digital GMSK filter, phase detector, charge pump circuit, and loop filter. Except GMSK filter, all elements are same as those of fractional-N synthesizer. Input binary data is fed into GMSK filter and signal bandwidth is limited by the GMSK filter. The filtered signal is oversampled by ΔΣ modulator and converted shorter bit length bat faster sampling data sequence. Based on this data sequence, the programmable divider changes its dividing ratio and VCO is

controlled. The transfer function from the dividing input to VCO is low pass characteristics which is same as closed loop characteristics of PLL. The ΔΣ modulator generate high frequency noise. For suppressing this noise, cutoff frequency of closed loop is not high enough compared with modulated signal bandwidth. Therefore this system is sensitive for loop characteristic variation.

The transfer function $T(s)$ of the closed loop of PLL is given as following;

$$T(s) = \frac{N \times Kv \times Icp \times H(s)}{N \times s + Kv \times Icp \times H(s)}$$

Here $H(s)$ is transfer function of loop filter, N is for dividing ratio, Kv is VCO sensitivity and Icp is current of charge pump. In above equation Icp, Kv, and $H(s)$ appear together as a product. Therefore, variation of $T(s)$ can be minimized with controlling only Icp.

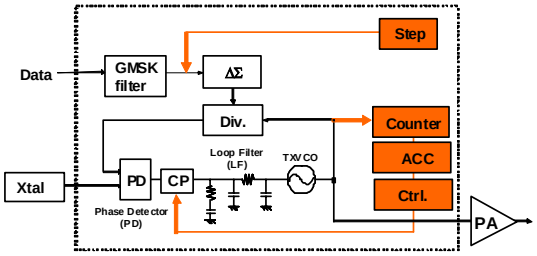

Figure 23 Fine loop gain calibration system with double counter

Figure 23 shows an example of a system, which calibrates above loop variation. A digital counter and accumulator are applied for detecting response of step frequency-setting operation. Figure 24 summarizes the procedure of this system. A step function signal is fed to the ΔΣ modulator. The PLL follows the change of frequency setting. The response of PLL depends on loop characteristic. If loop gain is larger, the response is faster. During the response, the counter operates and

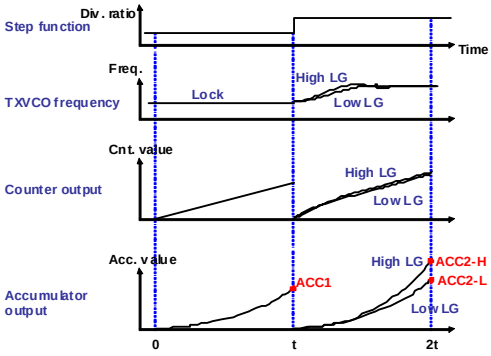

Figure 24 Operation summary of double counting system

counts VCO oscillation. Even if there is difference of loop gain, counting result is almost similar. However, if the counted result is accumulated, the difference becomes large enough to detect loop gain (See ACC2-H, and ACC-L in Fig. 24). For canceling constant term (ACC1: independent term from loop gain), VCO oscillation is counted and accumulated in the rock state and subtracted from accumulated result of step response.

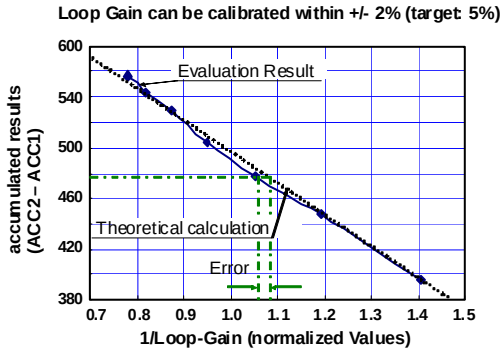

Figure 25 evaluation result

Figure 25 shows measurement result of accumulation. The horizontal axis is normalized reciprocal of loop gain and the vertical axis is accumulated result. The reciprocal of loop gain changes approximately 0.0004 per 1 of accumulated result. The error from theoretical line is only less than +/-2%. This performance is enough for GMSK transmitter.

8. Conclusion

Calibration techniques for direct conversion receiver, low-IF receiver, direct conversion transmitter and ΔΣ transmitter are introduced in this paper. Father integration not only just RF part but also with digital MODEM will be required for next generation terminals. For realizing such highly integrated solutions, calibration methods for analog parts will become mandatory techniques. .

9. References

[1] D. Haspeslagh, J. Ceuterik, L. Kiss, J. Wenin, A. Vanwelsenaers, and C. Enel-Rehel, "BBTRX: A Baseband Transceiver Fora Zero If Gsm Hand Portable Station," IEEE Proc. of CICC1992, pp. 10.7.1-10.7.4, May 1992

[2] J. Sevenhans, "An integrated Si bipolar RF transceiver for a zero IF 900 MHz GSM digital mobile radio frontend of a hand portable phone IEEE Proc. of CICC1991, pp. 7.7.1-7.7.4, May 1991

[3] S. Atkinson and A. Kontos, " Fractional frequency multiplier for use in GSM Direct Conversion Receivers, " IEICE MWE2001 Digest, pp. 253-257 Dec. 2001

[4] S. Tanaka, T. Yamawaki, K. Takikawa, N. Hayashi, I. Ohno, T. Wakuta, and B. Henshaw, "GSM/DCS1800 Dual Band Direct-Conversion Transceiver IC with a DC Offset Calibration System," IEEE, Proceedings of the 27th ESSCIRC pp. 492-495 Sep. 2001

[5] S. Tanaka T. Yamawaki, N. Hayashi, M. Kasahara, and B. Henshaw, "Circuit techniques for GSM/DCS1800 direct conversion receiver," IEICE MWE2001 Digest, pp. 269-274 Dec. 2001

[6] R. Magoon, A. Molnar, G. Hatcher, J. Zachan, G. Hatcher and W. Rhee, " A single-chip quad-band (850/900/1800/1900 MHz) direct conversionGSM/GPRS RF transceiver with integrated VCOs and fractional-n synthesizer, " IEEE, JSSC, Vol.37 No.12,pp. 1710 -1720, Dec 2002

[7] J. Ryynanen, K. Kivekas, J. Jussila, A. Parssinen, K.A.I. Halonen, " A dual-band RF front-end for WCDMA and GSM applications," IEEE, JSSC, Vol. 36, No. 8, pp. 1198-1204 Aug. 2001

[8] T. Yamaji, H. Tanimoto, and H. Kokatsu, "An I/Q active balanced harmonic mixer with

IM2 cancelers and a 45 deg. Phase shifter," IEEE JSSC Vol. 33 No. 12,, pp. 2240 -2246, Dec 1998

[9] K. Kivekas, A. Parssinen, J. Ryynanen, and J. Jussila, "Calibration techniques of active BiCMOS mixers", IEEE JSSC Vol. 37 No. 6, pp. 766 -769, June 2002

[10] M. Chen, Y. We, and M. F. Chang, "Active 2nd-order intermediation calibration for direct conversion receivers," IEEE ISSCC2006 Dig. Tech. Paper pp. 458-459 Feb. 2006.

[11] H. Darabi, H. J. Kim, J. Chiu, B. Ibrahim, and L. Serrano, "An IP2 improvement technique for zero-IF Down converter," IEEE ISSCC2006 Dig. Tech. Paper pp. 464-465 Feb. 2006.

[12] M. Kokubo, M. Shida, T. Ishikawa, H. Sonoda, K. Yamamoto, T. Matsuura, M. Matsuoka, T. Endo, T. Kobayashi, K. Oosaki, T. Henmi, J. Kudoh, and H. Miyagawa, "A 2.4GHz RF transceiver with digital channel-selection filter for Bluetooth," IEEE ISSCC2002 Dig. Tech. Paper pp. 94-95 Feb. 2002

[13] H. Ishikuro,, M. Hamada, K. Agawa, S. Kousai, H. Kobayashi, D. Nguyen, and F. Hatori, "A single-chip CMOS Bluetooth transceiver with 1.5MHz IF and direct modulation transmitter," IEEE ISSCC2003 Dig. Tech. Paper pp. 94-95 Feb. 2003

[14] A. A. Abidi, "RF CMOS come of age," IEEE Microwave Magazine, Volume 4, Issue 4, pp. 47-60 Dec. 2003

[15] S. Lerstaveesin, and B-S. Song, "A complex image rejection circuit with sign detection," IEEE ISSCC2006 Dig. Tech. Paper pp. 454-455 Feb. 2006.

[16] M. Hajirostam and K. Martin, "On-chip image rejection in a low-IF CMOS receiver," IEEE ISSCC2006 Dig. Tech. Paper pp. 456-457 Feb. 2006.

[17] I. Elahi, K. Muhammad, P.T. Balsara, "I/Q mismatch compensation in a 90nm low-IF CMOS receiver," IEEE, ISSCC2005 Dig. pp. 542-543 Feb. 2005

[18] K. Maeda, W. Hioe, Y. Kimura, and S. Tanaka, "Wideband image-rejection circuit for low-IF receivers," IEEE ISSCC2006 Dig. Tech. Paper pp. 476-477 Feb. 2006.

[19] T. Steztzler, I. Post, J. Havens, and M. Koyamae, "A 2.7V to 4.5 V single-chip GSM transceiver RF integrated circuits" IEEE JSSC, Vol. 30, NO.12 pp. 1421-1429 Dec. 1995

[20] D. Miyashita, H. Ishikuro, T. Shimada, T. Tanzawa, S. Kuusai, H. Kobayashi, H. Majima, K. Agawa, M. Hamada, and F. Hatori "A Low-IF CMOS single-chip Bluetooth EDR transmitter with digital I/Q mismatch trimming circuit," IEEE 2005 VLSI Symposium on VLSI

Circuit Dig. Pp298-301 June 2005

[21] A. Bellaouar, M. Frechette, A.R. Fridi, S.H.K. Embabi, “Highly-integrated SiGe BiCMOS WCDMA transmitter IC,” IEEE, ISSCC2002, pp.238-239, Feb. 2002

[22] H. Tomiyama, C. Nishi, N. Ozawa, Y.Kamikubo, H. Honda, H. Fujita, Y. Kondo, H. Iizuka, T. Takahashi, “A low voltage (1.8V) operation triple band WCDMA transceiver IC,” IEEE RFIC Symposium 2006, June 2006

[23] G. Brenna D. Tschopp, J. Rogin, I. Kouchev, and Q. Huang, "A 2-GHz carrier leakage calibrated direct-conversion WCDMA transmitter in 0.13um CMOS," IEEE JSSC Vol. 39 No. 8, pp. 1253 -1262, Aug. 2004

[24] C. P. Lee, A. Behzad, D. Ojo, M. Kappes, S. Au, M.-A. Pan, K. Carter, and S. Tian, “A highly linear direct-conversion transmit mixer transcondactance stage with local oscillation feedthrough and I/Q imbalance cancellation scheme,” IEEE ISSCC2006 Dig. Tech. Paper pp. 368-369 Feb. 2006.

[25] T. Yamawaki, M. Kokubo, K. Irie, H. Matsui, K. Hori, T. Endou, H, Hagisawa, T. Furuya, Y. Shimizu, M. Katagishi and J. R. Hildersley, "A 2.7V GSM RF Transceiver IC", IEEE JSSC, vol. 32, no.12, pp.2089-2096, Dec. 1997

[26] G. Irvine, S. Herzinger, R. Schmidt, D. Kubetzko, and J,Fenk, “An up-conversion loop transmitter IC for digital mobile telephone”, IEEE ISSCC1998 Dig. Tech. Paper pp. 364-365 Feb. 1998.

[27] S. Tanaka "A PLL Based Transmitter Architecture for GSM System," MWE2000 Digest, pp. 361-365, Dec. 2000.

[28] W. T. Bax, and M. Copeland “A GSM modulator using ΔΣ frequency discriminator-based synthesizer,”IEEE JSSC Vol. 36 No. 8, pp. 1218 -1227, Aug. 2001

[29] C. O’Keeffe, et al., ”A direct digital modulation technique for GSM/GPRS/DCS applications using a 24 bit multi-accumlator fractional-N Synthesizer ", IEEE System on Chip Workshop, pp. 6/1-6/11, Sept. 2000

[30] E. Hegazi and A. A. Abidi, "A 17-mW transmitter and frequency synthesizer for 900-MHz GSM fully integrated in 0.35-um CMOS ,” IEEE JSSC Vol. 38 No. 5, pp. 782 -792, May 2003.

[31] E. Gotz, H. Krobel, G. Marzinger, B. Memmler, C. Munker, B. Neurauter, D. Romer, J. Rubach, W. Schelmbauer, M. Scholz, M. Simon, U. Steinacker, and C. Stoger, “ A quad-band low power single chip direct conversion CMOS transceiverwith ΔΣ-modulation loop for GSM ,” ESSCIRC 2003 Dig., pp.217-220, Sept. 2003

[32] Y. Akamine, M. Kawabe, K. Hori, T. Okazaki, N. Tolson, M. Kasahara, and S.

Tanaka, ”A loop-band width calibration system for fractional-N synthesizer and ΔΣ PLL transmitter,” IEEE, ISSCC2005 Dig. pp. 314-315, Feb. 2005

[33] C. P. Lee, A. Behzad, D. Ojo, M. Kappes, S. Au, M.-A. Pan, K. Carter, and S. Tian, “A highly linear direct-conversion transmit mixer transcondactance stage with local oscillation feedthrough and I/Q imbalance cancellation scheme,” IEEE ISSCC2006 Dig. Tech. Paper pp. 368-369 Feb. 2006.

[34] 3GPP TS 05.05 version 8.14.0 Release 1999

[35] S. Tanaka "Circuit technique for integrated mixer," IEICE MWE2001 Digest, pp. 413-422 Dec. 2001

[36] S. Tanaka, “Circuit techniques for mobile communication transceivers”, IEICE Vol.J89, No.10, pp. 622-6

CMOS and SAW RFID Tags at UHF Frequencies

Robert Weigel[1)], Kay Seemann[1)], Leonhard Reindl[2)]

[1)] Institute for Electronics Engineering, University of Erlangen-Nuremberg, Germany

[2)] Institute for Microsystems Engineering, University of Freiburg, Germany

***Abstract* — Today, there exists a huge market pull towards radio frequency identification (RFID) and/or wireless sensing for high-volume applications as well as for professional applications based on the use of passive, i.e., battery-less, low-cost transponders (tags, labels). In order to arrive at smaller tag dimensions, higher transceiver-to-tag interdistances, and more flexible, i.e., application-dependent antenna designs, higher-than-LF/HF carrier frequencies in the UHF band are becoming extremely interesting. CMOS and SAW transponder technologies are of special interest while other technologies such as polymer-electronic RFID tags are not feasible for the use in today's applications. In what follows, we will report on the current status and future trends of both CMOS and SAW RFID backscatter techniques.**

***Index Terms* — Passive RFID transponders, CMOS tags, SAW tags, SAW sensors, RFID systems, RFID radar transceivers.**

I. Introduction

Over the last years ubiquitous identification and sensor networks gained a lot of interest in the RF communication community. In particular, the radio frequency identification (RFID) technology became a well known synonym for passive transponder systems. The passive RFID technology is announced to be an exceptional high-volume application. Typical applications are, e.g., theft/loss prevention, container/pallet monitoring, equipment/animal/personal tracking and identification, rental car parking monitoring, and access control. However the tag cost remains the limiting factor for item level applications. The typical item level barcode scenario for SCM (supply chain management) is depicted in Fig.1. In order to approach this vision, a lot of scientific work is also in progress in the area of low-cost technology development, for e.g. polymer electronics [1]. But, even if these emerging technologies may have future potential, most of today's RFID-systems are still implemented by using CMOS and SAW transponder technologies.

The applied frequencies for RFID applications vary from the kHz domain up to GHz domain. The corresponding frequency bands feature different data rates and operational distances, due to limitations in bandwidth and radiation power given by local regulatory. Beneath regulatory issues, the characteristic properties of passive RFID systems are determined by the air-interface physics. Low-frequency RFID systems are usually operated in the near-field of the interrogator's antenna and feature low attenuation by organic materials. Unfortunately, the implementation of high distance applications and multi-tagging scenarios is restricted by the underlying capacitive or inductive near-field physics. To overcome near-field limitations the efforts in realizing far field UHF-RFID transponder systems increased over the past few years.

Most of today's commercially available passive UHF RFID transponders, with standard communication protocol support, are made by using a CMOS bulk technology. This is because CMOS is the classical technology for low-cost integrated circuits with a high yield and high integration densities for digital circuits. Furthermore, there are many accurate models, simulation tools and digital IPs available. Additionally, there is a world-wide infrastructure for CMOS manufacturing and many IC designers are experienced in analog and digital CMOS design methodologies. CMOS is also well-known for its programmability due to the combination with non-volatile-memory (NVM) technologies like, e.g., EEPROM or FRAM [2]. CMOS is also known to be the solid-state technology best qualified for ultra-low-power digital applications [3].

In recent years, a great and important progress was made in SAW RFID tags and a variety of innovative applications were acquired. These developments are mainly based upon the combination of SAW RFID tags [4,5] with traditional SAW sensor techniques [6,7]. This combination results in passive transponders that are connected to their read-out unit solely by a wireless radio link [8-11].

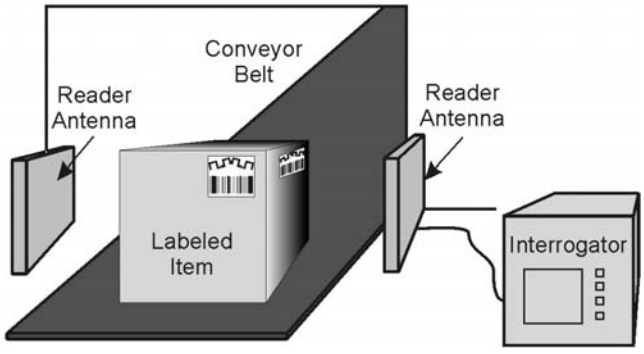

Fig. 1: CMOS RFID tags for barcode applications in supply-chain-management-systems.

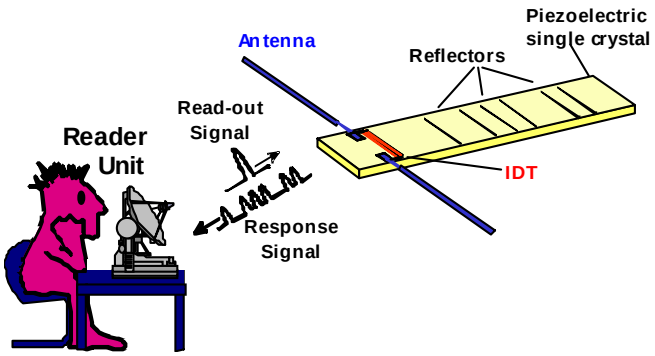

Fig. 2: Schematic of a SAW-based radio-link system which uses a reflective delay line.

The operating principle of such a system is as follows (see Fig. 2): An RF read-out signal is transmitted by a local radar transceiver (TRx). A small portion of this signal is picked up by the antenna of the passive SAW transponder where an interdigital transducer (IDT), connected to the antenna, converts the received signal into a SAW.

The RF micro-acoustic wave is stored in a SAW device and coded according the code number (or to the sensor variable) of interest. This storing can be done using either a delay line configuration or a resonator one. Due to the low velocity of SAWs, long delay times in the range of some microseconds can be achieved using rather small SAW chips. Therefore, at VHF/UHF frequencies, environmental echoes caused by electromagnetic multipath propagation phenomena are already safely faded away when the sensor response arrives at the radar transceiver. Hence, the sensor response can easily be separated from environmental echoes in the time-domain. This fact incorporates a great advantage of wireless SAW-based sensor systems compared to other radio link systems.

Within the next section a brief review of state-of-the-art passive transponder systems featuring integrated passive CMOS-transponders will be given. The concerning transponder architecture and important building blocks will be discussed in Section III. In Section IV SAW based transponder systems will be explained and Section V deals with state-of-the-art SAW-tags.

II. CMOS RFID Transponder Systems

Even if multiple and dense interrogator environments have been defined in widely used standards [12], state-of-the-art passive RFID transponder systems usually consist of one dominating single-tone interrogator and several passive transponder devices. Such an UHF RFID transponder system is schematically depicted in Fig.3.

In far-field UHF systems the physical layer of the tag-to-interrogator communication is based on the variation of the transponder's scattering characteristics. These characteristics

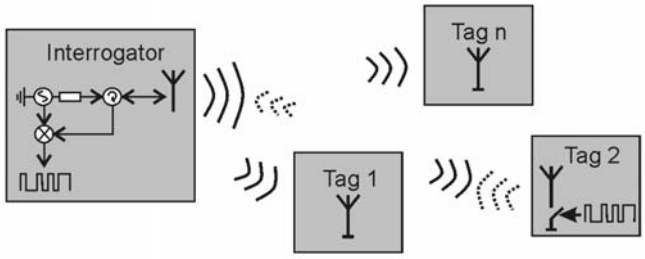

Fig. 3: Single reader RFID system with n passive Tags.

are usually specified by the transponder's radar cross section (RCS) [13].

In addition to the passive backscatter modulation approach the most important advantage of the passive transponder technology is the use of ambient energy for power supply. In order to obtain small transponder devices, the common energy-harvesting approach is based on the rectification of electromagnetic power. Therefore, the interrogator is responsible for information exchange and the power supply of the tag's integrated building blocks. This is achieved by emitting a continuous power wave, which used for rectification and backscatter modulation.

III. CMOS RFID Transponder Devices

The architecture of a typical state-of-the-art integrated CMOS UHF transponder is depicted in Fig. 4. Additional to the external antenna, this figure shows important integrated building blocks. These are the RF power-rectifier (RECT), several building blocks for RF voltage limiting (LIM-FB/LIM), the envelope-detection circuitry (DET/DECODE), a building block for the DC power management (REG), the voltage, current and time reference sources (REF), the power-on-reset circuitry (POR) and the backscatter modulation interface (CODE/MOD). Furthermore, the figure shows a

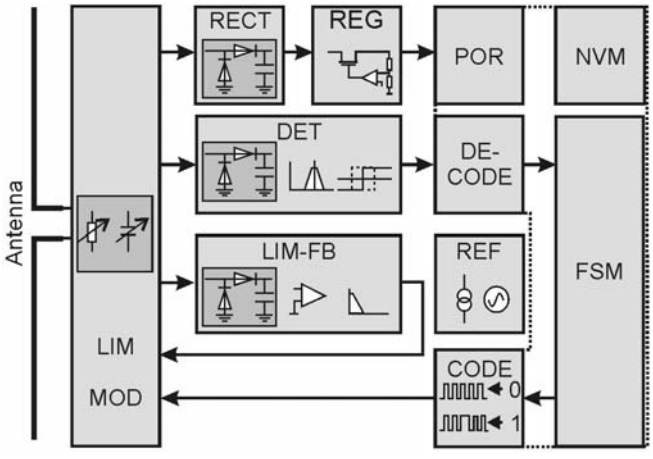

Fig. 4: Typical passive CMOS transponder device architecture.

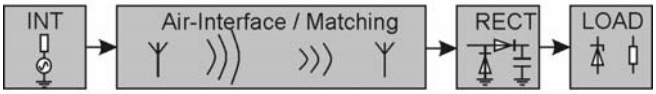

Fig. 5: Wireless power transmission setup in RFID systems.

digital finite-state-machine to support a standardized protocol (FSM). This state-machine controls the tag's analog building blocks and the non-volatile memory (NVM). The design issues can be divided into the design of the external antenna and matching structures, the design of the integrated RF components, the design of integrated analog baseband and auxiliary devices and the design of the digital components.

The antenna is the largest component of a high-distance UHF RFID tag and it is usually the only device which is not on the chip. As it has been presented in [14], it is also feasible to integrate embedded on-chip antennas for short range applications. The antenna is mainly responsible for the power matching of the IC's RF interface. Important design criteria are the general RCS behavior, the operational bandwidth and the antenna's efficiency. Several different approaches concerning antenna geometries and materials can be found in [14].

To operate the passive transponder devices at low RF power levels a consequent low-power design of the integrated circuits is mandatory. Fortunately, in the recent decades several important advances towards full scalable semi-physical low-power MOS device models have been presented by several authors [15,16]. Beneath a correct device modeling the use of ultra-low-power design techniques is necessary. In the following, the main important integrated analog building blocks of the passive UHF CMOS architecture will be summarized.

In most passive UHF RFID tags the DC power is generated by rectification of an incident RF power wave. As it has been already mentioned in Sec.II this power wave is provided by

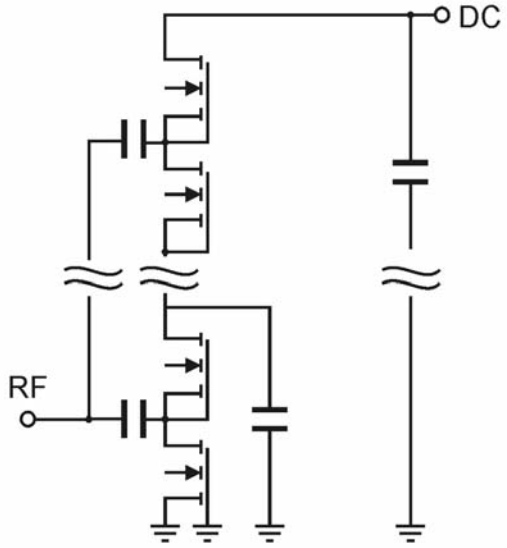

Fig. 6: Single-ended UHF CMOS n-stage power-rectifier.

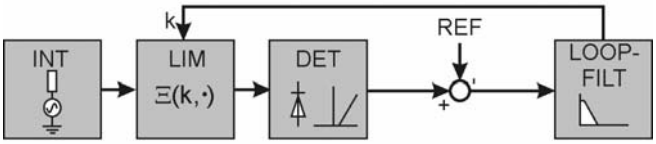

Fig. 7: Slow-dynamic RF voltage limiter of RFID systems.

the interrogator as it is depicted in Fig.5. To mitigate parasitic substrate losses (e.g. pad and contact wires) and for high integration density the rectification is commonly accomplished by parallel arranged dual diode rectifier stages [17]. The feasible integration of single-ended, differential and quasi-differential rectifier topologies has been already demonstrated by several authors [2]. The active nonlinear devices may be realized by using Schottky-diodes or MOS-transdiodes. The dimensions of the coupling capacitors and the size of the active devices are optimized for maximum power conversion efficiency at low-power levels. A commonly used single-ended CMOS rectification circuit is depicted in Fig.6

In addition to the efficient RF-to-DC power conversion, the protection of the passively powered transponder device against overvoltage hazards is a challenging task. Since broadband diode limiters lead to desensitization effects of the on-chip envelope detectors, the RF voltage limiting is subdivided by the dynamic of the RF envelope. Thus, fast high-voltage overshooting is usually prevented by broadband clamping devices and slow medium-voltage dynamics are limited by using narrow-band nonlinear feedback loops. A typical RF voltage limiting loop is schematically depicted in Fig.7. The RF voltage limitation loop consists of the feedback shunt device, the RF mean value amplitude detector and the loop filter. A mean value amplitude detection circuit realized in CMOS is depicted in Fig.8.

For power efficient implementation most RFID transponders feature incoherent receivers by using envelope detection devices. According to this, the standardized modulation modes are based on well-known amplitude-shift-keying techniques. The typically used envelope detection topology is depicted in Fig.9. These receivers consist of a nonlinear detection device, anti-aliasing devices and a comparator for 1-bit quantization. As it is depicted in Fig.10, the comparator usually features hysteresis to suppress unwanted small signals.

Contrary to near-field transponder systems, the response of UHF RFID transponders is based on the backscattering of the

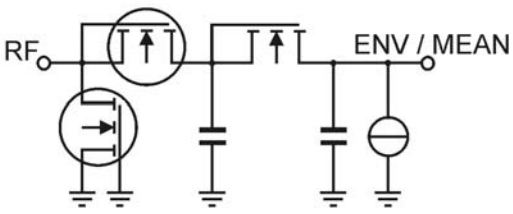

Fig. 8: CMOS RF envelope and mean detection circuitry.

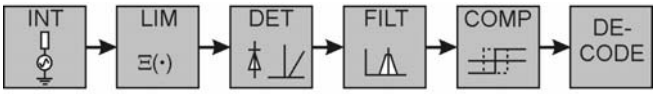

Fig. 9: Integrated envelope detector of a CMOS-Transponder.

incident RF power wave [19]. The modulation capabilities are usually specified by measuring the transponder's radar cross section (RCS). The information is coded into the carrier's phase and amplitude, respectively. The on-chip modulation devices may support resistive or reactive two-state shift keying modes. Due to the RZ (return-to-zero) implementation of common modulators the backscattered RF envelope is usually of a nonzero-mean complex value.

IV. SAW RFID TAG SYSTEMS

The SAW RFID stores the SAW wave. If the tag stores the SAW using a delay line configuration, then the coding can be achieved either by using a coded transducer or reflector array. In this case the information is encoded in the number, the time positions, and the phases of the response pulses. If resonant structures are used for storing, then the information is encoded by the number, the center frequencies, and the corresponding phases.

The coded RF micro-acoustic signal is re-converted into electrical signals by the IDT and re-transmitted to the radar TRx unit by the transponder antenna. This response contains any information about the number and geometries of the coding structures as well as the propagation and reflection properties of the SAW. Its evaluation in the radar unit may allow for the extraction of the desired information which is, e.g., a specific ID number or/and the sensor effect for a certain measurement.

The passive SAW transponders do not require any power supply, and their antennas are usually of a dipole, patch, slot, or loop type. In the VHF/UHF frequency range, the insertion loss of SAW transponders is in the order of 20-60 dB [4,5,10,11,21], depending on the operating frequency, the substrate material and the number of reflectors The achievable access rate is up to 10^5/s. The latter fact allows for communication with fast moving objects or vehicles.

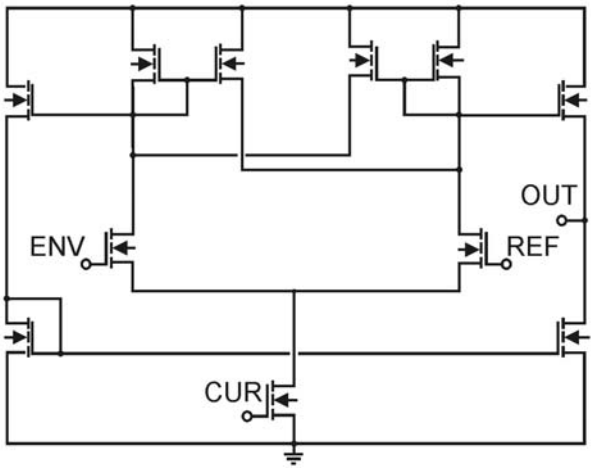

Fig. 10: Integrated CMOS comparator with hysteresis.

Because the distance between the radar TRx and the SAW transponder is unknown or varying, differential test arrangements are usually employed and differences in amplitudes, phases, frequencies, and propagation time delays are evaluated.

Because SAW transponders are passive components without any active logic on chip, they cannot be addressed individually. To access more than one transponder frequency division multiple access (FDMA), time division multiple access (TDMA), code division multiple access (CDMA), space division multiple access (SDMA), or combinations of them must be realized. For FDMA orthogonal frequency bands or subbands must be used for each individual transponder. This technique is feasible for several resonant transponders [9]. In combination with TDMA, the number of transponders can be enlarged. When implementing TDMA different time positions for each reflected signal have to be chosen to minimize intersymbol interferences. Typically 10 TDMA chips, each with 3-4 reflectors, can be realized. Using CDMA and an associated signal processing again approximately 10 code-orthogonal transponders can be addressed [27,28]. For SDMA techniques a certain space separation of the transponders has to be ensured. Since the field attenuation of the RX power decays with r^{-4} (with r being the interdistance between the reader and the tag), the near-far problem limits the multiple access of passive radio transponders.

When interrogated by an RF radio signal, a linear-distorted version of the read-out signal is re-transmitted by the SAW transponder. Therefore, a wireless one-port response measurement has to be performed with time division between the read-out signal and the tag response. Fig. 11 shows the time domain impulse response of a SAW transponder of the delay line type.

The frequency bandwidths used in SAW based radio link systems are quite large. Hence fading effects cause no major problems in these systems. Because the read-out principle is comparable to a radar system, all radar type measurement values like the distance to the SAW transponder, its velocity or angular velocity can be obtained with an accuracy of about 1% of the electromagnetic free-space wavelength.

The response signal of the SAW transponder, distorted by noise and interference, is received by the local TRx. Errors during transmission result in measurement errors not separable from a sensor effect. Therefore, special care has to be taken for the radio transmission systems [25]. The reader units for wireless SAW sensor system applications [8], [20]–[25] resemble those used in traditional radar systems. As is the

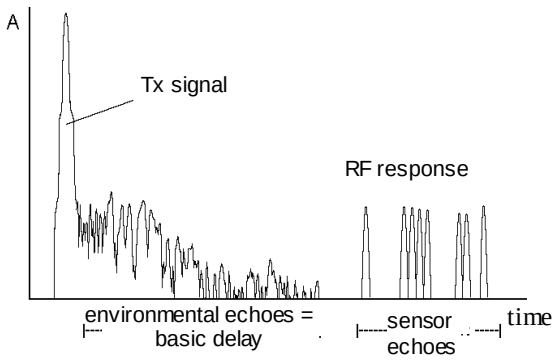

Fig. 11: Time domain response to the Tx signal.

case with radar systems, the receiver (Rx) usually is located nearby the transmitter (Tx) so that coherent detection is feasible.

For optimum free-space propagation conditions of the electromagnetic waves, the well-known radar equation predicts the (best case) level of the signal strength received by the reader unit. The maximum read-out distance *r* is given by Eq. (1), where is the electromagnetic wavelength, A_{SAW} is the insertion loss of the transponder, P_o denotes the transceiver's transmitted power, G_r and G_s are the respective gains of the TRx and the transponder antennas, kT_oBF is the relevant thermal noise power (Boltzmann's constant *k*, absolute temperature T_0, system bandwidth *B*, and noise figure *F*), and *SNR*, finally, is the minimum signal-to-noise ratio required to safely detect the received signal with a specified rate or probability of errors.

$$\frac{r}{\lambda} = \frac{1}{4\pi}\sqrt[4]{\frac{P_0 G_r^2 G_s^2}{A_{SAW} BFkT_0\ SNR}} \quad (1)$$

In Europe, three frequency bands at 433 MHz, 868 MHz and 2483 MHz suitable for SAW devices are allocated to unlicensed low power devices. The allowable equivalent isotropically radiated power (EIRP) in these bands is P_0 = 25 mW. In RF-shielded metallic process chambers, however, the operating frequency can be chosen arbitrarily and the Tx power can be enhanced. Typical values for the antenna gains are G_r = 12 dBi and G_s = 6 dBi,, respectively. The required signal-to-noise ratio *SNR* in the receiver is in the order of 10 to 20 dB.

Methods for data reduction can help to lower the effort of signal processing and even intersymbol interferences can be evaluated to extract the measurement value [24].

Apart from the time domain division between the request signal and the SAW sensor response, the read out of the sensor's characteristic can be done in time or frequency domain.

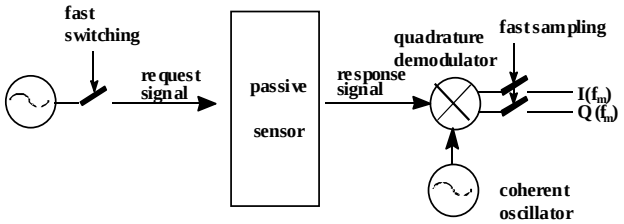

Fig. 12: Time-domain sampling technique.

A. Time-domain Sampling

For time-domain sampling devices (see Fig. 12) like pulse or pulse compression radar systems, the read-out signal spans the total system bandwidth *B*. Therefore, to avoid intersymbol interferences, fast sampling has to be performed in the receiver unit with at least twice the bandwidth *B*. Time-domain sampling is a single-scan measurement method, whereby the read-out repetition can be up to 10^{-5} s. Hence, this method is especially well-suited for reading fast changing measurement values or for read-out of fast moving objects.

For non-spread spectrum signals, the duration of one read-out signal T_{TDS} is low compared to the read-out repetition. With a restricted peak power P_0, the energy content P_0/B of one read-out signal and therefore also the maximum read-out distance will be small. Using typical values for these parameters the maximum read-out distance *r* is in the order of only 3 to 4 meters for one single reading cycle.

Using pulse compression methods, P_0/B can be increased by the time-bandwidth product *TB* of the pulse compression system thus enlarging the read-out distance. The maximum duration for *T*, however, is limited to the basic delay of the SAW devices, to avoid an overlapping between the read-out and the response signal. Using pulse compression technique a gain of 12 dB has been demonstrated which doubles the read-out distance [8]. At the expense of time resolution the sampled signal can be averaged over several read-out cycles thus lowering the measurement system bandwidth *B*. According to Eq. (1), an averaging factor of 16 doubles the read-out distance r. Using such techniques, read-out distances of 5-10 m have been demonstrated.

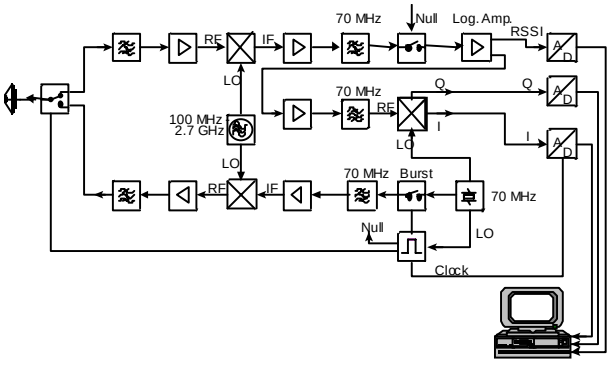

Fig. 13: Schematic diagram of a TRx using a pulse radar architecture.

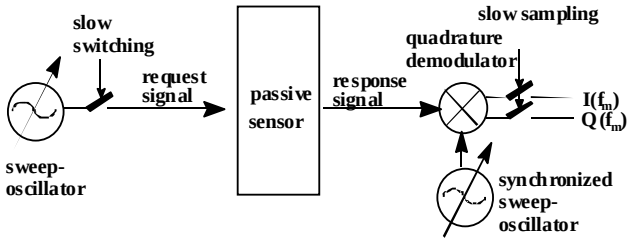

Fig. 14: Frequency domain sampling technique.

Fig. 13 shows a schematic diagram of a pulse radar TRx unit. The Rx uses a 70 MHz IF stage and a logarithmic limiter amplifier with a radio signal strength indicator (RSSI) output and a second output providing a limited signal for phase detection. Using conventional SAW IF band-pass filters, a system bandwidth of 40 MHz is achieved for operation in the 2.45 GHz ISM band. To compensate for the coherent cross--talk in the IF stage as well as for the DC offset of the mixers and A/D converters, a GaAs FET switch is included in the logarithmic amplifier [21].

The short read-out bursts of variable length are excited in the transmitter part (lower part in Fig. 13) by switching the output of a 70 MHz temperature-compensated crystal oscillator (TCXO). With a frequency synthesizer operating between 100 MHz and 2.7 GHz, these bursts are then converted to the RF band.

The response signal from a SAW transponder is first amplified in the receiver part (upper part in Fig. 13), then mixed down into the IF band, and then passed to the logarithmic amplifier. Quadrature demodulation is employed to extract the in-phase and quadrature components from the limited signal. After demodulation and digitizing, the data are processed further by a microprocessor. Table I summarizes the characteristics of the system.

B. Frequency-domain Sampling

For frequency domain sampling the total bandwidth is scanned in M steps in the frequency domain (Fig.14). The bandwidth of one step B_{res} can be rather low to achieve a high resolution. The Tx pulse can have a relatively long time period T_{FDS}. If T_{FDS} exceeds the basic delay of the SAW device, the duplexer switch at the TRx front-end has to be replaced by a circulator and a low noise amplifier with a high

Table I
Characteristic data of the Pulse RADAR read-out unit.

Quantity	Value
Frequency range /MHz	150 - 2700
Rx bandwidth B /MHz	1 - 36
Dynamic range /dB	85
Max. output power P_0 /dBm	40
Amplitude resolution /dB	±5
Phase resolution /°	±1
Noise figure F /dB	5

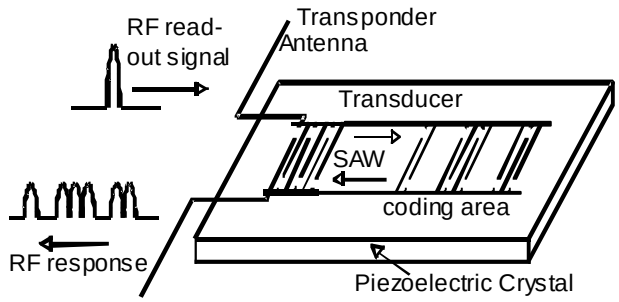

Fig. 15: Schematic layout of a SAW ID tag with several transducers wired together to a common bus bar.

dynamic range. Frequency domain sampling techniques enhance the SNR (E_b/N_0) in the receiver at the expense of the time resolution of the measurement value. Magnitude and phase of a narrow-band signal have to be detected in the Rx, which lowers the complexity and cost of the sampling and signal processing unit. Similar to time-domain sampling systems, the RF signals can be derived from a single oscillator for a coherent detection.

Frequency domain sampling is a multi-scan measurement technique. To achieve the information of M points in time-domain, M frequencies have to be scanned. The information about the sensor signal in time domain is received by a frequency to time transformation by, e.g., FFT or other more sophisticated algorithms. The total measurement time takes more than M times the minimum measurement cycle of a single time-domain sampling. Frequency domain sampling is therefore well suited for slow, high precision, and long-distance measurements. It can be performed using a network analyser or a frequency-modulated continuous wave (FMCW) radar architecture [21,22]. In order to eliminate the transmitted signal and all environmental echoes, also in a frequency domain sampling technique the first 1-2 µs of the sensor response can be suppressed in time-domain [20].

IV. SAW RFID TAGS

A SAW RFID tag usually incorporates a coupling IDT and a coding area. There are two ways of designing the coding area: either reflectors are used (see Fig. 16) or, alternatively, several coding transducers are wired together with a common bus-bar (see Fig. 15).

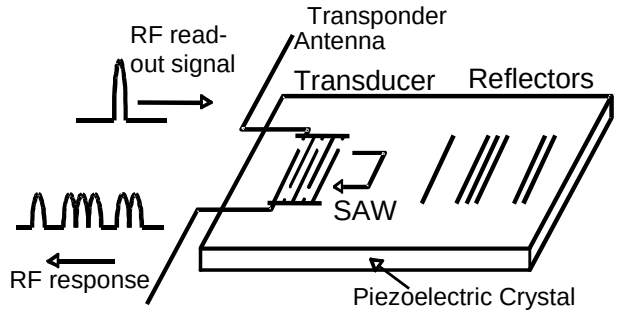

Fig. 16: Schematic layout of a reflective delay line.

A. Transducer Coded Delay Lines

The layout of a delay line with several coding transducers is similar that of a tapped delay line, where the tapped transducer is wired by a long bus-bar to the coupling transducer to build up a one-port device. In principle the coded transducer could also get wired to the coupling transducer and the antenna via a circulator.

The minimum length of this common bus-bar is given by the number of symbols *I* lined up multiplied by the minimum distance ΔT between two symbols, which is determined by the bandwidth *B* of the system.

The wavelength λ_{el} of an electric signal on $LiNbO_3$ is reduced by a factor of approximately 10 compared to free space, due to the high dielectric constant of this material. If the length of the bus-bar becomes larger than 10% of λ_{el}, the quasi-static approximation used in the simulation of the electrical connection is no longer valid and electric wave-guide effects on the bus-bar must be taken into account. If we demand, that the length of the bus-bar must remain smaller than 10% of λ_{el}, and, if we take into account, that the minimum resolution is given by the system bandwidth B, we get an upper limit N_{max} for the number of symbols *N*, which can be lined up on $LiNbO_3$ in this technique, with

$$N_{\max} \le \frac{0.1\lambda_{el}}{v_{SAW}/B} = \frac{10^3 B\lambda_{SAW}}{v_{SAW}} = \frac{10^3 B v_{SAW}}{v_{SAW} f_0} = 10^3 \frac{B}{f_0} \qquad (2)$$

Using a relative bandwidth B/f_0 of 2%, less than 20 symbols are possible with this technique. For a identification system incorporating only a few symbols, or, if a substrate with a low dielectric constant like quartz is used, a tag of this kind may be a promising concept.

B. Reflective Delay Lines

Most SAW RFID tags are designed using a reflective delay line, like the one sketched in Fig. 16. The SAW in a reflective delay line propagates towards reflectors distributed in a characteristic barcode-like pattern and is partially reflected at each reflector. The usage of reflectors halves the chip size compared to the non-reflective arrangement of Fig. 15. Furthermore, the electrical impedance of the transducers remains unattached by the number of coding elements and the actual code.

The coding of a SAW ID tag depends on the applied modulation technique and is obtained by a specific coding arrangement. In the simplest case, this coding is done by a binary amplitude shift keying ASK (on/off): each predetermined possible symbol position is set either by a transducer or reflector (on-bit) or not (off-bit). Fig. 17 shows a

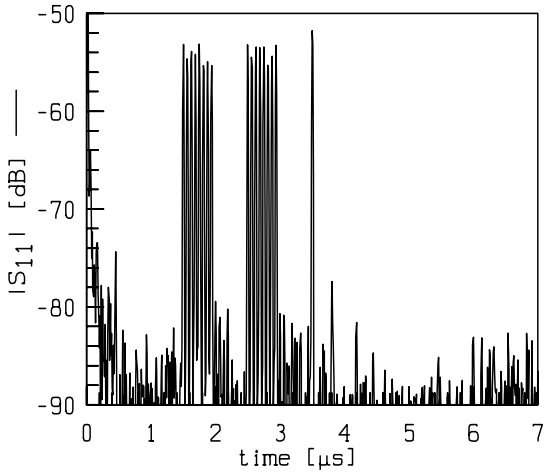

Fig. 17: Measurement of the SAW ID tag with 8 "ON", 8 "OFF", 8 "ON", 8 "OFF", and 1 "ON".

measurement of an ID tag using a reflective delay line structure and a ASK modulation scheme.

With 32 symbol positions, 2^{32} different tags can be coded. ID-tags with ASK modulation are already in use, e.g., in German subway systems [10], [26]. The system operates in the ISM band at 2.45 GHz..

The ASK on/off keying is outperformed by other modulation techniques such as phase shift keying PSK. Using a PSK modulation the phases of the time response are evaluated and not their amplitudes. A binary phase shift keying BPSK modulation obtains the same bit error rate with a 6 dB lower signal-to-noise ratio compared to an ASK modulation, thus enhancing the maximum readout distance. Higher-order PSK like quadrature PSK (QPSK) uses fewer symbols (reflectors) and therefore need less chip size and obtain lower insertion attenuation, but a higher signal-to-noise ratio is needed for the detection.

The requirements for a SAW transponder used in a phase modulation system, however, become more stringent, because all influences which change the delay time of a reflector, e.g., the SAW velocity or the accuracy of the fabrication process,

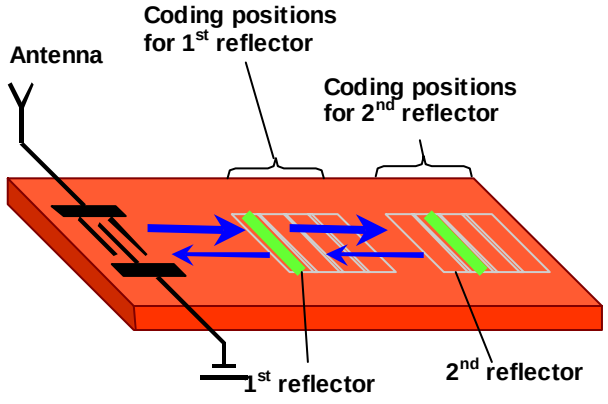

Fig. 18: Pulse position coding schema.

must be controlled within a small fraction of one single SAW wavelength.

A good choice for the modulation technique used in SAW transponders might be a pulse position modulation (see Fig. 18), which achieves the code-density of a higher phase-modulation and avoids their stringent sensitivity on small inaccuracies during the fabrication process. In a pulse position modulation scheme the symbol is set at one out of several time slots. The accuracy in the time resolution of one target is much higher than the time separation of two targets in most radar systems. Therefore, the time slots can be arranged with higher density, compared to the symbol separation in a ASK modulation. If each reflector is set in one out of 2^n time slots, each symbol codes for n bit.

VII. Conclusion

We have discussed the state-of-the-art of both CMOS- and SAW-based passive RFID techniques. Today, there is no other technology available that offers similar performance figures than these two technologies. Polymer-electronic RFID tags which offer low production costs are not feasible at UHF in the next future. Therefore, CMOS will take the lead in the high-volume UHF markets. Here, the development trends go towards bi- or even triple-frequent operation at the 13 MHz, 900 MHz and 2.4 GHz bands. Additionally, the research trends go towards integration of sensor functionalities and energy harvesting. SAW RFID techniques will find their market in professional applications with lower volume. Their great potential lies in the possibility to integrate sensor functionalities as an inherent feature or to add sensor functionalities by operating as an air interface for external non-SAW sensors. SAW RFID tags can operate in harsh environments and at temperatures higher than 400 ^{0}C. The principal difference between passive CMOS and SAW RFID systems is the high dynamic range of SAW systems. This is due to the fact that the SAW transponders can be viewed as linear devices and the systems dynamic range is determined by the reader's transceiver. On the other hand the dynamic range of CMOS RFID systems is limited by the CMOS transponders behaving like bandpass nonlinearities. Therefore, CMOS RFID systems suffer from desensitization effects when strong interferers hit the tag. Additionally, the lower end of the dynamic range of CMOS systems is given by the required minimum converted DC voltage, whereas the sensitivity of SAW systems is determined by the required SNR of the reader. So, we can say that passive SAW RFID systems are "noise-limited", and passive CMOS RFID systems are "voltage-limited", practically associating a higher read range with SAW systems. One major drawback of SAW RFID systems is due to the fact that the programming of the SAW tags has to be done during fabrication whereas CMOS tags can be programmed during operation. Another advantage of CMOS tags is due the possibility to make them smart, e.g., to run communication protocols or to implement multi-tag systems by using sub-carrier techniques. Moreover, encryption is not feasible with SAW tags. At the foreseeable future, there is no killer application, i.e. high-volume application for SAW RFID tags. However, this seems also to be the case with CMOS RFID tags where at the moment a huge market pull exists but the technology push clearly lacks behind. Thus, this situation differs from the mobile radio terminal situation in the 1990s where we had a win-win situation, i.e. there was a simultaneous market-pull/technology push situation. Another open issue in the RFID business is still international regulation and standards, especially at UHF frequencies. Electromagnetic irradiation issues have been already successfully addressed but privacy concerns ("Is RFID a snooper technology or a super technology?") are in no way regulated. So the passive RFID race is still far from end.

ACKNOWLEDGEMENT

The authors wish to acknowledge the assistance and support of the companies Infineon Technologies and EPCOS for device fabrications.

REFERENCES

[1] V. Subramanian, J.M.J. Frechet, P.C. Chang, D.C. Huang, J.B. Lee, S.E. Molesa, A.R. Murphy, D.R. Redinger, S.K. Volkman: "Progress toward development of all-printed RFID tags: materials, processes, and devices", Proc. of the IEEE,vol.93, No.7, pp. 1330-1338, Jul. 2005

[2] H. Nakamoto, D. Yamazaki, T. Yamamoto, H. Kurata, S. Yamada, K. Mukaida, T. Ninomiya, T. Ohkaw, S. Masui, K. Gotoh: "A Passive UHF RFID Tag LSI with 36.6% Efficiency CMOS-Only Rectifier and Current-Mode Demodulator in 0.35mm FeRAM Technology ", Conf. Dig. ISSCC,Feb 2006 pp.1201- 1210

[3] A. P. Chandrakasan, S. Sheng, and R. W. Brodersen, "Low-power CMOS digital design," *IEEE J. Solid-State Circuits*, vol. 27, pp. 473–484, Apr. 1992

[4] L. Reindl, W. Ruile: "Programmable Reflectors for SAW-ID-Tags", in Proc. of the 1993 IEEE Ultrasonics Symp., pp. 125-130

[5] V. P. Plessky, S. N. Kondratiev, R. Stierlin, F. Nyffeler: "SAW Tags: New Ideas", in Proc. of the 1995 IEEE Ultrasonics Symp., pp. 117-120

[6] G. Fischerauer, "Surface Acoustic Wave Devices," in: W. Göpel, J. Hesse, J. N. Zemel, H. Meixner, R. Jones (Eds.), Sensors. A Comprehensive Survey, Vol. 8. Weinheim: VCH, 1995.

[7] D. S. Ballantine, R. M. White, S. J. Martin, A. J. Ricco, E. T. Zellers, G. C. Frye, H. Wohltjen, Acoustic Wave Sensors: Theory, Design, and Physico-Chemical Applications. San Diego etc.: Academic Press, 1997.

[8] F. Schmidt, O. Sczesny, L. Reindl, V. Magori, "Remote sensing of physical parameters by means of passive surface acoustic wave devices ('ID TAG')," in Proc. of the 1994 IEEE Ultrasonics Symp., pp. 589-592

[9] W. Buff, F. Plath, O.Schmeckebier, M. Rusko, T. Vandahl, H. Luck, F. Möller, "Remote sensor system using passive SAW sensors," in Proc. of the 1994 IEEE Ultrasonics Symp., pp. 585-588

[10] L. Reindl, G. Scholl, T. Ostertag, H. Scherr, U. Wolff, F. Schmidt, "Theory and application of passive SAW radio transponders as sensors," IEEE Transactions on UFFC, Vol. 45, No. 5, Sep. 1998, pp. 1281-1292

[11] Pohl, R. Steindl, L. Reindl, "The 'intelligent tire' utilizing passive SAW sensors - measurement of tire friction", IEEE Transaction on Instrumentation and Measurement, Vol. 48, No. 6, Dec. 1999, pp. 1041-1046

[12] EPCglobal Inc GS1, EPC "Radio-Frequency Identity Protocols Class-1 Generation-2 UHF RFID Protocol for Communication at 860MHz-960MHz", 2005

[13] H. Kwon, B. Lee, "Evaluation of RFID Tag Antenna Performance Using Radar Cross Sections", 8th European Conf. on Wireless Technology, 2005, pp. 491- 493

[14] M. Usami *et al.*, "Powder LSI: An ultra small RF identification chip for individual recognition applications," in *IEEE ISSCC Dig. Tech. Papers*, Feb. 2003, pp. 398–399.

[15] K.V.V. Rao, P. V. Nikitin, S.F. Larn, "Antenna Design for UHF RFID Tags: A Review and a Practical Application", IEEE Transaction on Antennas and Prop.,Vol.53, Vo.12, Dec. 2005, pp. 3870-3876

[16] C. C. Enz, F. Krummenacher, E. A. Vittoz, "An Analytical MOS Transistor Model Valid in All Regions of Operation and Dedicated to Low-Voltage and Low-Current Applications", Analog Integrated Circuits and Signal Processing, vol. 8, pp. 83 - 114, 1995

[17] Y. Cheng, C. Hu, "MOSFET Modeling & BSIM3 User's Guide, " Kluwer Academic Publishers, 1999.

[18] K. Seemann, R. Weigel, "Ultra-Low-Power Rectification in Passive RFID Tags at UHF Frequencies", Frequenz, Journal of RF-Eng. and Telecommunications,Vol.59, Vo.5-6, Jun. 2005, pp. 112-115

[19] B.D. Rao, K.S. Arun: "Model Based Processing of Signals: A State Approach", Proc. IEEE, Vol. 80, no. 2, 1992, pp. 283-309

[20] Pohl, G. Ostermayer, C. Hausleitner, F. Seifert, L. Reindl: "Wavelet Transform with SAW Convolver for Sensor Application", Proc. IEEE Ultrasonics Symp. 1995, pp. 143-146

[21] G. Scholl, F. Schmidt, T. Ostertag, L. Reindl, H. Scherr, U. Wolff, „Wireless passive SAW sensor systems for industrial and domestic applications", Proc. 1998 IEEE Frequency Control Symp., pp. 595-601.

[22] G. Fischerauer, F. Schmidt, M. Voss, R. Bader, "Mechatronic Extension of a Tap Holder for Process Monitoring," in Proc. of the IECON 98

[23] A. Pohl, G. Ostermayer, F. Seifert, "Wireless sensing using oscillator circuits locked to remote high-Q SAW resonators", IEEE Trans. Ultrason,. Ferroelect., Freq. Contr., vol. 45, No. 5, pp. 1161-1168, Sep. 1998

[24] Pohl, "A low cost high definition wireless sensor system utilizing intersymbol interference", IEEE Trans. Ultrason,. Ferroelect., Freq. Contr., vol. 45, No. 5, pp. 1355-1362, Sep. 1998

[25] Pohl, "A Review of wireless SAW Sensors," IEEE Transactions on UFFC, Vol. 47, No. 2, March. 2000, pp. 317-332.

[26] Siemens Transportation Group, product description A19100-V700-B535-V1-76

[27] G. Ostermayer, A. Pohl, L. Reindl, F. Seifert, "Multiple Access to SAW Sensors Using Matched Filter Properties", Proc. IEEE Ultrasonics Symposium, Toronto, 1997, pp. 339-342

[28] G. Ostermayer, A. Pohl, R. Steindl, F. Seifert, "SAW sensors and correlative signal processing – a method providing multiple access capability", Proc. ISSSTA 98, South Africa, pp. 902-906

Ultra-Low Power UWB Wireless Communication System Using SAW Matched Filters

T. Sato, T. Sugiura, E. Otobe, K. Tanji, N. Otani, and M. Hasegawa
Wireless Communication Lab.
Samsung Yokohama Research Institute
Yokohama, Japan
tk-sato@ieee.org

***Abstract*—A novel ultra-wideband (UWB) communication system with surface acoustic wave (SAW) matched filters that consumes a small amount of power during operation is introduced. The system uses a unique pulse position modulation method combined with unique spreading codes that are achieved by using SAW matched filters for modulation and demodulation. We fabricated 4-GHz SAW matched filters and used them in a UWB module comprised of these filters, low-noise amplifiers, converters, baseband circuits, and an antenna. With the UWB communication system, we achieved 20-Mbps real-time video streaming. The TX and RX power consumption in the RF section were 50 mW and 150 mW, respectively. This system is suitable for a wireless personal area network (WPAN) that requires low power consumption.**

Keywords—UWB; SAW; wireless pulse communication; matched filter

I. INTRODUCTION

Ultra-wideband (UWB) communication is one of the most promising technologies for the next wireless personal area networks (WPANs) because of its extremely high data transmission rate with ultra-low power consumption [1]. Recently, two kinds of communication methods used for UWB systems have been the center of attention [2]. One method is called DS-UWB (Direct Sequence UWB), and it uses very short pulses covering an extremely wide bandwidth spectrum. The other is called Multi-Band OFDM (Orthogonal Frequency Division Multiplexing). This method uses an OFDM technique already applied in wireless LAN systems. Achieving ultra-low power consumption with these two systems is difficult because the DS-UWB system needs some power consuming devices such as a high-speed clock, synchronization, and tracking loop, for example, and the Multi-Band OFDM system needs very complicated circuits that in turn result in high power consumption.

The surface acoustic wave (SAW) matched filters have been studied since the 1960s [3]. In recent years, many studies of SAW matched filter applications for spread-spectrum-related communication systems have been presented [4-6]. These SAW matched filters can be used for high-speed signal processing devices that perform correlation of complex pulse waveforms [7]. Using them achieves lower power consumption, as well as simplification and miniaturization of circuits, as compared to that using digital correlators with semiconductor circuits.

In this paper, we introduce a novel UWB communication system with SAW matched filters that can be operated with ultra-low power consumption. The system uses a unique pulse position modulation (PPM) method combined with unique spreading codes. In the transmitter, two kinds of pulse trains corresponding to the reference and data signals are transmitted shifted by a specific delay time. These modulated pulse trains are generated with other spreading codes for the reference signal and the data signal, respectively, by using the SAW matched filter. In the receiver, detecting the data by comparing the peak position of two correlation signals demodulated from the data pulse train and the reference pulse train by SAW matched filters corresponding to the respective spreading codes is possible. The SAW matched filter enables low power consumption, simplification of the circuit, and miniaturization. Moreover, the PPM method is robust against multipass fading.

In section II, we briefly show the SAW-UWB system with the PPM method and present a unique spreading code to improve the ratio of the strength of the desired correlation signal to undesired signals (D/U ratio). In section III, we show the device configuration to provide the high-performance GHz-range SAW matched filter with fewer feed-through signals. In section IV, we describe the actual implementation in a UWB module comprised of these filters, low-noise amplifiers, converters, baseband circuits, and an antenna, to evaluate the performance of the SAW-UWB system. Then, we show the system performance of the UWB module and the SAW matched filters.

II. PRINCIPLE OF UWB COMMUNICATION SYSTEM WITH SAW MATCHED FILTERS

A. Basic Architecture

Our developed UWB communication system exploits a unique pulse position modulation (PPM) method [8] that is based on an impulse radio technique and a coding technique. The advantage of the PPM method is that the effect of multi-path fading can be suppressed. We adopted SAW matched filters for coding and decoding to achieve ultra-low power

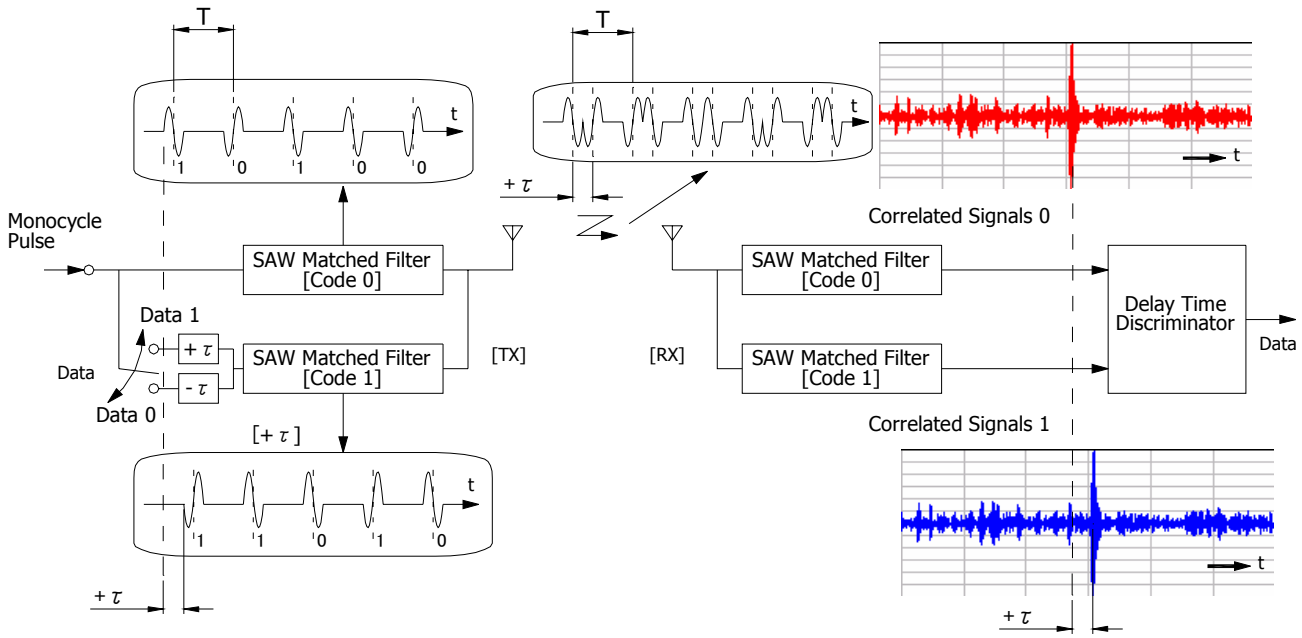

Fig. 1 Basic architecture of UWB communication system with pulse position modulation (PPM) method combined with spreading codes.

consumption. The transmitter and receiver architectures eliminate the need for mixers, an IF section, and most baseband signal processing, by using SAW matched filters. This is because the SAW matched filter can directly convert an RF signal to, or from, a baseband signal.

The basic architecture of the UWB system with the PPM method combined with spreading codes is shown in Fig. 1. The system uses two orthogonal spread pulse trains that are generated by the SAW matched filters from very short mono pulse signals. One filter refers to a reference pulse train and the other refers to a data pulse train. In modulation, the reference mono pulses are generated at some constant interval corresponding to the data rate, while the data mono pulses are generated at a delayed time $+\tau$ or $-\tau$ with respect to the reference pulse when sending Data 1 or Data 0, respectively. Moreover, the reference and data pulses are spread to pulse trains with orthogonal spreading codes by the TX SAW matched filters to distinguish these pulses in a receiver. In demodulation, the pulse trains are correlated by the RX SAW matched filters to regenerate the reference signals and $+\tau$ or $-\tau$ delayed data signals. The two correlated signals are distinguished at a delay time discriminator and converted to digital signals.

The system does not need a high-speed clock generator operating at a high chip rate. Furthermore, the demodulated reference signals are converted to digital signals, and then, these signals are used as clock signals for synchronization in digital signal processing. Hence, in addition, the system does not need power consuming synchronization for digital signal processing. This system with SAW matched filters operating in the GHz range can achieve asynchronous communication. As a result, we achieved ultra-low power consumption, as well as simplification and miniaturization of circuits.

B. New Spreading Codes for PPM Method

Some well-known spreading codes, such as the gold code and the barker code, for example, are used for wireless communication systems. However, they are not suited to the PPM method we present because their modulation method requires both a high D/U ratio and short code for a high transmission rate.

In our modulation method, the delay time τ between the reference pulse train and the data pulse train is shorter than the chip interval T of each pulse train. The data pulses are placed in the reference pulse train, shifted by the delay time τ. Therefore, the output of the SAW matched filter contains both autocorrelation and cross-correlation signals. The cross-correlation degrades the D/U ratio of the correlation of SAW matched filters. Assuming that the reference train is spread with a seven-chip barker code (1–1 1 1–1–1–1) and the data train is spread with a reversed barker code (–1–1–1 1 1–1 1), the D/U ratio of autocorrelation is 7:1. However, the D/U ratio of the correlation of SAW matched filters is degraded to 7:3 because the cross-correlation becomes 3, as shown in Fig. 2 (a). Therefore, detecting the peak position of the correlation stably is difficult.

To improve the D/U ratio, we propose a unique coding technique suited to the PPM method. The new spreading codes are expanded as the chip interval T' of the presented codes is half of that of the conventional codes, i.e., T' = T/2. The delay time τ is also set to T'. Compared to the conventional codes, the number of chips doubles, but the length of the pulse train is the same. The code employs three states: -1, 0, and 1. The

Transmitted Pulse Train of Data 1 for Barker codes	1	-1	-1	-1	1	-1	1	1	-1	1	-1	-1	-1	-1	1
Reference Pulses (code 0)	1		-1		1		1		-1		-1		-1		
Data Pulses (code 1 [t=+τ])		-1		-1		-1		1		1		-1		1	

Correlation Signal of Data 1 by RX Matched Filter (code 0)	-1	1	0	2	-1	3	0	0	-1	-3	0	-2	7	-1	0	2	-1	-3	0	0	-1	3	0	-2	-1	1
for Reference (auto correlation)	-1		0		-1		0		-1		0		7		0		-1		0		-1		0		-1	
for Data (cross correlation)		1		2		3		0		-3		-2		-1		2		-3		0		3		-2		1

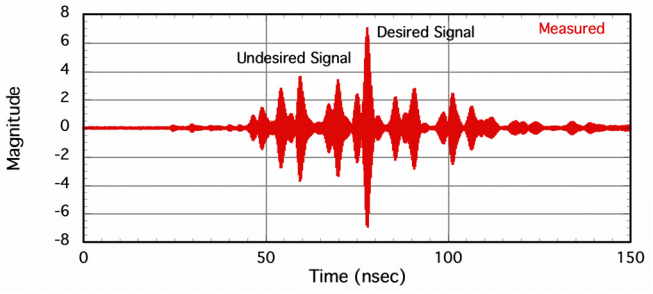

(a)

Transmitted Pulse Train of Data 1 for new codes	0	1	1	-1	0	2	2	1	0	-1	-1	1	-2	1
Reference Pulses (new code 0)	0	1	0	-1	0	1	1	0	0	0	-1	1	-1	
Data Pulses (new code 1 [t=+τ])		0	1	0	0	1	1	1	0	-1	0	0	-1	1

Correlation Signal of Data 1 by RX Matched Filter (new code 0)	0	-1	0	1	-2	-1	0	0	1	0	-2	0	10	0	1	-4	-1	2	1	0	-1	1	0	-2	1	0
for Reference (auto correlation)	0	-1	1	0	-1	0	0	1	0	-1	-1	-1	7	-1	-1	-1	0	1	0	0	-1	0	1	-1	0	
for Data (cross correlation)		0	-1	1	-1	-1	0	-1	1	1	-1	1	3	1	2	-3	-1	1	1	0	0	1	-1	-1	1	0

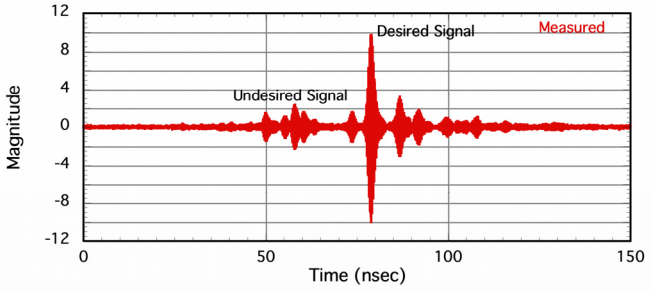

(b)

Fig. 2 Correlation signals of PPM method for (a) Barker codes and (b) new spreading codes.

autocorrelation and cross-correlation signals are also overlapped because the reference and data chips are permitted to overlap each other. If a cross-correlation is added to autocorrelation at the correlation peak and cross-correlations are canceled by autocorrelations in the side-lobe, we can obtain the bigger desired signal and the smaller undesired signals. Therefore, the D/U ratio can be improved using this idea.

Next, we show an example of the new spreading codes for the PPM. The correlation signals of the new spreading codes, where the reference spreading code is (0 1 0–1 0 1 1 0 0 0–1 1–1) and the data spreading code is (0 1 0 0 1 1 1 0–1 0 0–1 1), are shown in Fig. 2 (b). The effective number of chips is the same seven chips, as in the case of Fig. 2 (a). As shown in Fig.

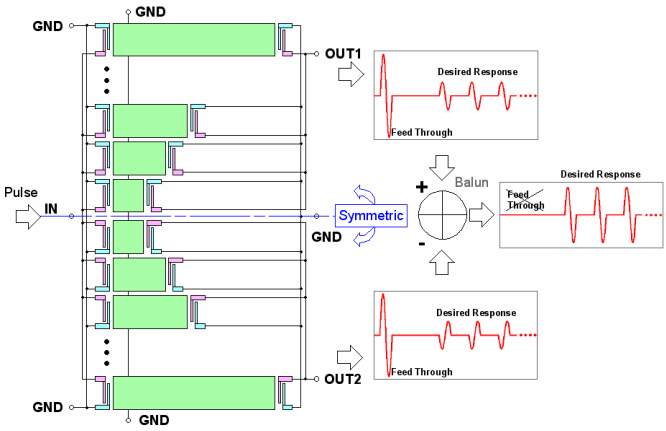

Fig. 3 Feed-through cancellation concept by symmetrical configuration.

2, a D/U ratio of about 10:2 can be achieved, and this improvement is twice that of the seven-chip barker code. This is because the correlation peak grows from 7 to 10 because of a cross-correlation and the side-lobe levels are suppressed to about 2.

III. SAW MATCHED FILTER FOR UWB COMMUNICATION SYSTEM

The tap arrangements of the SAW matched filter for our UWB communication system were designed on the basis of the new spreading codes described in the previous section. The structure of the SAW matched filter was designed by using a full-wave simulation method to reduce unwanted parasitic effects in the GHz range. We calculated the SAW responses with a SAW simulation based on the coupling of mode (COM) model. An electromagnetic (EM) simulation of the structure patterns without IDT was performed with an EM simulator based on a moment method. We also used the EM simulator to calculate the influence of a package. The total simulation results of both SAW and EM were combined on a circuit simulator.

Feed-through signals leaking directly from input to output transducers of the SAW matched filter, degrade a correlation performance, especially for wireless pulse communication systems operating in the GHz range. To suppress this feed-through response, we proposed a new configuration of SAW matched filters [9]. The feed-through cancellation concept is shown in Fig. 3. The pattern configuration has a single-ended input and balanced outputs. The input-output 1 and input-output 2 patterns were designed to be symmetrical. The individual feed-through signals of output 1 and output 2 are in phase and of the same magnitude because of the symmetrical device pattern. On the other hand, the SAW IDT structures are designed so that both desired output signals are out of phase. Consequently, the feed-through signals can be canceled and only the desired signal can be detected with a balun.

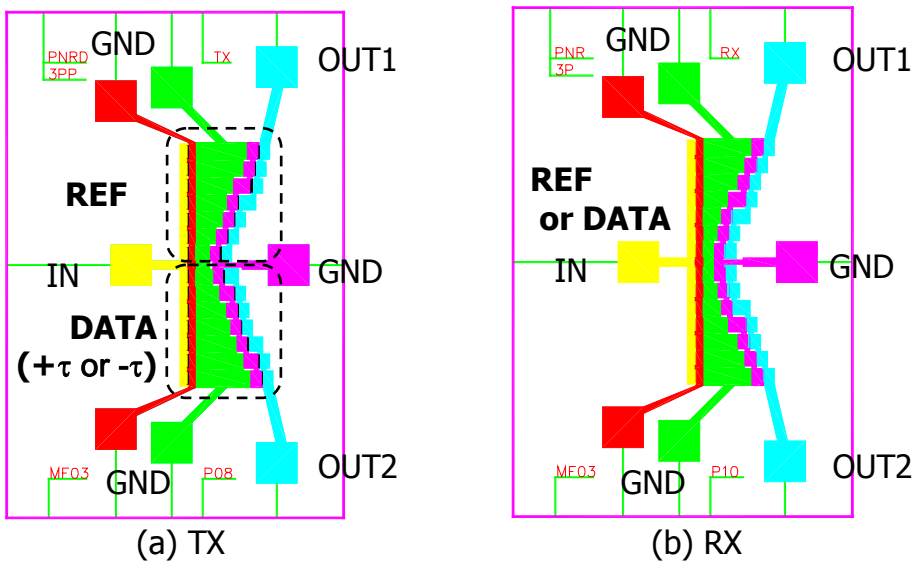

Fig. 4 Chip patterns of SAW matched filters in SAW-UWB module.
(a) TX and (b) RX. Chip size is 1.0 × 1.3 mm^2.

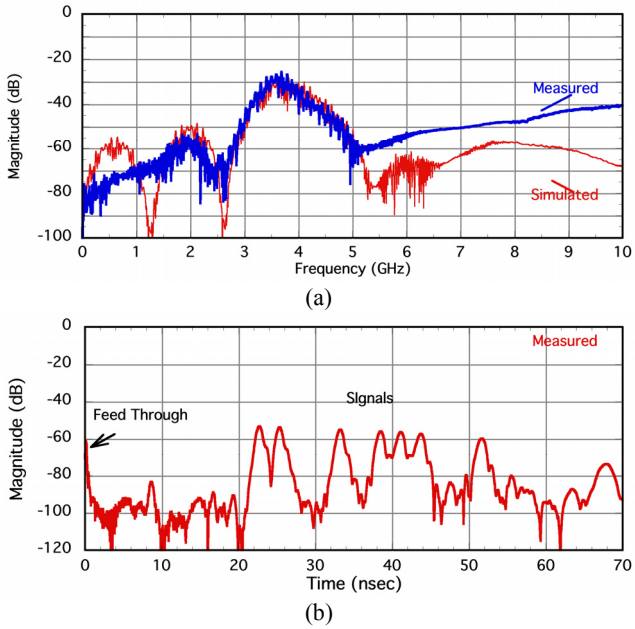

Fig. 5 Measurement results of 4-GHz RX SAW matched filter for spreading code (0 1 0 0 1 1 1 0–1 0 0–1 1).
(a) Frequency response and (b) time domain.

For the SAW-UWB system, two kinds of TX SAW matched filter and two kinds of RX SAW matched filter were fabricated. The chip layouts of the fabricated SAW matched filters are shown in Fig. 4. The TX SAW matched filter includes the reference spreading code and the data spreading code. One TX matched filter is for the delay time of $-\tau$ (Data 0), and the other is for the delay time of $+\tau$ (Data 1). One RX matched filter is for the reference signal, and the other is for the data signal. We adopted a single electrode IDT on a 42°-Y-X lithium tantalate substrate for a very high operating frequency range, and we adopted a multi-track structure to avoid the reflection effects between individual taps. The electrodes were made of Al-Cu with a thickness of 900 Å. Each IDT consists of three finger pairs. The line and space widths were 0.254 µm each. The propagation paths are metallized to reduce the propagation loss of leaky surface waves. The aperture of each track is 80 µm, and the chip size is 1.0 × 1.3 mm^2. The SAW matched filter was assembled in a 2.5 × 2.0 × 0.85 mm^3 ceramic package with a symmetrical interconnection pattern by using the flip chip technique.

The measurement results obtained for the fabricated SAW RX matched filter for spreading code (0 1 0 0 1 1 1 0–1 0 0–1 1) and our calculations are presented in Fig. 5. The measurement results are in good agreement with the calculations. In the time-domain response, the feed-through response is suppressed and a good modulated pulse train with seven chips is detected.

IV. IMPLEMENTATION OF UWB MODULE USING SAW MATCHED FILTERS

We fabricated a SAW-UWB module by the PPM method to evaluate the performance of this system.

An overview of our implemented UWB module with SAW matched filters is shown in Fig. 6. The size of the module is 110 × 45 × 13 mm^3, and the RF circuit area is 36 × 40 mm^2. The communication system is a half duplex system that switches TX/RX signals with one antenna. The interface is a USB (Universal Serial Bus) 2.0 port, and the only power for the module is supplied from a PC through the USB port.

A block diagram of the UWB module is shown in Fig. 7. In the RF circuit, four kinds of SAW matched filters, low-noise amplifiers, pulse generators, converters, and an antenna were developed specifically for the module, and the baseband chip is an FPGA (Field Programmable Gate Array) that was customized for our UWB system. The SAW matched filters with new spreading codes described in the previous section were used. Low-noise amplifiers, pulse generators, and

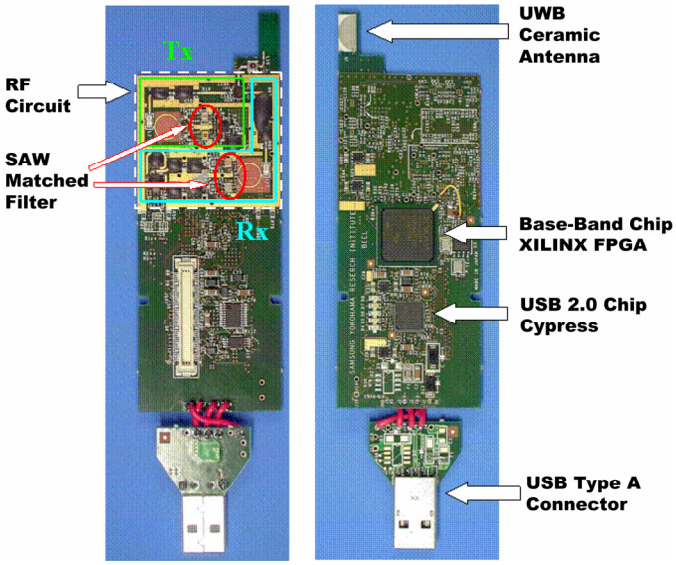

Fig. 6 Implemented UWB modules with SAW matched Filters.

converters were made with MMIC (microwave monolithic IC) by using the InGaP HBT process to attain high speed, low power consumption, and a small package. The UWB ceramic antenna was developed with a size of $10 \times 5 \times 1$ mm^3 [10]. The correlation signals of the RX SAW matched filter in the UWB module are shown in Fig. 8. A maximum data rate of 20 Mbps was achieved, as shown in Fig. 8.

We prepared two laptop PCs for transmission experiments with our implemented UWB module. The modules were put in the respective USB ports of the PCs. We transmitted MPEG1 data from one PC to the other through the modules. We achieved an effective speed of 14 Mbps real-time video streaming with UWB modules over a transmission distance of five meters. The transmission speed was degraded from 20 Mbps (Max) due to error correction sequences and switching between TX and RX. We have achieved ultra-low power consumption, 50 mW at TX and 150 mW at RX, in the RF section.

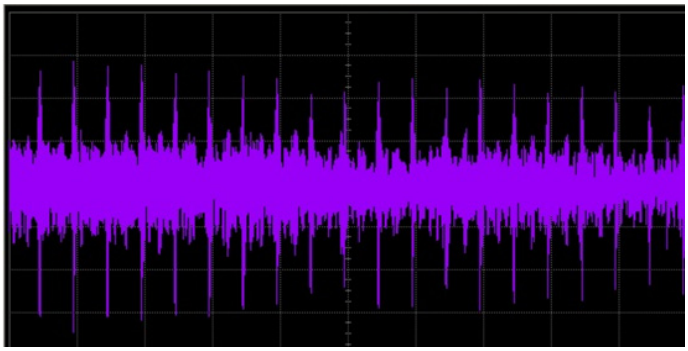

Fig. 8 Measured correlation signals of RX SAW matched filter. 100 nsec/div. The data rate is 20 Mbps.

We have also developed an integrated simulation tool for the UWB communication system that includes RF and baseband circuits. To achieve higher data transmission, the transmission characteristics of the SAW-UWB system using SAW matched filters with narrower pulse interval were calculated by this simulation tool. Our simulation verified that our UWB communication system achieves 112 Mbps data transmission as shown in Fig. 9.

V. Conclusion

We have presented a novel UWB communication system with SAW matched filters, that exploits a unique PPM method and new spreading codes.

We have fabricated UWB modules with SAW matched filters and achieved 20 Mbps (max) real-time video streaming with them. Ultra-low power consumption, 50 mW at TX and 150 mW at RX in the RF component, was obtained with the UWB communication system. The simulation verified that the SAW-UWB system achieves 112 Mbps data transmission. The system is suited to WPANs requiring low power consumption.

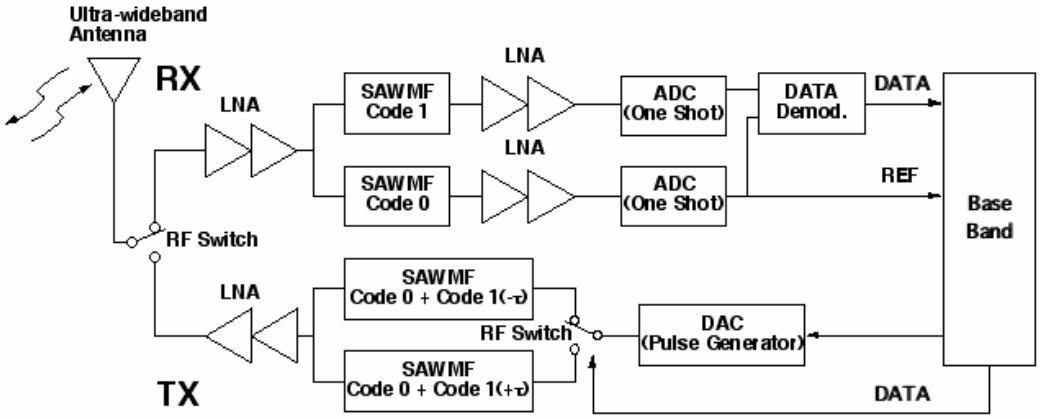

Fig. 7 Block diagram of UWB module with SAW matched filters. The RF section consists of four kinds of SAW matched filters, low-noise amplifiers, pulse generators, converters, and an antenna.

REFERENCES

[1] K. Siwiak, "Ultra-Wide Band Radio: Introducing a New Technology", IEEE Vehicular Technology Conference, May 2001, pp. 1169-1172.

[2] K. Siwiak and D. McKeown, "ultra-wideband radio technology", Wiley, 2004.

[3] S. T. Costanza, P. J. Hagnon and L. A. MacNevin, "Analog matched Filter Using Tapped Surface Wave Delay Line", IEEE Trans. MTT, vol. 17, pp. 1042-1043, 1969.

[4] K. Tsubouchi, H. Nakase, A. Namba and K. Nasu, "Full Duplex Transmission Operation of a 2.45GHz Asynchronous Spread Spectrum Modem using a SAW Convolver", Trans. UFFC, vol. 40, pp. 478-482, 1993.

[5] R. Weigel, C. Knorr, K. C. Wagner, L. Reindl and F. Seifert, "MSK SAW Tapped Delay Lines on LiTaO3 with Moderate Processing Gain for CDMA Indoor and Mobile Radio Applications", Proc. Ultrason. Symp., 1995, pp. 167-170

[6] R. Brocato, E. Heller, J. Wendt, J. Blaich, G. Wouters, E. Gurule, G. Omdahl and D. Palmer, "UWB communication using SAW correlators", IEEE Radio and Wireless Conf. 2004, pp.267-270.

[7] K. Hohkawa, H. Yoshida, C. Kaneshiro and K. Kho, "Design Consideration on Ultra-Wideband-SAW Devices at GHz Frequency Range", Proc. IEEE Ultrason. Symp., 2003, pp.825-828.

[8] H. Nagasaka, T. Sato, T. Sugiura, E. Otobe, M. Hasegawa, K. Tanji, N. Otani and T. Shimamori, "The MODEM for ultra-wideband communication employing surface-acoustic-wave devices", Proc. IEEE Symp. Circuits and Systems, 2005, pp. 3950 – 3953.

[9] T. Sato, T. Sugiura and H. Nagasaka, "Analysis of parasitic effects of GHz-range SAW matched filters for wireless pulse communication systems", Proc. IEEE Ultrason. Symp., 2004, pp. 1533 – 1536.

[10] D. H. Kwon, Y. Kim, M. Hasegawa and T. Shimamori, "A small ceramic chip antenna for ultra-wideband systems", Joint UWBST & IWUWBS, 2004.

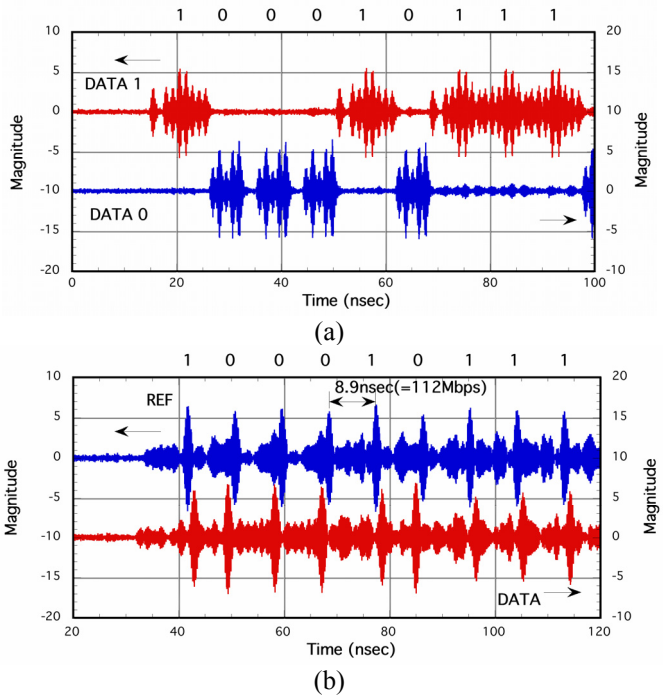

Fig. 9 Simulation results of transmission characteristics of SAW-UWB system with data transmission rate of 112 Mbps. (a) Modulated signals generated by TX SAW matched filter and (b) demodulated signals generated by RX SAW matched filters.

SH-SAW Sensor for Chemical Applications

Jun Kondoh
Graduate School of Science and Technology
Shizuoka University
Hamamatsu-shi, Japan
j-kondoh@sys.eng.shizuoka.ac.jp

***Abstract*—A shear horizontal surface acoustic wave (SH-SAW) has high potential for applying it to a liquid-phase sensor. The SH-SAW sensor can detect loaded mass on the surface, density and viscosity products, permittivity, and conductivity, simultaneously. Therefore, using the SH-SAW sensor, several information of the adjacent liquid are obtained. In this paper, we present fundamental properties of the SH-SAW and its application for evaluating binary-mixture solutions and methanol sensor for a direct methanol fuel cell.**

I. INTRODUCTION

A surface acoustic wave sensor (SAW) is widely used as filter and resonator in high frequency circuit [1]. The SAW propagates on a piezoelectric material surface with concerning its energy near the surface. Therefore, the SAW is influenced by chemical and/or physical changes of an adjacent media and then SAW velocity and amplitude are changed. By detecting the changes, the SAW sensor is realized. As the SAW on the piezoelectric material is coupled wave of particle displacements and static potential, it is varied by mechanical and/or electrical changes of the adjacent medium. Former is called mechanical perturbation and latter electrical perturbation. Simultaneous detection of the perturbations is one feature of the SAW sensor. The SAW sensor is categorized by a propagating mode. Rayleigh-SAW can be applied to only gas sensor [2]. For liquid-phase sensor application, it is necessary to use shear horizontal (SH) mode. In 1987, Moriizumi et al. proposed to use the SH-SAW on 36YX-$LiTaO_3$ for liquid sensing [3]. Then, the authors derived perturbation theories of the SH-SAW sensor for liquid [4]. There are several acoustic wave sensors other than the SAW sensors [5, 6]. Thickness shear mode (TSM) sensor, which is called quartz crystal microbalance (QCM), SH acoustic plate mode (APM) sensor, and Love wave or guided SH-SAW sensor have been developed. The advantage of the SH-SAW sensor is high sensitive and simultaneous detection of liquid mechanical and electrical properties. Especially, as 36YX-$LiTaO_3$ has the high electromechanical coupling coefficient, the SH-SAW sensor, which is fabricated on it, can detect liquid electrical properties with high sensitivity.

In this paper, two applications of the SH-SAW are described. First, the evaluation of binary-mixture solutions of glucose and ethanol is presented. The aim of this research is to apply the SH-SAW sensor for fermentation process monitoring. The second is the detection of methanol concentration. The development of fuel cells has rapidly progressed due to environmental issues regarding global warming and the need for a substitute fuel for petroleum [7]. A direct methanol fuel cell (DMFC) is one of such cells, in which methanol is used as the raw material. A peculiarity of the DMFC is the possibility of miniaturization, so it can be used as a cell for mobile electronics, such as laptop PCs. As the efficiency of the DMFC depends on the concentration of methanol, a methanol sensor is required. As the SH-SAW sensor can detect the permittivity of the solutions, the detection of methanol concentration at high temperature is performed. Moreover, the influence of the formic acid is discussed.

II. DETECTION MECHANISM

The velocity and field distributions of the SAW are calculated by the Campbell and Jones method [9]. Table I summarizes the velocity and particle displacement ratio at surface, when pure water was loaded onto the 36 YX-$LiTaO_3$. It is found from the table that the propagating wave on the 36YX-$LiTaO_3$ is the SH mode. Figure 1 shows the SH particle displacement, u_2, and piezoelectric potential, ϕ, profiles at the pure water and 36YX.LT interfaces. Figure 1(b) shows the magnification of the SH particle displacements in the water. Subscripts of f and s mean the electrical free and shorted surfaces, respectively. When the surface is electrically shorted, the potential becomes to zero.

Table I. SAW velocity and particle displacement ratio at propagating surface. Propagating surface is free or shorted. The particle displacements of u1, u2, and u3 show those of x1, x2, and x3 directions in Fig.3 respectively.

Surface	Velocity (m/s)	Particle displacement ratio (u1 : u2 : u3)
Free	4161.7	0.011 : 1.0 : 0.093
Shorted	4110.8	0.030 : 1.0 : 0.13

This work was partially supported by Industrial Technology Research Grant Program in '05 from New Energy and Industrial Technology Development Organization (NEDO) of Japan.)

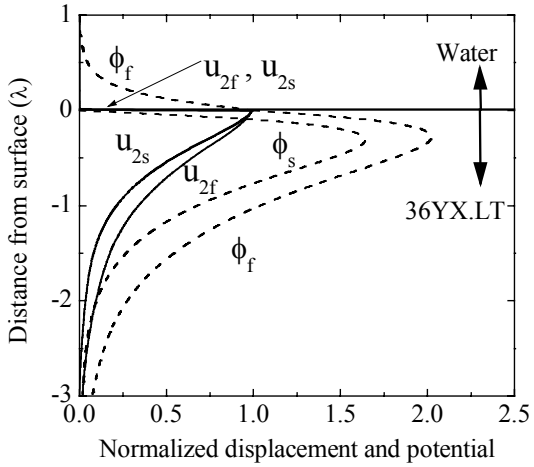

(a)

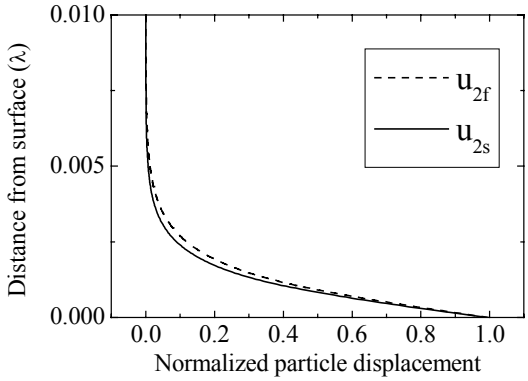

(b)

Figure 1. (a) Particle displacement, u_2, and piezoelectric potential, ϕ, profiles at the interface between 36YX.LT and water. (b) Magnification of particle displacement profiles in water. Subscripts of s and f mean electrical shorted and free surfaces, respectively. Here, λ : wavelength.

In such case, only particle displacement interacts with the adjacent liquid. This interaction is called as the mechanical perturbation or mechanical interaction. On the other hand, the particle displacement and potential interact with the adjacent liquid, when the propagating surface is electrical free. Interaction between the potential and the adjacent liquid is called as the electrical perturbation or the acoustoelectric interaction. If the electrical perturbation is only detected, the mechanical perturbation must be canceled.

III. THREE-CHANNEL SH-SAW SENSOR

Based on the detection mechanisms of the SH-SAW sensor, we designed a three-channel SH-SAW sensor as shown in Fig. 2 [9]. The propagating surfaces of channels 1 and 2 are metallized and electrically shorted by gold and chromium evaporated films. Channel 3 has a free surface area in a propagating surface. Two Liquid cells were placed on the propagating surface, as shown in Fig. 3. Reference or sample liquids are injected into the cells. The liquid cell on channel 1 is for reference liquid. Reference or samples are

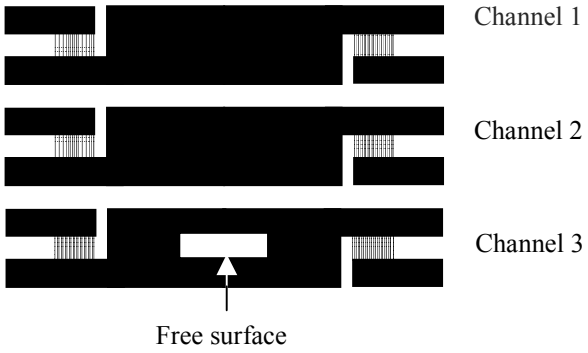

Figure 2. Schematic drawing of the three-channel SH-SAW sensor.

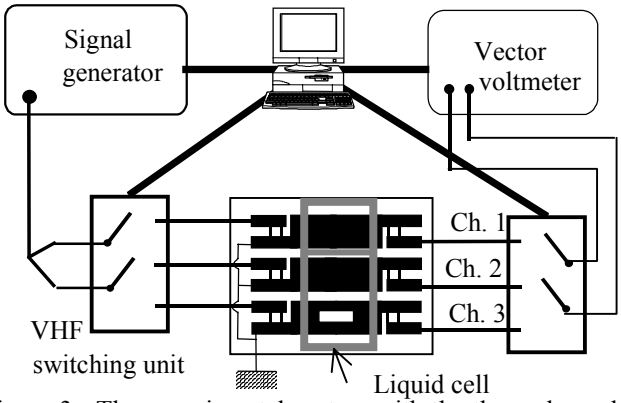

Figure 3. The experimental system with the three-channel SH-SAW sensor.

putted into the other cell on the channels 2 and 3. The differential signals between channels 1 and 2 involve the information about the mechanical properties of liquid and mass loading effect onto the surface. On the other hand, the electrical properties of liquid are obtained from the differential signals between channels 2 and 3. In this case, the mechanical perturbations are cancelled due to measuring the differential signals. Center frequency of utilized SH-SAW sensor is 50 MHz.

The experimental system is illustrated in Fig. 3. The system consists of a signal generator (Anritsu MG3601A), a vector voltmeter (Agilent 8508A), and a VHF switching unit (HP 3488A). All systems are controlled by an external PC via GPIB. The VHF switching unit was used for selecting the two channels of the three-channel SH-SAW sensor. The phase and amplitude are obtained from the vector voltmeter. A velocity shift, $\Delta V / V$, and an attenuation change, $\Delta\alpha / k$, are derived from the phase shift and amplitude ratio between reference and sensing channels. Here, k is a wave number.

IV. APPLICATION OF THE SH-SAW SENSOR

A. Evaluation of binary-mixture solutions

In the fermentation process, the glucose changes to alcohol due to catalytic reaction of the brewer's yeast at the anaerobic environment. One application of the SH-SAW

sensor is a monitoring system for a fermentation process for alcohol drink. At initial stage of this research, binary mixture solutions of glucose and methanol were measured. Four-dimensional date, which were phase shift and amplitude ratio between channels 1 and 2 and between channels 2 and 3, were obtained from a measurement. Five measurements were performed for each sample. All results of glucose and ethanol aqueous solutions are plotted in Fig. 4. The abscissa is concentration and the ordinates are phase shift or amplitude ratio between the reference and sensing channels. As the sample solutions were nonelectrolytes, similar results were obtained. The density and viscosity products increase with increasing the concentration, the phase shift and the amplitude ration between channels 1 and 2 decrease. The phase shift and the amplitude ration between channels 2 and 3 increase due to change of the electrical properties. Whereas magnification of phase shift for the ethanol solution is larger than that foe the glucose solution, it is difficult to evaluate the binary mixture solutions on the basis of the phase shift and amplitude change.

To evaluate the results, principal component analysis (PCA) was used [10]. The PCA transforms the original data set of variable into a smaller set of linear combination. The purpose of the PCA is to determine factors, which are called as principal components, in order to explain as much of the total variation on the data as possible with as a few factors as possible. Figure 5 shows the calculated results. The abscissa is the first principal component (PC1) and the ordinate the second principal component (PC2). The contribution ratios for PC1 and PC2 were 86.7 % and 11.5 %, respectively. These values mean that the information loss from the original four-dimensional data set is 1.8%. The PC1 indicates the concentration of the sample. Minus side of the PC2 is the glucose solutions and plus side of that is ethanol solutions. Therefore, using this figure, the evaluation of the samples can be carried out.

The mixed solutions of glucose and ethanol solutions were prepared and measured using the three-channel SH-SAW sensor. The obtained results were calculated on the basis of the PCA. The results are shown in Fig. 6. In the figure, the mixed solutions of 20 wt.% glucose and 20 vol.% ethanol, and 20 wt.% and 15 vol.% ethanol are plotted. The mixture ratio of the both samples is also written in Fig. 6. The points of the mixed solution locate on the line between the glucose and ethanol solutions. With increasing the ratio of ethanol, the points approach to the ethanol solution. Other glucose and ethanol solutions were also mixed, measured, and calculated. Similar results with Fig. 6 were obtained. Therefore, we have concluded that the three-channel SH-SAW sensor is able to apply for evaluation of the binary-mixture solutions.

B. Measurements of methanol concentration

The permittivity of the methanol solution is changed by changing its concentration. In the measurements, the SH-SAW sensor with Ch. 2 and Ch. 3 were used. The operating temperature of the DMFC is normally higher than 50° C. To apply the SH-SAW sensor for the methanol sensor of the DMFC, we must know the relationships between concentration, temperature and sensor responses. For this purpose, a desktop high-temperature chamber (Espec ST-120) was used for temperature control. The SH-SAW sensor with a liquid cell was placed into the chamber. Temperature was varied from 25 ºC to 60 ºC. Temperature was measured using a thermocouple thermometer (Fluke 51K/J). Also, methanol concentration was varied from 0 to 50 % by weight. Distilled water at 25 °C was used as the reference solution.

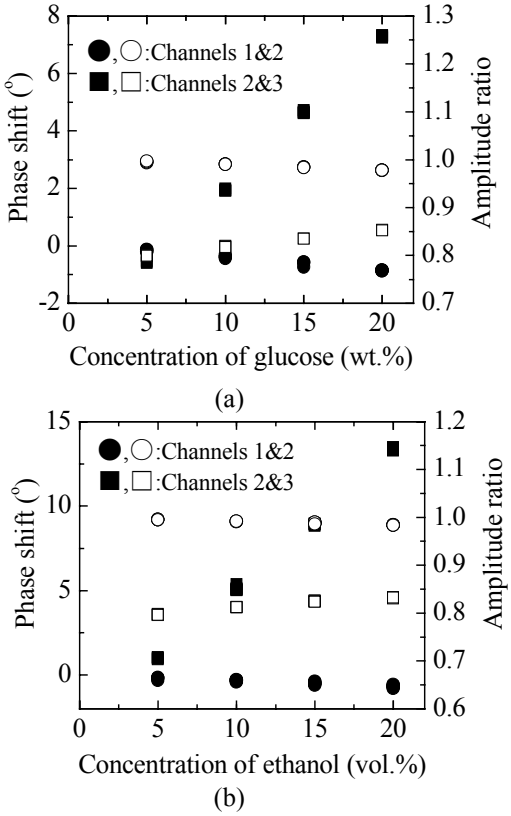

Figure 4. Phase shift and amplitude ratio between channels 1 and 2, or channels 2 and 3 as a function of concentration. (a) Glucose solution and (b) ethanol solution. ● and ■: phase shift, ○ and □: amplitude ratio.

Experimental results of the phase shift between reference water and samples are shown in Fig. 7. The lines in the figure are the best-fit lines. Linear relationships between concentration and phase shift are obtained. The slope increases with temperature. In other words, the sensitivity of the SH-SAW sensor increases with temperature. Also, high correlation coefficients are obtained. The concentration resolution was estimated on the basis of time stability. Concentration resolutions at 25 °C and 60 °C are 0.13 and 0.10 % by weight, respectively. The optimum concentration of methanol is determined for a DMFC. The estimated concentration resolution is sufficient for practical purposes.

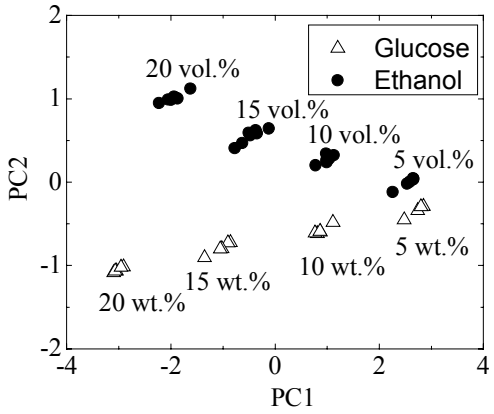

Figure 5. Scatter diagram of the experimental results of glucose and ethanol solutions.

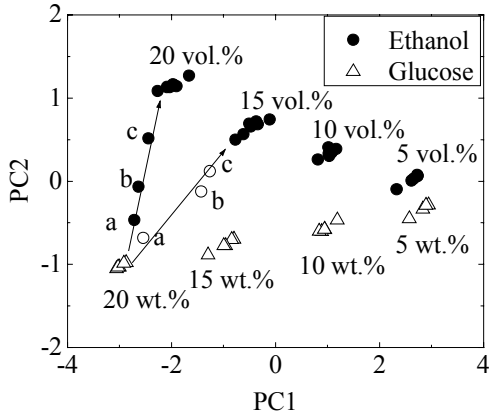

Figure 6. Estimation of glucose and ethanol mixture solutions with PCA. ● and ○: mixture solutions of 20 wt.% glucose and 20 vol.% ethanol, and 20 wt.% glucose and 15 vol.% ethanol. Labels, a, b, and c, show the mixing rations of 3:1, 1:1, and 1:3, respectively.

During electrode reactions in DMFC, hydrogen ions are generated from the methanol [7]. During the process of the electrode reaction, formic acid is also generated [7]. As the formic acid is mixed in the methanol solution, it is necessary to consider the method of methanol determining concentration in methanol-formic acid binary-mixture solution. The concentration of the formic acid in solutions is known to be less than 0.1 % by weight. Figure 8 shows the measured results of the mixture solution. The concentration of methanol was fixed at 10 % by weight. When the formic acid is not involved in the solution, the methanol concentration can be determined from the phase shift, as shown in Fig. 8. For the mixture solution, however, the sensor responses become complicated, because the conductivity increases with the formic acid concentration. Phase shift and amplitude ratio decrease with increasing formic acid concentration. These results are reasonable.

To consider the method of determining the methanol concentration, $\Delta V/V$ and $\Delta\alpha/k$ are derived from phase shift and amplitude change, respectively. The obtained values are plotted on the $\Delta V/V$-$\Delta\alpha/k$ plane, as shown in Fig. 9. The

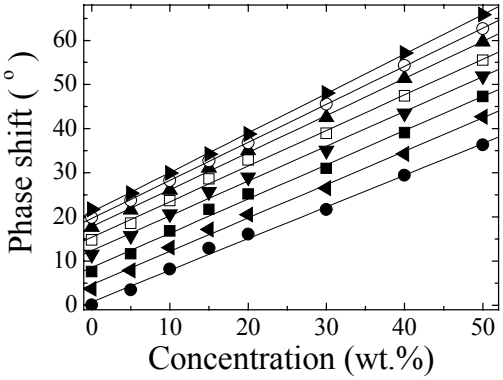

Figure 7. Experimental results of methanol solution. Symbols shows the temperature, as follows: ● 25 °C, ◀ 30 °C, ■ 35 °C, ▼ 40 °C, □ 45 °C, ▲ 50 °C, ○ 55 °C, and ▶ 60°C.4

plotted data were measured at room temperature. The dots denote the experimental data. M and F in the figure represent methanol and formic acid, respectively. The numbers indicate the concentration. For example, M5 is 5 % methanol by weight and M10+F0.1 is the mixture solution of 10 % methanol and 0.1 % formic acid. Straight lines in the figure are used to connect points. Now we consider the quadrilateral ABCD. Segments AD and AB indicate the

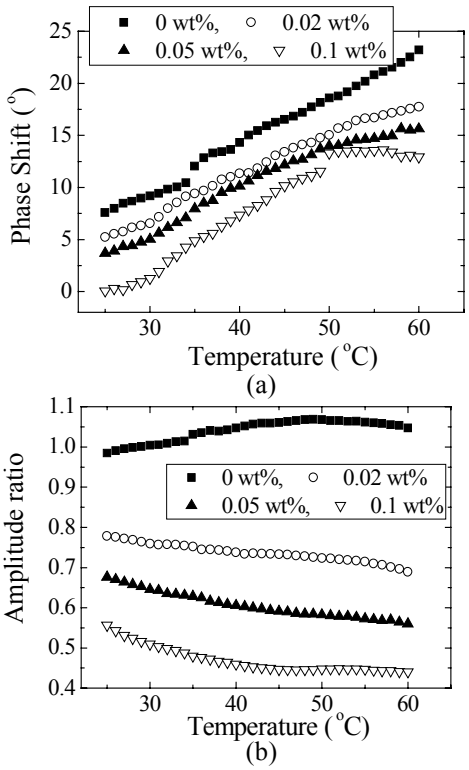

Figure 8. Experimental results of methanol and formic acid binary-mixture solution. (a) Phase shift and (b) amplitude ratio. Methanol concentration is fixed at 10 % by weight and formic acid concentration is a parameter.

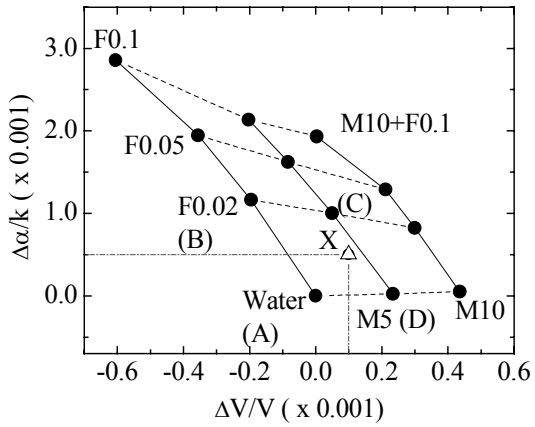

Figure 9. Evaluation of methanol and formic acid binary-mixture solutions. Black circles: experimental results, X (triangle): unknown sample. M and F denote methanol and formic acid, respectively. The numbers indicate the concentration of the solution.

concentrations of methanol (0-5%) and formic acid (0-0.02%), respectively. The measured data on $\Delta V/V$-$\Delta\alpha/k$ plane was performed the coordinate formation to AD-AB plane, and the concentrations were estimated using following equations.

$$x=21014(\Delta V/V) + 3543(\Delta\alpha/k) \quad (1)$$

$$y=-1.683(\Delta V/V) + 17.52(\Delta\alpha/k) \quad (2)$$

Where x and y are the concentrations of methanol and formic acid, respectively. For example, the experimental result of the unknown concentration is located at the point (X) denoted by a triangle in the figure. The results of velocity shift and attenuation change were substituted into eqs. (1) and (2). The estimated results are 3.9 % methanol by weight and 0.009 % formic acid by weight.

V. CONCLUSIONS

The advantage of the SH-SAW sensor on the 36YX.LT is simultaneous detection of the liquid properties. The three-channel SH-SAW sensor is proposed for the purpose. In this paper, the three-channel SH-SAW sensor is applied for evaluating of the mixed solutions of glucose and ethanol. The mixture solutions are evaluated using the PCA. Then, the SH-SAW sensor is applied for methanol concentration detection for the DMFC. The experimental results indicate that the sensitivity increases with temperature. Also, the resolution was derived from the experimental results to be 0.10 % by weight at 60°C. Therefore, the SH-SAW sensor is suited for use as a methanol sensor for DMFC. Moreover, the influence of formic acid was considered. A method of estimating methanol concentration in methanol and formic acid mixture solution was examined. A simple and effective method was proposed. Developing a SH-SAW sensing system for DMFC is future work.

ACKNOWLEDGMENT

The author thanks Dr. Showko Shiokawa, Mr. Yoshikazu Matsui for advises and comments for works.

REFERENCES

[1] M. Kadota, "Development of Substrate Structures and Processes for Practical Applications of Various Surface Acoustic Wave Devices, " Jpn. J. Appl. Phys., 44, pp.4285-4291 (2005).

[2] H. Wohltjen, R. Dessy, "Surface Acoustic Wave Probe for Chemical Analysis. I. Introduction and Instrument Description," Anal. Chem., 51. 9, pp.1458-1464 (1979).

[3] T. Moriizumi, Y. Unno, S. Shiokawa, "New Sensor in Liquid Using Leaky SAW", Proc. IEEE US Symp., pp.579-582 (1987).

[4] J. Kondoh, S. Shiokawa, Liquid Sensor Based on a Shear Horizontal SAW Device, Trans. IEICE, J75-C-II, 5, pp.224-234, May 1992 [in Japanese]; [translation] Electronics and Communications in Japan Part II: Electronics, 76, 2, 69-82, 1993.

[5] D. S. Ballantine, R. M. White, S. J. Martin, A. J. Ricco, E. T. Zellers, G. C. Frye, H. Wohltjen, Acoustic Wave Sensors, Academic Press, 1997.

[6] S. Shiokawa, J. Kondoh, Surface Acoustic Wave Microsensors, Trans. IEICE, J78-C-I, pp. 573-579, November 1995 [in Japanese]; [translation] Electronics and Communications in Japan Part II, 79, pp.42-50, 1996.

[7] J. Larmine, A Dicks, "Fuel Cell Systems, Explained," Tokyo: Ohmsha, 2004 (Japanese edition).

[8] J. J. Campbell, W. R. Jones, Propagation of Surface Waves at the Boundary Between a Piezoelectric Crystal and a Fluid Medium, IEEE Trans. Sonics and Ultrasonic., SU-17, 2, pp.71-76, 1970.

[9] J. Kondoh, K. Saito, S. Shiokawa, H. Suzuki, "Simultaneous Measurements of Liquid Properties Using Multichannel Shear Horizontal Surface Acoustic Wave Microsensor," Jpn. J. Appl. Phys., 35, 5B, pp.3093-3096 (1996).

[10] W. R. Dillon, M. Goldstein, Multivariate Analysis, John Wiley & Sons, Chap.2, 1994.

Liquid-Phase Sensor Using SH-SAW on Quartz

Hiromi Yatsuda and Takashi Kogai
Japan Radio Co., Ltd.

***Abstract*— In order to realize miniature biosensors for real-time, rapid and direct detection, a liquid-phase sensor using shear horizontal surface acoustic waves (SH-SAWs) on ST-cut quartz is presented. On the sensor chip, there is an SH-SAW delay line that is composed of a transmitting interdigital transducer (IDT), receiving IDT and a biochemical reaction area in between them. The biochemical reaction area is surrounded with epoxy wall to protect the IDTs from liquid. In order to evaluate the performance of an SH-SAW delay-line sensor, C-reactive protein antibodies with different concentrations are provided to the biochemical reaction area. The phase changes in the S21 response of a 250 MHz SH-SAW delay-line at a fixed frequency are measured on real-time and it is confirmed that different phase changes are obtained for different antibody concentrations. Furthermore, a concept of one-chip biosensor system that is composed of SH-SAW delay lines for sensing and additional IDTs to excite Rayleigh type SAWs for SAW streaming on a chip. In this paper, one-chip quartz-based liquid-phase SH-SAW delay-line sensor systems with pumping and agitating functions using Rayleigh type SAWs are demonstrated.**

Keywords; Sensor; SAW; SH-SAW; C-reactive protein;

I. INTRODUCTION

Miniature and low-cost liquid-phase sensor systems have been required in some applications such as environment, food industry, medicine and so on. Miniaturization can allow not only to realize portable but also to reduce the reagent volume and to shorten process time by diffusion driven reactions. Those sensor systems [1], such as a lab-on-a-chip or micro total analysis systems (uTAS), generally require a sensing function in liquid-phase and a fluidic function on the chip.

Acoustic wave based sensors are suitable for miniaturization. Those sensors have been successfully investigated for the detection of bio-chemical compounds due to the need for real-time, rapid and direct detection where the device is in direct contact with the solution. Quartz crystal microbalances (QCMs) are one of the most popular acoustic devices in the field of bio-chemical applications and there are many papers about QCM immunosensors [2]. On the other hand, it has been known that shear horizontal surface acoustic waves (SH-SAWs) are suitable for liquid-phase sensors [3-5]. Since SH-SAW has a horizontal polarization in the direction normal to the propagation direction parallel to the substrate, the SH-SAW energy is less radiated into the liquid. Although some SH-SAWs exist on several substrates, $LiTaO_3$ [3], $La_3Ga_5SiO_{14}$ [4] and Quartz [5], the liquid sensing systems using SH-SAW on $LiTaO_3$ substrate to detect the density and viscosity products, relative permittivity and conductivity of the liquid have been studied for a long time. However, there has been a few papers for miniature one-chip biosensor using acoustic sensor devices.

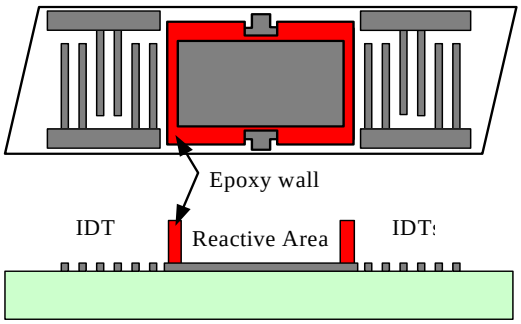

Figure 1. Configuration of SH-SAW liquid-phase sensor.

On the other hand, since a Rayleigh type SAW can be attenuated in liquid, it has been believed that the SAW cannot be utilized for liquid-phase sensor devices. However, after the phenomena that liquid on the surface of the device is dynamically moved and streamed toward the SAW propagation direction was found [6], some papers about the positioning systems of small liquid droplet using SAW [7,8] have been published. In those papers, $LiNbO_3$ substrates were generally used for the SAW fluidic-systems because there are some SAWs with a large electro-mechanical coupling coefficient that can be efficiently excited along some axes within the wafer plane.

This paper shows experimental results of quartz-based SH-SAW liquid-phase sensors using C-reactive protein and gives a concept of one-chip biosensor systems using SAW and SH-SAW. On one-chip sensor devices, the SH-SAWs can be utilized for sensing and the SAWs can be utilized for pumping or agitating. This work is the first step for a one-chip multifunctional biosensor or “lab-on-a-chip”.

II. SH-SAW DELAY LINE SENSOR WITH LIQUID CELL SURROUNDED WITH EPOXY

SH-SAWs on ST-cut Quartz substrates have a big advantage of excellent temperature stability in contrast to other SH-SAWs on $LiTaO_3$ substrate. The first order temperature coefficient of SH-SAW on Quartz is almost zero and the second order temperature coefficient is around -0.04 ppm / $°C^2$. On the other hand, the SH-SAW on $LiTaO_3$ substrate has a temperature coefficient of about -35 ppm / °C . In order to evaluate the basic performance of the SH-SAW liquid-phase sensor on Quartz, we designed an SH-SAW delay-line on 37° rotated y-cut Quartz substrate with a liquid cell as shown in Fig. 1. The transmitting and receiving SH-SAW IDTs are placed with a center-to-center distance of 6 mm between them. A liquid cell is placed between the IDTs that was surrounded with epoxy wall in order to protect the IDTs from liquid. The electrode periodicity of the IDT is a 20-micron-meter wavelength with double electrode fingers and the center frequency of the SH-SAW delay-line is around 250 MHz. The IDTs have an aperture of 2 mm and a number of finger pairs of 50. In the liquid cell, there is a reaction surface that was covered with evaporated gold film. The reaction surface was surrounded with epoxy wall with a height of about 60 micron meters. The wall was realized by a photo-lithography technique using photosensitive epoxy film with a 60 micron meters thickness, that is a popular material for Micro Electro Mechanical Systems technology. The SH-SAW can be attenuated under the epoxy wall. The propagation loss of about 0.75 dB/wavelength at 250 MHz SH-SAW was obtained in our experiments. The photolithography technique provided a thin wall with a thickness of 40 micron meters or about two wavelengths for the 250 MHz device. Then the increase of insertion loss of SH-SAW delay-line due to epoxy wall was about only 3 dB.

The frequency response of the SH-SAW delay-line sensor device is shown in Fig. 2. The dashed line shows the response without water. The insertion loss was 27 dB including the propagation loss of 3 dB at epoxy wall. The solid line shows the response with water. The increase of the insertion loss was about 12 dB due to liquid-phase sensing on the shorted layer at reaction area.

A schematic diagram of the measurement system is shown in Fig. 3. The sensor devices are placed in the oven with a constant temperature at a 25 degree centigrade. The phase response and the insertion loss of the SH-SAW delay-line are measured using a vector network analyzer and a personal computer. When the SH-SAW is propagating at the reaction area, the SH-SAW propagation characteristics which are the phase response and insertion loss can be changed.

Since the surface of the reaction area was covered with evaporated gold film, the mechanical perturbation can be efficiently detected. Then when buffer liquid with antibodies is injected into the liquid cell, the antibodies can be absorbed onto the gold surface. The velocity of the SH-SAW at the reaction area covered with gold film can be changed due to antibodies absorption. Figure 4 shows some experimental results using buffer liquid with C-reactive protein antibodies [2]. C-reactive protein antibodies with different concentrations were provided to the biochemical reaction area. The phase change in the S21 response of the SH-SAW delay-line at a fixed frequency has been monitored on real-time. In Fig. 4, the vertical axis is the

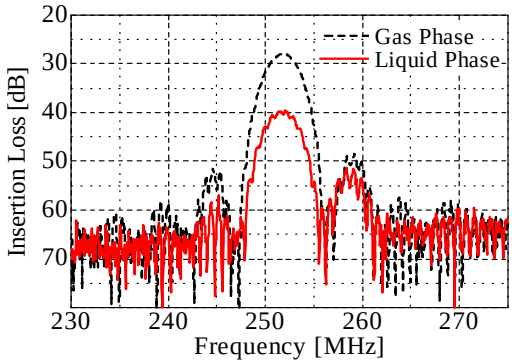

Figure 2. Frequency responses of SH-SAW liquid-phase sensor.

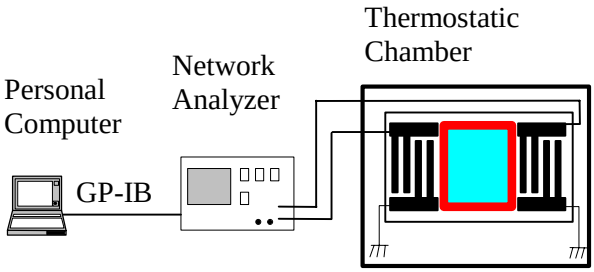

Figure 3. Measurement system.

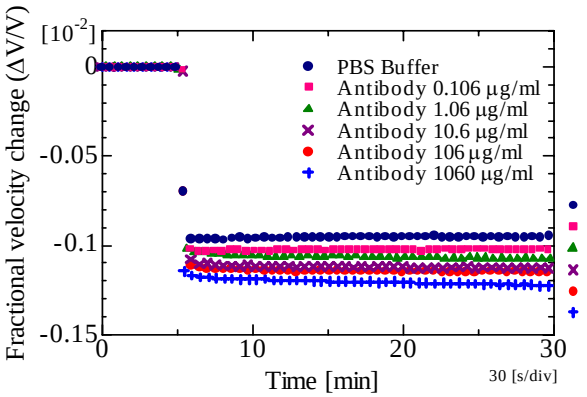

Figure 4. Fractional SH-SAW velocity changes with different antibody concentrations.

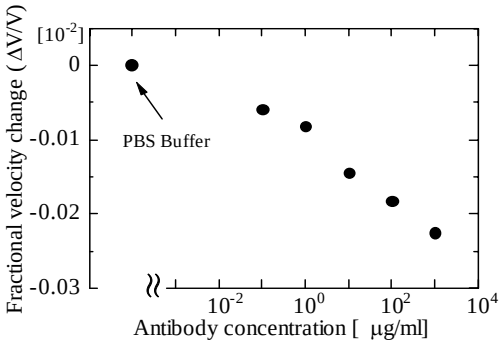

Figure 5. Fractional SH-SAW velocity changes with different antibody concentrations.

fractional velocity change of the SH-SAW that was obtained from the measured S21 phase changes. SH-SAW velocity can be changed by surface condition with antibody adsorption on the reaction area. It was confirmed that different velocity changes were obtained with different antibody concentrations. Antibody in the buffer can be adsorbed spontaneously to the gold surface on the reaction area in liquid-phase. The fractional velocity changes versus C-reactive protein antibody is shown in Fig. 5. The insertion losses were almost the same with different concentrations in liquid-phase. On the other hand, after rinsing and drying, the S21 responses were measured again. The insertion losses and fractional velocity changes are shown in Fig. 6 and Fig. 7, respectively. The results indicate that antibody in the buffer can be adsorbed spontaneously to the gold surface on the reaction area, even though after rinsing and drying.

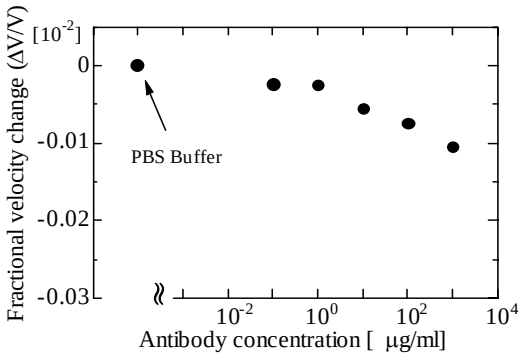

Figure 6. Fractional SH-SAW velocity changes with different antibody concentrations after rinse and dry.

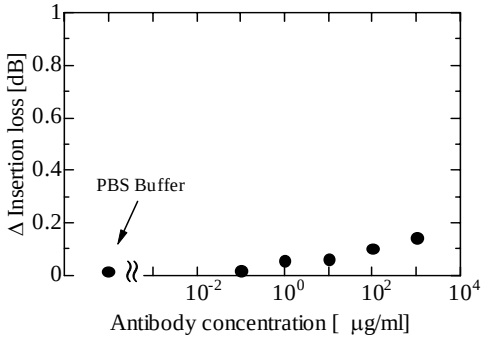

Figure 7. Insertion loss changes with different antibody concentrations after rinse and dry.

III. One-Chip Liquid-Phase Sensor Using SAW and SH-SAW

Two different acoustic waves, a Rayleigh type SAW and an SH-SAW can be efficiently excited on 37° rotated Y-cut Quartz substrate as shown in Fig. 8. The Rayleigh type SAW on 37° rotated Y-cut Quartz substrate can be effectively excited to x-direction on the surface. The elector-mechanical coupling coefficient of the SAW is about 0.16 %. It is not so big but good enough to excite SAW that can push or agitate a droplet on the substrate. On the other hand, the SH-SAW can be efficiently excited normal to the direction of the SAW propagation direction on the substrate. The SH-SAW can be suitable for liquid-phase sensors that can provide real-time, rapid and direct detection where the device is in direct contact with the solution.

A concept of one-chip liquid-phase sensor on Quartz substrate is shown in Fig. 9. On the sensor chip, there is a SH-SAW delay-line that is composed of a transmitting interdigital transducer (IDT), receiving IDT and a biochemical reaction area in between them. And there is another IDT that excites a Rayleigh type SAW to push or agitate a droplet. When a Rayleigh type SAW is propagating under the droplet on the substrate, the SAW is attenuated and radiated a longitudinal wave into the droplet [8]. If the SAW amplitude is high enough, the force induced by acoustic streaming is high enough to push the droplet in the SAW propagation direction. When the SAW amplitude is low, the droplet cannot be moved but the longitudinal wave that was radiated into the droplet can shake or agitate the droplet.

Two types of one-chip sensors using SAW and SH-SAW were demonstrated for pumping and agitating. Figure 9 shows the one-chip sensor system using a 50 MHz SAW and a 250 MHz SH-SAW in this study.

A. One-chip sensor using SAW for pumping

For biosensor devices, some processes may be required, which are to inject a droplet to the reaction area, to rinse the reaction surface and to react the immunoassay at the reaction area. After the droplet with 20 micro litters is placed at the

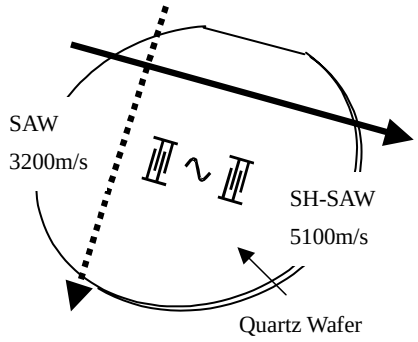

Figure 8. SAW and SH-SAW on Quartz substrate.

dispense area using a dispense machine, the droplet can be transported to the reaction area by the SAW launched at the SAW IDT. The Figure 10 shows an experimental result of this process. The insertion loss and phase changes of the SH-SAW delay-line response were measured during some steps, 1)a droplet with Latex with 20 micro litters was dispensed at the dispense area, 2)after 7.5 minutes, the SAW was exited for 2 minutes. As shown in Fig. 10, the droplet was transported to the reaction area by the SAW and the fractional velocity change of the SH-SAW delay-line was observed.

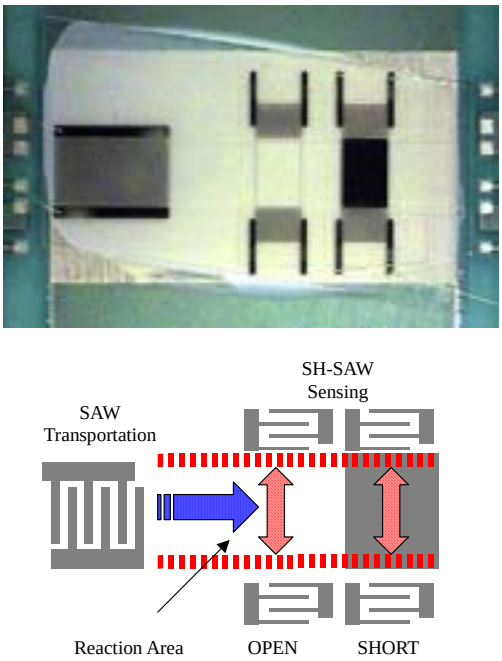

Figure 9. One-chip SH-SAW sensor with pumping and agitating system using SAW.

B. *One-chip sensor using SAW for agitating*

Figure 11 shows the insertion loss and phase changes of the SH-SAW delay-line response. Those were measured during some steps, 1)started the measurement, 2)after 5 minutes, a droplet with Latex with 20 micro litters was dispensed at the reaction area, 3)after 10 minutes, the SAW was exited for 2 minutes.

After the droplet was injected into the reaction area, the SH-SAW velocity was changed slowly for the next 10 minutes. After the SAW was excited, the SH-SAW velocity was changed rapidly. It means that the reaction between the gold layer on the reaction area and Latex in liquid can be accelerated by the SAW. The SAW can be used for agitating or mixing the liquid.

IV. CONCLUSION

A concept of a one-chip biosensor system using SAW and SH-SAW was presented. The SH-SAW can be utilized for sensing and the SAW can be utilized for pumping or agitating. On the sensor chip, there is an SH-SAW delay-line that is composed of a transmitting IDT, receiving IDT and a biochemical reaction area in between them. And there is another IDT on the sensor chip that can excite a Rayleigh type SAW to carry a droplet or to agitate a droplet at the biochemical reaction area. The one-chip quartz-based liquid-phase SH-SAW delay-line sensors with pumping and agitating functions using SAW were demonstrated. This work is the first step for a one-chip multifunctional biosensor or "lab-on-a-chip".

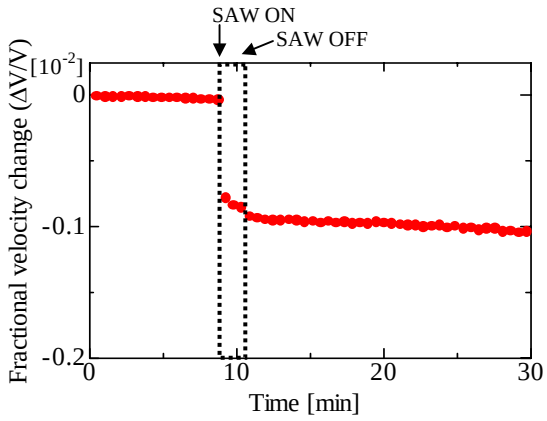

Figure 10. Experimental result of pumping system using SAW.

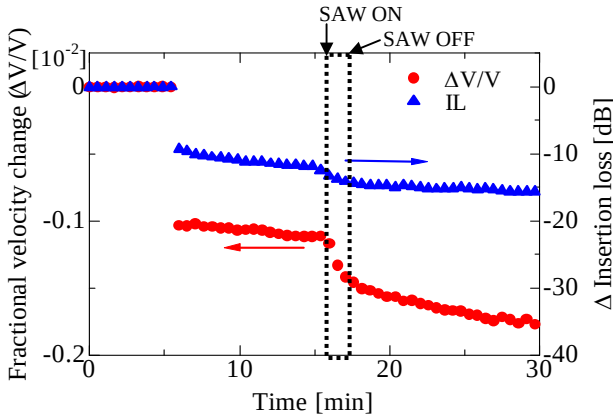

Figure 11. Experimental result of agitating system using SAW.

REFERENCES

[1] Kiichi Sato, Emi Mori, Masaya Kakuta, Manabu Tokeshi and Takehiko Kitamori, "Automatud micro ELISA sysyrm toward clinical diagnosis; determination of a heart failure marker, BNP," Micro TAS 2004, pp.135-137.

[2] S. Kurosawa, M. Nakamura, H. Aizawa, JW Park, M. Tozuka, K. Kobayashi, K. Yamada and M. Hirata, "Immunosensor for C-reactive protein using anti-CRP monoclonal antibody and its F(AB')$_2$ fragment immobilized quartz crystal microbalance," in proc IEEE Freq. Cont. Symp., 2002, pp.273-275.

[3] T. Moriizumi, Y. Unno, and S. Shiokawa, "New sensor in liquid using Leaky SAW," in proc IEEE Freq. Cont. Symp., 1987, pp.579-582.

[4] Eric Berkenpas, Shivashanker Bitla, Paul Millard and Mauricio Pereira da Cunha, "Pure Shear Horizontal SAW Biosensor on Langasite," IEEE Trans. Ultrason., Ferroelect,. Freq. Contr.,vol.51, 2004, pp.1404-1411.

[5] May Tom-Moy, Richard L. Baer, Darlene Spira-Solomon, and Thomas P. Doherty, "Atrazine Measurements Using Surface Transverse Wave Device," Anal. Chem 1995, 67,1510-1516.

[6] S.Shiokawa, Y.Matsui, and T. Moriizumi, "Experimental study on liquid streaming by SAW," Jpn J. Appl. Phys., vol 28, 126-128, 1989.

[7] K. Chono, N. Shimizu, Y. Matsui, J. Kondoh and S. Shiokawa, "Novel atomization method based on SAW streaming, " in proc IEEE Freq. Cont. Symp., 2003, pp.1786-1789.

[8] Christoph J. Strobl, Zeno von Guttenberg, and Achim Wixforth, "Nano- and Pico-Dispensing of Fluids on Planar Substrates Using SAW," IEEE Trans. Ultrason., Ferroelect,. Freq. Contr.,vol.51, 2004, pp.1432

Passive, Wireless, Orthogonal Frequency Coded SAW Sensors and Tags –Design and Systems

D.C. Malocha, D. Puccio and N. Saldanha – Lobo
School of Electrical Engineering & Computer Science
University of Central Florida, Orlando, Fl. 32816-2450
dcm@ece.engr.ucf.edu

Abstract- This paper presents the concept of orthogonal frequency coding (OFC) for applications to SAW device technology. OFC is the use of orthogonal frequencies to encode a signal, which spreads the signal bandwidth in a manner similar to a fixed M-ary frequency shift signal.[1-3] Also, a pseudo noise (PN) sequence can be added for additional coding. The OFC technique provides a wide bandwidth spread spectrum signal with all the inherent advantages obtained from the time-bandwidth product increase over the data bandwidth. The theory of OFC is presented and discussed; defining the fundamental equations and showing the time and frequency domain relationships. The application of OFC to SAW devices for tagging will be introduced.

I. I. Introduction

This paper presents the concept of orthogonal frequency coding (OFC) for SAW communication, tag and sensor applications. OFC is a spread spectrum technique for encoding the SAW device which has the inherent advantages of processing gain and security and allows both frequency and PN coding. This paper presents the basic theory, the OFC coding approach, a comparison to other approaches of tagging, SAW device implementation concepts and system considerations.

II. Single Frequency SAW TAG Discussion

Before proceeding to the OFC theory, it is useful to discuss a single frequency tagging SAW approach. This provides a basis for comparison of some properties and parameters. Currently, SAW tags and sensors are commonly implemented using several identical single frequency reflectors. The device is excited with a single carrier RF burst that generates a surface wave that is partially reflected from each of the N inline, unweighted reflectors shown in Figure 1. An amplitude shift keying (ASK) or phase shift keying (PSK) receiver can be used with this device in order to determine the reflected pulse locations that indicate the device code and/or the sensed information.[4-8] Alternatively, tag identification and sensor readout can be accomplished by applying the tag response to a matched filter based on the bit locations and phases [9,10]. In the following discussion, these receiver architectures are investigated with the goal of quantifying tag insertion loss excluding transducer and propagation losses. Figure 1 shows a schematic drawing of a single frequency SAW tag and the desired impulse response.

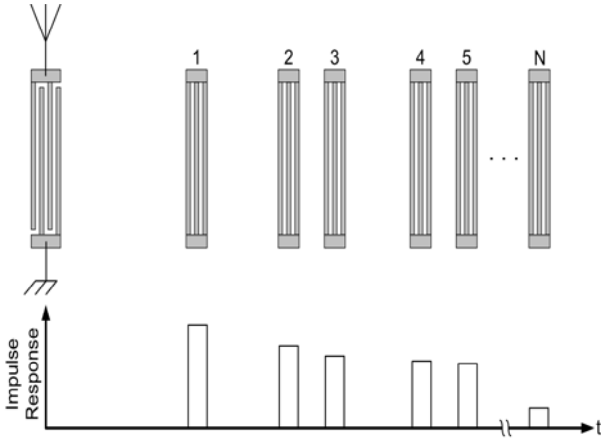

Figure 1. Schematic drawing and impulse response of single frequency SAW ID tag. All reflector gratings are in one track besides the input transducer.

The desired impulse response is a series of reflected pulses with time locations corresponding to the physical locations of the reflectors. The true impulse response of the device shown contains spurious pulses that are generated due to multiple reflections between the reflectors. In the following analysis, these undesired signals are not considered when considering the total power that is returned to the input transducer.

The amount of power received from n^{th} reflector is

$$P(n) = R \cdot T^{2(n-1)} \quad (1)$$

where R and T are the bit power reflection and transmission coefficients, respectively, and, assuming no propagation loss, conservation of power yields

$$R + T = 1 \quad (2)$$

where $R \le 1$ and $T \le 1$. In ASK and PSK receivers, the tag insertion loss is defined by the bit with the lowest power level which, using (1), is the furthest bit from the input transducer. Consequently, it is desirable to choose the reflection coefficient R in order to maximize the power returned from the last bit in the sequence. Given a bit count , N , (1) and (2) are used to define the power received from the last bit as

$$P_{last}(R) = R \cdot (1-R)^{2N-2} \quad (3)$$

The power received from the last bit P_{last} is plotted versus bit reflection coefficient in Figure 2 for three different bit counts.

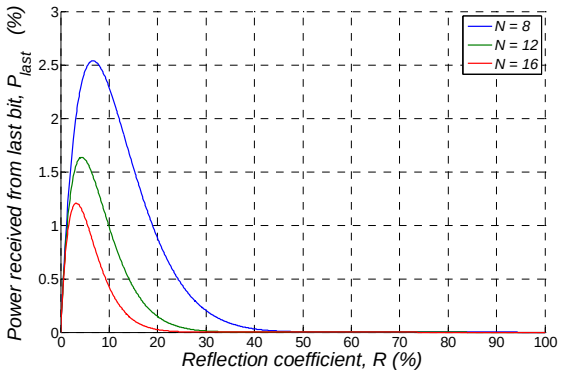

Figure 2. Power received from last bit vs. reflection coefficient, R, in single frequency SAW tag for bit counts equal to 8 (blue), 12 (green), 16 (red).

Note that the optimal reflection coefficients are represented by the peaks in Figure 2, and are defined for a given bit count N as

$$R_{opt}(N) = (2N-1)^{-1} \tag{4}$$

Substituting (4) into (3), the maximum power received from the last bit versus bit count is plotted in. As seen in Figure 3, the loss associated with the last bit is relatively high, which in ASK or PSK systems, limits the SNR accordingly and ultimately leads to a reduction in readout distance. Figure 4 shows the power received from the last bit relative to the first given that the bit reflectivity is R_{opt}. The plot gives a measure of reflected signal power variation versus bit count, N. For increasing bit count, the ratio asymptotically approaches e^{-1}, which implies that maximum power variation in the reflected signal is 4.34 dB.

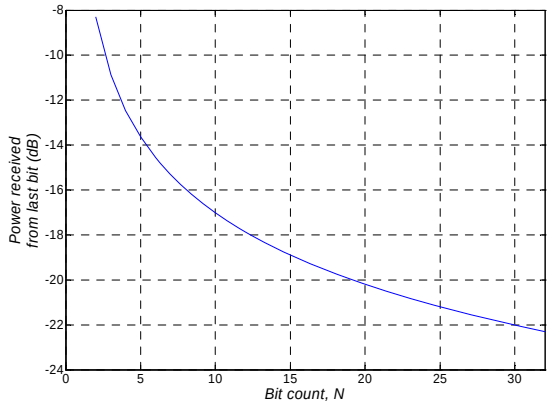

Figure 3. Power received from last bit, in dB, versus bit count N given R_{opt}. The plot gives a measure of tag insertion loss which is shown to be relatively high.

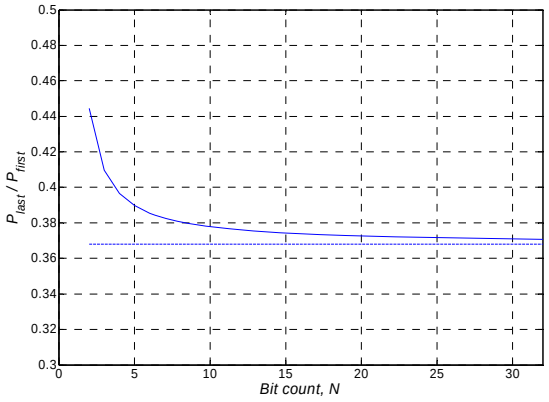

Figure 4. Power received from the last bit relative to the first bit versus bit count N given R_{opt}. Plot demonstrates the amplitude variation of the tag impulse response. For increasing bit count, N, the ratio asymptotically approaches e^{-1}.

The SNR of the single frequency SAW tag system can be improved by applying the received tag signal to a matched filter similar to DS/SS. In addition, the reflectors can be phase coded to provide multiple access operation similar to CDMA communication systems.[9,10] The following analysis considers an optimal reflection coefficient given that a matched filter is used for demodulation. Since the matched filter integrates the power received from all bits in the tag, the tag power is defined by the total amount of reflected power from all N reflectors, and is defined using (1) as

$$P_{tot}(N) = \sum_{n=1}^{N} P(n) = \left(\frac{1-T^{2N}}{1+T} \right) \tag{5}$$

In order to ensure the orthogonality of the PN codes used, the variation in power received from the bits is limited by the equation

$$\frac{P(N)}{P(1)} = \frac{P_{last}}{R} = x \tag{6}$$

where x defines an acceptable ratio of the powers in the last and first bits. For a given power ratio x, the bit transmission and reflection coefficients are defined using Equations (2) and (3) as

$$T = x^{1/(2N-2)}$$
$$R = 1 - x^{1/(2N-2)} \tag{7}$$

Furthermore, the total power received given the requirement in (6) yields

$$P_{tot}(N,x) = \frac{1-x^{N/N-1}}{1+x^{1/(2N-2)}} \tag{8}$$

Equation (8) can now be used to define the single frequency SAW ID tag insertion loss, excluding transducer loss, for a

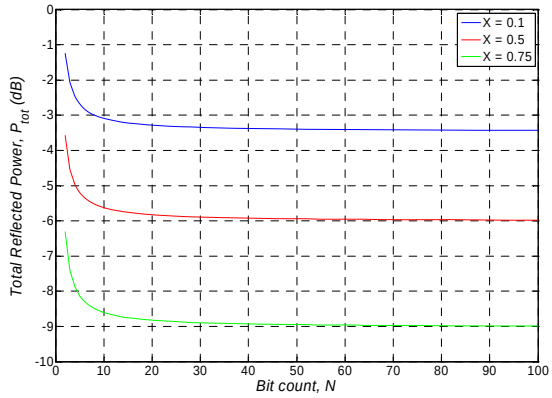

Figure 5. Total reflected power vs. bit count for three bit power variation ratios (blue - 10%, red - 50%, green - 75%).

given bit count N and bit power variation x. The total reflected power that contributes to the correlated compressed pulse is plotted for three bit power variations in Figure 5.

Note the power received is maximized for bit counts under five; however, such low bit counts severely limit the number of identifiable tags. For larger bit counts, the received power approaches a nonzero minimum value defined by

$$P_{tot}(x) = \frac{1-x}{2} \tag{9}$$

Equation (9) provides a theoretical upper limit of 3 dB for the tag loss of a single frequency SAW ID tag with practical code diversity. The 3 dB limit assumes no power is received from the last bit. In practice, a more sensible tag loss is 6 dB assuming that the last bit provides half the power of the first. Equation (9) implies that code diversity can be increased indefinitely with little increase in tag loss; however, what is practically realizable in a SAW device will set an ultimate limit.

III. Orthogonal Frequency Theory

Consider a time limited, nonzero time function defined as[11]

$$h(t) = \sum_{n=0}^{N} a_n \cdot \phi_n(t), \quad |t| \le \frac{\tau}{2}$$

$$= 0, \quad |t| \ge \frac{\tau}{2} \tag{10}$$

$$\text{where} \quad \phi_n(t) = \cos\left(\frac{n \cdot \pi t}{\tau}\right)$$

The function, $\varphi_n(t)$, represents a complete orthogonal basis set with real coefficients a_n. The members of the basis set are orthogonal over the given time interval if

$$\int_{-\frac{\tau}{2}}^{\frac{\tau}{2}} \phi_n(t) \cdot \phi_m(t)\, dt = K_n, \quad n = m$$

$$= 0, \quad n \neq m \tag{11}$$

where K_n = constant.

Given the basis set and constraints, two functional descriptions are obtained which have the forms:

$$h1(t) = \sum_{n=0}^{N} a_n \cdot \cos\left(\frac{2n \cdot \pi t}{\tau}\right) \cdot \frac{\text{rect}(t)}{\tau}$$

$$h2(t) = \sum_{m=0}^{M} b_m \cdot \cos\left[\frac{(2m+1) \cdot \pi t}{\tau}\right] \cdot \frac{\text{rect}(t)}{\tau} \tag{12}$$

Each cosine term in the summations in (12) represents a time gated sinusoid whose local center frequencies are given by

$$f_n = \frac{n}{\tau} \quad \text{and} \quad f_m = \frac{(2m+1)}{2\tau} \tag{13}$$

In the frequency domain the basis terms are well known Sampling functions with center frequencies given in (13). From (13), $f_n \cdot \tau$ must be an integer, which requires an integer number of wavelengths at frequency f_n, and similarly there must be an integer number of half wavelengths at f_m. Given that each basis term is a Sampling function, then the null bandwidth is known to be $2 \cdot \tau^{-1}$. The overall frequency function is defined given the choice of the even or odd time function in (12), the basis frequencies of interest, the weight of the basis function, and either the bandwidth or the time length. Figure 6 shows an example of the Sampling function basis frequency response terms described, normalized to center frequency and having all weights of unity.

IV. Orthogonal Frequency Coding Concept

A. Bit Function Description

Given a time function, $g_{bit}(t)$, having a time length τ_B defined as the bit length, the bit will be divided into an integer number of chips such that

$$\tau_B = J \cdot \tau_c \quad \text{where} \quad J = \#\ \text{of chips} \tag{14}$$

The chip interval τ_c is set as the time interval in (13) for the basis set. Allowing a time delay τ_D, such that $t = (t - \tau_D)$, and given a definition of each chip as $h_{cj}(t)$, then a bit is defined as the sum of J chips as

$$g_{bit}(t) = \sum_{j=1}^{J} w_j \cdot h_{cj}(t - j \cdot \tau_c) \tag{15}$$

Each chip is contiguous without time overlap and w_j is the bit weight and the functional form for the chip definition $h_{cj}(t - j \cdot \tau_c)$ is chosen from (12). In general, multiple local

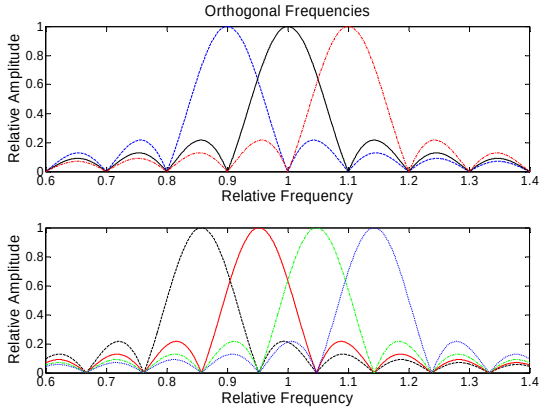

Figure 6. Example of three and four orthogonal sampling function frequency response terms.

carrier frequencies are possible in each chip depending on their weighting coefficient. Using the basis set with the integer number of half-wavelengths yields,

$$h_{cj}(t - j\cdot\tau_c) = \sum_{m=1}^{M} b_{jm}\cdot\cos\left(\frac{(2m+1)\cdot\pi\cdot(t-j\cdot\tau_c)}{\tau_c}\right)\cdot\mathrm{rect}\left(\frac{t-j\cdot\tau_c}{\tau_c}\right) \quad (16)$$

To generate the required signal, let $b_{jm} = 0$ for all m, except $m = C_j$ where $1 \le C_j \le M$. Then,

$$h_{cj}(t - j\cdot\tau_c) = b_j\cdot\cos\left(\frac{(2\cdot C_j+1)\cdot\pi\cdot(t-j\cdot\tau_c)}{\tau_c}\right)\cdot\mathrm{rect}\left(\frac{t-j\cdot\tau_c}{\tau_c}\right) \quad (17)$$

The form in (17) shows that each chip has a single local carrier frequency $f_{cj} = \frac{2C_j+1}{2\cdot\tau_c}$ and b_j is the chip weight. In order to build the desired time function, the following design rules are used: 1) $b_j = \pm 1$ for all j, 2) the bit null bandwidth is $BW_{bit} = J\cdot 2\cdot\tau_c^{-1}$, and 3) C_j is a sequence of unique integers which means that f_{cj} form a contiguous, non-repetitive set, similar to Figure 6. The rules, however, do not require that the local frequency of adjacent chips that are contiguous in frequency must be contiguous in time. In fact, the time function of a bit provides a level of frequency coding by allowing a shuffling of the chip frequencies in time.

B. OFC Properties

Figure 7 shows an example seven chip sequence where $f_{cm} \neq f_{cn}$ for all $m \neq n$, and there are an integer number of half wavelengths in each chip. The seven local chip frequencies are contiguous in frequency but are not ordered sequentially in time, and the chip weights are all unity. The given chip sequence represents the orthogonal frequency code for the bit. If there are *J* chips with *J* different frequencies in a bit, then there are $J!$ possible

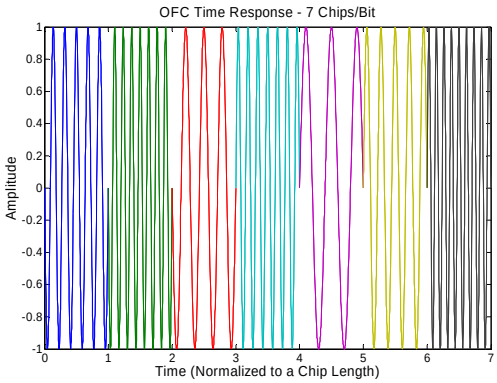

Figure 7. Example of seven chip time function using the basis set defined in (17).

permutations of the frequencies within the bit. A signal can be composed of multiple bits, with each bit having the same OFC or differing OFC. For the case of a signal, *J* chips long, $b_j = 1$, and having a single carrier frequency, the signal is a simple gated RF burst τ_B long.

In addition to the OFC coding, each chip can be weighted as ±1, giving a PN code in addition to the OFC, namely PN-OFC. This does not provide any additional processing gain since there is no increase in the time bandwidth product, but does provide additional code diversity for tagging. For conventional PN coding, the number of available codes is 2^J. When using PN-OFC coding, the number of available codes is increased to $2^J\cdot J!$.

Figure 8 shows the bit frequency responses of a seven chip OFC, seven chip PN and uncoded single carrier signal with time functions normalized to unity and having identical impulse response lengths. The uncoded single carrier is narrowband and has greater amplitude at center frequency than the PN (-9dB) and OFC (-17 dB) signals. The bandwidths of the PN and OFC signals are 7 and 49 times greater than the single frequency carrier bandwidth, respectively, as expected due to the spread spectrum nature of the signals. The power spectral density is lowest for the OFC signal. Figure 9 shows the autocorrelation functions of

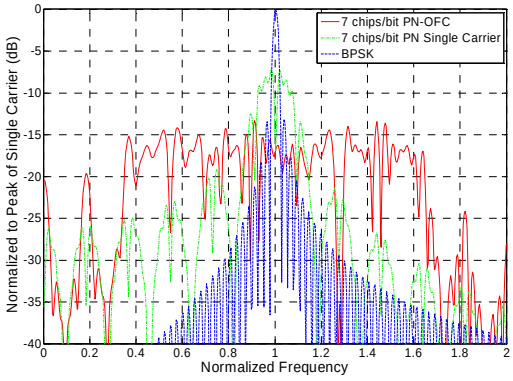

Figure 8. Frequency responses of seven chip OFC (red), seven chip PN (green) and single frequency carrier (blue) each with identical time lengths.

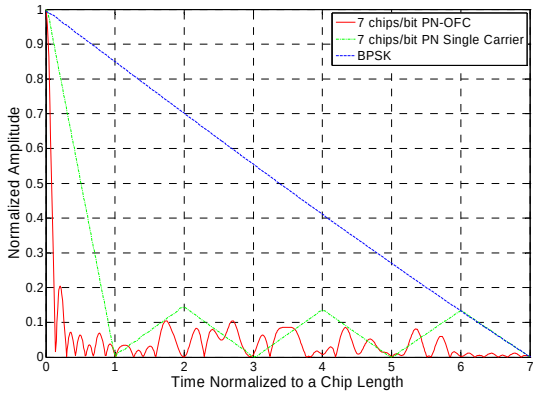

Figure 9. Time autocorrelation of seven chip PN-OFC, seven chip PN (Barker), and single frequency signals having identical time lengths. Only half of the autocorrelation is shown due to symmetry.

the signals used in Figure 8. The peak autocorrelation is exactly the same given the identical time amplitude and signal lengths, but the compressed pulse widths for the coded signals are narrower than that of the uncoded single carrier, as expected. This provides the measure of processing gain (PG), which is the ratio of compressed pulse width to bit length. The PG for the PN and OFC signals are 7 and 49, respectively, and PN-OFC provides a lower PSD than single carrier PN and uncoded signals of equal amplitude. As a result, PN-OFC yields the greatest correlated output in relation to peak spectral power.

V. OFC Reflector Design

In applying the OFC concept to a SAW reflector, the effects of the non-ideal reflector response needs consideration. A good measure is to examine the difference between the ideal time domain rect function and frequency domain Sampling function, versus the SAW chip reflector response in both domains. In addition, the parameters of interest to obtain near-optimum reflector bank performance were chip reflector insertion loss, chip processing gain (PG), intersymbol interference (ISI), chip correlation properties and inter- and intra- chip interactions. For this discussion, only a single in-line reflector bank is considered and the analysis assumes no reflector weighting is implemented. COM simulations of the complete chip and/or bit structure are analyzed and compared to the first order predictions for analysis to verify the accuracy of predictions. It is realized that multiple parallel tracks can be approached in a similar manner and that parallel tracks could be used to further optimize the OFC device performance.

A. Chip amplitude uniformity

For a fixed chip time length which is required for orthogonality, as the chip frequency increases the number of reflectors in a chip increase, since the number must equal an integer. Since reflectivity increases with the number of reflectors, the higher frequency chips will have greater reflectivity compared to lower frequency chips, assuming reflectivity per electrode is constant. If mechanical loading is significant, then the reflectivity will also increase at higher frequencies because the relative h/λ will also increase. Compensation using several techniques can help mitigate this effect, but this analysis approach will assume constant amplitude for all chips.

B. Chip frequency response

The desired chip frequency response is a sin(x)/x function, as shown in Figure 1. Figure 10 shows the frequency responses of COM simulated chip reflectors having a 1% reflectivity per electrode as a function of the number of electrodes. The number of reflectors (Ng) principally determines the null bandwidth while the product of the reflectivity (r) and electrode number determines the frequency selective response. As the product of Ng*r increases, the center frequency reflectivity increases, a desirable effect, but the frequency response begins to deviate from the desired sin(x)/x response, an undesirable effect. Figure 11 is the well known plot of reflectivity versus the product Ng*r. The figures shows that Ng*r>2 adds little additional reflectivity, but the frequency function distortion is severe. The implemented device OFC bit bandwidth is limited by bulk mode radiation caused by the mode matching of parts of the grating with in-band signals, which can be significant for quarter-wavelength electrodes. The practical limit is approximately 25% on lithium niobate.

C. Adjacent chip frequency reflectivity effects

Although OFC yields reduced reflections between reflectors compared to single frequency PN due to chip orthogonality, it is non-zero. Non-synchronous orthogonal frequencies are partially reflected from adjacent interrogator

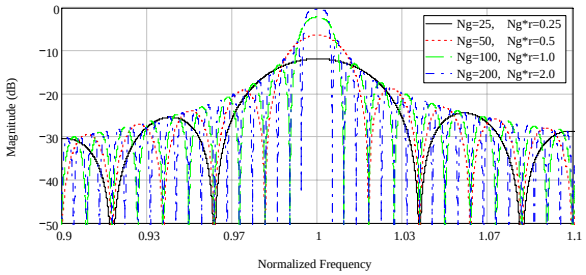

Figure10. COM simulation of grating frequency reflective responses for 1% reflectivity per strip, and 4 different grating lengths. Magnitude in dB versus normalized frequency, (f/f_o).

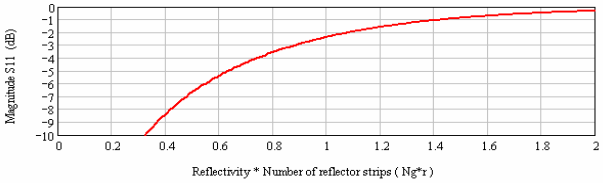

Figure 11. Plot of magnitude of reflectivity (S_{11}), in dB, versus the product of the number of strips and reflectivity per strip (Ng.r).

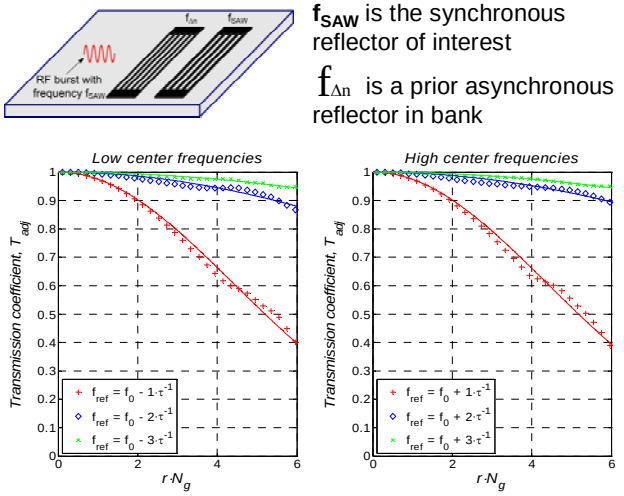

Figure 12. Frequency transmission versus Ng*r as a function of chip frequency offset. Schematic of the COM simulated device is shown that consisted of 2 chips and an RF interrogator pulse having duration of the chip length. The first chip has a synchronous frequency not equal to the RF burst frequency and the second chip has a synchronous frequency of the RF burst.

chip frequencies and the closer the adjacent frequency the larger the partial reflection. In order to understand the magnitude of this effect, simple COM simulations were conducted on a 2 chip reflector bank. Figure 12 shows a schematic of the device simulated. It consisted of 2 chips and an RF interrogator pulse having duration of the chip length. The first chip has a synchronous frequency not equal to the RF burst frequency and the second chip has a synchronous frequency of the RF burst. COM simulations were conducted for the 3 closest adjacent chip frequencies of the RF burst frequency, as shown in Figure 12. The simulations provide transmission versus Ng*r as a function of the asynchronous frequency offset. This will predict the transmission coefficient of asynchronous chips to an interrogation signal, with the desired transmission coefficient to be close to unity. Note that the reflected energy from the second reflector is proportional to the reflectivity of the second reflector less the transmission loss associated with propagating through the first reflector twice. Also realize that the term “transmission loss” as it is used here does not imply that the incident SAW energy is truly lost. In an OFC device, the portion of the incident wave that is reflected by non-synchronous reflectors is returned to the input transducer. Since this reflected energy does not correlate in the matched filter, it is considered to be a loss term. As expected, the closest adjacent frequency to the RF burst has the most significant transmission loss. For Ng*r < 2, over 90% of the energy is transmitted through for all asynchronous chips.

D. Chip reflector time response

The effect of the time response on the Ng*r product was also studied. Figure 13 shows COM

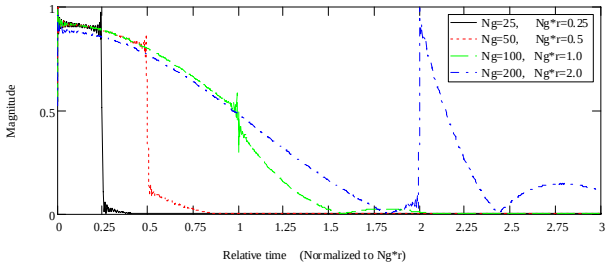

Figure 13. COM simulation of a SAW chip linear magnitude time response versus relative time,normalized to N_g*r, for 1% reflectivity and 4 different chip lengths.

simulations of the normalized linear magnitude time chip response versus time for 1% reflectivity per electrode. For N_g*r<0.5, the impulse responses show little stored energy beyond the desired chip length. For N_g*r=1.0, stored energy beyond the chip length is evident, but may be acceptable, and for N_g*r=2.0, the stored energy is very significant which would cause significant ISI and PG loss. This observation suggests that N_g*r<1 would be a criteria limit for chip design. From Fig. 11, this would indicate a chip reflector loss of approximately 2.5 dB.

VI. Experimental Device Results

As a first example, a 250 MHz, dual sided OFC reflector device was designed having 7 chips, a %BW=28 on YZ $LiNbO_3$. Al shorted-electrode reflectivity was ~3.4% and the number of electrodes was 24 @f_0, yielding Ng*r~0.72. Time domain RF probe measurements and COM simulation of the double sided OFC device time responses are shown in Figure 14; results include the input transducer effects. The agreement is very good and the chips are well defined, as expected. The predicted chip reflector loss is ~4dB and is predicted well by the COM theory.

As a second example, 250 MHz, dual sided OFC reflector device was designed having 8 chips, a %BW=11.5 on YZ $LiNbO_3$. Al shorted-electrode reflectivity was ~3.4% and the number of electrodes was 70 @f_0, yielding Ng*r~2.38. The larger number of electrodes allows a narrower fractional chip and bit bandwidth and lower

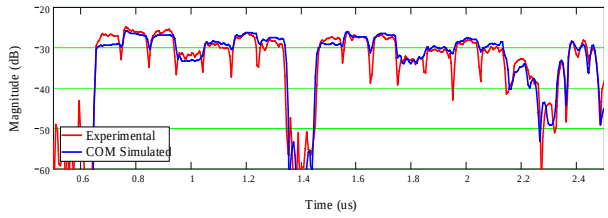

Figure 14. OFC 7 chip, dual sided device time response versus magnitude in dB. The COM simulation and measured data are superimposed and show good correlation. The chips are clearly distibuishable with little ISI, as expected.

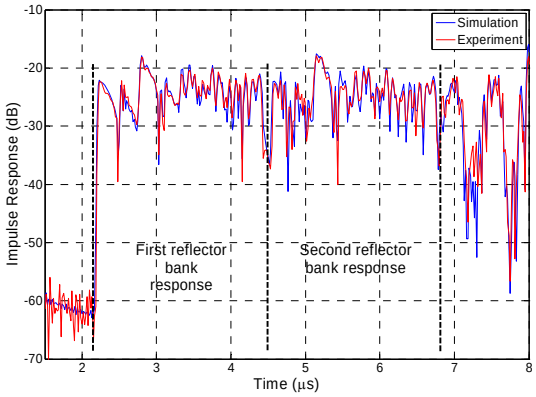

Figure 15. An example of an 8 chip, 250 MHz OFC SAW double sided reflector response.

reflector loss. Time domain RF probe measurements and COM simulation of the double sided OFC device time responses are shown in Figure 15; results include transducer effects. The COM and measured agreement is quite good. Note that the chips are less well defined, as compared to the first example, and there are intersymbol effects due to the longer chip impulse responses, as predicted. The measured chip reflector loss is lower than the previous example, as predicted, and is close to 0dB, and is predicted well by the COM theory.

VII. OFC System Discussion

A. *Transceiver Block Diagram*

For this discussion, the transceiver approach will use the device as a code for a correlator. For tagging, the device could be single sided, or for a use as a sensor, the device could have reflector banks on either side of a transducer and be used in the differential mode. The dual sided device type is shown Figure 16. A schematic of the system block diagram is shown in Figure 17 which depicts a chirp interrogation signal, the chirp matched filter at the receiver, the correlator and the compressed pulse which is used for further signal processing. A computer simulation was used to predict the system performance. Figure 18 shows the theoretically predicted compressed pulses, assuming two delayed signals, the simulated compressed pulses based on the COM model with the ideal code, and the

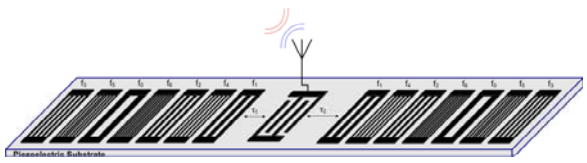

Figure 16. Schematic drawing of OFC SAW sensor using identical reflector banks on either side of input

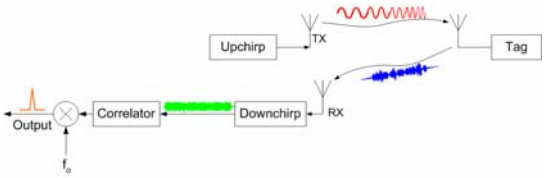

Figure 17. OFC SAW system block diagram showing up-chirp interrogation, the returned noise-like signal, the matched filter at the receiver, and the compressed pulse output of the correlator.

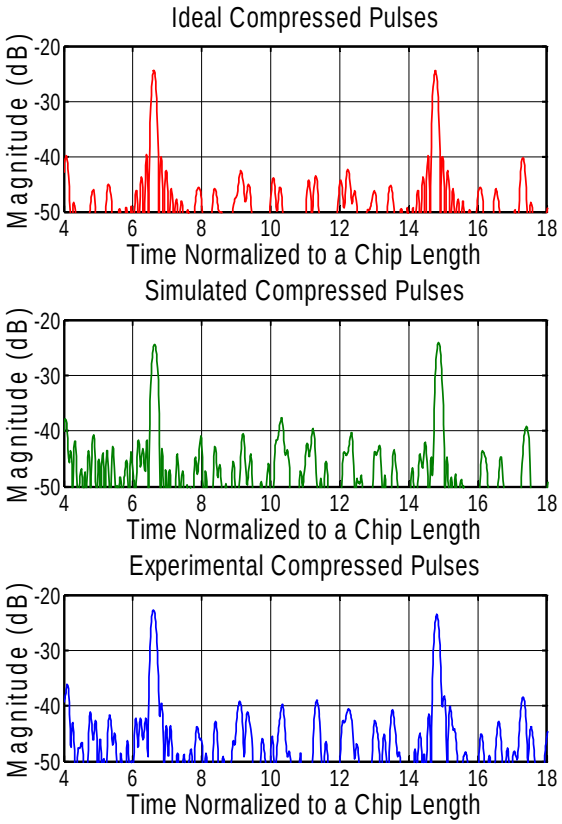

Figure 18. The OFC SAW sensor compressed pulses at room temperature. Upper trace is the ideal OFC autocorrelation; middle trace is the autocorrelation produced using the COM model; lower trace is autocorrelation using experimental data on YZ lithium niobate device.

correlation of an actual measured OFC coded device with the ideal code. The agreement is very good and there is a slight difference in the sidelobes adjacent to the main correlation peak. In a sensor application, the differential pulse delay is one method used to determine the temperature of the device.

B. Temperature Effects on Correlated Response

Lithium Niobate has been used as the OFC device substrate because of its high coupling coefficient, and it has a large TCD which provides good temperature sensitivity. However, the large TCD also degrades the compressed correlator response if no compensation is used. For this reason, an adaptive filter approach was used to maximize the compressed correlator response. Knowing the material TCD, it is possible to predict the changes in frequency of the matched filter code versus temperature. An algorithm modifies and scans the receiver matched filter coded until the peak correlation is maximized. This adaptive matched filter approach ensures that the correlation peak is very near its maximum value at any temperature. Figure 19 shows the effects on the correlated response with and without the adaptive matched filter. Figure 20 shows the simulator output correlation of a 7 chip OFC temperature sensor versus temperature and delay time using the adaptive filter; demonstrating the peak correlation uniformity versus temperature. Using this approach, the device was ramped over temperature and the simulator extracted the device's temperature versus the thermocouple measurements, as shown in Figure 21.

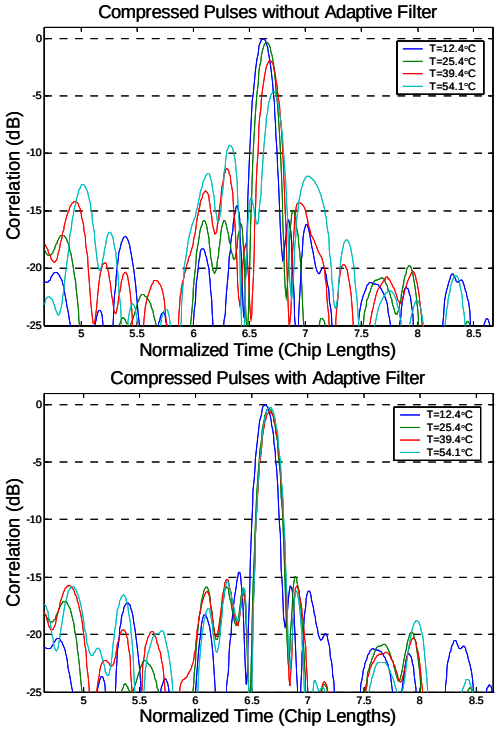

Figure19. Degradation of compressed pulse response over temperature using static matched filter (upper), and improved compressed pulse response using adaptive matched filter (lower).

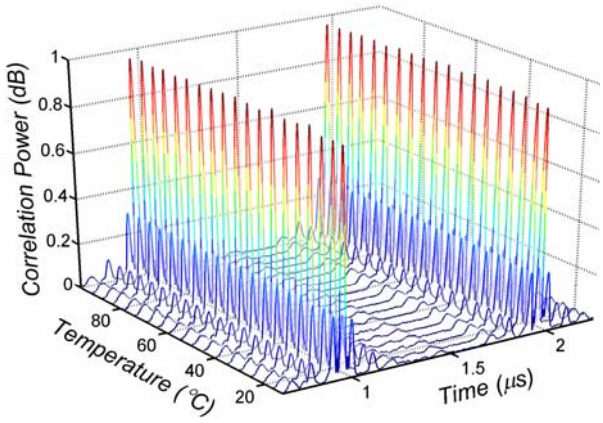

Figure 20. Cosine weighted OFC SAW sensor compressed pulses. Temperature varied between 15°C and 100°C. Adaptive matched filter yields uniform pulse amplitude as temperature varies.

C. OFC Device and System Discussion

The previous example given uses the SAW OFC sensor in a differential delay mode. However, there are other possible ways of using the returned sensor information. As an example, the adaptive filter itself is using an algorithm that is predicting the device temperature in order to modify the matched filter at the receiver based on optimization of the correlation peak. This would allow a single sided OFC reflector bank to be used which would reduce device size.

The current research efforts are developing devices and systems for operation in a multi-sensor environment, as well as sensors for operation in unusual or harsh environments. The transceiver system that is currently being developed at UCF is based on a software radio concept, and several variations are possible from the discussion to follow. The transmitter will use a chirped signal to interrogate the SAW OFC wireless sensor system. The devices will respond with their individual coded waveforms which will have embedded the device sensor information. The receiver will have an RF front-end which will match the chirp interrogation signal and will mix the signal to a near-zero IF. The signal will then be sampled using an A/D having the required bandwidth. It is currently possible to purchase commercial A/D chips or systems that have sampling rates of several GHz which allows bandwidths of several hundred MHz. It is anticipated that the signal will be buried in the noise with a single interrogation. The interrogator will be used to excite the devices multiple times and the data summed from all received signals until a suitable signal-to-noise ratio (SNR) is established. At this point, all the sampled data will be demodulated and analyzed using software and DSP

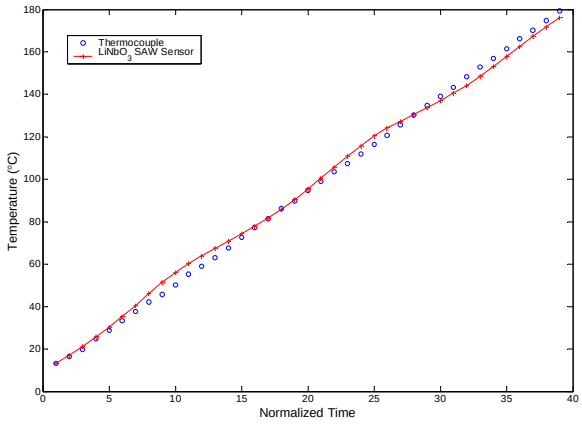

Figure 21. Seven chip OFC SAW temperature sensor tested between 10°C and 180°C and compared to thermocouple measurements.

techniques. Since the signal is now represented as a data file and is purely digital, the processing can be easily reconfigured to adapt to changing sensor or system conditions and requirements. This approach eliminates a great deal of electronic hardware in favor of digital processors. This approach should allow fairly easy reconfiguration of the transceiver system as center frequency and bandwidths of the system change. Current efforts have shown a demonstration of the feasibility of the approach and work continues on developing a complete system.

As a final example, results of initial work on the use of SAW OFC sensors at cryogenic temperatures has been conducted. Unlike semiconductor devices, piezoelectric devices appear to work at extreme temperatures, both hot and cold. Tests have been conducted near liquid nitrogen temperatures for use of the devices as temperature sensors for NASA ground and space applications. Results of the tests are shown in Figure 20, which demonstrates the robust performance of SAW devices working under extreme temperature conditions.

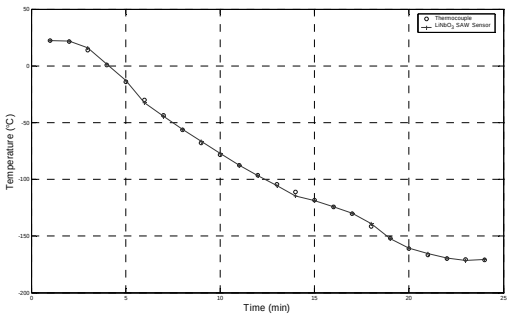

Figure 22. OFC SAW temperature sensor results and comparison with thermocouple measurements at cryogenic temperatures. Temperature scale is between +50 and -200 ^{o}C and horizontal scale is relative time in minutes.

VIII. Discussion and Conclusion

This paper has provided an introduction to the theory of OFC SAW wireless and passive devices for use in tagging and sensors. A brief discussion of single frequency SAW reflective tag devices was presented as background. The basic theory of OFC design and analysis was presented for application to SAW device implementation. The use of OFC reflectors for OFC implementation and some of the design considerations and experiments were provided. OFC SAW device experimental data shows the operation and the ability to design and synthesize and COM predictions and have shown good agreement compared to measurements. Several temperature sensor results were shown from near liquid nitrogen temperatures to 200 ^{o}C. System considerations were presented for obtaining and demodulating the OFC SAW sensor data.

The current research has used a center frequency of 250 MHz, which was chosen for convenience based on the fabrication capabilities currently used and for ease in test and measurement. Ultimately, it would be desirable to operate devices in the 1-3 GHz range. The higher frequency would produce smaller devices and would smaller, better efficient antennas.

At the present time, our work has not addressed the antenna issue. This is clearly important since the sensor footprint is a function of both the SAW and antenna. Further research is needed here to produce very small, possible integrated antenna design, for SAW wireless tagging and sensor applications.

IX. Acknowledgment

The authors wish to thank continuing support from NASA KSC and especially Dr. Robert Youngquist. The work has been partially supported through NASA Phase I and II STTR contracts with the industrial partner of Microsystem Sensors, Inc., and by the Florida Solar Energy Center (FSEC) at the University of Central Florida. Student support has also been provided through the NASA Graduate Student Research Program (GSRP).

X. References

1. R.W. Chang, “Synthesis of band limited orthogonal signals for multi-channel data transmission”, Bell System Technical Journal, Dec. 1966, pp. 1775-1796.
2. L. Vandendorpe, “Multitone Spread Spectrum Multiple Access Communication Systems in a Multipath Pician Fading Channel”, IEEE Transactions on Vehicular Technology, Vol. 44, No.2, May 1995, pp. 327-337.
3. L.L. Yang and L. Hanzo, “Overlapping M-ary frequency shift keying spread spectrum multiple access systems using random signature sequences", IEEE Transactions on Vehicular Technology, Vol. 48, #6, Nov. 1999, pp. 1984-1995.

4. F. Seifert, W. E. Bulst, and C. Ruppel, "Mechanical sensors based on surface acoustic waves," Sensors and Actuators, vol. A44, pp. 231-239, 1994.
5. C. S. Hartmann, "A global SAW ID tag with large data capacity," in Proc. IEEE International Ultrasonics Symposium, 2002, pp. 65-69.
6. W. E. Bulst, G. Fischerauer, and L. Reindl, "State of the art in wireless sensing with surface acoustic waves," IEEE Transactions on Industrial Electronics, vol. 48, no. 2, pp. 265-271, 2001.
7. C. S. Hartmann, "Design of global SAW RFID tag devices," presented at Second International Symposium on Acoustic Wave Devices for Future Mobile Communication Systems, Chiba University, Japan, 2004.
8. A. Pohl, "A review of wireless SAW sensors," IEEE Transactions on Ultrasonics, Ferroelectrics and Frequency Control, vol. 47, no. 2, pp. 317-332, 2000.
9. G. Ostermayer, A. Pohl, C. Hausleitner, F. Seifert, and L. Reindl, "CDMA for wireless SAW sensor applications," in Proc. IEEE International Symposium on Spread Spectrum Theory Techniques and Applications, 1996, pp. 795-799.
10. A. Pohl, C. Hausleitner, F. Seifert, G. Ostermayer, and L. Reindl, "Wavelet transform with a SAW convolver for sensor application," in Proc. IEEE International Ultrasonics Symposium, 1995, pp. 143-146.
11. D.C. Malocha, D. Puccio, D. Gallagher, “Orthogonal frequency coding for SAW device applications,” Proc. IEEE International Ultrasonics, Ferroelectrics and Frequency Control 50th Anniversary Joint Conference, 2004, pp. 1082-1085.

MEMS-Based SAW Devices

Jan H. Kuypers*, Andrew B. Randles, Marek E. Schmidt, Shuji Tanaka and Masayoshi Esashi
Department of Nanomechanics, Tohoku University, Sendai 980-8579, Japan
*jan@mems.mech.tohoku.ac.jp

***Abstract*—This paper gives an overview of current activities on developing wireless sensors, wafer level packaging technologies for piezoelectric substrates, and tunable SAW devices. Advanced results of a developed TDMA based wireless temperature sensor system featuring parallel sensor interrogation and in-situ accuracy evaluation are shown. Based on combining the experiences with wireless sensors and bulk etching of $LiNbO_3$ a monolithic design of a miniature wireless pressure sensor is proposed. Advances in using imprinted epoxy-based dry film resist for wafer level packaging of SAW devices are described. Finally, the design and recent results of a microelectromechanical switch to control the phase velocity of a SAW is presented. This technology is expected to achieve tuning ranges of 1~10 %.**

Keywords-Wireless SAW sensor, $LiNbO_3$ micromachining, wafer level packaging, SU-8 dry film resist, tunable SAW devices, SAW switches, Acoustic RF MEMS

I. INTRODUCTION

Microelectromechanical systems (MEMS) have found their way into a wide range of fields, including sensor, optic, RF, fluidic, power and biomedical applications. This paper discusses current developments on combining MEMS technology with acoustic devices, and focuses in particular on wireless sensing applications, wafer level packaging, and tunable SAW devices. Wireless sensor technology possesses a large potential concerning measurement flexibility, monitoring of moving objects, and measurement in hazardous environments. Passive SAW sensors have been proposed for this purpose, and are developing with numerous publications from as far back as 1987 [1]. We have applied this technology to the simultaneous interrogation of temperature sensors using a TDMA (time division multiple access) scheme, and have developed a design method for multi-reflector sensors [2, 3]. This work also discussed the importance of sensor mounting. The technology of the passive SAW delay line sensors is being extended to monolithic pressure sensors. To overcome the problems of size and packaging in current sensors [4, 5], a monolithic design based on the thermal inversion, deep bulk wet etching and direct bonding of lithium niobate substrates is proposed.

In order to minimize RF parasitics encountered with standard ceramic SMD packages and to reduce the overall size of packaged SAW devices, a new packaging technology using photosensitive epoxy has been developed. This approach enables wafer-level packaging and requires only a minimum addition of process steps. This miniature epoxy package can withstand temperatures up to 300 °C, and slightly deforms to match the thermal expansion of devices, which is generally anisotropic for piezoelectric substrates.

This work was supported in part by the Shinsei Foundation, SCOPE from the Ministry of Internal Affairs and Communications (062302002), and Grant-in-Aid for Scientific Research from the Ministry of Education, Science, Sports, and Culture of Japan (16201027).

The final section covers the development of a SAW tuning technology, which is promising for a vast number of applications, ranging from miniature SAW-based phase shifters, sensors, tunable resonators and filters. This technology uses electrostatically actuated MEMS bridges to modulate the SAW velocity under the bridge. The utilized micromachining processes and materials are compatible with standard SAW fabrication.

WIRELESS TEMPERATURE SENSOR

II. FUNDAMENTALS OF SAW DELAY LINE SENSOR AND WIRELESS SYSTEM

In previous studies [1, 6], the principle of the SAW delay line sensors for a wireless temperature measurement has been demonstrated. The principle is based on the temperature dependence of the propagation velocity of the SAW and the thermal expansion of the substrate. The typical layout of the SAW delay line sensor and its simulated time response are shown in Fig. 1. A radio wave emitted from a transceiver is received by the sensor's antenna, and SAWs are generated by an interdigital transducer (IDT) connected to the antenna. The surface wave propagates along the piezoelectric substrate, reflects at reflectors, and then returns to the IDT. The returned SAW is reconverted to a radio wave, which is transmitted back to the transceiver. The temperature is then evaluated by determining the time delay and phase difference between the sensor's time responses.

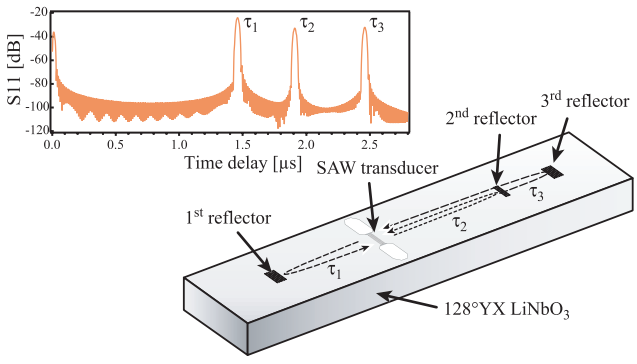

Figure 1. Typical structure of a one port SAW delay line sensor.

The temperature monitoring system which we have developed features simultaneous wireless interrogation of 4 sensors using a TDMA scheme [2, 3]. This system is compliant with the frequency regulations for short range devices operated in the ISM band at 2.45 GHz. In this study black 128°YX $LiNbO_3$ was used as the piezoelectric substrate material, as it features large piezoelectric coupling, which is important for low-loss and wide-band SAW transducers, negligible excitation of bulk waves, and a moderate temperature dependence of the SAW velocity. The chemical reduction of $LiNbO_3$ is effective to reduce pyroelectric effects, causing charge-up problems during fabrication and operation.

One of the most important specifications to be designed is temperature sensing accuracy. The estimation of the achievable sensing accuracy needs not only accurate SAW simulation but also the quantitative knowledge of sensing accuracy. The difficulty is, that the sensor accuracy depends on a number of dynamic parameters, e.g. the read-out range, the antenna-to-sensor alignment, and possible noise sources. This problem was solved by experimentally evaluating the dependence of the time and phase measurement accuracy on the SNR (signal-to-noise ratio) of the sensor time responses [2]. The relationship between effective SNR and the accuracies obtained using a commercially available SAW reader unit are shown in Fig. 2.

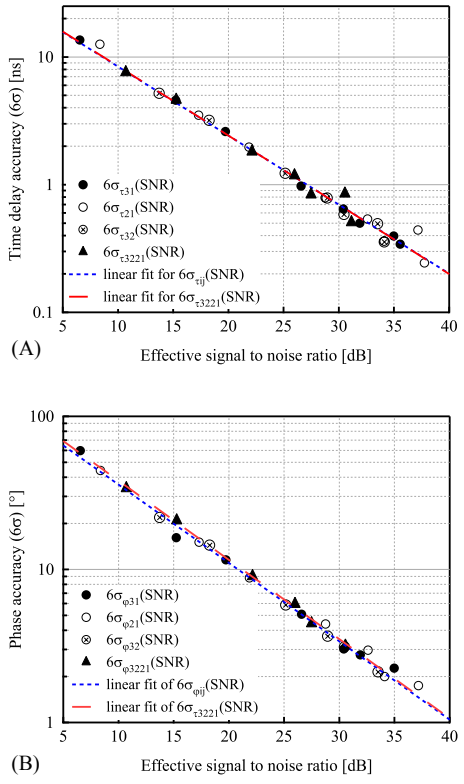

Figure 2. Experimentally derived relationships of the achievable time delay (A) and phase accuracy (B) versus the effective SNR [2].

The performance of the sensor system is derived from relating the achievable time delay or phase accuracy to a corresponding temperature accuracy. Finally, the temperature sensing accuracy is directly related to the SNR of the sensor time responses, and the designer of the wireless sensor system can modify read-out power, antenna gain, cable loss, averaging etc. by considering only the SNR to achieve a required performance. The SNR using the modified radar equation [7, 8] is given as

$$\mathrm{SNR} = \frac{P_t G_t^2 G_r^2 \lambda_0^4 t_i n}{(4\pi R)^4 k T F \mathrm{IL} L_{\mathrm{sys}}}, \tag{1}$$

where

SNR = Signal to noise ratio
P_t = Transmitting power [W]
G_t = Transmitting antenna gain
G_r = Receiving antenna gain
λ_0 = Free space wavelength [m]
t_i = Integration time [s]
n = Averaging factor
R = Read-out distance [m]
k = 1.38×10^{-23} J/K (Boltzmann constant)
T = Temperature [K]
F = Receiver noise factor
IL = SAW sensor insertion loss
L_{sys} = System loss (cables etc.).

The effective isotropic radiated power (EIRP), given as EIRP = $P_t G_t$, is restricted by frequency regulations.

III. Temperature Sensitivity

The temperature coefficient of delay (TCD), which is the rate of change in time delay of a SAW caused by a temperature variation, is defined as

$$\mathrm{TCD} = \frac{1}{\tau}\frac{\partial \tau}{\partial T} = \frac{1}{l}\frac{\partial l}{\partial T} - \frac{1}{v_0}\frac{\partial v_0}{\partial T} = \alpha - \frac{1}{v_0}\frac{\partial v_0}{\partial T}. \tag{2}$$

The first term in (2), α, corresponds to the thermal expansion coefficient of the substrate along the SAW propagation direction, which is found as 15.4 ppm/K [9]. The latter term corresponds to the change in the SAW velocity, which is computed as –55.8 ppm/K based on a temperature-dependent implementation of the method given by [10] using material data from [9, 11]. The resulting TCD for 128°YX $LiNbO_3$ is 71.2 ppm/K.

A. *Time Delay Dependence*

The temperature dependent formulation of a time delay τ is represented by

$$\tau(\Delta T) = \tau_0(1 + \mathrm{TCD}\cdot\Delta T), \tag{3}$$

where τ_0 refers to the initial time delay, and ΔT to the temperature variation.

The sensitivity for a given time delay is thus

$$S_\tau = \frac{\partial \tau}{\partial T} = \tau_0 \mathrm{TCD}, \quad (4)$$

suggesting that the temperature sensitivity for a typical time delay of $\tau_0 = 1$ µs is approximately 0.07 ns/K. Increasing the sensitivity requires either a material with larger TCD or a larger time delay. For 128°YX $LiNbO_3$, 1 µs of time delay corresponds to a chip length of ~2 mm. Larger time delays are obtained using a longer chip, however the propagation loss at 2.45 GHz increases at 5~6 dB/µs.

B. Phase Dependence

Higher sensitivity is achieved by evaluating the phase of the complex time response for a given reflector delay. The phase is related to the time delay as $\varphi = 2\pi f\tau$, where the frequency f corresponds to the center frequency of 2446 MHz. From (4) the temperature sensitivity of the phase is represented as

$$S_\varphi = \frac{\partial \varphi}{\partial T} = 2\pi f \tau_0 \mathrm{TCD}. \quad (5)$$

The temperature sensitivity for a typical time delay of $\tau_0 = 1$ µs is 63°/K, suggesting that high sensitivity is achieved even by a low-accuracy phase measurement. However, one phase value corresponds to many temperatures at an interval of 5.7 K (= 360°/63°/K), and a unique temperature cannot be determined just by evaluating the phase. Hereafter, this is referred to as "phase ambiguity".

IV. Multi-step Evaluation Schemes

We have proposed a multi-step evaluation scheme using a combination of time delay and phase to achieve both high sensing accuracy and a wide range in temperature measurement [2, 3]. Only differences of time delay and phase are used, as the time delay and phase depends on the distance between the sensor and interrogation unit.

A. Combined Time Delay and Phase Evaluation

The multi-step evaluation scheme is illustrated in Fig. 3. First, the largest and thus most sensitive relative time delay (e.g. $\tau_{31} = \tau_3 - \tau_1$ in Fig. 1) is chosen for the first rough temperature estimation (A). The temperature accuracy for this first evaluation is low judging from the achievable resolution of time delay measurement and the sensitivity determined by (4). Therefore, the following resolution refinement is performed using a relative phase (B). However, the temperature range corresponding to a phase change of 2π (= 360°/S_φ) must be smaller than the uncertainty of temperature determined using the time delay to avoid the phase ambiguity problem. Otherwise, one phase might correspond to two or more temperatures in the uncertainty of the first temperature evaluation. Therefore, a sufficiently small time delay is required for this second temperature evaluation (see (3, 5)). The required time delay is thus created as a delay difference using three reflectors, as

$$\tau_{3221} = \tau_{32} - \tau_{21} = (\tau_3 - \tau_2) - (\tau_2 - \tau_1). \quad (6)$$

Evaluating the phase φ_{3221} of this delay results in an increased accuracy of the sought-after temperature. Further resolution refinement is performed using a more sensitive phase, which corresponds to a longer time delay (C). Again, the temperature range corresponding to a phase of 2π must be smaller than the uncertainty of the temperature determined using φ_{3221}. In our design, the most sensitive phase φ_{31}, can be used for this second resolution refinement. Developing the inequalities which must be satisfied for this evaluation scheme yields

$$6\sigma_{\tau_{31}}(\mathrm{SNR}_1, \mathrm{SNR}_3) \cdot 6\sigma_{\varphi_{3221}}(\mathrm{SNR}_1, \mathrm{SNR}_2, \mathrm{SNR}_3) < \frac{2\pi}{f}, \quad (7)$$

where f corresponds to the center frequency, σ_X to the variance of a measured value X, and the $\mathrm{SNR}_{1,2,3}$ to the SNRs of the three time responses. Only if (7) evaluates to be true, phase ambiguities are prevented, and thus the multi-step scheme will work. It is interesting to note that this equation is independent from the material's TCD, the operating temperature range, and the choice of the maximum time delay τ_{31}, and thus the resulting accuracy via φ_{31}. Inserting the time delay and phase accuracies shown in Fig. 2 together with the definition of the effective SNR illustrated in Fig. 4 and the center frequency of 2446 MHz into (7) reveals that a SNR of 18 dB is necessary for the 3 reflector responses.

In case of the design shown in Fig. 1, the reflector strength of reflector 2 and 3 are designed to be identical. The reflection strength of reflector 1 will be largest, as a shorter delay time suffers smaller propagation loss. Reflectors 2 and 3 share the same acoustic track and due to the increased delay time, their reflection is generally 6~12 dB lower than the reflection of reflector 1. As the noise floor is assumed the be constant in the

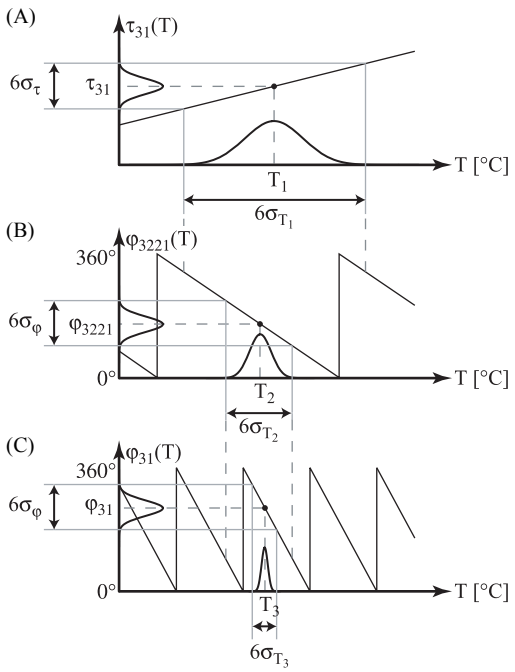

Figure 3. Principle of the three-step combined delay and phase evaluation scheme for temperature measurement.

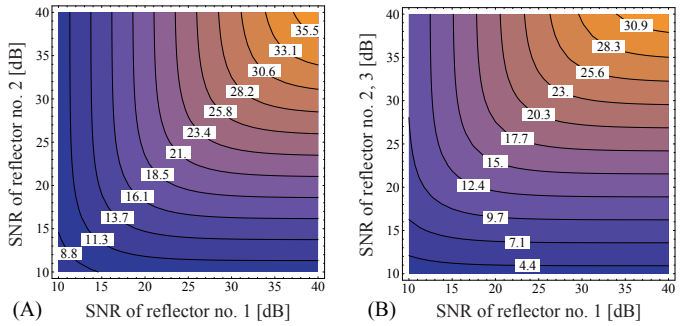

Figure 4. Relation of the reflectors SNRs to the effective SNR used in Fig. 2 for a relative time delay or phase using 2 reflectors (A) and 3 reflectors (B), assuming that the SNR of reflectors two and three are identical.

time domain, SNR_1 is 6~12 dB larger than $SNR_{2,3}$. Concerning the limitation of (7), this design requires SNR_1 to be at least 25 dB for an assumed difference of 8 dB between SNR_1 and $SNR_{2,3}$, for this scheme to work.

Although the accuracy does increase with increasing τ_{31}, so does the insertion loss of the reflector responses. For 128°YX $LiNbO_3$, having a TCD of 71.2 ppm/K, the SAW propagation loss is assumed to be 6 dB/µs. In this case, τ_{31} should be designed to be 1~2 µs to maximize the achievable temperature accuracy. This leads to the fundamental limitation of achievable accuracies for any kind of SAW delay line sensor.

B. All-Phase Evaluation

An alternative multi-step evaluation scheme using only phase relations is shown in Fig. 5 for comparison. First, a very small time delay τ_{3221} is chosen so that the phase φ_{3221} yields exactly a 2π phase change over the sensor's operating temperature range, e.g. –20 ~ +180 °C (A). Based on the phase evaluation of φ_{3221}, the first rough value of temperature is determined. Next, the phase difference φ_{21} is used for an increased accuracy (w. l. o. g. $\tau_{21} < \tau_{32}$) (B). Again, as seen above, the 2π phase ambiguity condition for φ_{21} is prevented by designing the temperature accuracy resulting from φ_{3221} to be sufficiently high. This choice is based on the minimum SNR required for this sensor design to operate properly, fixed in the specifications. The highest accuracy is finally achieved by evaluating the phase φ_{31} (C). Again the phase ambiguity condition must be prevented.

From the three restrictions originating from φ_{3221}, and the two transitions to $\varphi_{21}$and φ_{31}, in order for this scheme to work inequality (8) must be satisfied.

$$[6\sigma_{\varphi_{3221}}(SNR_1, SNR_2, SNR_3)]^2 + 4\pi 6\sigma_{\varphi_{21}}(SNR_1, SNR_2) < (2\pi)^2 \quad (8)$$

Compared to the restriction of the mixed time delay and phase evaluation scheme given by (7), the all-phase evaluation scheme only requires a SNR of 3 dB for the case of identical SNRs, whereas 18 dB had been necessary for the mixed scheme. The all-phase scheme generally allows for lower SNR levels.

The minimum SNR level for the all-phase evaluation scheme to work is determined by the choice of the delay time τ_{21}. A smaller delay time, which is thus less sensitive, allows for operation at lower SNRs. However, as τ_{3221} had been determined on the basis of φ_{3221} fulfilling a phase change of 2π over the operating temperature range, and now choosing τ_{21}, means that via $\tau_{31} = \tau_{3221} + 2\tau_2$, the time delay τ_{31} is already fixed. Although a smaller time delay τ_{21} enables operation at lower SNRs, τ_{31} also decreases, and thus leads to a lower accuracy achievable, as seen from (5).

The upper bound of the temperature accuracy for a three reflector design is found as

$$6\sigma(T_{min}) > \Delta T_{spec} \frac{6\sigma_{\varphi_{31}}(SNR_{31}) \cdot 6\sigma_{\varphi_{3221}}(SNR_{3221}) \cdot 6\sigma_{\varphi_{21}}(SNR_{21})}{(2\pi)^3}, \quad (9)$$

where ΔT_{spec} corresponds to the temperature operating range of e. g. 200 K. It is again interesting to note that both relations (8) and (9) are independent from the material's TCD. However, for both approaches using the mixed and all-phase evaluation scheme, the final sensor accuracy is determined by τ_{31} and its phase, as

$$6\sigma(T_{min}) = \frac{\sigma_{\varphi_{31}}(SNR_{31})}{2\pi f \tau_{31} TCD}. \quad (10)$$

Nevertheless, the maximum accuracy resulting from (10) for the all-phase evaluation scheme may not interfere with the upper bound given by (9).

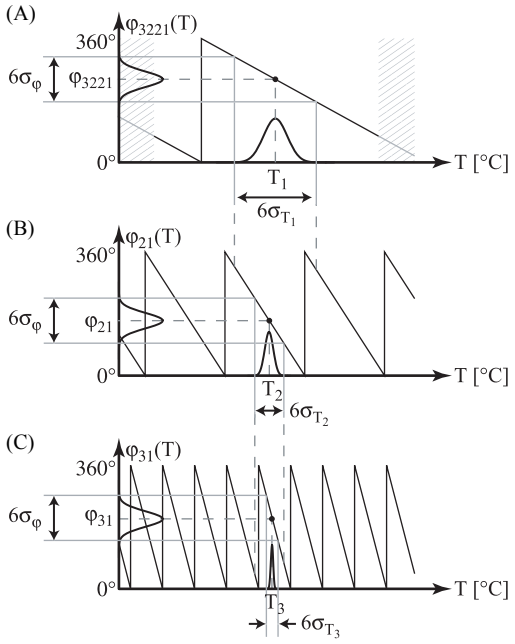

Figure 5. Principle of the three-step phase evaluation scheme for temperature measurement.

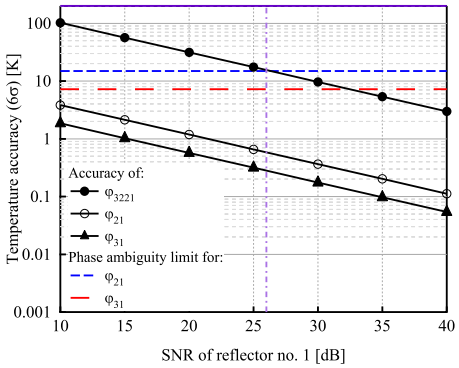

Figure 6. Temperature accuracy for the fabricated TDMA based sensors using an all-phase evaluation scheme.

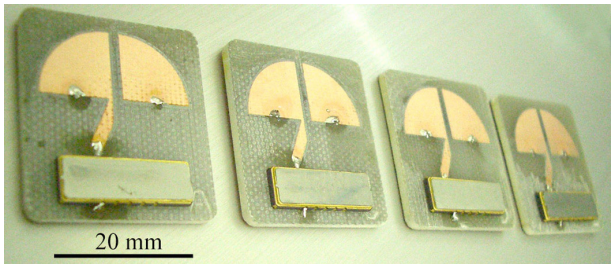

Figure 7. Developed 2.45 GHz wireless temperature transponders, consisting of packaged SAW delay line sensors mounted on a microstrip antenna.

C. *Comparison of Multi-step Schemes*

The all-phase evaluation scheme allows for evaluation at lower SNR levels, and requires only the knowledge of achievable phase measurement accuracy, and is easier to design as there are less degrees of freedom. However, for the design of a system featuring parallel sensor interrogation, more design freedom is sometimes necessary in order to prevent the overlap of time responses when using the TDMA scheme. The choice of the multi-step scheme should be made based on the system specifications of the temperature operating range, minimum SNR and temperature accuracy using the above equations. The design of tags for very large temperature operating ranges (> 260 K) will require a very insensitive phase φ_{3221}, achieved by choosing a very small delay time τ_{3221}, in the range of 10~20 ns. This requires exact knowledge concerning the propagation velocity including dispersion and strict process control in fabrication in order to prevent discrepancies in the range of up to 30 %.

However, the all-phase evaluation scheme features one particular advantage compared to the mixed time delay and phase evaluation scheme. This originates from the difficulty to determine the position of the time response peaks accurately. The delay times are determined by fitting the S11 peaks of the time responses and extracting their maximum position ($\tau_{1,\,2,\,3}$). Due to the finite width of the peaks in the time domain, originating from the used bandwidth of 75 MHz and the applied window function during FFT, any ripple from e.g. sidelobes of adjacent peaks of parallel sensors or non-white noise will lead to significant errors concerning the time delay evaluation. On the other hand, the phase is rather constant around the reflector positions, and ripple or noise has a negligible influence on altering the phase. Although the phase is to be extracted at exactly the peak positions ($\tau_{1,\,2,\,3}$), a slight deviation from this position still leads to a good estimation of the actual phase values ($\varphi_{1,\,2,\,3}$). This agrees with the experience that the all-phase evaluation design is more robust in operation.

V. Experimental Evaluation of All-Phase Design

This section discusses the design and experimental results of fabricated sensors using an all-phase evaluation scheme. Sensor systems using a mixed time delay and phase evaluation scheme have been demonstrated in the past [2, 3]. The achievable accuracy for the sensor using the all-phase evaluation design is shown in Fig. 6. The sensor is designed to operate in a temperature range of 200 K, with the time delays τ_{3221}, τ_{21} and τ_{31}, determined as 29 ns, 380.5 ns and 790 ns, respectively. As seen in Fig. 6 in order to prevent the phase ambiguity of φ_{21}, a SNR of 26 dB is required for the first reflector, whereas the SNR of reflector 2 and 3 are designed to be identical, being 7.5 dB smaller than SNR_1. Above the critical SNR level of 26 dB, the all-phase evaluation scheme works and switching the evaluation from φ_{3221} to φ_{21} leads to an accuracy improvement of factor 26. The phase ambiguity for changing from φ_{21} to φ_{31} is not critical as seen in Fig. 6, and leads to an accuracy increase of factor 2. In order to achieve an accuracy of 0.1 K, a SNR for reflector 1 of 35 dB is required for this design. In this case the minimum SNR level was traded against maximum achievable accuracy.

A. *Fabrication and Packaging*

The fabrication of the all-phase sensors is identical to the process described in [2]. This article had also discussed the importance of the sensor mounting during packaging, as it greatly influences the experimentally found TCD. We had shown that in particular for very small time delays, as used in our design for e.g. $\tau_{3221}/\varphi_{3221}$, any difference in TCD will be amplified by the ratio of τ_1/τ_{3221}, which is about 40~50 for the all-phase evaluation scheme presented here. This means that a difference as small as 5 ppm in the TCD for the delay of τ_1 compared to τ_2 and τ_3 leads to a change in the experienced TCD of 250 ppm/K. It was also shown that this change can lead to negative TCDs [3]. In order to prevent this effect the sensor chips are mounted outside of the acoustic track.

B. *Temperature Evaluation*

The temperature characteristics of the sensors were evaluated using a Pt100 sensor as reference, identical to the procedure reported in [3]. The results are shown in Fig. 8. Unfortunately, the results suffer from a rather low SNR during measurement, partly originating from the strong RF absorption of the oven glass, in which the sensors were set, as well as the

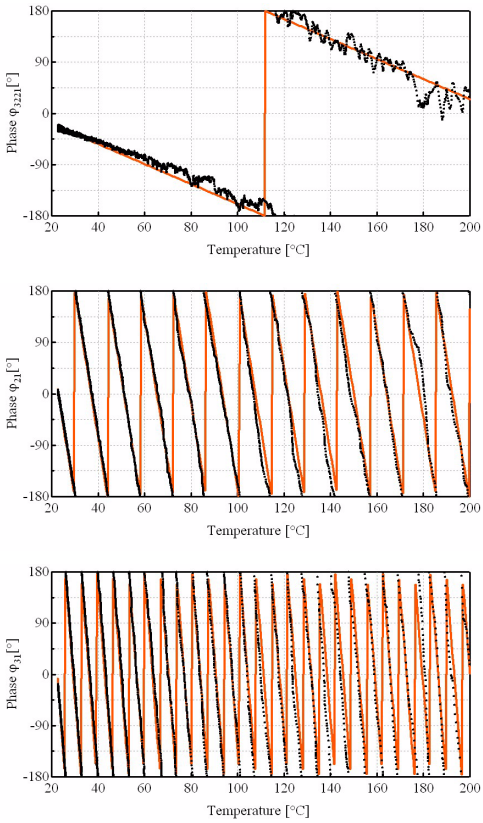

Figure 8. Measured temperature characteristics of the all-phase design using the three phase differences φ_{3221}, φ_{21} and φ_{31} to determine the temperature.

PCB based microstrip antennas not being suited for these high temperatures. Nevertheless, the data agree well with a linear best fit. Also, the corresponding TCDs for φ_{3221}, φ_{21}, φ_{32} and φ_{31} are 77.4 ppm/K, 75.9 ppm/K, 76.0 ppm/K, and 76.0 ppm/K, respectively, which are close to the theoretical value computed as 71.2 ppm/K.

VI. Conclusion

Based on the close agreement of our result and the theoretical expressions given above, we conclude that the sensors including packaging effects are well understood. This enables the precise estimation of the sensor performance based on the presented relationships of measurement accuracy in combination with modelling the relative insertion loss of the sensor by SAW simulation [12, 13]. The measured RF characteristics have been shown to agree well with simulation in the past [2, 13]. Nevertheless, the comparison of the measured and predicted SNR levels using the modified radar equation given in (1) shows poor agreement; the theory predicts larger read-out ranges by a factor of 2~5. In particular a poor radiation efficiency of the used tag antennas, as shown in Fig. 7, are thought to account for this discrepancy. Currently the read-out distances are in the range of 130-140 cm, corresponding to accuracies of 0.19-0.1 K (6σ) [2].

Monolithic $LiNbO_3$ based Pressure Sensor

VII. Background

Currently we are trying to combine $LiNbO_3$ micromachining technologies with the knowledge gained from the wireless temperature sensors to develop wireless passive pressure sensors for automotive applications. Reported wireless pressure sensors suffers from large size and non-hermetic sealing methods [4, 5]. These designs use standard substrates with thicknesses of 500 µm and 350 µm without the micromachining of the substrates themselves (bulk micromachining). This leads to membrane sizes of 20 mm and 8 mm in diameter, respectively, in order to achieve reasonable sensitivities for hydrostatic pressure measurement. So far epoxy adhesive has been used as sealant. However, such polymer-based non-hermetic sealing is not suitable for pressure sensing applications. Additionally, thermal expansion mismatches of substrates should be avoided, as accounts for [5].

The hermetic seal and thermal expansion problem are addressed in our work by choosing a monolithic sensor design. $LiNbO_3$ micromachining is employed to fabricate thin membranes in order to increase the sensitivity, and thus realize smaller designs. The structure of the sensor is illustrated in Fig. 9. Changes in pressure are evaluated by a change in the time delay τ_{41}, or rather the phase φ_{41}. In order to compensate for temperature effects, a temperature sensor, which is identical to the one described above is included, using the reflectors $\tau_{1, 2, 3}$.

VIII. $LiNbO_3$ Micromachining

The micromachining of $LiNbO_3$ by dry etching is limited to shallow depths due to the slow etching rates of 7~50 nm/min [14, 15]. Laser ablation features high speed, but suffers from debris deposition and inherent low throughput originated from a serial process [16, 17]. The debris deposition will generally make a subsequent polishing step necessary. Wet etching of $LiNbO_3$ in hot HF and HNO_3 solutions can achieve etch rates in the range of 10~55 µm/h [18]. This etching is found to be anisotropic and exhibits a strong dependence on the

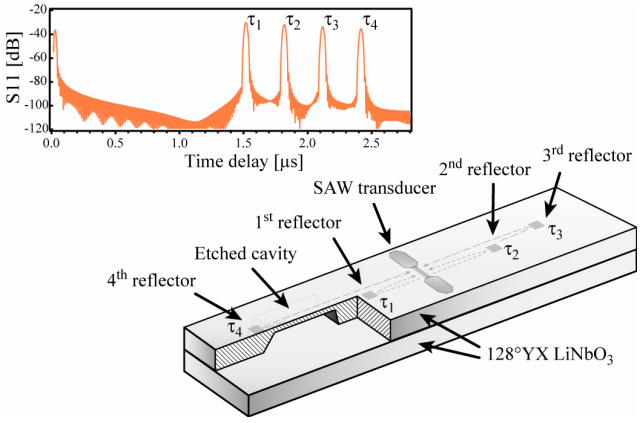

Figure 9. Design of the monolithic SAW delay line sensor for pressure measurement based on using $LiNbO_3$ bulk etching and wafer bonding.

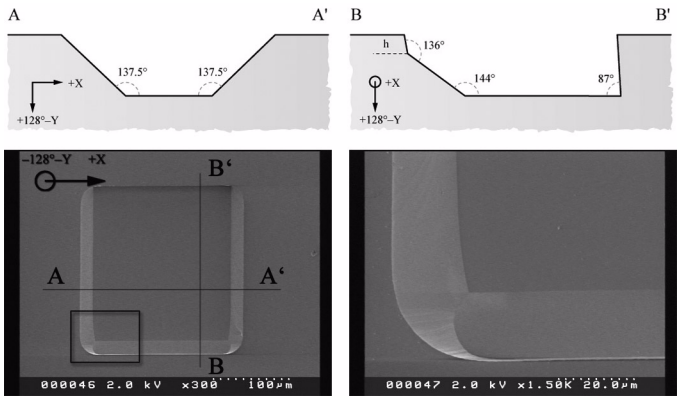

Figure 10. Wet etching results for square mask openings on –128°Y-cut $LiNbO_3$ with an etch depth of ~20 µm, and corresponding cross-sections.

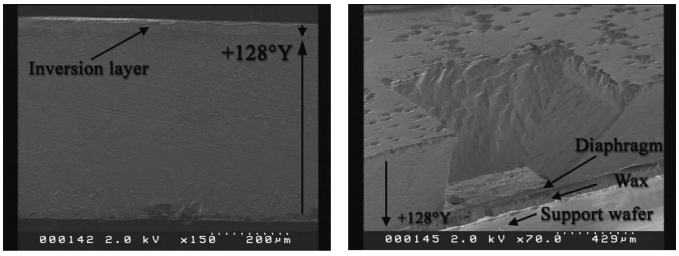

(A) (B)

Figure 11. Cross-section of thermal inversion layer on 128°Y-cut $LiNbO_3$ (A), and fabricated diaphragm of ~20 µm thickness using the inversion layer as an etch stop (B).

z-axis orientation. Etch rates on the positive *z*-face are found to be negligible in comparison to that on the negative *z*-face. The large difference in etch rates for the +*z* and –*z*-faces in combination with selective re-poling of domains has been used for the fabrication of waveguides on Z-cut $LiNbO_3$ [18].

Most etchants proposed in literature for $LiNbO_3$ are based on mixtures of hydrofluoric (HF) and nitric acid (HNO_3) at temperatures close to the boiling point of 110 °C [18, 19]. Our experiments showed that a 49% HF solution at 80 °C turned out to yield higher etch rates and lower under-cutting of the metal mask. Typical etch rates depending on the orientation of the substrate are in the range of 20~50 µm/h [20]. The patterning requires a masking layer, which is able to withstand hydrofluoric acid at elevated temperatures. A gold layer of 2 µm thickness on top of a 30 nm thick chrome adhesion layer have shown to give satisfactory results. High quality films deposited by RF magnetron sputtering at 170 °C combined with careful handling and cleaning procedures are the key to reduce pinholes in the masking layer.

A. Bulk Wet Etching on 128°YX $LiNbO_3$

We demonstrate that this differential etching technology is extendable to the deep etching of 128°YX $LiNbO_3$ substrates, which is of great technical interest due to its superior acoustic properties. For 128°Y-rotated substrates, the crystal z-axis is inclined by 38° from the substrate surface normal, as is understood from the Euler angles of (0, 37.86, 0). The substrate surface corresponding to an inclined positive *z*-face shows slow etch rates of ~0.4 µm/h, which agrees well with experiences with Z-cut substrates. Instead, the backside of the 128°Y-rotated substrate shows etching rates of ~21 µm/h for 49% HF solution at 80 °C. Double-side polished substrates are used due to a later direct bonding step, and as the roughness of standard SAW substrates makes it difficult to achieve satisfactory masking during etching.

The results for a ~20 µm deep square opening are shown in Fig. 10. The slope of the sidewalls along the positive and negative x-axis are found to be identical. The profile perpendicular to the x-axis is not symmetric. On one side two crystal planes appear, with the first section almost vertical, and the latter similar to the x-direction. The height of this first almost vertical section denoted by *h*, depends strongly on the etch depth and increases from ~4 µm for a depth of 20 µm to ~150 µm for a ~500 µm deep etch. The opposite side shows a slightly overhanging sidewall. The bottom of the etched area is parallel to the substrate surface and shows microstructures leading to a roughness of R_{max} of 1~4 µm, which becomes larger for longer etching times.

B. Thermal Inversion based Etch-stop

Although the membrane required for the proposed sensor structure can be obtained by wet etching alone, it is difficult to achieve a required accuracy of the membrane thickness based on time control. In silicon micromachining, the p^{++} etch-stop technique, which uses a heavily-boron-doped layer as an etch-stop, is widely used to make thin diaphragms, bridges, cantilevers etc. We make use of a similar technique to define the membrane thickness in $LiNbO_3$ substrates. A method referred to as thermal inversion discovered by Nakamura et al. [19] enables a domain inversion through a part of the thickness of the substrate. Although originally found with Z-cut substrates, it was shown to work as well on substrates with inclined spontaneous polarization as 36°, 163°, and 128° rotated Y-cut substrates. The mechanism of the thermal inversion has been explained based on the out-diffusion of Li_2O at elevated temperatures [19] and its defect gradient causing built-in electrical fields, which exceed the coercive field of $LiNbO_3$ of e.g. 5 V/cm at 1100 °C [21]. As rapid cooling was found to lead to thicker inversion layers, it has been suggested that pyroelectrically induced fields also contribute to the inversion [19].

The thermal inversion enables the formation of a head-to-head domain structure, and the thickness of the inversion layer can be controlled by the inversion temperature and time [19]. At a proper temperature and flowing argon gas containing water vapor, the growing speed of the inverted

domain becomes slow enough (~2 µm/h at 1100 °C) to control its thickness precisely. As can be seen from Fig. 12 (E), this inverted domain is used for an etch-stop as the inclined positive *z*-face of the inversion layer is exposed. The use of thicker substrates relieves handling issues during fabrication and packaging, especially in case of using large wafers. However, the surface roughness is found to increase with increasing etch depth. The second advantage of using the inversion layer as an etch stop is that a smoother surface can be obtained at a relatively uniform inversion boundary compared to time-controlled etching. Furthermore, selective thermal inversion is possible by masking the substrate with metals such as platinum, and not only diaphragms but also bridges and cantilevers can be made in a similar process.

Fig. 11 (A) shows the cross-section of a ~20 µm thick inversion layer on a 128° rotated Y-cut. In order to expose the different domain orientations the sample was briefly etched in hydrofluoric acid. The SAW device is later fabricated on the inversion layer, which corresponds to a –128°Y-cut substrate. Switching from the standard 128°Y-rotated plane to this 308°Y-rotated plane with Euler angles (0, 217.86, 0) leads to a difference in sign of the piezoelectric tensor, but identical acoustic properties.

IX. Fabrication Process

The process of the proposed sensor structure is illustrated in Fig. 12. First, the substrates are immersed in boiling NH_4OH:H_2O_2:DI water solution for cleaning (A). The samples are then placed in a quartz furnace at 1100 °C flowing wet argon for 8 hours for thermal inversion (B). Prior to the deposition of the masking layer, the inverted substrates are then cleaned again. Next, layers of Cr/Au/Cr are deposited on the inversion layer by RF magnetron sputtering with the substrates being heated to 170 °C. The sputtering is repeated to deposit layers of Cr/Au on the backside as well (C). The Cr/Au on the backside is then patterned with standard photolithography and wet etching of Au and Cr (D). The three-layer stack on the front-side thereby ensures, that the Au-layer is not attacked and thus the front-side is later protected during the $LiNbO_3$-etching. Alternatively, the top-side can be sealed-off from the etchant using a fluorinated O-ring. Finally, the samples are etched in a 49% HF solution at 80 °C. The etching is self terminating when it reaches the inversion layer (E). The Cr/Au masking layers are then removed and the etched substrate is bonded to a virgin substrate of the same orientation (F). After fabrication of this modified substrate containing a pressure cavity, a standard SAW fabrication process is used to complete the sensor (G).

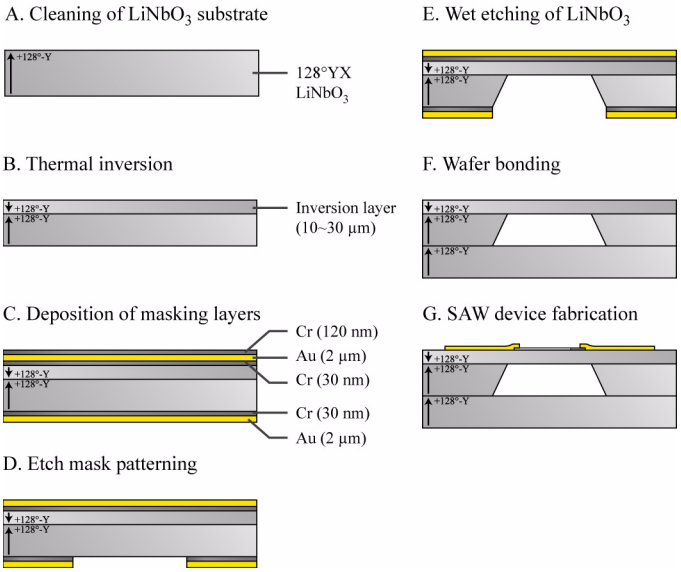

Figure 12. Process flow for the monolithic pressure sensor on 128°YX $LiNbO_3$.

X. Results and Conclusion

The effective method for etching $LiNbO_3$ using the metal mask has been presented. This method features reasonable etch rates and good dimension controllability. Thin membranes have been successfully fabricated on 128°Y-rotated wafers based on bulk wet etching and the use of a thermal inversion layer as an etch-stop, as shown in Fig. 11 (B). The etch-stop allows for long over-etching to yield a smoother membrane backside. In addition, ununiformity of etch rate throughout the wafer can be relieved by the over-etching. Hereby, the anisotropic etching characteristics determine the final shape of the fabricated diaphragm. Currently, wireless SAW sensors for pressure measurement are being developed based on this technology.

Wafer Level Packaging

The size of the developed temperature delay line sensors discussed in the first section measures 0.5 × 0.8 × 8~12 mm, where the rather large chip-length originates from the implemented time delays. Standard ceramic SMD SAW packages suitable for this size suffer from parasitic shunt capacitances in the range of about 1 pF. This leads to difficulties in matching as well as bandwidth restrictions. To escape from these parasitics as well as the overall size increase due to the package, we have investigated the wafer level packaging of SAW devices. The achievable decrease in size is illustrated in Fig. 13, by comparing these standard packages with a wafer level packaged sensor.

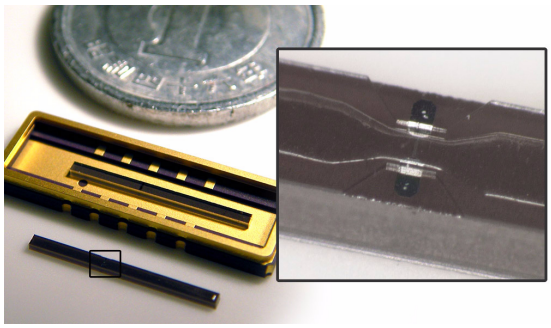

Figure 13. Size of a SAW delay line sensor packaged in a ceramic SMD SAW package compared to a wafer-level packaged sensor.

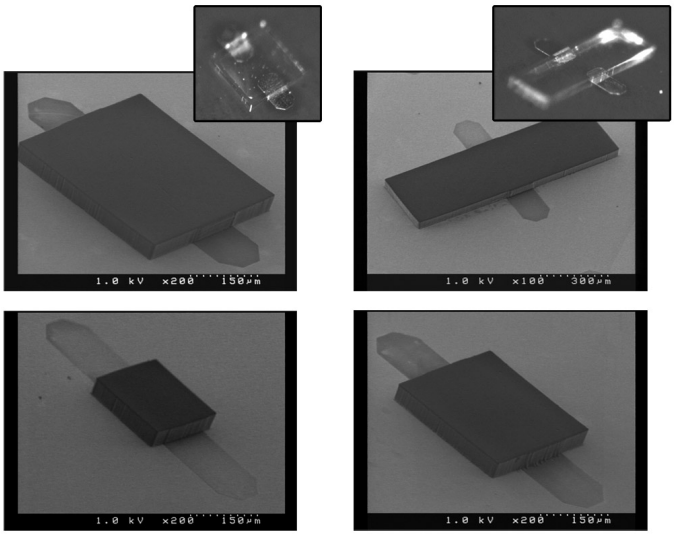

Figure 14. Wafer-level packaged SAW devices using imprinted SU-8 dry film resist and optical microscope image revealing the contained cavity.

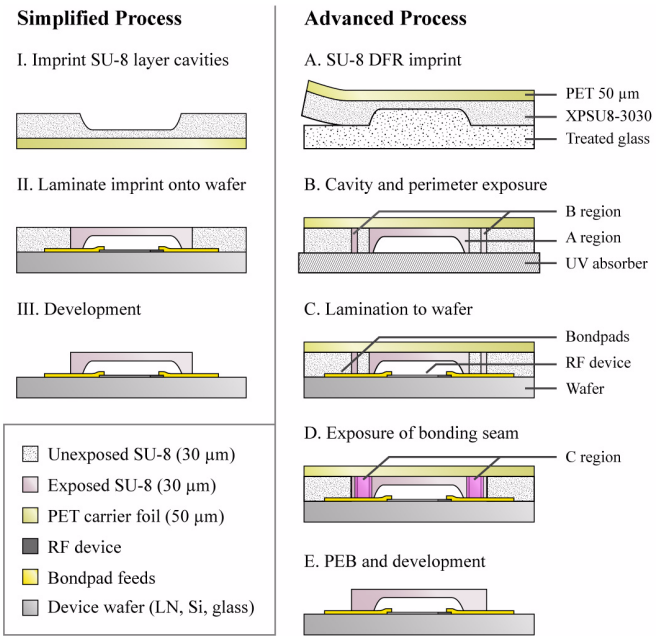

Figure 15. Simplified (left) and advanced process (right) for the wafer-level packaging of RF devices using imprinted SU-8 dry film.

A. Selection of Packaging Material

The largest difficulty in packaging devices fabricated on piezoelectric substrates is their inherent anisotropy in the in-plane thermal expansion. For the case of 128°YX $LiNbO_3$, an elliptical distribution of the in-plane thermal expansion coefficients exists. The thermal expansion coefficients range from 15.4 ppm/K along the *x*-axis, to 12.4 ppm/K along the *y*-axis. For a YZ-cut substrate this distribution resembles a dumb-bell-like shape with the thermal expansion along *x* being 7.5 ppm/K and the value for the transverse axis being 15.4 ppm/K. It is obvious that materials enabling a hermetic seal such as glass, metals or ceramics generally have isotropic in-plane thermal expansion properties, causing thermal expansion mismatch problems with $LiNbO_3$. A straightforward solution is to use the same material and the same orientation of the substrate material to solve this problem, as done for the presented pressure senor. This approach was also taken by [22] for SAW filters fabricated on $LiTaO_3$, however this process involves a large number of sophisticated process steps.

In order to develop a general packaging technology applicable to a wide range of substrates we have investigated the use of epoxy based micro-cavities. These epoxy packages are not hermetic. However, a similar packaging process has been proposed by Infineon for wafer-level packaging of SMR-type FBARs in combination with plastic overmold packages [23]. In this case, the instability problem due to the non-hermetic packaging is relaxed by a passivation layer. Another alternative shown in [24] uses silicon cavities transferred onto the device wafer by means of adhesive. It is stated that these packages can be hermetically sealed by depositing a final inorganic coating on top.

B. Imprinted SU-8 Dry Film Packaging

As the packaging material, we used SU-8, a photosensitive chemically amplified epoxy based photoresist. This resist is often used in the MEMS field to fabricate high aspect ratio microstructures. However, it does suffer from a narrow process window. The SU-8 3000 resist series used in this study features high temperature stability with a glass transition temperature of 200 °C, thermal degradation above 300 °C, and Young's Modulus of 1.5 GPa [25]. It has been shown that two layer spin-on SU-8 packages could withstand overmold conditions of 100 bar at 180 °C [23]. The large dielectric loss tangent of ~0.06 at 2.45 GHz [26] is compensated for by lithographically reducing the package wall dimensions and thus minimizing the effect on electrical feed-through connects. The large thermal expansion coefficient of ~50 ppm/K [25] is mitigated by its low Young's Modulus and reduction of the overall package dimensions. Based on the results of [24] we are investigating if these packages can be hermetically sealed by applying an additional inorganic coating.

C. Packaging Process

The basic process of the proposed packaging is illustrated in Fig. 15 (I - III). Initially, 30 µm thick SU-8 dry film resist (DFR) is imprinted with a glass master using a de-bonding agent. The imprinted DFR is then aligned to the device wafer by the means of imprinted alignment marks and laminated onto it. Finally, the packaged outline is defined by photolithography, and the unexposed regions removed during development. This initial process required certain modifications for improved yield, as shown in [27]. One problem is that the device cavities collapse at temperatures exceeding 48 °C. However, stable

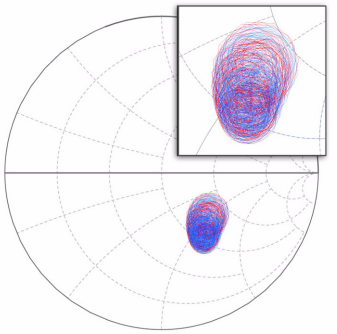

Figure 16. Smith chart of the delay line sensor before (red), and after packaging (blue) showing that additional parasitics are not observed.

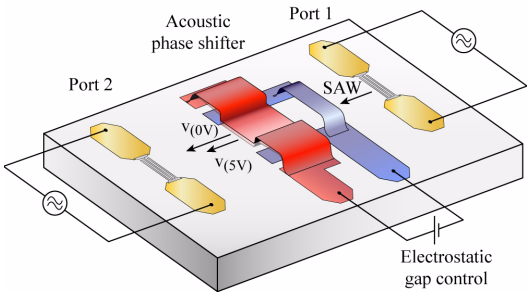

Figure 17. Acoustic phase shifter based on electromechanically controlling the phase velocity of a SAW by a MEMS structure.

results for the lamination of the DFR are achieved at 54 °C. This problem is prevented if the cavity region is exposed previously, as it cross-links and does not deform during lamination. Only a narrow region is not exposed, which is used as a sealing ring around the package, as shown in Fig. 15 (B). The package shape itself was found to be affected by a reflow effect during the post exposure bake (PEB), which was solved by exposing the perimeter of the package also during step (B) with the same mask. As this additional step occurs off-wafer, there is no influence on the device yield or processing time. The commonly encountered problem that SU-8 adheres to the photomask does not occur, as the PET-carrier film remains on top of the DFR during exposure (D). Fig. 13 and 14 show SAW devices packaged by this process.

The process has three main features: 1. The imprinted cavities are prepared off-wafer, and this process does not affect the device yield, 2. The packaging process requires only the aligned lamination to the device wafer, one exposure, and final development, 3. The device inside the cavity does not come in contact with liquid. The last point guarantees that there will be no residue affecting the acoustic device. It also means that no stiction effects of e.g. air gap type FBARs [28] will occur. This technique has recently been applied to the packaging of RF switches.

D. RF Characteristics of Packaged Devices and Conclusion

Packaged SAW delay line devices were characterized using an Agilent 5071B network analyzer and an angled Picoprobe Model-10 GS probe, which allows for on wafer level probing across the package. The measured forward reflection S11 before and after packaging is shown in Fig. 16. No changes observable in the impedance characteristic indicate that negligible parasitics are introduced. This is also expected from calculation, as the package section above the bondpad feeds measures only 25~30 µm. It is also interesting to note that the strength of the reflections from the sensor's time responses are not affected during packaging, which means that no additional propagation losses occur.

MEMS BASED SAW SWITCH TECHNOLOGY

We have developed a compact SAW phase shifter, which electromechanically controls the SAW propagation velocity. A metal sheet fabricated by surface micromachining is suspended above the piezoelectric substrate, and the gap in between is controlled electrostatically. The structure is illustrated in Fig. 17. This technology is of interest for phase shifters, tunable filters and resonators, programmable filter banks, devices using control of the propagation angle [29], etc.

A. Principle of Controlling the SAW Phase Velocity

The influence of a metal sheet in the vicinity of a piezoelectric substrate and its effect on the phase velocity of Rayleigh waves was theoretically formulated by Campbell et al. [10]. This model was used to derive the limiting conditions for a fully metallized and free surface. This case was also treated by Auld [30], giving a solution for the distance dependence based on perturbation theory. The velocity dependence computed for 128°YX $LiNbO_3$ based on both methods [10, 30] is shown in Fig. 18.

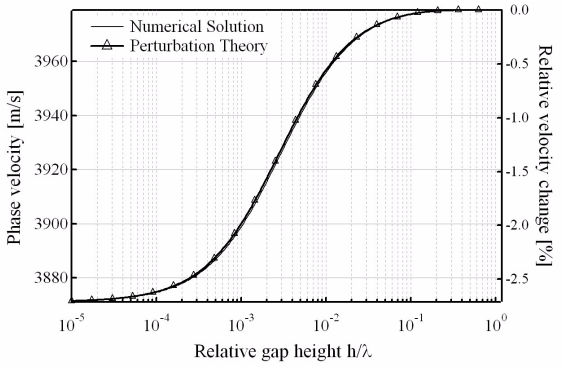

Figure 18. Computed dependence of the phase velocity of the Rayleigh wave on the gap height of a suspended metal sheet.

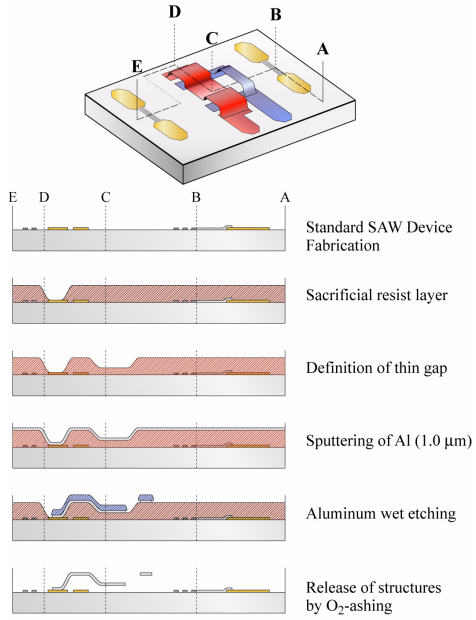

Figure 19. Process sequence for the SAW switch based on surface micromachining.

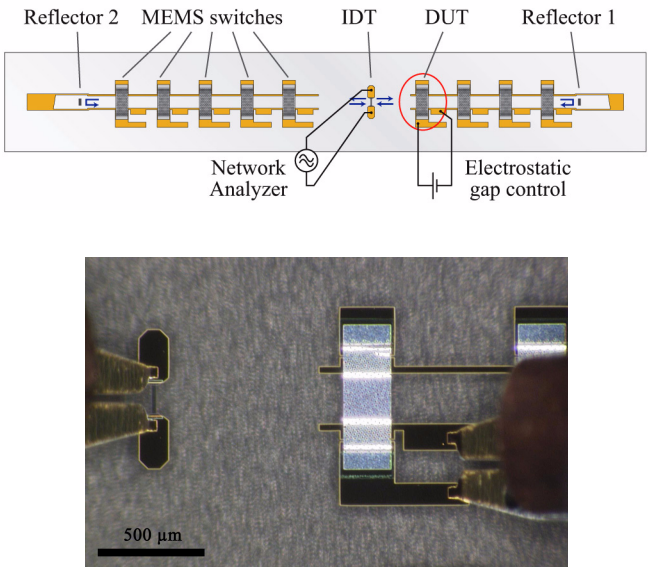

Figure 20. Experimental set-up of the test-device to evaluate the capability of controlling the phase velocity by the proposed structure.

The general approximation of the SAW coupling coefficient is given as

$$k^2 \cong \frac{v_0^2 - v_m^2}{v_0^2} \cong 2\Delta v / v_0 \,, \qquad (11)$$

where v_0 and v_m correspond to the propagation velocity for a free and metallized surface, respectively. By mechanically controlling the distance of a metal sheet above the substrate surface, the velocity can be tuned within the range given by v_0 and v_m. A larger coupling coefficient corresponds to more energy being stored in the electrical waves and thus a larger sensitivity towards changes in the electrical boundary conditions. Tuning of up to 1~10 % of the phase velocity is thus reasonable for the crystal cuts of $LiNbO_3$ and $LiTaO_3$ used in commercial SAW devices.

B. *Fabrication Process*

The fabrication was designed to be compatible with standard SAW processing, in respect of used materials and process temperatures. The process is outlined in Fig. 19. It assumes that the contact pads for the MEMS switches are fabricated together with the bondpads of the SAW device. A positive type sacrificial photoresist layer is then patterned to expose the anchor pads of the later switches. After development the resist is exposed again with a much shorter dose to define the gap height for the switches. Next a 1 µm thick aluminum layer is deposited by sputtering on top of the resist. The aluminum layer is then patterned by wet-etching. Finally, the masking resist as well as the underlying sacrificial resist layer are removed in an O_2-plasma asher.

C. *Experimental Verification*

For a first evaluation of the ability to control the phase velocity, an on-chip acoustic test-bench identical to a SAW delay line shown in Fig. 20 was fabricated. The initial gap height was chosen to be 2 µm, set by the exposure dose of the second exposure step of Fig. 19. The results shown in Fig. 21 were taken for a 230 µm wide switch. The measured phase shift corresponds to a sensitivity Δv/v of 40 ppm/V, a phase sensitivity of ~2°/V, and a decrease in velocity of ~3 m/s. However, the sensitivity is about 10-100 times smaller than expected, which suggests the existence of a residual gap under the switches. This seems to be caused by the slight buckling of the switches, which will be improved. Nevertheless, the measured sensitivity is two orders of magnitude higher than electrically-biased phase shifters [31, 32].

XI. CONCLUSIONS

This paper reviewed recent activities of our group in developing wireless sensors, wafer level packaging, and tunable SAW devices. A wireless temperature monitoring system featuring parallel sensor interrogation using TDMA and the multi-step evaluation was presented. Important general knowledge for designing various wireless SAW sensors was introduced. In addition, $LiNbO_3$ bulk micromachining technologies including thermal inversion and wet etching for a monolithic wireless pressure sensor were described.

Next, wafer-level packaging technology using imprinted SU-8 dry film resist for SAW device packaging was described in detail. This miniature wafer-level package features

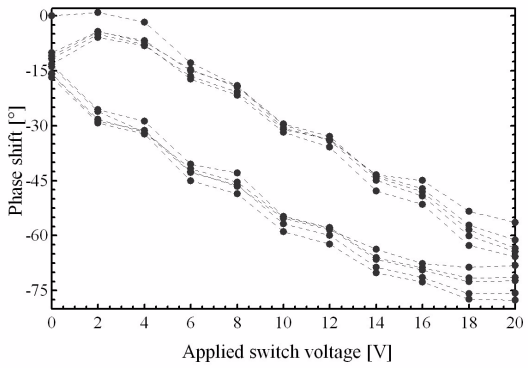

Figure 21. Measured phase shift for cycling the switch voltage 5 times between 0 and 20 V.

compatibility with a wide range of substrates, and prevents contamination or stiction of inside devices. Finally, an electromechanically-tunable SAW technology has been introduced, which enables tuning ranges between 1~10%. The developed surface micromachining is compatible with standard SAW device fabrication. The fusion of acoustic wave technology and MEMS technology is believed to create a variety of new devices.

ACKNOWLEDGMENT

J. H. K. would like to thank L. M. Reindl and K. Hashimoto for invaluable discussions and support over the years.

REFERENCES

[1] X. Q. Bao, W. Burghard, V. V. Varadan, and K. V. Varadan, "SAW Temperature Sensor and Remote Reading System", Proc. IEEE Ultrason. Symp. 1987, pp. 583-585

[2] J. H. Kuypers, D. A. Eisele, L. M. Reindl, "Passive 2.45 GHz TDMA based Multi-Sensor Wireless Temperature Monitoring System: Results and Design Considerations", Proc. IEEE Ultrason. Symp. 2006, pp. 1453-1458

[3] J. H. Kuypers, D. A. Eisele, L. M. Reindl, S. Tanaka, M. Esashi, "2.45 GHz Passive Wireless Temperature Monitoring System featuring Parallel Sensor Interrogation and Resolution Evaluation", Proc. IEEE Sensors 2006, in press

[4] H. Scherr, G. Scholl, F. Seifert, R. Weige1, "Quartz Pressure Sensor based on SAW Reflective Delay Line", Proc. IEEE Ultrason. Symp. 1996, pp. 347-350

[5] K. Lee, W. Wang, G. Kim, S. Yang, "Surface Acoustic Wave Based Pressure Sensor with Ground Shielding over Cavity on 41° YX $LiNbO_3$", Jap. J. Appl. Phys., vol. 45, no. 7, 2006, pp. 5974-5980

[6] L. M. Reindl, I. M. Shrena, "Wireless Measurement of Temperature using Surface Acoustic Waves Sensors", IEEE Trans. Ultra. Ferro. Freq. Cont., vol. 51, no. 11, 2004, pp. 1457-1463

[7] L. Reindl, G. Scholl, T. Ostertag, H. Scherr, U. Wolff, F. Schmidt, "Theory and Application of Passive SAW transponders as Sensors", IEEE Trans. Ultra. Ferro. Freq. Cont., vol. 45, no. 5, 1998, pp. 1281-1292

[8] K. Chang, "RF and Microwave Wireless Systems", John Wiley & Sons, 2000, pp. 200-201

[9] R. T. Smith, and F. S. Welsh, "Temperature Dependence of the Elastic, Piezoelectric, and Dielectric Constants of Lithium Tantalate and Lithium Niobate", J. Appl. Phys., vol. 42, no.6, 1971, pp. 2219-2230

[10] J. J. Campbell, W. R. Jones, "A Method for estimating Optimal Crystal Cuts and Propagation Directions for Surface Waves", IEEE Trans. Sonics Ultrason., vol. SU-15, no. 4, 1968, pp. 209-217

[11] G. Kovacs, M. Anhorn, H. E. Engan, G. Visintini, and C. C. W. Ruppel, "Improved Material Constants for $LiNbO_3$ and $LiTaO_3$", Proc. IEEE Ultrason. Symp. 1990, pp. 435-438

[12] J. H. Kuypers, D. A. Eisele, L. M. Reindl, "The K-Model - Green's Function based Analysis of Surface Acoustic Wave Devices", Proc. IEEE Ultrason. Symp. 2005, pp. 1550-1555

[13] J. H. Kuypers, D. A. Eisele, L. M. Reindl, "Design of Wireless Reflective Delay Line Devices using the K-Model", Proc. Piezo. Mat. Dev. 2005, pp. 97-102

[14] C. L. Lee, C. L. Lu, "CF4 Plasma Etching on $LiNbO_3$", Appl. Phys. Lett. 35, 10, 1979, pp. 756-758

[15] J. L. Jackel, R. E. Howard, E. L. Hu, S. P. Lyman, "Reactive Ion Etching of $LiNbO_3$", Appl. Phys. Lett. 38, 11, 1981, pp. 907-909

[16] N. Omori and M. Inoue, "Excimer Laser Ablation of Inorganic Solids", Appl. Surf. Sci., 54, 1992, pp. 232-236

[17] J. Greuters and N. Rizvi, "Laser Micromachining of Optical Materials with a 157 nm Fluoride Laser", Proc. of SPIE, 4941, pp. 77-83

[18] I. Barry, G. Ross, P. Smith, R. Eason and G. Cook, "Microstructuring of Lithium Niobate using Differential Etch-rate between Inverted and Non-inverted Ferroelectric Domains", Mat. Lett., 37, 1998, pp. 246-254

[19] K. Nakamura, H. Ando, H. Shimizu, "Ferroelectric Domain Inversion caused in $LiNbO_3$ Plates by Heat Treatment", Appl. Phys. Lett. 50, 20, 1987, pp. 1413-1414

[20] A. Randles, S. Tanaka, B. Pokines, M. Esashi, "Bulk-micromachined Lithium Niobate Sensor and Actuator for harsh Environments", Proc. Transducers 2005, pp. 1380-1383

[21] V. Kugel and G. Roseman, "Domain Inversion in Heat-treated $LiNbO_3$ Crystals", Appl. Phys. Lett., 62, 1993, pp. 2902-2904

[22] J.-h. Lim, J.-s. Hwang, J. Kwon, S.-J. Ham, W. Kim, T. H. Kim, W. K. Jeung, S. J. Yang, S., M. Choi and J. H. Park, "An Ultra Small SAW RF Filter using Wafer Level Packaging Technology,", Proc. IEEE Ultrason. Symp. 2006, pp. 196-199

[23] R. Aigner, "Volume manufacturing of BAW-filters in a CMOS fab", 2nd International Symposium on Acoustic Wave Devices for Future Mobile Communication Systems, 2004, pp. 129-134

[24] M. Goetz, C. Jones, J. Rao, at al., "Advanced SAW Packaging for Modular Integration", 2nd International Symposium on Acoustic Wave Devices for Future Mobile Communication Systems, 2004, pp. 279-286

[25] Nippon Kayaku, Prod. Cat. SU-8 3000, Jap. (2004)

[26] R. Osorio, M. Klein, H. Massler, J. Korvink, "Micromachined Strip Line with SU-8 as the Dielectric", 11th GAAS Symp., 2003, pp. 179-182

[27] J. H. Kuypers, M. Esashi, "Wafer-Level Packaging of RF Devices using Imprinted SU-8 Dry Film", Proc. APCOT 2006, 95-PAT-A0449, pp. 1-4

[28] M. Hara, J. Kuypers, T. Abe and M. Esashi, "Surface Micromachined AlN Thin Film 2 GHz resonator for CMOS integration", Sensors and Actuators, A 117 (2005), pp. 211-216

[29] B. D. Zaitsev, I. E. Kuznetsova, A. A. Teplykh, S. G. Joshi, "Theoretical and Experimental Investigation of the Influence of Electrical Shorting of the Surface on PFA of SH0 Wave in Thin Piezoelectric Plates", Proc. IEEE Ultrason.Symp. 2006, pp. 277-280

[30] B. A. Auld, Acoustic Fields and Waves in Solids, vol. 2, 2nd ed., pp. 291

[31] S. G. Joshi and B. B. Dasgupta, "Electronically Variable Surface Acoustic Wave Time Delay Using a Biasing Electric Field", Proc. IEEE Ultrason. Symp. 1981, pp. 319-323.

[32] A. J. Budreau, P. H. Carr, J. H. Silva, "New Configuration for Electronically Variable SAW Delay Line", Proc. IEEE Ultrason. Symp. 1982, pp. 399-400.

High-Speed and Phase-Sensitive Laser Probe System for SAW Device Characterization

Ken-ya Hashimoto, Hiroshi Kamizuma, Tatsuya Omori and Masatsune Yamaguchi

Dept. of Electronics and Mechanical Engineering, Chiba University
1-33 Yayoi-cho, Inage-ku, Chiba-shi, Chiba 263-8522, Japan
E-mail: {k.hashimoto, omori, masa} @faculty.chiba-u.jp

Abstract—This paper reviews recent progress of a high-speed laser probe system developed by the authors' group for surface acoustic wave (SAW) devices. The phase-sensitive knife-edge method is employed for the optical detection. This makes the system unsusceptible to low-frequency mechanical vibration caused by the fast stage translation. A fast scanning rate of 2.5 kS/s is realized by continuous stage translation and successive acquisition of the detector output by a high-speed data-logger. Timing for the data acquisition is synchronized with the stage movement: timing pulses are generated from a high-precision linear-scale installed in the translation stage and are fed to the data-logger as the trigger. Effectiveness of the system is demonstrated through the selective characterization of spurious resonance modes and scattered non-guided modes appearing in SAW resonators. It is also demonstrated how the wavenumber domain analysis is applied to two-dimensional images captured by the laser probe system for the characterization of RF SAW devices.

I. Introduction

Various types of the laser probe techniques have been proposed and used for the visualization of propagating surface acoustic wave (SAW)[1-4]. Owing to their recent enhanced measurement speed, dynamic range, maximum operation frequency, etc., they are believed to become one of the most effective diagnosis tools for sophisticated RF SAW devices[5-10].

It should be stressed that ultimate reduction in time consumption is still one of the matters of vital importance for applying the laser probe techniques to the research and development of SAW devices.

The authors have recently reported development of a very high-speed laser probe system for RF SAW devices [9,10]. In fact, we can now capture high quality two-dimensional (2D) data of 2,500×400 points in 20 min, and further speeding up and SNR improvement are demanded.

This system is based on the knife-edge method[2,3,6,11]. Since the method optically detects a surface microbend occurred by the SAW propagation, the system is inherently insensitive to low-frequency vibration caused by the fast stage movement.

The detector output is sampled by a high-speed data-logger synchronously with the stage movement; trigger pulses are generated from the output of the high-precision linear-scale and fed to the data-logger. This makes the translation stage driven at its maximum speed, and the sampling rate of 2.5 kS/s is achieved without degradation of the measured result.

The knife-edge method allows us to measure not only amplitude but phase distributions of propagating SAW fields. In addition, the distance between two adjacent measured points is constant and calibrated. Thus, the measured SAW field in the real space (x-y) domain is readily converted into the wavenumber (β_x-β_y) domain by the 2D Fast Fourier Transform (FFT) [10,12].

Similar to the time gating used for an output of vector network analyzers, the (β_x-β_y)-domain analysis offers various information; the types and characteristics of spurious signals, and where and how the spurious signals are generated and propagated[12].

This paper reviews recent progress of the SAW laser probe developed by the authors' group.

After fully describing the system setup, the system is applied to the characterization of spurious resonance modes in an SAW resonator on ST-cut quartz. In conjunction with skillful use of image processing in wavenumber domain, it is shown how the present system is effective in the diagnosis and development of SAW devices.

II. Laser Probe System

A. Optical system

The optical system of the developed laser probe system is shown in Fig. 1. The output of the laser diode (LD) (λ_O=635 nm) is beam-formed, and is incident to the polarized beam-splitter 1 (PBS1), where the s-polarized component is reflected and detected by the monitor photo-detector (PD). On the other hand, the p-polarized component is transmitted to PBS1 and PBS2, and focused on the surface of an SAW device by an objective lens with a large numerical aperture (NA=0.8).

Due to its two-way transmission in the λ/4 plate, the reflected beam is converted to an s-polarized beam on

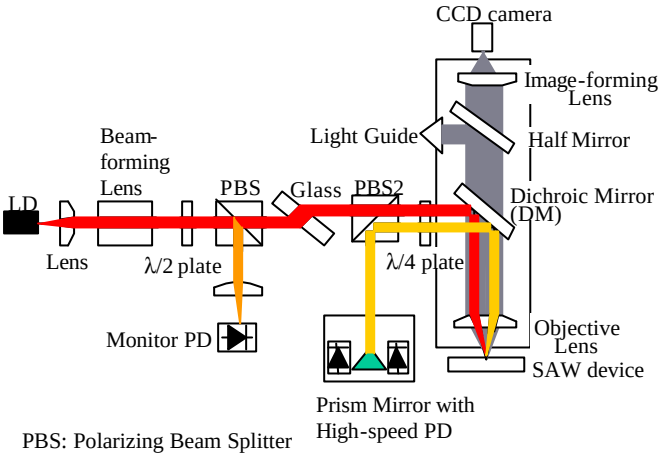

PBS: Polarizing Beam Splitter

Fig. 1 Setup of the optical system

PBS2. Then the beam is reflected by PBS2 and becomes incident to the prism mirror, which also acts as a knife-edge.

It should be noted that the laser beam incident to the SAW device surface becomes obliquely angled by the parallel glass plate inserted between the two PBSs. Therefore, the surface micro-bend caused by the SAW deflects the laser beam, which is to be intensity-modulated by the prism mirror and detected by the high-speed PD (NEWPORT AD-200, f_T=2.5 GHz).

The dichroic mirror reflects only red light, and the above laser path is installed coaxially in the microscope tube with the objective lens. Thus, the magnified image of the device surface with the laser spot can be observed during the measurement. The image is detected by the CCD camera and transferred to the microcomputer for system control.

The SAW device under test is placed on the motor-driven X-Y stage equipped with high-precision linear-scales (20 nm resolution).

The operation principle suggests that the laser spot size D should be smaller than half the SAW wavelength λ_S, and that the maximum deflection efficiency is obtained at D= $\lambda_S/2$.[2]

It should be noted that when D is slightly larger than the electrode width w, D is effectively reduced to w due to large difference in the optical reflectivity between electroded and unelectroded regions. Because of the minimum spot size of approximately 1.4 μm in the present system, maximum operation frequency of the system may be around 2GHz.

B. Detector circuit

A detector circuit with the analog output was developed for fast data acquisition. Figure 2 shows its configuration.

An RF signal is first divided into two paths. The signal in one path is applied to the SAW device under test, and the measured optical output is fed to the mixer after RF amplification. Then the output signal is down-converted to the IF frequency (0.455-10.7 MHz) and applied to an RF two-phase lock-in amplifier (Stanford Research, SR844) after IF filtering. The signal in the

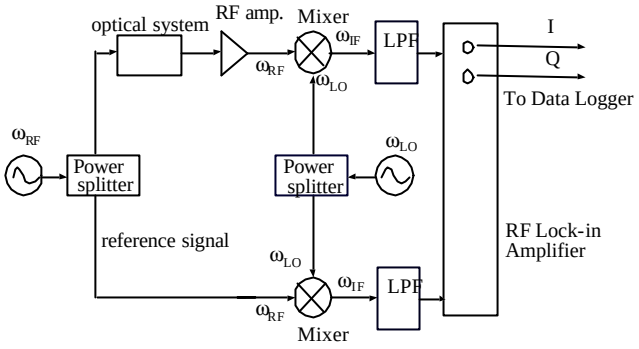

Fig. 2 Detection circuit.

other path is also down-converted to the IF frequency and fed to the lock-in amplifier as a reference signal. The output signals including both the amplitude and phase data of the lock-in amplifier are fed to the high-speed data-logger (Hioki 8841).

C. Measurement procedure

Figure 3 shows the setup of the laser probe system.

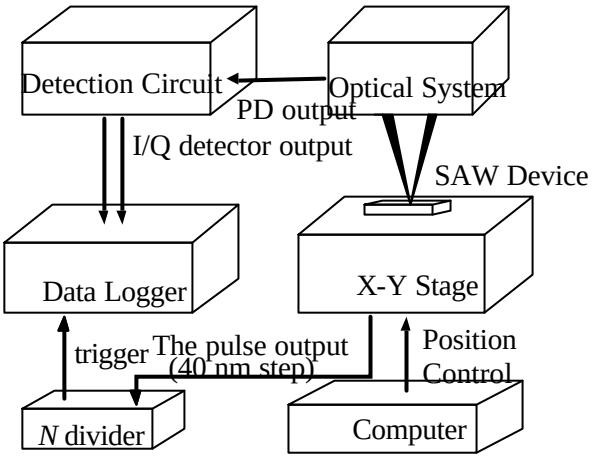

Fig. 3 Setup of laser probe system

Measurement is carried out by the following procedure. The translation stage moves continuously along the longitudinal (x) direction between the specified starting and ending points. The high-precision linear scale attached to the stage outputs two-phase pulse trains every 40 nm movement. Then output signals of the lock-in amplifier are acquired by the high-speed data-logger synchronously with the pulse trains. After one x scan is completed, the stage moves to the lateral y direction by a specified step, and the same measurement is again carried out along the reversed x direction. This process is repeatedly done until the two-dimensional scan is completed.

In the present system, the translation stage moves at its maximum speed of about 1.0 mm/s, and the sampling rate of 2.5 kS/s is achievable.

The sampling interval of 40 nm step is generally too dense resulting in a huge size of data. So the N-divider circuit was prepared by a one-chip micro-controller (Atmel ATtiny13) and inserted between the linear-scale output and the data-logger (see Fig. 3). Here, N can be set arbitrary by a program; when N=25, for example, the

data interval becomes 1 μm (=40 nm×25) step.

Fig. 4 shows the whole system developed. Owing to the knife-edge method which is very insensitive to low-frequency vibration, no tight anti-vibration systems are needed and the optical system occupies only a small area of 66×56 cm^2.

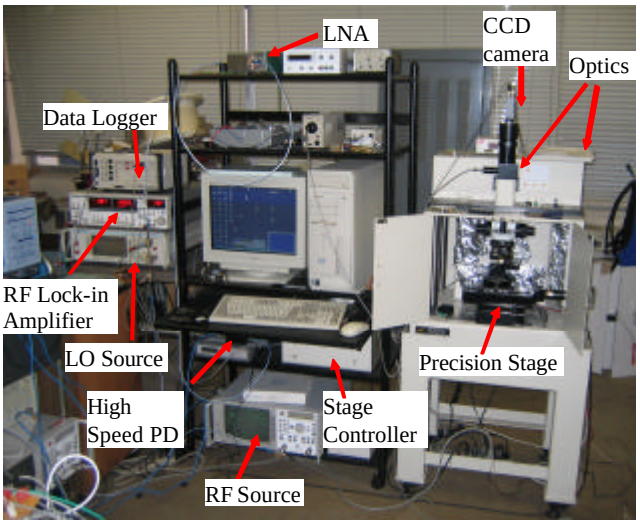

Fig. 4 Appearance of the laser probe system.

III. SAW Device Analysis

A. *Measurement*

The present system was applied to the characterization of an one-port SAW resonator on ST-cut quartz. The design parameters are as follows; the numbers of electrodes of the interdigital transducer (IDT) and reflectors are 356 and 182, respectively, the IDT periodicity is 7.19 μm, the aperture is 209 μm, and the Al electrode thickness is 140 nm.

Fig. 5 shows the input impedance of the resonator as a function of the driving frequency. In addition to the main resonance (b) at 433.00 MHz, several inharmonic resonances are observed.

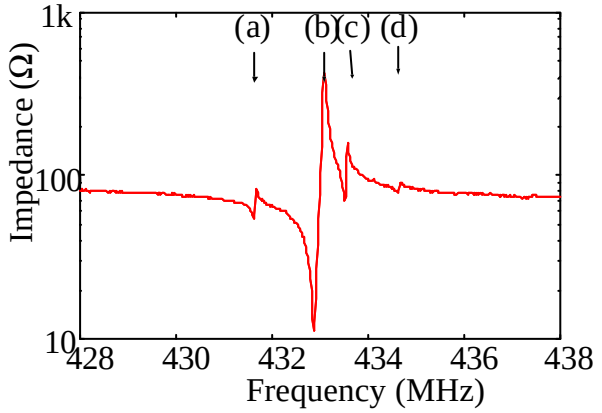

Fig. 5 Input impedance of the device.

The laser probe measurement was applied to the spurious resonances (a), (c) and (d) at 431.625, 433.51 and 434.635 MHz, respectively, as well as to the main resonance (b). At each frequency, it took approximately 20 min. to scan 2,620 (x) × 410 (y) points with 1 μm step.

Fig. 6 shows the result. SAW field distribution is clearly visible. At this frequency region, the dynamic range of about 40 dB is achievable when the detector bandwidth is 1 kHz. The dynamic range can be enhanced by narrowing the detector bandwidth, though the translation speed needs to be reduced as a trade-off.

At the main resonance (b), the SAW energy is confined within the IDT region, and the amplitude changes smoothly along the lateral (y) direction of the IDT. Since the detector output is proportional not only to the SAW amplitude but also to the coefficient of optical reflection on the surface, the periodic streaks parallel to the y direction is due to the difference in the reflection coefficient of the Al electrodes and quartz substrate.

At the spurious resonance (a), three bright loops are observed in the longitudinal (x) direction in the IDT region. This indicates that the SAW is trapped as one of the higher-order longitudinal resonances.

As to the spurious resonances (c) and (d), three and five bright loops are observed aligning in the longitudinal (x) direction in the IDT region. They show that the SAW is trapped as one of the higher-order transverse resonances.

B. *Wavenumber-Space Distribution*

Figure 7 shows the (β_x-β_y) spectrum $A(\beta_x,\beta_y)$ calculated by the 2D FFT of measured data $a(x,y)$ at 433.51 MHz (c). The spectrum on upper (β_x>0) and lower (β_x<0) half planes corresponds to the SAW propagating upward and downward on the device surface, respectively.

Two lines at $\beta_x=\pm\beta_S$ represent the contribution from the SAW propagation giving the main resonance. Each line is basically composed of two bright spots due to the oblique propagation of a guided transverse mode, smearing in the vertical direction owing to the finite width of the SAW beam.

A bright spot is also shown at the origin $(\beta_x,\beta_y)=(0,0)$, corresponding to the contribution of the electromagnetic (EM) feedthrough from the SAW device to the photo detector circuit. It should be noted that since IDTs can not ideally generate acoustic waves normal to the substrate surface, the acoustic contribution should be zero at the origin. Because of the finite measured area, the spot smears both in the vertical and horizontal directions.

An elliptic trace is seen around the origin in the figure. Since the trace includes the bright spots, this suggests that the trace could be the contribution of the SAW scattered at discontinuities.

In addition, several vertical lines are seen at $\beta_x=n\beta_S$, where n is an integer. They are caused by the fact that the IDT and reflector electrodes are aligned periodically and that their periodicities p are almost equal to each other[10]. Namely, the variation in the optical reflectivity generates the spectrum components of $\beta_x=\pm\beta_S+2n\pi/p$ from the SAW components at $\beta_x=\pm\beta_S$, while those of $\beta_x=2n\pi/p$ from the EM feedthrough component at $\beta_x=0$. Since β_S is equal to π/p at the

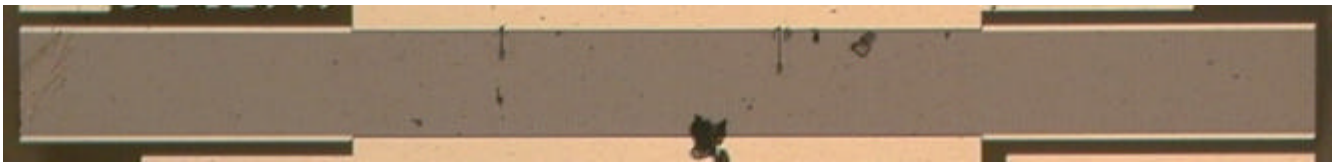

Chip Photo

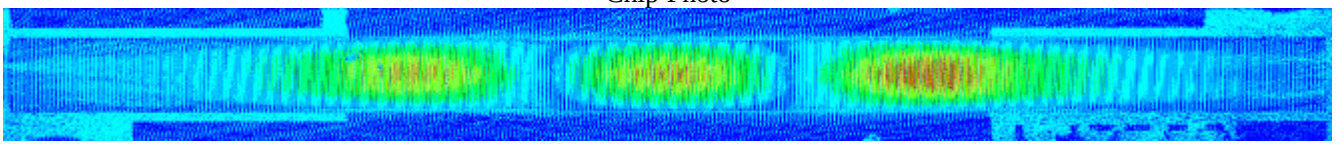

(a) Magnitude (431.625 MHz)

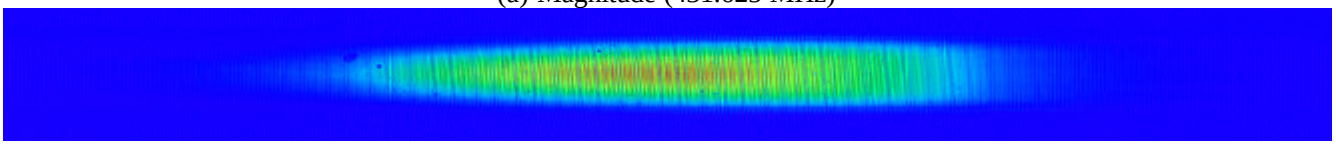

(b) Magnitude (433.00 MHz)

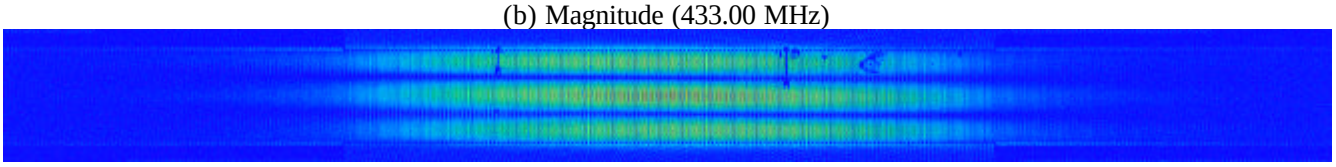

(c) Magnitude (433.51MHz)

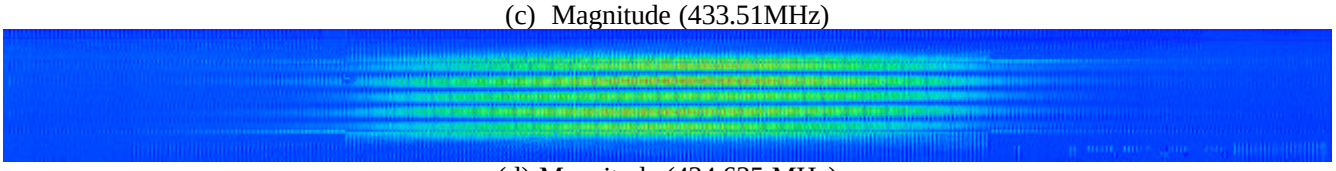

(d) Magnitude (434.635 MHz)

Fig.6 Observed SAW field pattern on the one-port SAW resonator (amplitude)

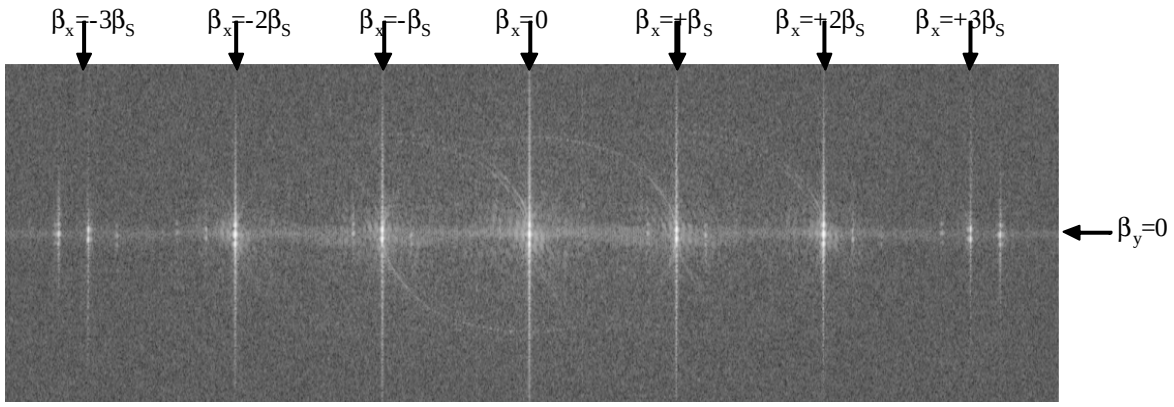

Fig. 7 Measured field distribution in (β_x,β_y) domain (433.51MHz)

resonance, bright lines appear at $\beta_x=n\beta_S$ in the (β_x-β_y) spectrum.

Remaining several lines at $\beta_x\neq n\beta_S$ may be due to the aliasing caused in the FFT calculation.

C. *Gating*

Particular contribution can be selectively characterized by extracting or removing corresponding spectrum and reconverting into the real (*x*-*y*) space by the inverse FFT[12].

Fig. 8 shows an example, where the EM feedthrough was removed by removing the spectrum around the bright line along $\beta_x=0$. Comparison of Fig. 8 with Fig. 6(c) clearly shows that the contrast is enhanced, and that the streaks seen in the bus-bar and reflector regions disappeared. The streaks are caused by the interference between the propagating SAW and EM feedthrough. This technique is expected to become effective with the increased measurement frequency, where the influence of the EM feedthrough is not negligible.

Fig. 9 shows another example obtained by extracting the spectrum around the oval in Fig. 7, which corresponds to the contribution of the scattered SAW. By comparing Fig. 9 with Fig. 6(c), the scratch at upper right is identified as the main scatterer, and the scattering by the surface contaminations is found negligible.

D. Instantaneous field distribution

Since the resonator structure under consideration is symmetric and quasi-periodic, the SAW field distribution (envelope) $\hat{a}(x,y)$ is estimated simply by

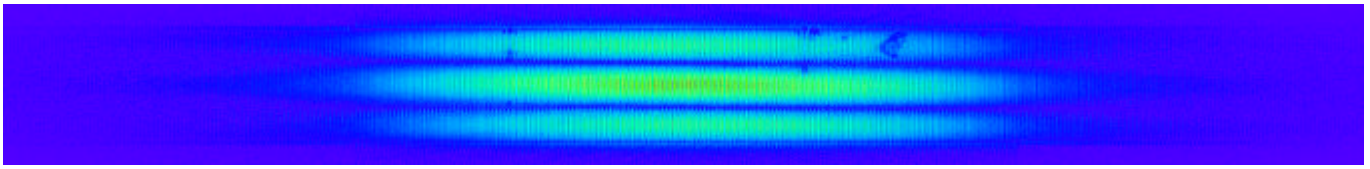

Fig. 8 Measured SAW field distribution after removal of EM feedthrough. (433.51MHz)

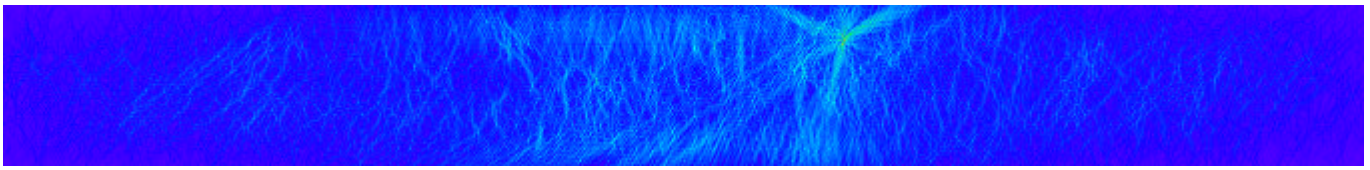

Fig. 9 Extracted scattered SAW field. (433.51MHz)

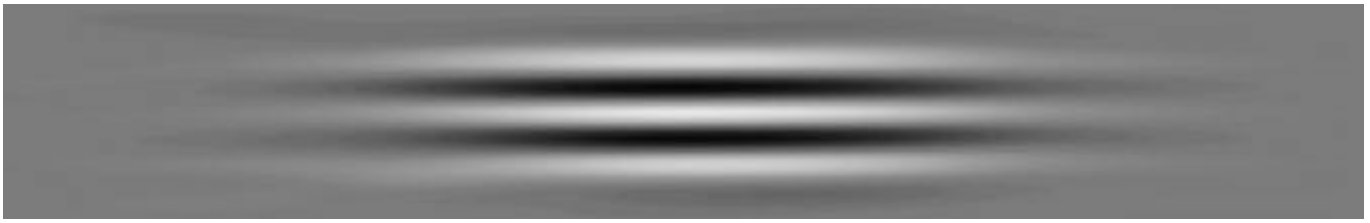

Fig. 10 Estimated SAW envelope in the one-port SAW resonator (434.635 MHz).

extracting the two-dimensional data $\hat{A}(\beta_x,\beta_y)$ around $\beta_x=+\beta_S$ from $A(\beta_x,\beta_y)$ and applying the inverse FFT to $\hat{A}(\beta_x-\beta_S,\beta_y)$[10]. An instantaneous amplitude distribution is estimated by $\mathrm{Re}[\hat{a}(x,y)\exp(j\omega t)]$ where ω is the driving frequency. This image processing technique might be understood from an analogy with the synchronous detection of modulated signals in the telecommunications.

Fig. 10 shows the instantaneous SAW field distribution (envelope) $\mathrm{Re}[\hat{a}(x,y)\exp(j\omega t)]$. The periodic streaks in the row data are completely removed and the reversal of sign amongst adjacent loops are clearly seen.

V. Conclusions

This paper introduced a high-speed laser probe system developed by the authors' group for SAW devices.

A fast scanning rate of 2.5 kS/s is realized by continuous stage translation and successive acquisition of the detector output. The acquisition is synchronized with stage movement detected by a high-precision linear-scale installed in the translation stage.

Owing to the phase-sensitive knife-edge method employed for the optical detection, the system is very unsusceptible to low-frequency mechanical vibrations caused by the fast stage translation.

The system was applied to the characterization of spurious resonance modes in an SAW resonator on ST-cut quartz. In conjunction with skillful use of image processing in wavenumber domain, it is shown how the present system is effective in the diagnosis and development of SAW devices.

Further reduction in the total measurement time may be possible by optimizing the acceleration and deceleration profiles for the stage translation.

Acknowledgements

It is a pleasure to thank Mr. S. Meguro of NEOARK Corp. for his technical support on the system construction, Mr. H. Nakamura and Mr. K. Nishimura of Panasonic Electronic Devices, Co. Ltd. for supplying SAW devices used in this work, and Mr. T. Ui, Mr. M. Watanabe, Mr. K. Kashiwa and Ms. H. Ohtami of Chiba University for their assistance. KH also thanks to late Prof. M.M. Salomaa of Helsinki University of Technology and Dr. S. Jen of Crystal Photonics, Inc. for their valuable suggestions at the initial stage of this work. This work was partially supported by the Mitsubishi Foundation, a Project to Develop "Innovative Seeds" from the Japanese Science and Technology Agency, and a Grant-in-Aid for Scientific Research from Japanese Ministry of Education, Culture, Sports Science and Technology.

References

[1] G.I. Stegeman, "Optical Probing of Surface Waves and Surface Wave Devices," IEEE Tran. Sonics and Ultrason., **SU-23** (1976) pp. 33-36.

[2] H. Engan, "Phase Sensitive Laser Probe for High-Frequency Surface Acoustic Wave Measurements," IEEE Tran. Sonics and Ultrason., **SU-25** (1978) pp. 372-377.

[3] S. Jen and C.S. Hartmann, "Recent Advances in SAW Laser Probe," Proc. IEEE Ultrason. Symp. (1996) pp. 33-36.

[4] A. Holm, R. Weigel, P. Russer and W. Ruile, "A Laser Probing System for Characterization of SAW Propagation on $LiNbO_3$, $LiTaO_3$ and Quartz," IEEE MTT-S Digest (1996) pp. 1541-1544.

[5] K. Kokkonen, J.V. Knuuttila, V.P. Plessky, and M.M.

Salomaa, “Phase-Sensitive Absolute-Amplitude Measurements of Surface Waves Using Heterodyne Interferometry,” Proc. IEEE Ultrason. Symp. (2003) pp. 1145-1148.
[6] H.E Engan and A. Rønnekleiv, “Enhancement of SAW Laser Probe Measurements By Signal Processing,” Proc. IEEE Ultrason. Symp. (1999) pp. 217-220.
[7] S. Wakana, A. Miyamoto, and A. Ito, “Backside Observation Technique for SAW Distribution under Electrodes,” Proc. IEEE Ultrason. Symp. (2003) pp. 1714-1717.
[8] T. Chiba, “Optical Measurement and Numerical Analysis of SAW Propagation,” Proc. IEEE Ultrason. Symp. (2003) pp. 1718-1721.
[9] H. Kamizuma, L.Y. Yang, T. Omori K. Hashimoto and M. Yamaguchi, “High-Speed Laser Probing System for Surface Acoustic Wave Devices Based on Knife-Edge Method,” Jpn. J. Appl. Phys., **44**, 6B (2005) pp. 4535-4538.
[10] H. Kamizuma, T. Omori, K. Hashimoto and M. Yamaguchi: “Development of Fast-Scanning Laser Probe System Based on Knife-Edge Method for Diagnosis of Surface Acoustic Wave Devices”, IEEE Trans. Ultrason., Ferroelec., and Freq. Contr., **52** (2006) pp. 1186-1191.
[11] R. Adler, A. Korpel and P. Desmares, “An Instrument for Making Surface Waves Visible,” IEEE Tran. Sonics and Ultrason., **SU-15** (1968) pp. 157-161.
[12] K.Hashimoto, H.Kamizuma, M. Watanabe, T. Omori, M. Yamaguchi: “Wavenumber Domain Analysis of Two-Dimensional SAW Images Captured by Phase-Sensitive Laser Probe System”, IEEE Trans. Ultrason., Ferroelec., and Freq. Contr., **53** (2007) [to be published].

Absolute Measurement of Surface Vibrational Distributions in Acoustic Wave Devices Using Laser Speckle Interferometer Technique

Yasuaki Watanabe, *Member, IEEE,* Shigeyoshi Goka, Takayuki Sato and Hitoshi Sekimoto, *Member, IEEE*
Graduate School of Engineering, Tokyo Metropolitan University
Hachioji, Tokyo 1920397, JAPAN

Abstract— **In this paper, two different methods for absolutely measuring the surface mode patterns in piezoelectric resonators are described. One is high-sensitive method that uses a semiconductor laser in synchronization with the device motions, and the other is wideband method that uses a burst resonator driving. Both methods are based on a two-dimensional laser speckle interferometer with a CCD video camera, and can provide very clear mode shapes with the absolute displacement scales. Some statistical approaches for the measured interference images are used for deriving the absolute vibrational-displacements in both methods.**

I. Introduction

A number of methods for plotting the mode shapes of piezoelectric resonators have been developed. In designing resonators or vibration devices, measuring the vibration mode shapes is very important. Many of these methods use the optical interference, which is the interaction between incident and reflected photons, produced by coherent laser beams [1]. The laser speckle method that uses the long coherence of modern lasers is a powerful tool for visualizing the displacement of deformed shapes. As a result, many techniques have been proposed [2-6]. When a coherent light such as that from a semiconductor laser irradiates a surface that has a surface roughness greater than the laser wavelength, reflected photons form a random speckle pattern. Because the speckle pattern is very sensitive to changes in the path length, this method can be applied to piezoelectric resonators with minute displacements.

Advances in computer technology have enabled the application of finite element analysis (FEA) to the design of high-frequency piezoelectric resonators such as quartz resonators and SAW devices. In designing the resonators, confirming the reliability of the calculated results is very important because the calculation renders many spurious resonances. Comparing of the mode shape as predicted by analysis and obtained by experiments is the best way to confirm the results.

High-frequency piezoelectric resonators are generally small and their surfaces are not rough enough to directly apply the laser speckle method. For this reason, we have developed many methods for visualizing the mode shapes that combine surface speckle interferometry and image processing techniques [7-13]. The process involves irradiating a roughly finished device surface with a visible-collimated laser beam, and the speckle field that is generated on the surface of the device is captured by a CCD video camera.

However, the absolutes value of the vibrational displacements had not been estimated by the previous method, and the measurement error had not been estimated.

In this paper, two different methods, based on the two-dimensional laser speckle method, for absolutely measuring the surface mode patterns in piezoelectric resonators are described. One is high-sensitive method that uses a semiconductor laser in synchronization with the device motions, and the other is wideband method that uses a burst resonator driving.

The calibration system for the absolute displace estimation is described in Section II. The principle, the measurement system and experimental results of the laser-synchronization method are described in Section III. The method based on the burst resonator excitation method is described in Section IV. We applied these methods to measure the fundamental thickness shear modes in a circular AT-cut quartz resonator with a roughly finished surface.

II. Calibration System [13]

A diagram of the system used to measure the absolute in-plane vibrational displacement is shown in Fig. 1. A small mirror is attached to a lateral face of a rectangular quartz plate having roughly finished surfaces. The plate is externally vibrated by a laminate ceramic actuator in the lateral direction.

Figure 2 shows a detailed drawing of the plate. The Michelson interferometer measures the out-of-plane vibrational displacement at the lateral face to which the mirror is attached. This displacement corresponds to the in-plane displacement observed at the upper side of the plate. The speckle images on the quartz plate are captured with a CCD camera placed over the plate.

The amplitude of the in-plane displacement on the plate surface is obtained from data and statistical processing of the speckle images: estimation of pixel brightness, calculation of

Email: y.watanabe@ieee.org

visibility, and an correction of the error in the vibrational amplitude based on the interference function.

Figure 3 shows the optical reflection and interferometric model of the resonator surfaces, which are roughly finished. The incident angle of the laser beam must be set almost parallel to the surface being measured. The light beams scattered on the surface interferes with each other; that is, the bright or dark spots on the device surface are amplitude modulated by the in-plane vibrations. In general, the surface roughness of devices ranges from several micrometers to a hundred micrometers, sufficiently large in relation to the wavelength of visible lasers and sufficiently small in relation to the coherence length of semiconductor lasers. Accordingly, the vibrational amplitude can be obtained by measuring the brightness changes at the interference points on the device surface.

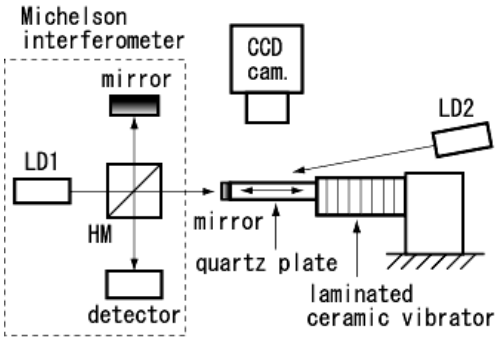

Figure 1. Measurement system.

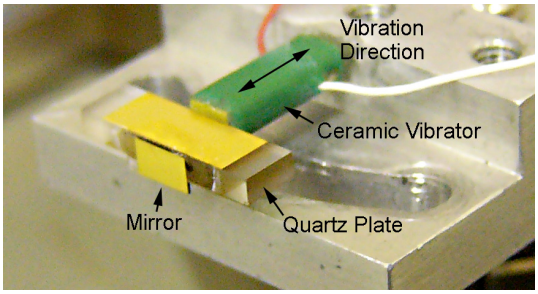

Figure 2. Quartz plate with small mirror.

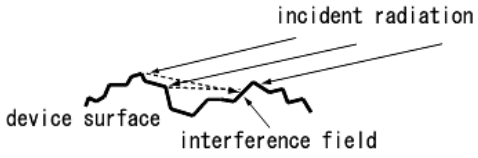

Figure 3. Optical model of device surface.

Assuming the optical model shown in Fig. 3, the interferometric intensity is given by the following equation when the laser beam is parallel to the resonator surface.

$$I = \bar{I}_0 + \gamma \cos 2kdx \qquad (1)$$

where $k = 2\pi/\lambda$, λ is the wavelength of the laser, $\bar{I}o$ is the average intensity of the interference, γ is the visibility of the fringes, and dx is the vibrational displacement of the resonator. The γ changes the surface condition of the resonator and its optical constructions.

III. Synchronized Laser Method

A. Principle

Based on the constituent relation for piezoelectric devices, the amplitude of the vibrational displacement is proportional to the driving voltage. Using this relationship, we can obtain visibility γ from arbitrary pairs of vibrational amplitude and interferometric intensity. We obtained γ by using resonator driving voltage V_1 and V_2 ($V_2 = V_1 / 2$). The absolute vibrational displacement was obtained using (1).

By rearranging (1), we can express γ as

$$\gamma = \frac{2 \cdot \Delta I_2^{\,2}}{4 \cdot \Delta I_2 - \Delta I_1} \qquad (2)$$

where ΔI_1 and ΔI_2 are the differences in optical intensities for V_1 and V_2, respectively.

We can thus obtain the absolute amplitude of the in-plane vibration by using

$$dx = \frac{1}{2k} \cos^{-1}\left(1 - \frac{\Delta I - |\varepsilon|}{\gamma}\right) \qquad (3)$$

where ε is the residual error caused by CCD and environment noise.

A practical approach for the application of the laser speckle method is as follows.

1) Calculate the mode shape and contour map from the set of images captured by the CCD camera using a two-dimensional correlation function.
2) Divide the set of image areas having approximately the same in-plane vibrational amplitude into smaller areas.
3) Find the pair of pixels that gives the maximum optical intensity difference in each divided area.
4) Repeat steps 2) and 3) using half the resonator driving voltage to derive visibility γ.
5) Repeat steps 2) and 3) without driving to estimate system noise ε.
6) Map the frequency distribution characteristics of the intensity differences in the divided areas.
7) Calculate the in-plane vibrational amplitude using Eq.(3).

B. Measurement System

Figure 4 shows a block diagram of the measurement system [13]. A reference oscillator phase locks the signal generators (SGs). A low-frequency oscillator generates the image capture triggers and the phase control signals for SG_1. A commercial CCD video camera captures images of the interference on the surface of the sample. These images are averaged to reduce system noise. The vibration patterns are obtained as correlation coefficients between the images for the maximum positive and maximum negative vibrational phases. A semiconductor laser with linear polarization generates a visible beam. In our measurements, the laser had an optical power and wavelength of 10 mW and 655 nm, respectively. The incident angle of the beam on the resonator surface was 10^{o}. The spatial resolution of the camera was 640 x 480 pixels. The kernel for calculating the correlation between two accumulated images had 5 x 5 pixels, so the kernel was sufficiently smaller than the wavelength of the acoustic wave on the resonator surface. After the correlation analysis, the small areas are classified by their amplitude levels for the frequency distribution analysis.

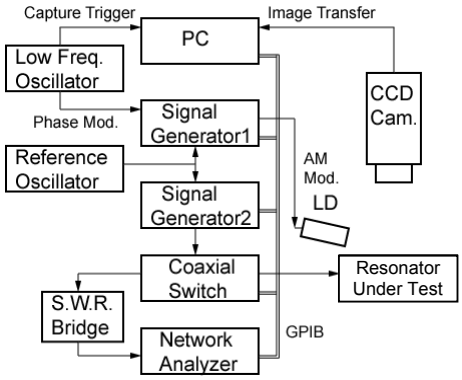

Figure 4. Experimental setup of full-field in-plane motion visualization system with synchronized laser diode.

C. Results

Figure 5 shows the frequency distribution characteristics of the intensity deviations in the divided areas. The drive frequency of the ceramic actuator was 1 kHz. The actuator driving voltage was adjusted to achieve the absolute displacement. Five thousand pairs of images were accumulated and averaged to reduce the CCD and environment noise. The ordinate axis is the frequency of the divided areas, and the abscissa axis is the deviation in pixel gradation. The peaks of the curves corresponding to changes in the vibrational displacement. Even the actuator driving level was zero, there was still a gradation-sequence error of about 0.2, caused by the CCD and environment noise.

Figure 6 shows the measured in-plane displacement vs. absolute displacement based on Fig. 5. The dotted line shows the ideal characteristics.

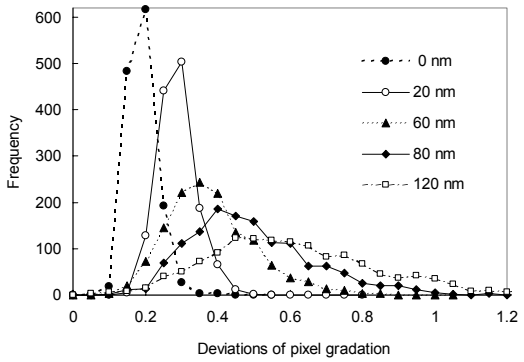

Figure 5. Frequency distributions of pixel gradation for vibrational displacement.

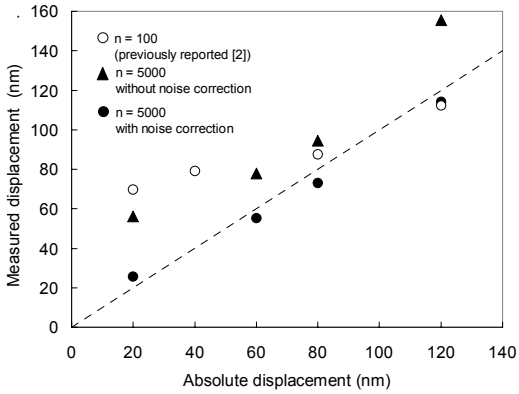

Figure 6. Comparison between measured and absolute vibrational displacements.

Visibility γ is taken into account to correct the systematic error caused by the optical measurement conditions. The filled circles and triangles represent the measured in-plane displacement. The filled circles were derived using system error ε, and the filled triangles were derived without ε. Very good correlation between the measured and absolute vibrational displacement was obtained with ε. The open circles show the experimental results [13]; 100 images were used for averaging, and ε was ignored. This figure shows that the absolute in-plane vibrational displacement can be measured using equation (3) with an appropriate number of images and system error correction.

Figure 7 shows the mode shape of the fundamental thickness-shear mode in a circular AT-cut resonator. We used a 10 MHz circular AT-cut quartz resonator with a roughly finished surface (#4000) with partial electrodes [10]. In this experiment, 500 pairs of images were used. The scale on the right was determined using the proposed method. This figure demonstrates that the vibrational amplitude is trapped in the midsection of the electrode area. The in-plane vibrational displacement was approximately 100 nm in the midsection and was below 20 nm at the circumference.

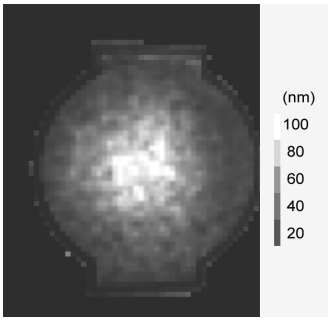

Figure 7. Experimental results for 10 MHz circular AT-cut quartz resonator. (N=500; Drive level = +3 dBm).

IV. Burst Excitation Method

A. Principle

In the burst resonator excitation system, the speckle interferometric intensity difference between the resonator-driven and resting phases is given by integrating equation 1 as,

$$\Delta I = \gamma\left(1 - \frac{\sin 2kdx}{2kdx}\right) \tag{4}$$

We can easily understand from the equation that γ is not explicitly obtained by changing dx as a parameter. Therefore, we used a second order polynomial function to approximate equation 4 at around $dx = 0$.

The second term in the parentheses in equation 4 can be formally expressed as,

$$\frac{\sin 2kdx}{2kdx} = \alpha dx^2 + \beta dx + 1 \tag{5}$$

where α and β are negative constants, and they can be derived by determining λ and the approximation range. By rearranging equation 5, dx can be obtained by the next relationship.

$$\Delta I = -\gamma\left(\alpha dx^2 + \beta dx\right) \tag{6}$$

γ can be obtained by solving equation 6 for two dx(s) of their amplitude ratio is 1 : 1/2.

$$\gamma = \frac{\alpha}{\beta^2}\frac{\left(\Delta I_1 - 4\Delta I_2\right)^2}{-2\Delta I_1 + 4\Delta I_2}, \tag{7}$$

where ΔI_1 and ΔI_2 are the differences in optical intensities for V_1 and V_2 (= V_1 / 2). This method is based on the linear piezoelectric relation and its potency is demonstrated in our previous paper [13]. In our proposed method the residual noise ε of the image is subtracted from each ΔI_1 and ΔI_2 before using equation 7 because the relationship between brightness of the interferometric filed and the vibrational displacement is not simply defined.

We can thus obtain the absolute vibrational amplitude of the in-plane vibration using equation 4. Figure 8 shows a flowchart for measuring and image processing.

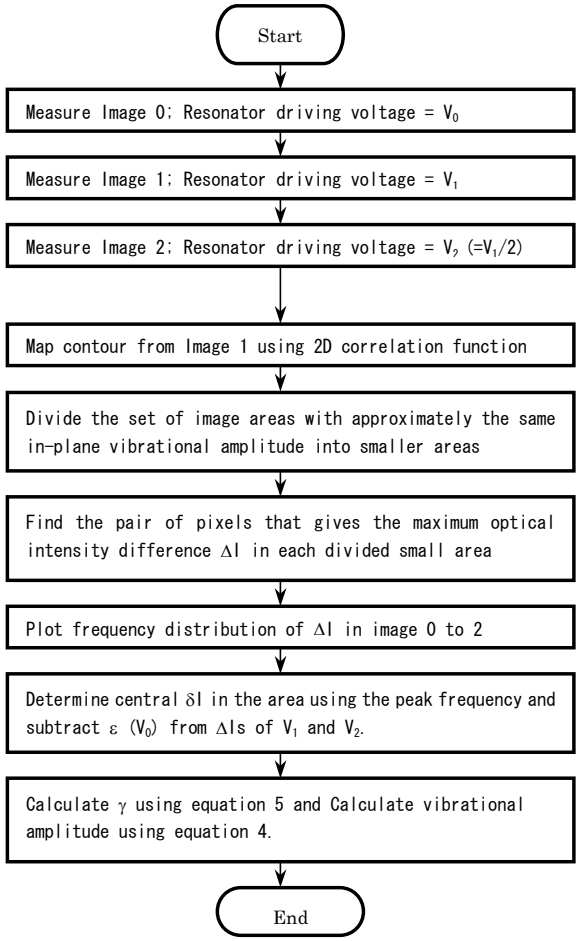

Figure 8. Flowchart of measurement and image processing

B. Measurement System

Figure 9 shows an optical layout of the burst resonator-driving system for measuring the in-plane mode shapes of the piezoelectric devices. A collimated beam from the laser diode (LD) illuminates the electroded sample surface and was scattered on the surface. Polarization of the laser beam was parallel to the sample surface. The reflected beam was illuminated on the mirror placed on the opposite side of the laser.

This optical system enhances the interference intensity of the sample surface when the in-plane vibrational displacement is measured. The incident angle of the laser in the system used is same as the system described in Section II.

Figure 10 shows a timing chart of the sample driving signal and image capture triggers. The resonator sample was driven by a burst wave signal at the resonant frequency of the sample. The burst period and duty ratio were 400 ms and 5%.

The period of the video trigger was half that of the burst period. Images for the driven and resting states are thus alternately obtained. The slow trigger rate is attributable to the image transfer and the image averaging.

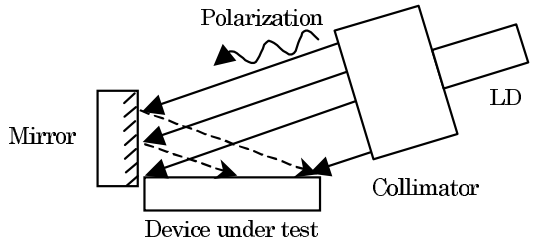

Figure 9. Optical layout of burst-drive laser speckle method.

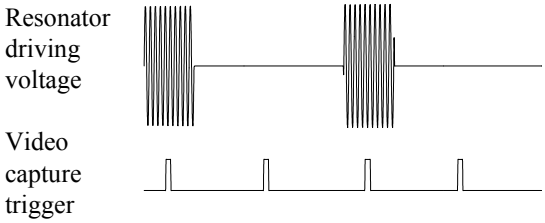

Figure 10. Timing chart of measurement.

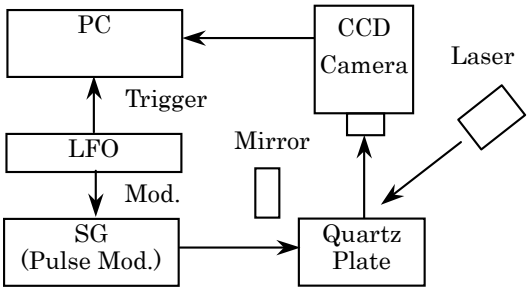

Figure 11. Measurement system.

Figure 11 is a block diagram of the measurement system. A charge coupled device (CCD) video camera was used to capture the diffusion light component on the surface of the sample. The vibration patterns were obtained as reciprocals of the correlation coefficients between the images for the driven and resting phases. This system was improved so that the frequency synthesizer's output frequency automatically traced out the resonant frequency of the device using the network analyzer.

The specifications of the laser and other equipment in this system are same as the system in Section II.

C. Results

We used the same calibration system as shown in Section I for estimating the burst method.

Figure 12 shows the measured in-plane displacement vs. the absolute displacement derived from the frequency distribution of the intensity deviations. The dotted line represents the ideal characteristics. Visibility γ and residual error ε were taken into account to correct for the systematic error caused by the optical measurement conditions and the CCD noise. The drive frequency of the ceramic actuator was 1 kHz. The actuator driving voltage was adjusted to achieve the specified displacement. Two thousand image pairs were accumulated and averaged to reduce the CCD and environment noises.

The dots represent the measured in-plane displacement. The error bar shows the standard deviations of measured data that were taken five times. The maximum standard deviation was 25 nm. A very good correlation between the measured and absolute vibrational displacements was obtained with regards to γ and ε.

Figure 13 shows the measured in-plane displacement without using ε. Very large errors are observed in the figure, that is, the error correction is necessary for this method.

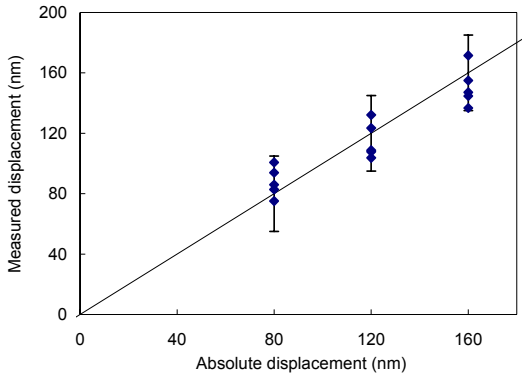

Figure 12. Comparison between measured and absolute vibrational displacements.

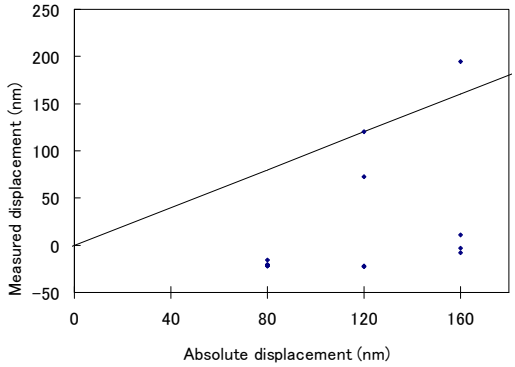

Figure 13. Comparison between measured and absolute vibrational displacements without concerning ε.

Figure 14 shows the mode shape of the fundamental thickness shear mode in a circular AT-cut resonator. We used a 23 MHz circular AT-cut quartz resonator with a roughly finished surface (#4000) with partial electrodes. We used 200 image pairs in this experiment. The resonator driving level was + 13 dBm of the SG output level. The scale on the right was determined using the proposed method. This figure demonstrates that the vibrational amplitude was trapped in the midsection of the electroded area. The in-plane vibrational displacement was approximately 200 nm in the midsection. The measurement time was approximately 300 s. The image transfer process occupied the majority of the measurement time.

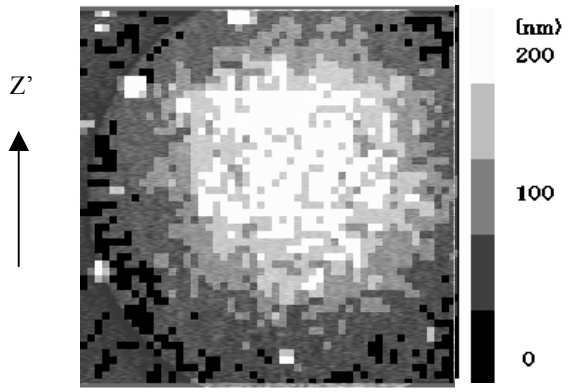

Figure 14. Experimental results for 23 MHz circular AT-cut quartz resonator. (N=200; Drive level = +13 dBm).

V. CONCLUSIONS

We have developed two full-field imaging methods that rapidly measures the absolute in-plane mode shapes of piezoelectric devices. By taking into account the error caused by CCD and environment noise, the absolute in-plane displacement on a device surface can be mapped. The full-field attribute of the method enables rapid data acquisition compared to mechanical scanning. The method will be further improved by introducing a low-noise CCD camera and incrementing the number of measurements.

References

[1] R. J. Williamson, "Non-Destructive Means for Determining Mode Shape in Thickness-Shear Resonators," in Proc. 44th Annu. Symp. Freq. Control, 1990, pp. 424-436.

[2] H. J. Tizianni, "Application of Speckling for In-plane Vibration Analysis," Optica Acta, Vol. 18, No.12, pp. 891-902, 1971.

[3] D. E. Duffy, "Moire Gausing of In-plane Displacement Using Double Aperture Imaging," Applied Optics, Vol. 11, No. 8, pp. 1778-1781, 1972.

[4] J. Monchalin, "Optical Detection of Ultrasound," IEEE Trans. Ultrason., Ferroelect., Freq. Contr., Vol. UFFC-35, No. 5, pp. 485-499, 1986.

[5] W. Wang, C. Hwang, S. Lin, "Vibration Measurement by the Time-Averaged Electronic Speckle Pattern Interferometry Methods," Applied Optics, Vol. 35, No. 22, pp. 4502-4509, 1996.

[6] C. Ma, C. Huang, "The Investigation of Three-Dimensional Vibration for Piezoelectric Rectangular Parallelepipeds Using the AF-ESPI Method," IEEE Trans. Ultrason., Ferroelect., Freq. Contr., Vol. 48, No. 1, pp. 142-153, 2001.

[7] Y. Watanabe, Y. Shikama, S. Goka, T. Sato, H. Sekimoto, "Mode Shape Measurement of Piezoelectric Resonators Using Image Processing Technique," Japanese. Journal of Appl. Phys. Vol. 40, pp. 3572-3574, 2001.

[8] Y. Watanabe, T. Tominaga, T. Sato, S. Gokaj H. Sekimoto, "Visualization of Mode Patterns of Piezoelectric Resonators using Correlation Filter," Japanese. Journal of Appl. Phys., Vol.41, Pt.1, No.5B, pp. 3313-3315, 2002.

[9] Y. Watanabe, T. Sato, S. Goka and H. Sekimoto, "Non-Scanning Means for Determining Vibrational Distribution in BAW and SAW Devices," in Proc. IEEE Ultrasonic Symp., 2002, pp. 928-931.

[10] Y. Watanabe, T. Sato, S. Goka and H. Sekimoto, "Measurement of In-Plane and Out-of-Plane Mode Shapes in Piezoelectric Devices Using Laser Speckle Interferometry," Acoust. Sci. & Tech. Vol.23, No.5, pp. 284-285, 2002.

[11] Y. Watanabe, S. Goka T. Sato and H. Sekimoto, "Non-Scanning Measurements for Determining In-Plane Mode Shapes in Piezoelectric Devices with Polished Surfaces," in Proc. IEEE Freq. Contr. Symp., 2003.

[12] Y. Watanabe, K. Tsuno, T. Tsuda, S. Goka, T. Sato and H. Sekimoto, "In-Plane Mode Shape Visualization of Piezoelectric Resonators using Stroboscopic Laser Irradiation," in Proc. 2004 Annu. Symp. Freq. Control, 2004.

[13] Y. Watanabe, T. Tsuda, S. Ishii, S. Goka and H. Sekimoto: : Jpn. J. Appl. Phys., Vol. 45, No. 5B, 2006, pp. 4585-4587

Picosecond laser based surface acoustic wave probing

Oliver B. Wright

Hokkaido University, Graduate School of Engineering, Sapporo, Japan, Email: assp@kino-ap.eng.hokudai.ac.jp

Abstract — **I show how by the use of an ultrafast optical technique one can excite broadband surface acoustic wave packets and track them on crystals, microstructres, and on 1D and 2D phononic crystals in two dimensions and in real time at frequencies up to ~1 GHz. The acoustic dispersion relation is obtained from the data by means of a spatiotemporal Fourier transform. In phononic crystals we find stop bands for both leaky longitudinal and Rayleigh waves.**

Keywords: phononic crystal, surface acoustic wave, stop band, ultrasonic

I. INTRODUCTION

Laser-based acoustics is an excellent method for investigating acoustic wave propagation in microstructured specimens. To achieve the sub-micron acoustic wavelengths required, picosecond laser pulses have been used to generate and detect high frequency bulk waves. Thin films [1], microstructures and nanostructures [2][3] can be characterized in this way with longitudinal waves. Furthermore, similar measurements with shear waves have been carried out [4]. It was also shown by myself and coworkers that picosecond laser pulses are suitable for generating and imaging surface acoustic waves (SAW) up to ~1 GHz [5]. These methods present the advantages of non-contact and nondestructive testing. Most recently we have been studying the interaction of laser generated surface acoustic waves with 1D and 2D microfabricated phononic crystals that exhibit stop bands. Phononic crystals can have a variety of geometries. For example, they can consist of periodically oriented grooves or lines, [6] or of cylindrical holes or cylinders [7-9] in a substrate. The superior acoustic features of phononic crystals, such as acoustic stop bands, have led to their incorporation in devices such as filters [9][10]. In this paper I shall illustrate our picosecond SAW imaging technique in relation to our recent work on phononic crystals.

II. EXPERIMENTAL SETUP

For the surface acoustic wave measurements we are using an optical pump and probe technique, shown in Fig. 1 (a), incorporating light pulses of duration ~1 ps. The detection is performed with two 800 nm probe beams by means of a common path interferometer [5][11] that measures the optical phase difference $\Delta\phi$ between these beams. The pump light pulses of

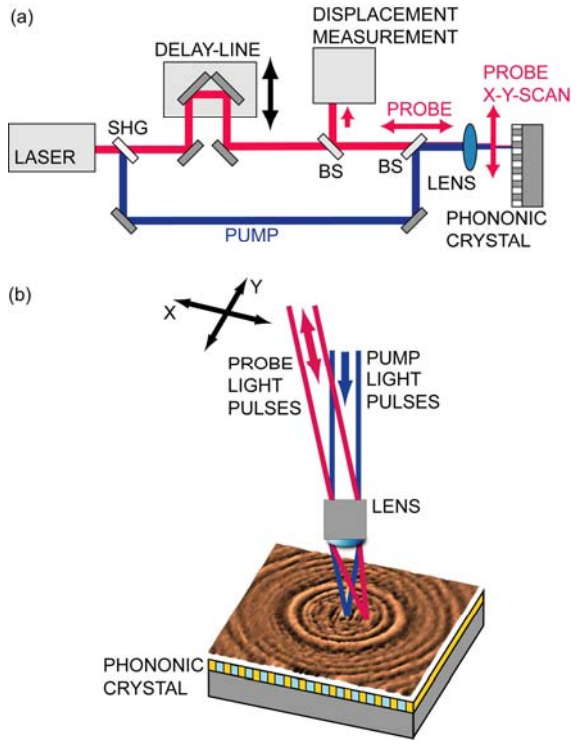

Figure 1. (a) Pump and probe setup for a phononic crystal sample. (b) Geometry for optical incidence on a 1D phononic crystal. The probe beam is scanned. (SHG: second harmonic generation crystal. BS: beam splitter.)

wavelength 400 nm are absorbed at a small spot (~2 μm in diameter) at the surface of the specimen, launching Rayleigh-like surface acoustic waves (RW) as well as leaky longitudinal acoustic waves (LW) along the surface. As shown by the optical incidence configuration in Fig. 1 (b), the probe laser spot (also of diameter ~2 μm) is scanned in the lateral (x, y) directions across the surface. We record the temporal variation of $\Delta\phi$, which is proportional to the time derivative of the out-of-plane surface motion ($\partial u_z/\partial t$), within an area of 150 μm × 150 μm. The 76.3 MHz repetition rate of the laser corresponds to a period of 13.1 ns. We typically record 40 images, equally spaced in time within 13.1 ns. The broadband SAW pulses have a maximum amplitude between 200 MHz and 700 MHz, corresponding to a dominant wavelength Λ~10 μm. Frequencies up to ~1.3 GHz are detected.

III. MICROFABRICATED PHONONIC CRYSTALS

Both 1D and 2D phononic crystals were prepared. To make a 1D phononic crystal of period a=4 μm, alternate 2 μm wide copper and silicon oxide lines of thickness 800 nm are deposited perpendicular to the [011] direction on a silicon (100) substrate [see Fig. 2 (a)]. As the cross section of the specimen in Fig. 2 (b) shows, a layer of tantalum of thickness 25 nm serves as a diffusion barrier for the copper. The industrial fabrication process involves lithography and chemical-mechanical polishing, leading to a very small surface roughness (<10 nm). On top of this specimen we sputtered a 30 nm gold layer to achieve uniform optical reflectivity. The gold layer and the tantalum diffusion barrier do not significantly affect the SAW dispersion [5].

The 2D phononic crystals consist of air-filled holes etched in silicon (100), arranged in regular square lattices. The holes have diameter d≈12 μm, depth h≈15 μm, lattice constant a≈15 μm, and filling fraction F≈50%. We also prepared a similar sample with d≈6 μm, h≈80 μm, a≈6.5 μm and F≈70%. These samples are metal coated to a 40 nm thickness.

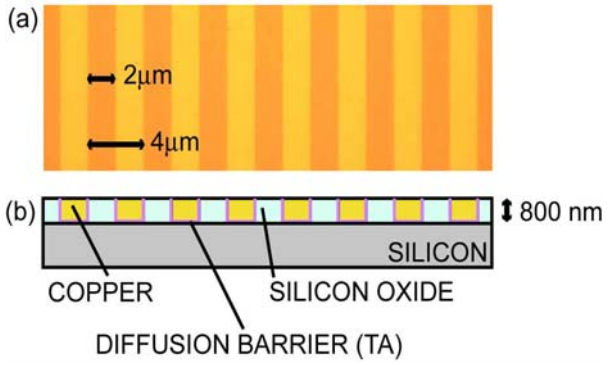

Figure 2. (a) Optical micrograph of the top surface of the sample. (b) Corresponding cross section of the specimen before gold film deposition.

IV. RESULTS

A. Real-time mesurements

Figure 3 shows four consecutive images of the measured optical phase difference $\Delta\phi$ over a 150 μm × 150 μm region of the 1D phononic crystal sample (corresponding to 37 copper lines). The images are spaced by 1 ns. The multiple wave fronts are caused by the laser pulse repetition, the multimode excitation, and the scattering by the periodic line array. The SAW penetrates to a distance $\sim\Lambda$. The SAW propagation, especially at low frequencies, is therefore affected by the anisotropic Si substrate. We observe a twofold symmetry in the wave front that is caused by the line array. The influence of the anisotropic Si can only be observed at low frequencies where Λ is larger (as described later).

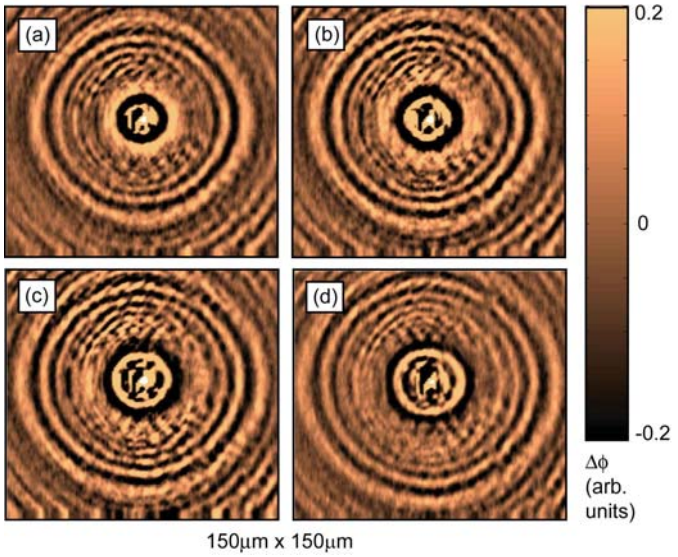

Figure 3. (a) – (d) Real-time images of the optical phase difference $\Delta\phi$ separated in time by ~1ns. The scanning area is 150 μm × 150 μm.

B. Dispersion relation

With a complete temporal series of these images, we have direct access to the complete dispersion relation using a combination of a 2D Fourier transformation in the space domain [12],

$$F(\mathbf{k},t)=\frac{1}{(2\pi)^2}\int_{-\infty}^{\infty} f(\mathbf{r},t)\exp\left(-i\,\mathbf{k}\cdot\mathbf{r}\right)d^2\mathbf{r}\,,$$

and a Fourier transformation in the time domain,

$$H(\mathbf{k},\omega)=\frac{1}{2\pi}\int_{-\infty}^{\infty} F(\mathbf{k},t)\exp\left(i\omega t\right)dt\ .$$

From the 40 recorded real-time images, the complete dispersion relation of the excited waves is calculated from the above Fourier transforms. Figure 4 shows two such constant frequency surfaces of the dispersion relation. The boundary of the first Brillouin zone (BZ) at $k_x=\pm\pi/a=\pm0.79$ μm^{-1} (period a=4 μm) is indicated by the white arrows. At 458 MHz [Fig. 4 (a)] the RW and LW modes form concentric rings, indicating an approximately isotropic wave velocity. Mode identification is provided on the right in Fig. 4. The RW ring is also visible as a ghost shifted in both the positive and negative k_x directions by a reciprocal lattice vector $\pm G=2\pi/a=1.58$ μm^{-1}, owing to the effect of acoustic scattering in the periodic structure. These ghosts are referred to as Bloch harmonics (see dotted lines in Fig. 4). At 534 MHz [Fig. 4 (b)], one sees stop bands persisting for propagation angles (to the k_x-direction) up to θ≈15° and 20° for RW and LW, respectively. The overall shape of the constant frequency surfaces becomes noticeably flattened with respect to a circle by the effect of the periodicity (that imposes zero group velocity at the BZ edges). We interpret the bridge-like features joining the RW and LW branches at θ≈30° (to the k_x-direction) to be RW Bloch harmonics inside the 1st BZ. At higher frequencies (> 600 MHz) we observe that the stop band closes.

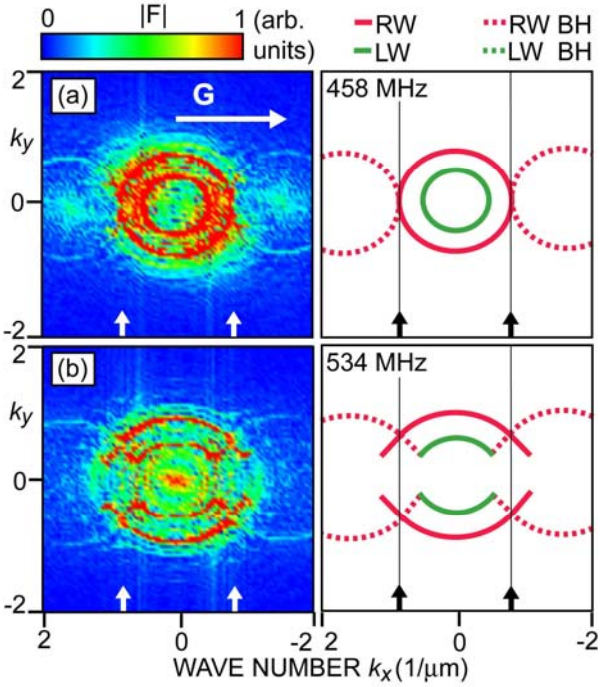

Figure 4. Left: experimentally obtained constant frequency surfaces for (a) 458 MHz and (b) 534 MHz. Right: Mode identification at both frequencies. BH: Bloch harmonics.

C. Comparison of real-time imaging and dispersion relation

The effect of the stop band, which we identified in the constant frequency surface at 534 MHz, can also be observed in real time. Figure 5 (a) shows the real-time data filtered with a band-pass filter around 229 MHz. As expected at these low frequencies the wave propagation is almost isotropic, and the wave front consists of concentric rings. The anisotropic silicon substrate causes a weak fourfold symmetry. Figure 5 (b) shows the filtered real-time data corresponding to a band-pass filter around 534 MHz [cf. Fig. 4 (b)]. In this case we observe strong attenuation for waves propagating in the *x*-direction for which the stop band occurs. After about 2-3 periods the waves almost completely disappear.

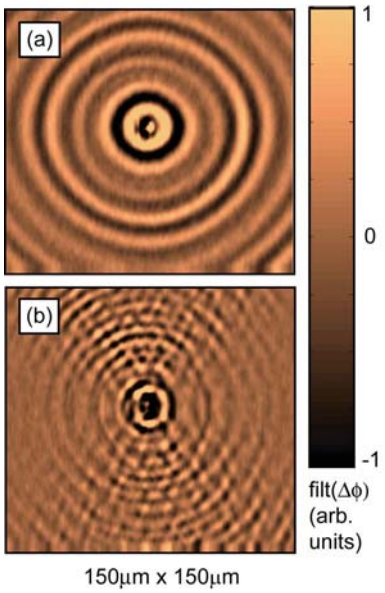

Figure 5. (a) Real-time data filtered around 229 MHz. (b) Real-time data filtered around 534 MHz, where the stop band occurs. The notation filt($\Delta\phi$) for the scale means the filtered value of the optical phase difference $\Delta\phi$.

V. 2D PHONONIC CRYSTALS

We have also applied the same experimental techniques to the two 2D phononic crystal samples, and preliminary results were obtained. For the $a\approx15$ μm sample, the wave fronts could be observed over the area of the 2D phononic crystal surface, as in the 1D case, and a stop band was discerned at ~250 MHz for *x*- or *y*- directed propagation. For the $a\approx6.5$ μm sample, the holes were too close together to allow imaging over the area of the 2D phononic crystal surface, but we were instead able to measure wave fronts reflected from the structure over an unpatterned portion of the surface. This indicated a stop band in the vicinity of 550 MHz for *x*- or *y*-directed propagation. We are at present analysing these results by comparison with simulations [13].

VI. CONCLUSIONS

In conclusion we have applied a real time imaging method to the detection of propagating surface acoustic waves in crystals, microstructures and 1D and 2D phononic crystals. By Fourier transformation the acoustic dispersion relation is directly obtained. So far the frequency resolution has been limited to ~76 MHz, the repetition rate of the laser used. In future the use of a lower repetition rate should allow much finer frequency resolution. We also intend to apply this method to study wave propagation phenomena on surface acoustic wave resonators or waveguides, and it should also prove useful for characterizing acoustic waves on 3D phononic crystals.

ACKNOWLEDGMENT

We would like to thank JSPS (the Japanese Society for the Promotion of Science) for financial support and Alex Maznev for donating the 1D phononic crystal specimen I also thank

Dieter Profunser, Osamu Matsuda Udo Lang, Abdelkrim Khelif, Sarah Benchabane, and Vincent Laude for their contributions to this work.

REFERENCES

[1] C. Thomsen, H.T. Grahn, H.J. Maris and J. Tauc, "Surface generation and detection of phonons by picosecond light-pulses", Phys. Rev. B., vol. 34, pp. 4129-4138, 1986

[2] D.M. Profunser, J. Vollmann and J. Dual, "Measurement of the bulk acoustic wave propagation in ultra-thin membranes", Proceedings of the IEEE Ultrasonics Symposium, pp. ,Munich, 2002

[3] D.M. Profunser, J. Vollmann and J. Dual, "Determination of the material properties of microstructures by laser based ultrasound", Ultrasonics, vol. 42, pp. 641-646, 2004

[4] O. Matsuda, O.B. Wright, D.H. Hurley, V.E. Gusev and K. Shimizu, "Coherent shear phonon generation and detection with ultrashort optical pulses", Phys. Rev. Lett., vol. 93, Art.No. 095501, 2004

[5] Y. Sugawara, O.B. Wright, O. Matsuda, M. Takigahira, Y. Tanaka, S. Tamura and V.E. Gusev, "Watching ripples on crystals", Phys. Rev. Lett., vol. 88, Art.No. 185504, 2002

[6] D.M. Profunser, O.B. Wright and O. Matsuda, "Imaging ripples on phononic crystals reveals acoustic band structure and Bloch harmonics", Phys. Rev. Lett., vol. 97, Art.No. 055502, 2006

[7] Y. Tanaka and S. Tamura, "Acoustic stop bands of surface and bulk modes in two-dimensinonal phononic lattices consisting of aluminium and a polymer", Phys. Rev. B, vol. 60, pp. 13294-13297, 1999

[8] Y. Tanaka and S. Tamura, "Surface acoustic waves in two-dimensinonal periodic elastic structures", Phys. Rev. B, vol. 58, pp. 7958-7965, 1998

[9] T.T. Wu, L.C. Wu and Z.G. Huang, "Frequency band-gap measurement of two-dimensional air/silicon phononic crystals using layered slanted finger interdigital transducers", J. Appl. Phys., vol. 97, Art.No. 094916, 2005

[10] S. Benchabane, A. Khelif, J.Y. Rauch, L. Robert and V. Laude, "Evidence for complete surface wave band gap in a piezoelectric phononic crystal", Phys. Rev. E, vol. 73, Art.No. 065601 2006

[11] T. Tachizaki, T. Muroya, O. Matsuda, Y. Sugawara, D.H. Hurley and O.B. Wright, "Scanning ultrafast Sagnac interferometry for imaging two-dimensional surface wave propagation", Rev. Sci. Instr., vol. 77, Art.No. 043713, 2006

[12] Y. Sugawara, O.B. Wright and O. Matsuda, "Direct access to the dispersion relations of multiple anisotropic surface acoustic modes by Fourier image analysis", Appl. Phys. Lett., vol. 83, pp. 1340-1342, 2003

[13] T.T. Wu, Z.G. Huang and S.Y. Liu, "Surface acoustic wave band gaps in micromachined air/silicon phononic structures – theoretical calculation and experiment", Z. Kristallogr., vol. 220, pp. 841-847, 2005

Bringing BAW Technology into Volume Production: The Ten Commandments and the Seven Deadly Sins

Robert Aigner, TriQuint Semiconductor, Florida
raigner@tqs.com

ABSTRACT:
This paper reviews the ten most important things required to bring a thin film resonator BAW process into volume production. Relationships between performance parameters are described and some of the obstacles are outlined.

Keywords: BAW (Bulk Acoustic Wave), SMR (Solidly Mounted Resonator), FBAR (Film Bulk Acoustic Resonator)

INTRODUCTION:

The list of companies who have succeeded in commercializing BAW/FBAR is equally long as the list of those who have failed and/or given up. Within the next few years both lists will become a lot longer. It is remarkable that BAW/FBAR used to be a topic of intense R&D mostly in companies not previously engaged in Surface Acoustic Wave (SAW) filters. The schematic cross-section of an FBAR or SMR BAW device looks very similar to thin-film capacitors or micromachined pressure sensors; things the IC industry has been doing for two decades. Lithography requirements for BAW are trivial as compared to the state-of-the-art in IC manufacturing. The idea of adding BAW to the technology portfolio of an IC company is an easy sell. However in the aftermath of this decision it is very difficult for management to accept that it takes so long to develop a BAW process and why progress in performance and improvement of yield is an uphill battle. In contrast to IC companies the major players in SAW engaged with BAW/FBAR very reluctantly and very late, probably because they had a better understanding on how difficult a task this may be.

Many of the obstacles found during the development of a BAW process pop up as a total surprise like rocks blocking a winding road; very often the engineers have to turn around and revisit things they had considered completed long ago. Some examples will be given later. It is also a very common mistake to trust that good modeling and simulation capabilities will compensate for deficiencies in resonator performance. The truth is that there is no software that will allow you to build good filters if your resonator performance is insufficient. However it should be pointed out that simulations and theoretical analysis are essential aids to figure out how to improve the resonator performance and what process changes are needed. It can take much longer than anticipated from a first "almost working" sample to a mature process because the improvement of one parameter usually harms other parameters in an unexpected way.

From a manager's point of view making a BAW filter seem like a trivial task. I have heard comments like "How hard can it be? It is just 8 elements! RF-ICs have millions of transistors!". True. But may I ask: how accurate is the gain of a transistor?

THE "TEN COMMANDMENTS" FOR BAW

1. Coupling coefficient
2. Q-values
3. Uniformity
4. Trimming
5. Spurious modes
6. Temperature coefficient
7. Passivation layer
8. Power handling
9. Nonlinearities
10. Packaging

I) COUPLING COEFFICIENT k^2_{eff}

Without any doubt this parameter is the biggest challenge in thin-film BAW. It is quite likely that FBAR/BAW would have emerged ten years earlier if the deposition methods for piezoelectric films would have been available. Numerous early activities in BAW failed because the coupling coefficients k^2_{eff} were too low and were not reproducible. The method of choice for thin-film piezolayers is reactive magnetron sputtering. The dominant material today is clearly Aluminum Nitride (AlN). The entrepreneur Ken Lakin succeeded building the first BAW filters in small volumes in the mid 1990's for military applications, but it was not until the late 1990's that groups at Hewlett Packard (now Avago) and Siemens (now Infineon) developed sputter processes yielding sufficient coupling coefficients for FBAR/BAW filters in handset applications. A definition of "good enough" will be given below. The know-how and process for sputtering AlN with perfect c-axis orientation is a well kept secret by those who have succeeded. From what is published about AlN growth [1, 2, 3, 4] there is apparently no consensus about the conditions under which excellent film quality is achieved. It is also clear that the "best known process" developed on one vendor's tool can not be copied to another vendor's tool without significant rework.

There is strong indication that the layer on which AlN is deposited plays an important role. The following parameters have been reported to influence k^2_{eff} significantly:

- material and orientation of bottom-electrode [1]
- smoothness of bottom-electrode surface
- chemical surface condition [3]

Material science groups often present AlN results in terms of XRD (X-Ray Diffraction) peak-width "rocking-curve FWHM angle", it is important to note that a small FWHM angle is a necessary condition for high coupling but it is by no means a sufficient condition. Even if XRD shows perfect orientation there can be an amorphous AlN "starting layer" on the bottom electrode. The X-ray signal of the amorphous starting layer would be hidden behind the large peaks of the oriented AlN. Amorphous layers between the electrode and the piezolayer harm a resonator badly, the effective coupling coefficient of a 2GHz resonator can degrade from 6.6% to 6.3% as a consequence of an only 30nm thick amorphous layer. A method to analyze if an amorphous starting layer is present is HR-TEM (High Resolution Transmission Electron Microscopy). In HR-TEM it is actually possible to image atomic lattice planes of AlN, identify the grains and check if they are correctly aligned. In bad AlN one may also observe mis-oriented grains of large size which slowly decay the thicker the film grows. In such a case the starting layer is not really amorphous but nevertheless it is a dead zone in terms of coupling and will harm performance badly.

Another case in which XRD would fail to detect a growth problem is the effect of flipped grains in AlN [3]. Flipped grains will counteract the actuation of their correctly oriented neighbors and generate "dead" regions (and potentially strong acoustic losses). 2% flipped grains will bring down coupling from 6.6% to 6.3%.

Fig. 2 sketches the hexagonal crystal structure of AlN (Wurtzite, class 6mm) in the two possible c-axis configurations. Note that in both configurations hexagonal monolayers of Aluminum and Nitrogen exist and that it is therefore not sufficient to start out with the "right" material as a first monolayer. What distinguishes the two configurations is the density of Al – N bonds from the first Al monolayer to the Nitrogen atoms above; in the upper picture the area density of bonds is a factor of three higher than in the lower picture. In addition it is reasonable to assume that the nature of the vertical Al – N bonds is different from the three other bonds (Al is a group III element, N is a group V element). Without offering scientific proof for this hypothesis it appears that growing high quality AlN requires a seeding condition that provides the right number and type of bonds during the initial seed formation phase of AlN. Reference [4] discloses amorphous Silicon as a good candidate to improve AlN quality.

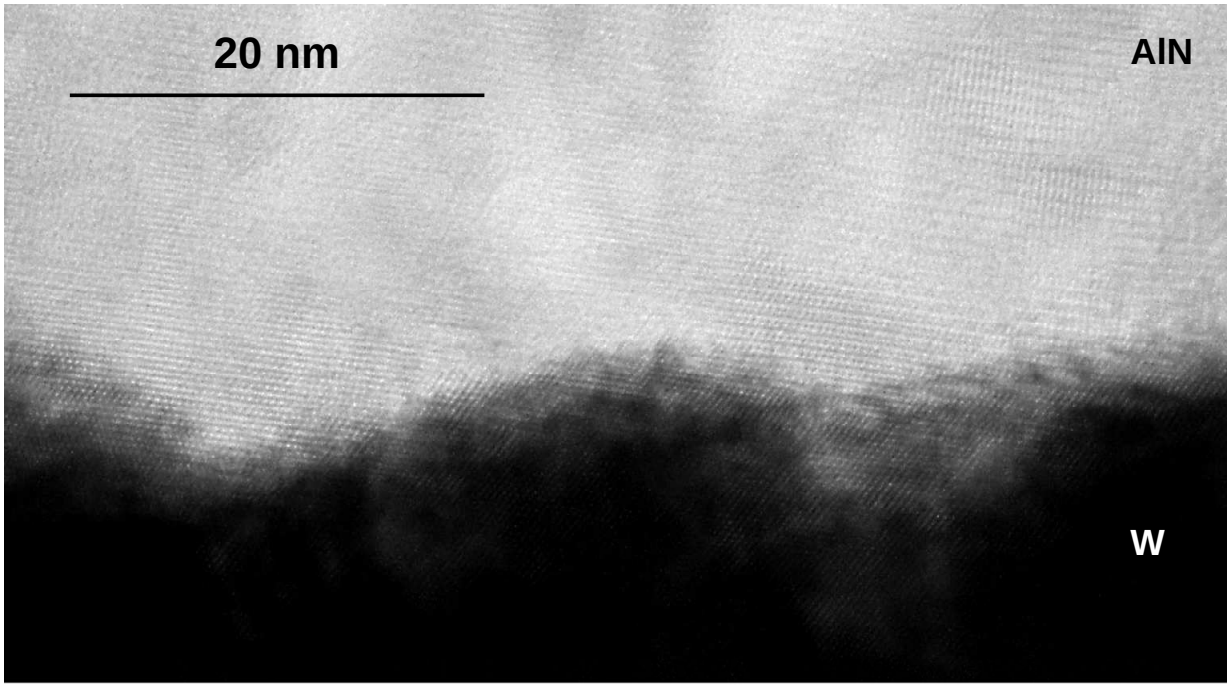

Fig. 1: HR-TEM image of AlN on an "as deposited" Tungsten bottom electrode as disclosed in [4] and [6], showing misaligned grains in the interface region.

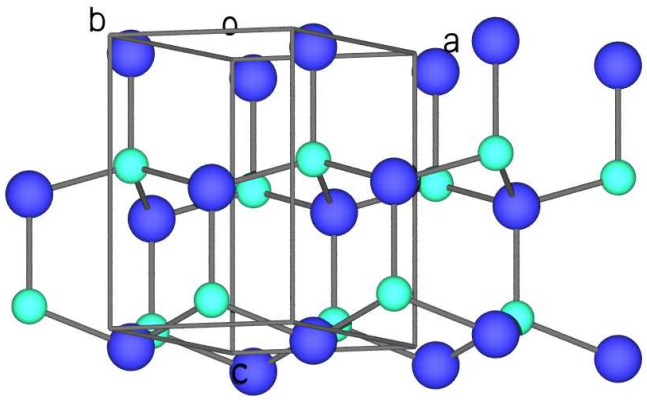

Fig 2a: AlN crystal structure, c-axis pointing upwards

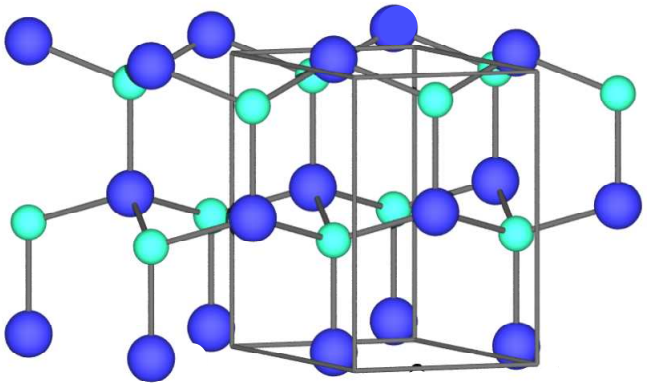

Fig. 2b: AlN crystal structure, c-axis pointing downwards (same as 2a but up-side-down)

The most reliable and relevant evaluation of k^2_{eff} is to build a simple BAW resonator that can be RF-probed. From the S-parameter data of resonators, the frequencies of resonance and anti-resonance can be extracted with high accuracy. Very short leads must be used between the RF-probe pads and the actual resonator in order to avoid series inductance which would result in an overestimation of k^2_{eff}. Wideband measurements should always be made to confirm that series inductance is negligible. Resonators with strong spurious modes can be problematic for k^2_{eff} extraction purposes as those may show distorted phase slopes and will introduce scatter in the determination of the resonance frequencies. It is highly recommended to fit a BVD model to the measurement data rather than just detecting the zero-crossings of the phase.

The value of k^2_{eff} can be straight forward calculated from the resonance frequency f_s and the anti-resonance frequency f_p. Unfortunately not all groups working in this field use the same formulas. On a first look the differences are not big but one should keep in mind that if k^2_{eff} drops from 6.6% to 6.3% it can lower yield from 80% down to zero. The following definitions are used by various groups:

$$k^2_{eff} = \frac{\pi}{2}\frac{f_s}{f_p}\frac{1}{\tan\left(\frac{\pi}{2}\frac{f_s}{f_p}\right)}$$ IEEE definition

$$k^2_{eff} = \frac{\pi^2}{4}\left(\frac{f_s}{f_p}\right)\cdot\left(\frac{f_p - f_s}{f_p}\right)$$ 2nd order Taylor approx.

$$k^2_{eff} = \frac{\pi^2}{4}\cdot\left(\frac{f_p - f_s}{f_p}\right)$$ 1st order Taylor approx.

$$k^2_{eff} = \frac{\pi^2}{4}\cdot\left(\frac{f_p - f_s}{f_s}\right)$$ "Optimist's favorite"

f_p/f_s = 1.0284	k^2_{eff}
IEEE standard	6.63 %
2nd order Taylor	6.62 %
1st order Taylor	6.81%
Optimist's favorite	7.01%

Table 1 shows by how much the four definitions differ for a good SMR-BAW. f_s = 1866 MHz and f_p = 1919 MHz.

The IEEE standard definition is fully consistent with the results derived for a resonator with infinitely thin electrodes in classical BAW literature [5]. The reason why this definition is not widely used is the trouble one runs into when inverting the transcendent function for modeling purposes. The 2nd order Taylor series is a very good approximation and should be used as a standard. However most groups and tool vendors use the 1st order Taylor (or even the "Optimist's favorite") because they show higher values for k^2_{eff}.

The values achieved in state-of-the-art deposition tools (on a regular basis and as an average over full wafer area) are k^2_{eff} = 6.7% (using IEEE standard definition) for an SMR-BAW at 2 GHz.

It should be pointed out that it makes no sense to benchmark this number against published data for mono-crystalline AlN. The layer stack and most importantly the electrodes used have a strong influence on coupling and this has nothing to do with the AlN quality. A properly designed layer stack can enhance coupling [6], a badly designed stack will degrade coupling. In addition to this a thin film piezolayer is laterally clamped and the d33 parameter of a crystal differs from a thin-film [1].

Despite the fact that ZnO has in theory a slightly higher coupling coefficient than AlN it has so far not been demonstrated as a viable alternative to AlN. The other prominent piezomaterial PZT is an interesting material for MEMS and low frequency devices as it has very high coupling along with extremely high dielectric constant. In the GHz range PZT appears to have too high intrinsic losses [7]. Moreover the high dielectric constant and low acoustic

velocity would result in extremely small resonators which in turn would make it very hard to control acoustic behavior.

II) Q-VALUES

It is a fact that the high Q-values achieved with FBAR were a key advantage over SAW in the frequency range up to 2 GHz at the time FBAR emerged on the market. In order for FBAR/BAW to remain competitive against SAW in this frequency range, the Q-values of next generation BAW products must improve significantly. Q = 2000 is a reasonable target.

Most groups working in FBAR/BAW use their own definition of Q-values. While in all cases the Q-value-definition is related to the impedance-phase-slope of a resonator, there are different ways to smooth and average the results obtained. Furthermore, the "de-embedding" of electrical losses can change results significantly.

Spurious modes may be present in the surrounding of f_s and/or f_p and it is not a good idea to use local derivatives to calculate Q because that can lead to huge scatter in the Q-value data extracted. A fit function based on a BVD model can be used to fit the slope before the extraction of Q is done.

In a really good resonator of reasonable size (20 to 150 ohm impedance level) the phase-slope is steeper at f_p because the series resistances of the RF-probes, pads and leads have no effect at this frequency. Whenever a resonator shows a bad phase-slope at f_p it is most likely an acoustic loss that causes this problem. In order to describe a resonator properly one would have to define 3 different Q-values:

- the "acoustic" Q_a-value represented by the acoustic branch resistance Ra in Fig.3
- $Q@f_s$ which includes the series resistance R_s
- $Q@f_p$ which includes R_{si}.

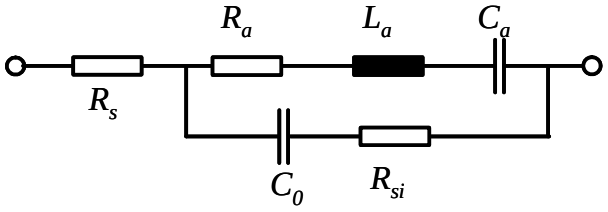

Fig.3 shows the electrical equivalent circuit of a resonator know as "modified BVD" [8]

In a good resonator R_{si} is extremely small or zero and $Q_a = Q@f_p$. The best values reported to date for FBAR are Q>2000 [9] and for SMR-BAW are Q=2500 [10].

The Q-values of SMR-BAWs were extremely poor until the discovery was made by Infineon's BAW group in year 2000 that shear waves generated as a by-product of thickness expansional vibration will leak out through the bottom reflector [11]. Up to this point in time reflectors were built from quarter wavelength thick layers of high- and low-impedance materials. After changing this to fix the dominant loss mechanism by modifying the reflector to work both for the longitudinal and the shear wave, the Q-values jumped from below 700 to above 1300 without any other concurrent changes.

Hunting down the loss mechanism that presently limits Q-values in SMR-BAWs is on the agenda of many groups. Attempts to explain part of the losses by lateral acoustic leakage or lateral redistribution currents in the electrodes [12] have been published. However it is not proven at this point in time that losses of this nature limit the Q-values we see in experiments. To my knowledge there is no publication about a method that would consistently predict the theoretical limit for Q for FBAR or SMR.

III) UNIFORMITY

Uniformity of layer thickness across a wafer is one of the obvious challenges in FBAR/BAW. Using a Mason-model approach one can derive the change of resonance frequency if a layer thickness is off target. Layer thickness uniformity has been discussed in many publications [13]. There are many aspects of uniformity that are less obvious and easily escape people's attention:

- uniformity of acoustic parameters (velocity, density) is equally important to thickness-uniformity.
- Uniformity of k^2_{eff} across the wafer is related to maximum yield.
- Some types of uniformity problems can be fixed by trimming while others can't. Some layers deep down in the stack do not change frequency by a significant amount but they are important with regard to acoustic wave dispersion.
- Uniformity on a small lateral scale is very important. A change of layer thickness or material parameters within one resonator can kill resonator performance. Any unintended change of parameters between the resonators comprising a filter or between neighboring filters on a wafer will cause severe yield losses. No trimming method is able to fix this type of problem.

While thickness uniformity, as it concerns frequency tolerance is somewhat overemphasized, the severity of the other aspects is clearly underestimated. At this point it is worth mentioning that many of the methods used to measure and map thickness are indirect and need very careful calibration. For transparent layers the standard tool is an optical spectrometer/ellipsometer. It measures thickness very accurately if refractive index and the optical properties of the layer underneath are well defined. A change in "optical length" is not necessarily related to "acoustical length". Another example is the thickness measurement of metal layers. The 4-Point-Resistance method is a standard method in many IC fabs. The result of the measurement is the "R_{square}" of a metal layer which is inversely proportional to thickness. The conductivity is a calibration parameter. It is wrong to assume that conductivity is in any way related to the acoustic properties of the film. There is no way to distinguish if a change in R_{square} is related to a thickness changes or if conductivity has changed. The 4-Point-Resistance method is not suited to verify the uniformity of metal layers for BAW. A somewhat better way to measure thickness is XRF (X-Ray Fluorescence). The calibration parameter is density and the assumption is that alloy

composition does not change. Thin and heavy layers can be measured with XRF quite well but it is not possible to measure multilayer stacks. The king of metrology methods for FBAR/BAW is Femtosecond Laser-Pulse Sonar. The tool measures acoustic delay time(s) of layer(s) and directly extracts the parameters needed for a Mason model. Even if the calibration parameter "acoustic velocity" is slightly off, the error will, to a large extent, self-correct when calculating the frequency. One of the nice features of this method is the small spot size (10 .. 20 μm) and the capability to measure multi-layers in one shot.

IV) TRIMMING

A typical PCS duplexer spec requires hitting a frequency target accurately to ±1 MHz, which is equivalent to ±0.05% relative error. Accordingly the layer thickness, acoustic velocity and density of several layers would have to be accurate to ±0.02% each. There is no hope to achieve such a high accuracy "as deposited". As a consequence frequency trimming is one of the key processes in FBAR/BAW. Run-to-run variations can be corrected by feed-forward control of deposition thickness. However correction of uniformity errors requires "localized processing". Off-the-shelf trimming tools for BAW and SAW are now available and they are all based on local Ion-beam etching. A very narrow Ion-beam is scanned over the wafer surface at a controlled speed which determines the local removal that occurs [14].

The challenge in trimming is to choose the right strategy. Trimming for volume production is a balancing act between accuracy and throughput. The input data for trimming comes from mapping the thickness and/or frequency. The mapping grid must satisfy Shannon's sampling theorem in both coordinate directions. The size and shape of the ion-beam is a very important parameter which determines the maximaum frequency gradient the tool can handle. Small diameter beams allow very large gradients but tend to have a very low volume etch rate which results in very long processing times. The stability of the beam shape over a long time is crucial for the accuracy the tool will achieve.

The topmost layer from which the Ion-beam is supposed to removes material must be chosen considering the following parameters:

- Trimming into heavy layers allows very high throughput but there are limitations in accuracy. Even at maximum scanning speed, the frequency shift can be larger than desired on certain spots on the wafer. The maximum speed and acceleration of the mechanical scanning system can accommodate is an important parameter for such a case.
- Metal layers may grow a native oxide layer in air. The thickness of this layer is not predictable. In most cases this native oxide exhibits a different etch rate than the metal below. This results in strong nonlinear behavior in the dose versus removal curve. The worst materials to trim are Al alloys. Al_2O_3 etches factor 5 slower than the Al below.
- Dielectric materials are well suited to trim very accurately. On the other hand, the frequency shift that can be obtained is very limited because suitable layers (SiO_2 or Si_3N_4) have a low mass density and low etch rate. In general dielectric layers show excellent reproducibility of trimming rate. The drawback of dielectric layers is that their presence generally degrades coupling coefficient without contributing to the conductivity of the electrode. The maximum thickness of a dielectric layer is determined by how much margin, in coupling coefficient, a filter has.

V) SPURIOUS MODES

Spurious modes are related to lateral standing waves in a BAW or FBAR resonator. Only a very tiny amount of spurious ripple is acceptable in filters with stringent amplitude ripple and group delay ripple specs. Moreover the presence of spurious modes usually goes along with degraded Q-values. There are different ways to fight spurious modes in FBARs and in SMRs. For SMRs it is certain that pronounced spurious modes will show up when the Q-values exceed 1000 (regardless of resonator shape) and they will be really bad at Q = 1500. At Q<1000 most spurious modes will be strongly damped which smears them out over a larger frequency range. In fact the vibrations associated with these modes can be a major source of energy loss. In order to achieve higher Q-values, those losses must be confined and as a consequence the modes by themselves will become more pronounced. The theory behind spurious modes and the methods for their suppression have been discussed in detail in [15, 16, 17].

As a precondition for the above referenced "border ring" concept, the dispersion relationship of the layer stack must be of "type I". This must be kept in mind while optimizing the acoustic reflector stack to provide high reflectivity for both longitudinal and shear waves as mentioned above. In fact this limits the freedom in designing an acoustic reflector significantly.

VI) TEMPERATURE COEFFICIENT

FBARs are slightly better in terms of temperature drift than conventional SAWs, but not by much. SAWs, based on $LiTaO_3$, have a typical TCF of -39 ppm/K, while FBARs can achieve around -30 ppm/K on average. SMRs on the other hand side utilize the inverted temperature behavior of (amorphous) SiO_2 to obtain partial compensation of the temperature drift of the other materials. The Young's modulus of SiO_2 increases as temperature goes up [18]. In addition the thermal expansion coefficient is very small. An SMR fulfilling the above mentioned conditions for dispersion type and utilizing a shear wave optimized reflector can have a TCF as low as -19 ppm/K [19]. In the most demanding duplexer applications, a low TCF is extremely important as it allows achieving spec-compliance over a wider range of temperatures. Moreover a low TCF helps to avoid thermal runaway (a situation where self-heating shifts the filter down and losses at the upper passband edge increase which in turn enhances self-heating, and so on) [20].

It is possible to further improve TCF in SMRs by increasing the SiO_2 content and by moving the SiO_2 closer to the high stress regions in the stack. SMRs with essentially zero TCF have been reported [21]. All of these approaches harm k^2_{eff} massively and can only be used for filters and resonators with small fractional bandwidth. In order to have a zero TCF one would have to accept k^2_{eff} of an SMR resonator below 4%.

VII) PASSIVATION LAYER

The purpose of a passivation layer is to protect the resonators from detrimental effects caused by humidity or corrosive fluids. Whether they are required or not has been a topic of heated discussions. This question can only be answered after reviewing the packaging options and preferences for FBAR/BAW.

The main challenge of passivation layers for BAW-SMRs at high frequencies is that, for acoustical reasons, one can not choose layers as thick as in traditional IC processes. While IC process typically use a combination of 300nm SiO_2 with 300nm Si_3N_4 on top, the maximum thickness for an SMR at 2GHz is less than 100nm (or else the k^2_{eff} degrades badly). It is possible to deposit a pin-hole free layer of that thickness. This layer can also serve as a "trimming layer".

VIII) POWER HANDLING

FBAR/BAW devices endure higher power levels better than SAWs mainly because the electrical currents distribute more evenly. There are no narrow IDT fingers like in SAW which are prone to electromigration damage. Even though the minimum feature size of BAW is much larger, the current densities can be enormous. For a BAW at 32dB transmit power at the upper passband skirt (worst case scenario) the following observation has been made. Depending on the electrode materials used the combined effect of current density and mechanical stress will cause the electrode material to migrate and form rough regions on the resonator surface. The losses of that resonator will increase and so will the temperature of the resonator. As migration effects follow an Arrhenius type law with temperature, the damage accelerates and the resonator will self-destroy within minutes. The power handling of BAWs is a strong function of the ambient temperature as suggested by the Arrhenius law. It is very important to keep the filter chip as cold as possible, therefore it is necessary to provide a good heat sink. The key to excellent power handling is to improve the electro- and stress-migration properties of the weakest material involved. This is an exercise the SAW vendors have successfully completed during the last years [22]. Significant material research activities will be required to find an optimum solution for BAW.

IX) NON-LINEARITIES

The discovery of nonlinear behavior in BAW and FBAR was first reported in 2005 [20]. It has long been known that solids exhibit nonlinear stress-strain relationships at high stress levels [23]. The binding forces of the atoms in a lattice are a strongly nonlinear function of distance. This effect is described by the 3rd order elastic constants of a material. In addition to that the piezoelectric constants change as the crystal deforms. It should not come as a total surprise that the elastic constants of a material are modulated by strain generated by large voltage swings at high RF-power levels or by bias voltages. To my knowledge no complete theory about the nonlinear behavior of AlN based BAW resonators has been published.

There are known tricks to improve the linearity of BAW filters. Cascading of two double sized resonators to replace one resonator in a filter is one of them, however this is not possible for all resonators in a filter as it would increase the size of a BAW by a factor of 4. Other tricks involve partial compensation of harmonic tones.

X) PACKAGING.

The fact that BAW filters can be processed on Silicon wafers is a big advantage for packaging. Silicon is much easier to handle than Lithium Tantalate or other piezo materials SAW filters are typically made from. Silicon is inherently stronger and less fragile, moreover it can be temperature ramped at a high rate which is a significant advantage over SAW. The thermal expansion coefficient of Silicon is small and isotropic and the heat conductivity is excellent.

FBARs and BAWs need a cavity above the top electrode which was also true for all SAW filters until the recent introduction of Boundary-Wave-Acoustic Devices [24]. Providing this cavity in a cost efficient way is a key for commercial success in consumer markets. The method of choice is to use a Wafer-Level-Packaging (WLP) approach in which the cavities are created in a batch process. FBAR [25] and BAW WLPs [26] are in volume production and details are published. [25] describes a process using wafer-bonding with a hermetic seal while [26] uses a polymer build-up approach which is not hermetic. The non-hermetic approach is potentially lower in cost but requires perfectly passivated resonators which do not corrode in a humid environment. Passivation is much easier to apply to BAW-SMR than to FBAR because there is no bottom cavity. For BAW-SMR a pin-hole free protection layer on the top surface is sufficient.

SUMMARY

The market share that FBAR/BAW will be able to gather is largely dependent on how well they support RF-integration. It is a clear trend in the wireless industry that companies building phones want to source functional blocks and modules rather than discrete filters. For the phone manufacturer the filters are invisible; it is the supplier's responsibility to make filters and active components work together smoothly. The determining factor will be whether SAW or FBAR/BAW will provide a more cost competitive solution that meets the necessary performance level.

THE "SEVEN DEADLY SINS" (AND HOW MANAGERS CAN AVOID THEM)

LUXURIA (extravagance)
Choose your target markets and applications wisely.

GULA (gluttony)
Don't build more capacity than you can fill.

AVARITIA (greed)
Don't be "penny wise and pound foolish"; don't try to save money in the wrong place.

ACEDIA (sloth)
Not applicable. Eningeers don't have this bad habit.

IRA (wrath)
Engineers do their best to meet your aggressive schedules; don't demand miracles.

INVIDIA (envy)
Don't think your competitors were just lucky.

SUPERBIA (pride)
Know what SAW is capable of doing and what your competitors are up to.

ACKNOWLEDGEMENTS:
Many thanks to Ben Abbott for discussions on the crystal structure of AlN and for introducing me to the world of SAW.

REFERENCES:
[1] M.-A. Dubois, P. Muralt, L. Sagalowicz, "Aluminum Nitride Thin Films for High Frequency Applications", Ferroelectrics, 1999, Vol. 224, pp. 243 – 250

[2] R. S. Naik, R. Reif, J.J. Lutsky, C. G. Sodini, "Low-Temperature Deposition of Highly Textured Aluminum Nitride by Direct Current Magnetron Sputtering for Applications in Thin-Film Resonators", Journal of The Electrochemical Society, 146 (2) 691 – 696, 1999

[3] J.A. Ruffner, P.G. Clem, B.A. Tuttle, D. Dimos, D.M.Gonzales, "Effect of substrate composition on the piezoelectric response of reactively sputtered AlN thin film", Thin Solid Films 354 (1999) 256-261

[4] US patent, US6878604B2

[5] J.F. Rosenbaum, "Bulk Acoustic Wave Theory and Devices", Artech House, Boston, London, 1988

[6] US patent, US6291391B1

[7] Q-X Su, P. Kirby, E. Komuro, M. Imura, Q. Zhang, R. Whatmore,"Thin-Film Bulk Acoustic Resonators and Filters Using ZnO and Lead-Zirconium-Titanate Thin Films", IEEE Transactions on Microwave Theory and Techniques, Vol. 49, No. 4, April 2001

[8] J.D. LarsonIII, P.D. Bradley, S. Wartenberg, R.C. Ruby, "Modified Butterworth-Van Dyke circuit for FBAR resonators and automated measurement system", IEEE Ultrasonics Symposium 2000, vol.1 page 863-868

[9] R. Ruby, J. D. LarsonIII, R. S. Fazzio, C. Feng, "Performance Degradation Effects in FBAR Filters and Resonators due to Lamb Wave Modes", Proceedings of IEEE Ultrasonics Symposium 2005, Rotterdam

[10] G. Fattinger, R. Aigner, S. Marksteiner, "Everything you always wanted to know about BAW", Workshop proceedings, APMC2006, Yokohama Dec. 2006

[11] S. Marksteiner, J. Kaitila, G. G. Fattinger, R. Aigner, „Optimization of Acoustic Mirrors for Solidly Mounted BAW Resonators", Proceedings of IEEE Ultrasonics Symposium 2005, Rotterdam

[12] R. Thalhammer, R. Aigner, "Energy loss mechanisms in SMR–type BAW devices", Proceedings of IEEE IMS-MTT-S 2005, Long Beach

[13] R. Lanz, et.al. "Aluminum-Nitride Manufacturing Solution for BAW and other MEMS Applications Using a Novel, High-Uniformity PVD Source", Proceedings of IEEE Ultrasonics Symposium 2006, Vancouver

[14] European patent EP1456947B1

[15] G. G. Fattinger, S. Marksteiner, J. Kaitila, and R. Aigner, „Optimization of Acoustic Dispersion for High Performance Thin Film BAW Resonators", Proceedings of IEEE Ultrasonics Symposium 2005, Rotterdam

[16] A. Link, et.al "Suppression of Spurious Modes in Mirror-Type Thin Film BAW Resonators Using an Appropriate Shape of the Active Area", Proceedings of IEEE Ultrasonics Symposium 2005, Rotterdam

[17] US patents US6182619 B1 and US6788170 B1

[18] National Institute of Standards (NIST) ceramic database, http://www.ceramics.nist.gov/srd/summary/emodox00.htm

[19] R. Aigner, "Volume manufacturing of BAW-filters in a CMOS fab", Acoustic Wave Device Symposium 2004, Chiba Japan, March 2004

[20] R. Aigner, N.-H. Huynh, M. Handtmann, S. Marksteiner "Behavior of BAW devices at high power levels" Proceedings of IEEE IMS-MTT-S 2005, Long Beach

[21] K.M. Lakin, "A Review of Thin-Film Resonator Technology", IEEE microwave magazine, Dec. 2003

[22] O. Nakagawara, et al. "High power durable SAW antenna duplexers for W-CDMA with epitaxially grown aluminum electrodes", IEEE Ultrasonics Symposium 2002

[23] W.P. Mason, "Physical Acoustics, Vol III, part A" chapter 5, pp 199. Academic Press, New York and London, 1966

[24] H. Kando, et. al. "RF Filter using Boundary Acoustic Wave", Proceedings of IEEE Ultrasonics Symposium 2006, Vancouver

[25] K. Wang, M. Frank, P. Bradley, R. Ruby, W. Mueller, „FBAR Rx filter for handset front-end modules with wafer-level-packaging", Proceedings of IEEE Ultrasonics Symposium 2003, Honolulu

[26] M. Franosch, K.-G. Oppermann, A. Meckes, W. Nessler, R. Aigner, "A Wafer-Level-Process using Photo-Epoxy to create Air-Cavities for Bulk-Acoustic-Wave RF-Filters", Proceedings of IMAPS 2004 conference, Long Beach California, Nov. 2004

An Air-Gap Type FBAR Filter Fabricated Using a Thin Sacrificed Layer on a Flat Substrate

Shinji Taniguchi, Tsuyoshi Yokoyama, Masafumi Iwaki,
Tokihiro Nishihara, Masanori Ueda and Yoshio Satoh
FUJITSU LABORATORIES LTD.,
64 Nishiwaki, Ohkubo-cho, Akashi 674-8555, Japan
E-mail:taniguchi.shinj@jp.fujitsu.com

***Abstract* – This paper describes the development of an air-gap type FBAR filter, fabricated using a thin sacrificed layer on a flat substrate. We focused development on the cost reduction of the wafer process. The formation of an air gap with a dome shape between the substrate surface and the bottom electrode is verified by both the simulation and experimental result and the possibility of the air-gap type FBAR structure is confirmed. Even if a thin sacrificed layer is used, the air gap can be formed on the flat substrate via stress control. Consequently, the Q-factor at the resonance, anti-resonance, and the effective k^2 were obtained as 1500, 1100, and 7.2 % at the 2-GHz range, respectively. The W-CDMA duplexer is designed using the proposed air-gap type FBAR filters in a 3.0 x 2.5 x 0.7 mm^3 ceramic package. The insertion losses are as small as 1.2 dB and 1.5 dB in the Tx and the Rx bands.**

I. INTRODUCTION

The study of thin film Bulk Acoustic Wave (BAW) technology is advanced as a filter device that plays a key role in broadband mobile communication systems [1, 2]. The BAW devices have several merits such as their high Q-factor, excellent electric power durability, and the possibility of integration with active devices by using the Si substrate compared to commercially widespread SAW devices. In various applications, the Wideband Code Division Multiple Access (W-CDMA) system requires an extremely low insertion loss, in other words, the demand for BAW devices becomes inevitable.

The BAW device includes a laminated structure, which consists of a top electrode film, a piezoelectric film, and a bottom electrode film. The laminated structure is formed on a substrate. In BAW device configurations, two structures are proposed in order to prevent acoustic emission into the substrate. The first is the membrane type, which creates a cavity by using Micro Electro Mechanical Systems (MEMS) fabrication under a bottom electrode. The other is the acoustic-mirror type, which installs an acoustic reflector consisting of multi layer films under a bottom electrode. The former is called a Film Bulk Acoustic Resonator (FBAR) [1], while the latter is called a Solidly Mounted Resonator (SMR) [2]. In general, the FBAR configuration, in which the resonator is isolated acoustically by the air gap, has the obvious advantage of better energy confinement compared with the SMR.

We have developed AlN film-based FBAR filters employing resonator configuration with a vertical via-hole, fabricated using deep-RIE technology [3]. We have also studied the properties of ruthenium (Ru) to be suitable for use as an electrode material [4], and proposed an AlN just-etched FBAR structure to reduce the lateral-leakage of acoustic waves and enhanced FBAR performance [5]. We recognize that not only development to improve the resonant characteristics but also the realization of a cost effective process, which leads to the supply of a low-cost device, is significant in terms of spread of the FBAR within the 2-GHz range system, which is occupied by the SAW filters.

We propose an air-gap type FBAR filter, fabricated using a thin sacrificed layer on a flat substrate in this paper. The air gap is formed under a bottom electrode by utilizing the stress of the film, which is an FBAR composition. We believe that the process involved in constructing this structure is cost-effective.

II. STRUCTURE OF THE AIR GAP

There are mainly two procedures used to form the air gap under a bottom electrode, which is the main feature of FBAR, as shown in Figure 1. Figure 1(a) shows the cross-sectional structure of FBAR with a cavity. The outline of the wafer process is as follows. The first step involves the cavity being formed and filled with the thick sacrificed layer. In the second step, the substrate surface is polished smoothly using chemical mechanical polishing technology. The third step sees the bottom electrode film, the piezoelectric film, and the top electrode film each stacked and patterned before finally, the sacrificed layer is etched to form the cavity. Figure 1(b) shows another structure with a vertical via-hole, which is formed at the final step. The method of fabricating a vertical via-hole involves etching a Si substrate from the rear side, using deep-RIE technology. The MEMS process technologies are used in both structures. As we mentioned above, the former structure contains several steps used to form the air gap. Alternatively, the latter incorporates a simple process, but includes photolithography and processing on the rear side of the substrate with high accuracy. Consequently, a relatively high production cost may be required. Of course, not all structures have problems relating to features for practical use.

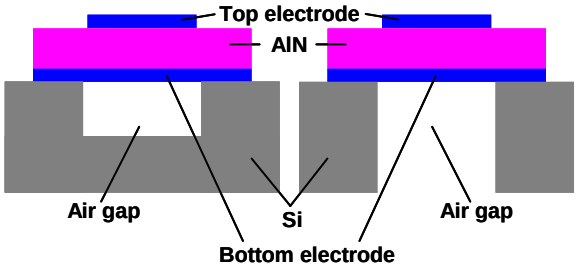

(a) Cavity type (b) Via-hole type

Fig. 1 Conventional structure of FBARs (side view).

We understand that constructing a simple structure with an easy process is important for cost reduction. With this concept in mind, we propose a simple procedure to form a dome-shaped air gap, as shown in Figure 2. This features a slight air gap, formed under a bottom electrode and fabricated using a thin sacrificed layer, with the procedure summarized in Figure 3. The outline of the wafer process is as follows. In the first step, a thin sacrificed layer is formed on a flat substrate of a Si wafer. Other materials such as the glass can be used as a substrate. Next, the sacrificed layer is patterned into a desirable shape by photolithography and etched, as shown in Figure 3(a). Subsequently, the bottom electrode film, piezoelectric film, and top electrode film are sequentially formed by sputtering. Compressive stress is applied to the laminated structure by controlling the sputtering condition. Each layer is patterned into a desirable shape by photolithography and etched, as shown in Figure 3(b). An overlapping region of the top and bottom electrodes through the piezoelectric film is ellipse-shaped to avoid unwanted resonances of lateral modes. The sacrificed layer has a patterned shape, similar to the shape of the overlapping region of the top and bottom electrodes. In the final step, the sacrificed layer is etched and removed. Subsequently, the compressive stress acts within the laminated structure, which consists of the bottom electrode, the piezoelectric film, and the top electrode. As a result, the laminated structure expands upward and a dome-shaped air gap is formed. The key point of development is to ensure that this air gap is formed effectively because there is a fear of sticking if only deleting the sacrificed layer. In order to avoid the sticking problem, a thick sacrificed layer is usually prepared. However, the quality of the AlN film represented by full width at half maximum of the rocking curve, which is one of the most important factors in determining the FBAR performance characteristics, is expected to be deteriorated because the surface roughness of the sacrificed layer loses its smoothness.

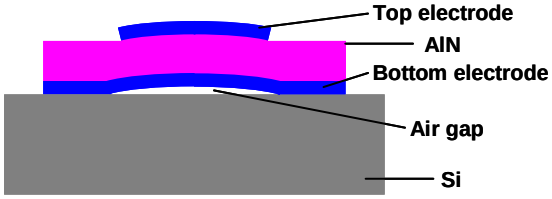

Fig. 2 Structure of proposed air-gap type FBAR.

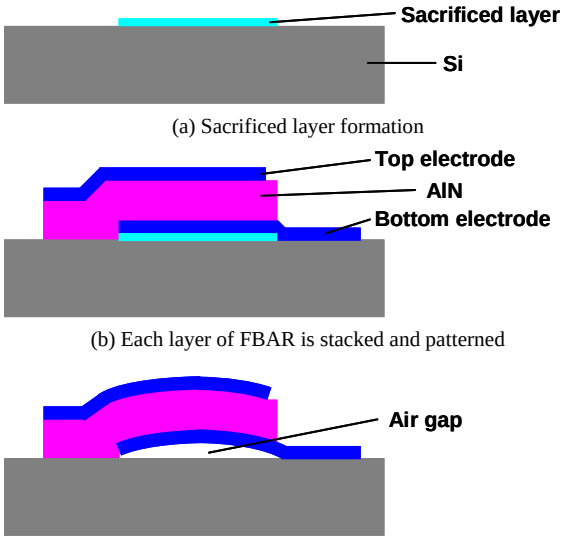

(a) Sacrificed layer formation

(b) Each layer of FBAR is stacked and patterned

(c) Air gap formation

Fig. 3 Fabrication processes of air-gap type FBAR.

III. Simulation

The possibility of the air gap formation with the thin sacrificed layer was examined. We simulated the three-dimensional shapes of the membrane that was obtained when the stress of each film, bottom electrode, piezoelectric film, and top electrode was changed by using the finite element method. Figure 4 shows the air-gap type FBAR structure used for the simulation. The region where the top and bottom electrodes overlap is ellipse-shaped, with dimensions of 250 um for the long axis and 180 um for the short axis, respectively. The relationships between the maximum membrane height and the film stress are as shown in Figure 5. Here, the film thickness of the sacrificed layer is assumed to be several ten nm, and the top and bottom electrodes are equal in terms of film thickness and stress. It is clear that the height of the membrane has risen as the compressive stress of either the electrode film or piezoelectric film increases. In addition, it is remarkable to see a high air gap obtained compared with the film thickness of the sacrificed layer.

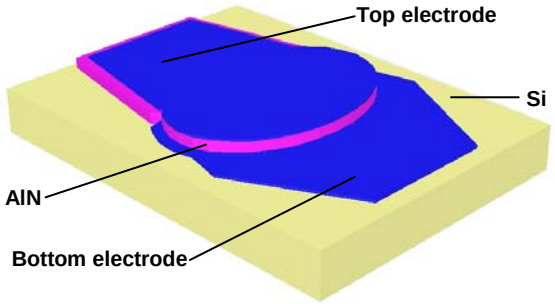

Fig. 4 Simulation model for the air-gap type FBAR.

A membrane shape of the simulation result is shown in Figure 6(a). Figure 6(b) is a cross-sectional view taken along a line A-A' in Figure 6(a). The displacement magnitude in the direction of height is shown by a contour line. We confirmed that a dome-shaped air gap was successfully formed under a bottom electrode. It is understood that the maximum displacement part shifts to the bottom electrode side. We confirmed that an air gap could be formed by the stress control through the structural examination and the simulation.

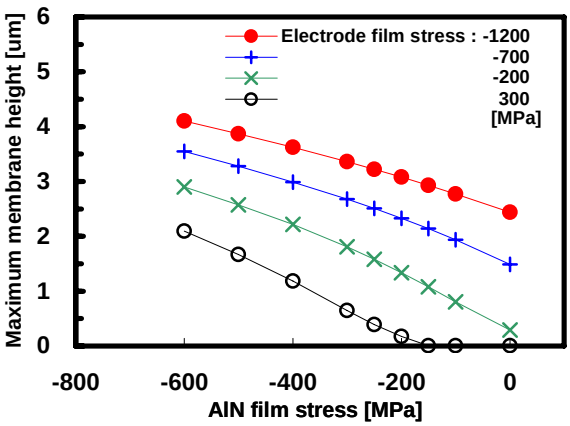

Fig. 5 Simulated maximum membrane height.

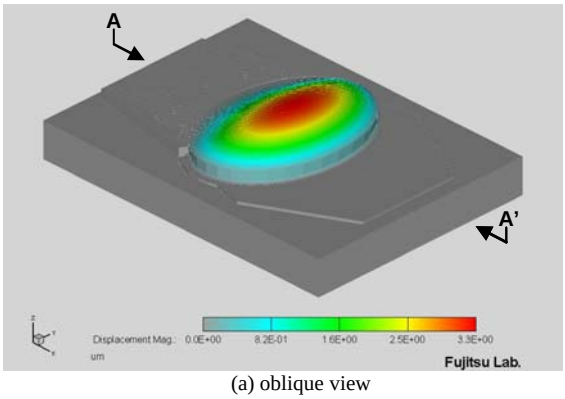

(a) oblique view

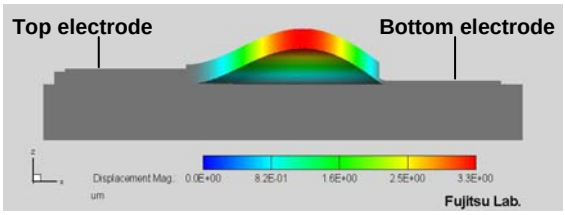

(b) Cross-sectional view

Fig. 6 Membrane shape from simulation result.

IV. Experiment

We fabricated an air-gap type FBAR in order to prove our concept. Ru and AlN were chosen as the electrode and piezoelectric materials, respectively. Each film was deposited via sputtering with different sputtering pressure to control the film stress. This technique is often used and is not special. Figure 7 is a micrograph of the air-gap type FBAR.

The three-dimensional measurement result of membrane shape is shown in Figure 8. Figure 8(a) is a top view of the contour line, while Figure 8(b) is a cross-sectional view taken along a line B-B' in Figure 8(a). It is understood that the actual sample shape corresponds well to the simulation result.

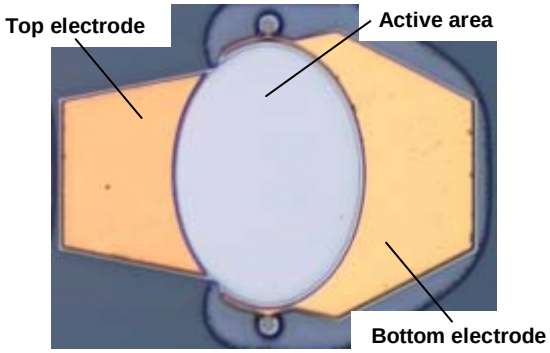

Fig. 7 Micrograph of top view of the air-gap type FBAR.

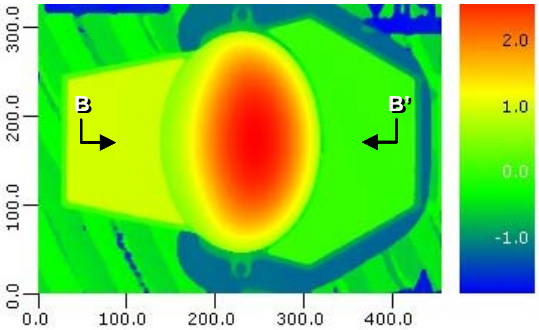

(a) Top view of contour line

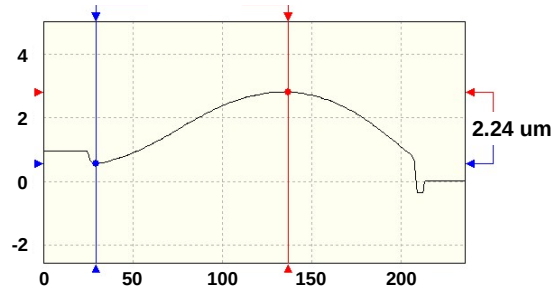

(b) Cross-sectional view

Fig. 8 Measurement result of membrane shape.

Figure 9 shows the result of examining the influence of the film stress on the maximum height of the membrane. Here, the top and bottom electrodes are equal in terms of film thickness and stress applied, the latter of which is about -1 GPa. The stress to which the AlN film is subject meanwhile, is about -170, -200, and -230 MPa, respectively. It was clarified that the height of the membrane is dependent on the magnitude of the compressive stress. This tendency corresponds well to the simulation result. The possibility of the air-gap process is confirmed by both the simulation and the experiment, simultaneously. An appropriate film stress enables us to

achieve high production reproducibility.

We discuss electrical performances. Figure 10 shows the Q-circle of 2-GHz FBAR, with the air-gap and via-hole types compared. The solid and broken lines indicate the air-gap and the via-hole type FBAR, respectively. We confirmed that the same characteristics could be obtained for both types of FBAR. The measured data was fitted to a Modified Butterworth-Van Dyke (MBVD) model [6]. The extracted resonator parameters are the loaded Q-factor of 1500 at the resonance, 1100 at the anti-resonance, and the effective k^2 of 7.2 %, respectively. The advantage of the air-gap type FBAR was indeed confirmed.

Finally, the application example is presented. The W-CDMA duplexer was designed by using air-gap type FBAR filters. The air-gap type Tx and Rx filters are mounted in a 3.0 x 2.5 x 0.7 mm^3 ceramic package. Figure 11 shows the measured frequency responses. The insertion losses of the Tx and Rx filters were 1.2 dB and 1.5 dB, respectively. Thus, we successfully developed a competent air-gap type FBAR filter for the W-CDMA duplexer.

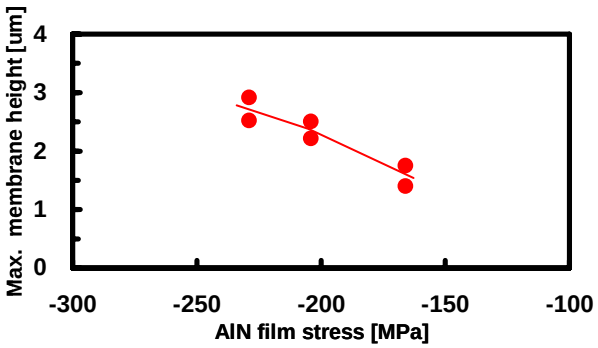

Fig. 9 Measured maximum membrane height.

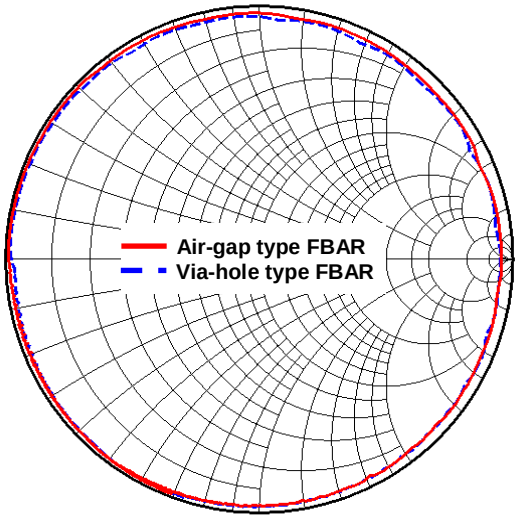

Fig. 10 Q-circle of fabricated 2-GHz FBAR.

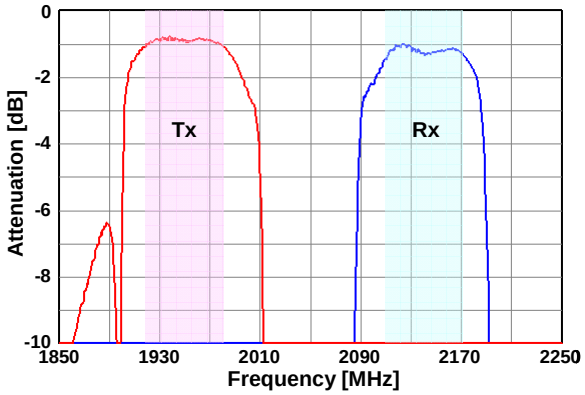

Fig. 11 Frequency response of W-CDMA duplexer.

V. Conclusion

We proposed an air-gap type FBAR filter, fabricated using a thin sacrificed layer on a flat substrate. We evaluated the suitability of this structure for the cost reduction of process. In order to form an air gap, we investigated the influence of the film stress, which is applied to the top electrode film, piezoelectric film, and bottom electrode film, respectively. Consequently, it was confirmed that the compressive stress of each film was significant to form the air gap via the simulation and experiment. The excellent characteristic could be verified, even if using a process that was suitable for the cost reduction. The Q-factor at the resonance, anti-resonance, and the effective k^2 were obtained at values of 1500, 1100, and 7.2 % within the 2-GHz range, respectively. We successfully developed a W-CDMA FBAR duplexer based on this structure with insertion losses of 1.2 dB and 1.5 dB in the Tx and the Rx bands.

References

[1] R. Ruby and P. Merchant, "Micromachined Thin Film Bulk Acoustic Resonators", Proc. IEEE 48th Symposium on Frequency Control, pp. 135-138, (1994).

[2] R. Aigner, "Bulk-acoustic-wave filters for cell phone applications", Proc. IEEE MEE-S Int'l. Microwave Symp. Workshop Note & Short Courses, WMB-14, (2004).

[3] T. Nishihara, T. Yokoyama, T. Miyashita, and Y. Satoh, "High Performance and Miniature Thin Film Bulk Acoustic Wave Filters for 5 GHz", Proc. IEEE Ultrasonics Symposium, pp. 969-972, (2002).

[4] T. Yokoyama, T. Nishihara, S. Taniguchi, M. Iwaki, Y. Satoh, M. Ueda, and T. Miyashita, "New Electrode Material for Low-loss and High-Q FBAR Filters", Proc. IEEE Ultrasonics Symposium, pp. 429-432, (2004).

[5] J. Tsutsumi, M. Iwaki, Y. Iwamoto, T. Yokoyama, T. Sakashita, T. Nishihara, M. Ueda, and Y. Satoh, "A Miniaturized FBAR Duplexer with Reduced Acoustic Loss for the W-CAMA Application", Proc. IEEE Ultrasonics Symposium, pp. 93-96, (2005).

[6] J. Larson, P. Bradley, S. Wartenberg, and R. Ruby, "Modified Butterworth-Van Dyke Circuit for FBAR Resonators and Automated Measurement System", Proc. IEEE Ultrasonics Symposium, pp. 863-868, (2000).

Hybrid SAW/BAW System-in-Package Integration for Mode-Converting Duplexers

S. Marksteiner*, D. Ritter, E. Schmidhammer, M. Schmiedgen, and T. Metzger
EPCOS AG
Anzinger Str. 13, D-81671 Munich, Germany
* stephan.marksteiner@epcos.com

Abstract — **During the last years the progressing integration of low-noise amplifiers into the transceiver chipset has driven the demand for (W-)CDMA duplexers that provide a balanced output signal at the receive port. Surface acoustic wave (SAW) filters can provide this mode-conversion functionality without any increase in processing complexity, however, for the closely separated receive and transmit bands of US-PCS (Band II) the steep roll-off and demanding power handling requirements make the design of a pure SAW based PCS duplexer not straight forward. On the other hand, bulk acoustic wave (BAW) devices have over the last couple of years proven their strength in particularly these disciplines. In this paper we present a hybrid SAW/BAW PCS duplexer that combines the mode-conversion properties of SAW with the steep skirts and superior power-handling capabilities of BAW filters. Both acoustic components have been integrated on a 3.0x2.5mm² LTCC substrate in which all the necessary matching components have been embedded.**

Keywords – CDMA Duplexer, BAW, SAW, Mode Conversion

I. INTRODUCTION

During the last decade the demand for ever smaller yet more capable mobile phone handsets has led to a dramatic reduction in both the size as well as the functionality of the various components on the circuit board. In many cases, this has made the development of new technologies necessary. One example for this is the antenna duplexer in CDMA telephone systems. This component serves as a passive cross-over network that directs RF-signals from the power amplifier (in the transmit or so called TX path) to the antenna while at the same time incoming signals from the antenna are directed to the low-noise amplifier (in the receive or RX path). The RX and TX paths use distinct but close-by frequency ranges that allow the *simultaneous* up- and downlink of RF-signals to and from the base station. The huge difference in the power level of the received and transmitted signals of up to 120dB leads to very demanding requirements on signal isolation, near-by selection, insertion loss and power durability of the duplexer. The basic building blocks of any duplexer are therefore two high-quality band-pass filters for the RX and TX frequency bands, respectively, and a proper matching network between them and the antenna.

One of the most demanding frequency bands for duplexers is the US-PCS or WCDMA Band II with its narrow gap of only 20MHz between the TX (1850-1910 MHz) and RX bands (1930-1990MHz). Until recently, the large temperature coefficient of high-coupling SAW substrates (like lithium tantalate or even worse lithium niobate) made this application inaccessible for SAW based filter solutions.

Until the end of the ninetieth, the only technology that was able to fulfil the demanding PCS specifications with an acceptable size for mobile handsets have been ceramic resonator type components. They make use of electromagnetic resonances (cavity modes) and are therefore quite large.

Around 2000, the first bulk acoustic wave based PCS duplexer components emerged [1] and showed due to the excellent quality factor of the BAW resonators a similar performance to ceramic components. Even though their footprint was initially not much smaller than the one of their ceramic counterparts they soon gained market share because of their significantly lower overall height of <2mm. In the mean time the size of these components has been systematically reduced to 3.8x3.8x1.3mm³ for high-volume applications and first data of duplexers with even smaller sizes have been presented [2]. At present, BAW PCS duplexers have more or less completely replaced ceramic duplexers in CDMA mobile phone handsets.

II. MODE-CONVERTING DUPLEXERS

The upcoming integration of low-noise amplifiers into the transceiver chipset and a trend towards cheaper CMOS based front-end architectures has created a strong demand for mode-converting filtering and duplexing components. If the single-balanced conversion is done in the traditional way (i.e., using a balun, e.g., in the form of a transformer) then there are basically two points where the balun can be positioned: either between the common TX/RX feed to the antenna and the RX filter (which in this case must then be a balanced-balanced type filter) or after the (single mode) RX filter. In the first case, the balun is an integral part of the duplexer and particularly of the intricate matching network between the RX and TX filters. It therefore needs to be carefully designed and matched into the system. In the second case, the design of the balun is somewhat more simple because it acts only as the mode- (and possibly impedance-) converting unit in a chain of

matched RF-components. However, in both cases discussed above, the conversion of the signal mode is linked with a signal loss due to mismatch and intrinsic losses in the balun.

A smart way of avoiding these balancing losses is the use of mode-converting band-pass filters. Both bulk acoustic as well as surface acoustic wave components provide this option, however, with significantly different impact on the design and/or manufacturing complexity. Whereas the signal balancing in SAW is established "simply" by wiring the various resonators and DMS (Double Mode SAW) tracks in an appropriate way, the mode-converting stacked crystal filters (SCF) or coupled resonator filters (CRF) necessitate the manufacturing of two properly coupled BAW resonators on top of each other [3-5]. This more or less doubles the photolithographic mask count, increases process complexity and poses significant challenges to the trimming strategy for these devices.

Since we at EPCOS are in the position of having both SAW and BAW filter technologies in-house, we chose to follow the way of a hybrid integration of a mode-converting SAW RX and a single-ended BAW TX filters. The integration platform is our **C**hip-**S**cale **S**AW **P**ackaging (CSSP) line [6], which is based on a low-temperature co-fired ceramic (LTCC) carrier. The advantage of this material is that the various matching components needed for a proper matching of the two filters can be embedded with excellent quality and good reproducibility in the LTCC.

III. MODE-CONVERTING SAW RX-FILTER

The design challenge for the Band II RX SAW filter lies particularly in the steep roll-off requirements especially on the low-frequency filter skirt. Due to the larger temperature coefficient of frequency (TCF) of -35ppm/K for uncompensated lithium tantalate (LT) based SAW resonators a larger safety margin to the passband edge is required. Fortunately, this situation is somewhat relieved at the low-frequency passband edge because the filter insertion loss improves for lower temperatures. This means that for lower operation temperatures the filter characteristic does shift upwards in frequency, but at the same time also shifts to lower insertion losses. This results in an "effective TCF" for the lower filter edge that can be significantly smaller than the intrinsic one.

In our design approach a standard LT SAW production process without additional expenses for the reduction of the temperature coefficient of frequency was used. The remaining effective temperature frequency drift and required manufacturing margins necessitate a steep filter skirt (from -3.5dB to -50dB) of better than approx. 12MHz. Further requirements for the RX filter of this duplexer are the transformation of the single-ended input signal to balanced mode at the output and sufficient power durability in the frequency range of the transmission band. In order to fulfill this variety of demands a combination of DMS filter and reactance filter was chosen. The balun functionality is realized by a 5IDT DMS track at the output. This design technique aids in the creation of a steep skirt of the RX filter and leads in general to excellent wideband behavior. The drawback of a somewhat limited power durability is compensated by adding several resonator structures at the antenna side. In order to achieve a good manufacturing stability all IDT (Inter Digital Transducer) finger structures are processed within one metallization layer of an Al-Cu sandwich structure. This electrode system allows a good insertion loss and a steep and stable skirt due to a low IDT finger resistance. The resulting limitations with respect to power durability for this metallization type were solved by optimizing the size of the resonator structures.

IV. SINGLE-ENDED BAW TX FILTER

We have already mentioned above, that BAW filters are currently the dominant filter technology for Band II duplexers. The advantages of using a BAW filter in the TX path are in particular:

- Good power handling capability: With respect to TX self-heating, the worst-case situation arises with a RF-signal transmission at the uppermost TX channel with a maximum radiated power of 500mW at the antenna and a typical signal attenuation of 3dB. In this case, the dissipated power in the BAW filter can be several hundred milliwatts. These power levels can be readily handled with BAW resonators, given that the resonator areas are appropriately designed and the filter die is properly connected to the circuit board via a heat sink. The reason for this lies in the large and robust electrode design of bulk resonators.
- Steep filter skirts: Even though the (intrinsic) TCF of AlN-based BAW filters in typically better than -20ppm/K the high-frequency shoulder suffers from the opposite effect as the low-frequency shoulder (c.f. the discussion in paragraph III). In this case now leads an increase in operation temperature to a downwards shift in frequency of the TX filter curve while at the same time the insertion loss increases. A proper design of the high-frequency filter shoulder with the goal of low insertion loss and steep roll-off is therefore extremely important.
- Low insertion loss: The higher quality factors of BAW resonators allow a somewhat lower insertion loss of the TX filter. Since the attenuation of the filter contributes a significant part to the losses in the TX path any improvement in filter attenuation translates directly into longer operating time of the mobile phone.

The design of the BAW filter is a ladder type with four series and three shunt resonator sections. In order to improve the power handling capability of the filter, all the series resonators have been doubled-up. The BAW technology used to manufacture the filter is a solidly mounted resonator (SMR) type process with AlN as the piezoelectric layer as described in [7].

V. CSSPLUS PACKAGE

As already mentioned above, the packaging of the two filter dies is done with EPCOS' proprietary CSSP process in its second development step, called CSSPlus. This packaging technology has proven over the last six year to be very reliable, scaleable, and most suitable high volume production. In addition, with advanced multi-domain simulation techniques (acoustic and electromagnetic, c.f. [8]), the number of redesign cycles has been significantly reduced over the last years and that has brought us significantly closer to a "first-time-right" design strategy. Note that the results presented here correspond to a part from the very first demonstrator run.

For the purpose of packaging, both acoustic dies are flip-chip mounted onto the LTCC carrier in which all necessary matching components have been integrated. The solder bumps are provided on the LTCC side by screen-printing. Please note that the pick-and-place during flip-chip assembly is the only sequential production step involved during the manufacturing process of the duplexer. After the reflow of the solder joints, a protective polymer foil is laminated over the dies and patterned using a laser. The package is then hermetically sealed by sputtering a plating base over the foil and galvanically reinforcing the metallic sealing. The duplexers are finally separated by sawing the LTCC panel. The final overall height of the duplexer is 1.3mm.

VI. DUPLEXER PERFORMANCE

The measured characteristics of the 3.0x2.5mm² mode-converting PCS CDMA duplexer are shown below. The specs shown are EPCOS-internal design goals. The part has been measured on a PCB with a soldered 15nH coil at the RX balanced port. The first two figures depict the TX and RX filter functions. The in-band attenuation is quite good over most of the passband, even though some adjustment of the centre frequency position of both the TX and RX filter is necessary.

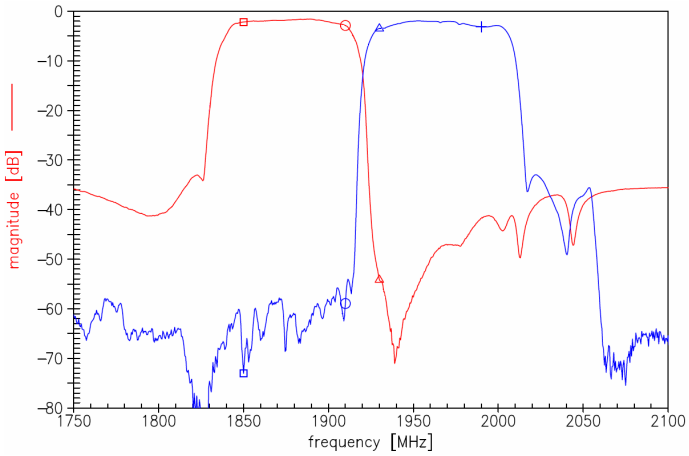

Fig. 1: TX (red) and RX (blue) transmission curves

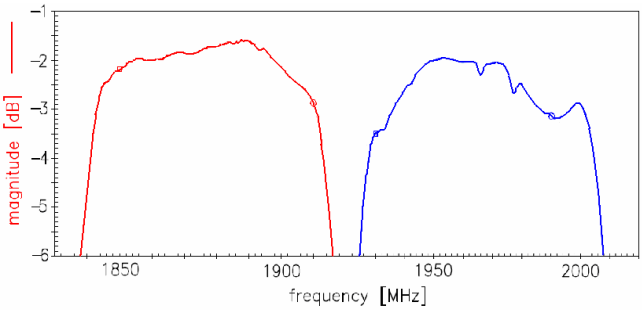

Fig. 2: Zoom-in on Fig.1 to show the in-band attenuation

The TX-RX-isolation shown in Fig. 3 is also excellent, particularly over the TX band. A moderate increase in the stopband attenuation of the TX filter should improve both the TX rejection as well as the isolation at the RX high-channel.

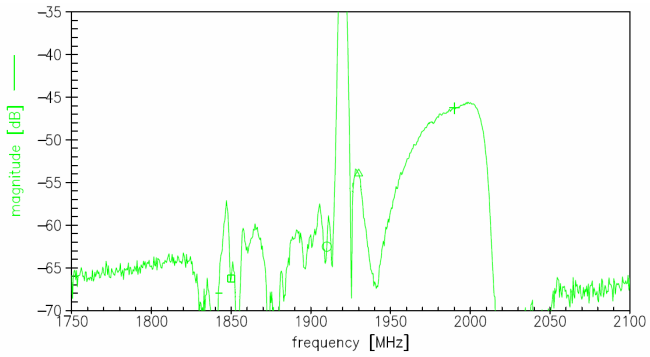

Fig. 3: TX-RX isolation

Fig. 4 shows the RX and TX reflection curves. They do not yet fulfil the return loss goal of -10dB. However, this is mostly due to somewhat off-target impedance levels of the filter dies. By redesigning the resonator areas and – if necessary – optimizing the internal matching components in the LTCC a return loss of better than -10dB is feasible.

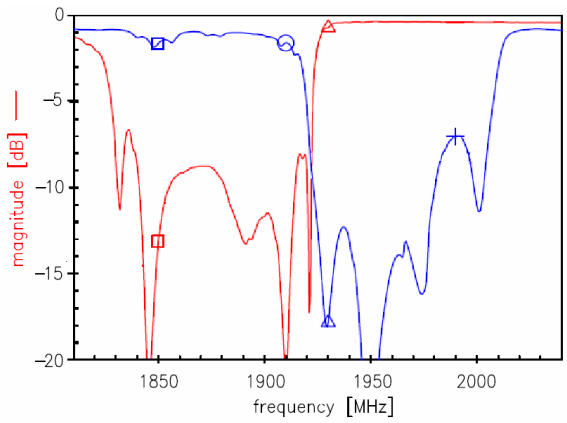

Fig. 4: TX (red) and RX (blue) matching curves

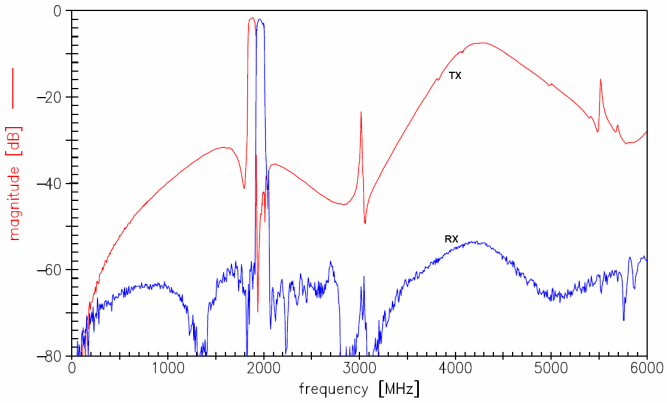

Fig. 5: Wideband insertion attenuation

The wideband behaviour (c.f. Fig. 5) is also very good. Only the 2nd-harmonic suppression at 3.8GHz needs some optimization. And finally, the symmetry of the mode conversion at the RX port is shown in Figs. 6 and 7. The signal symmetry meets the design goal of better than +/-1dB and the phase symmetry is better than +/-10 degree over the whole PCS band.

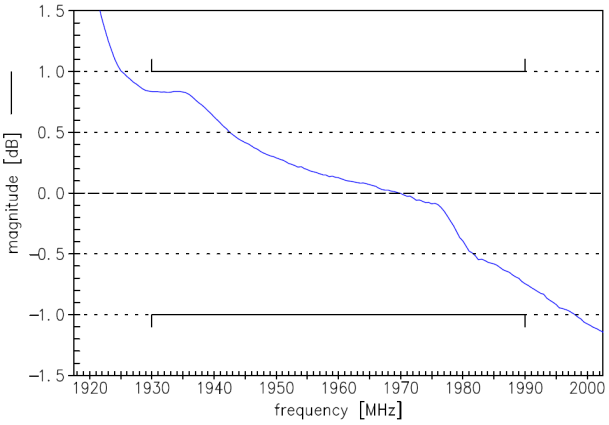

Fig. 6: Amplitude symmetry of balanced signal at RX port

VII. Conclusion

We have presented a 3.0x2.5x1.3mm³ fully matched mode-converting US-PCS CDMA duplexer based on the hybrid integration of a mode-converting SAW RX filter and a single-ended BAW TX filter. The integration platform is LTCC, in which all the necessary matching components have been embedded. Already the first samples from the demonstrator run show an electrical performance that fulfils in most parameters the design goals. The next steps in the commercialization of this component (besides a redesign to finally meet the electrical specifications) will be an intensive quality testing of the parts (humidity storage, high-power, temperature cycling, etc.) and a characterization with respect to non-linear behaviour.

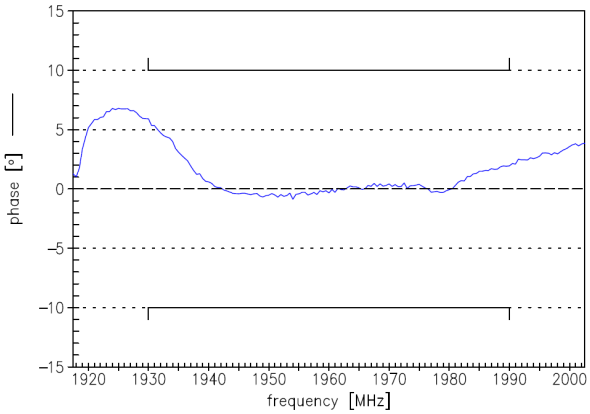

Fig. 6: Phase symmetry of balanced signal at RX port

Last but not least, we would like to mention, that the presented hybrid SAW/BAW integration strategy is of course not limited to fully matched single-duplexers but can also be implemented in more sophisticated components like quintplexers, PAiD or full RF front-end modules [9].

VIII. Acknowledgements

The authors are deeply grateful for the contribution of Isabel Gavela-Perez to the LTCC design. We would also like to express our appreciation to the whole BAW team for a record-breaking manufacturing time for the first hot lot.

References

[1] R. Ruby, et al., "*PCS 1900 MHz Duplexer Using Thin Film Bulk Acoustic Resonators (FBARS)*", Electronics Lett., vol. 35, pp. 794, 1999.

[2] R. Ruby, "*Overview of FBAR Filters, Duplexers, Quintplexers, and Front End Modules (FEM) at Avago (Formerly of Agilent)*", Workshop Proc. of the AMPC2006, pp. 399, 2006.

[3] A. Ballato and T. Lukasek, "*A Novel Frequency Selective Device: The Stacked Crystal Filter*", Proc. IEEE Freq. Contr. Symp., pp 262, 1973.

[4] K.M. Lakin, „*Coupled Resonator Filters*“, Proc. IEEE Ultrasonics Symp., pp. 901, 2002.

[5] G.G. Fattinger, et al.,"*Single-to-balanced Filters for Mobile Phones using Coupled Resonator BAW Technology*", Proc. IEEE Ultrasonics Symp., pp. 416, 2004.

[6] G. Feiertag et.al., "*Advanced Packages for Surface Acoustic Wave Components*", Proc. of Micro System Technology, Munich, p. 44, 2003.

[7] E. Schmidhammer et.al., "*BAW Components for PCS-CDMA Applications*", Proc. IEEE Ultrasonics Symp., pp. 89, 2005.

[8] F.M. Pitschi, et al., "*Accurate Modeling and Simulation of SAW RF Filters*", IEEE MTT-S Symp. Digest, pp. 2009, 2003.

[9] W. Faber, *"System in Package: from Discrete Components to Highly Integrated Devices and Modules"*, VDE Congress, Aachen, 2006.

Wafer Level Packaging (WLP) of FBAR Filters

Rich Ruby & Lexie Kekoa

Avago Technologies Inc.

***Abstract* — Although Wafer Level Packaging (WLP) was first introduced in the 1980's, the first publication describing WLP for FBAR and BAW devices was in 1999 [1]. In 2002, Agilent/Avago published their version of WLP to create microcapped FBAR devices [2]. And in 2004, Infineon described their version of microcapped BAW devices [3,4]. We describe some of the hermeticity tests and STRIFE tests developed for the evaluation of the microcapped FBAR filters.**

I. INTRODUCTION

Microcapped FBAR filters first appeared in the literature in 2002 and found their way into cell phones a year later. Their introduction into high volume commercial products was a paradigm shift in the packaging of moisture sensitive devices. Until 2003, devices such as SAW resonators and filters, BAW resonators and filters and Quartz crystal resonators were packaged in ceramic packages. The lid was constructed of either a ceramic or metal material and was typically sealed to the package via a seam sealing technique or soldering technique to create a hermetic, highly moisture resistant, environment. The electrical leads were brought out through the ceramic package. Motivation for making microcapped wafers was explained in an earlier paper [5].

II. TYPES OF WLP FOR FBAR AND BAW DEVICES

At the time of this writing, there are two companies selling BAW or FBAR devices using WLP in high volume – Infineon and Avago. The former company utilizes an organic seal, SU8, a negative, epoxy-type, photosensitive resist [6] that is extremely viscous and when applied to the wafer and patterned and cured leaves tall well-defined walls. In the "Infineon" process, the BAW device (a thin film bulk resonator –or FBAR – is deposited and formed on a stack of matched dielectric and metal layers that form a Bragg reflector). After the BAW device has been processed, a thick layer of SU8 is applied, patterned and partially cured. It is the Author's understanding that the wafer is then singulated, pick & placed onto a daughter board where the device pads are connected by wire bonds to pads on the daughter board. A silicon lid is then placed on top of the slightly sticky SU8 and more heat is applied to form a stronger attachment between the SU8 walls and the silicon lid.

Strictly speaking this is not Wafer Level Packaging. Only the walls are formed "en masse" while the devices are in wafer form. A newer generation Infineon process utilizes a sacrificial material to be placed on top of the BAW devices such that a SU8 layer can be placed on top, thus creating a protected region. This newer process is truly a WLP process. However, it is unknown to the Authors if this technique is in high volume manufacturing.

The Avago (previously Agilent and HP) approach is different and is a true WLP technique. Rather than using an organic epoxy as the bond, we use a "cold weld" technique using a high-pressure, high-temperature, wafer-to-wafer bond process to attach two wafers together and form a hermetic seal between the two wafers. The use of silicon as the "cap" wafer allows us to take advantage of the tremendous contributions from the MEMS field including deep silicon etching with high aspect walls and other MEMs techniques. In particular, using commercially available deep silicon etchers allow vias to be formed through the cap wafer.

There are several advantages inherent to this wafer-to-wafer bonding approach: 1) produce a high volume reliable, robust hermetic seal, 2) the ability to reduce chip area by "folding" the pads for the wire bonds back into the center of the device, and 3) the ability to integrate both passive and active devices into the lid.

Since both the Infineon and Avago approaches are in high volume, the level of hermeticity required by the end user (the cell phone manufacturer) is met by both techniques. The ability to "fold" the pads back into the center of the die gives an area advantage to Avago Microcap technique over both types of SU8 techniques – where the pads must be located on the periphery.

III. BACKGROUND ON HERMETICITY

Evaluation of the integrity of a hermetic package historically was performed by either or both fine and gross leak techniques. Gross leak detection is typically done by placing the device into a liquid and looking for bubbles. For fine leaks, a helium "bomb" technique was used where the packaged device was exposed to high pressure helium and then placed into a vacuum chamber to see if there was a residual leak of helium out of the package. Unfortunately,

neither technique works for microcapped FBARs, due to the very small volumes (~ 0.003 mm^3). Instead the shift in frequency of the FBAR filter is used as an indicator of whether the device was hermetically sealed or not. FBARs, like both SAWS and BAW (quartz and SMR [3]) devices have metal electrodes that can and will react to moisture. Conventional silicon nitride passivation is not compatible with Avago's FBAR processing. Aluminum nitride is employed as passivation but does not provide adequate protection and can –in non-hermetic instances – react with moisture. Even the slightest uptake of oxygen into the metal or aluminum nitride passivation can and will mass load the resonators that make up frequency devices and thus change its frequency.

The aluminum nitride passivation layer necessitates that the packaged device be truly hermetic. Non-hermetic packaging could potentially lead to catastrophic field failures. Harsh environmental conditions are employed using heat and moisture to accelerate failures, i.e. measured as frequency shift of devices after exposure.

A typical 6 inch wafer has fifteen thousand devices (assuming 1mm2 average die area). The bad news is that even an average of one bad part per wafer (one out of 15,000) got into a customer's phone, it would introduce 66 defects per million (DPM). Random pairing of a Tx die and Rx die (from two different wafers) in duplexer products double the DPM to 132 dpm and for the five filter Quintplexer products –> 330 dpm!

IV. HERMETICITY CRITERIA

The "good news" is that with an average of 15,000 die per 6" wafer (a WLP wafer), there is also the ability to gather a considerable amount of data per wafer and obtain insights based on solid statistics. One can use this to evaluate the relative merits of any process flow change on hermeticity. On wafer testing is very quick, uses testers in an identical way as they would be used in production (i.e. utilizes existing infrastructure) and the quantity measured – frequency shift – is a very sensitive measure of any degradation from a lack of hermeticity.

Moisture (humidity) accelerated by heat is the main culprit in frequency shift. High temperature storage (HTS) alone without the presence of moisture has not resulted in failure from 1000 devices stressed from 15 non-consecutive product lots.

Additionally harsh thermal cycling is considered a very challenging test that was thought to be very difficult to pass. Various conditions derived from JEDEC standards have been successfully evaluated. The harshest is liquid-to-liquid thermal shock rapidly transitioning from -65C to +150C typically in less than 10 seconds, involving repeated dipping of parts (on the order of hundreds of times in rapid succession) into hot liquid and then into a cold liquid. Hot/cold immersion of parts applies stresses on the microcap seals and, might create cracks and thus expose parts to moisture with the resultant frequency shift. Avago products have repeatedly shown no issues with respect to this test. Typical data from exposure to 1000 cycles of thermal shock is shown in Table 1 below, as well as other common environmental stress conditions.

Table 1-Thermal stress results

Stress Test	Stress Condition	Duration	Results
Temperature Cycling	-55°C /+125°C, 15 min dwell, 10min transition time (JESD22A-104B, Cond B)	1000X	0 failures of 1550 units stressed
Thermal Shock	-65°C /+150°C, 15 min dwell, <1min transition time (Liquid-liquid)	1000X	0 failures of 1000 units stressed
High Temperature Storage	Ta=+125°C	1000hrs	0 failures of 1000 units stressed
Low Temperature Storage	Ta=-40C	1000hrs	0 failures of 1000 units stressed

The useful life requirements vary from customer to customer but are typically less than 1000ppm for 7-10 year operation between 30°C ambient and 60-70%RH. The test conditions employed in demonstrating moisture robustness (with some variations depending on the customer) are i) MSL rating, ii) 1000 hours at 85°C at 85% relative humidity (85/85) and iii) 72-96 hours in autoclave (121°C at 100% relative humidity). MSL stands for Moisture Sensitivity Level and is a test of how well the part will survive assembly (including soldering to a printed circuit board) after seeing moisture. A MSL rating of 3 tells the customer that the parts can be left on the line for up to 168 hours exposed to the ambient moisture and still be "solderable" to the motherboard during assembly MSL ratings are applied to the packaged part (including the pc board, the epoxy, die attach and the microcap'd die) that has been "soaked" in moisture and then run thru IR reflow, a high temperature process step that is used by the vendor to attach all of the components onto the mother board of the phone. Moisture absorbed by the printed circuit board and the epoxy can cause delamination and "popcorning" types of failures not related to the microcap process. In contrast, the temperature/humidity tests look only to see if there is a slight frequency shift after the strife. Our goal is to have an

MSL rating no worse than the pc boards that they go on. However, to test the integrity of the microcap'd parts we use the more harsh tests such as 85/85.

Due to the length and sheer number of parts evaluated, Avago has employed 95C/98%RH and autoclave (121C/100%RH) as highly accelerated conditions for rapid process and new product evaluation/qualification. 95°C and 98% relative humidity is approximately 2.6 as accelerated a stress condition compared with the commonly specified 85°C/85%RH (due to different observed failure mechanisms between parts failing at 85/85 (or 95/98) vs autoclave, we cannot assign an acceleration factor between autoclave and 85/85). Failure rates are often expressed in terms of failures per million components operated for 1000hrs (FIT – Failures in Time in units in 10^9 hours). Avago's combined data from various reliability stress conditions results in a 90% confidence interval of 60 FITs (or 60 failures out of one billion hours of operation

V. ANALYSIS AND RESULTS

Table 2 shows the various ratings in our case and the various humidity tests used for strife and for qualification. Our parts are rates at MSL3 for assembly purposes. Data on the various performances of each strife test is also given in Table 2. The very large number of tested parts at 95/98 was the result of studies over the past 3 years and represents parts from all of our FBAR microcap'd FBAR lines.

Figure 1 shows a typical failure. This is a Band I UMTS duplexer whose Tx frequency shifted 2.5 MHz after 18 hours of autoclave.

Table 2-Moisture Robustness

Stress Test	Stress Condition	Duration	Results
MSL (Moisture-sensitivity level)	30C/60%RH	1 wk	Level 3
Temperature -Humidity	85°C/85%RH (JESD22A-113B)	1000hrs	0 failures of 1500 units stressed
	95°C/98%RH	96hrs	311 failures from 585,750 units stressed
Autoclave	121°C/100%RH	96hrs	3 failures of 1500 units stressed

Sometime in the middle of 2007, Avago will surpass the ½ billion FBAR filters sold to handset and data card manufacturers. Typical dpm (defects per million units processed) for all failure modes reported by our customers averages around 50 dpm.

With the advent of FBAR in high volume, hermetic WLP technology has demonstrated viability and maturity.

ACKNOWLEDGEMENT

The Authors wish to express their gratitude to the Fort Collins Fab engineers and management for bringing these products into commercial reality and to our management.

REFERENCES

[1] K. Lakin, "Thin Film Resonators and Filters", Ultrasonics Symposium Proceedings IEEE 1999

[2] R. Ruby, A. Barfknecht, C.H. Han,Y. Desai, F. Geefay, M. Gat, T. Verhoeven, "High-Q FBAR Filters in a Wafer Level Chip Scale Package", ISSCC 2002

[3] M. Franosch, K. Oppermann, A. Meckes, W. Nessler, R. Aigner, "Wafer-Level Package for Bulk Wave (BAW) Filters", Microwave Symposium Digest, 2004 IEEE MTT-S

[4] N. Huynh, H. Forstner, R. Aigner, T. Herzog, B. Gebatler, L. Elbrecht, S. Marksteiner, "Ultrasmall PCS Duplexer in Plastic Package using Bulk Wave (BAW) Filter Technology:, 34th European Microwave Conference 2004

[5] R. Ruby, "FBAR, From Technology Development to Production", 2nd International Symposium on Acoustic Wave Devices for Future Mobile Communiations, Chiba, Japan, March 2004

[6] IBM Patent #4882245

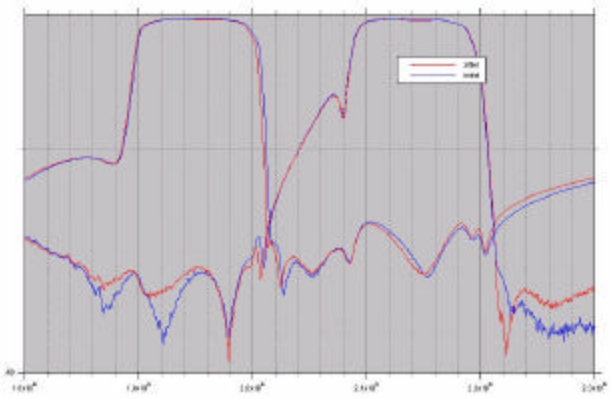

Figure 1 A typical failure due to hermeticity.

BAW Devices and Integration into System-in-Package (SiP).

A.B. Smolders, J.W. Lobeek, N.J. Pulsford, F.E. van Straten.

NXP Semiconductors, Gerstweg 2, 6534 AE Nijmegen, The Netherlands,
e-mail: Bart.Smolders@nxp.com

***Abstract* — This paper discusses the opportunities for integrating Bulk-Acoustic-Wave devices in to System-in Package (SiP) concepts, providing the smallest size and lowest cost in the end application. In future multi-mode wireless applications the main challenge lies in the front-end, where many high-performance filter/duplexers are needed to connect signals from several antennas to a single software-defined System-on-Chip (SoC). Minituarisation, reconfigurability and cost reduction are the key challenges. A novel low-cost IC process is developed to realise high-Q BAW resonators. Combined with advanced SiP technologies future challenges in (multi-mode) front-ends can be addressed. A couple of examples will be shown of recent developments at NXP Semiconductors.**

***Index Terms* — Bulk-acoustic-Wave (BAW) resonators, filters, System-in-Package (SiP), RF Front-ends, Passive Integration.**

I. Introduction

Advanced system integration will be one of the key trends in wireless applications in the upcoming year. This is particularly true in cellular handsets, where the number of features grows very rapidly and where the key-value-drivers are size and cost. This means that a high level of integration is required in order to meet the market needs.

With the growing number of wireless mobile applications, there is a strong need for a more efficient system partitioning in order to reduce the total Silicon area that is used and to increase flexibility and re-use (multi-mode) of various IC's. Already in today's high-end mobile phones we see various wireless applications combined, such as GSM/EDGE/UMTS, Bluetooth, FM radio, DVB-H TV reception, WLAN etc. For example, the penetration rate of Bluetooth is expected to be around 70% by 2008. In today's phones most wireless applications are added to the cellular system as "stand-alone" features, where the integration is only done on software level. No significant sharing of functions on a hardware-level is done yet. In the future mobile this will be different as illustrated in figure 1. The future mobile platform will consist of optimised flexible digital signal processors (Software Defined Radio) and re-configurable RF System-in-Package radios (Radio-SiP) that can be used to serve several wireless applications. As shown in the example of figure 1 we will have a dedicated cellular baseband taking care of all the signal processing that is required for 2G, 2.5G, 3G+ cellular standards. In addition, it includes a dedicated signal processing unit taking care of all the non-cellular and emerging standards, e.g. WLAN, Wibro/Wimax and DVB-H. The Radio SiP's are partly re-configurable as well and could potentially also be used to serve several applications operating at different frequency bands (multi-mode/multi-band). In addition, two Radio-SiPs could be used for MIMO (Multiple-Input-Multiple-Output) and/or diversity purposes as well. The radio's are connected to the digital modem via a high-speed serial interface.

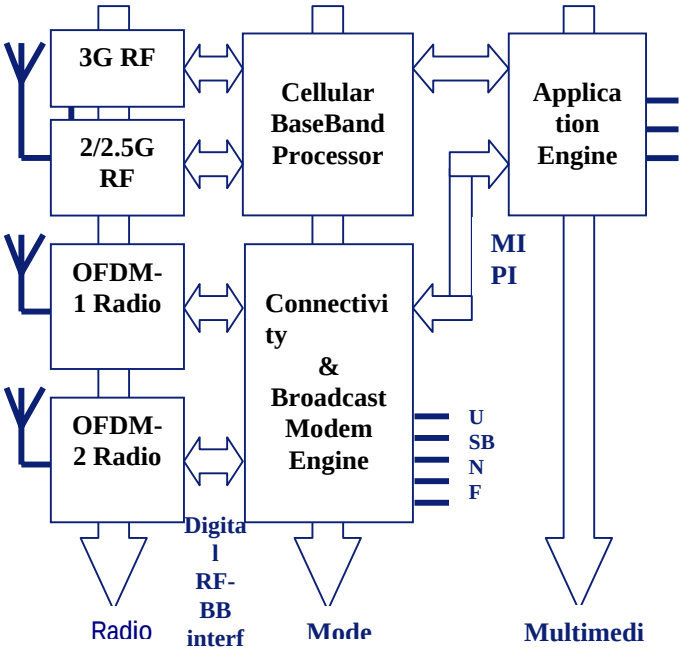

Fig 1:Embedding of baseband IP in future cellular platforms. There-configurable radio and corresponding front-end is highly integrated using System-in-Package technology.

II. Trends in Front-End integration for Wireless Applications

The key challenge in the route towards re-configurable or software-defined radios will be in the front-end. Many antennas need to be connected to the multi-mode digital signal processor. To illustrate this, let us investigate the potential evolution of the front-end from 2007 to 2012+. Figure 2 shows a typical front-end of a high-end cellular handset in 2006/2007. Note that only the cellular pipe is shown here. It consists of a transceiver for the 2G/2.5G mode and another transceiver for the 3G mode. Both transceivers are connected to a single baseband processor. In the front-end we have a low-band and a high-band antenna connected to a Front-End-Module (FEM) for the 2G/2.5G pipe and to a Power-Amplifier-with-Integrated-Duplexer (PAiD) module for the 3G pipe. In this example, the 3G pipe only uses the high-band. Further integration of the front-end of figure 2 can be done by expanding the FEM with the PAiD and antenna switch. Advanced SiP technology will be needed to further reduce size and cost.

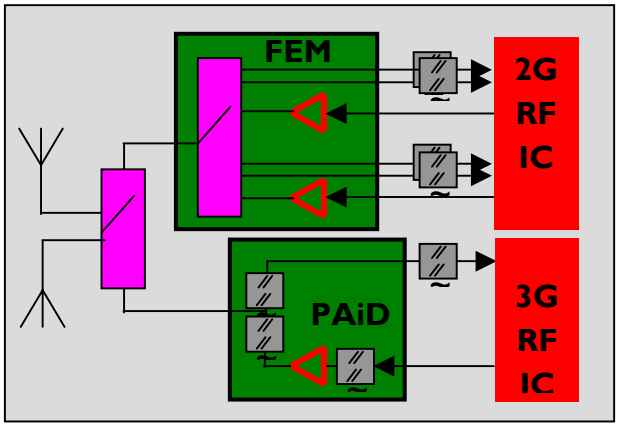

Fig 2: Cellular Front-End of a high-end multi-mode/band in 2007.

If we look somewhat further in the future we will see additional frequency bands and features coming into the front-end. If we use a similar approach/architecture as used in the 2007 front-ends, we will see the following trends:

- rapid growth of filters/duplexers
- multiple RF interfaces
- growth in number of Power Amplifiers
- Need for higher integration level in the front-end due to size/cost-constraints.
- more and broader-band antennas due to new frequency bands on system enhancements like MIMO.
- Co-existence issues with other standards will increase the requirements on the filters and duplexers.

This would lead to the front-end partitioning in 2010+ as illustrated in figure 3.

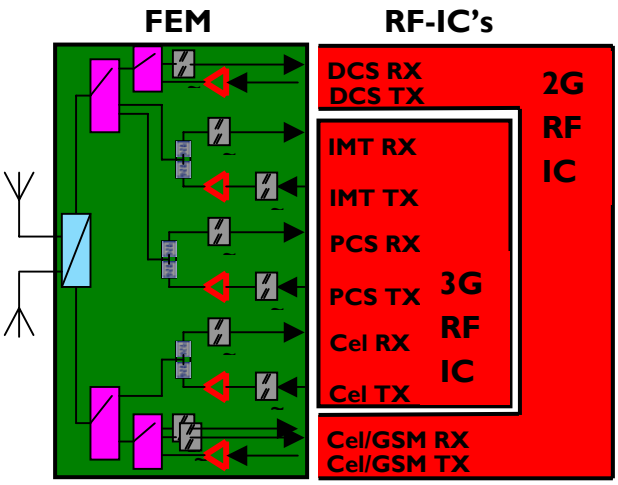

Fig 3: Cellular Front-End of a high-end multi-mode/band in 2010+. Additional frequency bands and performance-enhancement features (e.g. MIMO) are introduced.

The front-end would require 15 filters and 5 Power Amplifiers (PA's). The contribution of the filters to the total cost of a the front-end will grow significantly. It is clear that there is a strong need in the market for a high-performance, small-size, low-cost filter technology as a key building block for future FEM's. We believe that the Bulk-Acoustic-Wave (BAW) technology will make this happen, since it offers high-performance and is compatible with low-cost standard IC processing.

It is clear that the front-end architecture as shown in figure 3 is not the most cost-effective solution, since it uses many components. Therefore, if we look somewhat further in the future alternative front-end architectures can be expected with a high level of reuse of Silicon and other blocks. An example of such a front-end is shown in figure 4. This re-configurable SiP combines a multi-mode transceiver with a tunable front-end. The interface to the baseband processor is realised using a low-power high-speed serial link. It is clear that such a partitioning can only be achieved when high-Q "tunable" components are available for adaptive PA matching and adaptive filtering.

Both BAW as well as RF-MEMS are considered as potential technologies that can be used to build such tunable components. However, this is currently still in a research phase. Another function that will be embedded in the future front-end is a low-power high-frequency reference oscillator based on a high-Q BAW resonator. In this way, bulky and expensive crystal-based oscillators are not needed anymore. In addition, phase-noise performance will be improved significantly.

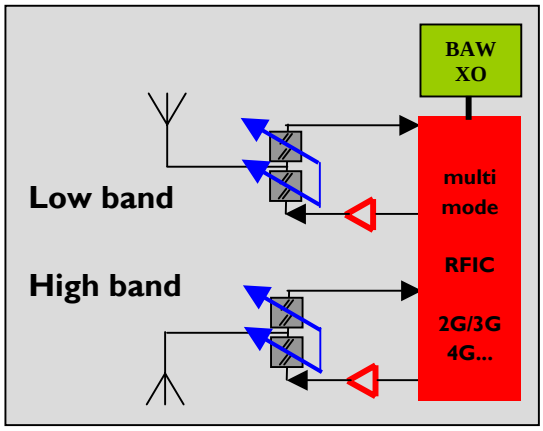

Fig 4: Re-configurable Radio in 2012+. It consists of a multi mode transceiver with digital high-speed interface to the baseband processor. The front-end uses high-Q tunable components for adaptive PA matching and tunable selectivity.

III. BAW Technology Overview

Two different concepts for BAW resonators are used in the market, namely: solidly mounted resonators (SMR) and membrane type resonators (FBAR). The membrane type is a suspended resonator with an air gap at both sides of the piezo-electric material. The other concept is the solidly mounted resonator where a Bragg reflector is used to reflect the acoustic energy. We have selected the SMR technology for several reasons, of which a key one is its compatibility with standard IC process flows.

A cross section of a basic resonator in the SMR technology is shown in figure 5. The reflector stack consists of various layers of low- and high-acoustic impedance materials to reflect acoustic energy. The low acoustic impedance material used is SiO_2. A well matched combination of both Pt as well as Ta_2O_5 layers is used for the high impedance layers. Patterning is used for the Pt layer to eliminate effects of parasitic capacitance. A more detailed description of the advantages of such a hybrid approach is given in [4].

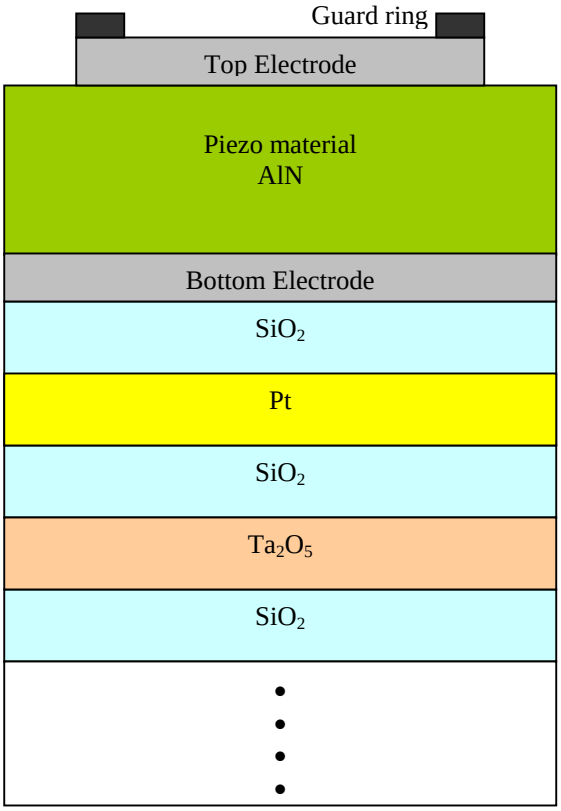

Fig. 5. Cross-section of a BAW resonator.

A complete chip-scale package is made by creating a cavity for protection purposes as illustrated in figure 6. Solder bumps are placed for flip-chip assembly. All processing can be done using standard IC processing equipment ensuring reliable and low cost production.

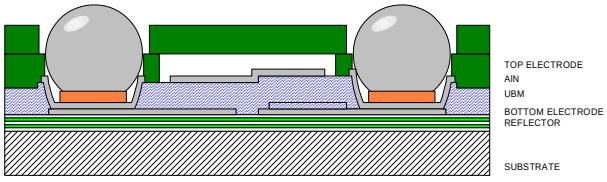

Fig. 6. Package concept of BAW resonator.

IV. SIP TECHNOLOGY

System-in-Package (SiP) offers the opportunity to integrate a complete system including all the required

passive components, such as bandpass filters, baluns, de-coupling and capacitors. This will result in the smallest possible total solution in the final application. Therefore, SiP technology is mainly used to integrate the front-end of a wireless system. We will describe here two different types of SiP technologies which are used in many applications [4].

The first approach uses a laminate substrate and is often used to realise Front-End-Modules (FEM). This platform offers the most flexible SiP solution and uses a low-cost 6-layer laminate substrate. Figure 7 shows a cross section of the laminate stack. It consists of two core layers, a prepreg layer and two sequential build-up (SBU) layers. The laminate substrate is used for interconnect using microvias. In addition, it integrates passive RF functionality such as striplines, inductors, baluns, filters and complete embedded antennas. The integration in laminate offers more design flexibility and better performance for some functions at high frequencies as compared to surface mount components (SMD's). Multiple active and passive dies (CMOS, BiCMOS, GaAs, BAW, MEMS) and SMD components can be mounted on the substrate. Wirebonding or flip-chip technology can be used to mounting the dies on the substrate.

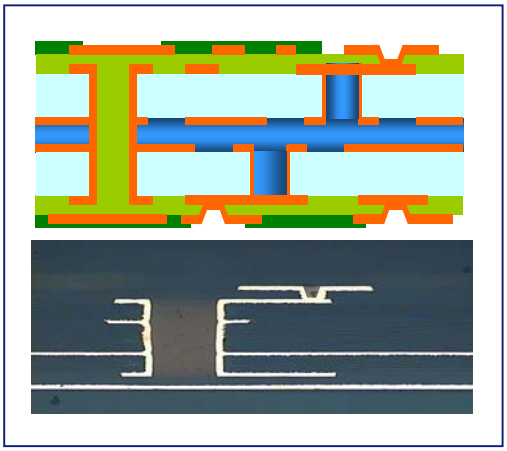

Fig. 7. Cross section of the 6-layer laminate substrate (LAMP). It consists of the following layers: solder-resist (dark-green), Metal Cu (orange), SBU (light-green), core (light-blue) and prepreg (dark blue), [4].

The second SiP platform is based on a low-cost thin-film passive integration IC technology build on a high-ohmic silicon substrate. The thin-film technology features a low number of mask steps and uses standard back-end IC processing with relaxed lithographic resolution in order to minimise manufacturing cost [4].

The active dies (CMOS, BiCMOS) and passive dies (BAW, MEMS) are placed on top of the substrate using flip-chip technology with solder bumps. Standard IC packages with a height of only 0.85mm can be used. Many passive functions can be realised including inductors, low- and high-density capacitors (up to 25-100 nF/mm^2), resistors and lateral PIN diodes. Figure 8 shows an example of a silicon-based SiP with double flip-chip technology.

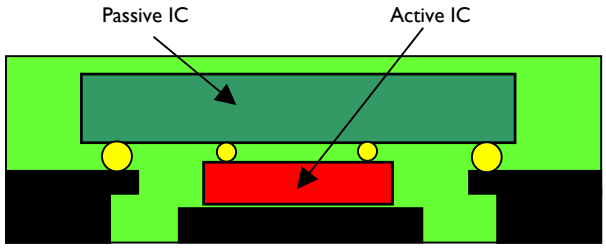

Fig.8. SiP build up using a passive thin-film IC. A double flip-chip technology with solder bumps is used in a standard IC package. Multiple active dies can be mounted on the passive die.

V. RECENT EXAMPLES

In this section we will describe a few examples of using BAW devices in a system-in-package concept. The first example concerns a BAW duplexer for the USPCS WCDMA bands. The close separation of the TX and RX bands of only 20MHz makes the USPCS system an ideal application for BAW technology due to the superior loaded Q-values compared to SAW technology. The duplexer function is composed out of 2 BAW filter dies one for the TX band (1.85-1.91GHz) and one for the RX band (1.93-1.99GHz) mounted onto the SiP laminate substrate as shown in Figure 9. The multilayer laminate integrates the high quality RF inductors (typ. 1-3 nH) required to complete the wideband response of the filter. Both the laminate response and BAW filter die response can be co-simulated with commercial quasi-3D electromagnetic simulation software. An excellent response is obtained with passband insertion loss of 3dB and a RX-TX isolation of 50dB.

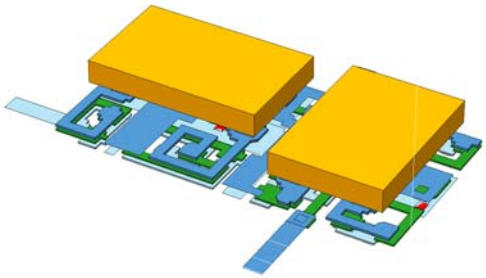

Fig. 9. BAW-duplexer build on laminate based SiP technology.

The second example is a BAW-based high-frequency oscillator [5]. In this case the BAW resonator is placed on top of passive silicon die using flip-chip technology. An active die that contains the feedback amplifier and additional control circuits is also placed on the Si-carrier. The BAW oscillator operates at 2 GHz and can replace low-frequency crystal based oscillators. Main advantages are size, cost and improved performance (e.g. power consumption and phase noise). Figure 10 shows a photograph of the three dies.

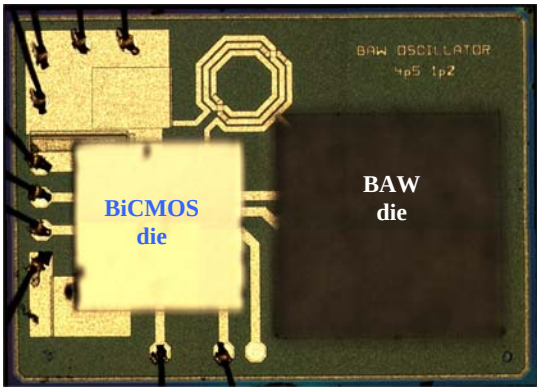

Fig. 10. Photo of a BAW-based high-frequency oscillator consisting of a BAW-die, a BiCMOS-die and a passive silicon carrier [5]. The BAW and BiCMOS dies are flip-chipped on the passive silicon carrier.

In last example a BAW filter is used to provide the required selectivity in a wide-band tuner concept. Figure 11 shows the basic block diagram. The tuner front-end is a highly linear LNA+mixer that upconverts the input frequency to an IF frequency. The BAW filter is then used to provide the selectivity and to remove interfering signals. The back-end part of the tuner that converts the IF signals to a digital representation has now very relaxed specifications. Figure 12 shows an example of such an IF BAW filter with a relative narrow-bandwidth. This up-converter concept can be used to realise low-cost high-performance TV tuners for DVB-H/T. In addition, this concept could also be a route to solve the future multi-mode/band problem as illustrated in figure 4.

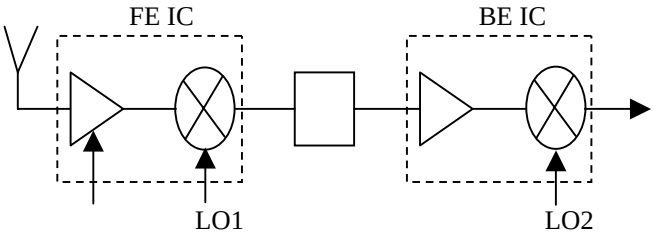

Fig. 11. A wideband upconverter tuner using a high-Q BAW filter to realise the required selectivity.

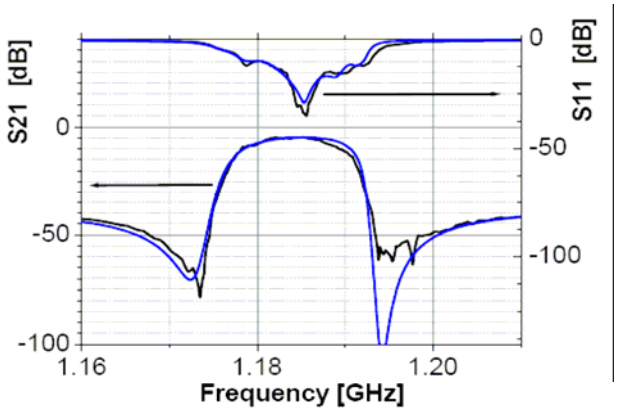

Fig.12 Narrow-band BAW filter characteristic with 8 MHz bandwidth used for up-converter architecture.

V. Conclusion

BAW technology opens the door to tackle many future challenges in wireless application. Combined with advanced System-in-Package concepts, low-cost highly integrated systems can be realised. A few examples were presented to illustrate the variety of potential applications.

VI. Acknowledgements

The authors wishes to thank all the members of the BAW development team at NXP for their contribution. In addition, we thank Eduard Stikvoort of Philips Research for the design of the tuner circuits.

REFERENCES

[1] Straten, F. van, A.B. Smolders, A. van Zuijlen, R. Ooijman,
"Multiband Cellular RF Solutions"
IEEE Journal of Solid-state circuits, Vol 39, October 2004.

[2] Lobeek, J.W. , A.B. Smolders,
"Design and Industrialisation of Solidly-Mounted BAW Filters"
Digest IEEE MTT-S 2006, San-Fransisco, p. 386-389, June 2006.

[3] Lobeek, J.W. , R. Strijbos, A. Jansman, N. Xin Li, A.B. Smolders, N.J. Pulsford,
"High-Q BAW Resonator on Pt/Ta2O5/SiO2 Based Reflector Stack"
Accepted for publication in Digest IEEE MTT-S 2007, Honolulu, June 2007.

[4] Smolders, A.B., N.J. Pulsford, P. Philippe, F.E. van Straten
"RF SiP: The Next Wave for Wireless System Integration"
Proceedings of the IEEE RFIC Symposium, Forth-Worth, pp. 233-236, June 2004.

[5] van Helmont, F., P. Philippe, A.B.M. Jansman, R.F. Milsom, J.J.M. Ruigrok, A. Oruk,
"A 2 GHz Reference Oscillator incorporating a Temperature Compensated BAW resonator "
Proceedings of the IEEE Ultrasonics Symposium, Vancouver, pp. 333-336, 2006.

Above-IC Integration of BAW Resonators and Filters for Communication Applications

Marc-Alexandre Dubois [(a)], Christophe Billard [(b)], Guy Parat [(b)], Mohammed Aissi [(c)], Hocine Ziad [(d)], Jean-François Carpentier[(e)], Kim B. Östman[(f)]

(a) Swiss Center for Electronics and Microtechnology (CSEM), Neuchâtel, Switzerland
(b) CEA-LETI, Grenoble, France
(c) LAAS-CNRS, Toulouse, France
(d) AMI Semiconductor Belgium BVBA, Oudenaarde, Belgium
(e) ST Microlectronics, Crolles, France
(f) University of Technology, Tampere, Finland.

***Abstract*— This paper demonstrates the feasibility of an above-IC bulk acoustic wave technology for wireless applications in the 2 to 6 GHz frequency range. Examples of low phase noise FBAR based oscillators are used to show the potential of this technology.**

***Key words*—Bulk acoustic wave devices, integrated circuit fabrication, micromachining, piezoelectric resonator filters, oscillators, radio receivers.**

I. INTRODUCTION

BULK acoustic wave (BAW) piezoelectric resonators have been developed over the last few years to be used in wireless communication systems, mainly in mobile phones. They consist in a piezoelectric thin film sandwiched between two electrodes, and isolated acoustically from the substrate over which they are built [1]. Due to their high Q factors, large power handling capability, and reasonable coupling coefficient, they can indeed be used advantageously in passive ladder filters and hence in duplexers with the low loss and steep skirts required by the latest communication standards. The duplexer is a key component in a mobile phone since it is responsible for cleaning the spectrum around the received or transmitted signal, just next to the antenna. It has then a very strong impact on the transceiver architecture and the RF design specifications. The need for efficient duplexers with small form factors has been the main driving force for the development of the thin film BAW technology, which is now mature and industrial [2][3].

Besides their use in passive high performance filters, miniature resonators can also be associated with active circuitry to provide specific electronic functions, where a high Q can be leveraged, such as low noise amplifiers or oscillators. In the latter case, the high Q factor of the resonator translates directly into a reduced phase noise, which is often the key specification for an oscillator.

Although BAW resonators and filters are processed, usually, on silicon wafers, the applied technologies are those used in the micro-electromechanical systems (MEMS) world, rather than in the IC fabrication facilities. Among the differences are the need for different materials—high resistivity silicon substrates, a piezoelectric layer and specific electrodes—fabrication tolerances either relaxed or much more stringent depending on the parameter, and possibly the wafers' size.

This paper describes results obtained in an exploratory work aiming at bringing together the BAW and IC technologies by co-integrating active and passive components on the same substrate. More specifically, piezoelectric thin film resonators and filters have been fabricated at the wafer level above BiCMOS integrated circuits in a post-processing approach.

Ultimately, such a co-integration could reduce the size of high performance RF systems and boost their perfomances through the reduction of interconnection parasitics. However, this would probably come at the expense of the fabrication yield and hence of the production cost, limiting this technological approach to high end markets where the cost is not the primary concern, unlike in the mobile phone business.

II. ABOVE IC BAW TECHNOLOGY

The two available types of BAW resonators—differentiated by the way the acoustic isolation between the vibrating film and the substrate is carried out [1]—have been shown recently to be compatible with such a co-integration scheme [4][5]. In this work, the *film bulk acoustic resonator* (FBAR) fabricated by surface micro-machining has been chosen in order to keep

Contact author: marc-alexandre.dubois@csem.ch

the technology for connecting the resonators to the topmost metal of the IC as simple as possible. Indeed, as only a very thin isolating air gap is created underneath each resonator, the latter are placed very close to the circuit and low loss interconnections can be realized without manufacturing metal-filled vias through a thick acoustic reflector.

Over the years, aluminium nitride (AlN) deposited by reactive sputtering has emerged as the technology of choice for BAW resonators because it is an excellent compromise between performance and manufacturability. Its coupling coefficient is not as high as that of ZnO or PZT, but it is chemically very stable, has an excellent thermal conductivity, and a low temperature coefficient. These properties enable the fabrication of resonators featuring coupling factors of 6-7%, good resistance to corrosion, excellent power handling capability, and limited drift with temperature. Another advantage of AlN is the low process temperature and the fact that it does not contain any contaminating elements harmful for semiconductor devices, unlike most other piezoelectric materials.

Furthermore, owing to these excellent material properties and because of the very stringent specifications on thickness accuracy and uniformity set by the BAW resonator's architecture—resonance frequency is inversely proportional to thickness—equipment manufacturers developed and optimized sputtering systems specifically for AlN, rendering the process industrial and widely available [6].

The sputtering process used in this work takes advantage of the properties of a platinum (Pt) electrode, which promotes efficiently the growth of AlN films with excellent piezoelectric properties. This is due to the hexagonal symmetry of the (111)-plane of Pt that matches the (002)-plane of AlN, and to an extremely smooth surface [7][8]. The drawback of Pt is its lower electrical conduction compared to aluminium or molybdenum, which is one of the limiting factors for the series Q factor of the BAW resonator. The crystalline properties of AlN films deposited with this process have been assessed by X-ray diffraction measurements, yielding a very narrow rocking curve FWHM of 1.07° for the (002) peak. This high crystalline quality has been confirmed by a direct measurement of the piezoelectric $d_{33,f}$ extensional coefficient with a double beam Mach-Zehnder interferometer. A value of 5.3±0.22 pm/V has been obtained, representing a potential coupling coefficient k_{eff}^2 in BAW resonators larger than 6.5%.

The fabrication sequence of the BAW resonators (and filters) above IC is the following: First, silicon oxide is deposited over the passivated IC-carrying wafers and planarized by CMP, in order to get a smooth and flat surface for the FBAR fabrication. A photoresist sacrificial layer is deposited, patterned, and cured at high temperature for defining each resonator's position, and then protected by silicon nitride. Next, the active part of the devices is built up, with the subsequent deposition and patterning of the Pt bottom electrode, the piezoelectric AlN layer, and the top electrode. Via holes are then etched through the different dielectric layers until the last metal level of the integrated circuit (M5), and a thick metal interconnect is deposited and patterned to link the BAW resonator to the IC. A thin silicon oxide loading layer is then deposited and patterned to shift down the frequency of some resonators in the case of filters. Finally, the sacrificial layer is etched and the membranes are released. Fig. 1. shows a schematic cross-section of a FBAR connected to the last metal level of an IC wafer.

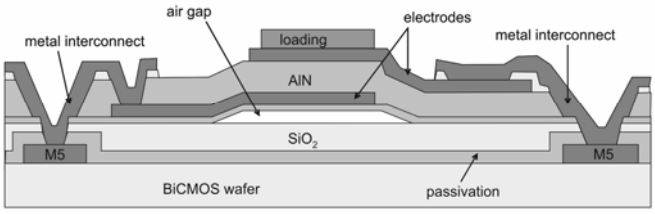

Fig. 1. Cross-section of FBAR integrated above IC

It has to be mentionned that the technology has been kept as simple as possible for these proof-of-concept integrations. Consequently, additional processing steps that would be required for large-scale production, such as the passivation of the devices for example, have been omitted.

Two different sources of IC wafers have been used: either BiCMOS 0.25µm SiGe:C technology from ST Microelectronics, or BiCMOS 0.35 µm SiGe technology from AMI Semiconductor. Likewise, two different FBAR frequencies have been explored, 2.14 GHz and 5.5 GHz.

III. Cross-influence of technologies

When post-processing MEMS of any kind above IC, it is crucial to control that the semiconductor devices do not suffer from the additional processing steps, and most particularly from the many thermal cycles applied to the wafer.

Table 1. Impact of post-process on BiCMOS technology

	unit	before	after	delta
NMOS 10x0.35 V_{bd}@10nA	V	9,4682	9,5689	-1.06%
PMOS 10x0.35 V_{bd}@10nA	V	-8,6168	-8,6625	-0.53%
NMOS 10x0.35 V_{t0}	V	0,60358	0,59291	1.77%
PMOS 10x0.35 V_{t0}	V	-0,63017	-0,6334	-0.51%
M3/M2 via chain	Ω/via	0,84329	0,85834	-1.78%
M2 resistance	mΩ/sq	48,498	48,805	-0.63%
HIPO resistor W100L10	Ω/sq	1090,4	1073,52	1.55%

As an example, in the case of post-processing above BiCMOS 0.35 µm SiGe wafers, about 50 different test devices characterizing globally the performance of the semiconductor technology have been measured, before and after the fabrication of BAW resonators and filters. Table 1 shows an

excerpt of this measurement campaign with only a few relevant parameters. The stable breakdown voltage V_{bd} of the transistors show that there is no significant alteration of the gate oxide integrity. The MOS threshold voltage V_{t0} is likewise not affected. The resistance measurements indicate that the thermal cycles experienced by the circuits do not lead to any intermetallic formation in the interconnections since the resistive paths are nearly unchanged. In general, no major deviation due to the post-process have been observed in any measured parameter. All differences are below 2% except for 2 leakage measurements, which seem actually to have been improved by the BAW processing. This show that the impact of the BAW fabrication upon the BiCMOS circuits is very limited.

The opposite has also been observed, namely that the BiCMOS wafers do not impact the performances of the resonators. Indeed, individual resonators exhibit the same performances above-IC as on plain silicon wafers, meaning that the presence of active circuits underneath the FBARs does not modify their performances. Typical coupling and quality factors measured on test resonators are 6.5% and 900 in the 2 GHz range, and 6.6% and 750 in the 5GHz range. If the coupling coefficients confirm the high quality of the AlN layer, the Q factors could be further improved with a better thickness and acoustic impedance ratio between the electrodes and the piezoelectric film and the suppression of the lateral modes propagating in the membrane. The latter can be seen as wavelets on the fundamental resonance circle of a test rectangular FBAR in Fig. 2.

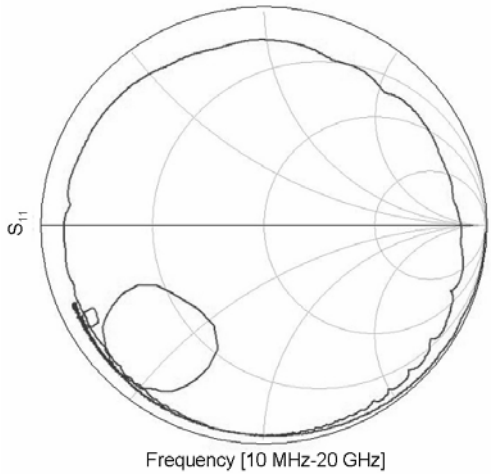

Fig. 2. Smith chart of a test FBAR at 5.5 GHz. The large circle is the fundamental resonance, whereas the 2 smaller ones are harmonics at 12.5 and 17.8 GHz respectively.

IV. WCDMA RF FRONT-END

The potential of this above-IC technology has been demonstrated through the design and fabrication of the receiver part of a simplified RF front-end set at 2.14 GHz. The latter is described thoroughly in [5]. This front-end chip contains a low noise amplifier, a single-to-differential converter, a high rejection double lattice FBAR filter, a matching network and a mixer. For the characterization of the circuit, the differential mixer was fed by an external signal generator.

Fig. 3. shows pictures of a newer version of the same RF front-end, which includes this time an FBAR-based VCO (seen at the right of the micrograph).

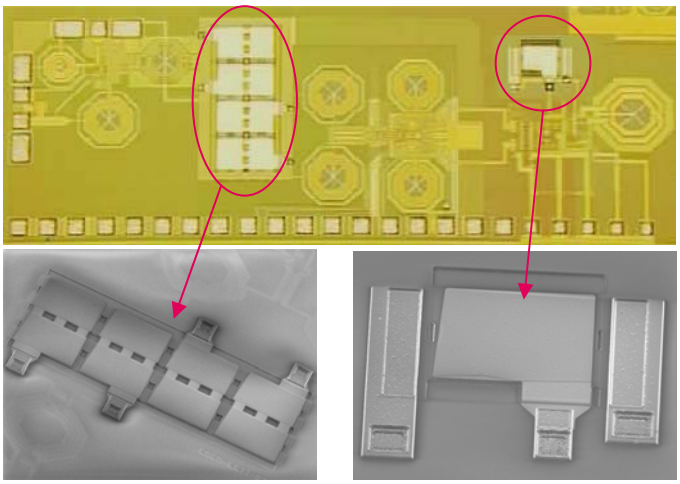

Fig. 3. Chip micrograph (top) of an integrated WCDMA receiver and SEM inserts of the BAW filter (bottom left) and resonator (bottom right).

The architecture and the performances of this differential VCO are described in details in [9]. Fig. 4. shows the measured phase noise of the FBAR VCO compared to the noise of a reference LC VCO, as well as a micrograph of the Si chip including the BAW resonator. The phase noise of the FBAR VCO is significantly lower than the one of the LC tank VCO, with a value as low as -143.7 dBc/Hz at the optimum operating voltage. The tuning range of the VCO is 15 MHz. It is not yet sufficient to cover the whole frequency band as required by the WCDMA standard, but it is much more than what has been obtained until now with FBAR oscillators [10][11].

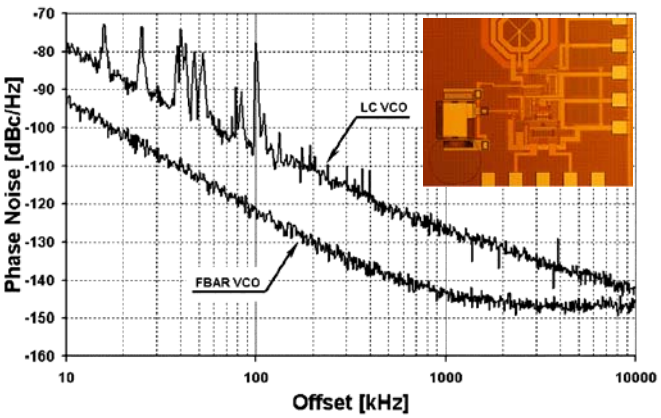

Fig. 4. Phase noise measurement of the FBAR differential VCO compared to a reference LCVCO.

Despite this limited tuning range, the receiver of Fig. 3. is functional, as it is shown by Fig. 5. It represents the spectrum

measured at the output of the mixer with a -40dBm signal at 2.1138GHz fed at the LNA input. The supply voltage and VCO control voltage have both been set at 2.4V.

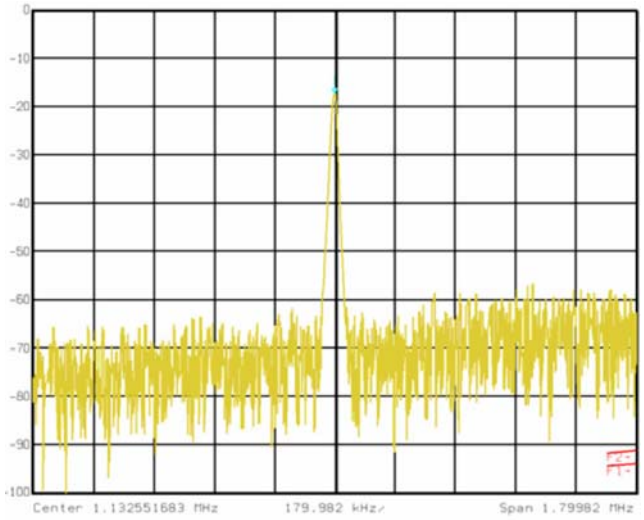

Fig. 5. Output spectrum of the monolithic WCDMA receiver, with the demodulated output at 1.13 MHz.

V. WLAN OSCILLATOR

As a second example of co-integrated system, an oscillator with Colpitts architecture has been designed for operating at 5.5 GHz. A micrograph of the chip and the schematic of the circuit are shown in Fig. 6. The core of the oscillator is a common collector transistor T_1, with the feedback capacitors C_1 and C_2 ensuring the negative resistance necessary to compensate the losses in the resonating FBAR. Transistor T_2 is used as a buffer to isolate the resonator from the load impedance. The active circuit has been implemented in the BiCMOS 0.35 µm SiGe technology from AMI Semiconductor.

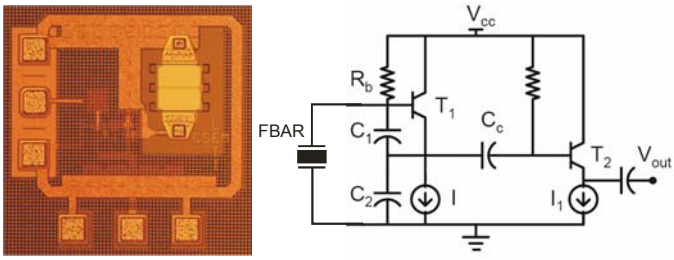

Fig. 6. Chip micrograph (640×650µm^2) and schematic of the oscillator

The active circuit and the ground line have intentionally been kept away from the resonator to prevent any possible coupling with the FBAR. However, it is certainly possible to reduce further the silicon area of the oscillator, by placing the FBAR over the active elements. In that case, a careful shielding of the sensitive part would be needed.

The output power of the oscillator is –8.4dBm for a total current consumption of 4.7mA at 2.7V, out of which 3mA are drawn by the buffer amplifier. Fig. 7. shows the output power spectrum of the circuit. A phase noise of –117.7dBc/Hz has been measured at 100kHz offset from the carrier.

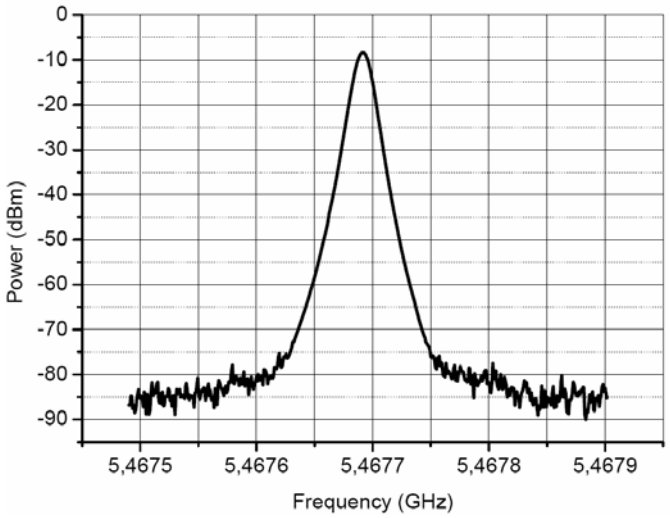

Fig. 7. Output power spectrum of Colpitts oscillator

Further information about FBAR Colpitts oscillators can be found in [12][13].

VI. CONCLUSION

FBAR processing is compatible with advanced BiCMOS technology, and hence enables the co-integration of RF high-Q passive and active devices on a single chip. Many circuit blocks such as LNAs or VCOs can take advantage from such a co-integration with high Q BAW devices. Performances can be further enhanced through the reduction of size, the limitation of interconnection parasitics, and the possibility to use the IC metal layers for shielding the BAW devices.

However, the complexity of the technology will certainly limit the fabrication yield in a production environment. Hence the validity of this above-IC approach is restricted to high-end applications, where RF performances outweight the cost issues.

ACKNOWLEDGMENT

This work was funded by the Swiss Office for Education and Science and the European Commission under Grant IST-2001-37362. Part of the processing has been realized at CMI-EPFL.

REFERENCES

[1] K. M. Lakin, "Thin Film Resonators and Filters," presented at IEEE Ultrasonics Symposium, Lake Tahoe, NV, 1999.

[2] R. Aigner, J. Kaitila, J. Ellä, L. Elbrecht, W. Nessler, M. Handtmann, T.-R. Herzog, and S. Marksteiner, "Bulk-Acoustic-Wave Filters: Performance Optimization and Volume Manufacturing," presented at IEEE IMS, Philadelphia, PA, 2003.

[3] R. C. Ruby, P. Bradley, J. Larson, Y. Oshmyansky, and D. Figueredo, "Ultra-Miniature High-Q Filters and Duplexers Using FBAR Technology," presented at IEEE International Solid-State Circuits Conference, San Francisco, CA, 2001.

[4] L. Elbrecht, R. Aigner, C.-I. Lin, and H.-J. Timme, "Integration of Bulk Acoustic Wave Filters: Concepts and Trends," presented at IEEE MTT-S, Fort Worth, TX, 2004.
[5] M.-A. Dubois, J.-F. Carpentier, P. Vincent, Ch. Billard, G. Parat, C. Muller, P. Ancey, P. Conti, “Monolithic above-IC resonator technology for integrated architectures in mobile and wireless communication”, *IEEE Journal of Solid State Circuits*, vol. 41, pp. 7-16, 2006.
[6] R. Lanz, C. Lambert. E. Kuegler, L. Gabathuler, L. Senn and K. Onuki, "Properties of Sputter deposited AlN, Mo, W and SiO_2 Thin-Films for Bulk-Acoustic-Wave Applications on 200mm Si Substrates", Proc. of 8th Int. Symposium on Sputtering and Plasma Processes (ISSP 2005), June 2005, Kanazawa, Japan.
[7] M.-A. Dubois and P. Muralt, "Stress and piezoelectric properties of aluminium nitride thin films deposited on metal electrodes by pulsed direct current reactive sputtering," *J. of Appl. Phys.*, vol. 89, pp. 6389-6395, 2001.
[8] H. P. Loebl, M. Klee, C. Metzmacher, W. Brand, R. Milsom, and P. Lok, "Piezoelectric thin AlN films for bulk acoustic wave (BAW) resonators," *Materials Chemistry and Physics*, vol. 79, pp. 143-146, 2003.
[9] K. B. Östman, S. T. Sipilä, I. S. Uzunov, and N. T. Tchamov, “Novel VCO Architecture Using Series Above-IC FBAR and Parallel LC Resonance”, *IEEE Journal of Solid State Circuits*, vol. 41, pp. 2248-2256, 2006.
[10] Y. H. Chee, A. M. Niknejad, and J. Rabaey, “A sub-100 _W 1.9-GHz CMOS oscillator using FBAR resonator,” in *IEEE RFIC Symp. Dig. Papers*, 2005, pp. 123–126.
[11] A. P. S. Khanna, E. Gane, and T. Chong, “A 2 GHz voltage tunable FBAR oscillator,” IEEE MTT-S Dig., pp. 717–720, 2003.
[12] M. Aissi, E. Tournier, M.-A. Dubois, G. Parat, and R. Plana, “A 5.4GHz 0.35µm BiCMOS FBAR resonator oscillator in above-IC technology,” presented at IEEE International Solid-State Circuits Conference, San Francisco, CA, 2006.
[13] M. Aissi, E. Tournier, M.-A. Dubois, Ch. Billard, H. Ziad, and R. Plana, “A 5 GHz above-IC FBAR Low Phase Noise Balanced Oscillator”, presented at IEEE RFIC Symposium, San Francisco, CA, 2006.

High-Q Thin Film Bulk Acoustic Wave Resonator and Tunable MEMS Capacitor using Highly Oriented Aluminum Electrode

T. Kawakubo[1)], K. Itaya[2)] and R. Ohara[2)]

1) Toshiba Research Consulting Corporation,

2) Corporate Research & Development Center, Toshiba Corporation

***Abstract* — RF MEMS devices, such as FBARs, variable capacitors and switches, are indispensable in the reconfigurable RF front-end for multi-mode multi-band mobilephone systems. High quality aluminum nitride piezoelectric films must play a key role in the high-Q FBARs, as well as the piezoelectrically actuated variable capacitors and switches in low voltage operation.**

In this paper, high-Q FBARs and variable capacitors with high capacitance ratios using AlN piezoelectric films and Al electrodes are presented. An amorphous metal underlayer enables fabrication of highly <111>-oriented Al thin films with XRD rocking curve FWHM of 0.6°. Using these high quality Al films, we have obtained highly c-axis oriented AlN films. These AlN films showed excellent crystallinity even at the initial stages of the AlN film deposition.

The fabricated resonators showed good resonance characteristics, such as high-Q values (loaded-Q ~800) and high effective coupling constants (~6.7%). The variable capacitor showed the highest tuning ratio of 10 at a low operation voltage of 5.5 V. The tunable built-in antenna in the UHF range is also examined.

I. INTRODUCTION

Recently, the requirements for RF circuits have made it difficult to develop RF devices. In particular, for multi-mode, multi-band mobile phone terminals, it is necessary to decrease the number of components and miniaturize the device size without compromising performance. To satisfy these requirements, new technologies are desired.

The reconfigurable RF front-end must be one of the best solutions for the requirements. The RF front-end should contain high-quality resonators, variable capacitors and switches and is preferably integrated on RF chip with CMOS-compatible materials and processes.

FBAR (Film Bulk Acoustic wave Resonator) technology [1-2] enable realization of high-frequency, low- loss RF filters manufactured by means of LSI-compatible processes.

In regard to designing and fabricating FBARs, there are several key issues. The first key issue is the selection of piezoelectric materials. Although several piezoelectric materials have been investigated for FBARs, AlN and ZnO are the only ones which can be manufactured. From the viewpoint of compatibility with LSI processes, AlN is the best choice.

Second, we have to decide the bottom electrode material. In this selection, we have to take into account three points: 1) acoustical properties, 2) electrical properties, and 3) crystallinity. This selection is the most important because the bottom electrode is the base for all FBAR structures[3].

From the acoustic viewpoint, the electrode should be a heavy, stiff material, such as Mo, W or Ru[4]. This is because materials with large mass density enhance effective coupling constant (k_{eff}^2) and stiff materials improve Q-values.

To achieve high Qr values, the resistivity must be low. The resistivity of thin films is often higher than that of the ideal value, in the case of materials with high melting points. Therefore, Cu and Al are highly advantageous in terms of their electrical properties.

The crystallinity and crystal structure of the bottom electrode are the most important considerations because the crystallinity of the AlN films strongly depends on both that of the bottom electrode. In general, as the melting point increases, more energy is needed to fabricate highly oriented films. This tendency supports the view that low melting point materials are a good choice for improving the crystallinity. Based on these discussions, we have chosen Al as the bottom electrode material.

The next item is the variable capacitors. Much research is being performed to develop RF MEMS tunable capacitors. Most researches have focused on the electrostatic types, which are free from restrictions of materials and processes, but operate at very high voltages of over 20 V [5]. Moreover, the “pull-in” phenomena limit the continuous tuning range to below 50 %. Other types of RF MEMS actuation

mechanisms, such as electro-thermal or electromagnetic drives have also been developed, but have the serious drawback of large power consumption.

Piezoelectric actuation is a promising mechanism for realizing RF MEMS tunable capacitors with a low operation voltage and a wide tuning range [6]. We proposed a piezoelectric actuator using AlN piezoelectric layers and Al electrodes, which uses fundamentally same process with the FBARs stated above, and demonstrated that a continuous tuning ratio of more than 3 is possible with an operation voltage of 3-5 V and high Q-factors [7,8].

These capacitors were applied to wideband built-in tunable antennas for digital terrestrial broadcasting as an example of reconfigurable RF systems.

II. Fabrication Method

There are the various fabrication methods for highly oriented Al(111) films. The first method utilizes the Si(111) substrate. Although epitaxial Al(111) films can be obtained by using this method, it has a big problem in that the interface between Si and Al is very thermally unstable. The second method uses the polycrystal Ti/TiN seed layer. Although this structure is thermally stable, it needs a thick seed layer to improve the crystallinity of Al(111) films. The third method utilizes the amorphous underlayer and this is the most suitable method for FBARs and piezoelectric actuators because the thin amorphous layer is sufficient to achieve highly oriented Al films. This technique was developed more than 10 years ago and first applied to aluminum interconnection in LSIs.

This underlayer must not only be amorphous, but have a large surface energy. When Al deposits on it, 2D layer-growth of Al films occurs due to the high surface energy of the underlayer. This continuous layer is thought to have the most stable (111) closely-packed configuration for fcc metals. Furthermore, an amorphous substrate enhances this tendency, because it has no specific crystal structure to prevent formation of Al(111) 2D island. Using this technique, we have obtained highly <111>-oriented Al films with XRD rocking curve FWHM of 0.6 degrees as shown in Figure 1.

Figure 2 shows the relationship between AlN thickness and the XRD rocking curve FWHM of AlN(0001). During deposition, we did not use a heater. The FWHM of 50nm AlN film is 1.1 degrees and the crystallinity improves slightly with an increase of thickness. This result indicates that AlN films are highly oriented even at the initial stage of deposition. Therefore, these AlN films are suitable for high -frequency applications.

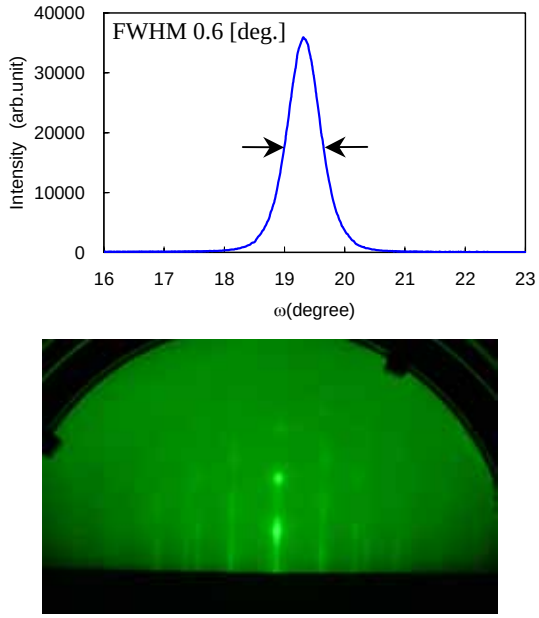

Figure 1 Al(111) XRD rocking curve and RHEED pattern of Al films formed on amorphous under layer.

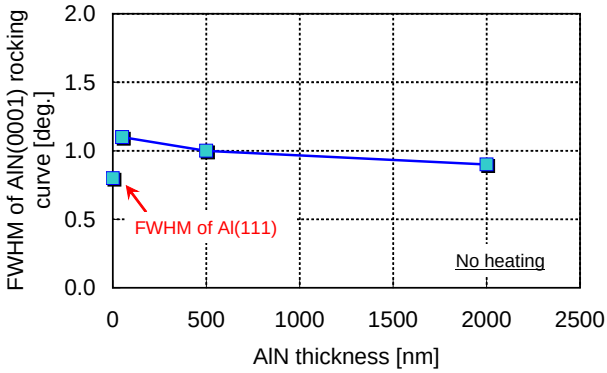

Figure 2 Relationship between AlN thickness and the XRD rocking curve FWHM of AlN(0001)

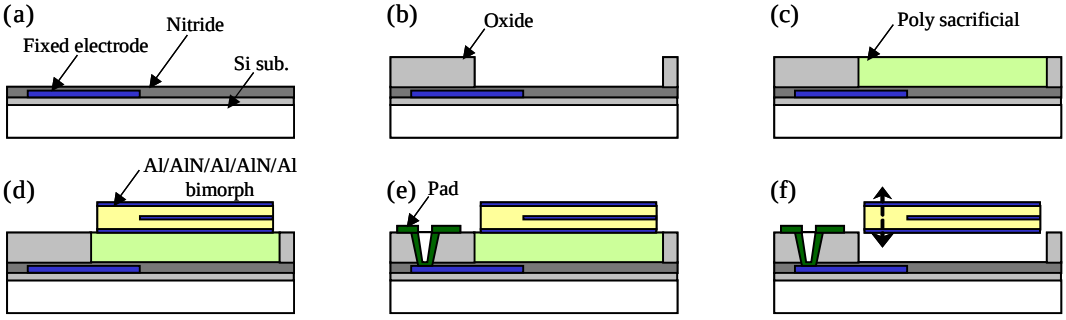

Figure 3 Process sequence of RF MEMS tunable capacitor

Figure 3 shows a schematic fabrication sequence of the tunable capacitors. 8-inch Si wafers having normal and high resistivity, or quartz wafers were used for the experiment. First, a fixed electrode was deposited and patterned, then buried by silicon nitride and oxide layers. Next, a thick TEOS layer was formed and patterned, and a poly-Si sacrificial layer was filled and flattened by CMP (Chemical-Mechanical Polishing). A piezoelectric bimorph was stacked on the flattened surface. Contact holes were opened and contact pads were formed. Finally a poly-Si sacrificial layer was selectively etched using a XeF_2 etching gas.

III. Development of FBAR

Since Al has a large temperature coefficient of elastic constant (-320ppm/°C) and also large acoustic attenuation[9] the FBAR characteristics are likely to degrade. We estimated the influence of Al electrode based on 1-dimensional Mason equivalent circuit. As a result, the acoustic-Q of over 2000 and temperature coefficient of frequency (TCF) of about -27 ppm/°C were obtained. These values differ little from those of conventional FBARs[10].

These results can be understood in terms of the strain energy distribution shown in Figure 4. The Nowotony-Benes[11] model was used for the calculation. The strain energy concentrates on Al electrode because acoustic impedance of Al is smaller than that of AlN. However, the percentage of strain energy in Al electrode is only 3.1%. This is why the adverse influence of Al electrode is limited.

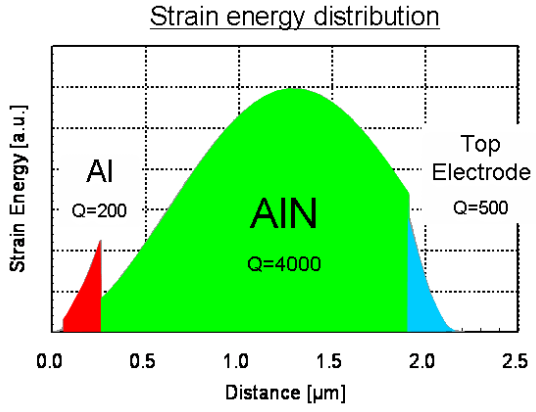

Figure 4 Strain energy distribution with Al bottom electrode.

The MBVD model is used to fit the measured resonant characteristics[12]. Figure 5 shows the calculation method of Q-values from the measured data. The diameter of the impedance circle corresponds to Qa and the diameter of the admittance circle related to Qr. The advantage of this method is its insensitivity to spurious responses.

Both figure of merit (FOM) and impedance ratio (Za/Zr) are used as the indices of overall performance of the FBARs. Equation(1) represents the relationship between the impedance ratio and the figure of merit. If Qa is not equal to Qr, Q is defined as a geometrical mean of Qa and Qr.

$$\frac{Z_a}{Z_r} \cong \left(\frac{8}{\pi^2} \cdot k_{eff}^2 Q \right)^2 = 0.657 \times \left(k_{eff}^2 Q \right)^2 \cdots\cdots (1)$$

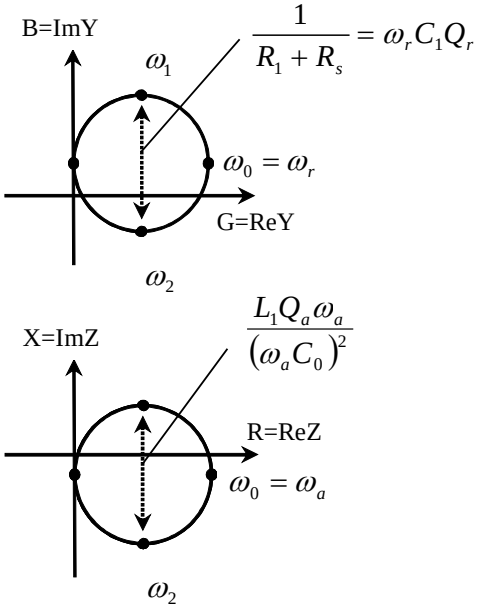

Figure 5 The calculation method of Q-values from the measured data.

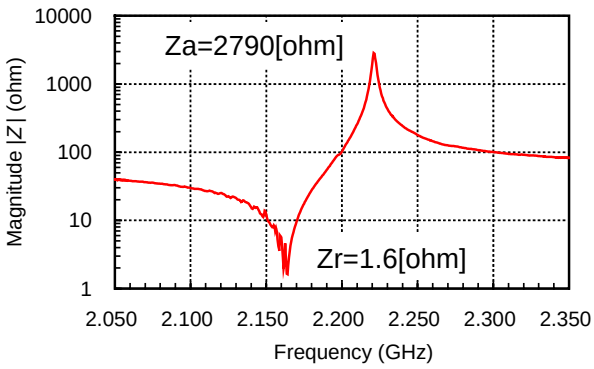

k^2_{eff}=6.2%
Qr=815
Qa=810

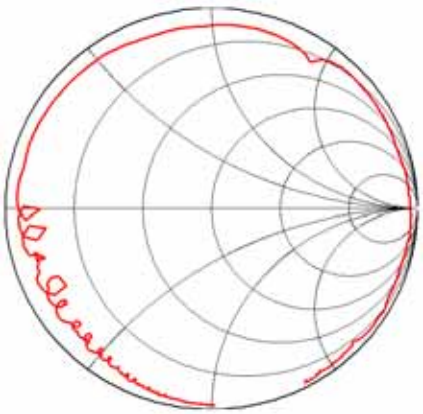

Figure 6 Impedance characteristics and Smith Chart of the measured data.

The measurement data is shown in Figure 6 and Figure 7. These figures represent two typical characteristics of 1port FBARs with slightly different structures. Please note that these results include all parasitic effects.

Figure 6 shows that the effective coupling is 6.2% and both Q values are over 800. The impedance ratio is over 1500 and this corresponds to figure of merit of 51. The extracted parameters of the MBVD model are: C0=1.2[pF], C1=0.067[pF], R1=0.67[Ω], L1=81[nH], Rs=0.87[Ω], and R0=0.48[Ω]. As expected, it is confirmed that there is no evidence of degradation due to aluminum electrode.

Figure 7 shows larger coupling constant of 6.7%, and smaller Q values. The extracted parameters of the MBV model are: C0=1.07[pF], C1=0.062[pF], R1=0.87[Ω], L1=86[nH], Rs=0.81[Ω], and R0=1.15[Ω]. In both cases, series resistances are slightly larger values than expected. This is due to structural problems and attempts to decrease the series resistance are under way.

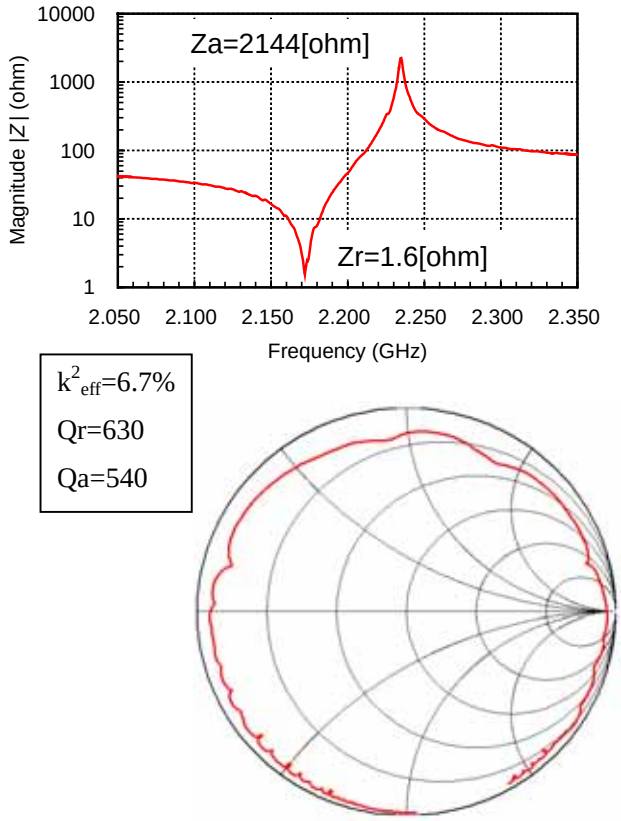

Figure 7 Impedance characteristics and Smith Chart of the FBAR with larger coupling constant.

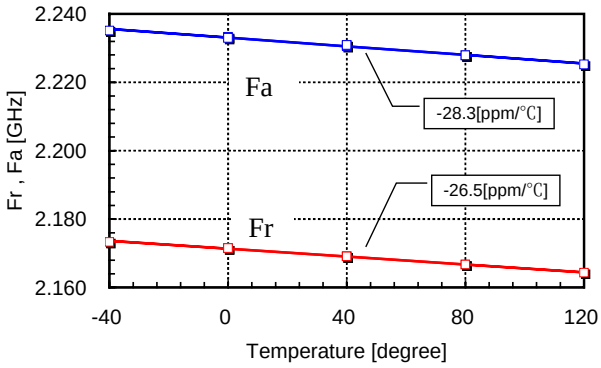

Figure 8 Temperature dependence of the resonance frequency (red line) and the anti-resonance frequency (blue line)

Figure 8 shows the temperature dependence of the resonance and anti-resonance frequency. TCFs of resonance and anti-resonance frequency are -26.5[ppm/°C] and -28.3[ppm/°C], respectively. These values are almost the same as the calculated values. Although the TCF of our FBAR is slightly larger than the reported value[10], however, this difference can be ignored.

The design of the stacked layer structure of FBARs significantly influences on the FBARs characteristics. The measured coupling constants and TCFs of FBARs are almost same as the calculated values using the 1-dimensional Mason equivalent circuit. On the other hand, Q-values can hardly estimate correctly. This is due to the energy radiation from the electrode edges. The Qa is also sensitive to the stacked layer structure, especially the bottom electrode thickness. The bottom electrode thickness also influences on the spurious responses.

IV. Development of Tunable Capacitor

The basic structure of a tunable capacitor with a piezoelectric bimorph actuator is shown in Fig.9. The electric voltage is applied between the intermediate electrode and the top/bottom electrodes. Within the two piezoelectric layers, the polarization direction is the same while the polarity of driving voltage is opposite. One piezoelectric layer expands while the other contracts. The net result is a bending deflection.

One of the most serious issues in the piezoelectric MEMS actuators is curling of the actuator beams due to residual stresses. Piezoelectric AlN actuators are composed of thin and long multiply stacked layers, tend to suffer from a large curling effect due to unbalanced residual stress in the stacked AlN layers.

Novel folded bimorph structures have been introduced to cancel the curling effect as shown schematically in Fig. 10. Using symmetrically

designed forward and backward beams can compensate the curling. Further, the piezoelectric actuation is doubled when reversed voltages are applied to the forward and backward bimorphs.

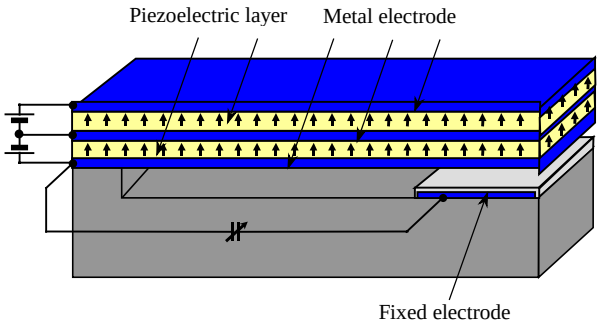

Figure 9 Basic structure of tunable capacitor with piezoelectric bimorph actuator.

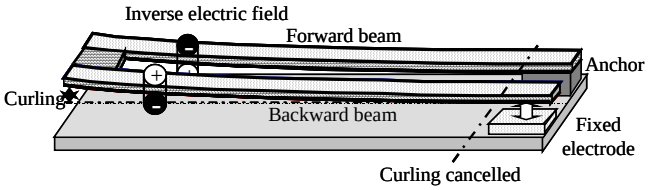

Figure 10 A schematic drawing of proposed folded structure piezoelectric tunable capacitor having forward and backward bimorph actuator beams.

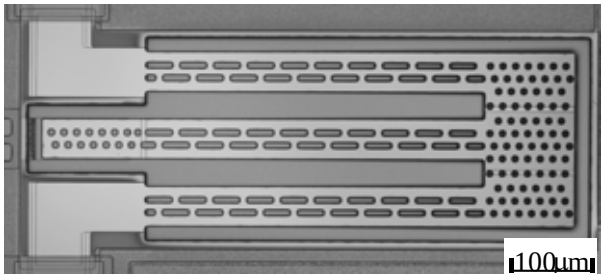

Figure 11 Laser microscope image of tunable capacitor, with singly clamped folded bimorph actuators.

An optical image of the RF MEMS tunable capacitor with a singly clamped folded bimorph actuator is shown in Fig. 11. Height measurements using laser microscopy revealed the curling at the actuation point was suppressed to less than a few microns while curling at the folding point reached a few tenth microns.

Smooth continuous capacitance changes were observed with a hyperbolic relation up to the contact point of the movable and fixed electrodes of the tunable capacitors. The lowest operation voltage of 2.5 V was obtained with a tuning ratio of 3, for the first time as shown in Fig. 12. The Q-factor of the tunable capacitor was less than 10 at 2 GHz because of a low-resistivity Si substrate.

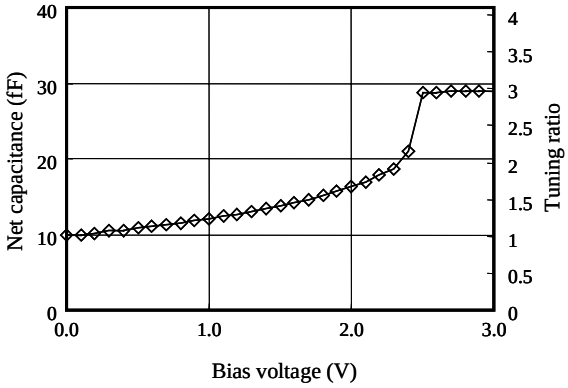

Figure 12 Measured net capacitance changes of the fabricated piezoelectric RF MEMS tunable shunt capacitor on normal resistivity Si substrate.

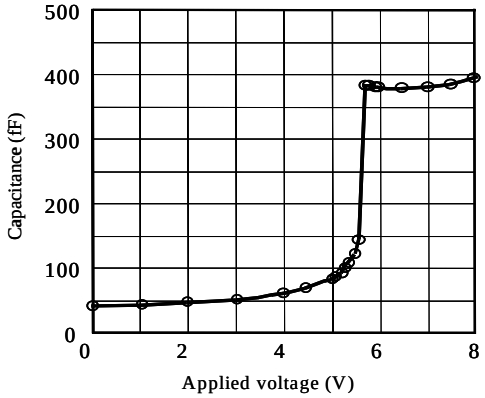

Figure 13 Capacitance changes of the piezoelectric RF MEMS tunable shunt capacitor on quartz substrate.

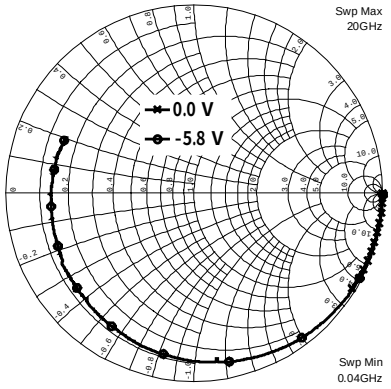

Figure 14 S_{11} of the piezoelectric RF MEMS tunable capacitor on quartz substrate.

To increase the Q-factor and decrease parasitic capacitance around signal pads, piezoelectric tunable capacitors were also made on insulating quartz substrates.

Figs. 13 and 14 show capacitance changes and the S_{11} plot of the capacitor. A very large capacitance change was observed from 40 to 385 fF at an operation voltage of 5.5 V, along with a minimum Q-factor of 40. The performance indicators, such as tuning ratio/operation voltage and Q show our results exceed these of previously published works.

V. Application for Tunable Antenna

Currently developed FBARs and tunable capacitors will likely be key components in the reconfigurable RF front-ends, such as tunable antennas, filter banks or tunable filters, tunable impedance machers, and wide range VCOs as shown in Fig.15.

One of the largest advantages of the MEMS tunable capacitors is their very high IIP3 characteristic compared with varactor diodes. A wideband built-in tunable antenna for digital terrestrial broadcasting has been targeted for the first application. It is difficult to realize a built-in antenna because the system requires a wideband antenna in a UHF band and its frequency bandwidth gets narrower as the antenna's size is reduced.

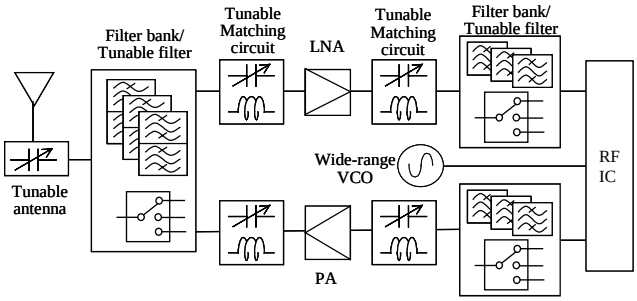

Figure 15 Reconfigurable RF front-end using RF MEMS devices.

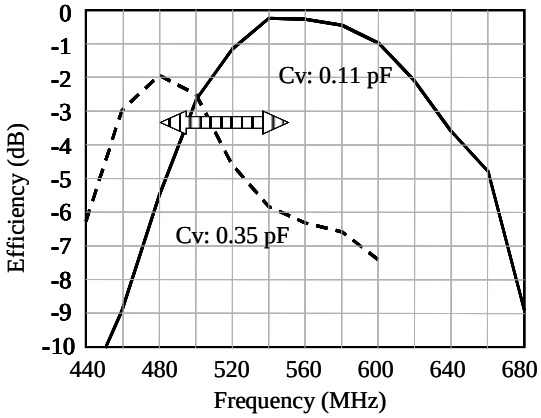

Figure 16 Efficiency of the tunable antenna using piezoelectric MEMS tunable capacitor.

The shape of the antenna element is a meander structure, and one point of the antenna connects to the PCB board through the tunable capacitor. Figure 16 shows efficiency of the tunable antenna. A wide tuning range from 450 to 650 MHz was realized at an efficiency of more than –5dB under a tuned capacitance from 0.11 to 0.35 pF.

VI. Conclusion

High-Q FBAR and RF MEMS tunable capacitor have been developed using the AlN piezoelectric layer and the Al electrodes.

As for FBAR, it is confirmed both theoretically and experimentally that the disadvantages of the Al electrode can be ignored because the strain energy in the Al electrode is very small. On the other hand, the advantages of the Al electrode are also confirmed, that is, the highly c-axis oriented AlN films are obtained by using high-quality Al films. These results indicate that aluminum is a promising electrode material for high-Q FBARs and low-loss filters.

A novel RF MEMS tunable capacitor with a folded beam piezoelectric bimorph actuator has been developed. Its continuous wide tuning ratio of more than 3 was realized at operation voltages of 3-5 V for the first time.

These piezoelectric RF MEMS devices are quite promising as key components for multi band/mode reconfigurable RF systems. Our process that uses CMOS compatible materials and temperatures makes it possible to easily adopt RF MEMS into RF CMOS processes.

References

[1] K. M. Lakin, "Thin Film Resonators and Filters", 1999 IEEE Ultrasonics Symposium, Proceedings, pp. 895-906

[2] J. D. Larson III, R. Ruby, P. Bradley, and Y. Oshymansky, and D. Figueredo, "A BAW antenna duplexer for the 1900MHz PCS band", 1999 IEEE Ultrasonics Symposium, Proceedings, pp. 887-890

[3] S. Mishin, D. R. Marx, and B. Sylvia, "Sputtered AlN thin films on Si and electrodes for MEMS resonators: relationship between surface quality microstructure and film properties", 2003 IEEE Ultrasonics Symposium, Proceedings, pp. 2028-2032

[4] T. Yokoyama, T. Nishihara, S. Taniguchi, M. Iwaki, Y. Satoh, M. Ueda, and T. Miyashita, "New electrode material for low-loss and high-Q FBAR filters", 2004 IEEE Ultrasonics Symposium, Proceedings, pp. 429-432.

[5] J. J. Yao, S. T. Park, and J. DeNatale, "High tuning-ratio MEMS-based tunable capacitors for RF

communication applications," in *Proc. Solid-State Sensors Actuator Workshop*, Hilton Head, SC, Jun. 1998, pp.124–127.

[6] J. Y. Park, Y. J. Yee, H. J. Nam, and J. U. Bu, "Micromachined RF MEMS tunable capacitors using piezoelectric actuators," in *IEEE Int. Microwave Symp. Dig.*, Phoenix, AZ, May 2001, pp. 2111–2114.

[7] T. Kawakubo, T. Nagano, M. Nishigaki, K. Abe, and K. Itaya, "Piezoelectric RF MEMS tunable capacitor with 3 V operation using CMOS compatible materials and process," in *Proc. IEEE Int. Electron Devices Meeting*, Dec. 2005, pp. 303–306.

[8] T. Nagano et al, T. Nagano, M. Nishigaki, K. Abe, K. Itaya, and *T. Kawakubo, "Fabrication and Performance of Piezoelectric MEMS Tunable Capacitors Constructed with AlN Bimorph Structure" *IEEE MTT-S Int. Microwave Symp. Digest*, 2006, pp.1285-1288.

[9] G. D. Mansfeld, S. G. Alekseev, and I. M. Kotelyansky, "Acoustic HBAR spectroscopy of metal (W, Ti, Mo, Al) thin films", 2001 IEEE Ultrasonics Symposium, Proceedings, pp. 415-418

[10] J. D. Larson III, and Y. Oshmyansky, "Measurement of Effective kt2, Q, Rp, Rs vs. Temperature for Mo/AlN FBAR Resonators", 2002 IEEE Ultrasonics Symposium, Proceedings, pp. 939-943

[11] H. Nowotny and E. Benes, "General one-dimensional treatment of the layered piezoelectric resonator with two electrodes", J. Acoust. Soc. Am. Vol.82, no.2 (1987) pp. 513-521

[12] J. D. Larson III, P. Bradley, S. Wartenberg, and R. Ruby, "Modified Butterworth-Van Dyke Circuit for FBAR Resonators and Automated Measurement System", 2000 IEEE Ultrasonics Symposium, Proceedings, pp. 863-868

[13] M. Nishio et al., *Shingakugiho* (2006) AP2005-170 **105** 600 (in Japanese).

Basic Deposition Process and Ferroelectric Properties of Stress Free Pb-based Ferroelectric Thin Films of Perovskite Structure

K. Wasa, I. Kanno, T. Mino, S. Kuwajima, K. Suzuki, and H. Kotera
Faculty of Mechanical Eng. , Kyoto Univ. Sakyouku Yoshida Honmachi, Kyoto, Japan

Abstract—Basic deposition process of stress free single crystal thin films of perovskite is described. The deposition process comprises sputtering deposition at epitaxial temperature followed by quenching in air. Based on the quenching process thin films of stress free single crystal $(PbMg_{1/3}Nb_{2/3}O_3)_{1-x}(PbTiO_3)_x$, PMNT were heteroepitaxially grown on (001)$SrTiO_3$ and (001)MgO substrates by rf-magnetron sputtering. The lattice parameters of the sputtered PMNT thin films were almost the same to the bulk values independent of the substrate lattice parameters. Planar thin film bulk acoustic wave resonator, FBAR, was fabricated for a measurement of electromechanical coupling k_t of PMNT thin films. The k_t near the morphotropic phase boundary, MPB, composition, x≅0.33, was found to be 45.2% at 1.3 GHz for the film thickness of 2.3μm. The k_t was almost the same values to the bulk single crystals.

INTRODUCTION

Thin films of Pb-based ferroelectric perovskite are essential for a production of piezoelectric devices, since the Pb-based ferroelectric perovskite exhibits the highest electromechanical coupling. The environmental pollution of lead component could be reduced by two orders in magnitude, if the Pb-based materials are used in a form of thin films [1]. To achieve bulk like high electromechanical coupling, thin films of single crystal perovskite are essential. The single crystal films are fabricated by heteroepitaxial growth process. The MgO and/or $SrTiO_3$ are widely used for the substrates. The heteroepitaxial films include the stress due to the lattice mismatch between thin films and substrates. The heteroepitaxial temperature is around 500 to 600°C. The thermal stress is also induced during the cooling stage after the deposition due to the differences in a thermal expansion coefficient between thin films and substrates. The electromechanical coupling of heteroepitaxial perovskite thin films is lower than bulk values due to the epitaxial stress [2]. Reduction of stress in the heteroepitaxial films is essential for the achievement of bulk like high electromechanical coupling. .

Recently we have found quenching after the deposition in the heteroepitaxial growth reduces the epitaxial stress and achieves the fabrication of stress free single single crystal thin films of Pb-based ferroelectric perovskite PMNT [3]. This paper describes the basic sputtering deposition process and the structure and ferroelectric properties of the stress free single crystal PMNT thin films.

BASIC SPUTTERING PROCESS

The solid solution of relaxor ferroelectric $Pb(Mg_{1/3}Nb_{2/3})O_3$ (PMN) and normal ferroelectric $PbTiO_3$ (PT), PMNT, exhibits an exceptionally high coefficient of electromechanical coupling [4]. The PMNT shows a morphotropic phase boundary (MPB) at x≅0.33 for bulk single crystals. Several deposition processes are reported including a sputtering [5], MOCVD [6], PLD [7], and sol-gel method [8]. These PMNT thin films often include isometric compound of pyrochlore, $Pb_2(Mg,Nb)_2O_7$ type and comprise grains and/or interfacial dislocated layers. The structure looks like polycrystalline ceramics and their density is not high. Heteroepitaxial growth was applied for the deposition of single crystal PMNT thin films. These heteroepitaxial films frequently include grains and/or dislocated interfacial layer to reduce the lattice mismatch strain. Their micro-structure is different from bulk single crystal. Among these deposition processes the sputtering is one of a promising process for the deposition of the bulk like single crystal thin films, since the high energetic sputtered adatoms enhance the growth of high density single crystal thin films [9].

A planar rf-magnetron sputtering was used for the heteroepitaxial growth. The PMNT thin films were directly sputtered from PMNT powder target on (001)$SrTiO_3$ and/or (001)MgO single crystal substrates. The powder target was composed of the mixture of PT, PbO, MgO, Nb_2O_5, and TiO_2. The key growth conditions of single crystal PMNT thin films are: (1) stoichiometric composition of thin films, (2) substrate temperature > epitaxial temperature, (3) substrate temperature < re-evaporation temperature of Pb. The chemical composition of the sputtered thin films was easily changed by the composition of the mixed powder. The epitaxial temperature was 500~600°C. According to the key growth condition, the substrate temperature should be higher than the epitaxial temperature. However, the substrate temperature should be lower than the Pb re-evaporation temperature of about 600°C. The higher temperature enhances the growth of Pb-reduced structure, $Pb(Mg_{1/3},Nb_{2/3})_3O_7$. Typical sputtering conditions are shown in Table 1. The optimum growth temperatures showed a narrow window of 500 to 550°C. The sputtered

thin films were quenched after the deposition in air in order to reduce the re-evaporation of lead and/or to suppress the growth of the pyrochlore phase during cooling down stage.

Table 1. Sputtering conditions

Target*[1]	mixed powder: PbO, MgO, Nb_2O_5, PT
Substrates*[2]	La-0.75wt% doped(001)ST, (001)MgO
Buffer layer	(110)SRO, (001)PLT
Sputtering gas	0.5 Pa (Ar/O_2=20/1)
Growth temp	500-600°C
Growth rate	5-15 nm/min
Film thickness	20-8000 nm
Quenching rate	100°C/min. in air

*[1] Typical composition: stoichiometric + 10%PbO
*[2] Conductive base electrode: (001)Pt for (001)MgO

STRUCTURE AND FERROELECTRIC PROPERTY

Figure 1 shows typical XRD patterns of the sputtered 0.67PMN-0.33PT (PMN-33PT) thin films on the (001) MgO substrate. The XRD Θ-2Θ pattern showed the sputtered film was highly (001) orientation (Fig.1a). The pole figure of the (110) direction showed a strong four-fold intensity describing 3-dimensional epitaxy (Fig.1b). The similar epitaxial properties were also observed for the different substrates.

The lattice parameters of the sputtered PMNT thin films for different substrates are shown in Table 2. It is noted the lattice parameters of the PMNT thin films are almost the same to the bulk lattice values independent of the substrate lattice parameters. The sputtered PMNT thin films are almost relaxed and show stress free structure.

Table 2. Lattice parameters of sputtered PMNT thin films for different substrates.

	a-lattice (nm)	c-lattice (nm)
Bulk PMN	0.405	0. 405
Thin Films		
(001)MgO	0.405	0.406
(001)Pt/(001)MgO	0.405	0.406
(001)$SrTiO_3$	0.405	0.406
Substrates		
MgO	0.420	0.420
$SrTiO_3$	0.3905	0.3905

The cross-sectional SEM and TEM images show that the sputtered PMNT thin films exhibit continuous single crystal-like structure without grains and/or interfacial dislocated layer between the PMNT thin films and the substrates as seen in Fig.2. These structural analyses describe the sputtered PMNT thin films comprise bulk like single crystal structure without stress.

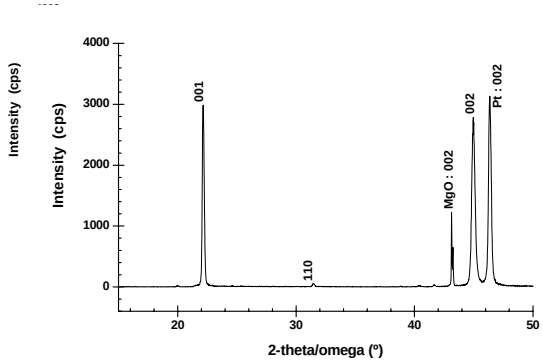

(a)

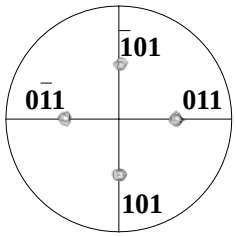

(b)

Figure1. Typical XRD patterns of the sputtered PMN-33PT thin films on (001)MgO substrates (film thickness: 2.3μm).

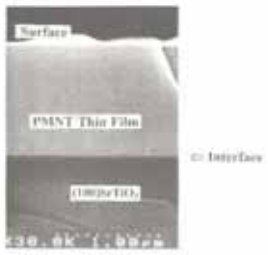

(a)

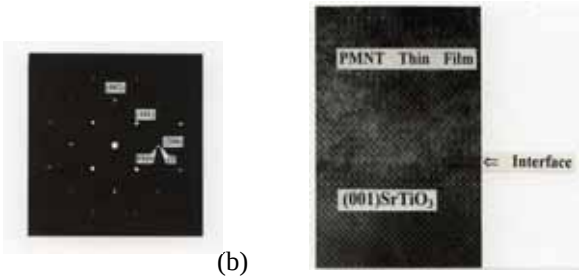

(b)

Figure 2. Cross-sectional SEM and TEM images of (001)PMNT thin films on (001)ST: (a) SEM image(film thickness: 1170nm), (b) TEM lattice image with SAD patterns at interface (film thickness:300nm).

The TEM images suggested the point defects were present at the interface between the thin films and the substrates. However, the dislocated interfacial layer could not be observed [10].

When the film thickness of heteroepitaxial PMNT thin films exceed a critical values, typically 2 to 3 μm, a small high angle grain grow from the interface between the film and the substrates probably for a reduction of the stress accumulated in the films. The typical SEM image of the grain is shown in Fig.3a. The growth of the grains could be suppressed in a multi-layered structure shown in Fig.3b. The layered structure is fabricated as follows: (1), a 1st layer of around 1μm thick, i.e. below the critical thickness, is deposited at 550°C and the film is quenched to room temperature in air. (2), after several hours later of the 1st deposition, 2nd layer of PMNT of around 1μm thick is deposited on the 1st layer. It is interested the growth of the high angle grains is suppressed in the layered structure. The stress will be relaxed at the interface between the layers. The multi-layered PMNT thin films exhibit stress free single crystal structure. We have confirmed the single crystal PMNT thin films of 8μm in thickness fabricated in the multi-layer structure. The multilayered epitaxial process is available for a deposition of single domain /single crystal thick films of smooth surface without the growth of grain.

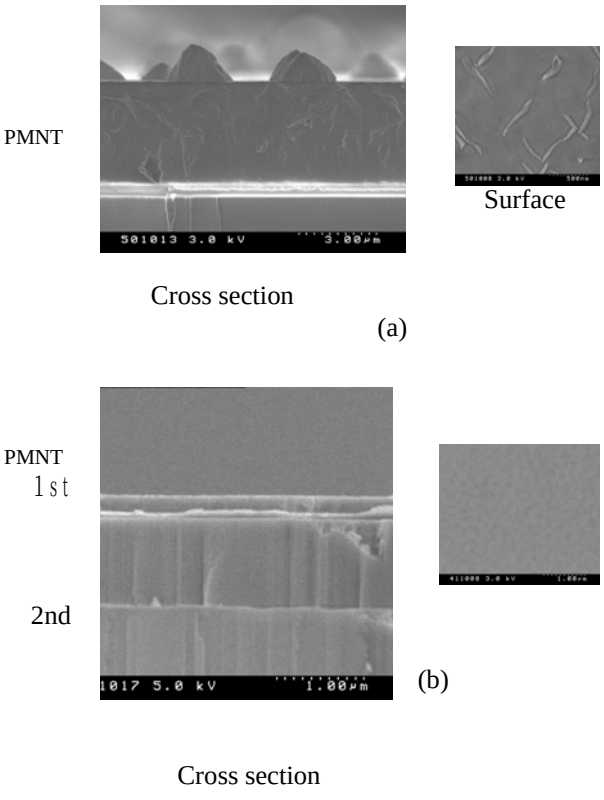

Figure 3. Cross section and top surface SEM images of PMNT single layer, Fig.3a, PMNT multi-layer, Fig.3b.

Dielectric properties of PMNT thin films were evaluated in the Pt/PMNT/(110)SRO/(001)Pt(001)MgO heterostructure. Typical P-E curves are shown in Fig.4. The Pr increases with the addition of PT into PMN similar to the bulk materials. Electromechanical coupling k_t was measured by a resonance spectrum method [11].

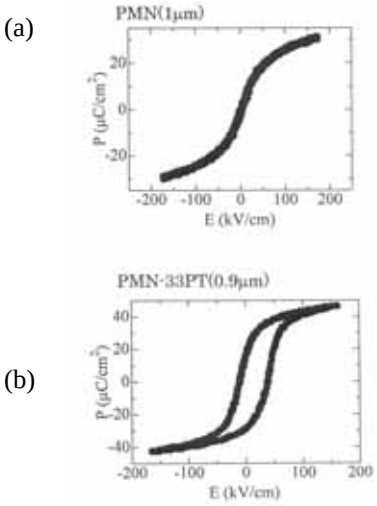

Figure 4. Typical P-E curves for PMNT thin films on (001)MgO substrates: (a) PMN thin films, (b) PMN-33PT thin films.

Planar PMNT thin film BAW resonator was fabricated for the measurement of the resonant spectrum [12]. Typical resonant spectrum for the PMN-33PT thin films of 2.3μm in film thickness is shown in Fig.5. The resonant frequency was observed at about 1.3 GHz indicating the longitudinal phase velocity of 5500 to

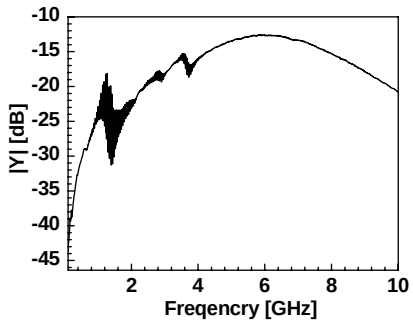

Figure 5. Typical resonant properties of PMN-33PT thin film planar BAW resonator.

6000m/s. The multi-reflection mode superposed on the main spectrum was caused by the acoustic multi-reflection of a longitudinal standing wave excited in the MgO substrate. The electromechanical coupling k_t evaluated by the Mason's equivalent circuit was about 45% at the resonant frequency of 1.3GHz with ε_{33}^{s} =500, Q_{ms}=2000, Q_{mp}=20, where Q_{ms} and Q_{mp} are mechanical Q values of the MgO substrate and PMNT thin films, respectively.

DISCUSSIONS

It is known to sinter pyrochlore free bulk PMN, magnesium and niobium oxides are first to form the columbite $MgNb_2O_6$ and then followed by a reaction with lead oxide [13]. The present sputtering process achieves the direct synthesis of the perovskite without the prereaction process. It is described sputtering deposition at epitaxial temperature followed by quenching after the epitaxial growth achieves the growth of c-axis single crystal PMNT thin films of bulk like high density structure independent of the lattice parameters of substrate crystal. The multi-layered structure provides stress reduced and/or stress free single crystal PMNT thin films without interfacial layer. The film surface was smooth without visible crystallites. The structural properties are different from the structure of PMNT thin films provide by a conventional deposition process. The bulk PMN shows cubic structure at room temperature. The structure of PMN thin films shown in Table 2 is almost the same to the bulk PMN except a small enlargement of c-axis. The bulk PMN-33PT shows rhombohedral and/or mixture of rhombohedral and tetragonal structure [14]. The lattice parameters of the present PMN-33PT thin films are shown in Table 3.

Table 3. Lattice parameters of PMN-33PT thin films on (001)MgO(2.3 μm in thickness).

	Thin Films	Bulk PMN-33PT[13]	
	PMN-33PT	Rhomb.	Tetra.
a	0.4012 nm	0.4024nm	0.4018nm
b	0.4018	0.4017	0.4018
c	0.4049	0.40178	0.4041
α	90.003°	89.910°	
β	89.799°		
γ	90.024°		

The lattice parameters indicate the possible structure of nm, c=0.405nm, $\alpha = \beta = \gamma = 90^o$ and/or monoclinic structure, i.e. $\beta = \gamma = 0$. It is reasonably considered the in-plane structure of heteroepitaxial films is governed by the substrate surface structure. If the structure of substrate crystal is cubic, $\beta = \gamma = 90^o$ for the epitaxial films, even if the bulk structure is rhombohedral. If the epitaxial films on cubic substrates show the rhombohedral structure, the epitaxial films surely include interfacial dislocated layer. So, it is reasonably understood present quenched PMN-33PT thin films do not show rhombohedral structure but tetragonal and/or monoclinic structure, i.e. $\beta = \gamma = 90^o$. The fact the quenched epitaxial PMNT thin films on different substrates show the same in-plane lattice close to bulk lattice parameters is considered as following growing process of the heteroepitaxial PMNT thin films. The crystal structure of the PMNT thin films during growing stage will be c-axis oriented tetragonal form, since the c-plane is the densest package plane. At the growing stage the film structure is not tightly governed by the substrate lattice. Their lattice spacing is almost the same to their bulk lattice values regardless to the substrate lattice spacing. The quenching surely freezes the crystal structure of the growing stage. The polar axis of the PMNT is c-axis. The high electromechanical coupling will be observed for the quenched PMNT thin films, although the crystal structure of the PMNT thin films is modified from bulk rhombohedral structure.

These expectations have been confirmed by the measurements of electromechanical coupling at PMNT thin film planar bulk acoustic wave resonator FBAR. The electromechanical coupling of the PMNT thin films was 45% at 1.3 GHz. The value is almost the same to the bulk value, i.e. 47% for rhombohedral structure [15]. Slow cooling after the film growth is conventionally used for the epitaxial growth. The crystal structure and the lattice parameters are fully controlled by the substrate lattice structure during the slow cooling stage [16]. The present quenching has prohibited the growth of the conventional epitaxial mode. The high electromechanical coupling of the present PMNT thin films has been confirmed by the measurement of piezoelectric constant of d and/or e values. The e_{31} values were measured by a deflection of cantilever [17]. The cantilever comprised MgO beam deposited PMNT thin films of 2 to 3μm in film thickness. The thickness of MgO was 0.3mm with 2 mm width. Base electrode and top electrode were sputtered Pt films. It was found the deflection of cantilever beam was 1 to 5μm at 10V for 7mm in beam length, which corresponded e_{31}=- 5 to -8(C/m^2). These values are same order or higher than bulk PZT ceramics bimorph cantilever [18].

The higher coupling thin films and/or higher Q thin films will be achieved by a selection of chemical composition of the piezoelectric films. Complex

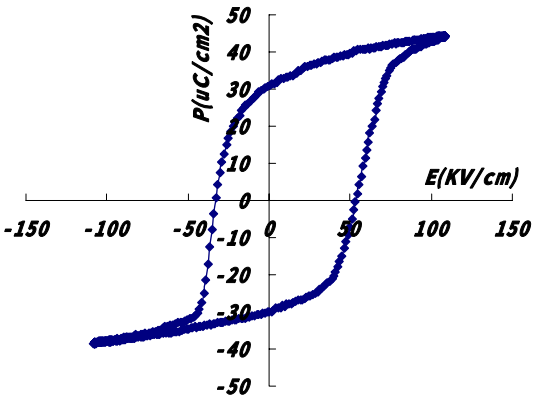

Figure 6 P-E hysteresis curve of Sr-doped PMN-PT-PZ thin films on SRO/Pt/(001)MgO. (film thickness: 1.9um).

composition with small additive is used for the bulk ceramics piezoelectric materials. The present sputtering process easily achieves the complex composition using powder target. Figure 6 shows an example of ferroelectric properties of complex compound PMN-PT-PZ with addition of Sr [19].

Excellent ferroelectric P-E curves with large Pr was observed. In the bulk materials the addition of Sr increases the dielectric constant. The present sputtered PMN-PT-PZ films also show the increase of dielectric constant with the addition of Sr. The selection of chemical composition with variety of small additive will achieve the well-designed ferroelectric thin films including dielectric properties, piezoelectric properties, and mechanical properties for the fabrication piezoelectric thin film devices. For the

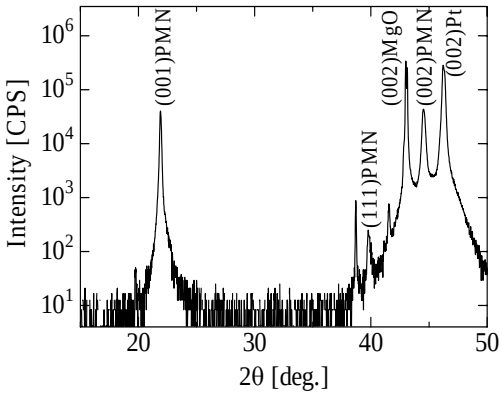

Figure 7. Typical XRD pattern of quenched thin PMN-33PT thin films (film thickness: 300nm).

fabrication of FBAR of GHz operation the thickness of the piezoelectric thin films is smaller than 1μm. Absence of interfacial dislocated layer is essential.

Figure 7 shows the XRD pattern of quenched PMNT thin films of thickness below 1 μm. It is seen sharp (001)PMNT peak is observed. This suggests the present quenching process provides high quality thin PMNT films and the process is one of a candidate for the fabrication of FBARF of high coupling and/or high Q perovskite materials.

CONCLUSION

Sputtering deposition followed by quenching provided stress free/ single c-domain /single crystal thin films of PMNT. The lattice parameters of the quenched sputtered films are almost the same to the bulk values independent of substrate materials. The electromechanical coupling k_t of the PMNT thin films near the MPB composition was 45% which was almost the same to the bulk single crystal value 47%. The selection of cathode target materials provides wide variety thin films with designed composition. The multi-layered structure is also useful for a fabrication of thick films of flat surface single crystal perovskite.

ACKNOWLEDGEMENTS

The authors thank Prof. K. Nakamura (Tohoku Univ.), Dr. H. Adachi, and T. Matsunaga (Matsushita Elec. Ind.) for their measurements and analyses of planar resonator and XRD , respectively with their useful discussions.

REFERENCES

[1] K. Wasa, “Materials engineering for a better global environment”, Bulletin of Materials Science, India, vol.18,p.937-953,1995.

[2] V. Nagarajan,C.S. Ganpule, B. K. Nagaraj, S. Aggarwai, S. P. Alpay, A.L. Roytburd, E.D. Williams, and R. Ramesh, “Effect of mechanical constraint on the dielectric and piezoelectric behavior of epitaxial $Pb(Mg_{1/3}Nb_{2/3})O_3$(90%) -$PbTiO_3$(10%)”, Appl. Phys. Lett.,vol.75, pp.4183 -4185 , 1999 .

[3] K. Wasa, I. Kanno, and T. Suzuki, “Structure and Electromechanical Properties of Quenched PMN-PT Single Crystal thin Films”,Advances in Science and Technology, vol.45, pp.1212-1217, 2006.

[4] K.Uchino, “High electromechanical coupling piezoelectrics: relaxor and normal ferroelectric solid solutions”, Solid state Ionics, vol.108, p.43-52, 1998.

[5] M.C. Jang and T.B.Wu, “ The effect of electrode composition on rf magnetron sputtering deposition of Pb [$Mg_{1/3}Nb_{2/3}$] 0.7-Ti0.3O_3, J. Mater. Res., vol.9, pp.1879 -1885,1994.

[6] Y. Takaeshima, K. Shiratsuyu, H. Takagi, and K. Tomono, “Preparation of Lead Magnesium Niobate Titanate Thin Films by Chemical Vapor Deposition”, Jpn. J. Appl. Phys., vol.34, Part 1, No.9B, p.5083-5085, 1995.

[7] C. Tantigate, J. Lee, and A. Safari, “ Processing and properties of Pb $(Mg_{1/3}Nb_{2/3})O_3$-$PbTiO_3$ thin films by pulsed laser deposition”, Appl. Phys. Lett., vol.66, p.1611-1613,1995.

[8] N. Wakiya, J. Shiihara, K. Shinozaki, and N. Mizutani, “Raman Spectroscopic Determination of Pyrochlore-Type Compound on the Synthesis and Decomposition of Sol-Gel-Drived $Pb(Mg_{1/3}Nb_{2/3})O_3$ (PMN)”, J. Sold State Chem., vol.142, pp.344-338 ,1999.

[9] K. Wasa, M. Kitabatake, and H. Adachi, “Thin Film Materials Technology”, Springer, William Andrew Pub., New York(2004) P.71.

[10] Seon Hee Seo, PhD Thesis, Kwangju Institute of Science and Technology, 2004, p.109.

[11] S. Ito, K. Nakamura, and K. Ishikawa, “Piezoelectric Properties of BaTiO3 Thin Films grown by ECR-PLD”, Proceeding of 2005 IEEE International Ultrasonic Symposium (Rotterdam, 2005) P1L-7.

[12] K. Wasa, K. Nakamura,T. Matsunaga, I. Kanno, T. Suzuki, H. Okino, T. Yamamoto, S.H. Seo, and D. y. Noh, “Electromechanical coupling factors of single domain $0.67Pb(Mg_{1/3}Nb_{2/3})_3$-$0.33PbTiO_3$ single crystal thin films”, Appl. Phys. Lett.,vol.88, p.122903-1-122903-3,2006.

[13] S.L.Swartz, T.R. Shrout, W.A. Schulze, and L.E. Cross, “Dielectric Properties of Lead-Magnesium Niobate Ceramics”, J.Am, Ceram. Soc., vol.67, p311-315, 1984.

[14] O. Noblanc, P. Gaucher, and G. Calvarin, “Structural and dielectric studies of Pb(Mg1/3Nb2/3)3-PbTiO3 ferroelectric solid solutions around the morphotropic boundary” J. Appl. Phys. Vol.79, p.4291, 1996.

[15] R. Zhang and W. Cao, “Transformed Material Coefficients for Single Domain $0.67Pb(Mg_{1/3}Nb_{2/3})$-$0.33PbTiO_3$ Single Crystal Under Differently Defined Coordinate System”, Appl. Phys. Lett. Vol.85, p.6380, 2004.

[16] R. Ai , H. Ito, and K. Wasa “Domain Control of Sputtered Perovskite Thin Films”, Proc. of SPIE (Florida, 2001)p.4058-49.

[17] I. Kanno, Y. Yokoyama, H. Kotera, and K. Wasa, “Thermodynamic study of c-axis-oriented epitaxial $Pb(Zr,Ti)O_3$ thin films”, Phys. Rev. B vol.69, pp.064103-1－064103-7, 2004.

[18] K. Wasa, I. Kanno, T. Suzuki, S. H. Seo, D. Y. Noh. H. Okino, and T. Yamamoto, “Structure and Ferroelectric Properties of Sputtered PMNT Thin Films”, Proc. of 2004 IEEE UFFC 50^{th} Anniversary Joint Conf.,(Montreal, 2004)FE1A-5.

[19] H. Ouchi,”Piezoelectric Ceramic Materials”, National Technical Report, vol. 22, p.720-740.

Some Recent Advances in SAW Duplexers and PA Duplexers Modules

M. Solal, PA. Girard, M. Aguirre, A. Bayram, C. Carpenter, F. Sinnesbichler, K. Cheema, S. Malocha and B. Abbott

TriQuint Semiconductor
Apopka, Florida and Munich, Germany

***Abstract*— The growth of WCDMA is leading to an increased interest for duplexers. Addition of new bands and features continue to drive the need for higher integration and lower cost. For duplexers used as discrete components, the goal is to avoid the addition of external elements. We developed a 3x2.5x1,6 mm^3 LTCC package CDMA duplexer. For modules application, a small 2x1.5x0.5 mm^3 package is used for the SAWs and external components are added on a laminate. A CDMA duplexer with balanced RX output is presented. In order to support 100 ohm output impedance, a new configuration is proposed. Good isolation and symmetry are maintained. New bands for WCDMA have been defined. In particular, for band 4, the distance between RX and TX band is about 400 MHz. A new ladder architecture using external inductors to improve isolation is proposed and demonstrated. PA duplexer modules are presented. They allow for better performances while simplifying the design for the phone manufacturer.**

I. INTRODUCTION

	TX band (MHz)	RX band (MHz)	Region	Comments
1	1920..1980	2110..2170	EU, Asia	UMTS band
2	1850..1910	1930..1990	USA	PCS band
3	1710..1785	1805..1885	EU	DCS band
4	1710..1755	2110..2155	USA	
5	824..849	869..894	USA	CDMA band
6	830..840	875..885	Japan	Part of CDMA
7	2500..2570	2620..2690	Discussed worldwide	
8	880..915	925..960	EU	EGSM band
9	1750..1785	1845..1880	Japan	Part of DCS band

TABLE I. WCDMA FREQUENCY BANDS

While GSM is a half-duplex system, meaning that a switch can separate the TX and RX paths in a mobile, CDMA and WCDMA are full duplex systems. Thus, the separation between RX and TX must be done in the frequency domain using filters, or duplexers. The growth of the WCDMA and the emergence of several new frequency bands (see table 1) increase the interest for high performance duplexers. 3G handsets include typically the four GSM edge bands and WCDMA band 1 for operation in Europe or WCDMA band 2 and 5 for operation in USA or these three bands for worldwide operations.

A general trend in the handset world is the replacement of discrete components by modules [1]. The main advantage of this approach is in the manufacturing of the mobile phones, which benefits from a drastic simplification of the RF design effort, allowing for a reduction of the design cycle time. In addition, the reduction of components diminishes the manufacturing cost. Furthermore, when possible, the co-design of various components in a module can give a better result. Opportunities for improvements in over all performance are expected when optimizing for the global specification rather than splitting this responsibility between different teams. This trend is also true for both duplexers and PAs, and the PA duplexer module solution developed by TriQuint Semiconductor.

The way duplexers are implemented is closely related to the way they are used. For discrete devices, the goal is to provide to the customer a complete duplexer solution. A match to 50Ω, without the need of additional components, is preferred. The duplexer needs to integrate the SAW die, an impedance inverter and some inductors. The device thickness is less critical than for modules application. Several ways are possible to get this result. One approach is to embed the SAW die and the passive in a ceramic package. This can be done by embedding the passive in the ceramic by using the LTCC technology, or by adding an integrated passive device die inside the package. Another possibility is to use a small module approach. The package contains only the SAW die. It can be mounted on a laminate with the extra passive or on a LTCC support for example. It is very difficult to determine what "the best architecture" is and the choice is probably different from one company to another, depending on its available technologies and cost structure. We chose the LTCC package approach mainly because it was the one yielding the lowest cost for us.

For the module applications, we developed a very compact 2x1.5x0.5 mm^3 ceramic package. Using advanced flip chip process, it is possible to embed the TX and RX SAW in this package. The impedance inverter as well as extra ground inductors are implemented as a part of the module on a laminate. To be able to get good duplexer performances requires complete control of the implementation. As it is usual for RF, the laminate layout has an important impact on the duplexer isolation. In particular, for duplexers, the ground paths in the laminate and in the package have to be carefully designed. Another point is the position of the different inductors on the module and the control of their mutual couplings. Our experience has shown that best results are obtained when a real co-design of all parts of the module is done. In this case, the laminate layout can be included when designing the SAWs.

II. SAW DESIGN MODELLING TOOLS

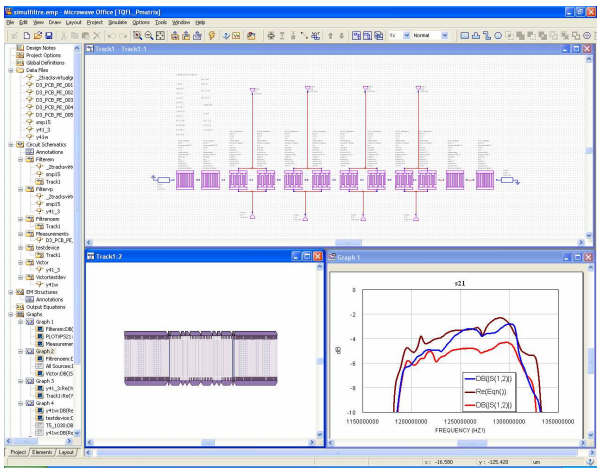

Figure 1. Example of a CRF design inside Microwave Office™. The top window is the schematic for one track of CRF including several gratings and transducers sections. The left bottom window is the corresponding layout and the right bottom window is some simulation response.

Two aspects are important when discussing of design and modeling tools: the first aspect is obviously the accuracy while the second aspect is the integration of the SAW design inside the complete design flow. Two main models are used at TriQuint to design SAW duplexers. The first model [2,3], so called harmonic admittance model, is based on prof. Hashimoto FEMSDA free software [4]. This software allows us to compute the harmonic admittance for an infinitely long periodic grating. By inverse Fourier transform, the mutual admittances from one electrode to another electrode inside the periodic grating are obtained. Then, the admittance of a synchronous resonator is calculated by summing the mutual admittances. The summation can also be replaced advantageously by an integration in the slowness domain [5] Some numerical problems have to be solved to get a good accuracy, in particular the leaky SAW pole has to be extracted and its contribution needs to be computed analytically. The main advantage of this method is that it takes into account directly for all acoustic modes and in particular the bulk mode is included. Its main drawback is that it only allows the analysis of synchronous resonators with infinite gratings. In particular, the losses and ripples due to the finite grating length are neglected. If the computation time is too long for purposes of optimization, simple perturbation methods may be used to account for variations of the resonators geometry.

The second model used currently in TriQuint is a P matrix model. As described in [6], it is possible to extract from a harmonic admittance, computed using a FEM/BEM or FEMSDA model, the dispersion curve for the Leaky SAW. The second step is to compute the P matrix parameter from this dispersion curve. The P matrix parameters (reflection coefficient, velocity, propagation loss, acoustic conductance) are frequency dependent. It is impossible to suppress the ambiguity between velocity and reflectivity using only a periodic model and an assumption is needed. We used the same assumption as [6], i.e. we assumed that the reflection coefficient is frequency independent.

Under this assumption, it is possible to extract from the dispersion curve all P matrix parameters. The result is a file containing the values of the parameters for a sample of normalized metal thickness h/2p, duty factor a/p and normalized frequency 2pf, where p refers to the pitch. This file is computed once for each couple of substrate and electrode material. It is then interpolated to find the parameter for the actual geometry and frequencies. In this model, the difficult part is the process of extraction of the dispersion curve. The solution to this problem must be very robust in order to be able to work for a large variety of piezoelectric materials, metal thickness, duty factors and frequency. Typically, the presence of the bulk mode and of the hybrid mode [7] makes it tricky to write an extraction routine isolating the LSAW mode. The result can be very dependent on the extraction algorithm or even on its parameters (for instance, convergence criteria).

As shown in [8], it is possible to give a very accurate representation of the harmonic admittance, which includes as well the LSAW, the bulk mode and the hybrid mode. Even if only the LSAW is included in the P matrix model for now, this allowed us to get a very robust algorithm to extract the parameters.

The need for a good integration of the SAW design tools inside the global design flow led us to integrate our SAW models inside commercial EDA tools [ADS™, Microwave Office™] by the way of "Process Design Kits" or "User Compiled Models". In particular, for the P matrix model, we implemented a transducer as a 4-port model (2 electrical ports and 2 acoustic ports). The EDA tool treats the acoustic ports as electrical ports. This is made possible by defining an arbitrary acoustic impedance of 50Ω. The P matrix cascade is then replaced simply by equivalent electrical connections [9].

This approach is very powerful in terms of design environment. When the SAW model is implemented in the EDA, all the features of this EDA are directly available for the SAW designer. For example, several optimizers of different kinds are present. It is possible to perform a Monte Carlo analysis of a module including manufacturing variations of the SAW as well as variations of the other elements. In addition, the layout is done directly in the EDA, based on the design parameters. This approach enables a direct link to the EM

simulator. The integration of all the elements of the module in the same tool is also very important for a true collaboration between the SAW, modules and PA designers.

III. CDMA- WCDMA BAND V DESIGNS

A. *Discrete solution*

For a discrete duplexer component, it is important to simplify its utilization and to avoid the need of external components. Typically, the duplexer contains a phasing element and two or three small inductors connected in series of the shunt resonators. With the increasing number of competitors who are able to manufacture duplexers meeting technical requirements, the cost continues to become a more significant factor. Our approach was to use passive elements embedded in a 3x2.5 mm^2 LTCC package. The main factors driving the cost are the number of layer in the LTCC and the size of the SAW die. We chose to use only four LTCC layers (counting from the input pads to the bump pads) to embed the elements.

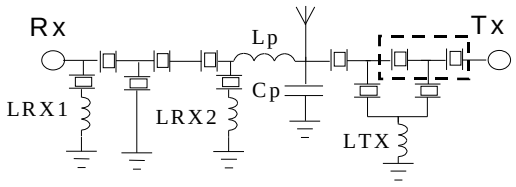

Figure 2. Architecture of the LTCC CDMA duplexer. The two series resonators grouped in ths dashed line box are acoustically coupled to reduce the die size

The duplexer architecture was chosen to minimize the die size while maintaining good performance. The architecture is shown on figure 2. To connect the TX and the RX filters, an impedance inverter is needed. Embedding one quarter-wavelength line in the package is a typical solution. Using three passive elements (2 capacitors and 1 inductor or 2 inductors and 1 capacitor) an inverter may be implemented. By choosing to use a series inductor between two shunt capacitors, we were able to embed the two capacitors on the SAW die. From the antenna, the first element for the RX filter is a shunt resonator, which is able to assimilate one of the shunt capacitors required for the inverter. For the TX filter, the first element on the antenna is a resonator in series so that the shunt capacitor Cp has to be present. A very simple and compact way to do a capacitor is to place on the SAW die an IDT in a different direction than the used LSAW direction. If its period is chosen appropriately, this IDT behaves like a capacitor in the frequency band of interest.

A way to make the die more compact is to use acoustic coupling between series resonators. Typically, these resonators have small sizes. When the size is not a concern, they are generally not laid out one in front of the other in order to avoid acoustic coupling between them. Actually, these resonators can be acoustically coupled without performance losses [10] if this is accounted in the model. Furthermore, one of the two resonators acts like a reflector for the second one, which results in even smaller sizes. For this example, the two last (from antenna) series resonators of the TX filter are acoustically coupled. The filter was designed with the P matrix model inside ADS™. EM simulation of the LTCC and die was performed using HFSS™ (see figure 3).

The definition of ports inside the electromagnetic simulator is very important. HFSS™ allows the definition of so called differential ports. One differential port consists in two electrical nodes. It is assumed that all the current coming from one of these nodes will enter the second node. If this is a good approximation when a standard resonator is connected to the port, it is no more valid when the resonators are acoustically coupled. Similar problem happens when analyzing CRFs. The solution we found in this case was to add a "virtual" common reference potential (i.e. adding a metallic pad) between the bus bars and to define the ports between one bus bar and this common reference (see fig. 4). Using this method, we were able to reduce the die size down to 1.4x0.9 mm^2. Figures 5-9 show the comparison between measured and simulated results. The insertion loss is 2 dB for TX and 3 dB for RX while the isolation is 53 dB in the TX band and 45 dB in the RX band. As shown on the figures, the correlation between measurements and simulation is very good.

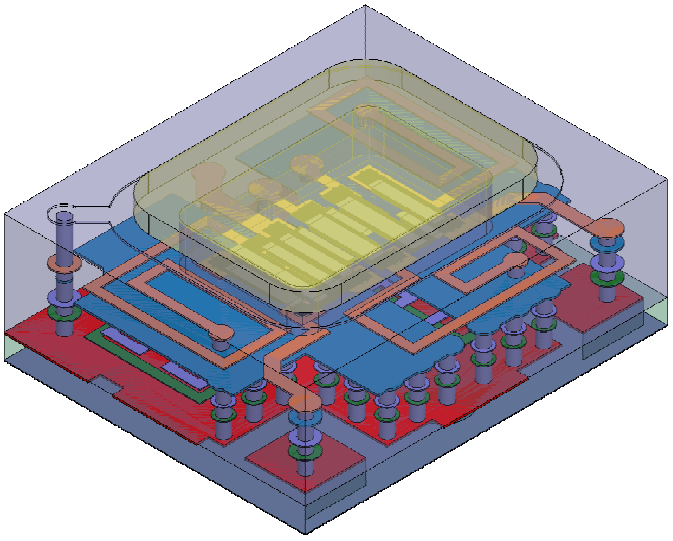

Figure 3. 3D view of the duplexer including the LTCC package and the die

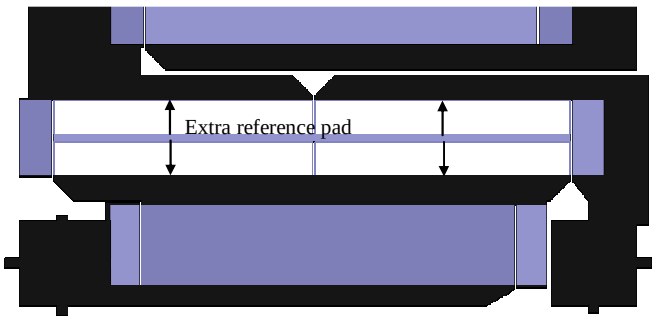

Figure 4. Detail of the die showing the acoustically coupled resonators and the ports (arrows) in HFSS™

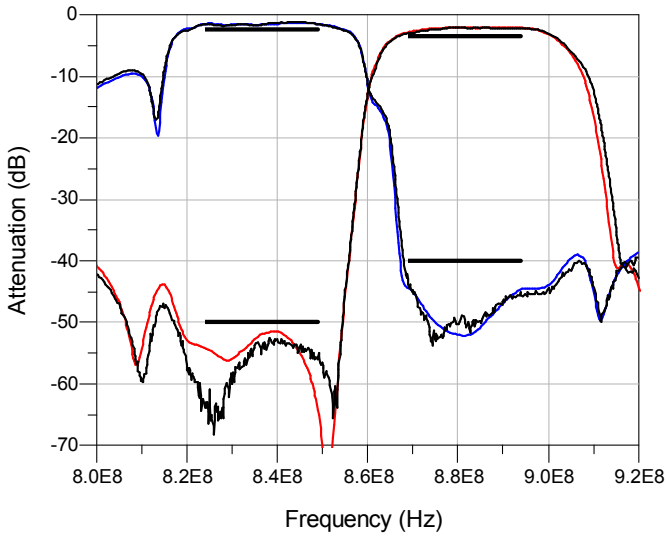

Figure 5. Comparison of mesurement and simulation for the LTCC duplexer RX and TX paths. Black measurement. Blue TX path. Red RX path.

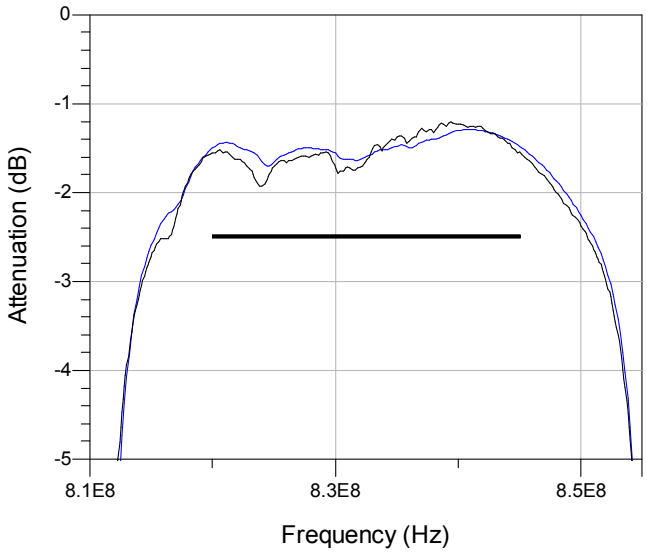

Figure 6. Comparison of measurement and simulation for the LTCC duplexer TX path. Black measurement. Blue simulation

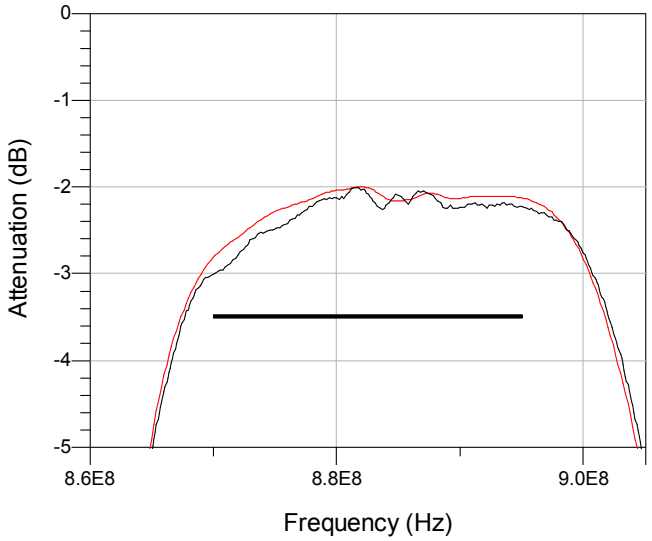

Figure 7. Comparison of measurement and simulation for the LTCC duplexer RX path. Black measurement. Red simulation

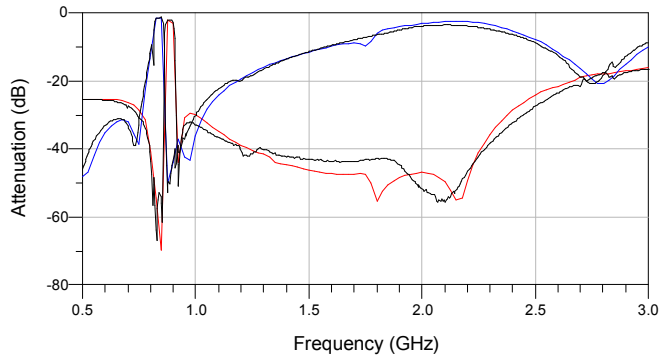

Figure 8. Comparison of mesurement and simulation for the LTCC duplexer top RX and TX paths

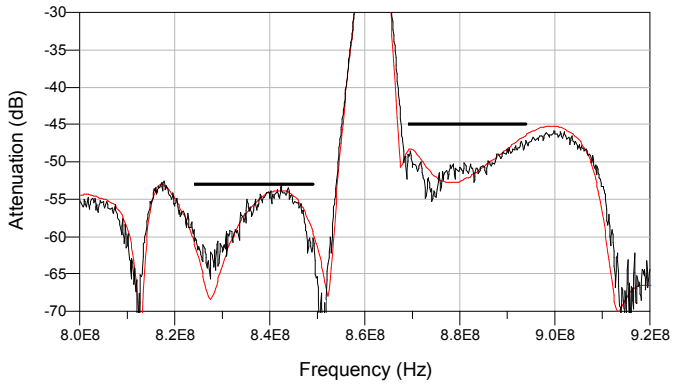

Figure 9. Comparison of measurement and simulation for the LTTC duplexer RX/TX isolation. Black measurement, red simulation

B. Single-balanced duplexer

A new requirement is to design duplexers having a 100 Ω balanced output for the RX side while maintaining the 50 Ω terminations for the TX and antenna ports. Therefore, the RX ladder filter was replaced by a coupled resonator filter. In

addition, the 100Ω output impedance makes it difficult to use the common configuration where the balanced output IDT is implemented using two transducers connected in series. To obtain the required output match, we chose to use a RX filter structure where the balanced output is produced by a single IDT (see figure 10).

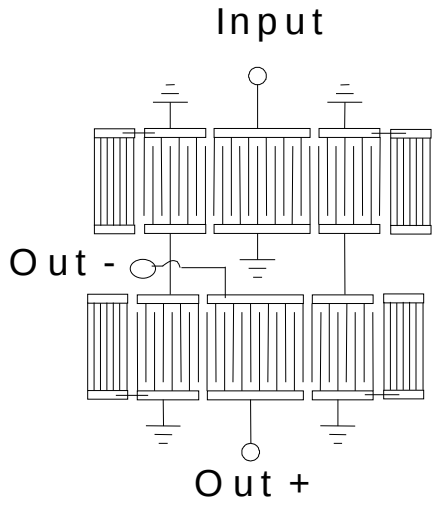

Figure 10. 50 Ω output impedance structure 2 tracks CRF

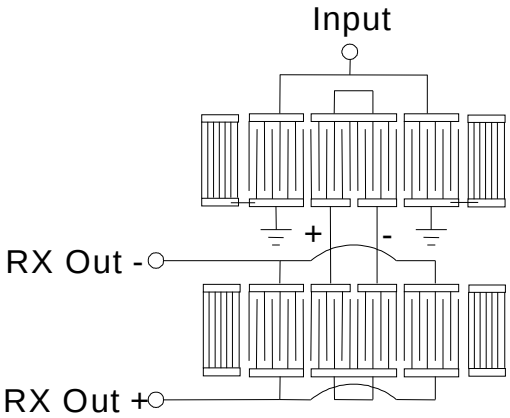

Figure 11. Architecture of the RX filter of the S/B duplexer

The natural impedance on the output side is 50Ω. The reason for this choice is that it is much easier to increase by design the impedance from 50Ω to 100Ω than to reduce it from 200Ω to 100Ω. The problem with the structure of figure 10 is that the (out-) connection is very close to one of the connections between the tracks so that the capacitances between the two lines are not negligible, especially when crossovers are used on the die. This can result in isolation and rejection deterioration. In addition, because of the presence of the ground connection for the input transducers, a space-consuming bump is needed between the two tracks. To avoid this, we chose to use a balanced connection between the two tracks (figure 11).

The input, of the structure in figure 11, is associated with the two outer transducers. The center transducer is split into two parts with invert phase and connected in series so that their common point is naturally at the ground. One advantages of this approach is its lower size due to the suppression of the center bump. Even more importantly, the capacitances between (RX Out 1) and (+) and (–) are identical. The two corresponding spurious are out of phase and cancel each other, and result in good isolation.

Seen from the antenna side in TX band, the CRF is equivalent to a small capacitance easy to match with a parallel inductor. The two SAW dies are embedded in our 2x1.5 mm^2 package. With two additional inductors, this package has been mounted on a 3x2.5 mm^2 laminate. Obviously, as discussed before, this solution is well suited to integration in a module.

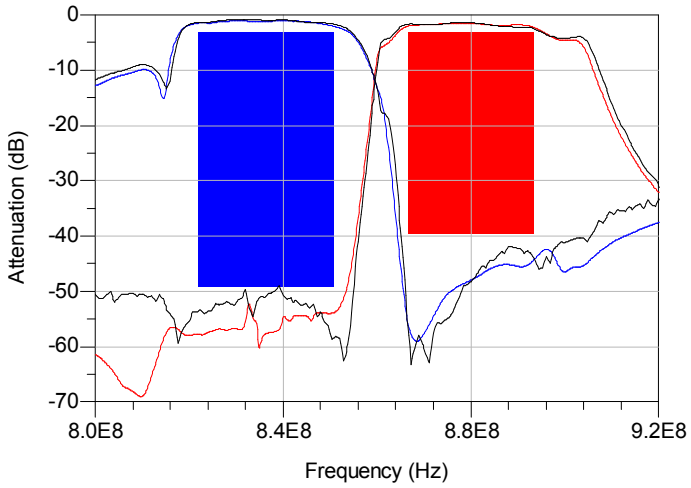

Figure 12. TX and RX paths for the single balanced duplexer (Black=simulation/ red=measurement)

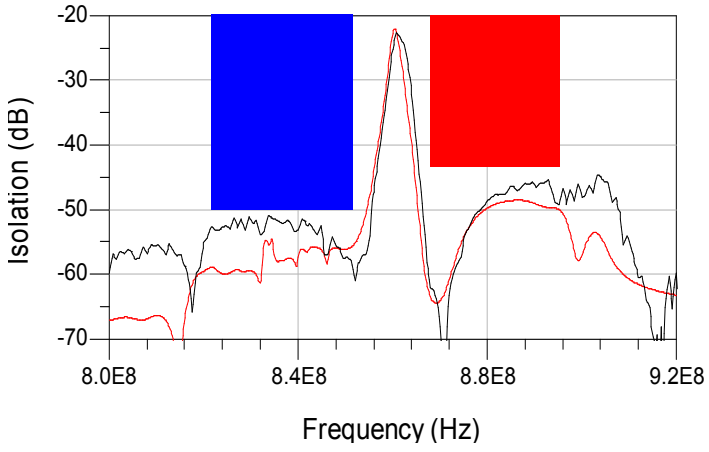

Figure 13. RX/TX isolation for the single/balanced duplexer (Black=measurement, red=simulation)

Very good performance is obtained. The typical insertion loss is -1.5 dB and -2.3 dB in the TX and RX band respectively. A typical isolation of –52 dB in the RX band and -45 dB in RX band has been demonstrated. In addition, the amplitude imbalance is less than +/-0.5 dB and the phase

imbalance is less than +/-3 degrees. Figure 14 shows the wide band comparison between the single LTCC duplexer and the single balanced duplexer. The TX wide rejection is similar for both duplexers. For the RX path the rejection is improved by 20 dB at 3 GHz for the single balanced duplexer. This is due to the use of CRF instead of a ladder filter.

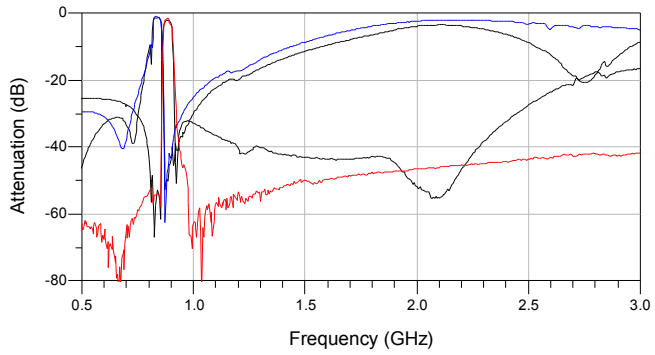

Figure 14. Wideband comparison of the LTCC (in black) and the single balanced duplexer(in red and blue)

IV. WCDMA BAND 1

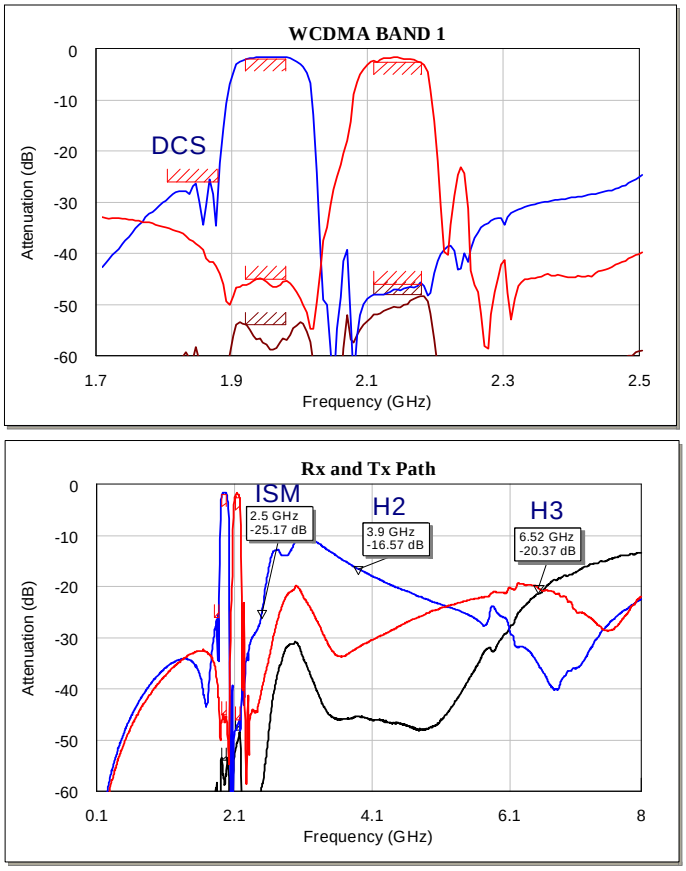

Figure 15. Narrow band (top) and wideband (botton) measured response for the WCDMA band 1 duplexer. Blue TX path, red RX path, black TX/RX isolation.

A WCDMA band 1 duplexer was designed and manufactured for our PA duplexer module (see section VI). Again, the small 2x1.5 mm^2 is used to embed the SAWs. The extra passive components are on the module laminate. Ladder filter architectures were used for both TX and RX. The difficulty was to get good insertion loss and isolation while maintaining a reasonable wide band rejection. Typically, adding inductors to the shunt elements helps to improve the close in performance (i.e. passband and isolation) while producing a degradation of the far out rejection. Figure 15 shows typical results for our band 1 duplexer measured inside our PA duplexer module. Typical insertion losses are 2 dB and 2.5 dB for the TX and RX band respectively while the TX/RX isolations are –54 dB in the TX band, and –48 dB in the RX band. The TX path has 26 dB of rejection in the DCS band. The TX harmonics are rejected by 16 dB and 20 dB, and the RX path exhibits a rejection better that 20 dB up to 8 GHz.

V. WCDMA BAND 4 DUPLEXER

An example of a new WCDMA band is band 4. The bandwidth (40 MHz) is relatively narrow for the 2 GHz range. Compared to the other bands, an important point for the band 4 is that the spectral distance between the TX and RX bands is about 400 MHz, which is 20% of the center frequency and thus very large. If this large distance reduces the required steepness and seems to make the design easier, it is not the case upon examining the problem in more detail.

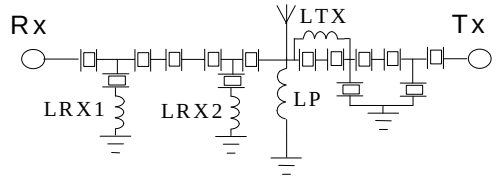

Figure 16.

When using a ladder structure, the best rejection of the filters is obtained close to the notches at the resonance of the shunt resonator and at antiresonance of the series resonators. For band 4, the RX band is very far from the TX and it becomes difficult to meet the rejection and isolation requirements. It is well known that adding inductors in series to the shunt resonators of a ladder filter decreases the resonance frequency of the resonator while keeping constant its antiresonance frequency. This has the effect of shifting the low side notches of the RX frequency response to lower frequencies, and permits the design of a duplexer with sufficient TX band rejection in the RX path.

Similarly, it is very important to have a good rejection of the RX band in the TX path. To obtain this result, we chose again to use inductors to increase the equivalent coupling coefficient of some resonators. For the TX path, this is done by placing inductances in parallel with the series resonators, which has the effect of increasing the antiresonance frequency of the composite resonant element, while maintaining the resonance frequency. This approach places a notch in the RX band.

The chosen duplexer architecture is shown on figure 16. Again, the SAW dies were encapsulated in our 2x1.5 mm^2 package while the 4 inductors are externally connected. The duplexer is used in a module. We were able to obtain typical insertion losses of 1.5 dB and 2 dB for the TX and RX band respectively. The typical TX/RX isolation is about 55 dB in the TX band and 47 dB in the RX band. To be able to get such performances, a careful design of the laminate layout is the key. In particular, it is very important to control the grounding paths of the duplexer. In addition, it is important to be careful with the layout of the inductors in order to avoid inductive coupling. Using this approach we were able to obtain a minimum TX rejection of 30 dB, up to 6 Ghz.

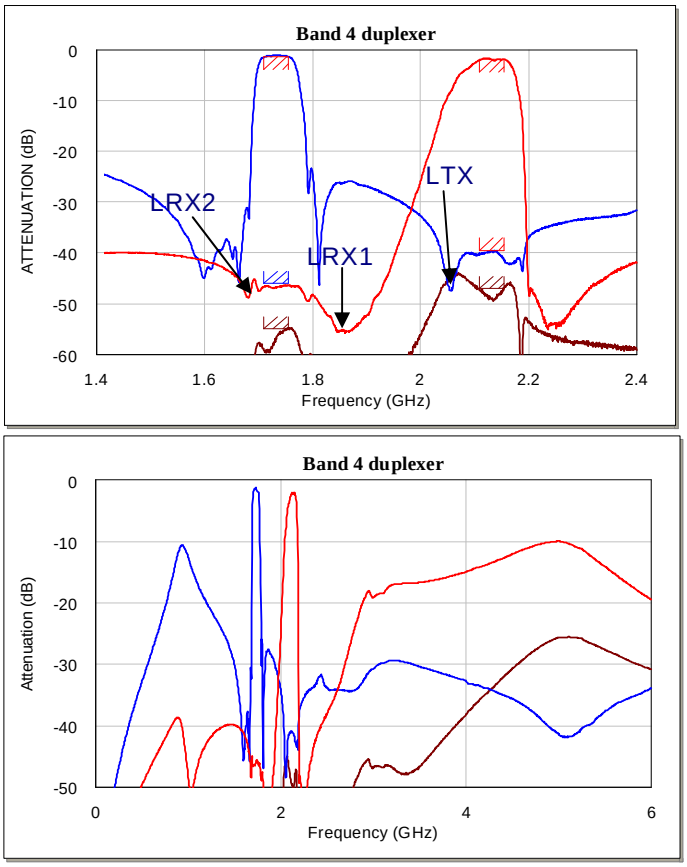

Figure 17. Narrow band (top) and wideband (botton) measured response for the band 4 duplexer. Blue TX path, red RX path, black TX/RX isolation.

VI. PA Duplexer Modules

While first generation WCDMA phones typically used a discrete approach for the front-end, the integration of several components into PA Duplexer modules (transmit modules) has recently become a widely adopted approach. Typically such a module includes an interstage filter, a power amplifier, a directional coupler, optionally a power detector, and the duplexer, as well as all required matching and phasing components (figure 18).

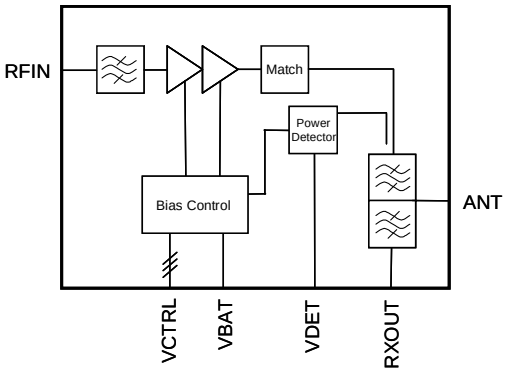

Figure 18. Block diagram of a PA duplexer module

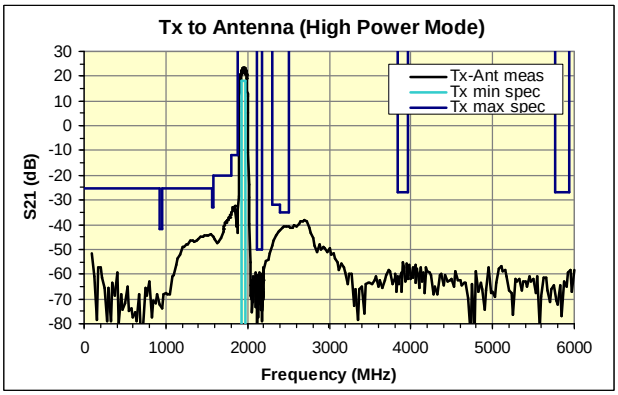

Figure 19. TX-ANT rejection of a complete Band I PA duplexer module

For the phone manufacturer, this architecture provides several advantages:

-The phone design effort is significantly reduced. All interfaces are well-defined 50Ω ports, all mutual coupling and grounding effects are addressed within the module. Also component count is dramatically reduced.

- The phone PCB area for the WCDMA front-end is reduced. First generation PA Duplexer modules integrate all above mentioned functionality into a size of only 5.0x8.0x1.5 mm³, second-generation module size is 4.0x7.0x1.1 mm³ and further size reduction is visible.

- Overall electrical performance of the module is improved over the discrete approach by carefully aligning all components within the module and by optimizing all internal interfaces.

An example for optimized component alignment is the total noise performance. The measured noise power at the antenna port and at the RX port of the module N_{comp} is a function of the noise at the input of the amplifier N_{RX}, the noise generated by the amplifier N_{amp} and of mixing effects of the input noise with the carrier signal. The total noise can be calculated as

$$N_{comp} = N_{Rx} \cdot G_{Rx} + N_{amp} \cdot G_{amp} + N_{Rx} \cdot G_{conv} \qquad (1)$$

In (1), G_{RX} and G_{conv} depend on the interstage filter, the amplifier, and the duplexer while G_{amp} is a function of the duplexer only. Since all input and amplifier related noise contributions are known during the design phase of the module,

the filters rejection requirements can be optimized resulting in better insertion loss of the duplexer and therefore in a reduction of the total current consumption of the module. As an example, figure 19 shows the measured wide band rejection of a band 1 PA duplexer module.

Another important optimization process during the module design is related to the interfaces between the power amplifier, the directional coupler and the duplexer. The natural impedance of the TX port of the duplexer is not necessarily 50Ω while the required impedance at the PA output is in the range of 5Ω for a typical WCDMA amplifier. Since the presented line up does eliminates the option of using an isolator between PA and duplexer to achieve load insensitivity, this optimization process takes into account all required load mismatch conditions. Typically this means that the linearity has to be maintained even for load mismatch of up to 3:1, depending on further losses of the overall front-end architecture.

TriQuint designed and fabricates a complete product line of PA duplexer modules. It is applied for CDMA and WCDMA in the cellular, pcs and IMT band 1 frequency ranges. As an example, figure 20 shows a photograph of our band 1 PA duplexer module.

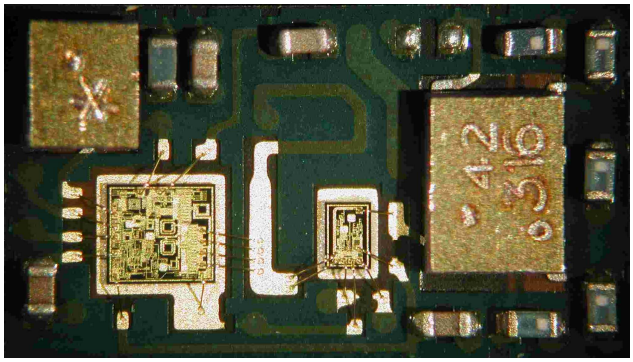

Figure 20. Band I PA duplexer module

VII. CONCLUSION

To serve the growth of WCDMA, a continuous improvement and size reduction of duplexers is required. For discrete solutions, we chose to use LTCC package in order to avoid the need for external components. A 3x2.5 mm^2 duplexer was designed. To reduce the cost, the package was simplified at maximum and the SAW die size reduced. Typical isolation as good as 53 dB in the TX band and 45 dB in the RX were obtained while keeping 2 dB insertion loss for the TX band and 3 dB for the RX band.

Modules provide for phone manufacturers as well cost reduction as reduction of their design efforts. For modules applications, we use a small 2x1.5x0.5 mm^3 package to embed only the SAW dies while the additional passive are laid on the module. To obtain good results it was necessary to design the module and the SAWs together. This is made easier by embedding the SAW models in an EDA tool. We were able to design and manufacture a duplexer having a balanced RX output. A new architecture was presented in order to handle 100 Ω output impedances. Among the new WCDMA bands, band 4 has a very large frequency difference between TX and RX. To make a duplexer for this band, a new architecture was defined using intensively inductors to increase the equivalent coupling coefficient of resonators.

Duplexers and PA duplexer modules are a very exciting technical field. Designers have to deal with the SAW design as well as the PA and the definition of the complete module. All aspects have a major impact on performance and a lot of possibilities exist to improve the combined performance. In future, the co-design of the duplexer and the complete module is foreseen to become more and more important. This will continue to drive the integration trend. In addition, the new SAW emerging technologies like temperature compensation and high coupling substrates [11-14] will probably become more and more common for duplexers.

REFERENCES

[1] Peter V. Wright, “Integrated Front-end modules for cell phones”, 2005 IEEE Ultrasonics symp. Proc., pp 564-572

[2] Pascal Ventura, Jean-Michel Hode and Marc Sola1, “A New Efficient Combined FEM and Periodic Green's Function Formalism for the Analysis of Periodic SAW Structure”, 1995 IEEE Ultrasonics symp. Proc., pp 263-268

[3] S. Malocha, B. P. Abbott, N. Naumenko,” Numerical Modeling of One-Port Resonators Based on Harmonic Admittance”, 2004 IEEE Ultrasonics symp. Proc., pp 2027-2030

[4] Ken-ya Hashimoto and Masatsune Yamaguchi, “Free Software Products for Simulation and Design of Surface Acoustic Wave and Surface Transverse Wave Devices”, 1996 IEEE Ultrasonics proc., pp 300-307

[5] Julius Koskela, Victor P. Plessky, and Martti M. Salomaa, ”Analytic Model for STW/BGW/LSAW Resonators”, 1998 IEEE Ultrasonics symp. Proc., pp 135-138

[6] Th. Pastureaud, “Evaluation of the P-Matrix parameters frequency variation using periodic FEM/BEM analysis”, 2004 IEEE Ultrasonics symp. Proc., pp 80-84

[7] Yann Fusero, Sylvain Ballandras, Jean Desbois, Jean-Michel Hode, Pascal Ventura, “SSBW to PSAW Conversion in SAW DevicesUsing Heavy Mechanical Loading”, IEEE trans. UFFC, vol. 49, no 6, june 2002, pp 805-814

[8] Natalya Naumenko, Benjamin Abbott, “Approximation of propagation loss in rotated Y-cuts of lithium tantalate with a periodic grating”, 2005 IEEE Ultrasonics proc., pp 1876-1879

[9] Xavier Perois, Marc Solal, J.Bernard Briot ,Stephane Chamaly, Martine Doisy, P.-Alexandre Girard, “AN ACCURATE DESIGN AND MODELING TOOL FOR THE DESIGN OF RF SAW FILTERS”, 2001 IEEE Ultrasonics symp., pp 75-80

[10] Victor Plessky, J.-Bernard Briot, Laurent Kopp and Marc Sola1, “Balanced lattice filter with acoustically interacting resonators”, 2002 IEEE Ultrasonics symp., pp.143-145

[11] J. Tsutsumi, S. Inoue, Y. Iwamoto, M. Miura, T. Matsuda, Y. Satoh, T. Nishizawa, M. Ueda and O. Ikata, “A Miniaturized 3 x 3-mm SAW Antenna Duplexer for the US-PCS band with Temperature-Compensated LiTaO3/Sapphire Substrate”, 2004 IEEE Ultrasonics proc. pp 954-958

[12] Ken-ya Hashimoto, Hiroki Asano, Kenji Matsuda, Naofumi Yokoyama, Tatsuya Omori and Masatsune Yamaguchi, “Wideband Love Wave Filters Operating in GHz Range on Cu-Grating/Rotated-YX LiNbO3-Substrate Structure”, 2004 IEEE Ultrasonics symp. Proc, pp. 1330-1334

[13] N. Naumenko, B. Abbott, “Analysis of Highly Piezoelectric Non-Leaky SAW Propagating in Rotated Y-Cuts of Lithium Niobate with Thick Metal Films or Gratings”, 2006 IEEE Ultrasonics symp. proc., pp 493-496

[14] H. Kando, D. Yamamoto, M. Mimura, T. Oda, A. Shimizu,K. Shimoda, E. Takata, T. Fuyutsume, R. Kubo and M. Kadota, “RF Filter using Boundary Acoustic Wave”, 2006 IEEE Ultrasonics symp. proc pp 188-191

ADVANCEMENT OF SAW DUPLEXER BY USING SiO2

R.Takayama, H.Nakanishi, Y.Iwasaki, and H.Nakamura

Panasonic Electoronic Devices Co., Ltd.
1006 Kadoma, Osaka, 571-8506, Japan

Abstract **–** We have studied a method to improve and enhance the characteristic of SAW filter by using SiO2. In a standard of Third Generation Partnership Project (3GPP), there are some operation bands for FDD/CDMA system. So, the SAW filter which has become widely used as a key device used in cellular phone is required to satisfy the specification of every band. However the band width of SAW filter is almost determined by electro-mechanical coupling coefficient (K2) and temperature coefficient of frequency (TCF) of substrate material. Then it is necessary to change the material characteristics of substrate to design filters for several operation band. Against this background, we paid attention to temperature compensation technology using SiO2. It has been known that low TCF can be realized with SiO2. Additionally, K2 also changes because of SiO2 coating.

In this paper, we will show the possibility to realize the resonator characteristics by coating LiTaO3 (LT) or LiNbO3 (LN) with SiO2 which can be applied to SAW duplexer of several operation frequency bands in 3GGP standard.

I. INTRODUCTION

The antenna duplexer, which is needed to transmit (Tx) and receive (Rx) signals simultaneously, is an essential device for the cellular phone in FDD communication. Because antenna duplexers require high quality characteristics that are low insertion loss (*IL*), high attenuation (*ATT*) and high power durability, dielectric types have been used conventionally. However, recent improvements of the quality of SAW filters lead to emergence of SAW antenna duplexers in 800 MHz applications [1]. However, in a standard of Third Generation Partnership Project (3GPP), there are some operation bands for FDD/CDMA system (Table 1). So, the SAW filter is required to satisfy the specification on every band with high quality.

A SAW filter is a filter using a characteristic of piezoelectric material and the performance of SAW filter is almost determined by a substrate material property and the design. Especially, in resonator type like DMS-type and Ladder-type SAW filter, the band width is almost determined by electro-mechanical coupling coefficient (K2) and temperature coefficient of frequency (TCF) of substrate material. One of the reasons for realizing the SAW duplexer for 800 MHz applications, which corresponds with Band V, is that K2 and TCF of 36-48^{o}Ycut LiTaO3 substrate suited frequency allocation of band V. However the situation is different in other FDD/CDMA operating frequency bands. Thus the technology to control K2 and TCF of substrate material is needed. From the table1, the small TCF and steep skirt characteristic are needed to realize the SAW duplexer for operating band II, III, VII and VIII(Figure1-a). It is necessary to strike a balance between bandwidth and TCF to form required pass-band and rejection-band width for operating band I, IV, VI and IX(Figure1-b). Against this background, many researchers have tried several methods to change k2 and TCF of substrate material [2][3]. We paid attention to temperature compensation technology using SiO2. Although this method might improve the TCF, SiO2 degrades the performance of SAW devices. It has never put into practical use. In case of the conventional technique, the degradation of Q-factor at anti-resonance frequency (Qp) is the most serious problem. From our experimental results, the shape of SiO2 has seemed to play an important role in

Table1. UTRA Fdd frequency bands

Operation band	(Tx Band)	(Rx Band)	relative pass band width	relative duplex gap
Band Ⅰ	1920-1980	2110-2170	2.93%	6.36%
Band Ⅱ	1850-1910	1930-1990	3.13%	1.04%
Band Ⅲ	1710-1785	1805-1880	4.18%	1.11%
Band Ⅳ	1710-1755	2110-2155	2.33%	18.37%
Band Ⅴ	824-849	869-894	2.91%	2.33%
Band Ⅵ	830-840	875-885	1.17%	4.08%
Band Ⅶ	2500-2570	2620-2690	2.70%	1.93%
Band Ⅷ	880-915	925-960	3.80%	1.09%
Band Ⅸ	1750-1785	1845-1880	1.93%	3.31%

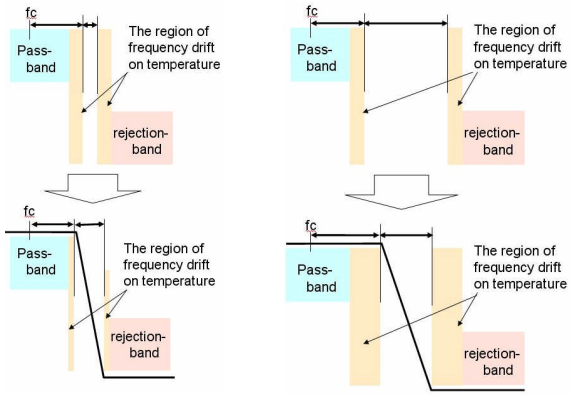

(a) narrow relative duplex gap (b) wide relative duplex gap

Fig. 1 The image of band width control direction

this phenomenon. In order to overcome this problem, we have tried not only to form high quality SiO2 layer but also to control the cross-sectional structure of the SiO2 layer. They are achieved by an advanced deposition method that we developed. The purpose of this study is to investigate how the layer-profile of SiO2 affects the characteristics of 1-port resonator and how to get useful SAW resonators which can be applied to SAW filters for SAW duplexers.

II. Conventional SAW RESONATORS HAVING SiO2/IDT/LiTaO3 STRUCTURE

For investigating influence of SiO2 coat on the characteristics of SAW device, we employed the synchronous 1-port SAW resonator as a test device. A SiO2 thickness was optically measured on the square pattern that was located close by the test SAW resonator. The sectional structure of the test SAW resonator is illustrated in figure 2.

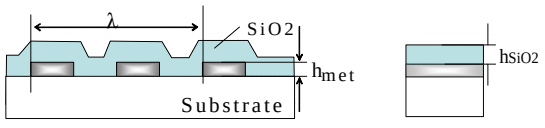

(a)IDT/refractor (b) Square pattern

Fig.2 A sectional structure of test device

II-1. SiO2 coat using conventional RF-sputtering

Figure 3 (a) and (b) shows the variations of transmission characteristics of SAW resonator having IDT/LT structure and SiO2/IDT/LT structure with different hmet, respectively. Both minimum *IL* of the SAW resonator with and without SiO2 structure is

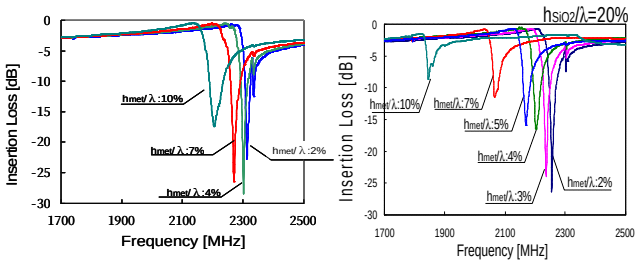

(a) IDT/LT structure (b) SiO2/IDT/LT structure

Fig. 3 Transmission characteristics

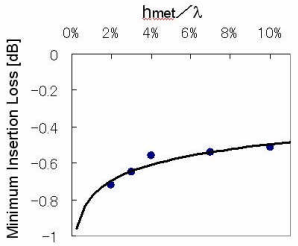

Fig. 4 Minimum insertion loss

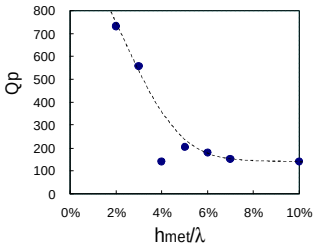

Fig. 5 Qp of the SAW resonator with SiO2/IDT/LT structure

shown in figure 4, and Qp of SAW resonator with SiO2 structure is shown in figure 5.In case of SAW resonator without SiO2, the characteristic of anti-resonant frequency becomes to deteriorate after peaking in hmet/λ = 4% with hmet/λ increasing. Minimum *IL* becomes small with hmet/λ increasing. On the other hand, in case of SAW resonator with SiO2, The characteristic at anti-resonant frequency (fp) is deteriorated with increase in hmet. Especially, Qp is deteriorated remarkably over 3% of hmet/λ. Figure 6 shows the reflection coefficient (| r |) roughly estimated from resonant frequency and frequency of spurious which appears at higher frequency than fp.

| r | of SAW resonators with SiO2 increases more than those of SAW resonators without SiO2 as the hmet/λ increase. The acoustic impedance of SiO2 is similar to that of Al. Then, if IDT/reflector is embedded in SiO2 and the SiO2 layer is formed homogenously on SAW propagation path, the factors of discontinuity in SAW propagation is almost only electric-loading effect.

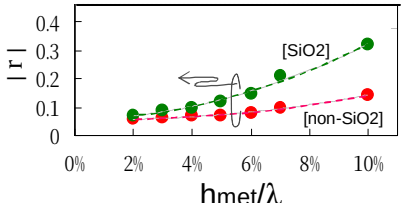

Figure 6. The reflection coefficient (| r |)

Therefore, in this case, | r | of every SAW resonator with every hmet/λ would becomes almost the same and smaller than that of SAW resonator without SiO2. However the results of our experiment were much different from anticipated results. To investigate the reason for this inconsistency, we observed the cross-section views of some test resonators (Fig.7).

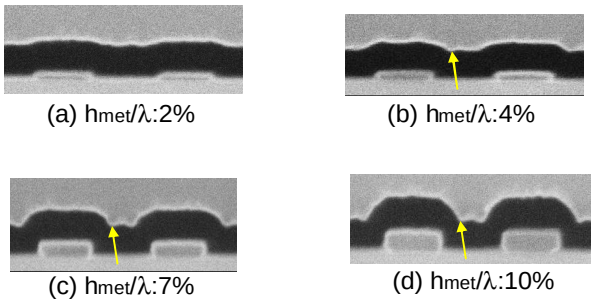

Fig. 7 Cross-section views of SiO2/IDT/LT structure SAW resonators of which SiO2 was coated using conventional RF-sputtering instrument. (h_{SiO2}/λ =20%)

From figure 7, it can be seen that the layer-profile of SiO2 depends on the hmet. As the hmet becoming thicker, the thickness between top and bottom of convexoconcave of SiO2 becomes thicker. Especially, clear another actual reflection surface, which is different from the edge of IDTs/reflectors, seems to be formed in over 4% hmet/λ.

II-2. SiO2 coat using advanced deposition method

From the experimental results shown in previous section, it seems that hmet/λ should be less than 4% to get a good Qp performance in SiO2/IDT/LT structure. However, the resistance of Al thin film which is less than approximately 150nm dramatically increases due to thin film effect. In the GHz band SAW filter, hmet/λ <4% correspond to thickness of less than 100nm. The increasing of *IL* with change of hmet/λ in the resonators without SiO2 are caused by the increasing of electric resistance (Fig.4). Then both the control of shape of SiO2 not to form another reflection surface which is different from the edge of IDTs/reflectors and the thick IDT would be necessary to enhance both Qp and Qs of SAW resonators with SiO2. Thus we have developed an advanced deposition method to control a shape of SiO2 layer, which covers the thick IDTs/reflectors. Figures 8(a) to 8(d) show the cross-sectional views of IDT of four test resonators, which are coated with SiO2 using this advanced deposition method under different deposition conditions. The hmet/λ and the hSiO2/λ of resonators, of which cross-sectional views are shown in figure 8, are 7% and 20%, respectively. By changing the deposition conditions of advanced deposition method, the convexoconcave of SiO2 becomes smaller and smoother in spite of every test resonator having the same hmet/λ? and the same hSiO2/λ. The transmission characteristics of these resonators and the dependence of Qp on the deposition conditions are shown in figures 9(a) and (b). Additionally, the dependence of K2 and | r | on the deposition conditions are shown in figures 10 and 11, respectively.

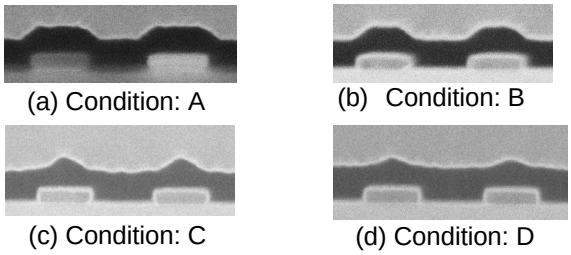

Fig. 8 Cross-section views of SiO2/IDT/LT structure SAW resonators of which SiO2 was coated using advanced deposition method. (hmet/λ =7%, hSiO2/λ =20%)

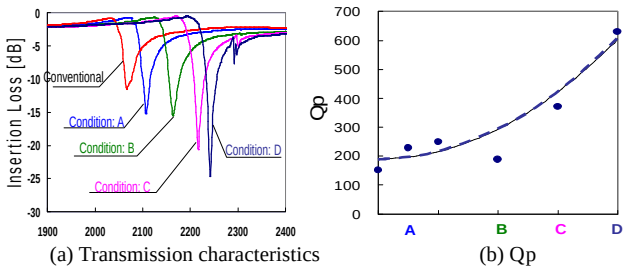

Fig. 9 Transmission characteristics and Qp of SiO2/IDT/LT structure SAW resonators with different hmet

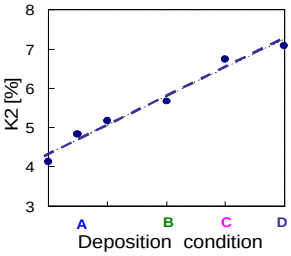

Fig. 10 The dependence of K2 on deposition condition

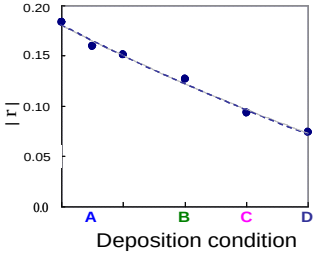

Fig. 11 The dependence of | r | on deposition condition

Both Qp and K2 were improved dramatically as the convexoconcave of SiO2 surface profile becomes small and smooth. At the same time, | r | decrease predictably. In case of deposition condition D, the | r | is nearly equal to SAW resonator without SiO2 which has 4% of hmet/λ. | r | is important factor for SAW resonator, and a suitable value is required. From point of view of Qp and K2, a flat surface of SiO2 layer seems better in this system of SiO2/IDT/LT, but a certain convexoconcave of SiO2 is needed to get suitable | r | for SAW resonators [4].

Figure 12, 13 shows the dependence of Q-value and K2 on hSiO2/λ in case of deposition condition D.

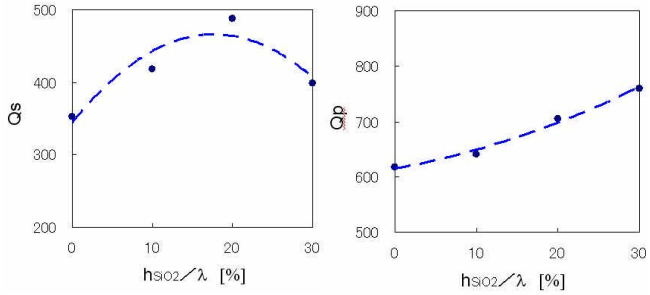

(a) Qs (b) Qp

Fig.12 The dependence of Q-value on h_{SiO2}/λ in case of deposition condition D.

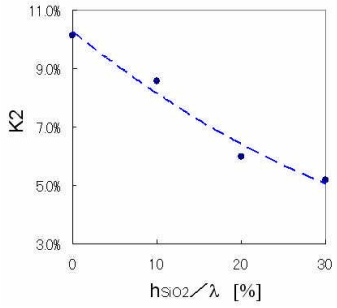

Fig.13 The dependence of K2 on h_{SiO2}/λ

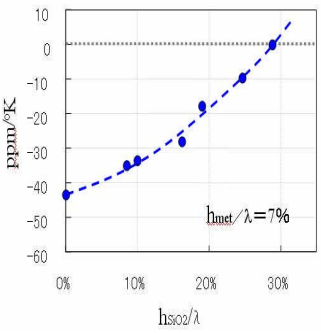

Fig.14 The dependence of TCF on h_{SiO2}/λ

The TCF variations at fr as a function of hSiO2/λ in case of SiO2 deposition conditions D is shown in Figure 14. Under this sputtering condition, every Qp was over 600 and Qs was the best in case of hSiO2/λ= 20%. It has been reported the Qs is a function of electrode thickness and cut angle of substrate with the exception of electric resistance [5]. So we guessed there was some relationship between surface profile of SiO2 and cut-angle of LT substrate. Figure 15 shows the Q-factors of SAW resonators with SiO2/IDT/LT structure with different cut-angle LT. In Fig.15, every SAW resonator has hSiO2/λ= 20%, hmet/λ=7%.

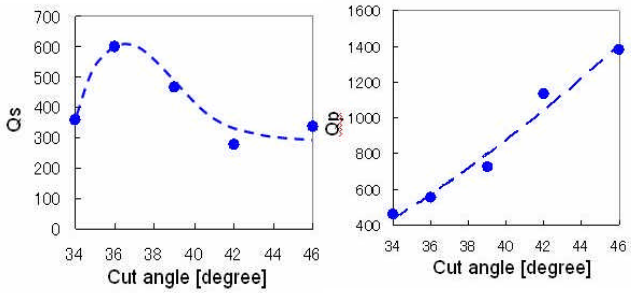

(a) Qs (b) Qp

Fig.15 The relationship between Q-factor and cut angle of LT in case of hSiO2/λ= 20%, hmet/λ=7% (deposition condition of SiO2 is D)

In this system, the best value of Qs was gotten around 37 degree and Qp is increasing as a cut angle becames higher. We think the Qs depend on the profile of SiO2.

Concerning K2, it can be seen that K2 becomes small as hSiO2/λ becomes large. And concerning TCF, it is improved as hSiO2/λ becomes large. Especially, zero-TCF at fp can be achieved at hSiO2/λ of approximately 30% in SAW resonator with hmet/λ of 7%. From these results, we believe it is possible to realize a SAW resonator with steep cut off characteristic and small TCF through the optimizing the K2 with high-Q by controlling hSiO2/λ, hmet/λ, cut angle of LT and SiO2 shape in this SiO2/IDT/LT system.

III. Band II (PCS) SAW Duplexer

We have applied SAW resonator with SiO2/IDT/LT structure mentioned in section II to Band II (US-PCS) SAW duplexer. In the case of ladder-type filter, a higher frequency part of the pass-band and attenuation characteristics of filter is to be mainly determined by the resonators that are located on series arms. Then, the rough estimation of the hSiO2/λ of resonators with SiO2/IDT/LT structure that are used for series arm resonators in Tx filter, is given as follows (Fig. 16,17),

$$\alpha < PZD / fc < \beta$$

where

PZD = *fa* – *fr*
fr: resonant frequency,
fa: anti-resonant frequency
fc: center frequency
α = [(A / 2) +(C / 2)] / *fc*
β?= [(A / 2) + B - (C / 2)] / *fc*

A = pass-band width (60MHz)
B = cross-band width (20 MHz)
C = frequency drift on temperature change
[TCF x (85°C-(-35°C)) x 1920MHz]

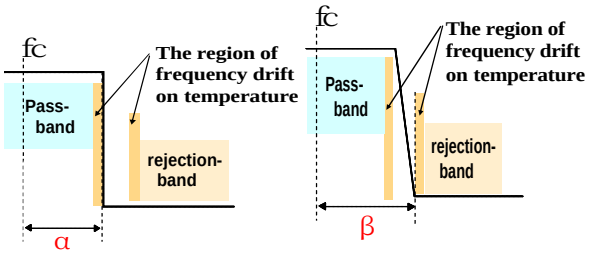

Fig.16 The definition of α,β in rough standard

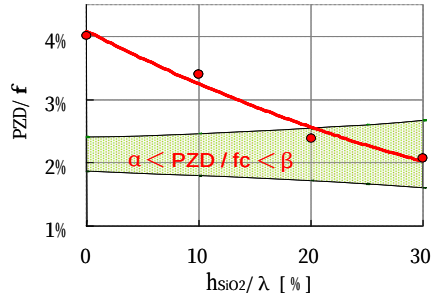

Fig.17 The rough standard of the extent of the PZD of resonators that are used for series arms in Tx filter

To take all data shown in Fig.17 into account, the resonator with SiO_2/IDT/LT of hmet/λ = 7% and hSiO2/λ = 20% is selected for the resonator of filter used in US-PCS SAW duplexer. The frequency characteristics of the filter used such resonators at -30 °C, 25 °C and +85 °C and temperature characteristic are shown in Figures 18(a) to (d).

The Tx filter has an insertion loss of 2.7dB at the Tx pass band, and a rejection of 42dB at the Rx band at 25 °C. The Rx filter also has an insertion loss of 3.6dB at the Rx pass band, and a good rejection of 52dB at the Tx band at 25°C. Concerning isolation characteristics between Tx and Rx, attenuations at the Tx/Rx bands were 55dB/46dB at 25 °C. TCF of Tx/Rx filters at center frequency were -14.4/-15.6ppm/°K, respectively. TCF at center frequency of Rx filter is a little bit larger than that of Tx filter. However, TCF of critical frequency region of Rx filter, which is the cross-band between the Tx pass band and the Rx pass band, is smaller than TCF at center frequency. It's owing to this small TCF, the US-PCS duplexer shows good performance over the whole operation

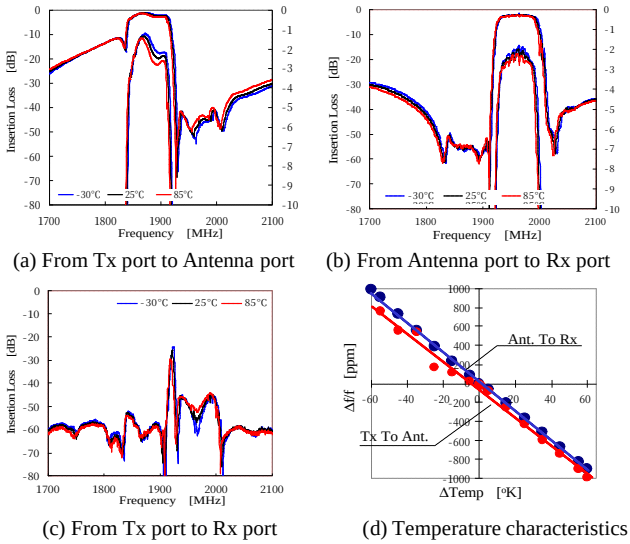

(a) From Tx port to Antenna port
(b) From Antenna port to Rx port
(c) From Tx port to Rx port
(d) Temperature characteristics

Fig.18 Frequency characteristics and Temperature characteristics of US-SAW duplexer using SAW resonators with SiO2/IDT/LT structure

temperature range from -30 °C to +85 °C. The insertion losses of Tx/Rx filter at the pass bands were less than 3.5dB/4.0dB. The attenuations at the rejectionbands were more than 50dB/40dB over the whole operation temperature range. Concerning isolations at the Tx/Rx bands were more than 53dB/44dB, respectively.

IV. SAW RESONATORS HAVING SiO2/IDT/LiNbO3 STRUCTURE

In section II, we discuss SiO2/IDT/LT structure. We show that SAW filter with steeper characteristic and smaller TCF than conventional SAW filter using LT are realized by controlling a shape of SiO2 in that structure. However, SiO2 coat makes K2 be small. Thus we have tried to cover LN with SiO2 to get larger K2 substrate than SiO2/IDT/LT. Figure19(a) shows the relationship between K2 and cut angle of LN in SiO2/IDT/LN concerning hmet/λ = 3% and 5%. We used conventional RF-spattering instrument for depositing SiO2 here. Figure 19(b) shows the minimum insertion loss of every sample. From fig.19 (a), K2 is increasing as cut-angle of LN is decreasing, and K2 which is larger than that of SiO2/IDT/LT can be gotten at lower than 41 degree. A difference of minimum insertion loss between the SAW resonator with electrodes thickness of hmet/λ=3% and that of 5% becomes small with the cut-angle of LN becoming lower. At the low cut-angle such as 5 and 15degree,

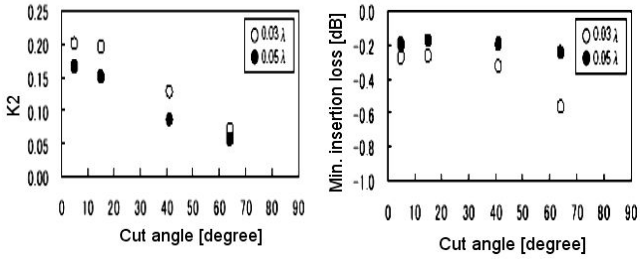

(a)K2 (b)min.I.L.

Fig.19 The relationship between K2/min.I.L. and cut angle of LN in case of hSiO2/λ= 20%

the difference of insertion loss between the electrode with hmet/λ=3% and that with 5% seems to come mainly from the difference of electrical resistance between them. Y11 characteristic of the SAW resonator with SiO2/IDT/LN structure using 15 degree cut LN was shown in figure20.

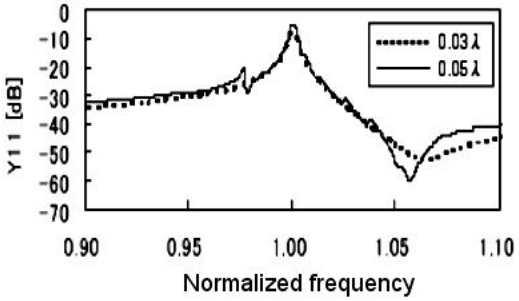

Fig.20 Y11 characteristic of SiO2/IDT/LN structure using 15 degree cut LN (SiO2 was deposited by using conventional RF-spattering instrument)

The characteristic around anti-resonant frequency of the resonator with hmet/λ=5% is better than that of the resonator with hmet/λ=3% despite of thicker electrode in this SiO2/IDT/LN system. This tendency is different from case of SiO2/IDT/LT structure. Additionally, there is comparable large spurious about 7.0 dB is found at lower frequency side of fr of SAW resonator in case of hmet/λ=5%. This spurious seems to come from response of Rayleigh mode by judging from propagation velocity [2]. This spurious makes a characteristic of filter which consist of these resonators deteriorate. For suppressing this spurious, we tried to apply the shape of SiO2 control technology mentioned in previous section. The result is shown in figure21. A spurious was suppressed to 1.7dB and the distance between resonant frequency and spurious became wider. Additionally, we confirmed the K2 and

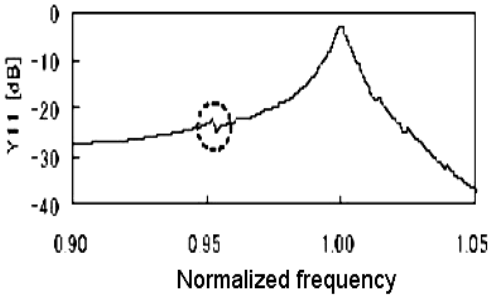

Fig.21 Y11 characteristic of SiO2/IDT/LN structure using 15 degree cut LN (SiO2 was deposited by using advanced RF-spattering instrument)

insertion loss was almost same the SAW resonator with SiO2 which is deposited using conventional sputtering instrument. In this case, TCF was approximately -40ppm/K. This resonator is available to design a filter for duplexer of Band I.

V. CONCLUSION

We have tried to change the characteristic of SAW resonator by using SiO2 coating technology in order to realize SAW duplexer for several operation bands. As the results, we realized the characteristics of the SAW resonator with small TCF and steepness by using SiO2/IDT/LT system. We realized the characteristics of the SAW resonator with high K2 by using SiO2/IDT/LN system as well. In our series of study, SiO2 layer-profile control technology played important roll to get a high performance SAW resonator with high-Q and low insertion loss in SiO2/IDT/substrate system. We also show the usefulness of advanced sputtering instrument we newly developed to control a shape of SiO2. We believe SAW duplexers for several operating band in 3GPP standard are realized using this technology.

REFERENCE

[1] O.ikata, Y.Satoh, H.Uchishiba, H.Taniguchi et al., *Proc. 1993 IEEE Ultrasonic Symp.*, pp111 .
[2] K.Yamanouchi and T.Ishii, *Proc. 2001 IEEE Ultrasonic Symp.*, pp189-192.
[3] K.Asai , M.Hikita, A.Isobe,et al , *Proc 2002 IEEE Ultrasonic Symp.*, pp226-229
[4] G.Kovacs, W.Ruile, M.Jakob,et al., *Proc. 2004 IEEE Ultrasonic Symp.*, pp974-977
[5] K.Hashimoto, M.Yamaguchi,et al., *Proc. 1997 IEEE Ultrasonic Symp.*, pp245-254

Small SAW Duplexer for W-CDMA Full-Band with Good Temperature Characteristics

Michio Kadota, Takeshi Nakao, Kenji Nishiyama, Shunsuke Kido, Masanori Kato, Ryoichi Omote, Hiroshi Yonekura, Norihiko Takada and Ryoichi Kita

Murata MFG. Co.,Ltd., Yasushi, Shiga, 520-2393, Japan.

Abstract— **Small sized surface acoustic wave (SAW) duplexer for wide band code division multiple access (W-CDMA) system with a good temperature coefficient of frequency (TCF) and good frequency characteristics has been required. However, the size of conventional SAW duplexer for W-CDMA using Al-electrode/50-70°YX-$LiNbO_3$ is large ($3.8\times3.8mm^2$) and its TCF is not good (-80ppm/°C). So, this duplexer can't satisfy its severe specifications in the all temperature range from -30 to 85°C. When SiO_2 film is deposited on this substrate to improve the TCF, the frequency characteristics is deteriorated by convex portions on the SiO_2 surface caused by SiO_2 sputtering. This time, by applying a flip chip bonding process, a flattened-SiO_2/Cu-electrode/substrate structure, and a YX-$LiNbO_3$ substrate, a small sized ($3\times2.5\times1.2mm^3$) SAW duplexer having good characteristics (such as low insertion loss and large attenuation) and good TCF has been realized for the first time. Here, the SiO_2 film is used to improve the TCF, the flattened-SiO_2 to obtain high Q, the thick Cu-electrode to obtain the large reflection coefficient, and the YX-$LiNbO_3$ substrate to obtain the large coupling factor and not to generate Rayleigh wave which causes spurious at the SiO_2 of 0.3λ and the Cu-electrode of 0.05λ.**

I. INTRODUCTION

Antenna duplexers composed of dielectric ceramic resonators have widely been used for mobile phone systems. However, the size miniaturization has been strongly demanded, because the size is large as $4.0\times9.0\times2.0mm^3$. So, currently the duplexers consisting of surface acoustic wave (SAW) or AlN film bulk acoustic resonators (FBAR) have been developed actively [1-5]. The pass-bands of a transmission (Tx) and a receiving (Rx) of wide band code division multiple access (W-CDMA) in Japan such as FOMA and Universal Mobile Telecommunication Service (UMTS) in foreign countries are 1920-1980MHz and 2110-2170MHz, respectively. A transition bandwidth between Tx and Rx is wide as 130 MHz compared with that (20MHz) of a duplexer for Personal Communication Services (PCS) handy phone in US. But demands for a low insertion loss (as small as possible) and a large attenuation at the rejection bands (as large as possible) is very hard. Therefore, in order to realize their specification, a SAW substrate satisfying both an optimum electromechanical coupling factor and a good temperature coefficient of frequency (TCF: a frequency shift per 1°C) is required. As the temperature changed by surrounding environment and the heat due to the input power of about 1W causes a large frequency shift of the SAW duplexer, that duplexer doesn't often satisfy their specification in the full temperature range from -30°C to 85°C. In order to suppress the large frequency shift and to satisfy their specification, a good TCF is also required.

An FBAR duplexer of size of $3.8\times3.8\times1.4mm^3$, which has the TCF of -20 to -30ppm/°C and the insertion loss at the pass bands/attenuation at the rejection bands of Tx: 1.6dB/45dB and Rx: 2.0dB/51dB, has been reported[6]. On the other hand, a SAW duplexer using leaky SAW (LSAW) on Al-electrode/50-70°YX-$LiNbO_3$ substrate has been developed, but its frequency characteristics and its TCF are not so good (Tx: 1.5dB/38dB、Rx: 2.2dB/ 46dB, and TCF: -80ppm/°C, respectively) compared with these of the FBAR.

Authors have developed and put to practical use a small SAW deplexer for US-PCS with a good TCF and frequency characteristics using a flattened-SiO_2/Cu-electrode/36-48°YX-$LiTaO_3$ structure for the first time[2][3]. This structure has too small coupling factor to realize the SAW duplexer for W-CDMA requiring a wide band. In order to realize SAW duplexer for W-CDMA with good characteristics and good TCF, authors applied the SAW structure of the flattened-SiO_2-film/Cu-electrodes/YX-$LiNbO_3$ substrate instead of $LiTaO_3$. As the result, the SAW duplexer for W-CDMA 60MHz Full-Band※, which has almost the same insertion loss and attenuation, but better TCF and smaller size ($3\times2.5\times1.2$(height)mm^3) compared with the FBAR, has been realized. (※ As shown in Fig.6, 60MHz bandwidth of W-CDMA in Japan covers three bands by 20MHz for three mobile communication carriers.)

II. Substrate for W-CDMA Duplexer

Conventionally, the LSAW on an Al-electrode/50-70°YX-$LiNbO_3$ substrate has been used as the SAW duplexer for W-CDMA Full-Band. It has leaky component and a bad TCF (-80 to -90ppm/°C), though it has a large electromechanical coupling factor. So, it is difficult to realize both a good low insertion loss and a large attenuation using this substrate in full temperature range from -30°C to +85°C. Thus, the characteristics of the duplexer using this LSAW is not good compared with that of the FBAR. Authors have investigated a substrate with suitable electromechanical coupling factor to satisfy the bandwidth of the W-CDMA duplexer

with the good TCF. At first, authors have tried to apply the SAW structure of the flattened-SiO_2-film/Cu-electrodes/$LiTaO_3$, which is one for the US-PCS SAW duplexer developed by authors [2][5], to the duplexer for W-CDMA. In this structure, the SiO_2 overlay film, the flattening SiO_2 film surface, and the high density metal electrode are used to improve the TCF, to obtain high Q, and to obtain a large reflection coefficient without the deterioration in the frequency characteristics, respectively [2][5]. However, this substrate structure is not suitable for the W-CDMA duplexer requiring the wider bandwidth, because its structure has too small coupling factor. Then, authors tried to use $LiNbO_3$ instead of $LiTaO_3$ as a substrate of flattened-SiO_2-film/Cu-electrodes/substrate, which has larger coupling factor than $LiTaO_3$. Figure 1 shows a coupling factor of a Rayleigh SAW and a LSAW on $SiO_2/LiNbO_3$ and $SiO_2/Cu/LiNbO_3$ with the SiO_2 film of thickness 0λ to 0.4λ as a function of θ, where λ is a wavelength of SAW and θ is an angle of Euler angle $(0°, \theta, 0°)$. The θ $+90°$ corresponds a rotation cut angle of conventional notation. The calculation has been based on the reference [7]. When the LSAW has the lower velocity than that of a slow shear bulk wave by depositing the SiO_2 film and the high density metal electrodes, it becomes an shear horizontal (SH) type SAW without the leaky component. It is called Love wave in this paper. When both of the thickness of the SiO_2 film and the Cu-electrode are zero at about θ =90°(Y-cut), a spurious response is generated because the coupling factor of Rayleigh SAW is not zero. The coupling factor of Rayleigh SAW depends on the angle θ , the SiO_2 film thickness, and the Cu-electrode thickness. An angle θ , at which the coupling factor of Rayleigh SAW becomes zero, shifts to lower angle as the SiO_2 film thickness increases as shown in Fig.1. It is about 100°, when the thickness of SiO_2 film is 0.3λ to 0.4λ and that of the Cu-electrode 0. When the SiO_2 film thickness is 0.3λ and the Cu-electrode thickness is 0.05λ, the coupling factor of Rayleigh SAW is about zero, in other words a spurious response is not generated, and that of Love wave becomes maximum at about θ =90°(Y-cut). So, Y-cut X propagation of Love wave on the $SiO_2/Cu/LiNbO_3$ structure is the best cut angle. Table I shows the TCF and the coupling coefficient of the SAW substrates tried for the W-CDMA duplexer. The Love wave on the $SiO_2/Cu/YX$-$LiNbO_3$ structure has similar coupling factor of the LSAW on the Al electrode/64°YX-$LiNbO_3$ substrate, which has been conventionally used for the W-CDMA SAW duplexer, and the Rayleigh SAW on this structure to generate the spurious responses has zero coupling factor. So this new structure is very suitable for the substrate for the W-CDMA duplexer.

Figure 2 shows the calculated reflection coefficient of the Love wave on this structure at an electrode finger when a metalization-ratio of interdigital transducer (IDT) is 0.5. The enough reflection coefficient as 0.15 is obtained when the thickness of the SiO_2 film and the Cu-electrode are 0.3λ and 0.05λ, respectively, though it is smaller than that of the structure having convex portions on the SiO_2 surface. Where the reflection coefficient was calculated by reference [8].

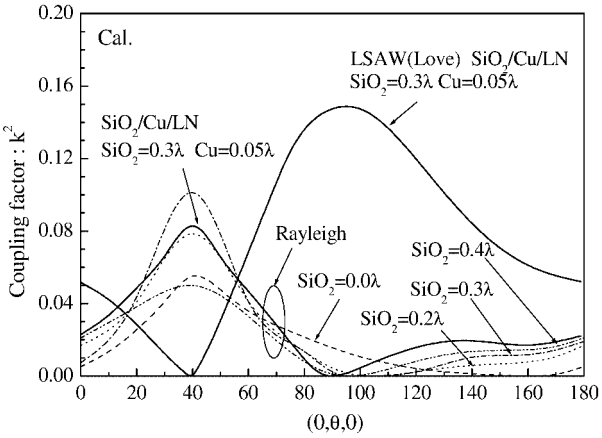

Fig1. Electromechanical coupling factor of Rayleigh SAW and LSAW on $SiO_2/Cu/LiNbO_3$ or $SiO_2/LiNbO_3$ as function of θ at $(0°, \theta, 0°)$.

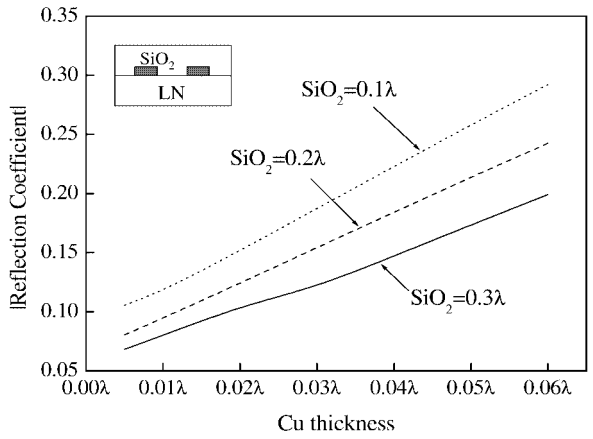

Fig2. Absolute value of Reflection coefficient of flattened-SiO_2/Cu-electrode/YX-$LiNbO_3$ as a function of Cu-electrode thickness at SiO_2 thickness of 0.1λ, 0.2λ, and 0.3λ.

Table I
Properties of SAW substrates for duplexer.

substrate	TCF ppm(°C)	Coupling factor k^2
Al/64°Y-X·LN	-80	0.18
SiO_2/Cu/36°Y-X·LT	0∼-10	0.06
SiO_2/Cu/Y-X·LN	0∼-20	0.15

The Love wave combining all of the SiO_2 film, the high dencity metal electrode (Cu-electrode), and $LiNbO_3$ substrate has been reported in 2003 by the authors [9] and in 2005 by Yamanouchi [10]. However, the reflection coefficient considering the structure with the IDT and the flattened SiO_2 film was reported in the former, not in the latter.

III. Characteristics of One-port Resonator

Figure 3 shows the measured impedance characteristics of the one-port resonators composed of an Al-electrode/64°YX-$LiNbO_3$ substrate and a flattened-SiO_2/Cu-electrodes/YX-$LiNbO_3$ substrate structure. A wavelength of SAW is 1.9μm, a number of IDT pair is 120, an aperture is 32μm, the thickness of Al and Cu-electrodes is 0.045λ and 0.05λ, the thickness of the SiO_2 film is 0.3λ, and a metalization-ratio of IDT is 0.5. The frequency of the impedance characteristics has been normalized by the resonant frequency fr (about 1.9GHz). The latter has wider bandwidth and larger impedance ratio than the former one. Where impedance ratio is 20 log(impedance of anti-resonant frequency/that of resonant one). Figure 4 shows the shifts of the anti-resonant frequency fa of both resonators in the temperature ranges from -20 to 80°C and Table II shows the resonant Q values (Qr), the anti-resonant Q values (Qa), the relative bandwidths, and TCFs of the anti-resonant frequency of both resonators. Although a spurious response appears near of the resonant frequency, it is clarified that the bandwidth, the resonant Q value, and the TCF of the flattened-SiO_2/Cu-electrodes/YX-$LiNbO_3$ structure is considerably improved as shown in Figs. 3, 4 and Table II.

As mentioned above, an angle θ , at which the coupling factor of Rayleigh SAW shows zero, depends on the thickness of the SiO_2 film and the Cu-electrode. The metalization-ratio of the IDT also influences this coupling factor. Therefore it is necessary to optimize θ precisely to suppress the spurious due to Rayleigh SAW according to the thickness of the SiO_2 film and the Cu-electrode, and the metalization-ratio of the IDT.

Figure 5 shows the measured impedance characteristics of the one-port resonators at the various angles θ of 88, 89, and 90°. The characteristics are normalized by the resonant frequency of about 1.9GHz. As shown in Fig.5, it is possible to suppress the spurious response due to the Rayleigh SAW by fine-tuning θ without deteriorating the main response.

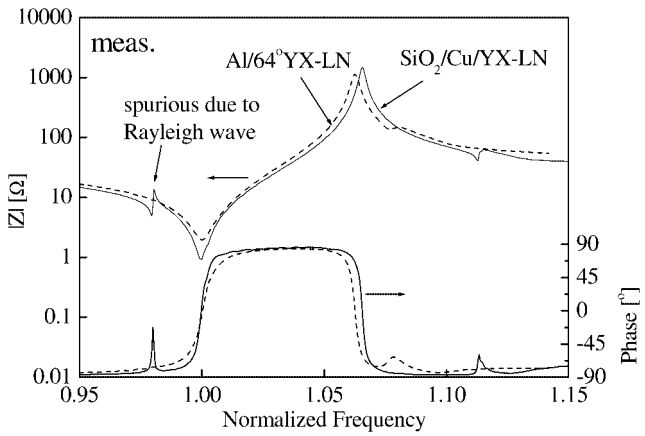

Fig3. Frequency characteristics of Al-electrode/64°YX-$LiNbO_3$ (dashed line) and flattened-SiO_2/Cu-electrode /YX-$LiNbO_3$(solid line).

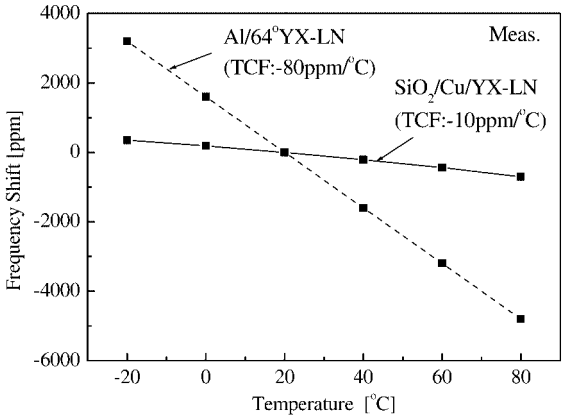

Fig4. Frequency shifts of Al-electrode/64°YX-$LiNbO_3$ and flattened-SiO_2/Cu-electrode/YX-$LiNbO_3$ as function of temperature change.

Table II
SAW properties of Al-electrode/64°YX-$LiNbO_3$ and flattened-SiO_2/Cu-electrode/YX-$LiNbO_3$ structure.

substrate	Qr	Qa	Band width (fa-fr)/fr	TCF(fa) (ppm/°C)
Al/64°Y-X·LN	155	330	0.063	-80
SiO_2/Cu/Y-X·LN	310	430	0.066	-10∼-20

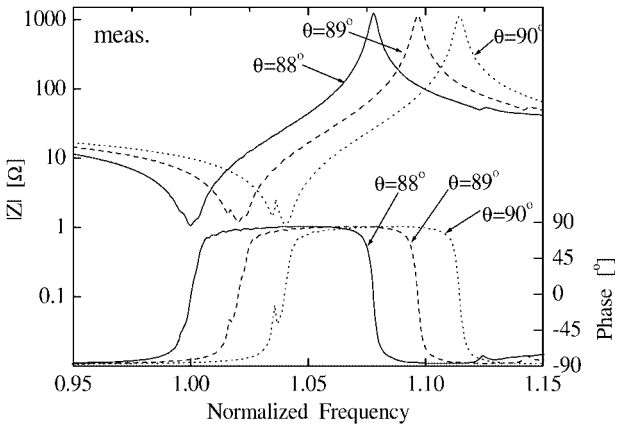

Fig5. Frequency characteristics of flattened-SiO_2 Cu-electrode /YX-$LiNbO_3$ at the various θ.

IV. Characteristics of SAW W-CDMA Duplexer

The small SAW duplexer for W-CDMA with good TCF has been realized by using this structure (flattened-SiO_2/Cu-electrode/YX-$LiNbO_3$). The Tx filter of the duplexer is a ladder type SAW filter composed of four series arm resonators and four parallel arm resonators. The Rx filter is also a ladder type one composed of three series arm resonators and three parallel arm resonators. Figs. 6 and 7 show the measured characteristics of the Tx and Rx filters of the newly developed duplexer, respectively. The bands used by three mobile communication carriers in Japan are shown in Fig. 6 for example.

Full band W-CDMA means the total 60MHz bandwidth of these three bands. The duplexer has good characteristics. The insertion loss of the Tx filter at the Tx band and the attenuation at the Rx band are comparatively good as 1.6dB and 45dB, in the full temperature range from -30 to +85°C. The insertion loss and the attenuation of Rx filter are also good as 2.0dB and 50dB, respectively, in the same temperature range. The frequency characteristics of this SAW duplexer are almost same compared with those of the FBAR.

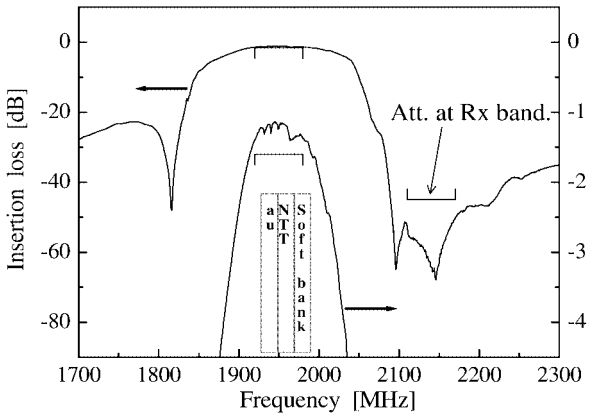

Fig6. Tx filter characteristics of newly developed SAW duplexer for W-CDMA.

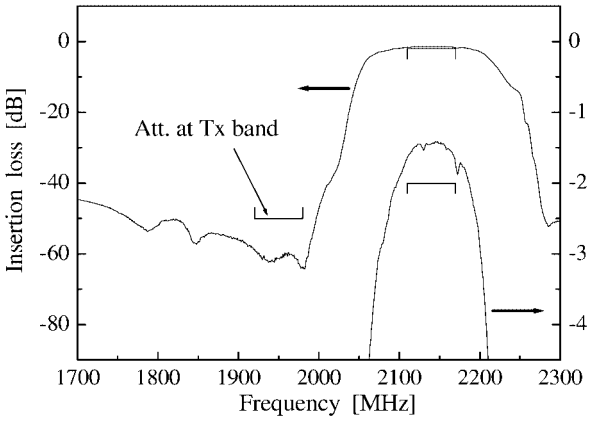

Fig7. Rx filter characteristics of newly developed SAW duplexer for W-CDMA.

Figures 8 and 9 show the measured characteristics of the Rx filters of the conventional duplexer composed of the Al-electrode/50-70°YX-$LiNbO_3$ and newly developed one composed of the flattened-SiO_2/Cu-electrode/YX-$LiNbO_3$ at the temperatures of -30°C, 25°C and 85°C, respectively. Though the duplexer composed of the Al-electrode/50-70°YX-$LiNbO_3$ shifts significantly by the temperature change, but that composed of the flattened-SiO_2/Cu-electrode/YX-$LiNbO_3$ shift slightly. By depositing the SiO_2 film of thickness 0.25λ, the TCF of the duplexer has been improved as -10 to -20ppm/°C which is about one-fourth of the conventional duplexer composed of the Al-electrode/50-70°YX-$LiNbO_3$. The package size of this duplexer is very small as $3.0\times2.5\times1.2mm^3$. The TCF of the newly developed SAW duplexer is better compared with that of the FBAR. The size is very small compared with those of the FBAR duplexers ($3.8\times3.8\times1.4mm^3$) and the dielectric ceramic duplexers($4.0\times9.0\times2.0mm^3$). The small SAW duplexer for 60MHz Full-Band W-CDMA having the good characteristics, the good TCF, the small size has been realized for the first time in the world. Moreover, a reliability of power handling and a climatic reliability have been guaranteed at a practical use condition.

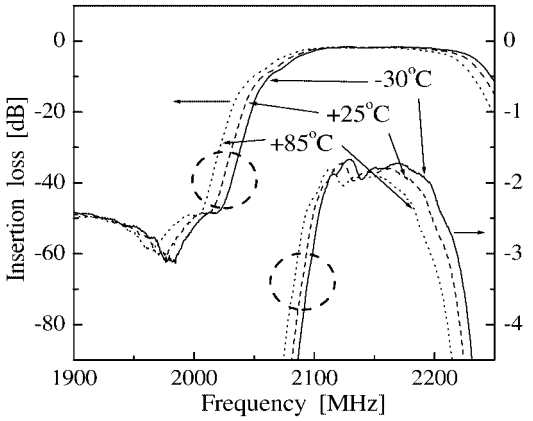

Fig8. Rx filter characteristics of conventional SAW duplexer at -30°C, 25°C, 85°C.

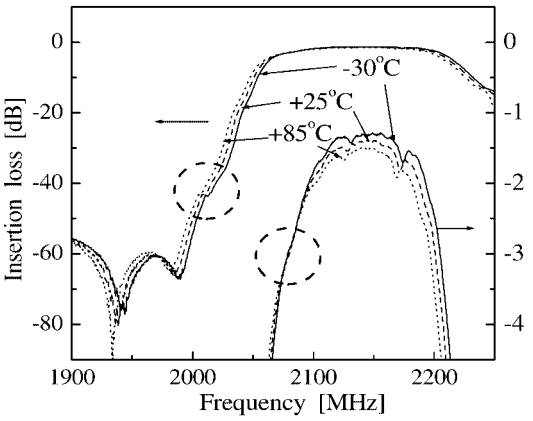

Fig9. Rx characteristics of newly developed SAW duplexer at -30°C, 25°C, 85°C.

V. Conclusion

By using the Love wave and by combining the flattened-SiO_2 film, the high density metal (Cu) electrode, and the YX-$LiNbO_3$ substrate, a new SAW substrate structure having a good resonant Q value, a good TCF and an optimum electromechanical coupling factor suitable for the W-CDMA duplexer have been obtained. By composing this structure, the new SAW duplexer for W-CDMA with 60MHz Full-Band having the good frequency characteristics and the good TCF (-10 to -20ppm/°C) and the small size ($3.0\times2.5\times1.2mm^3$) has been realized for the first time. The frequency characteristics are almost same, the TCF is best (smallest),

and the size is smallest compared with conventional duplexers.

Acknowledgement

The authors thank Mr. M. Hasegawa, Mr. K. Ikada, Mr. K. Sakaguchi, and so on for their assistance.

References

[1] P.D.Bradley, R. Ruby, A. Barfknecht, F. Geefay, C. Han, G. Gan, Y. Oshmyansky and J. Larson: Proc. IEEE Ultrason. Symp. (2002), p.861.

[2] M. Kadota, T. Nakao, N. Taniguchi, E. Takata, M. Mimura, K. Nishiyama, T. Hada and T. Komura: Proc. IEEE Ultrason. Symp. (2003)p.2105.

[3] J. Tsutsumi, S. Inoue, Y. Iwamoto, M. Miura, T. Matsuda and Y. Sato: Proc. IEEE Ultrason. Symp. (2004) p.954.

[4] R. Takayama, H. Nakanishi, Y. Iwasaki and T. Kawasaki: Proc. IEEE Ultrason. Symp. (2004)p.959.

[5] M. Kadota, T. Nakao, N.Taniguchi, E. Takata, M. Mimura, K. Nishiyama, T. Hada, and T.Komura: Jpn. J. Appl. Phys., 44, p.4527, 2005.

[6] AVAGO catalogue ACMD-7601(2006).

[7] J. J. Campbell and W.R.Jones: IEEE trans. Sonics & Ultrason., SU-15, p.209, 1968.

[8] T.Kojima and N.Kawai: Proc. IEEE Ultrason. Symp., (1996)p.299.

[9] M. Kadota, T. Nakao, and T. Hada: Japan Patent number P2003-346280(2003)(in Japanese).

[10] K. Yamanouchi, T. Yokoyama, and Y. Sato: 150th Committee on Acoustic Wave Device Technology 91th Technical Meeting p.33(2005)(in Japanese).

Prediction and Measurement of Boundary Waves at the Interface Between $LiNbO_3$ and Silicon.

S. Ballandras, V. Laude, H. Majjad, W.Daniau, D. Gachon, E. Courjon
Institut FEMTO-ST, UMR 6174 CNRS-UFC-ENSMM-UTBM,
Département LPMO, 32 Avenue de l'Observatoire, F-25044 Besançon Cedex, France
Ballandr@Femto-St.Fr

Abstract— **Interface acoustic waves (IAW) propagate along the boundary between two perfectly bonded solids. For a loss-less IAW, all displacement fields are evanescent along the normal to the boundary inside both solids, but a variety of leaky IAWs also exist depending on the selected combination of materials. When at least one of the bonded solids is a piezoelectric, the IAW can be excited by an inter-digital transducer (IDT) located at the interface provided one can fabricate the transducer and access the electrical contacts. Since the IDT always exhibits a finite thickness, this must be properly taken into account in the fabrication of actual devices. We discuss here the fabrication and characterization of IAW resonators made by indirect bonding of lithium niobate onto silicon. In our fabrication process, IDTs are first patterned over the surface of a Y-cut lithium niobate wafer. A thin layer of SU-8™ photo-resist is then spun over the IDTs and lithium niobate to a final thickness below one micron. The SU-8™ covered lithium niobate wafer is then bonded to a silicon wafer using a wafer bonding machine. The stack is subsequently cured and baked to enhance the acoustic properties of the interfacial resist. Measurements of resonators are presented with an emphasis on the dependence of propagation losses with the resist properties. Comparison with theoretical computations based on our periodic finite element/boundary element code allows for explaining the actual operation of the device**

Index terms – ***IAW, wafer bonding, Silicon, $LiNbO_3$, finite elements, boundary elements.***

I. INTRODUCTION

Wafer bonding for piezoelectric substrates is an application which has the potential to establish a key technology to realize passive devices for high frequency signal processing. Surface acoustic wave (SAW) devices classically are used for the fabrication of frequency references, sensors and filters. Several points related to aging, Q factor limitation, low cost packaging or sensitivity to electrical disturbances of the surface have to be enhanced. Interface acoustic waves (IAW) are at least in principle able to push back these restrictions. IAW, also named boundary waves, were first described by Stoneley [1]. Theoretical studies and the conditions of existence of interface acoustic waves for some piezoelectric substrates have been reported [2], [3]. Analysis methods used for SAW, i.e., the effective permittivity and the harmonic admittance computed within the Blötekjaer approach [4] were extended to IAW in classical piezoelectric cuts to estimate polarization, attenuation and coupling [5]. These first theoretical calculations more or less meet Hashimoto's results computed in a very similar approach [6]. Also more accurate predictions were achieved using our periodic mixed finite element analysis/boundary element method (FEA/BEM) computation code to take into account the actual shape of one transducer's period [7,8]. This approach provides a better analysis of the actual device operation modes.

Experimental results for IAW were claimed to be obtained with a $LiTaO_3$ substrate covered with a thick silicon oxide layer [9]. However, we consider that since the higher interface between SiO_2/air or SiO_2/vacuum is seen by the waves, they are much closer to Sezawa modes than to actual IAW. Note that other groups progress in the development of technological approach capable to provide true IAW devices [10].

Wafer bonding is a promising alternative to the deposition of thick layers. The main problem while bonding pre-processed wafers is the effect of surface roughness. We here report on the design and the fabrication of a device using a Y-cut lithium niobate ($LiNbO_3$) wafer bonded thanks to a thin epoxy-based photo-resist layer (SU-8™) to a silicon wafer [11]. The developed process uses IC-compatible micro-machining technologies which permit, in our case, batch fabrication of complete 3-inch wafers and wafer level packaging. The presence of this adhesive layer between the $LiNbO_3$ substrate and the Silicon wafer yields guiding conditions significantly different than the ideal wafer-to-wafer bounding hypothesis as considered in the Blötekjaër model. The agreement between theory and experimental results is finally emphasized.

The first section of the paper shows theoretical work dedicated to understand the wave guide operation accounting for the presence of the SU-8 ™ adhesive layer. Particularly, one can see the influence of the bounding thickness on the spectral density and the electromechanical coupling of the IAW guided at the interface. The following part presents technological developments achieved to build real devices (single port synchronous resonators). The third section is dedicated to experimental measurements, emphasizing the pertinence of our theoretical analysis. As a conclusion, we propose new perspectives for IAW-based devices.

II. THEORETICAL ANALYSIS

Figure 1. shows a schematic view of the structure considered in the analytical simulations. The effect of an intermediate layer was studied for the following structure, corresponding to the one of the devices manufactured.

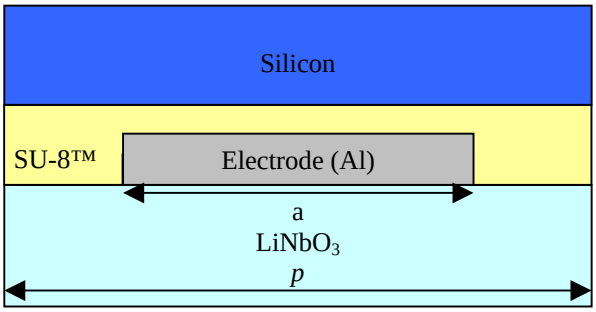

Figure 1. One period of a $LiNbO_3$/ SU-8™/ Si IAW structure with an aluminum electrode structured on the $LiNbO_3$ wafer.

In practice, the aluminum IDTs are deposited on the lithium niobate surface. Their actual thickness is not taken into account when simulating using the effective permittivity method. The silicon in the stack is considered as a (YX) cut semi-infinite substrate, the SU-8™ resist is 1 µm thick, the SiO_2 layer is a 360 nm thick PVD layer and the lithium niobate wafer corresponds to (YXl)/128° cut. The parameters (elastic, dielectric and piezoelectric constants) of the various materials are well-known in the literature, except for the SU-8™ resist. This resist is not dedicated to this type of application, however we will show that is possible to obtain interface acoustic wave devices, although the resist presents more acoustic losses than a single-crystal material. The SU-8™ resist parameters (considered as an isotropic dielectric) are as follows:

- density : 1190 kg/m^3,
- Young's modulus : 4.02 GPa,
- Poisson's ratio : 0.22,
- Dielectric permittivity : 3.

The Young's modulus is particularly low (nearly 50 times lower than the lithium niobate c_{11}), SU-8™ is in fact a material far from rigid and has very low longitudinal and transverse acoustic velocities. The components of the SU-8™ elastic tensor are: c_{11} = 4.59 GPa, c_{12} = 1.29 GPa and thus c_{66} = 1.65 GPa.

Simulations first were carried out with different values of SU-8™ losses in order to check the influence of this fundamental but initially unknown parameter. Losses are measured by a visco-elasticity coefficient η, so that an imaginary part is added to the elastic constant according to the visco-elasticity coefficient by the angular frequency product: $\omega\eta$. The simulations depicted in Figure 2 and Figure 3 show that moderate SU8 losses (the fitted visco-elasticity coefficient is approximately ten times that of silicon) can lead to relatively important losses for the interface mode. These results will be compared with experimental results.

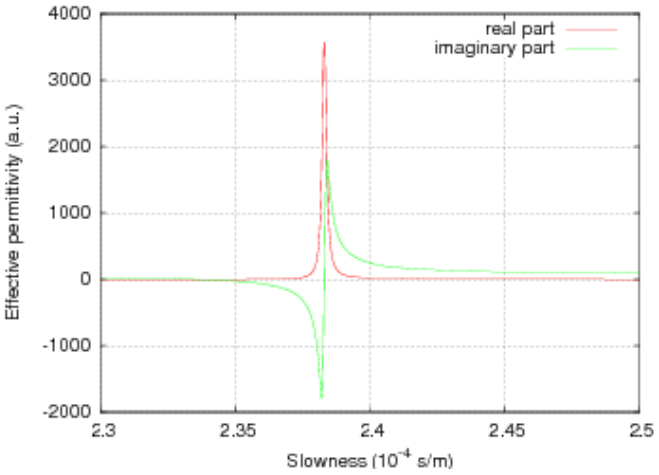

Figure 2. Resonance calculated by the interface effective permittivity method by neglecting the SU8 acoustic losses. Losses are 0.01 dB/λ (Q around 2000) and are only due to imperfect guiding at the interface.

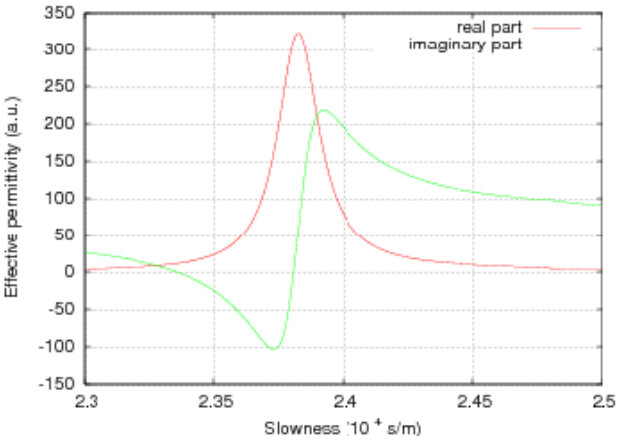

Figure 3. Resonance calculated by the interface effective permittivity method by considering acoustic losses in the SU8 (η=10 Ns/m2). The losses are 0.23 dB/λ (Q around 100).

Once those parameters fixed, one can simulate the structure to be fabricated. A first computation is performed considering the assembly of (YX) silicon and (YX) $LiNbO_3$ but neglecting the presence of the adhesive SU-8™ layer and considering silicon as perfectly dielectric. A shear-polarized interface mode is found with a phase velocity close to 4600m.s^{-1} exhibiting an electromechanical coupling of 4%. Introducing then the SU-8™ layer significantly change the spectral behavior of the device, showing two modes contributing to the harmonic admittance at lower frequencies (phase velocity respectively near 3800m.s^{-1} and 4200m.s^{-1}). The slowing down of the wave is easily explained by the presence of the SU-8™ adhesive layer for which bulk wave velocities are respectively in the vicinity of 2000m.s^{-1} (longitudinal) and 1200m.s^{-1} (shear). Figure 4 compares the two situations by superposing the corresponding harmonic admittances.

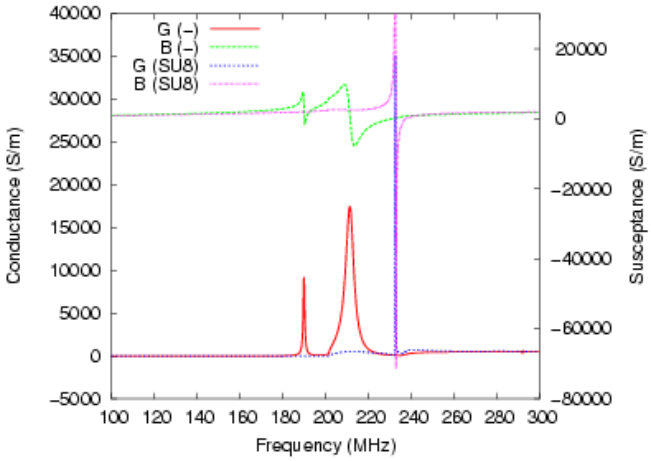

Figure 4. Harmonic admittances computed using the Blötekjaër model, without and with the adhesive layer accounted for.

One can note of course the increase of losses due to the adhesive layer, but also the strong value of the electromechanical coupling coefficient of the second mode (16%) that approaches the one of the leaky shear mode on the free surface of $LiNbO_3$ (YX) cut. We then compare both cases of SAW excitation at the surface of semi-infinite $LiNbO_3$ (YX) cut and at the Si/LiNbO3 interface accounting for the 1 µm thick adhesive layer. The corresponding harmonic admittance are reported if fig.5.

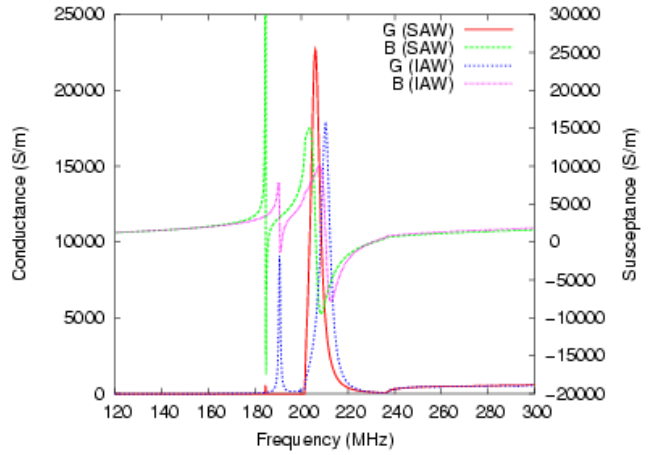

Figure 5. Harmonic admittances computed using the Blötekjaër model, comparison between IDT response on a semi-infinite (YX) LiNbO3 wafer and at the Silicon/Niobate interface accounting for the adhesive layer.

This plot tends to demonstrate that a wave exhibiting a polarization close to the one of the Rayleigh wave still exists but is accelerated at the Silicon/Niobate interface because of the presence of the adhesive layer, whereas the leaky shear wave of the free surface is slowed down due to the very small shear velocity in the SU-8™ layer. Consequently, we assume that reducing the SU-8™ layer should increase the wave velocities, reduce the shear mode electromechanical coupling and yields the spectral behavior of the device closer to the one without adhesive layer. This is shown in fig.6, where the SU-8™ thickness has been reduced to 0.5 µm, the corresponding admittance being compared to the one with 1µm thick SU-8™ layer.

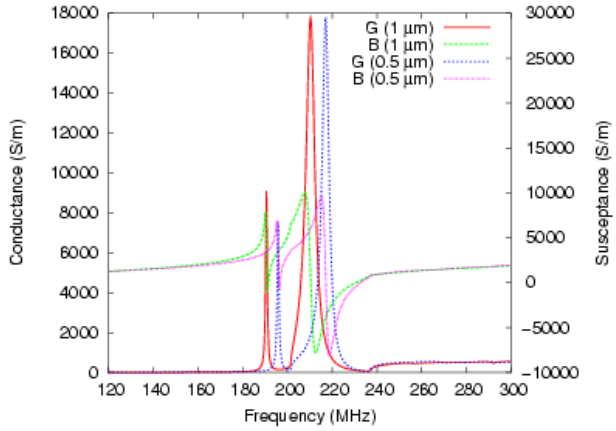

Figure 6. Harmonic admittances computed using the Blötekjaër model, comparison between IDT response at the Silicon/Niobate interface for 2 different thickness of the adhesive layer.

It clearly appears in fig.6 that the Rayleigh-like wave velocity increase whereas its coupling decreases when reducing the SU-8™ thickness. In the same time, the Q factor of the shear mode tends to increase and its electromechanical factor falls down. Further reduction of the adhesive layer thickness is expected to provoke the vanishing of the Rayleigh -like wave, the admittance tending asymptotically to the one of the Blötekjaër analysis without Su-8™.

To confirm these results, mainly concerning the nature of the wave and their polarization, we have computed the harmonic admittance considering the nominal adhesive layer thickness using our periodic FEA/BEM code [7] and compared it to the Blötekjaër analysis results. The implemented mesh is plot in fig.7, giving the definition of the computation conditions.

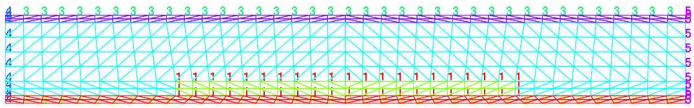

Fig.7 Implemented mesh for the simulation of interface wave excitation and guiding using a periodic FEA/BEM computation code. The boundary numbers correspond to the applied boundary conditions, i.e. unit voltage excitation applied on boundary #1 , periodicity conditions applied to boundaries #4 and #5, radiation in silicon applied to boundary #3 and radiation in lithium niobate applied to boundary #2.

Figure 8 shows a very nice agreement between both theoretical approaches (as expected), the only difference being due to the massive electrode taken into account in the FEA/BEM computation. We have reported in fig.9 and 10 deformed mesh sequences illustrating the Rayleigh-like and shear mode polarizations. They correspond to a decomposition of one time period in a 4 phase sequence (φ=0 to $3\pi/4$), providing clear evidence of the above analysis of the wave polarization. The iso-values correspond to displacement along x1 (propagation direction). For both modes, the polarization is general, but one can easily recognize the dominance of elliptic (fig.9) and shear polarization (fig.9).

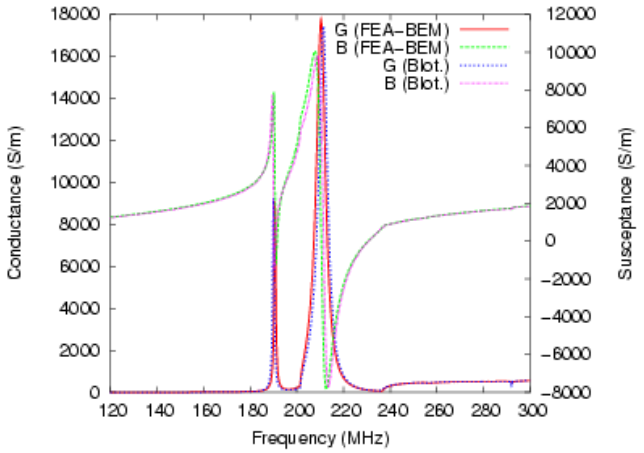

Fig.8 Comparison between harmonic admittances of the Si/SU-8™/$LiNbO_3$ IAW guide provided by the Blötekjaër and the FEA/BEM analyses. The slight differences between both results is due to mass loading accounted for in the FEA/BEM simulation (200 nm thick Al electrode)

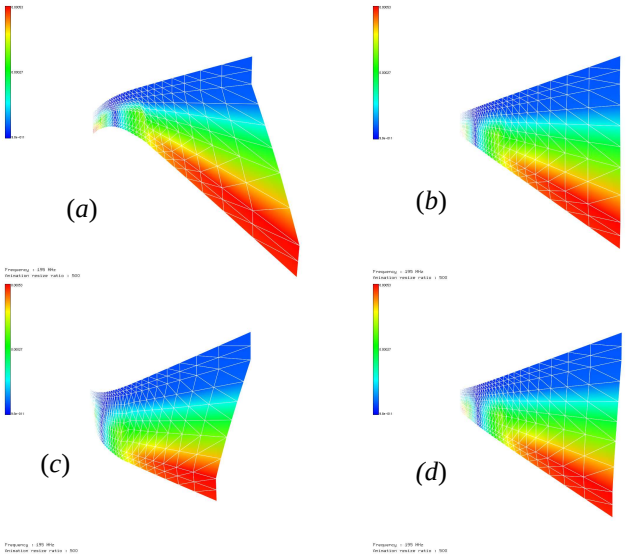

Fig.9 Quadrature sequences of the dynamic deformation of the Rayleigh-like mode (*a*)φ=0 ; (*b*) $\varphi=\pi/4$; (*c*) $\varphi=\pi/2$; (*d*) $\varphi=3\pi/4$

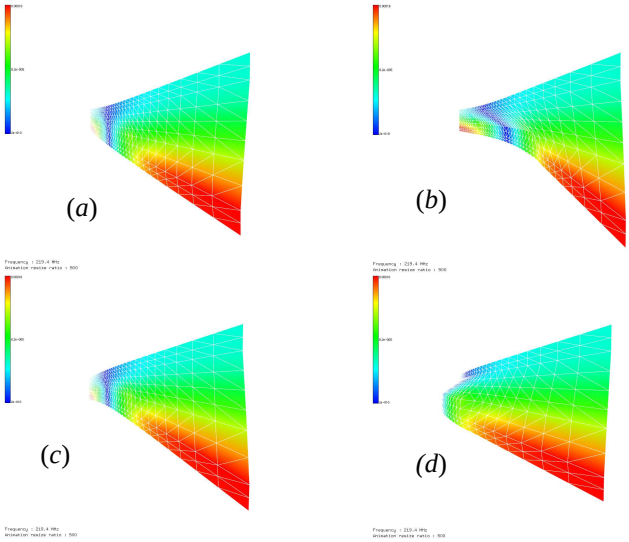

Fig.10 Quadrature sequences of the dynamic deformation of the shear mode (*a*)φ=0 ; (*b*) $\varphi=\pi/4$; (*c*) $\varphi=\pi/2$; (*d*) $\varphi=3\pi/4$

III. IAW Device Fabrication

General wafer bonding technology can be divided in two main branches, direct bonding and intermediate layer bonding [12]. Currently, wafer bonding of piezoelectric substrates receives a certain interest [13]. However wafer surface waviness and roughness are critical issues in direct bonding. Hence a low temperature bonding method using photosensitive material as adhesive intermediate layer was developed that is based on chemical surface hydrophilization and SU-8™ resist. First, the aluminium (Al) inter-digital transducers (IDT) are realized on the lithium niobate wafer. A SU-8 layer is spun on the $LiNbO_3$ wafer. A silicon wafer with wet-etched vias then is bonded to the $LiNbO_3$ substrate. The possibility to combine in this case IAW devices with silicon microelectronics is a significant long run motivation. The fabrication and wafer bonding process are schematically summarized in Figure 11.

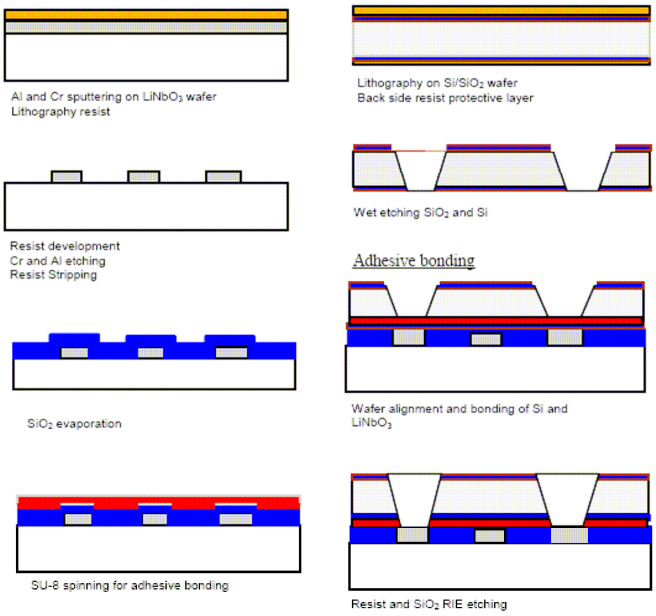

Fig.11 Flow chart for the adhesive wafer bonding process.

The starting substrate is a 0.5 mm thick 3-inch (YX) cut $LiNbO_3$ wafer. A 220 nm thick Chromium-Aluminum layer is sputtered on the polished side of the wafer. The photo-resist then is spun to form a 1.4 µm thin layer, on which prebake and hardbake are applied. The mask used for the photolithographic step has typical IDT patterns with a minimum finger size of 1 µm.

Once the resist developed, the metal layer is wet etched providing the usual IDT's grating pattern. The $LiNbO_3$ substrate then can be passivated using a SiO_2 layer. This silicon dioxide layer is assumed to protect the aluminum resonators during the harsh cleaning treatment before bonding, but this step can be well omitted because the SU-8™ also acts as an insulating layer.

Before any bonding operation, vias must be achieved in the silicon plate to access the electrodes and to probe the device. The starting substrate is a 0.25 mm thick 3 inch silicon wafer (100) covered with a uniform 1.4 µm thermal oxide layer. The SiO_2 layer then is etched locally thanks to a standard

lithography process, creating an in-situ mask for potassium hydroxide (KOH) silicon anisotropic deep etch. Afterwards, A re-oxidation of the wafer is done to obtain a SiO_2 thickness of 0.4 µm.

The wafers are cleaned to remove any kind of contaminants due to the process. Hydrophilic treatment on the Si/SiO_2 is achieved. The exact cleaning process is detailed in [9]. After that, Epon SU8-2001 is conventionally spun on the $LiNbO_3$ wafer to obtain 1 µm thick layer. A 30 min relaxation time on a flat support is respected to get an uniform coating on the wafer. The Si and $LiNbO_3$ wafers are aligned in an EVG 620 aligner. The pair is subsequently transferred to an EVG 501 bonder. The chamber of the wafer bonding machine is purged and evacuated to 10^{-3} mbar. The temperature rate in the heating process of the wafers is 1◦C/min from room temperature to 65◦C. Bonding occurred at 65◦C under a pressure of 500 N for 1 h. After bonding, the stacked wafers are annealed at 65 °C, for 1 hour in atmospheric N_2 ambient to enhance the bonding strength. The temperature then is decreased to room temperature with a 1◦C/min slope. Figure 12 displays the result obtained after the low temperature wafer bonding process.

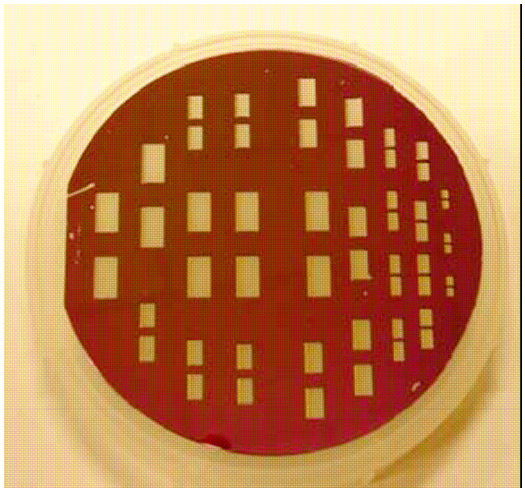

Fig.12 Picture of the 3-inches bonded wafers (LN/Si) from the silicon side

Cross-sectional cuts are made with a dicing saw on the bonded device to analyze the bonding process, by imaging the bonded interface using scanning electron microscope (SEM). An example of a SEM picture is shown in Fig. 13, showing a very high quality bonding between the two wafers.

After the bonding process, SU-8™ and SiO_2 layers still remain inside the vias devised for electrical contact. SU-8™ hashing and SiO_2 etching are performed in a PLASSYS reactive ion etching reactor. The remaining resist is dry etched with a gas mixture composed of oxygen and C_2F_6. We chose to dry etch SiO_2 using CHF_3 and C_2F_6 reactive ion etching (RIE). A thin resist layer is deposited on the $LiNbO_3$ back side to reduce spurious bulk acoustic wave (BAW) reflections. The stack then is diced for measurement.

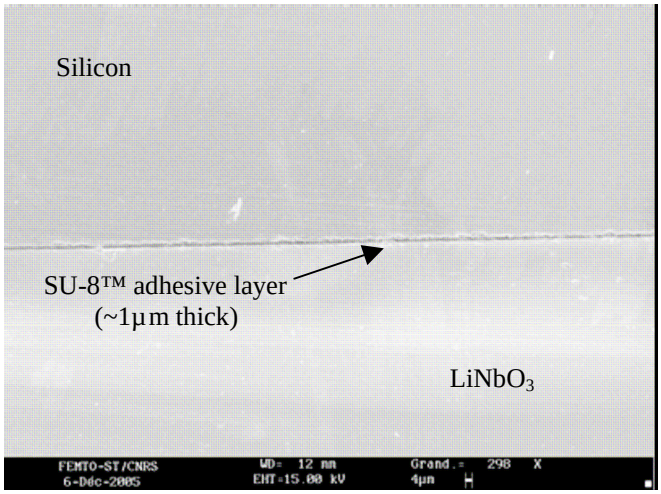

Fig.13 SEM picture of the stack after sawing. It shows the Lithium Niobate wafer, the adhesion interface and the Silicon substrate.

IV. MEASUREMENTS

The devices first have been characterized under RF probes connected to a network analyzer Rohde & Schwarz ZVCE. The wavelength of the tested devices has been set to 5µm, 3.3 µm and 2.8 µm respectively, yielding a minimum strip width of 0.7 µm near the very limit of our mask aligner. Most devices have been successfully tested but also have been found to suffer from parasitic elements limiting the measurement quality. Figures 14, 15 and 16 display the admittance derived from the S11 parameter of the tested devices. They show the existence of two modes as expected theoretically, corresponding to phase velocities near 3600 $m.s^{-1}$ and 4600 $m.s^{-1}$. Although this data are not that close from the above theoretically predicted values, one should keep in mind that the operation condition also are far from the reported analysis, explaining the enlargement of the frequency gap between the Rayleigh-like and the shear interface modes (the relative thickness of the adhesive layer is much larger than the one considered in our computations). Consequently, these results can be considered as rather satisfying assessment of the proposed analysis.

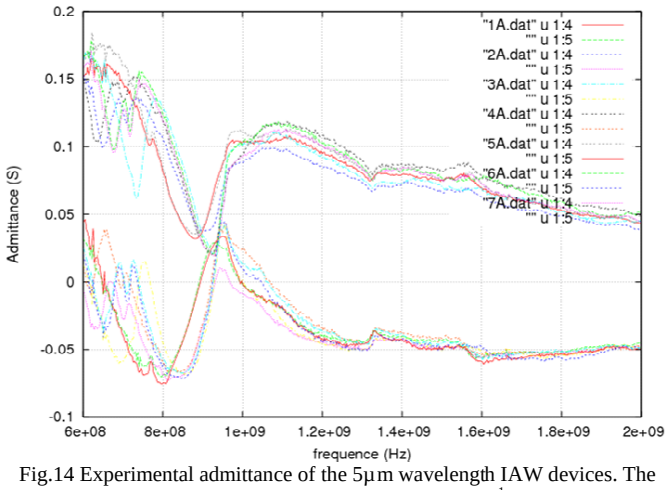

Fig.14 Experimental admittance of the 5µm wavelength IAW devices. The Rayleigh-like mode is found to propagate near 3600 $m.s^{-1}$ whereas the shear mode exhibits a phase velocity close to 4500 $m.s^{-1}$.

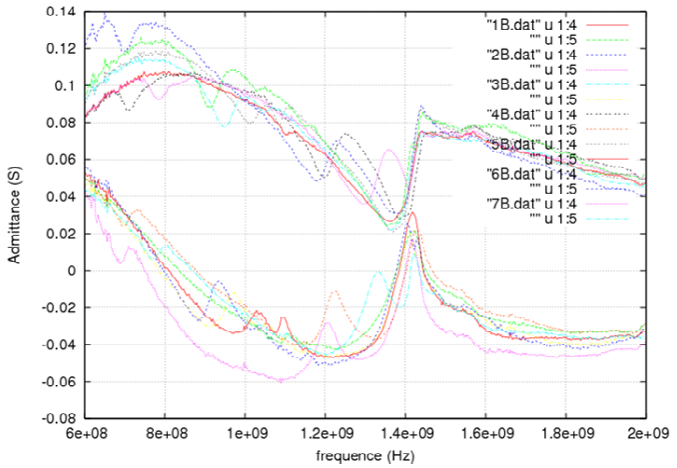

Fig.15 Experimental admittance of the 5µm wavelength IAW devices. The Rayleigh-like mode is found to propagate in the range [3100-3800] m.s^{-1} whereas the shear mode exhibits a phase velocity close to 4620 m.s^{-1}.

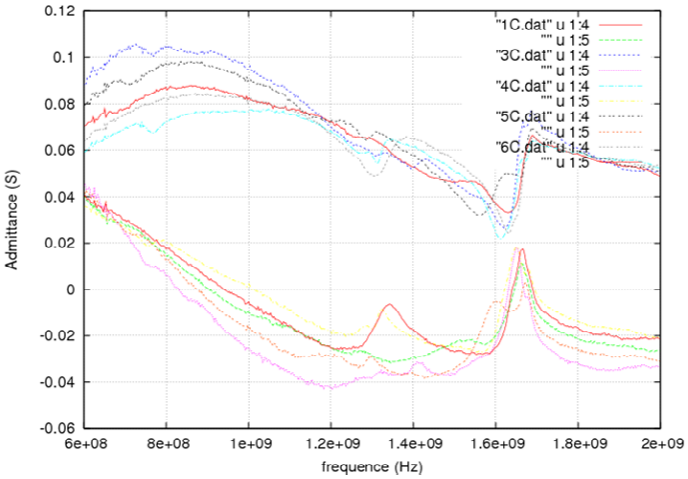

Fig.15 Experimental admittance of the 5µm wavelength IAW devices. The Rayleigh-like mode is found to propagate near 3640 m.s^{-1} whereas the shear mode exhibits a phase velocity close to 4760 m.s^{-1}.

V. Conclusion

A theoretical analysis of the operation of IAW has been proposed to describe the characteristics of a wave guide composed of a Silicon wafer and a Lithium Niobate wafer bonded together thanks to an adhesive layer, accounting for the presence of the excitation/detection electrode grating. Two modes are guided at the interface, the first being close to the free-surface Rayleigh wave and the second exhibiting a quasi-shear polarisation. A low temperature wafer hetero-bonding process of Lithium Niobate onto Silicon also has been achieved, exploiting a thin spin-coated SU-8™ film as an adhesive layer. It is the first experimental demonstration of interface acoustic wave devices made with the wafer bonding technique and operating at frequencies larger than 1 GHz. It is found that the presence of an adhesive layer between the $LiNbO_3$ wafer and the Silicon wafer leads to losses on the IAW modes, but allows for the excitation of a highly coupled shear mode (K_s^2>10%). Experiments are on going to increase device frequencies up to 2 GHz. Investigations are under way in order to decrease losses due to the adhesive wafer bonding by using harder layers obtained by spin on glass (SOG). The extension of the developed processes to other piezoelectric substrates such as lithium tantalate is also planned.

Acknowledgments

This work was supported by DGA/STTC under contract n° 04.34.017.

References

[1] R. Stoneley, “Elastic waves at the surface of separation of two solids,” Proc. Roy. Soc., vol. A106, pp. 416–428, 1924.

[2] C. Maerfeld and P. Tournois, “Pure shear surface wave guided by the interface of two semi-infinite media,” Appl. Phys. Lett., vol. 19, pp. 117–118, 1971.

[3] Y. Shimizu and T. Irino, “Stoneley waves propagating along an interface between piezoelectric material and isotropic material,” Proc. of the IEEE Ultrasonics Symp., pp. 373, 1983.

[4] K. Blötekjaer, K. A. Ingebrigtsen, H. Skeie, “A method for analysing waves in structures consisting of metal strips on dispersive media,” *IEEE Trans. Ultrason.,Electron., Devices*, vol. 20, no. 6, pp. 1133-1138, 1973.

[5] S. Camou, V. Laude, T. Pastureaud, S. Ballandras, “Interface acoustic waves properties in some common crystal cuts,” *IEEE Trans. Ultrason., Ferroelect., Freq. Contr.*, vol. 50, no. 10, pp. 1363-1370, 2003.

[6] K.Y. Hashimoto, T. Yamashita, M. Yamaguchi, “Highly piezoelectric shear-horizontal-type boundary waves”, Jpn J. Appl. Phys., V. 36, pp. 3057-3059, 1997

[7] S. Ballandras, V. Laude, A. Reinhardt, M. Wilm, R. Lardat, W. Steichen, T. Pastureaud, “Optimisation and Improved Convergence of Coupled Finite Element/Boundary Element Analyses”, proc. of the IEEE Ultrasonics Symp., pp. 679- 682, 2005

[8] S. Clatot, V. Laude, A. Reinhardt, M. Wilm, W. Daniau, S. Ballandras, R. Lardat, M. Solal, “Sensitivity of Interface Acoustic Waves to the Nature of the Interface”, Proc. of the IEEE Ultrasonics Symp., pp. 2126-2129, 2003

[9] K. Yamanouchi, K. Iwahashi, and K. Shibayama, “Piezoelectric acoustic boundary waves propagating along the interface between SiO2 and LiTaO3,” IEEE SU 25 (6) 384-389, 1978.

[10] Nobuhiro Tai‡, Tatsuya Omori, Ken-ya Hashimoto, Masatusune Yamaguchi, “Fabrication of Si/inlaid-IDT/LiNbO3 structure for acoustic boundary wave devices”, 27th Symposium on ULTRASONIC ELECTRONICS, Nagoya, 2006

[11] D.Gachon, G. Lengaigne, H. Majjad, S. Benchabane, S. Ballandras, V. Laude, “High frequency bulk acoustic wave resonator using thinned monocrystalline lithium niobate,” Proc. of the 20th European Frequency and Time Forum, March 27-30, 2006, Braunschweig (Germany), to be published.

[12] C.T. Pan, P.J. Cheng, M.F. Chen and C.K. Yen, “Intermediate wafer level bonding and interface behavior,” Microelectronics Reliability, Volume 45, Issues 3-4, pp. 657-663, 2005.

[13] T. Ohtsuchi, M. Sugimomto, T. Ogura, Y. Tomita, O. Kawasaki, K. Eda, “Shock sensors using direct bonding of LiNbO3 crystals,” Proc. of the IEEE Ultrasonics Symp., pp. 331-334, 1996.

Low-loss and Extremely-wideband SAW filters on a Cu-Grating/Rotated-YX-$LiNbO_3$ structure

Tatsuya Omori, Ken-ya Hashimoto and Masatsune Yamaguchi
Department of Electronics and Mechanical Engineering, Chiba University
Inage-ku, Chiba 263-8522, Japan

***Abstract*— This paper discusses a very low-loss and extremely-wideband SAW devices employing highly piezoelectric Love wave propagating on Cu-grating/15°YX-$LiNbO_3$ structure. Theoretical analysis followed by some experiments shows that the structure supports non-leaky Love wave with its coupling factor K^2 of 30% and makes Rayleigh wave spurious responses considerably small. Width and length modulated dummy electrodes are proposed for the suppression of transverse mode spurious responses in one-port resonators based on Cu-grating/15°YX-$LiNbO_3$ structure. Finally, one-port resonators on Cu-grating/15°YX-$LiNbO_3$ are applied to the development of ladder type filters in 1 GHz range. As a result, the minimum insertion loss and −3 dB bandwidth obtained are 0.8 dB and 19%, respectively, showing superior performance of the Cu-grating/15°YX-$LiNbO_3$ structure.**

I. Introduction

Filter devices having low-loss and extremely wide passband width are required for future wireless communication systems. Such wideband filters may also become one of the breakthroughs for developing novel inductor devices for MMICs. Against this situation, research interest in wideband filter devices has long been focussed upon highly piezoelectric SH type surface acoustic waves (SAWs) propagating on YX-$LiNbO_3$, which are really promising and possess their K^2 of nearly 25%[1]. Because of their higher velocities than slow-shear bulk waves, however, SH type SAWs on YX-$LiNbO_3$ are substantially of leaky nature. This means that either an Au film or a very thick (more than 0.12λ) Al grating is needed to convert leaky SH type SAWs into non-leaky Love wave[2], [3]. When applying non-leaky Love wave on YX-$LiNbO_3$ to practical devices, however, one should also be careful how the effect of Rayleigh type SAWs (Rayleigh wave) simultaneously launched is avoidable to minimise spurious responses. For the minimised Rayleigh wave excitation, the previous work[2] also suggested that 15°YX-$LiNbO_3$ could be superior to pure YX-$LiNbO_3$.

From this point of view, this paper proposes the application of Cu as a grating electrode material aiming at developing extremely-wideband and low-loss RF SAW filters using Love wave on 15°YX-$LiNbO_3$.

First, theoretical analysis of Love and Rayleigh wave propagation on Cu-grating/15°YX-$LiNbO_3$ structure is made showing how Cu grating electrodes are effective in reducing the velocity of Love wave without badly affecting K^2. It is also shown that the excitation of spurious Rayleigh wave gets considerably suppressed by the combination of Cu grating electrode and 15°YX-$LiNbO_3$. The result of theoretical analysis is followed by some experiments.

Then, the effect of weighted dummy electrode is analysed by the potential theory, from which a novel method emerges for suppressing transverse mode spurious responses. The design consideration of dummy electrodes based on the method is confirmed in one-port Love wave resonators on Cu-grating/15°YX-$LiNbO_3$.

Finally, one-port Love wave resonators on Cu-grating/15°YX-$LiNbO_3$ are applied to the development of ladder type SAW filters having extremely wide passband and very low-loss properties. Although a considerable passband dip originating in Rayleigh wave is not easily removed by the weighted dummy electrodes, an additional experiment reveals that a viscous film coated on the device surface is most effective in suppressing the dip to less than a half without badly affecting the overall filter performance.

II. SAW propagation on Cu-grating/rotated-YX-$LiNbO_3$ structure

Ref. [2] reported that two types of SAWs propagate under a grating structure on YX-$LiNbO_3$; one is Love wave and highly piezoelectric. The other is Rayleigh wave and its electromechanical coupling is quite small. Although Love wave is substantially of leaky nature, its velocity decreases with an increase in the thickness of grating electrodes and finally becomes non-leaky, when its velocity gets smaller than the slow-share bulk acoustic wave velocity V_B. If one attempts to apply this highly piezoelectric and non-leaky Love wave on YX-$LiNbO_3$ to practical devices, however, spurious responses originating in Rayleigh wave appear. In order to deal with this problem, Refs. [2] and [3] showed that the electromechanical coupling of Rayleigh wave is minimised in 15°YX-$LiNbO_3$, where either expensive Au films or very thick Al films is needed as a grating electrode material to make Love wave non-leaky.

In accordance with the previous work, Love and Rayleigh wave propagation in Cu-grating/15°YX-$LiNbO_3$ structure[4] was theoretically analised, where Cu gratings are expected to be more effective in reducing Love wave velocity than Al gratings. The analysis was made by using the input admittance $Y(f)$ for infinitely long IDTs[5]. Once the resonance frequency f_r and anti-resonance frequency f_a are determined by $Y(f)$, they can be converted to the effective SAW velocities V_r and V_a, respectively, by multiplying the grating pitch $2p$. The effective electromechanical coupling factor K^2 was estimated by $(\pi f_r/2f_a)\cot(\pi f_r/2f_a)$.

Figure 1 shows the Love and Rayleigh wave velocities as a function of the normalised Cu film thickness $h/2p$ of grating electrodes. It is seen from the figure that Love wave becomes non-leaky when $h/2p$ is greater than about 5%, where both V_r and V_a are smaller than V_B. The calculation also showed that

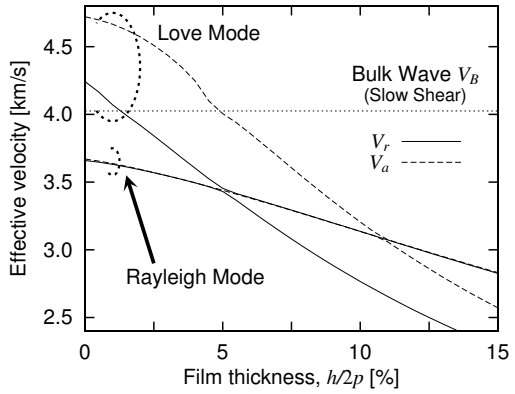

Fig. 1. Film thickness dependence of the effective velocities of Love and Rayleigh waves propagating in Cu-grating/15°YX-$LiNbO_3$ structure.

when Al is used as a grating electrode material, its film thick making Love wave non-leaky should be more than two times the thickness shown in Fig. 1.

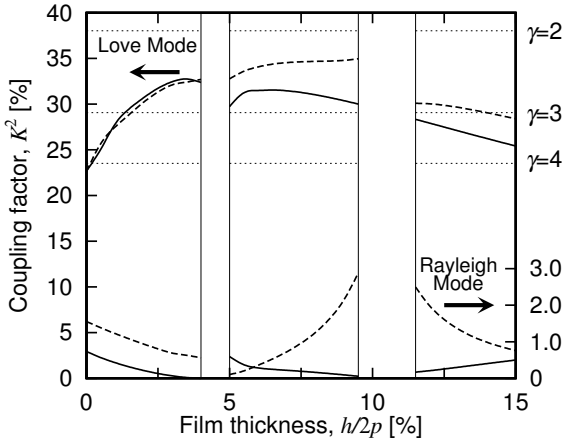

Fig. 2. Film thickness dependence of the effective electromechanical coupling factor K^2 of Love and Rayleigh waves propagating in Cu-grating/YX-$LiNbO_3$ (broken line) and Cu-grating/15°YX-$LiNbO_3$ (solid line) structures. (γ is the capacitance ratio estimated by $\gamma = \{(V_a/V_r)^2 - 1\}^{-1}$)

Fig. 2 compares K^2 in Cu-grating/15°YX-$LiNbO_3$ and Cu-grating/0°-YX-$LiNbO_3$ structures. In the figure, K^2 is not shown in a certain range of $h/2p$, where the strong coupling between Love and Rayleigh waves occurs.

It is seen that K^2 for Love wave in both structures is more than 30% in the range of $h/2p$ of about $5 \sim 10\%$. On the other hand, K^2 for Rayleigh wave is remarkably reduced in Cu-grating/15°YX-$LiNbO_3$ structure. This suggests that Cu-grating/15°YX-$LiNbO_3$ structure could be applied to spurious free devices.

According to the above discussion, one-port resonators were fabricated on Cu-grating/0°YX-$LiNbO_3$ and Cu-grating/15°YX-$LiNbO_3$ structures. Both resonators possess the electrode configuration shown in Fig. 3 with $h \simeq 300$ nm ($h/2p \simeq 7.5\%$).

Figure 4 shows the measured input admittance of the two resonators. Comparing Fig. 4(a) with Fig. 4(b), one can see that the spurious response caused by Rayleigh wave is

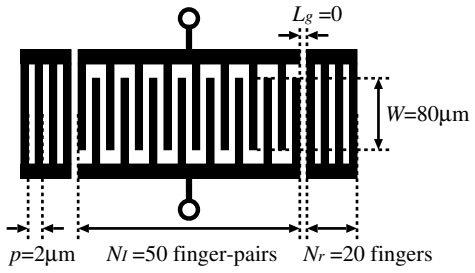

Fig. 3. Electrode configuration of fabricated one-port resonator.

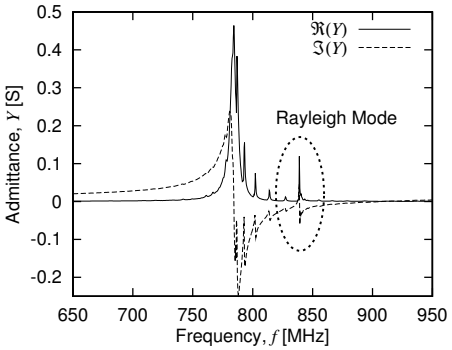

(a) Cu-grating/YX-$LiNbO_3$

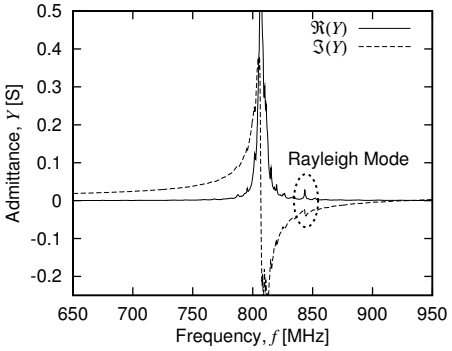

(b) Cu-grating/15°YX-$LiNbO_3$

Fig. 4. Admittance characteristics of fabricated one-port resonators.

markedly reduced by using 15°YX-$LiNbO_3$; it is still not negligible in practical device applications, though.

In addition to the Rayleigh wave spurious response, different kinds of spurious responses are observed in both structures. They are thought to be the contribution from transverse modes propagating obliquely in the waveguide structure composed of the grating and bus-bars.

III. Suppression of Transverse Mode Spurious Responses

The section discusses a technique of suppressing the transverse mode spurious responses appearing in the resonators on Cu-grating/15°YX-$LiNbO_3$ structure by applying weighted dummy electrodes.

A. Design of weighted dummy electrode

The length weighting for dummy electrodes (see Fig. 5) is known as one of the effective methods of suppressing spurious

responses caused by transverse modes[6]. If the dominant S_0 mode is trapped in the interdigital electrode region and much of the energy of all other spurious modes penetrates into the dummy electrode region, it is very likely that the spurious modes are only affected and suppressed by the weighted dummy electrodes. In Cu-grating/15°YX-$LiNbO_3$, however, there is a situation where the transverse spurious modes are also trapped in the interdigital electrode region because of their high electromechanical coupling. This suggests that careful design procedures should be needed to suppress the spurious responses by the dummy electrodes.

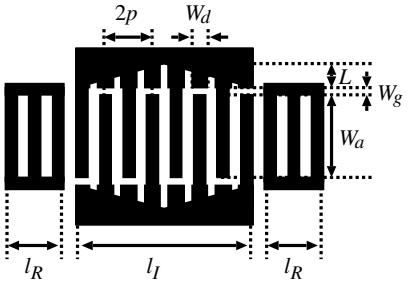

Fig. 5. Configuration of resonator with weighted dummy electrodes.

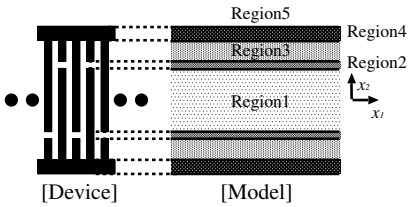

Fig. 6. Simplified model used in calculation.

By applying the scalar potential theory[7], the calculation was carried out to make it clear how the dominant and spurious modes behave in a planer transmission line structure consisting of gaps, dummy electrodes and bus-bars as well as interdigital electrodes[8]. Figure 6 shows the simplified model, in which Regions 1 to 5 represent the interdigital electrode region, gaps, dummy electrode regions, bus-bars and free surface, respectively. In the calculation, the anisotropic acoustic and piezoelectric properties were taken into consideration using the parabolic approximation, and it was assumed that the parabolic curves for the approximation are similar figures each other in the whole region, i.e., in Region 1 to 5. This is because the mechanical and electrical effect of the electrodes and bus-bars results in a small change in the anisotropy parameter in the parabolic approximation[9], [10].

Figure 7 shows the relation between the resonance frequencies of the transverse modes ($S_0, S_1, \cdots$) and the length of the dummy electrodes L. The IDT pitch $2p$, IDT aperture length $W_a/2p$, gap width $W_g/2p$ and electrode film thickness $h/2p$ are assumed to be 4 μm, 6.0, 0.125 and 0.065, respectively. In the calculation, the relative width of the dummy electrodes $W_d/2p$ was set at 0.25 and 0.28 in Figs. 7(a) and 7(b), respectively. As a matter of course, the relative Love wave velocity in Region 3 to Region 1, i.e., (V_d/V_s) also changes

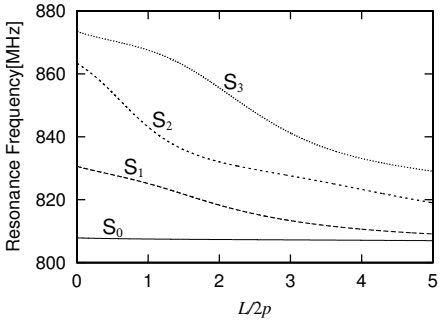

(a) $W_d/2p = 0.25$ $(V_d/V_s = 1)$

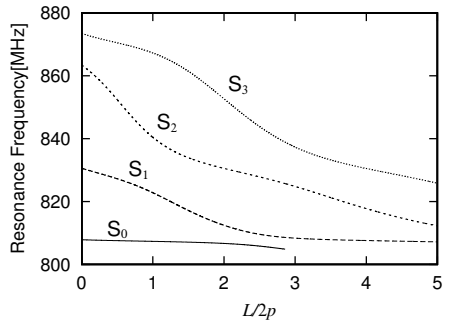

(b) $W_d/2p = 0.28$ $(V_d/V_s = 0.99)$

Fig. 7. Dependence of transverse mode (S_i ; $i = 0, 1, 2, \cdots$) resonance frequencies on dummy electrode length L.

with $W_d/2p$ as shown in the figure caption.

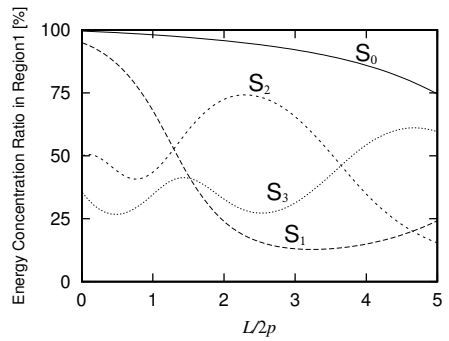

Fig. 8. Dependence of energy concentration ratio on dummy electrode length L $(W_d/2p = 0.25)$.

It is seen from Fig. 7(a) that the resonance frequency of the dominant S_0 mode is almost independent of L when $L/2p < 5$. The result suggests that because of the high electromechanical coupling, the energy of S_0 mode may be confined in Region 1. Defining the energy concentration ratio for a specific mode as the energy in Region 1 upon the total energy, one can see more quantitatively from Fig. 8 (see S_0 mode) how S_0 mode is strongly confined in Region 1, in particular, when L is relatively short. That is, L should not unnecessarily be long so that most of the energy of the dominant S_0 mode is confined within Region 1; this makes the S_0 mode scarcely be affected by the dummy electrodes.

On the other hand, it is seen from Fig. 7(a) that the resonance frequencies of S_1 and higher order transverse modes

strongly depend on L, which may mean that the energy of these modes transfers from Region 1 to other regions. In fact, the energy concentration ratio for S_1 mode in Fig. 8 decreases with an increase in L and takes the minimum value of 13% around $L/2p = 3$. This suggests that the propagation of S_1 mode could strongly be affected and suppressed (scattered) by the length modulated dummy electrodes, whereas S_0 mode is scarcely affected because of its energy concentration in Region 1. The similar effect of L on other higher order modes is also expected by the length modulated dummy electrodes.

Attempting to perturb the propagation of higher order transverse modes only by L, one may be unable to design the length modulated dummy electrode with ease, because there is a situation where L becomes unacceptably long for practical applications. In addition, the energy concentration ratio for S_0 mode also decreases with an increase in L (see Fig. 8); this may cause the reduction of resonance Q-factor. This suggests that the use of the width modulated dummy electrodes together with the length modulated dummy electrodes could really increase the degree of freedom to control the mode profile in the design. By comparing Fig. 7(a) and (b), it can be seen that if $W_d/2p$ is increased from 0.25 to 0.28, then $L/2p$ necessary for perturbing the propagation of higher order transverse modes is reduced by about a half. This means that the width modulation for dummy electrodes is effective in reducing the dummy electrode length.

B. Experiment

According to the discussion in III-A, One-port Love wave resonators were fabricated on a Cu-grating/15°YX-$LiNbO_3$, and the effect of L and W_d on the resonator performance was experimentally discussed. The device configuration used in the experiments and its basic parameters are shown in Fig. 5 and Table I, respectively. A microscope image of the device is shown in Fig. 9.

TABLE I

BASIC DESIGN PARAMETERS FOR 1-PORT RESONATORS.

IDT pitch ($2p$)	4 μm
Gap length (W_g)	0.5 μm
Length of reflectors (l_R)	$20p$
Length of IDT (l_I)	$100p$
Electrode thickness ($h/2p$)	7%

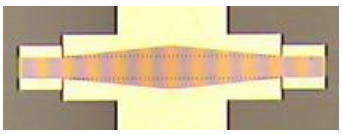

Fig. 9. Microscope image of fabricated device using width- and length-modulated dummy electrodes.

Figure 10 shows the admittance of the resonators with L as a parameter, where $W_d/2p = 0.25$ and $W_a/2p$=6. As can be seen from Fig. 10, S_1 mode is effectively suppressed when $L/2p = 2.375$ and 4.875. Note here that L for the conventional structure is zero. However, the resonance Q-factor for the dominant S_0 mode decreases monotonically with an increase in L. This may be caused by an increased ohmic loss, and/or by the fact that part of energy of S_0 mode has transferred to Region 3 (see Fig. 8).

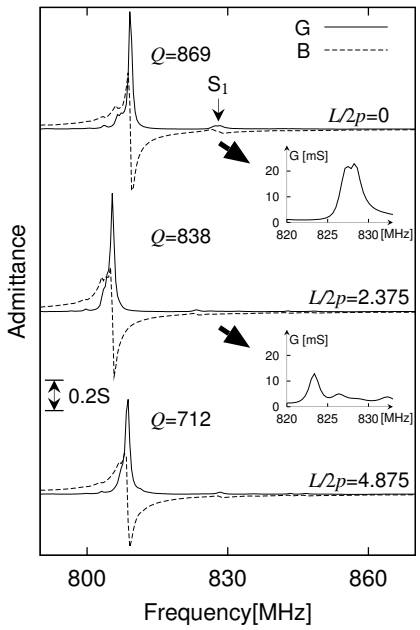

Fig. 10. Admittance of resonators with different dummy electrode length L.

Figure 11 shows the admittance of the resonators with W_d as a parameter, where $L/2p = 2.5$ and $W_a/2p = 5$. It is expected by the calculation that when $W_d/2p = 0.125$, S_1 mode is also trapped in Region 1 resulting in a strong spurious response. However, the spurious response is suppressed effectively with an increase in $W_d/2p$. As to Q-factor of the dominant resonance, it is still grater than 750 even when $W_d/2p = 0.375$. Although Q-factor for $W_d/2p = 0.125$ is extraordinary high, this may be attributed to the fact that there is a longitudinal spurious mode whose resonance frequency almost coincides with that of the S_0 mode; because of this longitudinal spurious response, it seems difficult to independently determine Q-factor for S_0 mode resonance with reasonable accuracy.

IV. APPLICATION TO ULTRA-WIDEBAND AND LOW-LOSS LADDER TYPE FILTER

An extremely-wideband Love wave ladder type filter was fabricated as one of the applications of the wideband one-port resonators on a Cu-grating/15°YX-$LiNbO_3$ structure to practical filters. The fabricated four-stage filter is shown in Fig. 12 and its fundamental design parameters are listed in Table II.

The frequency response of the filter is shown in Fig. 13(a), where the minimum insertion loss of 0.61 dB and the fractional -3dB bandwidth of about 19% are obtained. Comparing Fig. 13(a) with 13(b) in which no dummy electrodes are employed, it is clearly seen that the ripples in the passband caused by higher order transverse modes are effectively suppressed without notable deterioration of the filter performance, that is, the insertion loss, bandwidth, etc. The results shows

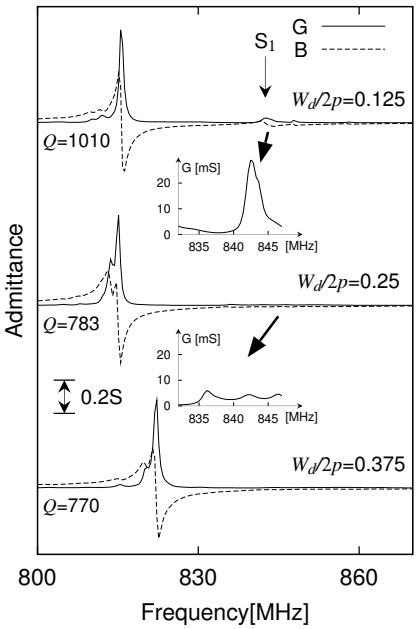

Fig. 11. Admittance response of resonators with different dummy electrode width $W_d/2p$.

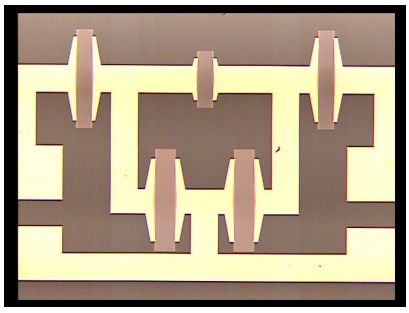

Fig. 12. Fabricated four-stage Love wave ladder type filter on Cu-grating/15°YX-$LiNbO_3$ structure.

that the method of suppressing transverse spurious responses for ultra-wideband resonators using the width and length modulated dummy electrodes is also applicable to suppress passband ripples appearing in ladder type filters on the Cu-grating/15°YX-$LiNbO_3$ structure.

On closer observation of Fig. 13(a), one may finds a moderate dip caused by Rayleigh wave still remaining near the lower passband edge. Although the combination of 15°YX-$LiNbO_3$ and a heavy metallic material like Cu for the grating electrodes tends to reduce the effect to Rayleigh wave, it seems rather difficult to make the dip negligible for practical device applications.

Since Rayleigh wave is basically supported by longitudinal and share-vertical components, it should be very susceptible to surface mechanical disturbance. On the other hand, the present filter owes its ultra-wideband and low-loss response to the highly piezoelectric SH type Love wave, which is relatively insensitive to mechanical disturbance on the surface. From this point of view, some experiments were carried out to investigate the effect of a viscous film coated on the filter surface upon

TABLE II

DESIGN PARAMETERS FOR LADDER TYPE FILTER

Substrate	15°YX-$LiNbO_3$	
Electrode material	Copper	
Electrode thickness, h [μm]	0.26	
Number of stages	4-stage	
	for parallel arms	for series arms
IDT period, $2p$ [μm]	2.8	3.6
$(h/2p)$ [%]	9.3	7.2
Aperture, W [μm]	56.	72.
Number of IDT pairs, N_I	112	86
Number of electrodes in each reflectors	20	20
Maximum length of dummy electrode, $L/2p$	2.0	2.0
Width of dummy electrode, W_d [μm]	0.9	1.1
Gap length, W_g [μm]	0.4	0.4

the selective suppression of the dip caused by Rayleigh wave.

Since the dip caused by Rayleigh wave in the series arm resonators is out of the passband, the surface of the parallel arm resonators has only to be coated with viscous films. As one of the experimental trials, an EB resist ZEP520-22 (ZEON Co.) film was coated as a selective damping material for Rayleigh wave. The resist film was spin-coated and selectively removed by Electron-Beam lithography as shown in Fig. 14, where the film thickness was about 0.16 μm. Figure 15 shows the frequency response of the filter thus prepared. As is seen in the figure, the depth of the dip caused by Rayleigh wave appearing at about 900 MHz was reduced to about 2.5 dB from 5.5 dB, while the increase in the minimum insertion loss was only 0.16 dB.

The result confirmed that the proposed technique using a viscous film coated on the filter surface is effective in suppressing the spurious response caused by Rayleigh wave. However the dip was made small, it still remained in the passband. More effective suppression could be realised by choosing a proper film material and controlling the film thickness.

V. CONCLUSION

Aiming at suppressing transverse mode spurious responses, this paper discussed the design and application of length and width modulated dummy electrodes to Love wave resonators on a Cu-grating/15°YX-$LiNbO_3$.

The Love and Rayleigh wave propagation on a Cu-grating/15°YX-$LiNbO_3$ structure was theoretically discussed showing that by Love wave could be applied to the development of low-loss and extremely-wideband filters with the minimised Rayleigh wave spurious response.

Based on the scalar potential theory, the analysis was made on the effect of the length L and width W_d of the dummy electrodes upon transverse mode profile (field distribution), that is, the energy distribution in interdigital electrode region, gaps, dummy electrode region, bus-bars and free surface.

The result showed that with an increase in L, the energy of the higher order transverse S_i $(i = 1, 2, \cdots)$ modes oozes from the interdigital electrode region and concentrates in the dummy electrode regions. On the other hand, S_0 mode was found quite insensitive to L and most of its energy is trapped

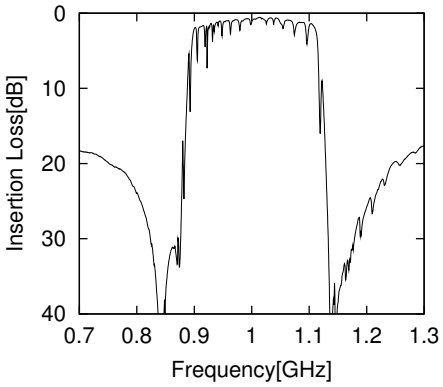

(a) without dummy electrodes

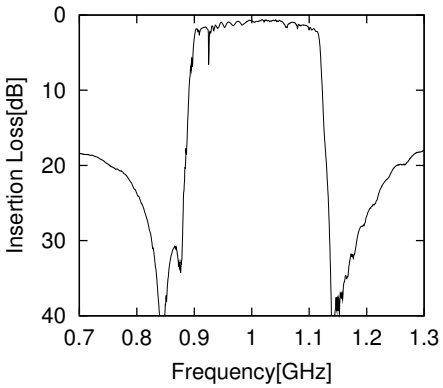

(b) with width and length modulated dummy electrodes

Fig. 13. Frequency responses of four-stage Love wave ladder type filter on Cu-grating/15°YX-$LiNbO_3$ structure.

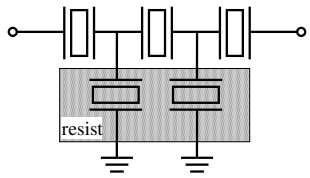

Fig. 14. Resist coating on the parallel arm resonators.

within the interdigital electrode region. This suggests that by the properly designed length modulated dummy electrodes, the propagation of S_i modes could strongly be affected and suppressed (scattered), whereas S_0 mode is scarcely affected because of its energy concentration in the interdigital electrode region.

The result also showed that a small change in W_d markedly enhances the effect of L. This suggests that the use of the width modulated dummy electrodes together with the length modulated dummy electrodes could increase the degree of freedom to control the mode profile and be effective in suppressing (scattering) S_i modes.

Based on the theoretical discussion on the length and width modulated dummy electrodes, one-port Love wave resonators were fabricated on a Cu-grating/15°YX-$LiNbO_3$ with L and W_d as experimental parameters. The experimental result was in good agreement with the theoretical prediction, showing that

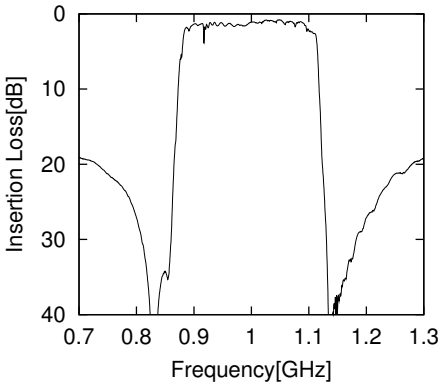

Fig. 15. Frequency response of four-stage Love wave ladder-type filter with a viscous film coated as an absorber for Rayleigh wave.

the proposed technique is most effective in suppressing the spurious responses caused by the transverse modes.

The one-port Love wave resonators were applied to ladder type filters, where the length and width modulated dummy electrodes are also found effective in minimising passband ripples caused by S_i mode. In addition, the viscous films were experimentally shown to be useful for suppressing the Rayleigh wave spurious response.

Acknowledgments

The authors wish to thank H. Asano, N. Yokoyama, K. Matsuda, Y. Sugama and T. Tanaka for their valuable assistance. This work was partially supported by a Grant-in-Aid for Scientific Research from the Japanese Ministry of Education, Culture, Sports, Science and Technology.

References

[1] K. Yamanouchi and K. Shibayama: "Propagation and amplification of Rayleigh waves and piezoelectric leaky surface waves in $LiNbO_3$", J. Appl. Phys., **43** (1970) pp. 856–862.

[2] H. Shimizu, Y. Suzuki and T. Kanda: "Love-type-SAW resonator of small size with very low capacitance ratio and its application to VCO", Proc. IEEE Ultrason. Symp. (1990) pp. 103–108.

[3] A. Isobe, M. Hikita, K. Asai and A. Sumioka: "Grating-mode-type wide-band SAW resonators for VCOs", Proc. IEEE Ultrason. Symp. (1998) pp. 11-114.

[4] K. Hashimoto, H. Asano, T. Omori and M. Yamaguchi: "Ultra-wideband surface acoustic wave devices using Cu-grating/Rotated-YX-$LiNbO_3$-substrate structure" Jpn. J. Appl. Phys. **43** 5B (2004), pp. 3063–3066.

[5] K. Hashimoto, J. Koskela and M. Salomaa: "Fast determination of coupling-of-modes parameters based on strip admittance approach", Proc. IEEE Ultrason. Symp. (1999) pp. 93–96.

[6] Y. Yamamoto and S. Yoshimoto: "SAW transversely guided mode spurious elimination by optimization of conversion efficiency using $W/W0$ electrode structure", Proc. IEEE Ultrason. Symp. (1988) pp. 111-114.

[7] R. V. Schmidt and L. A. Coldren: "Thin film acoustic surface waveguides on anisotropic media", IEEE Trans. Sonics & Ultrason. **SU-22** (1975) pp. 115–122.

[8] R. Nakagawa, T. Yamada, T. Omori, K. Hashimoto and M. Yamaguchi: "Analysis of excitation and propagation characteristics of leaky modes in SAW waveguides", Proc. IEEE Ultrason. Symp. (2002) pp. 405–409.

[9] T. L. Szabo and A. J. Slobodnik, Jr.: "The effect of diffraction on the design of acoustic surface wave devices", IEEE Trans. Sonics & Ultrason. **SU-20** (1973) pp. 240–251.

[10] K. Hashimoto, G. Endo, M. Ohmaru and M. Yamaguchi: "Analysis of SAWs obliquely propagation under metallic-gratings with finite thickness", Jpn. J. Appl. Phys. (1996) pp. 3006–3009.

Miniaturized SAW Package with Hermetic Performance

O. Ikata, Y. Kaneda, S. Ono, K. Sakinada, O. Kawachi, Y.Tanimoto

Fujitsu Media Devices Limited
Shin-Yokohama 2-3-12,Kohoku-Ku, Yokohama, Kanagawa, 222-0033,Japan

Abstract—Cellular-phone markets are moving quite aggressively towards module integration and as a result, the miniaturization of devices has been accelerated. Especially SAW filters, which are one of the key devices in RF circuit, are demanded to realize a small size, low profile, with high reliability performance for RF Module applications.

Conventional SAW filters use a ceramics (High Temperature Co-fired Ceramics; HTCC) package with cavity structure and metal sealing cap to obtain high reliability performance. At first, assembling technology improving to reduce the size of SAW filters, from the chip & wire to flip chip condition. However this structure changed not enough cover the demand for the miniaturization of SAW filters on RF module application. In order to reduce the size, HTCC package without cavity structure and resin sealing are commonly used. However, this structure does not contribute to the high reliability performance.

This paper describes the realization of a miniaturized SAW filter with keeping the hermetic condition. By using a unique packaging technique to achieve a low profile with high reliability performance based on the HTCC package without cavity structure and metal sealing. The technique has been realized by using cluster sealing with solder.

The optimization of the PKG design and sealing pressure was performed in solder sealing. In addition, by using plating in the outer coating, a high reliability performance can easily be achieved. Results of reliability testing including mechanical, electrical and moisture sensitivity will be discussed.

I. INTRODUCTION

Recently, the competition for miniaturizing, the cellular phone and making progress of multi-band and systems has intensified, as the cellular phone market expands. Therefore, the modulation of parts used has rapidly advanced. The demand for miniaturizing and making progress of low profile is growing very much on RF module solutions.

Basically, SAW devices have the advantage of easily obtainable steep characteristics and small-size design compared to the dielectric and multi-layer ceramics filters.

Therefore, the saw device market for cellular is widely expanding. On the other hand, the SAW filters have the feature that the filter characteristics the reliability cannot be maintained if an active surface is not protected in the air-gap. Because it is important for miniaturizing the SAW devices to secure the air-gap, a new technology is essential. [1-2]

At first, assembling technology improved by using flip chip type from the chip and wire structure as show the Figure 1.

This structure is keeping the surface space minimized to realizing the electrical performance and reliabilities.

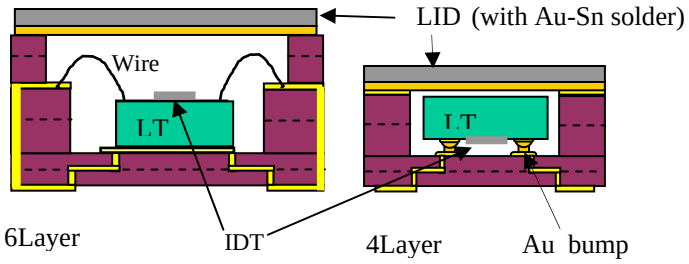

Figure 1. Schematic view of C&W and Flip Chip SAW

II. DEVELOPMENT CONCEPT OF MINATUALIZATION

The size of current flip chip type of RF SAW filters for the cellular phone and the size of newly developed filters are shown in Table.1.

The dimension of new single-band filter is 1.4mm x1.0mm x0.5mm height, which is 37% of volume reduction from the current single-band filter.

Table.1 Comparative table of RF-Filter Size

	Single-band	Dual-band
Current one	2.0*1.6*0.6mm	2.5*2.0*0.6mm
Developed one	1.4*1.0*0.5mm	1.8*1.4*0.5mm
Volume ratio	63%	60%

Development is aimed to keep both the electrical characteristics and reliability performance. Especially, high hermetic performance is absolutely necessary for humid environment.

In the past, not good reliability performance had confirmed in the resin type molding condition. One thing is frequency drift phenomena observed under the several time reflow test. The resin material has a characteristic of humidity absorption. This characteristic makes distortion of the SAW chip and influence to the filter performance as a frequency drift. For examples, the distortion makes 0.002micron variation influence to 2MHz frequency drift at 1.9GHz range filter. Of course these distortions are related to molding material Tg.[3]

To selected the molding materials, not only hermetical condition but also the frequency stability are important.

III. CURRENT PACKAGING TECHNOLOGY

Conventional flip chip type SAW filters use 4Layer ceramic (HTCC) PKG with cavity structure. The SAW chip is connected to the PKG by Flip Chip Bonding (FCB) using Au bumps. Then the cavity is encapsulated with an Au-Sn alloy coated LID. This sealing method is used to obtain high reliability performance. On the contrary, the miniaturization is difficult.

IV. NEW PACKAGING TECHNOLOGY

Figure 2 shows a new package structure.

Developed SAW filters use 2Layer HTCC PKG without cavity structure. The SAW chip is connected to plain PKG HTCC base by FCB. The SAW chip is molded with Sn-Ag solder, and the outside is coated by the Ni plating. Ni protects Sn-Ag solder from heat -treatment.

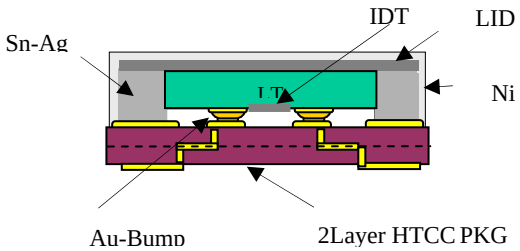

Fig.2 Developed filter structure

Fig.3 shows the cross-section photo and the EPMA map of the completed device. The plated Ni layer forms the outside wall and the Sn-Ag solder forms the inner part of wall homogeneously. Au diffuses from the plating layer of PKG, and its composition is uniform without segregation.
Generally, the melting point of Sn-Ag Solder series is about 220degree C. When the SAW device is mounted on the board of cellular phone, the temperature goes up to the Sn-Ag melting point again. Therefore, Sn-Ag melts again when mounting, and a high reliability securing is difficult. However, if the Ni plating is carried out properly, enduring the reflow becomes possible.

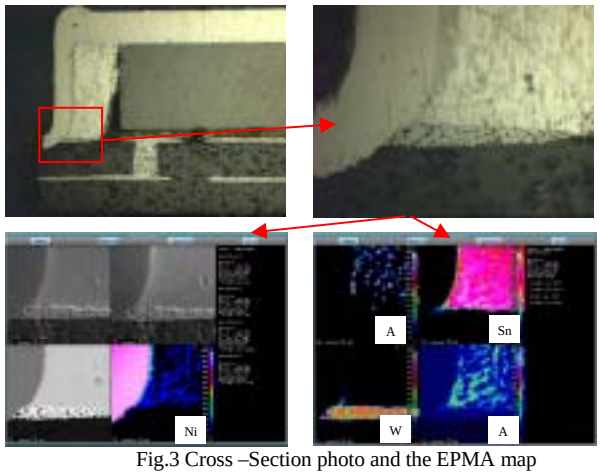

Fig.3 Cross –Section photo and the EPMA map

In the resin sealing that uses a conventional epoxy, cannot avoid the penetration of moisture over a long term. Therefore, an excellent result cannot be obtained for THB and PCT. This structure has the reliability of THB1000H, PCT96H and Moisture Sensitivity Level 1(JEDEC-MSL1), because it can achieve the hermetic performance.

V. PROCESS FLOW

Fig.4 shows the manufacturing process flow to achieve the new packaging structure. The main flow becomes Flip Chip Bonding, Sealing, Half-dicing (Ditch formation), Coating (Ni Plating), and Full-dicing.

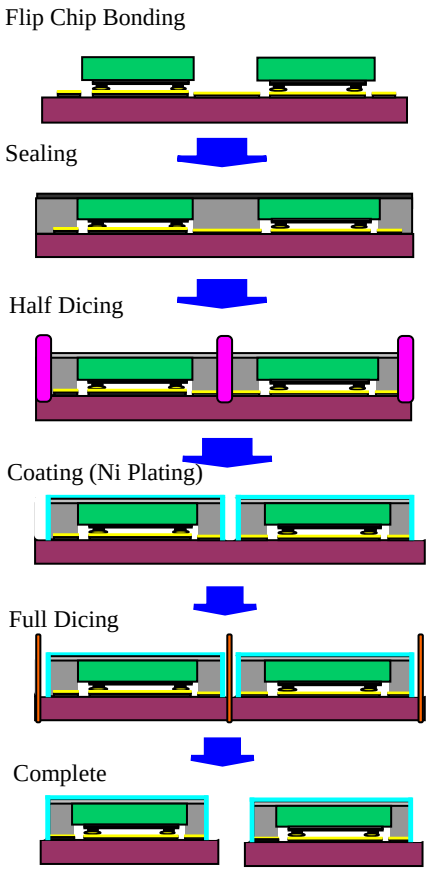

Fig.4 Image of Process flow

VI. DETAIL OF SEALING

The most unique technology in sealing is the use of Sn-Ag to achieve a new packaging. Sn-Ag is a very common material used also for SMD mounting, and has examples of practical use such as bumps and dams in various packaging.[4]

However, the new package is an unparalleled structure in the point of covering the whole chip with Sn-Ag. Details of sealing are as follows.

Fig.5 shows the image of the contact angle of melting Sn-Ag. Left figure shows the state that the SAW chip is mounted with the flip chip like the array in a HTCC package. In this situation, Sn-Ag is supplied from the upper side and heat is applied. If pressure is not applied to Sn-Ag, melting Sn-Ag becomes the Ball shape, like the Right figure. Because the Sn/LT contact angle is 90 degrees or more, this figure shows the state that the capillary action doesn't occur to the space of the SAW chip.[4]

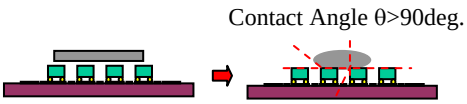

Fig.5 Image of contact angle

The pressure to push melting metal into a constant space is shown by the formula of Washburn eq.(1). This formula is used to show the pressure magnitude to push mercury into the hole of the radius=R. Moreover, the relation between pressure (P) and GAP (2r) can be led from this formula.

Formula of Washburn $Pr=-2\gamma\cos\theta$ **(1)**

The chip space and pressure have the relation of negative correlation. High pressure is needed when the space is narrow.

Fig.6 shows the image of the sealing process.

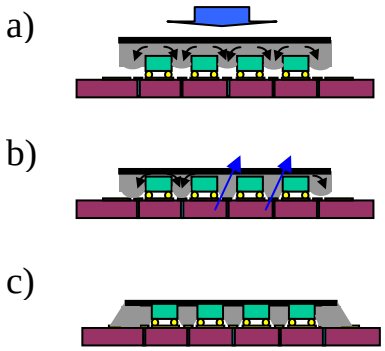

Fig.6 Image of sealing process

Sheet LID from which Sn-Ag is combined to KOV is supplied from the upper side of the chip as the first step. The sheet LID is clad-processed with KOV material of 25μm thickness on Sn-Ag sheet of 150μm thickness. Afterwards, if an appropriate pressure is applied at a temperature higher than the melting point of Sn-Ag, melting Sn-Ag starts to infiltrate into the GAP of the chips. (a)

When Sn-Ag reaches the Au plating pattern on the surface of the HTCC, Sn-Ag starts the capillary action. This is because the contact angle of melting Sn-Ag to Au is 90 degrees or less. Sn-Ag begins to flow in the depth direction of figure (b). Afterwards, sealing is completed(c).

When the press power is improved further, it is also fundamentally possible to fill Sn-Ag to a space under the chip. However, Sn-Ag inflows in GAP of the chips only by the wet phenomenon, because pressure that pushes Sn-Ag becomes 0 when the KOV reaches the back of the chip.

Therefore, designing GAP sizes, the space under the chip, and the Au plating pattern can control the sealing shape in this method.

Fig.7 shows one design example. Clearance(GAP) between the chip edge and the Au plating pattern edge is shown with X-axis, and a failure rate that Sn-Ag does inflow under the chip with Y-axis. If GAP is 0μm or more, Sn-Ag cannot infiltrate under the chip.

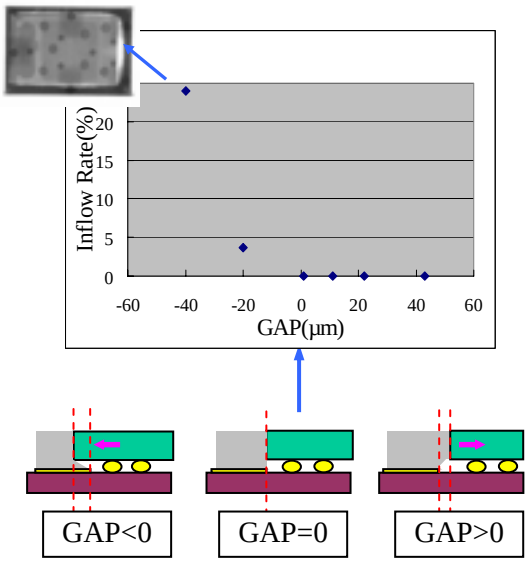

Fig.7 Relationship of GAP/ Inflow Rate

Moreover, the sealing temperature confirms that it does not influence the state of sealing within the wide range from 220 to 360degree C. The example of the temperature and GAP shows that the margin is considerably wide in this process compared with the case of resin molding. The reason the process margin is wide is that this process applies the wet character (contact angle) of melting Sn-Ag solder.

However, there is a supplementation to make sealing succeed. When sealing starts, it should exhaust the gas that exists around the chip. Melting Sn-Ag confines the gas if the exhaust is not done well, and excellent sealing cannot be done.

To cancel this issue, ventilation hole that penetrate the HTCC was arranged.

Fig.8 shows the effect of the ventilation hole. An upper X-ray photograph shows the sealing example without the ventilation holes. The gas is confined and the void defect is observed. On the other hand, a lower X-ray photograph arranged the ventilation holes in a red point, and shows the appearance where the void defect doesn't occur. The mass production of this process is very easy. The SAW chip that consists of several 100 pieces can be sealed in the batch.

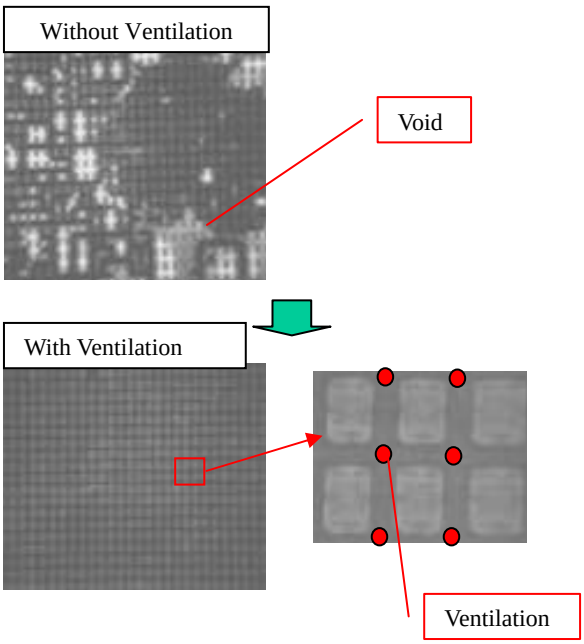

Fig.8 Effect of Ventilation hole

VII. RESULTS OF RELIABILITY TEST

Table.2 Results of Reliability tests

Test item	Condition	Result
6times reflow	260deg.C peak (FMD standard)	Pass
Bending	PCB bend,4mm,5sec (JIS C /IEC60068-2-21Ue1)	Pass
Vibration	98m/s^2 max,15min/sweep3D., 2H (JIS C/IEC60068-2-6)	Pass
Mechanical shock	14700m/s^2,0.5sec 6D., 5times (JIS C/IEC60068-2-27)	Pass
Solder heat resistance	260degreeC,10sec (JIS C/IEC60068-2-58)	Pass
Drop test	1.8m,150g, 6D.,each 3times (JIS C/IEC60068-2-32)	Pass
Temperature cycle	-40to125deg.C 100cyc. (JIS C0025/IEC60068-2-14,33)	Pass
Humidity bias	85deg.C, 95%RH,DC5V,1000H EIAJ ED-4701(IEC pub.60749)	Pass
Moisture sensitivity	125deg.C,16h>>+85deg.C,85% RH,168h>>260deg.C,6times reflow (JEDEC J-STD-020C)	Pass
Pressure cooker test	121deg.C,95%RH,96H EIAJ ED-4701(JESD-A100)	Pass

Table 2 shows the results of the reliability test on the new structural SAW filters. In all items, the reliability of the new structural SAW filters and current structural SAW are the same level.

VIII. CONCLUSIONS

New structural SAW filters sealed with the Sn-Ag solder was developed. The reliability of a new structural SAW filter and current structural SAW filter are the same level in all items. New structural SAW filters have a humidity tolerance MSL level 1. The volume of new structural SAW filters decreases by 60% compared with the current structural SAW filters, and is the smallest RF filters in the world. And these type filters are in practical use of RF module applications. Fig.9 shows the appearance of the developed SAW filters.

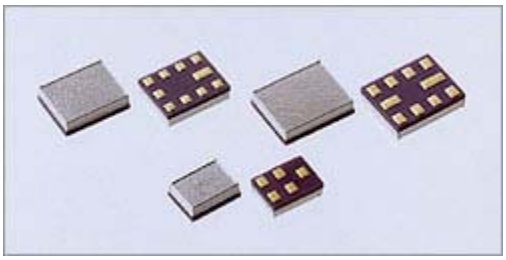

FIG.9 APPEARANCE OF PRODUCTS

ACKNOWLEDGMENT

The authors would like to express many thanks to relate all of people of the Fujitsu Laboratories LTD and the Fujitsu media device products LTD.

REFERENCES

[1] M.Koshino, M.Kawase, Y.Kuroda, N.Mishima, T.Takagi, K.Sakinada, Y.Ebata and S.Kimura “Small-sized Dual-band SAW Filters using Flip-Chip Bonding Technology” in Proc 1999 IEEE Ultrason,Symp,pp.341-346

[2] H.Meier,T.Baier and G.Riha “Miniaturization and Advanced Functionalities of SAW Devices” in Proc 2001 IEEE Trans. Microwave Theory and Tech,pp.341-346

[3] Nobutaka ITOH, Tadashi TATENO, Mami NAGATAKE, Akira TAKASHIMA, Osamu KAWACHI “Reliability Problem and Structural Analysis in New Electronic Packaging and Product (Three dimension Electronic Packaging and Mobile Equipment, etc.)” in Journal of Japan Institute of Electronics Packaging. Vol.6 No.7 2003

[4] P.Selmeier, R.Grünwald, A.Przadka, .Krüger,G. Feiertag and C.Ruppel “Recent Advances in SAW Packaging” in Proc 2001 IEEE Ultrasonic Symp,pp.283-291

[5] da Silva,M.F.P., R.Surmas., dos Santos,L.O.E., Philippi,P.C. “Analysis of contact angle in capillary invasion” in Proc 2005 International Congress of Mechanical Engineering.,

Development of Monolithic CMOS-SAW Oscillator

M. Furuhata, A. Yajima, K. Goto, H. Sato, T. Funasaka, S. Kawano, S. Fujii, T. Higuchi, M. Ueno
SEIKO EPSON Co., Ltd.
3-3-5 Owa, Suwashi, Nagano 392-8502, Japan
Furuhata.Makoto@exc.epson.co.jp

T. Karaki, M. Adachi

Toyama Pref. Univ.
5180 Kurokawa, Kosugimachi, Toyama 939-0398, Japan
chen@pu-toyama.ac.jp, adachi@pu-tpyama.ac.jp

***Abstract*— In recent years, miniaturization and high accuracy of mobile communication systems have become essential. Because of good phase noise performance, the SAW clock has become a viable option for data transmission. However, a SAW oscillator is usually made up of a SAW device and a CMOS-IC separately, and this large size limits its use in mobile communication systems. This paper covers the development of the smallest monolithic SAW oscillator using thin film ZnO deposited on a CMOS-IC. The SAW device and the IC have been combined into a single unit, and the total thickness is nearly the same as the IC.**

Keywords-component; SAW, oscillators, monolithic.

I. INTRODUCTION

In recent years, transmit technology has come to require both miniaturization and a high transmit rate. The SAW oscillator with good phase noise performance is suitable for high transmit rates. The passive components are fabricated in a single chip by two methods, SIP (System in Package)[1] and SOC (System on Chip)[2][3]. Since the SAW device is one of the largest components in the system, a monolithic SAW device with good phase noise performance is a desirable solution.

Because of the velocity dispersion of the thin film SAW device, the relationship of the IC's layered structure, which consisted of $SiN_x/SiO_2/Si$ between frequency, coupling coefficient k^2 and thickness of film were calculated. Inter Digital Transducer (IDT) with $1 \times 1.6mm^2$ sized oscillators were designed using a refined version of Smith's method.

The transistor's gate size was optimized using the Agilent ADS simulator. In IC fabrication, after standard 0.25um CMOS, ZnO film SAWs that easily crystallize at low temperatures without circuit damage were formed above the IC using RF sputtering.

In Fig. 1, the left side is the circuit area and the right side is the SAW area. Al lines connected the pad of the IC and the electrode of the SAW.

Fig. 2 shows that the monolithic SAW device oscillated clearly at 545MHz.

In addition discrete solution with good phase noise performance was already developed. This oscillator consisted of ZnO film SAW device and other individual components. [4]-[6]

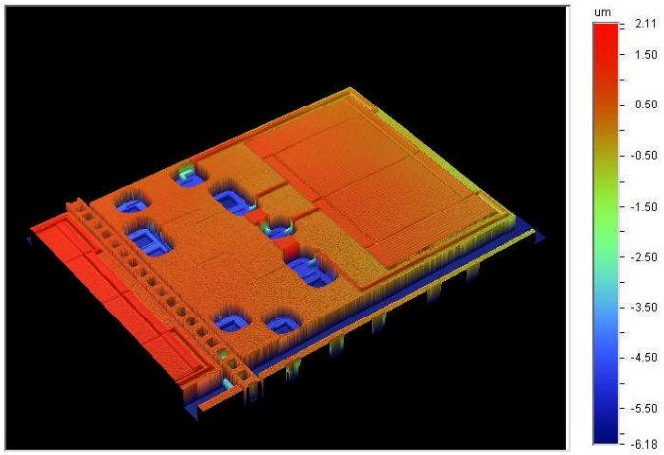

Fig. 1 Die of the monolithic SAW oscillator

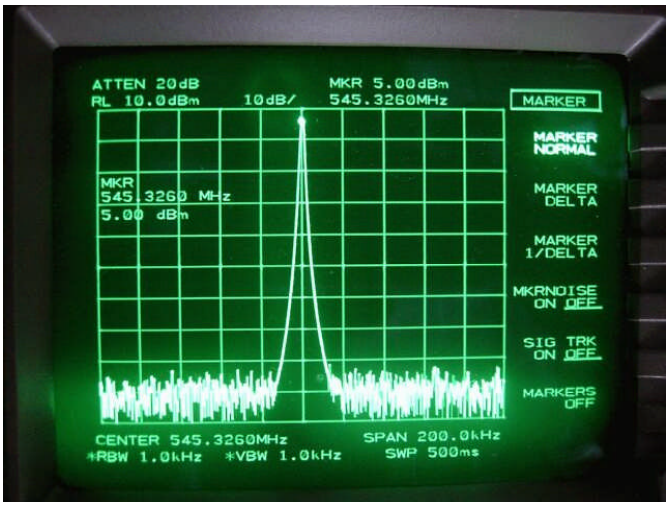

Fig. 2 Spectrum of oscillation

II. DESIGN

A. *SAW DESIGN*

Fig. 3 shows the calculated result using Campbell's method. [7]-[10] It shows that high k^2>1% needed the thickness of ZnO film being kh=1.5 with k(=$2\pi/\lambda$) being the wave number and λ being the SAW wave lengths. In this case, the thickness of isolation layers was kh=5 and the number of that

（SiO_2/SiN_x） layer was 4. At this thickness the Sezawa 3rd had the largest k^2.

As a high IDT reflection factor miniaturizes the SAW area, a thick Al (of kh>0.2 above ZnO/IC) was deposited. Fig. 4 shows that the simulated IL (Insertion Loss) =-10dB using Smith's method.

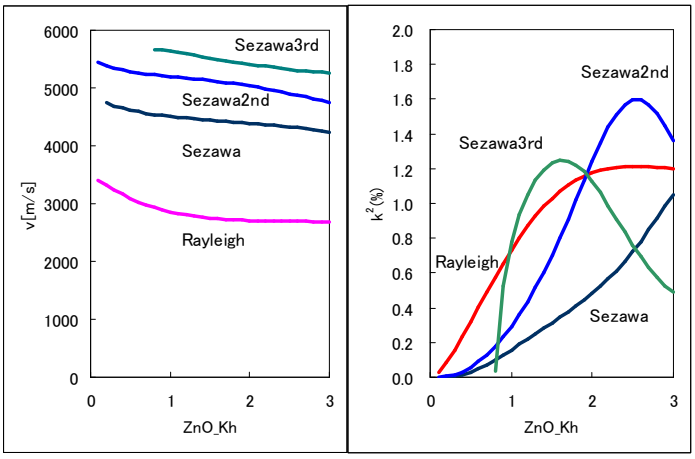

Fig. 3 Velocity depended on ZnO film thickness

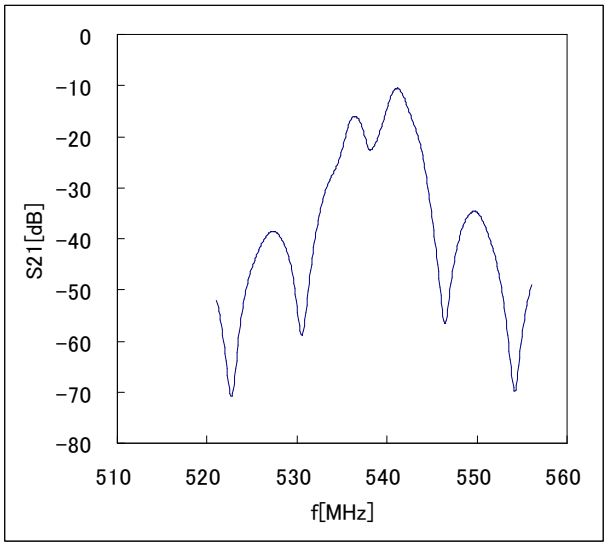

Fig. 4 Calculated SAW characteristics

B. CMOS CIRCUIT DESIGN

Fig. 5 shows the schematic circuitry of the colpitts oscillator. In this figure, as the IL of thin film SAW is often larger than that of single crystal, large transistor gain needed 3 stage inverters that connected 3 times in a series.

The analytical result of the relationship simulated with the Agilent ADS between transistor gain and power consumption in proportion to the transistor's gate size is shown in Fig. 6. In this simulation, the gain required 15dB that exceeded SAW IL=-10dB. As an upper limit of circuit power consumption of about 70mW, the maximum gate size was calculated. The relationship between gain and power consumption was presented. Therefore, optimized range of gate size W/L was from PMOS=60/0.3, NMOS=24/0.3 to PMOS =140/0.3, NMOS=47/0.3 with W/L transistor dimensions.

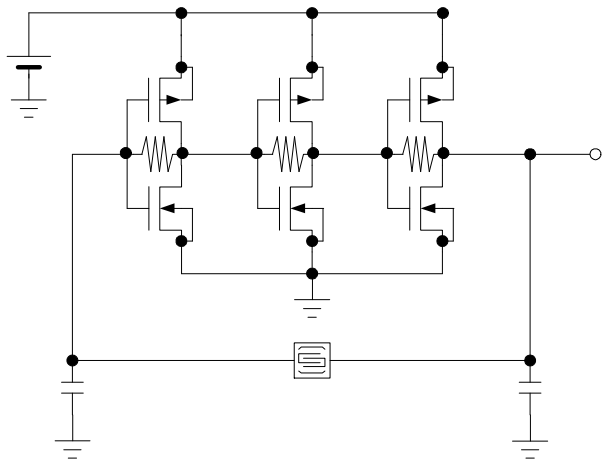

Fig. 5 Oscillatory circuit

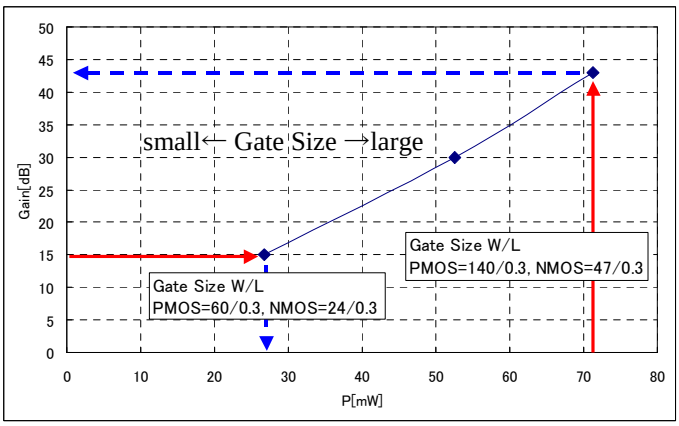

Fig. 6 Simulated result of gate size

C. CMOS FABRICATION

The IC was fabricated in the standard CMOS 0.25um process. Fig. 7 shows that the schematic surface of the chip with uneven distribution of Al lines was rough. To deposit thin film SAW on the chip, Chemical Mechanical Polish (CMP) was implemented to flatten the chip surface, as shown in Fig.8. If the wafer has a rough surface with an uneven distribution of devices, the SAW propagation loss also worsens. SAW area and circuit area were arranged mutually like a lattice figure because of SAW area having no lines in isolation layers.

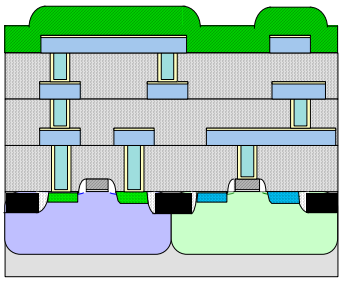

Fig. 7 Rough surface of standard IC chip

Identify applicable sponsor/s here. *(sponsors)*

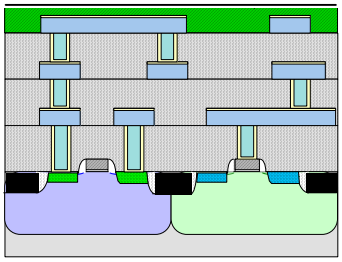

Fig. 8 Flat surface of IC chip by CMP

D. MONOLITHIC INTEGRATION PROCESS

It is easy to fabricate monolithic SAW device using the previous method. After CMP made the wafer surface flat, ZnO and Al films were deposited above it. IC pads and SAW electrodes were connected at the same time as the deposition of Al. Finally Al formed IDT by etching. Note that IC pads are not always needed, since they increase chip scales.

To avoid damages in circuit, a process under 400°C was selected. Moreover, post-process was chosen because of a possibility that ZnO could affect transistors. Fig. 9 and Fig. 10 show those schematic processes. First, ZnO film was deposited on a wafer with a flat surface and pads opened by etching. The next process was the Al deposition. Lastly, IDTs were formed by etching. Washing and etching processes that do not damage the circuit should be selected.

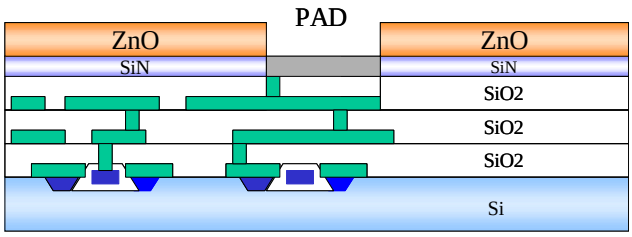

Fig. 9 ZnO deposition and PAD fabrication

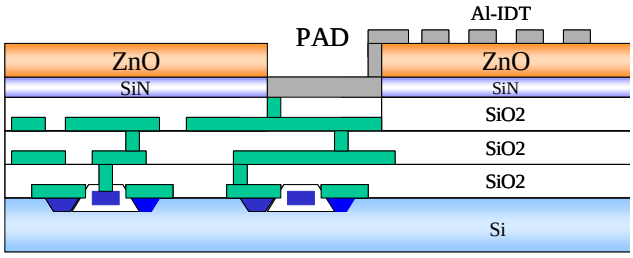

Fig. 10 Al deposition and IDT fabrication

III. MEASUREMENT RESULT

A. SAW MEASUREMENT

Fig. 11 shows that monolithic SAW got low IL=-14dB at Sezawa3rd. And the rayleigh, sezawa and sezawa2nd waves had an IL larger than -14dB. Although the IL was enough to oscillate, it did not reach -10dB. For a lower IL, the quality of ZnO film will need further improvement.

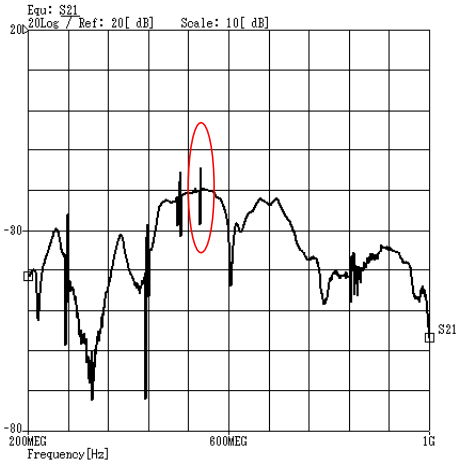

Fig. 11 SAW characteristics

A cross section photograph is shown in Fig. 12. The ZnO film formed a good c-axis. Fig. 13 shows the X ray diffraction (XRD) result. Its full width at half maximum (FWHM) was 3° , which indicated that the film quality was good.

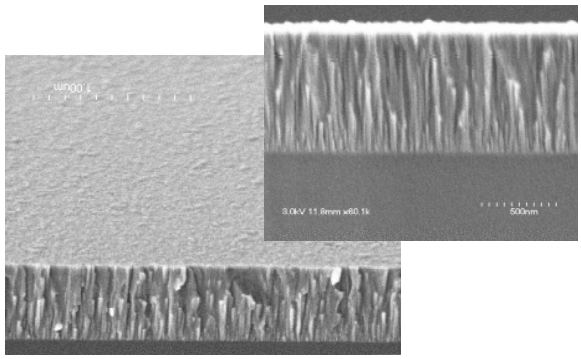

Fig. 12 Cross section photograph of ZnO film

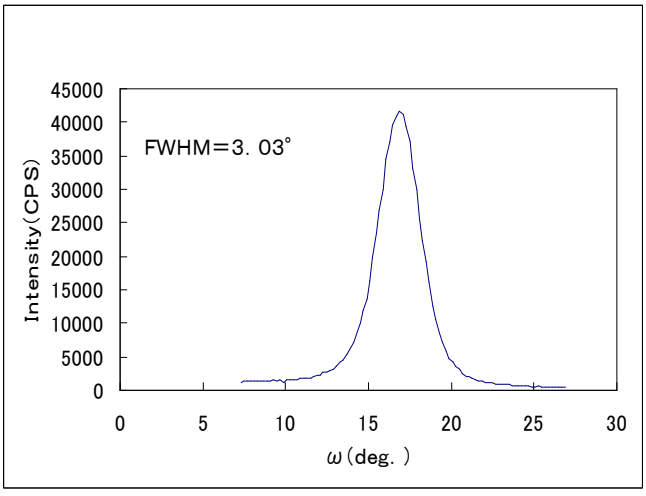

Fig. 13 XRD rocking curve

B. CMOS CIRCUIT MEASUREMENT

The oscillatory circuit obtained the gain over 14dB of thin film SAW.

In advance, the phase noise of the circuit covered with ZnO film was measured to check for influences. Fig. 14 shows that the difference of phase noise between the circuit and ZnO/IC was small. Therefore, the film had little effect on the circuit.

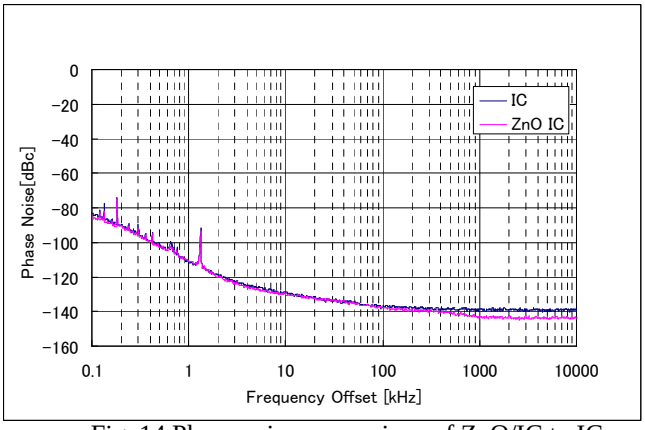

Fig. 14 Phase noise comparison of ZnO/IC to IC

The measurement result of components is shown in Table 1 below. The ZnO film also affected C, L and R very little. As the largest difference of resistance was only less than 5%, the film did not influence the circuit.

	L[nH]	C[pF]	R[Ω]
IC	4.84308	4.367	548.493
ZnO /IC	4.79307	4.356	476.786
Δ	0.05001	0.011	71.707

Table 1

C. MONOLITHIC SAW OCSILLATOR MEASUREMENT

The oscillatory condition at 545MHz was shown in Table 2 below. At 2.7[V], phase noise was measured. At 2.0[V], the oscillator worked steadily. But at 1.5[V], it sometimes stopped oscillating.

V[V]	I[mA]	P[mW]
2.7	13.7	36
2.0	7.5	15
1.5	3.2	5

Table 2 Oscillatory condition

Fig. 15 shows that measured phase noise of monolithic oscillator was almost equal to that of discrete solution, which was -120dBc/Hz@10KHz. [1][2][3]

At 1KHz monolithic SAW had –95.5[dBc/Hz], but LC oscillator that integrated typically in IC had –40[dBc/Hz]. [11] Therefore, SAW/IC showed an advantage regarding phase noise. In addition CMOS LC oscillated at 900MHz. But this monolithic SAW oscillated at 550MHz. Generally, the phase noise at a high frequency is worse than that at a low frequency. In this case there was little effect, since there was almost twice the difference.

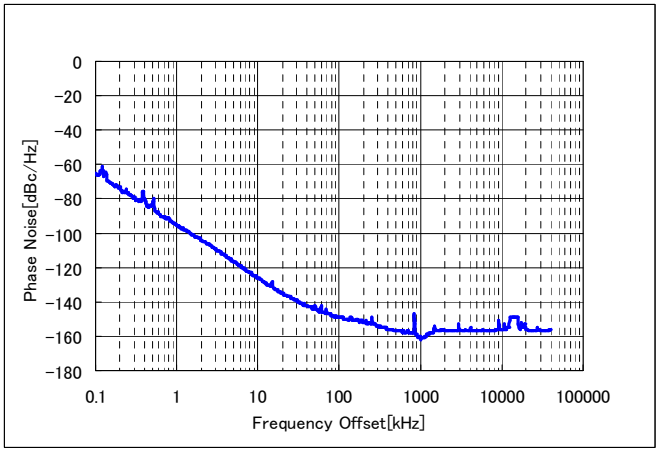

Fig. 15 1chip SAW oscillator Phase Noise

Frequency Offset	CMOS ZnO_SAW	CMOS LC
1KHz	−96	−40
10kHz	−120	−70

Table 3 Phase noise [dBc/Hz]

IV. CONCLUSION

The SAW device and the IC were combined into a single unit, and the total thickness was nearly the same as the IC.

A high performance Al reflector with a thickness of kh>0.1 was set up to minimize the SAW area to 1x1.6mm. To achieve a high gain at a low voltage power source, we optimized the gate size of the transistor and the parasitic element for phase adjustment in IC design using the Agilent ADS simulator.

Measurement results showed that the phase noise achieved an excellent value of –120dBc/Hz@10kHz. This indicates that the ZnO thin film did not affect the performance of the IC.

REFERENCES

[1] R. E. Jones, et al., IEEE RF-IC Symp.(2004) pp. 307-310

[2] M. J. Vellekoop, et al., 1987 IEEE Ultrason., pp. 641-644

[3] J. H. Visser, et al., 1989 IEEE Ultrason., pp. 195-200,

[4] M. Furuhata, et al., Proc. Symp. Ultrason. Electron., Vol. 25, (2004) pp. 211-212

[5] K. Goto, et al., Proc. 2004 IEICE Society Conf., pp. 152

[6] A. Yajima et al., IEE Jap. ECT-04-86~98, pp. 51-54

[7] J. J. Campbell, W. R. Jones: IEEE Trans. Sonics and Ultrason., pp. 209-217, 1968

[8] H. Nakahata, et al., 2002 JJAP Vol. 41 pp. 3489-3493

[9] A. Hachigo, et al,. 1995 IEEE Ultrason. pp. 371-374

[10] F. Takeda et al., JJAP. Vol.24 (1985) pp. 124-124

[11] A. Rofougaran, et al., ISSCC Dig. Tech. IEEE J. Solid-State Circuits, vol. 31, pp. 2042–2045, Dec. 1996.

RF FRONT-ENDS FOR MULTI-MODE, MULTI-BAND CELLULAR PHONES

Ulrich Bauernschmitt, Christian Block, Peter Hagn, Günter Kovacs, Enrico Leitschak, Andreas Przadka, and Clemens C.W. Ruppel

EPCOS AG, Munich, Germany

***Abstract* - This paper describes front-end architectures of modern multi-mode, multi-band cellular phones and will discuss the requirements on RF filtering in such applications. Special focus will be on dual mode (GSM and WCDMA) cellular phones with four GSM and three WCDMA bands. On the one hand driven by forward integration – e.g., from PA function via transmit front-end to a fully integrated radio – on the other hand influenced by new requirements of 3G systems and the integration of complementary access, filtering components such as SAW and BAW filters have to solve several increased requirements simultaneously. New technologies are required to follow the demand of increased RF performance, reduced PCB area consumption and continuously decreasing component costs.**

I. Introduction

Cellular systems worldwide are reaching maturity, especially the GSM system, accounting for more than 60% of global (cellular) sales in 2004. At its introduction, only the 900 MHz band was used; a few years later, the DCS band at 1.8 GHz was added. In Europe and Asia, these are still the bands occupied. In the U.S., the GSM system gained interest after the PCS band at 1900 MHz became available. Triple-band GSM phones can be considered the first single-system global phones. Today, with the addition of the 850 MHz band in the U.S., the GSM system spans four bands. In response to consumers asking for higher data rates, the GSM system expanded toward General Packet Radio Service (GPRS) and recently to enhanced data rate for GSM evolution (EDGE). Next to the GSM system, the 3-GPP committee has defined the Universal Mobile Telephone System (UMTS) as a global standard able to deliver data rates exceeding the GSM-EDGE standard by a factor of three. Upcoming high-end multi-mode, multi-band cellular phones will provide operation in several WCDMA bands. The bands of operation depend on the regions, as not all nine bands assigned for WCDMA are available all over the world. Thus, advanced cellular phones will operate in two different modes and will cover up to seven different frequency bands. This increased complexity was a driver for the development of integrated RF front-ends, which include ESD protection, switches, SAW and LC filters, and matching networks at least. In some cases power amplifiers (Pas) and duplexers are integrated too.

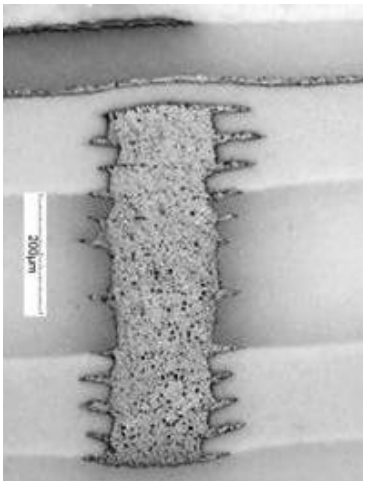

Fig. 1: Stacked via within different layers of ceramic materials.

In the coming years, handsets will increasingly have more features and functionality, e.g., internet, streaming audio/video, and games. Differentiation between handset manufacturers is no longer based on technical performance: features, fashion aspects, and cost determine the choice. Key value drivers for component and subsystem suppliers are therefore cost and size.

II. Key Materials and Core Technologies for RF Front-End Integration

A. LTCC Technology

In the nineties LTCC was mainly used to create discrete components like inductors, filters or baluns. Using LTCC as a substrate for passive integration and making modules or a complete system in package

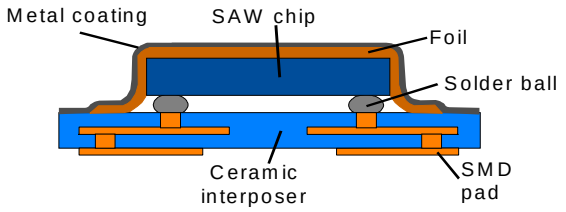

Fig. 2: Schematic cross section of Chip Sized SAW Package 2rd generation (CSSPlus).

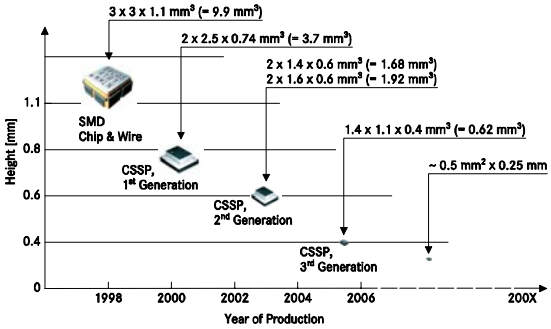

Fig. 3: Evolution of packaging for RF filters used in cellular phones.

was very often a burden to the user because of long turnaround times. A typical design cycle took three to four month and at least two or three cycles were required to get acceptable performance. Beside this, the range and achievable tolerances of embedded components were limited.

We have reduced the cycle times drastically. By making use of a non shrinkage 8''x8'' LTCC technology it is possible to combine different materials to extend the range of capacitance and inductance values but also to embed new semi-conductive ceramics for ESD/EMI protection. Furthermore, LTCC technology is the right choice for packaging for applications with severe temperature conditions like in automotive (e.g., gear controls) or communication (e.g., power devices) systems.

To produce an advanced LTCC panel existing of different materials in a competitive 8''x8'' format there are at least two major challenges. The first is to manufacture thousands of holes layer per layer fast and in high quality; the second one is to perform the shrinkage without any delamination between the layers or cracks around the metal structures and holes. Both have been achieved, e.g., 3000 holes/second are punched by using of special multi-punching tool.

Sintering of different materials (Fig. 1) is possible by adjusting the ceramic and metal material compositions in a way that the sintering starts at similar temperatures [8]. The so-called non shrinkage process has the big advantage that there is no shrinkage in the lateral dimensions. This is made possible by using top layers which do not shrink like the remaining functional body. The remaining shrinkage is only happening in the vertical dimension, so that delamination can be avoided.

B. Advanced Packaging Technology

Recent trends to integrate filtering into modules holding PAs, switches or the transceiver ICs are putting even more pressure towards the miniaturization of packages for electro-acoustic components. For the operation of SAW or BAW components it is necessary to realize hermetically sealed cavity-packages fulfilling stringent reliability requirements.

Traditionally, these requirements could be fulfilled using SMD type cavity packages. The packages were made of high temperature cofired ceramic (HTCC) and bonding wires between chip and package are used for the electrical connection. The inner metal pads of the package are connected by vias or metallized castellations to SMD pads on the bottom side of the package. A metal lid is welded or soldered to hermetically seal the package.

Further miniaturization was obtained by optimizing the ratio of active area (SAW or BAW chip). Novel approaches were needed to reduce the foot print of the package. Fig. 2 shows a chip size SAW packaged (CSSP) device, a flip chip package where the cavity is formed by laminating a polymer foil over the chips. Cu and Ni layers with a total thickness of 40 µm are used to seal the package hermetically.

With these steps in packaging it was possible to reduce the package volume in 2006 to 6 % (Fig. 3) of the 1998 value, a must for space saving integration of SAW filters into front-end modules. The next step will be the integration of bare dies on the surface of the module. Thus CSSP technology is directly applicable to highly integrated and miniaturized RF front-end modules.

III. WCMDA Frequency Bands

Today, nine different pairs of frequency bands for WCMDA applications (table 1) are specified. Not all

Band	up-link [MHz]	Down-link [MHz]	Comment
I	1920-1980	2110-2170	Europe, Japan, Korea, China
II	1850-1910	1930-1990	N.America, same as GSM 1900
III	1710-1785	1805-1880	Europe, same as GSM 1800
IV	1710-1770	2110-2170	US, Tx is subset of band III, Rx same as band I
V	824-849	869-894	N.America, same as GSM 850
VI	830-840	875-885	Japan, subset of band V
VII	2500-2570	2620-2690	Worldwide
VIII	880-915	925-960	Europe, same as GSM 900
IX	1750-1785	1845-1880	Japan, subset of band III

Table 1: WCDMA frequency bands

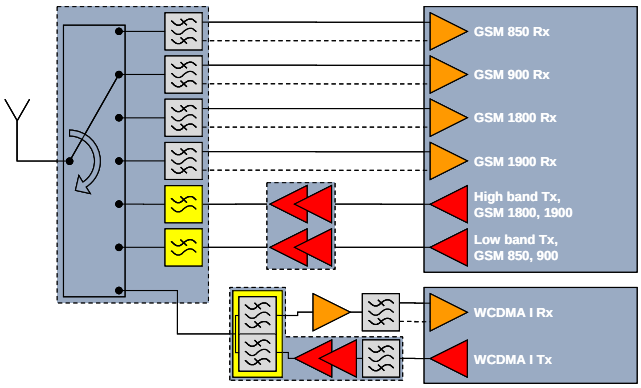

Fig. 4: Schematic block diagram of the front-end for a quad-band GSM and single band WCDMA cellular phone.

these bands are available all over the world, and not all frequency bands are available today. E.g., band VII will be included by 2009 or later. In order to reduce the complexity (and the costs) of a WCDMA cellular phone up to three different frequency bands are implemented only. Possible combinations depend on the main area of usage of the cellular phone. Examples are

- World (I, II, V)
- Japane (I, IX, VI)
- Europe (I, III, VIII)
- USA (II, IV, V).

IV. QB GSM + Band I WCDMA Front-End

In fig. 4 a schematic block diagram of a dual-mode (GSM/WCDMA) cellular phone is depicted. A quad band GSM transceiver in combination with a single band WCDMA transceiver is used. In the receiver section of the GSM portion a front-end module (FEM) with a switch and four SAW filters, one for each GSM frequency band, is used. Typically, these filters have a single-ended input and a balanced output [9], which eliminates the balun in front of the GSM transceiver. Doing the transformation from a single-ended to balanced signal in the SAW filter adds no additional insertion loss as a balun would do.

For the two GSM transmit bands (1 GHz and 2 GHz) a dual power amplifier module is used. GSM PAs with high efficiency require low-pass clean-up filters to suppress harmonics. Typically these filters are LC filters and are integrated into the front end module. In addition the complex matching required at the input of the GSM transceiver may be integrated too [1]. This reduced the component count by 12!

On the WCMDA side a module with a power amplifier and duplexer (PAiD) is used. Interstage filters are provided in Rx path after the LNA, and in the Tx path before the PA (integrated into the PAiD). To connect the GSM and WCDMA transceiver to the antenna an SP7T switch is included into the front-end module.

The proposed front-end for the dual mode cellular phone consists of three modules:

- a front-end module with an SP7T switch, a quad band filter bank, and Tx clean-up filters
- a dual power amplifier module
- a WCDMA PAiD module with PA, Tx interstage filter, and duplexer.

As is obvious, this is not the only solution for partitioning the front-end of a dual mode cellular phone. Another concept would result in the combination of a power amplifier switch module (PSM), a PAiD, and a filter bank with integrated matching. The decision for the modularization of the front-end depends strongly on size requirements, cost aspects,

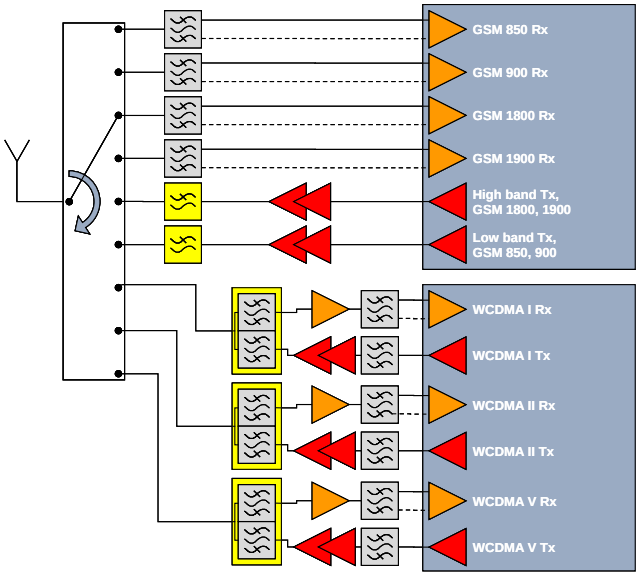

Fig. 5: Schematic block diagram of the front-end for a quad-band GSM and a triple band WCDMA cellular phone.

time to market considerations, and sourcing issues. All concepts result in technically equivalent solutions.

V. QB GSM + TB WCDMA Front-Ends

Advanced multi-mode, multi-band cellular phones will support four GSM frequency bands and up to three WCDMA frequency bands. This concept will be discussed in more detail for cellular phones operating in frequency bands I, II & V. The same ideas can be applied to other band combinations as well.

A. Separate GSM & WCDMA Transceivers

In this approach the GSM front-end described in chapter IV can be reused. Only the SP7T switch has to be replaced by an SP9T switch to allow for the two additional frequency bands. The WCDMA front-end has to be expanded by two more duplexers, four additional interstage filters, two PAs, and two more sections in the WCDMA transceiver.

Following this concept reduces the effort for the development of a dual-mode, multi-band cellular phone. Thus time-to-market and development costs are minimized. But this concept results in a not cost efficient system solution. Compared to today's systems a higher order switch (SP9T) results in higher costs and contributes to higher insertion loss in the radio front-end. As can be seen in fig. 5 the number of receivers is increased to seven, and the

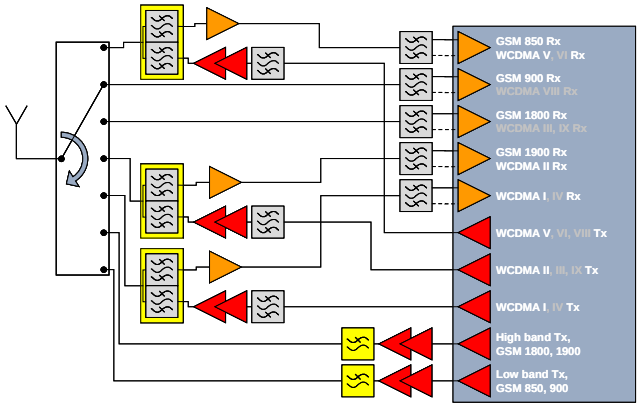

Fig. 6: Schematic block diagram of the front-end for a quad-band GSM and a triple band WCDMA cellular phone.

number of transmitters to five! This results in high pin count and large package size. Overall, costs for transceivers and filters are significantly increased.

B. Dual Mode Receivers

To overcome some of these drawbacks, new concepts have to be found. A possible solution is depicted in fig. 6. One prerequisite for this concept are reconfigurable multi-mode receivers [2, 3, 4, 5, 6, 7], because the same receiver path has to be capable to handle GSM and WCDMA signals. Thus the number of receivers can be reduced by two resulting in a total number of five receivers. This has direct impact on the antenna switch and only an SP7T switch is required. Compared to the solution described in chapter IV, the SP7T switch has five Tx ports and thus the die area is almost the same as of an SP9T switch.

By inspection of the frequency bands in table 1, one can see that GSM 850 and WCDMA band V share the same Rx frequency band. The same holds for GSM 1900 and WCDMA band II. Thus the first idea is to use the Rx filter of the respective WCDMA band for GSM too. The same concept may be applied to GSM/WCDMA cellular phones with frequency bands chosen for Europe I, III, VIII, and Japan I, III (IX), V(VI).

Implementing this concept requires two conventional GSM Rx filters and two dual mode interstage Rx filters. This dual mode filter has to fulfill specifications arising from both standards. Fig. 7 shows the frequency response (S_{21}) of such a

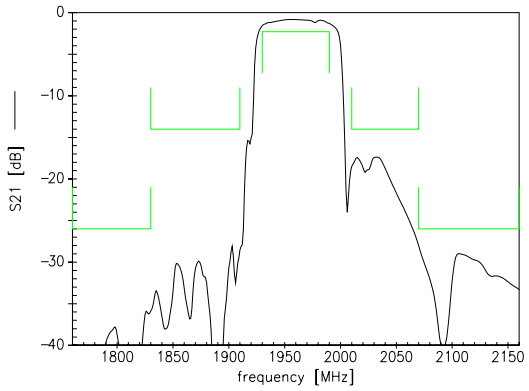

Fig. 7: Frequency response of a dual mode Rx interstage filter vs. GSM 1900 specification.

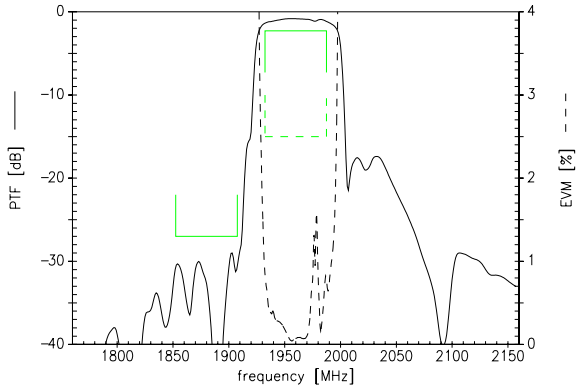

Fig. 8: Power transfer function and error vector magnitude of a dual mode Rx interstage filter vs. WCDMA II specification.

dual mode Rx filter vs. a typical GSM 1900 blocking specification. Fig. 8 shows power transfer function (PTF) and error vector magnitude (EVM) of the same filter vs. a typical WCDMA band II specification. PTF is a measure of attenuation for a WCDMA modulated signal. Basically, it is an average frequency response (S_{21}) weighted with the spectral power distribution of a WCDMA signal. EVM is a measure of signal distortion due to non-uniform attenuation and non-uniform group delay over a 5 MHz wide WCDMA channel [10]. Both, power transfer function and error vector magnitude are plotted as function of center frequency of the respective WCDMA channel.

C. Dual Mode Receivers without Rx Filters

A possible next step could be the attempt to remove the interstage filters in all WCDMA bands [6].

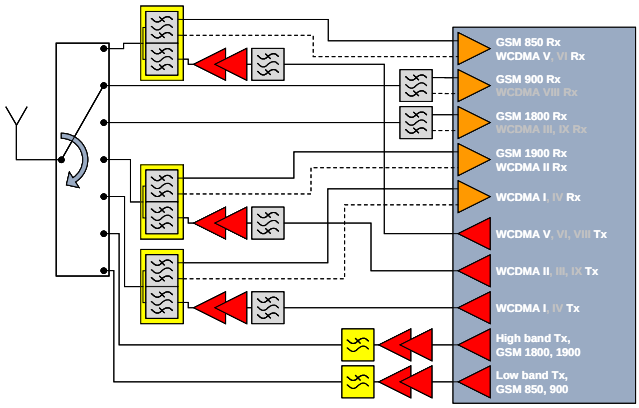

Fig. 9: Schematic block diagram of the front-end for a quad-band GSM and a triple band WCDMA cellular phone.

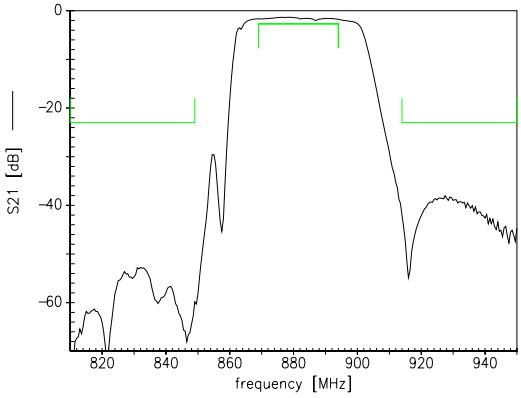

Fig. 10: Frequency response of a dual mode Rx duplex filter vs. GSM 850 specification.

Thus, the Rx filter of the WCDMA duplexer has not only to fulfill the tightened WCDMA specifications, but also the respective GSM specifications. Furthermore, the balun functionality of the interstage filters should also be shifted to the duplexer.

To point out the requirement for such an Rx filter of a duplexer, we have chosen a WCDMA band V duplexer with balanced Rx as an example. Fig. 10 shows the frequency response (S_{21}) of such a dual mode Rx duplex filter vs. a typical GSM 850 specification. In particular, the GSM blocking specifications above the pass band have to be fulfilled. Fig. 11 shows power transfer function (PTF) and error vector magnitude (EVM) of the same filter vs. a typical WCDMA band V specification. Besides a high suppression of Tx frequencies, this filter needs to suppress blockers at $2*f_{Tx}-f_{Rx}$ (Rx image) and at

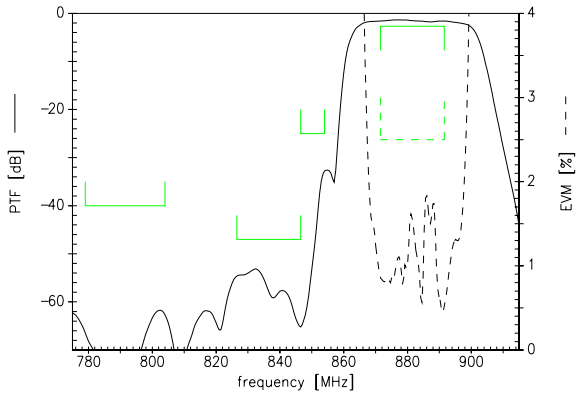

Fig. 11: Power transfer function and error vector magnitude of a dual mode Rx duplex filter vs. WCDMA V specification.

(f_{Tx}-f_{Rx}) / 2 (half duplex image) due to third order intermodulation products.

VI. Example of a Multi-Mode Front-End Module

In this chapter, the EPCOS module M104 is described as an example for a state of the art multi-mode front-end module. The block diagram of the module is shown on fig. 12. The module contains an SP7T CMOS switch, four SAW-filters for the GSM receive paths, low pass filters for the low and high band GSM transmit paths, an output branch for WCDMA operation and a network for protection against electro-static-discharges (ESD). The antenna pin of the module is connected to the input of the switch by means of the ESD protection network. The seven output branches of the switch are connected to the four GSM receive filters, the two GSM transmit low pass filters and the WCDMA output pin.

Fig. 13 presents the photo of the actual implementation of the module currently running in volume production. The encapsulation material has been left off, therefore the components mounted on the top side can be seen. The substrate is multilayer-LTCC which contains integrated passive components to realize the two low pass filters as well as matching components for the receive path. This allows the realization of customized Rx output impedances as part of the module, thereby saving board space and design-effort for the customer. On the top of the substrate are two SAW-filter packages in CSSPlus technology, each of them contains two of the GSM receive filters (2in1). In the lower left the SP7T-

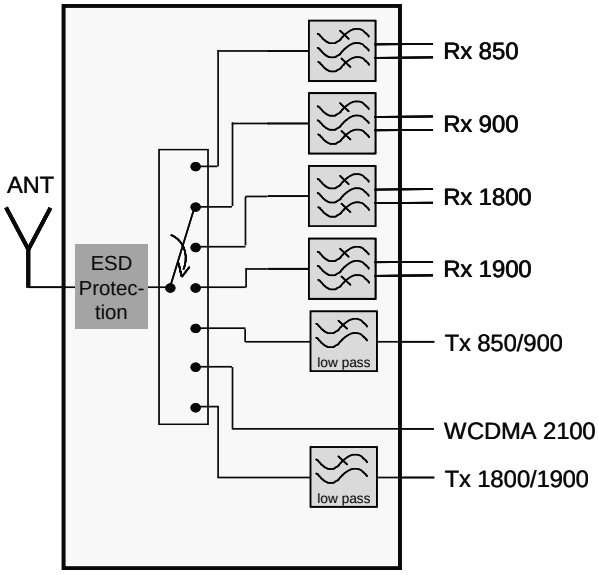

Fig. 12: Block diagram of EPCOS multi-mode module M104.

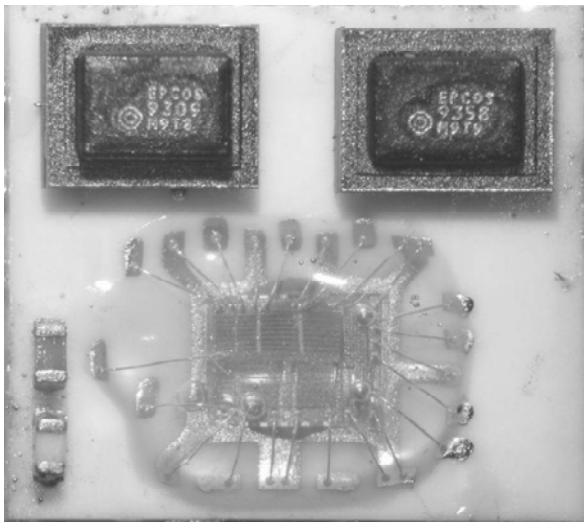

Fig. 13: Photo of the EPCOS multi-mode module M104 with the encapsulation material removed. Discernible are the SAW-filters in CSSPlus packages, wire-bonded SP7T switch and discrete SMD components.

switch is mounted. This was done by first die-bonding the chip onto the module substrate and afterwards connecting the switch electrically with wire-bonds. The elements for the ESD-protection network are added as discrete SMD components, located in the lower right. The module has a size of 5.4x4.7 mm².

Key performance parameters for a multi-mode module are insertion loss, prescribed attenuation

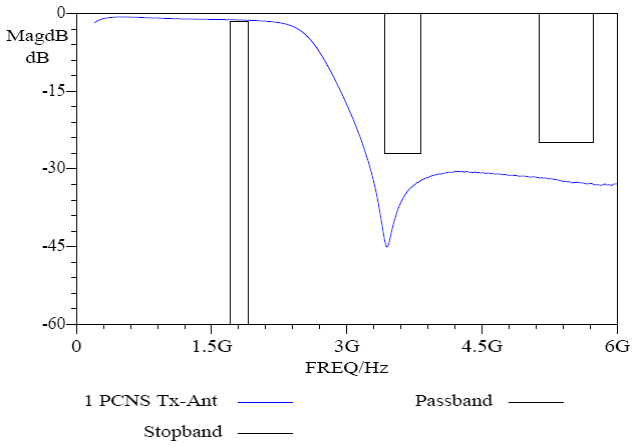

Fig. 14: Transfer properties of the EPCOS M104 for the GSM 2 GHz transmit mode.

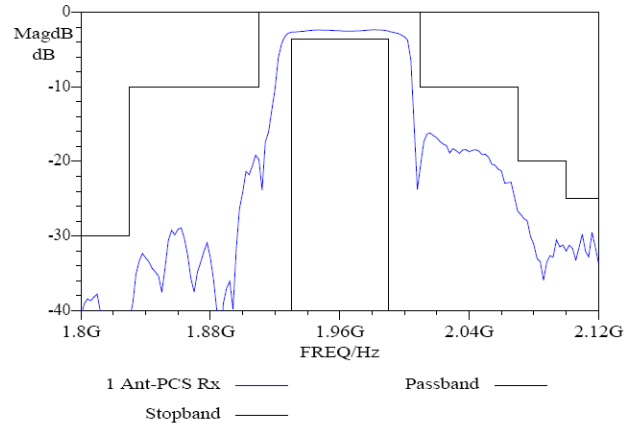

Fig. 15: Transfer properties of the EPCOS M104 for the GSM 1900 receive mode.

levels, low harmonic generation for the GSM transmit modes, excellent intermodulation properties as well as low current consumption and resistance against ESD. All this has to be realized within a minimum of space at low cost. On Fig. 14 and 15 we show as examples the transfer properties of the module for the GSM transmit (high band) and GSM 1900 receive modes, respectively.

The insertion loss for the low and high band GSM transmit modes is 1.2 dB and 1.3 dB, respectively. The insertion loss for the GSM receive bands is between 2.3 dB and 2.8 dB, depending on the frequency band.

For the WCDMA mode the transfer curve has low insertion loss over a broad bandwidth (fig. 16). This allows that the WCDMA mode of the module can be used for all currently used bands. The band to be used

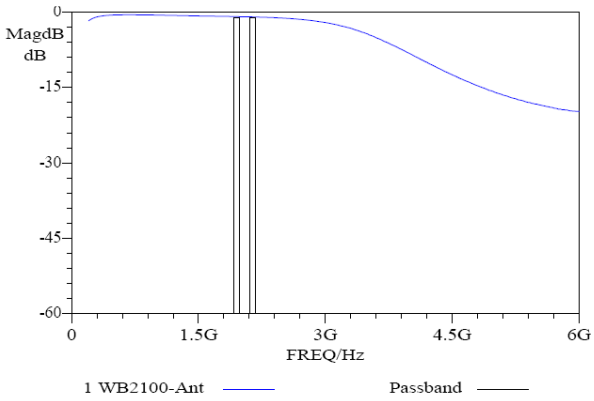

Fig. 16: Transfer properties of the EPCOS M104 for the WCDMA mode.

is chosen by the appropriate duplexer. A typical case is the use of band I, the relevant passbands are indicated on fig. 17. The EPCOS M104 displays an insertion loss of less than 1 dB, even at the highest frequency needed.

Besides the transfer curves the non-linear characteristics are key for successful use of a multi-mode front-end module. In the GSM transmit modes the M104 second and third order harmonic power is better -45 dBm, even when the antenna is mismatched. This provides enough margins against the GSM-specification and allows for the design of robust RF-transmitters. The non-linear parameter of most interest for the WCDMA mode is the intermodulation power generated in the receive band, when a blocking signal is applied to the antenna. In the typical test case the transmit power is set to 20 dBm at the antenna and the blocking signal to -15 dBm. A third order intermodulation product is formed according to:

$$f_{IM} = 2*f_{Tx}-f_{block}$$

The measured power of the third order intermodulation product is shown on Fig. 17. The power is displayed as a function of the relative electrical delay between the WCDMA pin of the module and the duplexer. The power is below -108 dBm for the worst case phase. It is important that the intermodulation power is low for all phases, because the module can be used on any phone PCB, independent of the distance between the module and the WCDMA duplexer.

Besides the RF-performance of the module, equally important are current consumption and ESD-

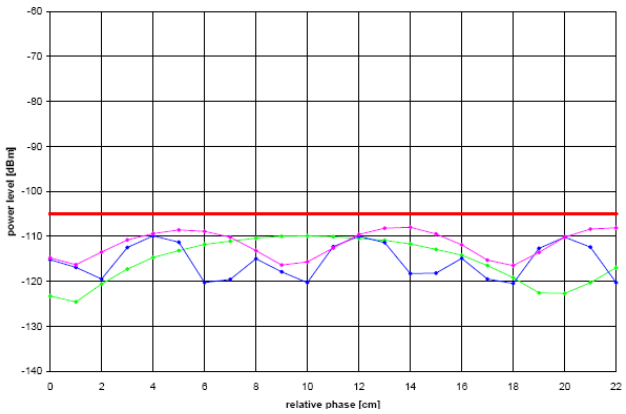

Fig. 17: Third-order intermodulation power of M104 for the M104 in the WCDMA receive band. The transmitter power was 20 dBm and power of the blocking signal -15 dBm at the antenna. The three curves are for WCDMA band I, II, and V.

resistance. With a current consumption of only 50µA and an ESD-resistance of 8kV contact discharge according to IEC1000-4-2 the M104 has the best performance known to the authors for these parameters.

Next steps are targeted towards further miniaturization. This will be achieved by the use of EPCOS next generation ultra-small SAW-packages in CSSP3 technology in combination with innovative assembly technologies for the switch.

VII. Conclusion

A prerequisite for successful development of RF front-ends for multi-mode, multi-band cellular phones is the control and availability of key materials, core technologies, advanced filter techniques, and comprehensive system knowledge. At EPCOS we have an in-house LTCC development and fabrication, we have introduced CSSP for acoustic filters, and extensive know-how with respect to SAW and BAW filters development, synthesis, simulation, and fabrication.

We have discussed different partitionings of RF front-ends for multi-mode, multi-band cellular phones which yield technically equivalent system solutions. Reuse of existing GSM subsystems can lead to shorter time-to-market, but either increases the component count, the complexity, and/or the cost of the system. Combining the requirements given by GSM and WCDMA specifications results in using the same Rx filter twice - for GSM and WCDMA – and eliminates one Rx filter. Thus the filter count and complexity for the QB GSM + TB WCDMA front-end module could be reduced. Adding GSM blocking specifications and balun functionality to the Rx filter of the duplexer, facilitated elimination of interstage filters.

More efficient solutions require more effort in design and development, but result in cost efficient implementations and will be used in future multi-mode, multi-band cellular phones.

VIII. References

[1] P. Hagn, A. Przadka, and C.C.W. Ruppel, "Acoustic Frontend Modules", 2004 IEEE International Microwave Symposium, pp. 921-922

[2] B. Bakkaloglu, and P.A. Fontaine, "Multi-Mode, Multi-Band RF Transceiver Circuits for Mobile Terminals in Deep-Submicron CMOS Processes, 2005 IEEE Radio Frequency IC Symposium, pp. 483-486

[3] J. Ryynänen, K. Kivekäs, J. Jussila, L. Sumanen, A. Pärssinen, and K.A.I. Halonen, "A Single-Chip Multimode Receiver for GSM 900, DCS 1800, PCS 1900, and WCDMA", IEEE Journal of Solid-State Circuits, Vol. 38, No. 4, April 2003, pp. 594-602

[4] A. Kruth, M. Simon, K. Dufrene, R. Weigel, Z. Boos, and S. Heinen, "A Multimode Receiver Front-End for Software Defined Radio", Proceedings of the 9th European Conference on Wireless Technology, 2006, pp. 19-22

[5] A. Baschirotto. R. Castello, F. Campi, G. Cesura, M. Toma, R. Guerrieri, R. Lodi, L. Lavagno, and P. Malcovati, "Baseband Analog Front-End and Digital Back-End for Reconfigurable Multi-Standard Terminals", IEEE Circuits and Systems Magazine, First Quarter 2006, pp. 2-28

[6] N.K. Yanduru, D. Griffith, S. Bhagavatheeswaran, C.C. Chen, F. Dulger, S.J. Fang, Y.C. Ho, and K.M. Low, "A WCDMA, GSM/GPRS/EDGE Receiver Front-End without Interstage SAW Filter, 2006 IEEE Radio Frequency IC Symposium

[7] M. Brandolini, P.Rossi, D. Manstretta, and F. Svelto, "Toward Multistandard Mobile Terminals – Fully Integrated Receiver Requirements and Architectures", IEEE Transactions in Microwave Theory and Techniques, Vol. 53, No. 3, March 2005, pp. 1026-1038

[8] C. Block, “Miniaturization of LTCC Modules Through the Application of New and Highly Dielectric Materials,” ZVEI Podium, Electronica, November 2002

[9] U. Bauernschmitt, C.C.W. Ruppel, and C. Block, " Filtering Challenges For Multi-Band, Multi-Link RF Front Ends For Cellular Phones", MWE 2005, Yokohama, Japan

[10] S. Freisleben, "Semi-Analytical Computation of Error Vector Magnitude for UMTS SAW Filters", 2002 IEEE International Ultrasonics Symposium, pp. 109-112

Wafer Level Packaging of SAWs Enables Low Cost 2.5G and 3G Radio Modules

Brent Wilkins
RFMD
5617 Scotts Valley Drive
Scotts Valley, CA 95066

***Abstract* - Cellular handset developers are adding features to their handsets while designing them to be smaller and thinner. This drives the need for highly integrated radio solutions that use minimal space and are easy to integrate with other functions. Module integrated circuit packaging technology, combined with appropriate semiconductor process technologies can provide handset manufacturers a very compact radio solution while enabling shortened time to market and low cost of ownership.**

In this paper I will show how module technology helps achieve a reduced time to market and size reduction for handsets. Additionally, I will show how wafer level packaged SAW filters play a key role in enabling these small and highly integrated modules.

I. Introduction

The year 2007 is the last year that GSM/GPRS handsets dominate the production of handset volumes [1] as indicated in Fig. 1. While many of the historic GSM and GPRS handsets has been dual band, today the majority of EDGE handsets are quad band. Volumes are also shifting to multimode handsets, increasing the number of unique frequency bands in each handset. Additionally, the use of full duplex radios for 3G handsets is driving explosive growth for duplexers, now exaggerated as multiple frequency bands are supported. This provides SAW and duplexer manufacturer with a growing market opportunity, at least in terms of units shipped. It also presents a challenge to the handset manufactures to find room the number of filters and duplexers.

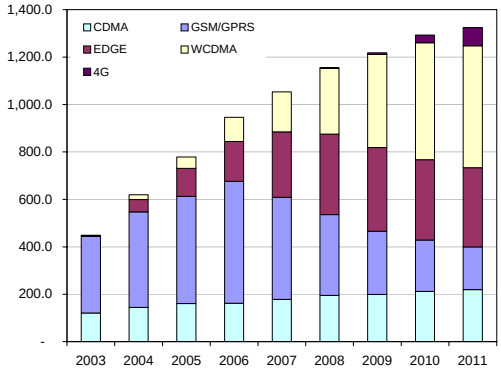

Fig. 1. Shows declining GPRS and increasing EDGE and WCDMA handset production. Source: RFMD

II. Modules vs MMICs

Just a few years ago, handset designers selected RF MMICs, discretes and passives components from a variety of suppliers and spent a considerable amount of time and resources debugging and relaying out printed circuit boards. Semiconductor companies have taken over these responsibilities by providing RF modules. The trend started when semiconductor companies combined the power amplifier (PA) die with passive components onto a laminate substrate to provide a complete tested module matched to 50 ohm impedance. The industry now recognizes the value of reducing the overall board area while improving factory yields and time to market. Nearly all handsets a now manufactured using power amplifier modules. This integration trend is now moving to the transceiver function, further reducing size and development effort, again improving time to market and therefore time to money.

A fundamental benefit of module technology includes the ability to combine different semiconductor process technologies into the same package creating a complete function using the optimal technology for the function. Fig. 2 shows a transmit module and includes pHEMT for the Rx/Tx switch, high and low band GaAs HBT die for the power amplifier, CMOS for the biasing and control functions and passives devices for harmonic filtering and impedance matching.

Additional benefits to the users of modules include the fact that the module manufactures have taken the responsibility for managing much of the supply chain based on the fact nearly all of the radio functions are provided in two or three modules by one suppler.

Fig. 3 shows two generations of advanced quad-band EDGE radios. Both solutions include integrated SAW filters inside the transceiver module and utilize multi technology modules to achieve the small size and high level of integration. Minimal external passive components are achieved partly due to the fact the impedance matching components are inside the module

To achieve cost effective radio module and achieve the correct selling price at acceptable production margins, the majority of the functions integrated into the module need to be manufactured by the module vendor. The SAW and duplexer devices are no exception.

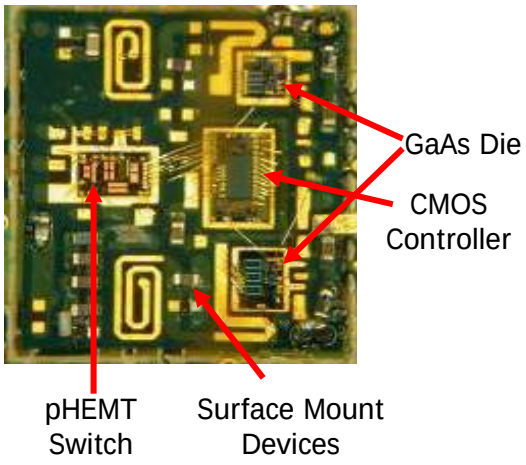

Fig. 2. The transmit module includes low band and high band GaAs HBT die, a pHEMPT switch, and CMOS controller Source: RFMD

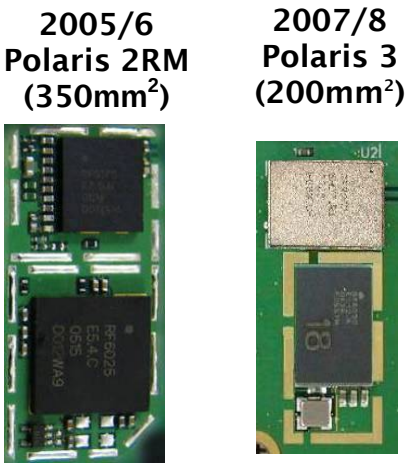

Fig. 3. Polaris 2 Radio Module includes pre packaged SAW filters. Polaris 3 includes WLP SAWs contributing to a smaller size module. Source: RFMD

III. WAFER LEVEL PACKAGING

The primary goals associated with the development of Wafer Level Packages SAWs and duplexers included both technical and commercial aspects.

Securing SAW filter supply for very large volumes of front end and transceiver modules was a key goal. Additionally, reducing the cost of SAWs already in high volume would drive immediate improvements in margins or enable a lower selling price. Supporting the size and integration goals for 3G front end modules also drove the need for smaller sized SAWs and duplex filters.

Reducing height was another key goal, as handsets are getting thinner and thinner and the ceramic pre-packaged SAWs were and continue to be the limiting factor in achieving lower module heights.

WLP SAWs are clearly the better choice compared to ceramic packaged SAWs when integrating the SAWs inside the transceiver or front end module.

RFMD's WLP SAW and duplexer devices are not intended as stand alone devices for use on standard printed circuit boards. They are designed to be included inside plastic modules and protected by the plastic over-mold compound.

The general strategy was to develop a reliable high volume capable SAW and duplexer technology, using wafer level manufacturing techniques, while achieving industry acceptable performance.

IV. WHERE DO SAWS BELONG?

When integrating SAWs or duplexers into modules, one of the first questions is where do they belong? It seems there is no one answer, however there are specific considerations to keep in mind.

Fig. 4 shows a two module 2.5G radio solution which can be achieved if the SAWs are integrated with the transceiver. The diagram also shows the power amplifier, switch and controller are integrated together in a transmit module. Alternatively some manufactures integrate the SAWs with the switch yielding a three module radio as shown in Fig. 5. These partitioning decisions are driven by many things, but as a minimum include historic product offerings, partnerships, willingness to manage more of the supply chain, and general technical capabilities.

In 3G handsets, the minimal number of modules appears to be achieved when the SAWs and duplexers are included in a front end module with the LNAs and a multi-port switch as shown in Fig. 6.

This enables the ability to include the matching components within the module and to minimize the pin count in the transceiver. Including the LNAs with the transceiver can lead to more pins as a second SAW is frequently employed right after the LNA requiring three pins per LNA.

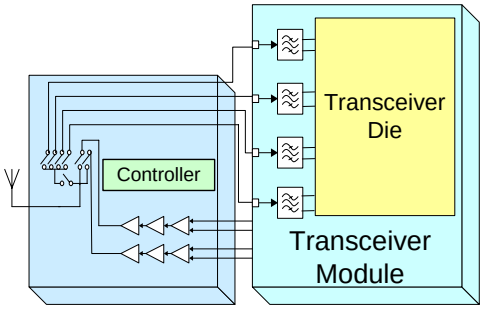

Fig. 4. Two module 2.5G solution with SAWs inside the transceiver module Source: RFMD

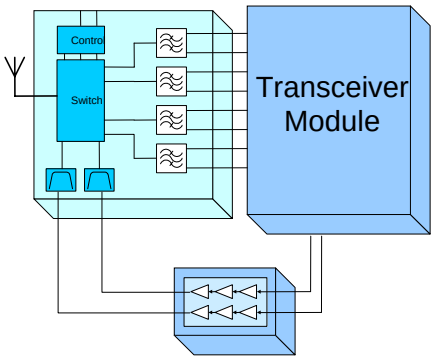

Fig. 5. Three module 2.5G solution with SAWs inside the switch module Source RFMD

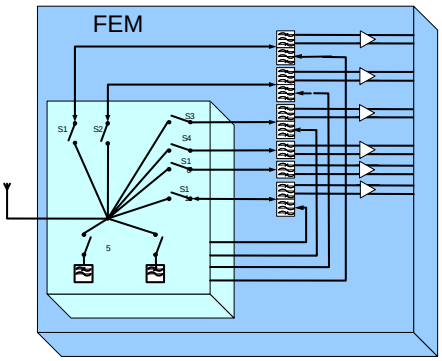

Fig. 6. The above 3G front end module with SAWs and duplexers integrated between the switch and LNAs Source: RFMD

V. WHAT IS WAFER LEVEL PACKAGING?

Wafer level packaged devices are processed at the wafer level where the complete wafer is processes, instead of the individual die. Singulation of the device is performed after the packaging steps are complete. Some refer to WLP as a true chip-scale packaging technique. Presently there is no one standard method for wafer level packaging, however many companies are deploying WLP processes for various products. Fig. 7 shows an overview of the wafer level packaging process used at RFMD.

A key priority was to develop a process to create an open cavity to enable the proper performance of the SAW device. Developing a method to etch open a cavity using a sacrificial material and then over coating the area to create the hermetic cavity was fundamental to enable use of the WLP process.

To achieve the benefits outlined in the goals listed above for using wafer level packaging, the product process had to be compatible with established wafer level semiconductor processing yet be benign to the performance of the SAW filter. For example the process had to handle the product using wafer handling methods and the deposition and etching techniques needed to be identified that would not damage the SAW fingers or substrate materials.

Other key requirements included the need to use a standard photolithographic processes, and use of standard back end wafer handling procedures for the following process steps:

- Wafer Singulation
- Die pick and place
- Die attach
- Wire bonding or flip chip
- Lead-free solder reflow
- Plastic encapsulation

One more difficult challenge was identifying a sacrificial material that would etch off without damaging the SAW fingers. This is used to create the critical open cavity to enable the SAW to operate properly.

Fig. 8 shows there was no damage introduced to the SAW fingers as the sacrificial material was removed.

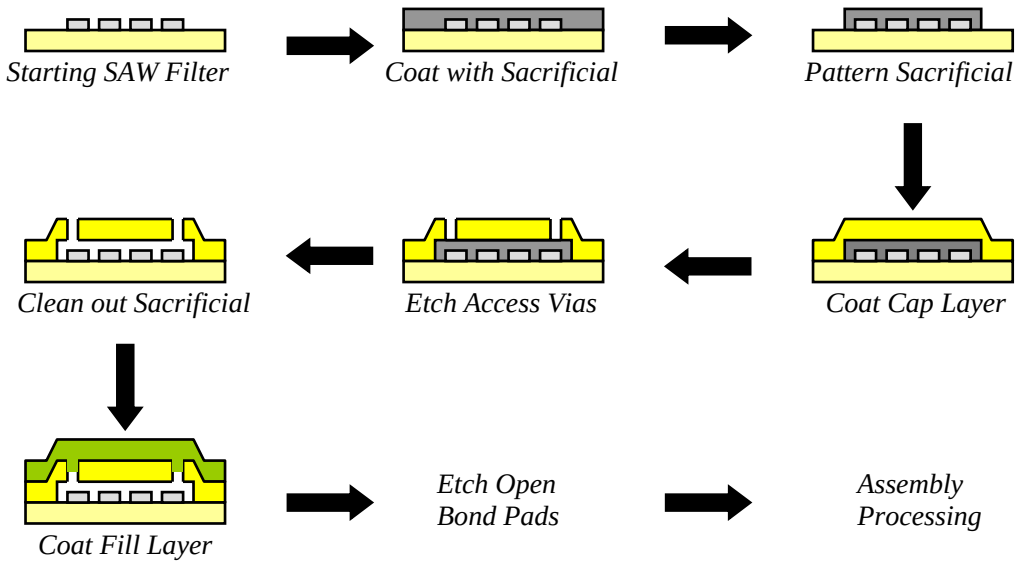

Fig. 7. Shows the process flow for wafer level processing.
Source: RFMD

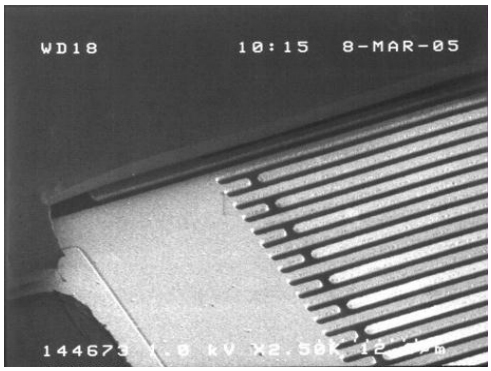

Fig. 8. Shows the SAW fingers after the sacrificial material has been removed. Source: RFMD

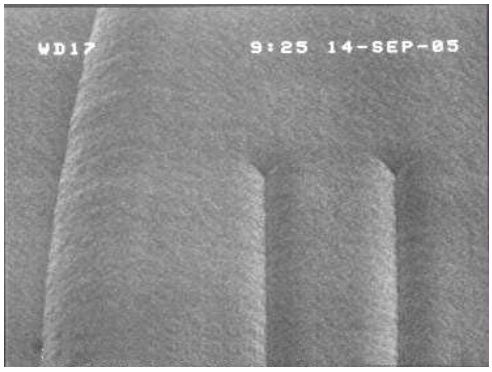

Fig 9. Shows an SEM image after the fill coat layer has been added sealing the etched vias Source: RFMD

Completing the fill coat layer and properly sealing the vias used to etch out the sacrificial layer is one of the critical and final steps in the process.
Although the via will never completely fill to be the same level as the top of the cap, the vias are successfully sealed to provide a hermetic cavity for the underlying SAW.

VI Reliability

To support the high volume goals for the WLP SAWs as part of the transceiver module programs, reliability goals of just a few PPM were required.

As with standard SAW devices long term cavity integrity is critical to maintain the performance of the WLP SAW.

The primary challenge was to maintain the cavity integrity through all the assembly and integration process steps without compromising the hermeticity of the package. Thermal stress is introduced when the devices is processed through the lead-free solder bump reflow. Additional stress is produced when the WLP device is processed through the high pressure transfer molding step.

VII WLP Electrical Test Results

The test results shown in Fig. 10 indicate that the WLP performance doesn't appreciably change through the manufacturing process steps including integration into the transceiver module.

In the case of Polaris 3 Total Radio, there are four SAW filters configured as two dual band WLPs; one for the low bands and the other for the high bands. The WLP SAW filters are solder-bumped along with the RF6030 die and are flip chip mounted onto the RF6030 transceiver module laminate as shown in the picture below. The SAW impedance designed to match the impedance of the LNAs to reduce the number of matching elements, and also to achieve optimum performance.

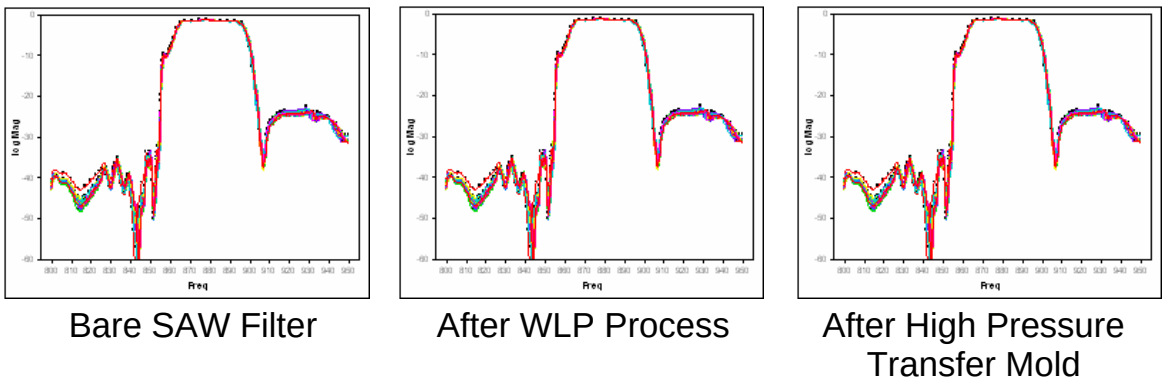

Fig 10. Shows the WLP SAW performance before and after the process steps Source: RFMD

Fig. 11 shows the bottom side of dual low band SAWs in wafer level packaging format and Fig. 12 shows the bottom side of dual high band SAWs. Flip chip solder bumps are evident in support flip chip assembly which is consistent with the CMOS based transceiver die.

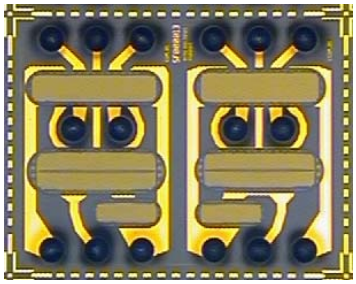

Fig. 11. Bottom side of dual low band SAWs in WLP Format. Source: RFMD

Fig 12. Bottom side of dual high band SAWs in WLP format. Source: RFMD

VIII. CONCLUSION

We have seen that quad band 2.5G and multi band 3G handsets provide an enhanced market opportunity for SAW and duplexer manufacturers.

We discussed how the use of module technology provides benefit to handset manufacturers in terms of size, ease of use, cost of supply chain management and cost of manufacturing.

Placement of SAWs in the transceiver module enables a two module radio today where placing SAWs with the switch enables a three module radio.

Using wafer level packaged SAWs provides an advantage in size and manufacturability compared to historic packaging techniques of ceramic hermetically sealed devices.

Wafer level packaging also helps reduce the cost of SAWs through use of wafer handling process methodologies providing advantage in manufacturing scale.

We have shown that the WLP process does not affect the performance of the SAW even through the bumping and transfer molding process.

The WLP process enables an industry leading size for transceiver modules, as shown in Fig. 13, targeted at GPRS/EDGE handsets today.

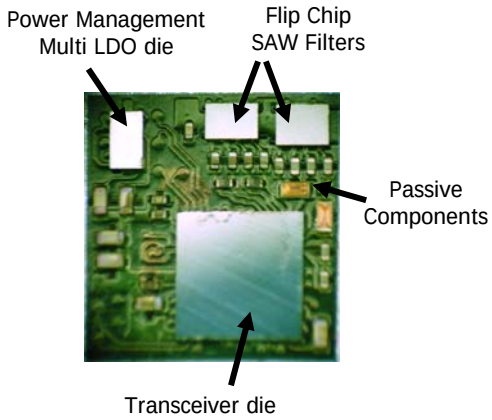

Fig.13 . Shows WLP SAWs in an EDGE transceiver module for handset applications Source: RFMD

ACKNOWLEDGEMENTS

The author would like to thank all the people at RFMD who have worked and are working on the various module and WLP SAW process technologies to enable products like those described above.

References

[1] M Press “RFMD Market Model, handset production” release Dec., 2006

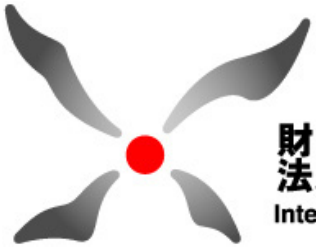

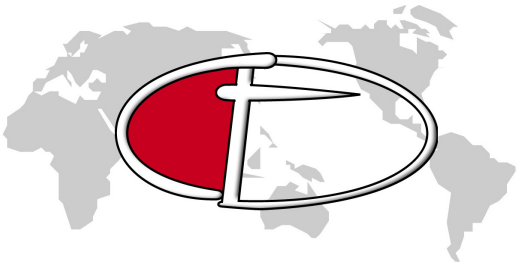

Japan-Taiwan Workshop on Future Frequency Control Devices

Thursday, 8th - Friday, 9th March, 2007
Keyaki Hall, Chiba University

Sponsored by
Interchange Association Japan
and Chiba University

Welcome to the First Japan Taiwan Workshop!

On behalf of Chiba University and the Organizing Committee, I am most delighted to invite you to the Japan Taiwan Workshop on Future Frequency Control Devices, which is held in conjunction with the Third International Symposium on Acoustic Wave Devices.

Presently frequency control devices are well recognized as key components in various modern electronic systems, for example, mobile communications and digital home electronics, and their technological progress and growth in the worldwide market are significantly owed to rapid evolution of the frequency control devices. Here, the frequency control devices involve resonators, filters, sensors and oscillators based on bulk and surface acoustic waves, MEMS and quantum effect technologies.

Although Japan and Taiwan are technological leading edges in this area, it seemed that technical interaction between their specialists has been scarcely made. I discussed with my friends in Taiwan on this matter, and we concluded that such an interaction will offer various benefits to both sides, especially for young engineers and professors. I proposed Taiwan professionals to organize joint Japan Taiwan workshops regularly, and this motion was seconded favorably. Fortunately, we could receive the financial support from the Interchange Association Japan just on time, and this workshop was organized as the first attempt.

Finally, the organizing committee would like to express its special thanks to Prof. T.T. Wu of National Taiwan University and Dr. C.S. Lam of TXC Corp. for their efforts on the program preparation. The organizing committee is most indebted to the Interchange Association Japan, Chiba University and the Venture Business Laboratory of Chiba University for their sponsorship.

8th March, 2007

K. Hashimoto

Ken-ya Hashimoto
Chairman of the Organising Committee
Professor of EEE
Chiba University

日本と台湾との架け橋
財団法人 交流協会
Interchange Association,Japan (IAJ)

Thursday, 8th March

Opening Remarks

13:50 K.Hashimoto, Chiba University

JA RF Devices (Chair: T. Omori)

JB Oscillator Technologies (Chair: C.S. Lam)

Friday, 9th March

JC SAW Sensors and AO Modulators (Chair: H. Yatsuda)

JD New Thin Films and Characterization (Chair: I.N. Lin)

Integration of RF Front-End Modules for the Handsets

by Wang-Chang Albert Gu，Yuantonix Inc.

Abstract

RF front-end (FE) of modern wireless terminals and handsets has evolved from a nearly all-discrete implementation to highly integrated RF IC's and RF front-end modules (RF FEM). This trend of RF FE integration is continuing, and will eventually lead to RF front-end engines, which are characterized not by circuit functionalities, but by standard interfaces. This paper reviews the current trends of RF front-end integration along with its constituting technologies, followed by technical discussions on the advancement from RF FEM to RF FE engines for future multi-band and multimode terminals and handsets.

Current Trends in RF Front-End Integration

A. GSM/GPRS Radios

GSM/GPRS handsets are undoubtedly one of the most successful products of consumer electronics in history. Contributing to this success are its system as well as hardware specifications, which include time-division duplexing (TDD), Gaussian minimum shift keying (GMSK) modulation, channel spacing of 200 kHz, and a peak power about 2 watts. TDD avoids the use of costly and bulky duplexers, and the phase-only GMSK modulation entails the use of high-efficiency PA operated at saturation. Although GSM's wide channel spacing and relatively high transmitter power is not the best use of spectrum resource and battery power, it significantly relaxes the hardware requirements for the desired data rate and receiver sensitivity. To prolong battery life, GSM employs elaborate power control schemes by closely monitoring the strengths of received signals at the basestation to minimize the handset transmit (Tx) power. In terms of radio architecture, GSM radios almost universally adopt the direct conversion, or the zero IF (ZIF) receiver and the translational loop, or the offset phase-lock loop (OPLL) transmitter architectures. The ZIF architecture relaxes the front-end RF filter requirement since there is no need to attenuate signals at the image frequencies any more, while the narrow-band nature of OPLL circuit eliminates the interstate Tx filter (before PAM). Currently, the level of RF FE integration in GSM/GPRS handsets is the highest among all the handsets, which comprises an antenna switch module (ASM), a power amplifier module (PAM), a zero-IF (ZIF) transceiver IC, multiple receive (Rx) bandpass filters (BPF), and crystal a oscillator (XO) as shown in Figure 1.

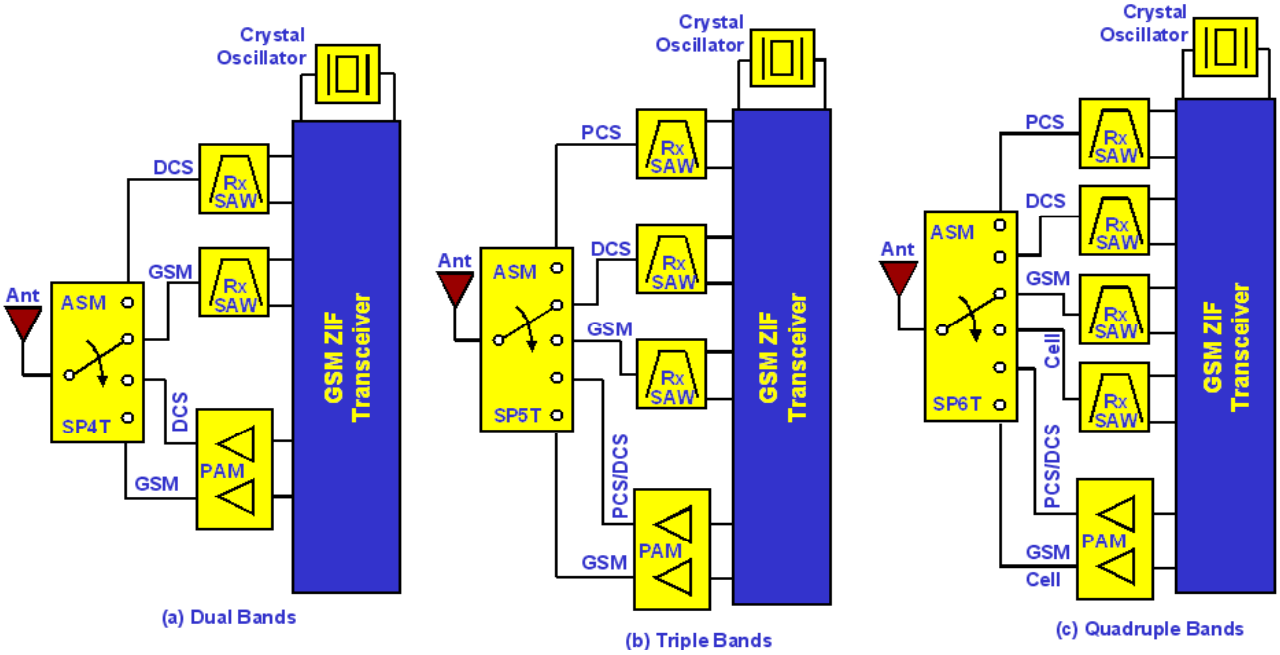

Figure 1. RF FE diagrams of GSM handsets: (a) dual bands, (b) triple bands and (c) quadruple bands.

ASM for multi-band handsets is a highly integrated RF FEM, which consists of a diplexer, multiple single-pole-dual-throw (SPDT) PIN diode switches, phasing circuits, and low pass filters (LPF) as shown in Figure 2. Key advantages of PIN diode switch include maturity, low costs, as well as single control line for each SPDT switch, however, it suffers from the fact that its circuit complexities increases linearly with the number of throws in the overall switching requirements. Further increase beyond four throws using the PIN switches will unavoidably put them in a cascade configuration, which doubles the overall insertion loss, and consequently, adversely impacts the receiver's noise figure and transmitter's efficiency. It is clear that future handsets are all multi-band and multi-mode in nature, and current PIN diode switches will be short in meeting their front-end switching requirements. PHEMT and UltraCMOS transistor switches are poised to replace PIN diode switches in coming years, which will be discussed later..

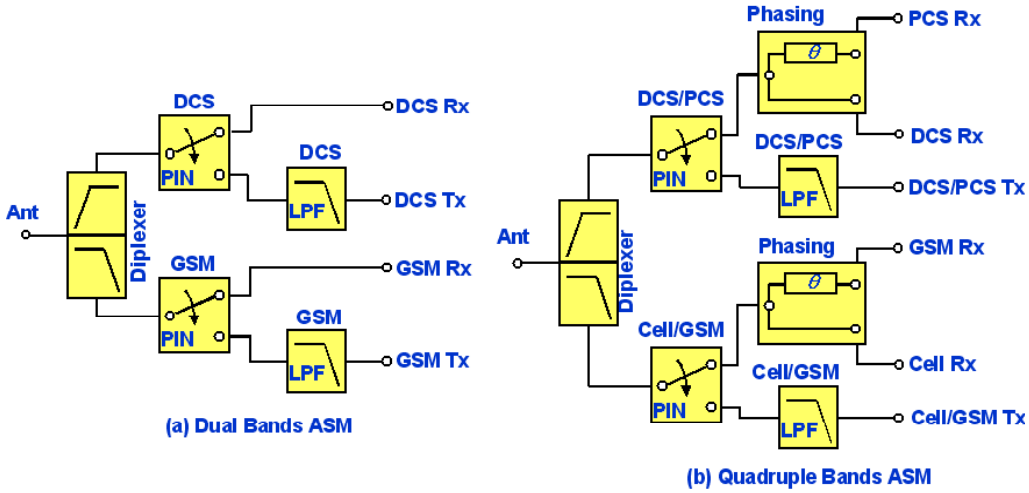

Figure 2. Circuit block diagrams of (a) dual-band and (b) quad-band ASMs.

PAM in GSM handsets today may be better referred to as a transmitter module rather than just a simple PA module, which encloses multiple-stage RF amplifiers on IC's, input/output matching circuits, power detectors, and a control IC encompassing close-loop power control, temperature compensation and logical functions as shown in Figure 3.. For the amplifiers, GaAs HBT remains as the technology of choice for its power added efficiency (PAE), power density and long-term reliability. CMOS based PA is slowly gaining ground for its cost and ease of system-on-chip (SOC) integration, but still lacks in PAE performance, while the increased die size is offset due to SOC integration.

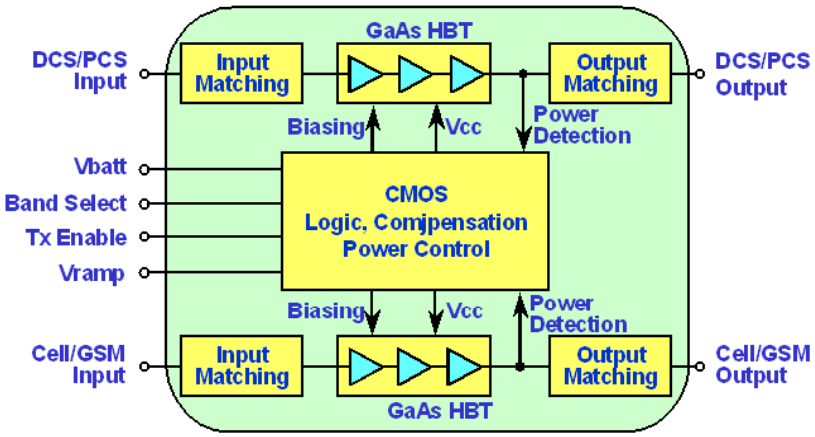

Figure 3. Block diagram of a quad-band GSM PAM.

Rx SAW filters are universally adopted in GSM handsets in single-end-to-balanced configuration to minimized interference to the received signals. By slowing down the RF signals by more than ten thousand times into surface acoustic wave signals, the size of the filter is greatly reduced. In addition, the discoveries of leaky-wave crystal cut such as 36^{o} to 42^{o} Lithium Tantalate crystals in the 80's paved the ways for the low-loss RF SAW filters. The path of integration in SAW filters starts with two filters in one package, or the 2-in-1 filter, and is moving to filter bank solutions. While RF SAW industry enjoys tremendous success today, it also faces challenges not in the areas of material, manufacturing and design, but in the miniaturized hermetic packages first in chip-scale package (CSP), and next on the wafer-level package. The hermetic requirement is not likely to go away for SAW devices, and the exotic nature of its crystalline substrate prevents it from SOC integration onto the transceiver IC, which propels handsets makers along with component suppliers to develop RF filter solutions more suitable for SOC integration such as BAW filter, which will be discussed later.

The trend of RF FE integration in GSM/GPRS handsets is continuing to a high level. On the transceiver side, complete absorption of the VCO control and frequency synthesizer circuitries is underway, leaving behind a simple crystal oscillator to provide stable frequency reference, which is made of quartz, and requires hermetic package as well. Yet to be seen is the proposals to develop a all-digital baseband processor, and move all the mixed-signal functions to the transceiver, which include the analogue-to-digital converter, digital-to-analogue converter, low pass filters, and various control and driver circuits. The benefits of such approach are three folds: First, by separating the digital circuitries from mixed-signal and analogue circuitries, the all-digital baseband processors are much more conducive to application-oriented solutions, which falls mostly into the digital signal processing (DSP) domains; Secondly, design and manufacturing cycles for the all-digital IC can be more easily and efficiently streamlined; Finally, the most advanced digital-IC technologies can be adopted immediately before the corresponding mixed-signal technologies becoming available. Other trends of further integration of RF FE in GSM/GPRS handsets include: 1) PA/Switch module incorporates the PAM and ASM into a single FEM; 2) Filter bank module puts multiple Rx filters into a single package; and 3) Transceiver/filter module either integrates the RF filters onto the transceiver IC, or into a common package.

B. EDGE Radios

The transitional standard called "enhanced data rate for GSM evolution" (EDGE) presents a unique set of problems in radio design. As a transitional standard, it implies the coexistence of both GSM/GPRS and EDGE systems in the same coverage areas with the same service provider, and dual-mode handsets are necessary wherever such systems exit. Relevant to radio hardware, EDGE standards are similar to GSM/GPRS standards, with only one noticeable difference, i.e., the linear modulation scheme of 8-PSK. The common TDD specifications and Tx/Rx bands imply the FE ASM and Rx filters can be shared between GSM and EDGE signals, however, the narrowband OPLL architecture and non-linear PA are unique to GSM transmitter, and EDGE radio requires a linear transmitter. Linear transmitter will be appropriately covered in the next section when CDMA radio is discussed. Currently, the most widely used solution for the GSM/EDGE transmitter is a hybrid of OPLL and direct up-conversion architectures. The GSM signal is still processed through the OPLL circuits bypassing the direct up-conversion circuit, while the EDGE signal is processed through both circuits with the OPLL serving as a local oscillator in converting the baseband I/Q signals directly into RF signals. Such hybrid approach allows a common PA to be used for both GSM/GPRS and EDGE signals. In terms of RF FE hardware, EDGE radios add a companion IC for direct up-conversion to the existing ZIF transceiver containing the OPLL transmitter circuit. In addition, a Tx interstage filter is needed to filter out-of-band noises.

C. CDMA/CDMA2000/WCDMA Radios

After its initial success in the North American market and later in segmented markets in South America and Asia, CDMA technology is becoming the dominant technology in third generation (3G) standards with 3 variants: 1) CDMA2000, 2) WCDMA, and 3) TD-SCDMA. Except the nationalistic TD-SCDMA standards, the radio architectures and hardware implementation in RF FE are similar in all CDMA handset, which is depicted in Figure 4. The major differences between GSM and CDMA handsets are two folds: 1) The frequency division duplexing (FDD) in CDMA requires a duplexer to provide a low-impedance path for the desired signal (Tx or Rx) while simultaneously attenuating the other signal separated by a frequency guard-band; and 2) The widely used OPLL Tx architecture in GSM is not suitable for linear modulations with amplitude modulated (AM) components, and broadband Tx architectures such as direct up-conversion or polar architecture has to be adopted, which requires filtering the Tx signal before the PA. Finally, it is more common to use chipset solution for separate transceiver functions than a single transceiver IC today, however, a single-chip transceiver will become more popular in the near future for the obvious reasons of implementation simplicity, size and costs.

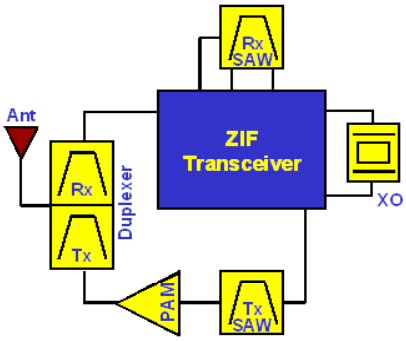

Figure 4. RF FE diagram of a CDMA handset.

The evolution in duplexer technologies is much more lengthy and complicated than SAW filters. The whirlwinds of RF SAW's miniaturized size and weight have swept the filter landscape clean of RF ceramic filters in the mid 90's, while similar forces has only taken the SAW technologies halfway into the duplexer application in CDMA handsets. More specifically, although SAW duplexers dominate in 850-MHz (cellular) band, the 1900-MHz (PCS) band duplexers is dominated by the film bulk acoustic resonator (FBAR) technology. FBAR technology, or the bulk acoustic wave (BAW) technology in general, has advantages over SAW in three important areas: 1) higher resonator quality (Q) factor for better insertion loss and steeper filter roll-off, or the so-called skirt, 2) better thermal stability for relaxed temperature margins in the duplexer design, and 3) better power handling capabilities for passing amplified Tx signals. Furthermore, SAW technology is reaching it's upper frequency limits in RF filter applications. As the frequency of SAW device is determined by the finger widths of its interdigit transducers, its insertion loss suffers as these fingers become narrower and thinner at higher frequencies. The upper frequency limit for low-loss RF SAW filter applications is probably around 2.0 to 2.5 GHz, which covers most wireless handset applications today, however, as mentioned earlier, the PCS duplexer presents great challenges to SAW manufacturers, and the upcoming WiMAX applications with frequencies in the range of 2 to 10 GHz are definitely beyond the scope of SAW.

BAW devices come in two distinct flavors, they are: FBAR with suspended piezoelectric thin-film membrane, and solidly mounted resonator (SMR) technology with piezoelectric thin-film sitting on top of a multi-layered acoustic mirror. FBAR duplexer enjoys the first-mover advantages in the market places, however, it requires great attention in controlling the residual stress in the membrane after the suspended film is released. Both FBAR and SMR devices also require precise control of the crystalline structure in the thin-film as well as its thickness, which are mostly made of Aluminum Nitride (AlN) or Zinc Oxide (ZnO) materials. Finally, all SAW and BAW devices require hermetic packages to protect their active surface from particulate and condensate, which may adversely affect their frequency precision and performance in frequency selectivity.

Hermetic packaging not only adds to the costs for these acoustic devices, it also prevents them from an easy integration path in RF FEM's and transceiver IC as well. In RF FEM integration, SAW and BAW devices are first enclosed by a chip-scale package (CSP) with hermetic cavities before packaged again in the RF FEM package. Therefore, these devices will see at least three high-temperature environments during the manufacturing cycles of the phone boards, which are especially hostile to SAW devices due to their pyroelectric nature. The BAW processes are compatible to CMOS processes, which opens the door for transceiver SOC integration. Strictly speaking, the FBAR processes are of the MEMS varieties, and its transceiver SOC integration is feasible but may not be economical. Although SMR is the best candidate for future transceiver SOC integration, it still requires hermetic protection at the wafer level, or a micro-cavity, before it is packaged along with the transceiver IC.

Moving on to the PAM for CDMA handsets, all CDMA standards adopt linear modulations with AM and phase modulated (PM) components. Unlike PM-only modulation as in GSM, designers of CDMA transmitters face difficult design trade-offs in linearity, complexities and PAE. Fortunately, CDMA PA's are operated at about 6 dB lower than GSM ones, and linearity and complexities are of the primary concerns for signal fidelity and lower costs. Today most CDMA transmitters adopt the direct up-conversion architecture for its simplicity with PA operating at a "back-off" point from saturation for best linearity, while PAE is compromised. With more and more power-hungry applications added to the handsets such as MP3/4's, mobile TV's, and prolonged internet connection, there is no doubt that saving battery power has to become higher priority in the CDMA PAM design.

To date, the best candidate for the high-efficiency as well as high-linearity performance is the so-called polar-loop architecture, where the amplitude and phase components of the modulated signal are processed separately. The PM components are amplified in a “non-linear PA”, which is operated at saturation point without loss of fidelity, while the AM components are processed and added back to the overall signal via the dynamic biasing voltages presented to the PA, which is proportional to the AM components of the original signal. For power control considerations, the polar loop is implemented with a feedback loop and power detection circuits at the output of the PAM.

The PAM’s for CDMA handsets are noticeably smaller and simpler than GSM PAM’s due to the fact that most control, compensation and logic circuitries are not integrated into the PAM. Figure 5 shows a typical CDMA PAM with its functional blocks, which comprise a two-stage amplifiers, input/output matching circuits and biasing circuit. The CMDA PA’s are predominantly of the GaAs HBT varieties, and GaAs pHEMT running as a distinct second. The integration path for CDMA PAM’s will follow that of GSM PAM’s by incorporating the control, compensation and logic functions into the PAM. In the markets supporting dual-band CDMA system, dual-band CDMA PAM will become more common as well. Finally, as will be discussed later, future 3G handsets are inherently multi-band and multi-mode, which calls for a single-pole-multiple-throw RF FE switch, and pHEMT technology is the leading candidate to provide such challenging RF FE switching functions. pHEMT technology is appealing in that the power-amplifying and switching functions can be integrated onto a single RF IC along with the required control, compensation and logic functions using the emerging enhance/depletion (E/D) mode pHEMT technology.

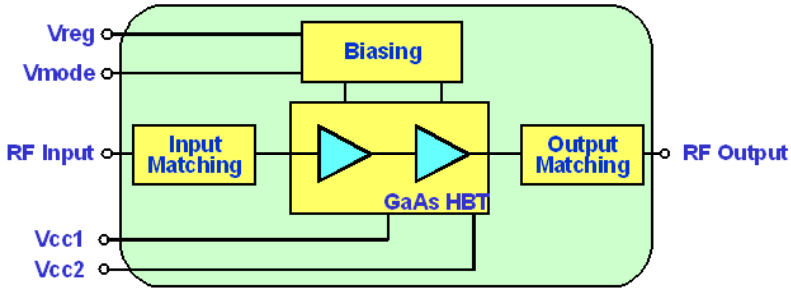

Figure 5. Block diagram of a CDMA PAM.

To illustrate its complexities, Figure 6 shows the FR FE of a CDMA/CDMA2000 handset. It is noticed that the global positioning system (GPS) is becoming a standard feature for handset sold in the North American market, and a FE triplexing circuit or a SP3T switch is required. Using a triplexer has the advantage of receiving the GPS signals and simultaneously making a CDMA phone call, while the SP3T switch forbids such simultaneous operations. Like GSM radios, the RF FE of CDMA/CDMA2000/WCDMA handsets are moving to a higher level of integration with the following trends: 1) 2-in-1 filters puts two Rx or Tx filters into a single package; 2) PA/duplexer/Tx filter module incorporates the PAM, duplexer and Tx SAW filter into a single FEM; and 3) Triplexer/duplexer module incorporates the triplexer and duplxers into a single FEM.

RF FE Engines for the Multi-Band, Multi-Mode Handsets

As mentioned earlier, 3G handsets are inherently multi-band and multi-mode, and modular approaches in its RF FE is the only way to achieve the desired time-to-market for handset manufacturers. Figure 7 depicts the RF FE diagram of a WCDMA/GSM/GPRS handset, where all the blocks have been discussed in the previous sections except the SP7T switch. This new SP7T switch has very stringent requirements in linearity, insertion loss and power handling. The linearity requirement for conventional ASM used in GSM/GPRS handsets is much relaxed than CDMA/CDMA2000/EDGE/WCDMA handsets due to its constant-amplitude GMSK modulation. CDMA and all 3G radios adopt linear modulations with signals containing both AM and PM components, and linearity is essential to prevent cross modulations between these AM and PM components, otherwise, loss of digital data will be prevalent. In addition, this SP7T switch has to provide at least 3 low-loss ports for passing GSM/GPRS and WCDMA Tx signals. Several manufacturers are currently developing this SP7T switch using different technologies such GaAs E/D pHEMT, GaAs E/D JFET and UltraCMOS technologies, in the mean time, cascading SP4T

switches or the combination of a diplexer and SP3T/SP4T switches serve as a interim solution. Finally, it is worthwhile to mention that single control line is required for the SP2T PIN diode switch such that only 2 control lines is needed for a SP4T PIN diode switch. This is not the case for transistor switches, where a control line is needed per “throw” of the switch, e.g., four control lines are needed for a SP4T transistor switch. To reduce the complexities between baseband IC and FEM, the control logics of transistor switches has to be simplified, and the GaAs E/D modes is an enabling technology for this advanced switching solution, where the depletion-mode switches and enhancement-mode logic circuits are integrated onto the same RF IC.

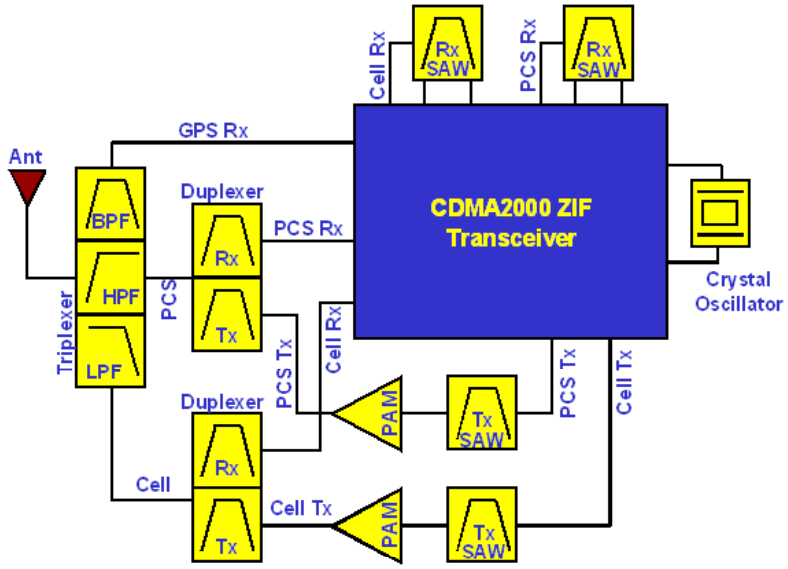

Figure 6. RF FE diagram of a dual-band CDMA/CDMA2000 handset.

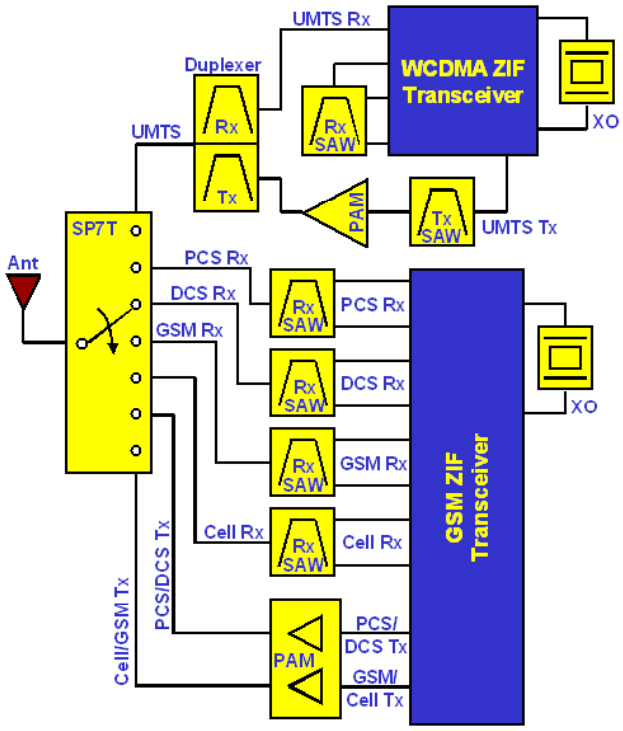

Figure 7. RF FE diagram of a WCDMA/GSM/GPRS multi-mode handset.

As a 3G standard, CDMA2000 adopts evolutionary paths for improved high-speed data communications. CDMA2000 consists three evolutionary networks: 1xRTT (single carrier radio transmission technology), 1xEV-DO (1x revolution data optimized), and 1xEV-DV (1x revolution data & voice), which are also backward compatible with 2G CDMA/IS-95 networks. Since there is no added spectrum resource in CDMA2000 networks, further improvement in voice capacities and high-speed data traffic has to be accomplished via advanced radio hardware as well as software in both basestations and handsets. On the handset side, the most important development is the so-called "diversity receiver" technology, where a 2nd independent receiver is added to counter the problems of multi-path fading for improving the sensitivity of the overall receiver. A typical CDMA2000 handset with diversity receiver is depicted in Figure 8. It should be noticed that there is no protection of a duplexer in the diversity path from the Tx blockers in the main path, and this job of added protection is partially fallen onto the Rx filters in the diversity path.

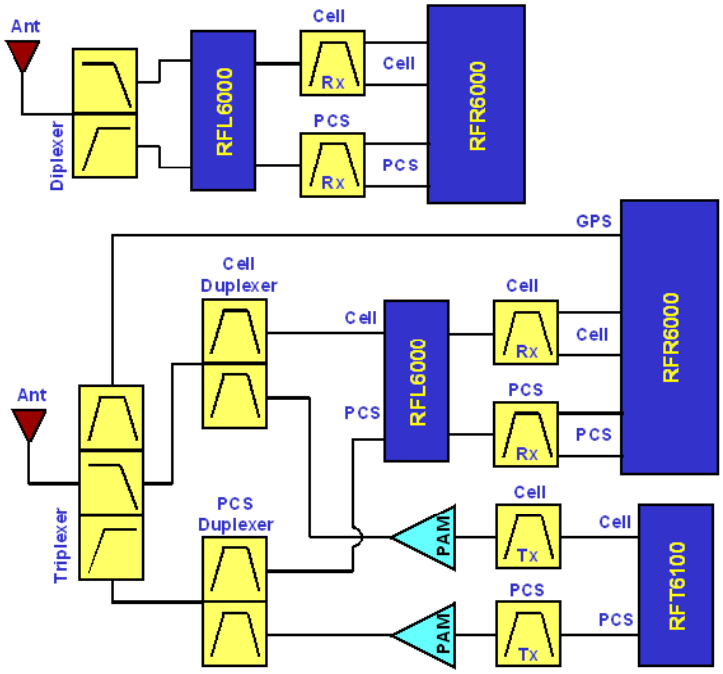

Figure 8. RF FE diagram of a CDMA2000 handset with diversity receiver.

3G cellular technologies are capable of delivering rich services in voice, audio, video and high-speed data communications. Handset manufacturers are facing ever-increasing complexities in hardware and software of application processors, and radio FE's have also grown considerably as seen in Figures 7 and 8, not to mention the yet-to-be-implemented polar loop PA for extending battery life. The trends for handset manufacturers to focus more on developing application-oriented solutions in baseband processors will undoubtedly shift the development of radio FE solutions to RF FEM providers. Radio hardware is notoriously known for its long development cycle due to the coexistence of strong Tx and weak Rx signals spanning as high as 100 dB apart, i.e., 10 billions to one. Even in its highly modular forms, interactions and interferences between FE modules and other supporting circuits can still be overwhelming in the multi-modes and multi-bands configurations. The time-to-market of handsets can be greatly improved if the radio FE is provided in a single shielded package called "RF FE engine," or RF FEE. For example, figures 9 and 10 illustrate, respectively, the RF FE engines of a quadruple-bands GSM/GPRS radio and a single-band CDMA/WCDMA/CDMA2000 radio. It is noticed that RF transceivers are not included in above mentioned RF FEE's due not to technical reasons, but to the market reality of separate suppliers of transceiver and RF FEM, furthermore, RF transceiver IC's are mostly provided with baseband IC's in a chipset arrangement. Inclusion of RF transceiver in RF FEE will eventually come about for technical considerations of optimized RF performance and completely shielded circuits from outside interference.

In conclusion, RF FE engines allow handset manufacturers to acquire fully debugged, trouble-free radio FE solutions for the emerging multi-bands and multi-modes handsets with greatly reduced time-to-market. Future handset manufacturers should be able to efficiently and quickly configure radio FE hardware similar to adding

standardized components and features of personal computers, and the burden of designing radio FE's will be shifted from handset manufacturers to RF FEM providers today.

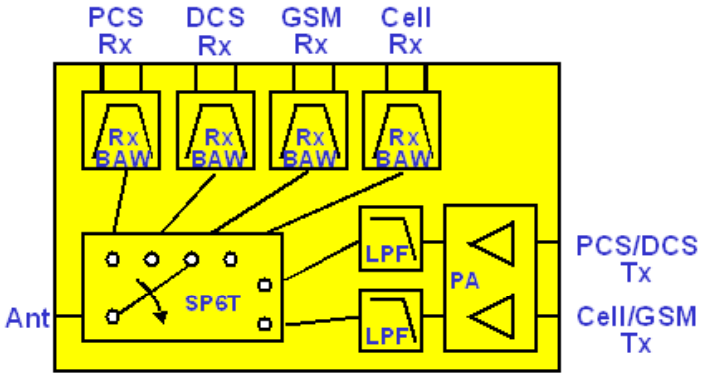

Figure 9. RF FE engine of a quadruple-bands GSM radio.

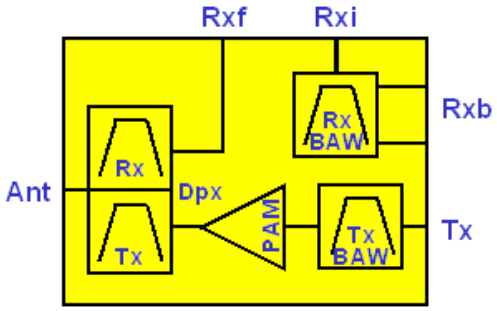

Figure 10. RF FE engine of a single-band CDMA/WCDMA/CDMA2000 radio.

Smaller SAW Duplexer($3\times2.5mm^2$) for US-PCS having Good Temperature Characteristics

Takeshi Nakao, Michio Kadota, Kenji Nishiyama, Yasuharu Nakai, Daisuke Yamamoto, Yutaka Ishiura, Tomohisa Komura, Norihiko Takada and Ryoichi Kita

Murata MFG. Co.,Ltd., Yasushi, Shiga, 520-2393, Japan.

Abstract— **Using flattened-SiO_2/Cu-electrode/36∼48° $LiTaO_3$ structure, small size ($5\times5mm^2$) surface acoustic wave (SAW) duplexer with a good temperature coefficient of frequency (TCF) for US-PCS was realized by authors. However, a smaller duplexer has been strongly required. Using flip-chip bonding process of SAW chips and Rayleigh SAW propagating on the flattened-SiO_2/Cu-electrode/126∼128°YX-$LiNbO_3$, which has larger coupling factor than above-mentioned substrate, a smaller sized ($3\times2.5mm^2$) SAW duplexer with a good TCF has been realized.**

I. INTRODUCTION

To realize the SAW duplexer for US Personal Communication Services (PCS), a SAW substrate having a suitable electromechanical coupling factor, a good temperature characteristic, and a large reflection coefficient is required. Authors have already realized the $5.0\times5.0\times1.7mm^3$(5050) size SAW duplexer for US-PCS with a good temperature coefficient of frequency (TCF) by using the flattened-SiO_2/Cu/36∼48°YX-$LiTaO_3$(LT) structure, and this SAW duplexer is widely used in a market[1][2]. The authors investigated further miniaturizing to a $3.0\times2.5\times1.2mm^3$(3025) size duplexer according to the market requirement.

As above-mentioned 5050 SAW duplexer are used bonding wires to connect SAW chips with the package, it is effective to employ a flip-chip bonding technique to miniaturize duplexer. However, the bonding wires in Tx filter of the SAW duplexer is operated to expand its bandwidth as expansion inductors, but the flip chip bonding can't be operated as the expansion inductor. And the 5050 sized duplexer uses the external components for impedance matching on the printed board but those external components cannot be used in the case of 3025 size because these is no space. So, in order to realize a 3025 sized US-PCS SAW duplexer, the SAW substrate for Tx filter should have the electromechanical coupling factor of 1.2 times larger than that of previously reported Tx filter of the 5050 size duplexer. Although it is possible to enlarge a coupling factor by thinning a thickness of SiO_2 film from the proper thickness to compensate the TCF, it introduces degradation of the TCF. Then authors investigated $LiNbO_3$ (LN) substrate having larger coupling factor than 36∼48°YX-$LiTaO_3$ instead of $LiTaO_3$ of the SiO_2/Cu/36∼48°YX-$LiTaO_3$ structure. And this new structure of the flattened-SiO_2/Cu-electrode/$LiNbO_3$ was applied to Tx filter of US-PCS SAW duplexer, then smaller sized ($3.0\times2.5mm^2$) SAW duplexer with a good TCF has been realized.

II. Rayleigh wave on SiO_2/Cu/$LiNbO_3$ structure

A. Calculation results

In order to realize a large coupling factor, authors investigated a new structure of the flattened-SiO_2/Cu-electrode/$LiNbO_3$ using $LiNbO_3$ substrate instead of previous reported $LiTaO_3$ substrate[1]. The structure of flattened-SiO_2/Cu-electrode/substrate previously reported by authors is shown in Figure 1. The SiO_2 film and Cu-electrode were composed in order to compensate the TCF and realized the large reflection coefficient, respectively.

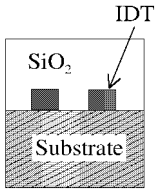

Fig1. Flattened-SiO_2/Cu/$LiNbO_3$ structure.

The electromechanical coupling factors of Rayleigh wave and leaky SAW (LSAW) on the SiO_2/$LiNbO_3$ structure are shown in Fig.2 as function of θ of Euler angles (0°, θ, 0°). The theoretical results are calculated by the reference[2]. Figure 2 shows results of the SiO_2 film of thickness 0, 0.2λ, 0.3λ and 0.4λ, where λ is a wavelength of SAW. In the case of SiO_2 thickness of 0.3λ , the results of Cu film of 0.05λ is also shown. It is clarified that the coupling factor of Rayleigh wave becomes maximum when θ is about 38° (it is called as 128° rotated Y cut) and then that of LSAW becomes minimum. The maximum coupling factor at the SiO_2 thickness of 0.3λ, Cu electrode one of 0.05λ, and θ=38° is about 1.2 times larger than that of LSAW on the previously reported SiO_2/Cu/36∼48°YX-$LiTaO_3$ structure[1]. The reflection coefficient of Rayleigh wave on the generally used Al-electrode/128°YX-$LiNbO_3$ structure is not large enough to be applied to a resonator with grating reflectors. So, Wen et al reported that

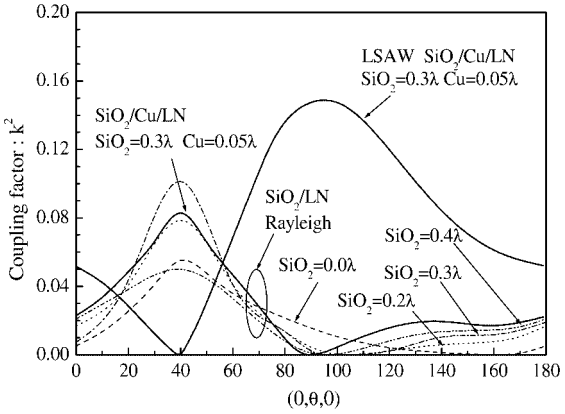

Fig2. Coupling factor of Rayleigh SAW and LSAW on $SiO_2/LiNbO_3$ or $SiO_2/Cu/LiNbO_3$ as a function of θ at (0°, θ, 0°).

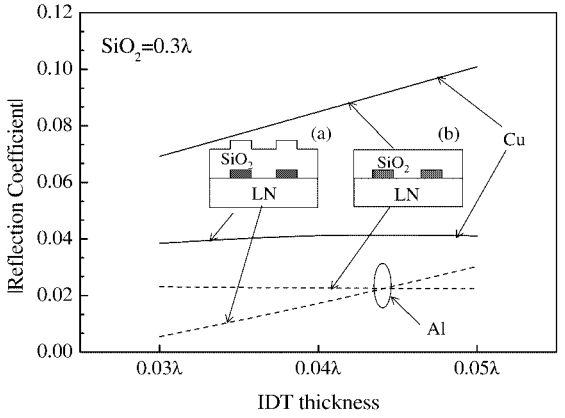

Fig3. Reflection coefficient of SiO_2/IDT/128°YX-$LiNbO_3$ on IDT-thickness.

large reflection coefficient is obtained by substituting Al-electrode to Cu-electrode[4]. But there were not reported $SiO_2/Cu/128°YX\text{-}LiNbO_3$ structure and its TCF.

Figure 3 shows the reflection coefficient at a finger electrode on Rayleigh wave on the surface flattened-SiO_2 structure and not flattened one as the function of thickness of Cu and Al electrodes at the SiO_2 thickness of 0.3λ. The Finite Element Method (FEM) was used in the calculation. The reflection coefficient at the Al electrode of Rayleigh wave is too small to be applied to resonator devices whether the surface of an SiO_2 film is flattened or not. On the other hand, the reflection coefficient at the Cu-electrode in the case of a flattened-SiO_2 surface is significantly larger than that of a not flattened one. This phenomenon has the opposite tendency to that of the SiO_2/Cu-electrode/36∼48° Y X-$LiTaO_3$ structure applied to the 5050 sized duplexer[1]. That is, the reflection coefficient of the flattened-SiO_2/Cu-electrode/36∼48° Y X-$LiTaO_3$ is smaller than that of non-flattened one. These results means that flattening of the SiO_2 surface is effective to obtain a sufficient reflection coefficient of Rayleigh wave on the $SiO_2/Cu/120∼128°YX\text{-}LiNbO_3$ structure. It is clarified that the Cu-electrode thickness should be thicker than 0.03λ in order to obtain sufficient reflection coefficient and low resistivity.

B. Application to a one-port resonator

Figure 4 shows the frequency responses of the one port resonators of the previously reported SiO_2/Cu-electrode /36∼48°YX-$LiTaO_3$ structure and above-mentioned newly developed SiO_2/Cu-electrode/128°YX-$LiNbO_3$ one. The wavelength of either resonator is 1.9μm, the number of IDT pairs is 120, the aperture is 32μm, the Cu-electrode thickness is 0.03λ, the SiO_2 film thickness is 0.3λ, and metalization ratio of fingers is 0.5. In the figure, the frequency is normalized by each resonant frequency.

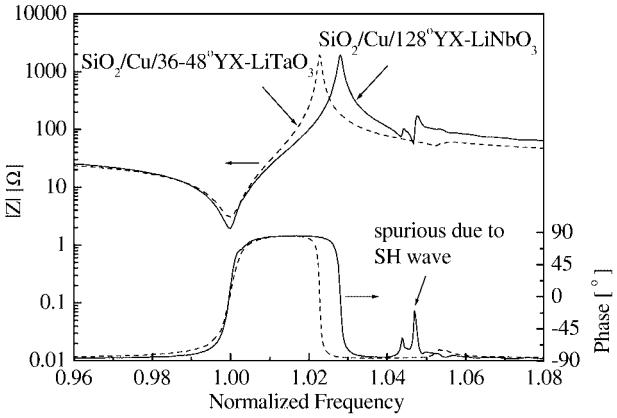

Fig4. Frequency responses of resonators composed of conventional and newly developed structures.

Table I shows the Q values at the resonant frequency and anti-resonant frequency, the relative bandwidth normalized by the resonant frequency, and the TCF of the anti-resonant frequency of each resonator. The coupling factor, which is relative to the bandwidth, of the newly developed Rayleigh wave on the flattened-SiO_2/Cu-electrode/128°YX-$LiNbO_3$ structure is 25% larger than the $SiO_2/Cu/36∼48°YX\text{-}LiTaO_3$ structure without degradation of the Q value and TCF, though a spurious response is generated at a little higher frequency than the anti-resonant frequency as shown in Fig.4. This spurious response is due to a LSAW.

Figure 5 shows the frequency responses of a one-port resonator on 120°, 124°, and 128°YX- $LiNbO_3$ with SiO_2 film and Cu-electrode. The Cu-electrode thickness is 0.03λ, the SiO_2 thickness is 0.3λ, and the metalization ratio is 0.5. In Fig.5, the spurious responses

Table I
SAW resonator properties of $SiO_2/Cu/LiTaO_3$ and $SiO_2/Cu/LiNbO_3$ structures.

substrate	Qr	Qa	Band width (fa-fr)/fr	TCF(fa) (ppm/°C)
SiO_2/Cu/36-48°YX-LT	320	1080	0.0226	-8
SiO_2/Cu/128°YX-LN	320	1070	0.0281	-7

of the LSAW are observed on a rotated cut angle of the $LiNbO_3$ substrate. In addition to the cut angle, the spurious response also depends on the thickness of Cu-electrode and SiO_2 film. It is confirmed that the spurious response would be able to be eliminated by optimizing a cut angle according to the design parameters such as a Cu-electrode thickness, a metalization ratio, and an SiO_2 film thickness.

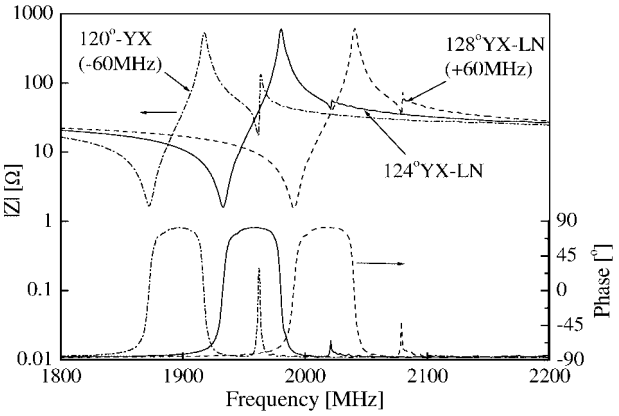

Fig5. Frequency responses of resonators on SiO_2/Cu/120~128° YX-$LiNbO_3$.

III. Applying to a US-PCS duplexer

The newly developed flattened-SiO_2/Cu/120~128° YX-$LiNbO_3$ structure was applied to the Tx filter of the 3025 sized US-PCS SAW duplexer. The Tx filter of the duplexer is ladder type consisting of three series resonators and three parallel resonators, while the 5050 sized duplexer has two parallel resonators. The Rx filter used a SiO_2/Cu-electrode/36~48°YX-$LiTaO_3$ structure as same as the previous report[1]. Both SAW chips of Tx and Rx filters are connected to the package by a flip chip bonding technique.

Figure 6 shows the frequency response between the Tx filters of the newly developed 3025 sized duplexer and the previously reported 5050 sized one. The improvement of the insertion loss of 0.2dB is realized compared with the previous 5050 sized duplexer.

Figure 7 shows response in wide range of frequency (0 to 6GHz) of the Tx filters of the newly developed 3025 sized duplexer and the previously reported 5050 sized one. In addition to the improvement of the insertion loss, the improvement of the attenuation in the frequency range of 2.4GHz to 6GHz is realized by employing above-mentioned third parallel resonator.

Figure 8 shows the frequency responses at -30°C, 25°C, and 85°C of the Tx filter. The temperature coefficient of frequency of higher side slope of the filter is -10~-15ppm/°C as same as the previous Tx filter of 5050 duplexer. As the results, it is realized that the maximum insertion loss of Tx band (1850~1910MHz) is 3.4dB and that the minimum attenuation of Rx band (1930~1990MHz) in 43dB in the temperature full range from -35°C to 85°C. And it is also confirmed that the newly developed duplexer can satisfy enough power handling capability and long term reliability required for a duplexer.

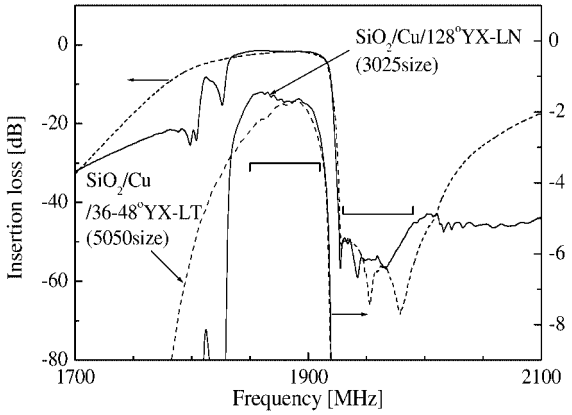

Fig6. Tx filter responses of conventional (dashed line) and newly developed (solid line) duplexers.

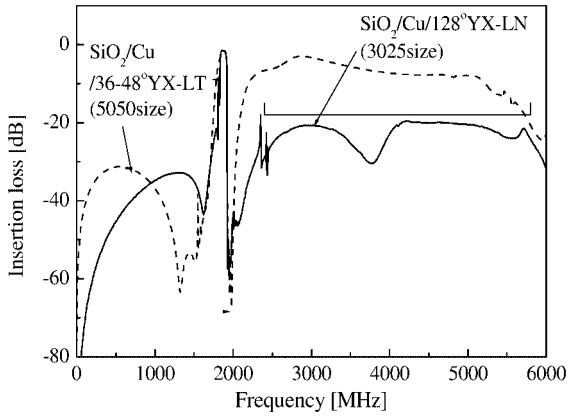

Fig7. Tx filter wide range spurious responses of conventional (dashed line) and newly developed (solid line) duplexers

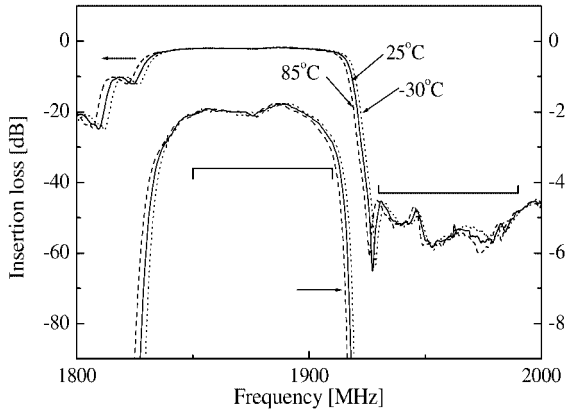

Fig8. Tx filter responses of newly developed duplexers at -30°C, 25°C and 85°C (with the loss of the measurement kit, about 0.2dB)

IV. Conclusion

The one port resonator with 25% wider bandwidth and without degradation of the Q values and TCF has been realized by using Rayleigh wave on the newly developed flattened-SiO_2/Cu-electrode/120∼128°YX-$LiNbO_3$ structure, compared with that of the previously reported the flattened-SiO_2/Cu-electrode/36∼48°YX-$LiTaO_3$ structure. These new resonators are applied to the Tx filter of SAW duplexer for US-PCS and the Rx filter is composed of previously reported flattend-SiO_2/Cu-electrode/36∼48°YX-$LiTaO_3$. In the addition to them, by using flip chip bonding, authors have realized significantly miniaturizing of US-PCS SAW duplexer from $5\times5\times1.7mm^3$ to $3.0\times2.5\times1.2mm^3$. The Tx filter with lover insertion loss and the lager attenuation in the range from 2.4GHz to 6GHz and the same TCF value of -10 to -15ppm/°C has been realized compared with the previous developed 5050 size duplexer.

Acknowledgement

The authors thank Mr. M. Hasegawa, Mr. K. Ikada, Mr. K. Sakaguchi, and so on for their assistance.

References

[1] M. Kadota, T. Nakao, N.Taniguchi, E. Takata, M. Mimura, K. Nishiyama, T. Hada, and T.Komura: Jpn. J. Appl. Phys., 44, (2005) 4527.

[2] J.J.Campbell and W.R.Jones: IEEE Trans.Sonics & Ultrason., SU-15, (1968) 209.

[3] M. Kadota, T. Nakao, N.Taniguchi, E. Takata, M. Mimura, K. Nishiyama, T. Hada, and T.Komura: IEEE MTT-S,WE1B-2, 382(2006)

[4] H.L Li, J.G.Wen, K. Hashimoto, T. Omori, and M. Yamaguchi: Proc. Symp. Ultrason. Electron., Vol.26, (2005) 193.

SHF Resonators Using Piezoelectric Lamb Waves Propagating in Mo/AlN/Mo Composite Membranes

Hisanori Matsumoto, Atsushi Isobe, and Kengo Asai
Wireless Systems Research Department
Hitachi, Ltd., Central Research Laboratory
Kokubunji-shi, Tokyo 185-8601, Japan
Email: hisanori.matsumoto.sn@hitachi.com

***Abstract*—Next generation wireless broadband systems should use higher carrier frequencies, and thus RF devices operating in the super high-frequency (SHF) band have become increasingly important. A novel piezoelectric Lamb wave (PLW) resonator composed of a Mo/AlN/Mo composite membrane is described for applications in the SHF band. We numerically and experimentally investigated the characteristics of PLWs propagating in the composite membrane. In both simulation and fabrication results, we found that a PLW with a phase velocity exceeding 25,000 m/s can be excited in the membrane. These results indicate that the membrane is suitable for PLW resonators in the SHF band.**

I. INTRODUCTION

Mobile broadband systems have been rapidly developed to enable Internet-access and multimedia- and data-based services as fast as those provided by wire communication technologies. Carrier frequencies of future systems such as mobile WiMAX and IMT-advanced systems (4G) should be in the super high-frequency (SHF) band, and thus RF devices operating in the SHF band have attracted much interest. Surface acoustic wave (SAW) resonators in RF circuits of conventional mobile terminals have been widely used because of their small size and high quality factor [1]. The resonant frequency of SAW resonators is uniquely determined from the wavelength and acoustic velocity. A short wavelength and/or high acoustic velocity are necessary to obtain high frequency SAW resonators. The excitation of short-wavelength SAWs requires a finely fabricated interdigital transducer (IDT), which results in an increase in the manufacturing cost. On the other hand, the SAW velocity is dependent on the materials and the cut angles of the substrates and the wave modes. Various attempts have been made to obtain a high-velocity SAW [2]-[7]. The highest SAW velocity reported up to now is approximately 10,000 m/s, and it was obtained using a layered structure with a diamond film [5]. However, SAW resonators operating in the SHF band require a higher acoustic velocity.

RF resonators using piezoelectric Lamb waves (PLWs) have a great potential for application in the SHF band because PLWs propagating in thin plates with a thickness comparable to the wavelength have a velocity that exceeds that of SAWs. Pioneering research on RF resonators based on PLWs has been conducted [8], [9]. Nakagawa *et al.* reported a PLW resonator that uses an AT cut quartz substrate and showed that their resonator obtained a frequency approximately three times higher than that of an SAW resonator when using the same substrate [8]. Bjurström *et al.* reported a PLW resonator that consisted of a sputter-deposited AlN piezoelectric film and Al electrodes [9]. Their resonator was fabricated with a freestanding AlN membrane using micromachining technology. However, to extend the operating frequency of PLW resonators to the SHF band, we need to investigate the propagation characteristics of PLW modes that have a higher velocity.

We suggested a novel PLW resonator composed of a Mo/AlN/Mo composite membrane for application in the SHF band [10]. Using simulated and experimental methods, we investigated the PLW characteristics propagating in the composite membrane for resonators operating in the SHF band. We obtained the impedance of a fabricated PLW resonator with a resonant frequency of 3.128 GHz and a relative bandwidth of 0.60%. The results indicate that the phase velocity of the excited PLW mode was as high as 25024 m/s.

II. SIMULATION

We used a finite element method (FEM) simulation to examine the characteristics of the PLWs propagating in the Mo/AlN/Mo composite membrane.

A. Mo/AlN/Mo Composite Membrane Model

Figure 1 shows the composite membrane model for our FEM simulation. The membrane consists of an AlN layer, an IDT in the middle plane of the AlN layer, and top and bottom Mo layers. The polarization direction of the AlN

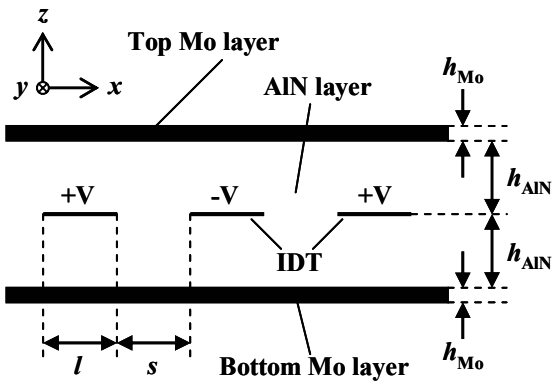

Fig. 1. Mo/AlN/Mo composite membrane model for FEM simulation.

layer is the same as the *z*-axis direction. The top and bottom Mo layers enhance the electromechanical coupling by directing the electric field in the same direction as the polarization. The top and bottom surfaces of the membrane are stress-free boundary conditions. The IDT fingers periodically arrange toward the *x*-axis direction and alternatively are applied positive and negative voltages. In Fig. 1, l is the line width of the IDT fingers, s is the space between adjacent fingers, h_{AlN} is half of the AlN layer's thickness, and h_{Mo} is the Mo layer's thickness. The top and bottom Mo layers have the same thickness in this model. We assumed that the model had an infinitely thin IDT. The IDT's period, $2l+2s$, equals the excited piezoelectric Lamb wavelength, λ_0. Therefore the normalized thickness of the composite membrane is defined as h/λ_0, where $h = 2h_{AlN}+2h_{Mo}$ and $\lambda_0 = 2l+2s$.

A two-dimensional model in the *zx* plane was used in the FEM simulation because the dimension along the *y*-axis direction is far larger than that along the *z*- and *x*-axis directions. A pair of IDT fingers was under periodic boundary conditions in the *x*-axis direction. The AlN material constants used in the simulation were those reported by Tsubouchi and Mikoshiba [3].

B. FEM Simulation Results

The FEM simulation estimated PLW modes with a high phase velocity and a large relative bandwidth excited in the composite membrane. The relative bandwidth is defined by $(f_a-f_r)/f_a$, where f_r and f_a are the resonant and anti-resonant frequencies. Figures 2(a) and 2(b) show the particle motions of the estimated PLW modes (L_1 and L_2) with good electromechanical coupling. The vector base and direction shown in Figs. 2(a) and 2(b) represent the maximum point and the direction of the particle displacement. For both L_1 and L_2, the displacement components in the *x*- and *z*-axis directions were asymmetric and symmetric. Symmetric modes were not excited in the composite membrane because the polarization direction of the AlN layer is asymmetric with respect to the middle plane of the membrane.

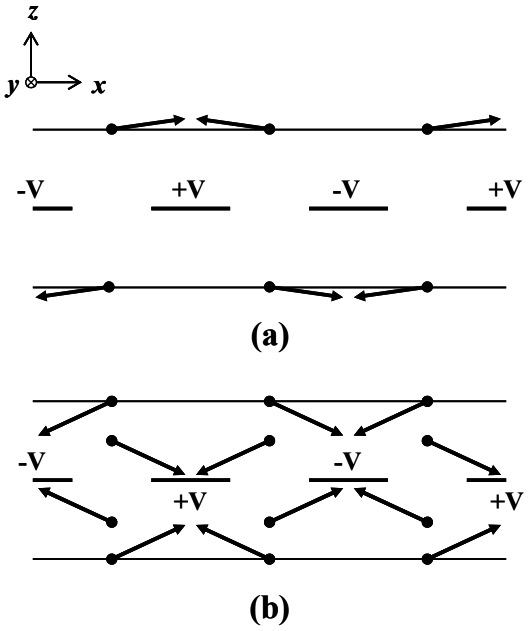

Fig. 2. Particle motions of PLW mode L_1 (a) and mode L_2 (b) estimated using FEM simulation.

Figures 3(a) and 3(b) show the estimated dispersion curves and bandwidths of L_1 and L_2 propagating in the membrane when the top and the bottom Mo layers were infinitely thin. Figure 3(a) shows that the phase velocities of L_1 and L_2 increase steeply when h/λ_0 decreases. As shown in Fig. 3(b), L_1 and L_2 obtained maximum bandwidths of 1.47% and 0.57% at an h/λ_0 of 0.5. When L_1 and L_2 reached the maximum bandwidth, their phase velocities were 11,446 m/s and 18,893 m/s.

Figures 4(a) and 4(b) show the estimated dispersion curves and bandwidths of L_1 and L_2 propagating in the composite membrane when the ratio of h_{Mo} to h_{AlN} was 0.2. The reason for L_2 being absent at an h/λ_0 of 0.1, as shown in Figs. 4(a) and 4(b), is that the bandwidth of L_2 at an h/λ_0 of 0.1 was below 0.05%, and we opted to exclude modes with a bandwidth below 0.05% in this study. The phase velocities of L_1 and L_2 shown in Fig. 4(a) are lower than those shown in Fig 3(a) because the model shown in Fig. 4(a) contained Mo layers with finite thickness. The maximum bandwidths of L_1 and L_2 were 0.89% and 1.38% at an h/λ_0 of 0.5, as shown in Fig. 4(b). When L_1 and L_2 reached the maximum bandwidth, their phase velocities were 8,870 m/s and 15,539 m/s. By comparing the results shown in Figs. 3(b) and 4(b), we found that when the Mo layers have a finite thickness, the bandwidth of L_1 decreases, and the bandwidth of L_2 increases. When heavy metals were put at the maximum displacement point, the bandwidth increased due to the mass loading effect. On the other hand, when metals were put at the maximum stress point, the bandwidth decreased due to a lowering of the piezoelectric efficiency. Therefore, the increased L_2

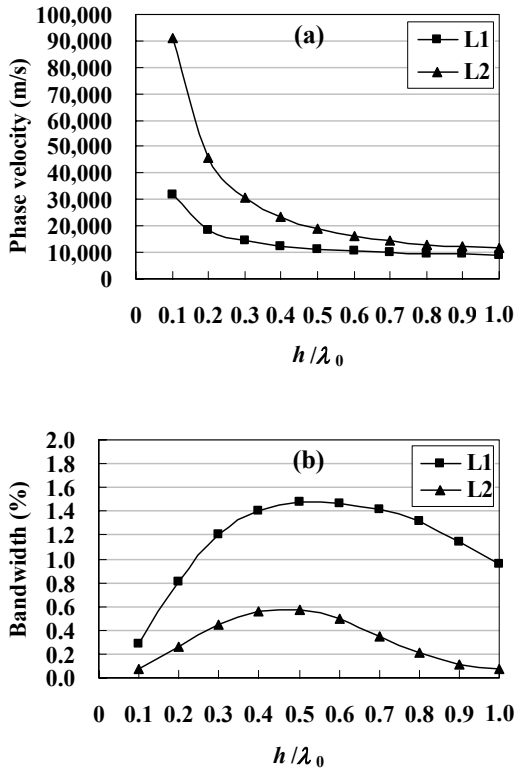

Fig. 3. Estimated dispersion curve (a) and bandwidth (b) of L_1 and L_2 propagating in composite membrane, where h_{Mo}=0.

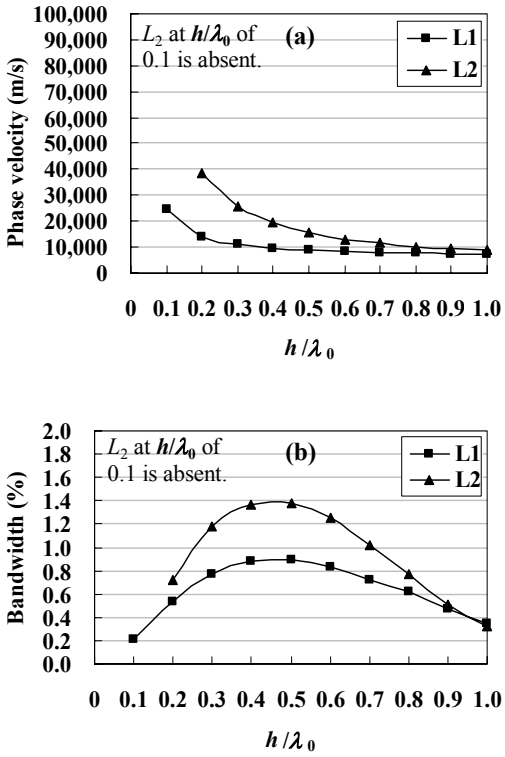

Fig. 4. Estimated dispersion curve (a) and bandwidth (b) of L_1 and L_2 propagating in composite membrane where h_{Mo}/h_{AlN}=0.2.

bandwidth can be attributed to the mass loading effect of Mo. However, the maximum displacement and stress points for L_1 were concentrated on the top and bottom surfaces of the composite membrane, as shown in Fig 2(a). We believe that the lowering of piezoelectric efficiency is more influential than the mass loading effect for L_1 when the surfaces are covered with a thick Mo layer.

To achieve high velocity PLW excitation with bandwidths greater than 1.0% for applications in the SHF band, we need an L_2 around an h/λ_0 of 0.3 to get acceptable performance, as shown in Figs. 4(a) and 4(b). L_2 obtained a phase velocity of 25,741 m/s and a bandwidth of 1.18% at an h/λ_0 of 0.3.

III. Fabrication

To support the simulation results, we fabricated composite membrane PLW resonators, as shown in Figs. 5(a) and 5(b). A 76-mm-diameter (100) silicon wafer was used as the substrate. The AlN and the Mo layers were deposited by RF and DC magnetron sputtering. The AlN layers were grown with a highly *c*-axis-preferred orientation normal to the surface of the substrate. An air gap was formed underneath the composite membrane to prevent acoustic energy leakage to the substrate.

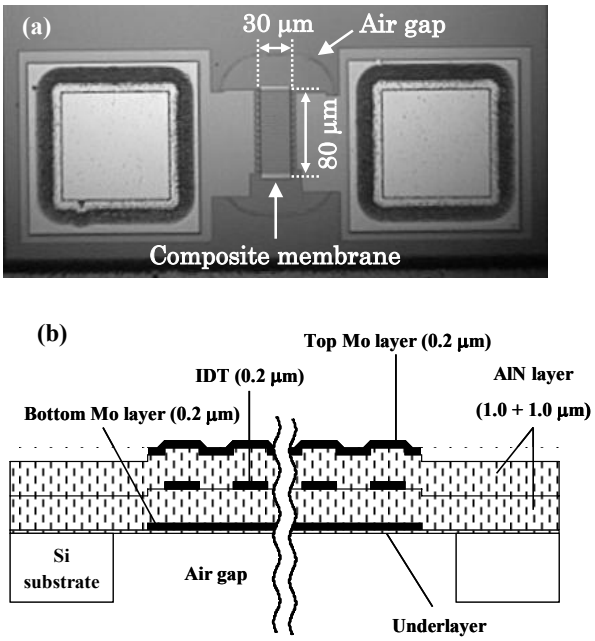

Fig. 5. Micrograph (a) and cross-sectional structure (b) of fabricated composite membrane PLW resonator.

The fabricated PLW resonators had an IDT with 12.5 pairs of fingers. Four PLW resonators with IDTs of different periods (6.2, 8.0, 9.6, and 12.0 μm) were fabricated, and the *l* and *s* were the same for each IDT. Figure 5(a) shows the PLW resonators with the IDT period of 6.2 μm. As shown in Fig. 5(b), an h_{AlN} of 1.0 μm, an h_{Mo} of 0.2 μm and an IDT thickness of 0.2 μm were used in each resonator, and an *h* of 2.4 μm was assumed when the IDT thickness was not taken into consideration. Therefore, the h/λ_0 of the fabricated PLW resonators were 0.375, 0.300, 0.250, and 0.200. An underlayer was inserted beneath the bottom Mo layer to enhance the crystalline quality of the composite membrane [11].

Figure 6 shows X-ray diffraction (XRD) patterns (θ-2θ scan) of a fabricated PLW resonator. Diffraction peaks indicating AlN(0002)- and Mo(110)-preferred orientations were detected. The full width at half maximum of the AlN(0002) and Mo(110) rocking curves were as good as 1.5 degree and 2.5 degrees, respectively.

IV. Results and Discussion

The composite membrane PLW resonators were measured in *S* parameters using a network analyzer and a wafer probe, and then the impedances of the resonators were calculated from the *S* parameters. Figures 7(a) and 7(b) show the impedance of the composite membrane PLW resonator with an h/λ_0 of 0.300. In Fig. 7(a), two PLW modes have a large relative bandwidth at 1.420 GHz and 3.128 GHz, respectively. The phase velocities of these modes of the resonant frequencies at 1.420 GHz and 3.128 GHz were estimated to be 11,360 m/s and 25,024 m/s, which correspond with those of L_1 and L_2 derived during the FEM simulation. In Fig. 7(a), we noticed that L_2 has prominently good electromechanical coupling that is consistent with the simulation results, indicating great potential for use with RF

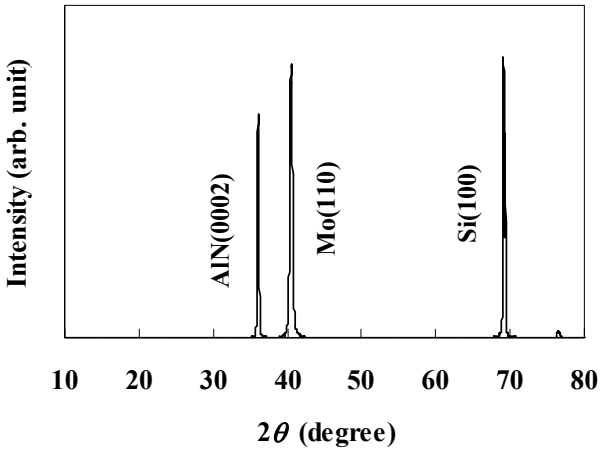

Fig. 6. XRD pattern of Mo/AlN/Mo composite membrane deposited on Si(100) substrate.

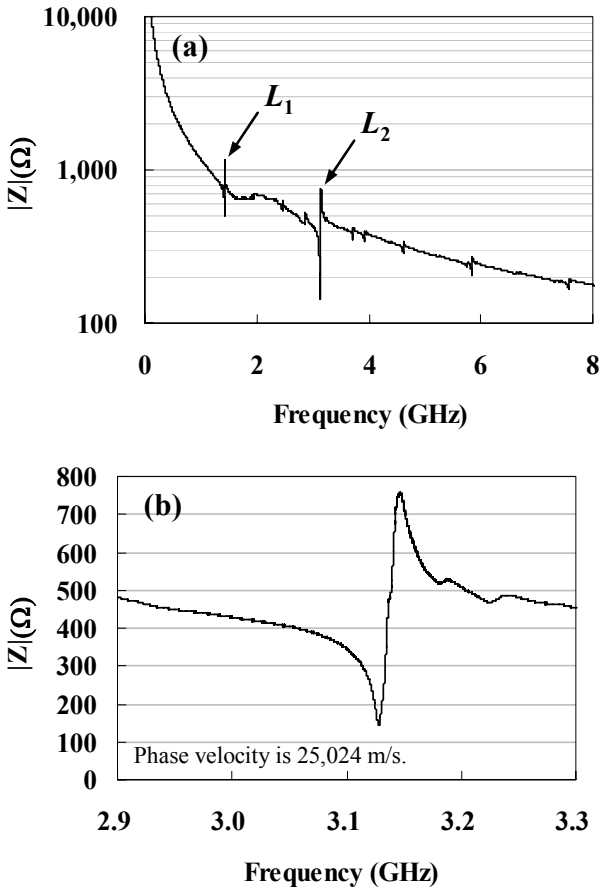

Fig. 7. Impedance of fabricated composite membrane PLW resonator with h/λ_0 of 0.3, measured wide frequency range from 0.05 to 8.0 GHz (a), and narrow frequency range from 2.9 to 3.3 GHz (b).

resonators. In Fig. 7(b), the measured bandwidth of L_2 is 0.60%, which is about half of the simulated value. The decrease in bandwidth is may be caused by imperfections in the crystal quality of the AlN layers. We assumed that the AlN layers were a single crystal in the FEM simulation. However, sputter-deposited AlN layers contain grain structures, and hence, they may cause deterioration in the electromechanical coupling.

The quality factor of the PLW resonator was derived from the impedance [7]. For a PLW resonator with an h/λ_0 of 0.300, as shown in Fig. 7(b), the quality factors at the resonant and antiresonant frequency were 408 and 107. The energy loss of our PLW resonator may be due to sub-optimal components such as incorrect sized IDTs and the absence of acoustic reflectors.

It should be noted that a fabricated PLW resonator with an h/λ_0 of 0.300 had an IDT period as large as 8.0 μm. Therefore, the results shown in Fig. 7(b) indicate that a high operating frequency above 3 GHz is achievable despite a

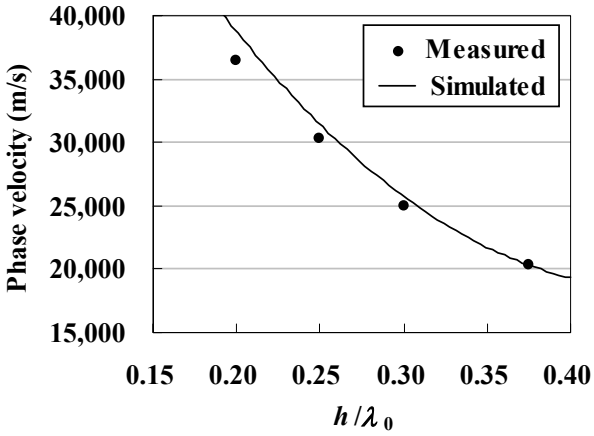

Fig.8. Relationship between phase velocity and normalized thickness using measured (solid circles) and simulated (line) data.

large IDT period, such as 8.0 μm, by using the composite membrane PLW resonator.

Figure 8 shows the relationship between the phase velocities and h/λ_0 in which the solid circles and line indicate the phase velocities obtained using the fabricated PLW resonators and simulated results. The measured phase velocity had good agreement with the simulated phase velocity, as shown in Fig. 8. In the simulation, the IDT thickness was assumed to be infinitely thin, as mentioned previously. The smaller the h/λ_0 is, the more the IDT thickness influences the propagation characteristics of PLWs. Therefore, as the h/λ_0 decreased, the differences between the measured and simulated phase velocities increased, as shown in Fig. 8.

The measured and simulated results obtained in this study demonstrate that the composite membrane structure is suitable for an exciting high velocity PLW with a large bandwidth and has great potential for use with RF resonators in the SHF band.

V. SUMMARY

We examined the PLW characteristics propagating in a novel composite membrane structure for RF resonators operating in the GHz range. The simulated results show that a PLW with a high phase velocity of 25,741 m/s, which is 2.5 times larger than the highest SAW velocity [5], and a relative bandwidth of 1.18% can be excited in a composite membrane structure. The simulated results were supported experimentally. We fabricated composite membrane PLW resonators and demonstrated that the phase velocity of the excited PLW mode was as high as 25,024 m/s and that the relative bandwidth was 0.60%. These results show the potential use of the composite membrane PLW resonators in applications that operate at higher GHz ranges.

ACKNOWLEDGMENTS

We are grateful to Professor Mitsutaka Hikita of Kogakuin University and Associate Professor Koji Hasegawa of Muroran Institute of Technology for their helpful advice.

REFERENCES

[1] M. Hikita, Y. Ishida, T. Tabuchi and K. Kurosawa, “Miniature SAW antenna duplexer for 800-MHz portable telephone used in cellular systems”, IEEE Trans. Microwave Theory Tech., vol. MTT-36, pp. 1047-1056, 1988.

[2] J. H. Collins, P. J. Hagon and G. R. Pullian, “Evaluation of new single crystal piezoelectric materials for surface acoustic-wave applications”, Ultrasonics, vol. 8, pp. 218-226, 1970.

[3] K. Tsubouchi and N. Mikoshiba, “Zero-temperature-coefficient SAW devices on AlN epitaxial films”, IEEE Trans. Sonics Ultrason., vol 32, pp. 634-644, 1985.

[4] K. Yamanouchi, N. Sakurai and T. Satoh, “SAW propagation characteristics and fabrication technology of piezoelectric thin film/diamond structure”, *Proc. IEEE Ultrason. Symp.*, 1989, p. 351-354.

[5] H. Nakahata, H. Kitabayashi, T. Uemura, A. Hachigo, K. Higaki, S. Fujii, Y. Seki, K. Yoshida and S. Shikata, “Study on surface acoustic wave characteristics of SiO_2/Interdigital-transducer/ZnO/diamond structure and fabrication of 2.5 GHz narrow band filter”, Jpn. J. Appl. Phys., vol 37, pp. 2918-2922, 1998.

[6] T. Sato and H. Abe, “Propagation properties of longitudinal leaky surface waves on lithium tetraborate”, IEEE Trans. Ultrason., Ferroelect., Freq. Contr., vol. 45, pp. 136-151, 1998.

[7] A. Isobe, M. Hikita and K. Asai, “Q values of longitudinal leaky SAWs propagating on rotated Y-cut LN substrates along the perpendicular to the x axis”, IEEE Trans. Ultrason., Ferroelect., Freq. Contr., vol 52, pp. 1812-1816, 2005.

[8] Y. Nakagawa, S. Tanaka and S. Kakio, “Lamb-wave-type high frequency resonator”, Jpn. J. Appl. Phys., vol. 42, pp. 3086-3090, 2003

[9] J. Bjurström, I. Katardjiev and V. Yantchev, “Lateral-field-excited thin-film Lamb wave resonator”, Appl. Phys. Lett., vol. 86, p. 154103. 2005.

[10] H. Matsumoto, A. Isobe and K. Asai, “Multilayer Film Piezoelectric Lamb Wave Resonator for Several GHz Applications”, *Proc. IEEE Freq. Contr. Symp.*, 2006, pp. 797-800.

[11] H. Matsumoto, K. Asai, N. Kobayashi, S. Nagashima, A. Isobe, N. Shibagaki and M. Hikita, “Influence of underlayer materials on preferred orientations of sputter-deposited AlN/Mo bilayers for film bulk acoustic wave resonators”, Jpn. J. Appl. Phys., vol. 43, pp. 8219-8222. 2004.

A Study on MOS Temperature Compensated Crystal Oscillator

Takehiko Adachi
Department of Electrical and Computer Engineering
Faculty of Engineering
Yokohama National University
Yokohama, Japan 240-8501
Email: ada@ynu.ac.jp

***Abstract*— The "Temperature Compensated Crystal Oscillator (TCXO)" is widely used as a stable frequency source of a mobile communication equipment. Demand for low-power operation of TCXOs stimulates the development of fully integrated CMOS analog TCXOs. A TCXO is composed of a voltage controlled crystal oscillator and a temperature characteristics compensation circuit. We have proposed a new CMOS temperature characteristics compensation circuit for TCXO. The proposed circuit is composed of a new temperature sensor and a new compensation function generator. The performance of the proposed sensor and compensation function generator are evaluated by simulation. The sensor shows the sensitivity of 1.17mV/˚C and nonlinearity less than 0.4% for the temperature range between -30˚C $\sim$ 80˚C. And the total performance of TCXO is estimated. The compensated frequency deviation is within $\pm$ 0.5ppm and the total DC consumption current is under 1.0mA.**

I. INTRODUCTION

The "Temperature Compensated Crystal Oscillator(TCXO)" is widely used as a stable frequency source of a mobile communication equipment. A variety of TCXOs have been developed since 1956 when the first idea of TCXO is published. TCXOs can be classified by the compensation method of frequency-temperature characteristics of a crystal oscillator: analog TCXO and digital TCXO. The analog TCXO is classified into direct analog TCXO and indirect analog TCXO. The direct analog TCXO compensates the frequency-temperature characteristics by using the temperature dependence of a load capacitance circuit of the oscillator[1]. The load capacitance circuit is composed of capacitors, resistors and thermisters. The indirect analog TCXO is composed of a temperature sensor, a compensation function generator, and a voltage controlled crystal oscillator[2]. The VCXO is controlled by the analog compensation voltage generated by the compensation function generator[3][4]. The analog TCXOs have been widely used because of their superiority in phase noise. The digital TCXOs were developed by responding to the needs of high precision temperature compensation[5][6][7]. Further improvements of digital TCXOs are under study, e.g. a TCXO using SC-cut oscillator [9][10]. Until the end of the 20th century, most of TCXOs are made by bipolar transistors because of their low noise property. But in the early 21st century, a fully integrated CMOS analog TCXO was developed to meet the demands for low power and low noise operation [11]. In these days, there is the demand for further improvement of TCXOs.

In this paper, we have proposed a new MOS TCXO. A new temperature sensor and compensation function generator have been introduced in the proposed TCXO. The performance of the proposed TCXO has been tested by simulation.

II. CIRCUIT STRUCTURE

Fig 1 shows a block diagram of a TCXO. A TCXO is composed of a compensation function generator and a voltage controlled crystal oscillator. Usually, a VCXO uses a AT-cut crystal resonator and its temperature dependence of frequency is a cubic function of temperature. Therefore, a compensation function generator is composed of a temperature sensor and a cubic function generator. In this section, the structure and property of each block are explained in detail, placing an emphasis on the temperature sensor and compensation function generator.

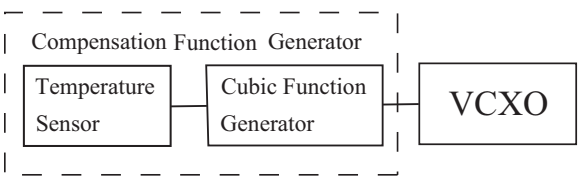

Fig. 1. Block Diagram of TCXO.

A. Temperature sensor circuit

In CMOS integrated circuits, there are a several temperature dependent characteristics which can be used for temperature sensors. Most commonly used ones are the bias current of a substrate bipolar transistor and the threshold voltage of a MOS transistor. Recently, a current source type temperature sensor was developed using the temperature dependence of threshold voltage [12][13]. We have introduced the new structure of a temperature sensor. Fig. 2 shows the temperature sensor circuit. The temperature sensor core is the voltage source consisted of MOS FET M_{n4} and M_{n5}. The voltage $V_{ref}(= R_2 I_{ref})$ is the reference voltage for the sensor core and is made by the bootstrap reference source[13][14] indicated by dotted line. The reference voltage V_{ref} is independent of power supply

voltage variation. The principle of operation is outlined in the following paragraphs.

All MOS transistors are supposed to be operating in the saturation region. The channel-length modulation effect is assumed to be negligible. The drain currents of M_{n4} and M_{n5} are given as follows;

$$I_{D4} = K_0 S_4 (V_{GS4} - V_{tn})^2 \tag{1}$$

$$I_{D5} = K_0 S_5 (V_{GS5} - V_{tn})^2 \tag{2}$$

where $K_0 = \dfrac{\mu C_{ox}}{2}$, μ is the surface mobility, C_{ox} is capacitance per unit area of the gate oxide, and V_{tn} is the threshold voltage of n-channel MOS FET.

$$S_{n4} = \frac{W_4}{L_4} \tag{3}$$

$$S_{n5} = \frac{W_5}{L_5} \tag{4}$$

where L_4 and L_5 are the channel length of M_{n4} and M_{n5} and W_4 and W_5 are the channel widths.

The currents I_{D4} and I_{D5} are equal because the gate current of M_{n4} and M_{n5} are negligibly small and the reference current I_{ref} fed from M_{p3} is drawn into M_{n5}. Using the relations $V_{out} = V_{GS4}$ and $V_{GS5} = V_{ref}$ and equate Equation (1) and (2), the output voltage of the sensor is expressed by the following equation.

$$V_{out} = \left(1 - \sqrt{\frac{S_{n5}}{S_{n4}}}\right) V_{tn} + \sqrt{\frac{S_{n5}}{S_{n4}}} V_{ref} \tag{5}$$

where, the temperature dependence of the threshold voltage V_{tn} is expressed by the following equation.

$$V_{tn}(T) = V_{tn}(T_0) - \alpha(T - T_0) \tag{6}$$

where T_0 denotes the reference temperature and α denotes the temperature coefficient of V_{tn}.

Therefore, the output voltage V_{out} is rewritten as

$$\begin{aligned} V_{out} &= \alpha(\sqrt{n}-1)T - (\sqrt{n}-1)\{V_{tn}(T_0) + \alpha T_0\} \\ &+ \sqrt{n} V_{ref} \end{aligned} \tag{7}$$

The output voltage V_{out} varies linearly according to the temperature change. The sensitivity of V_{out} to the temperature is shown to be

$$S_T^{V_{out}} = \frac{dV_{out}}{dT} = \alpha(\sqrt{n}-1) \tag{8}$$

where $n = \dfrac{S_{n5}}{S_{n4}}$.

The reference current I_{ref} is expressed as follows,

$$I_{ref} = \frac{V_{tn}}{R_1} + \frac{1}{\beta_{n1} {R_1}^2} + \frac{1}{R_1}\sqrt{\frac{2V_{tn}}{\beta_{n1} R_1} + \frac{1}{{\beta_{n1}}^2 {R_1}^2}} \tag{9}$$

where, $\beta_{n1} = K_0 S_{n1}$, $S_{n1} = W_1/L_1$.

The fact that drain current of MOS FET is constant against temperature variation at the specific point on gate-voltage to gate-current characteristics is known generally. Then the reference voltage V_{ref} can be made constant against temperature and power supply voltage variation, when the reference current I_{ref} is set to this value. And the output voltage of the sensor varies only proportional to the temperature change, independent of power supply voltage.

Simulation has been made by the circuit parameters of Table I. These parameters are determined to get the sensitivity $2mV/℃$ at $T_0 = 25℃$for the temperature range $-30℃ \sim +80℃$. The power supply voltage V_{CC} is 3.3V. Fig. 3 shows the temperature dependence of the output voltage of the sensor. This sensor can operate for the power supply voltage above 2.6V. Obtained sensitivity is $1.17mV/℃$ and the nonlinearity is less than 0.4%. The obtained performances are sufficient for the application to TCXO. This sensor can be used for other applications.

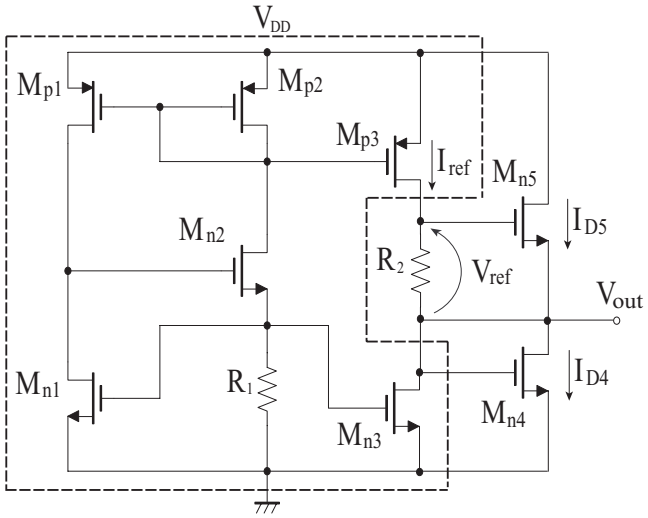

Fig. 2. Temperature sensor.

TABLE I
CIRCUIT PARAMETER OF TEMPERATURE SENSOR.

Parameter		Value
M_{n1}, M_{n2}, M_{n3}	W/L	$50\mu m/10\mu m$
M_{p1}, M_{p2}, M_{p3}	W/L	$50\mu/10\mu m$
M_{n4}	W/L	$10\mu m/2\mu m$
M_{n5}	W/L	$132\mu m/2\mu m$
R_1		$53k\Omega$
R_2		$43k\Omega$

B. Compensation function generator circuit

Fig. 4 shows the compensation function generator. The compensation function is the sum of a cubic and a linear function of temperature. The sensor output voltage is applied to the multiplier MUL1 and the MUL1 generates the square

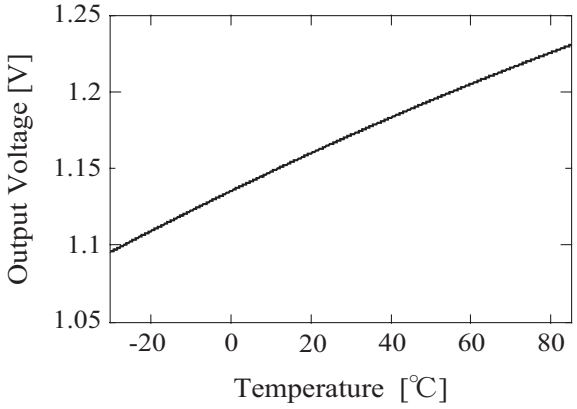

Fig. 3. Characteristics of temperature snesor.

TABLE II
PERFORMANCE OF TEMPERATURE SENSOR.

Parameter	Value
Temperature range	-30℃∼80℃
Sensitivity	1.17 mV/℃
Nonlinearity	$\leq 0.4\%$
DC current	$104\mu A$

function of temperature. The output of MUL1 and sensor output is applied to the second multiplier MUL2 and the MUL2 generates the cubic function of temperature. The analog adder sums the sensor output and the MUL2 output. Gilbert cells depicted in Fig. 5 are used as the multipliers.

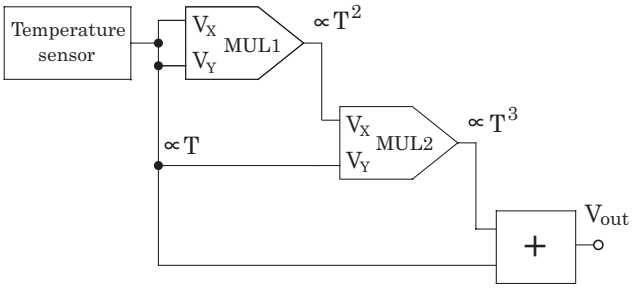

Fig. 4. Compensation function generator.

Simulation has been made using $W/L = 20\mu/5\mu$ for $M_1 \sim M_6$, $I_{SS} = 10\mu A$, $R = 100k\Omega$. Fig. 6 shows the temperature dependence of the output voltage MUL1. The obtained curve is distorted from square curve. The cause of the distortion is presumed to be the temperature dependence of the gain factor of the multiplier. To solve this problem, we have adopted the following approach. At first, we have divided the temperature range into a few sections and generated the linear function of temperature with different coefficient in each section. Then the obtained linear functions and sensor output are multiplied by the multiplier. And the approximate square function of temperature is obtained in the whole temperature

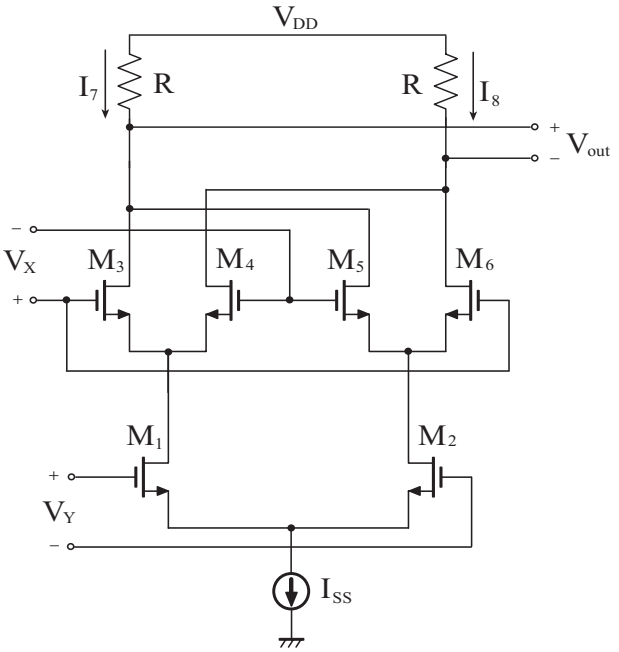

Fig. 5. Gilbert cell.

range. Fig. 7 shows the modified square function generator circuit. $VGA1 \sim VGA2$ are the variable gain amplifiers. Fig. 8 shows the structure of the variable gain amplifier. R_1, R_2, R_3, MOS FET M_8 and operational amplifier constitute a negative amplifier. The part surrounded by dotted line is a comparator which outputs 0 for $V_{C1} < V_{C2}$ and outputs V_{DD} for $V_{C1} > V_{C2}$. MOS FET M_8 switches on and off according to the comparator output and changes the gain of the amplifier. The amplifier gain is expressed as follows;

$$Gain = \begin{cases} -\dfrac{R_3}{R_1} & V_{C1} \leq V_{C2} \\ -\dfrac{R_3}{R_1 // R_2} & V_{C1} \geq V_{C2} \end{cases} \tag{10}$$

where $R_1//R_2$ is the pararell resistance of R_1, R_2.

The operational amplifier is a two-stage amplifier which is made by a differential input stage and a source follower. Fig. 9 shows the structure of the operational amplifier.

TABLE III
PARAMETER OF COMPARATOR.

MOS FET	$W[\mu m]$	$L[\mu m]$
M_1	3	1
M_2	3	1
M_3	15	1
M_4	15	1
M_5	4.5	1
M_6	94	1
M_7	14	1

Fig. 7 shows the case when the temperature range is divided into four sections and the gains of $VGA1 \sim VGA3$ are set

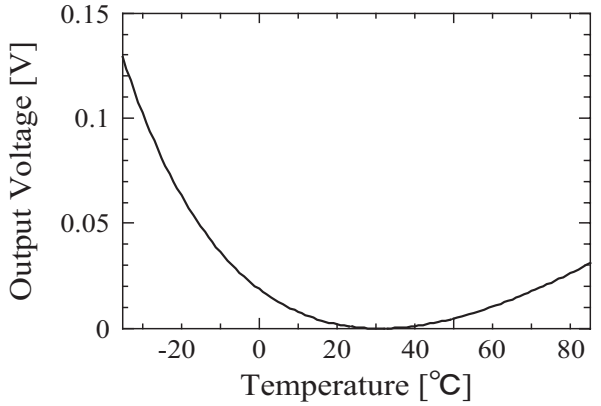

Fig. 6. Output voltage of multiplier MUL1 in Fig. 4.

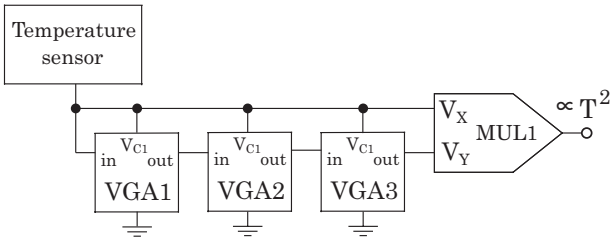

Fig. 7. Modified square function generator.

at the temperatures T_1, T_2, and T_3 ($T_1 < T_2 < T_3$). At first the whole temperature range is divided into two parts at the center temperature 25℃. Then the high temperature region is divided into three parts having almost same temperature range. The dividing points are trimmed slightly by minimizing the difference of the generated compensation function and the temperature dependence of a crystal resonator. In this case, temperatures 30℃, 50℃, 60℃ are selected to the dividing points. Table III, Table IV, and Table V shows the circuit parameters of the comparator, the variable gain amplifier, and the operational amplifier. Fig. 10 shows the linear functions of temperature corresponding to four temperature regions. Fig. 11 shows the output of the modified square function generator. The solid line shows the output voltage and the dotted line shows the square function approximating the output voltage. Fairly good square function of temperature is obtained for the whole temperature range.

Fig. 12 shows a modified compensation function generator. $MUL1$ generates a square function of temperature V_2 and $MUL2$ generates a cubic function of temperature V_3 by multiplying V_1 and V_2. The analog adder generates the compensation function by summing the cubic component V_3 and the linear component V_4. V_4 is the linear function of temperature whose coefficient changes at 30℃. Fig. 13 shows the compensation function. Although there is a slight unsmoothness near 65℃, the obtained compensation function approximates well the temperature dependence of a crystal resonator.

TABLE IV
PARAMETER OF VARIABLE GAIN AMPLIFIER.

VGA	$R_1[k\Omega]$	$R_2[k\Omega]$	$R_3[k\Omega]$
VGA1	70	300	70
VGA2	70	100	70
VGA3	100	70	100
VGA4	100	190	87

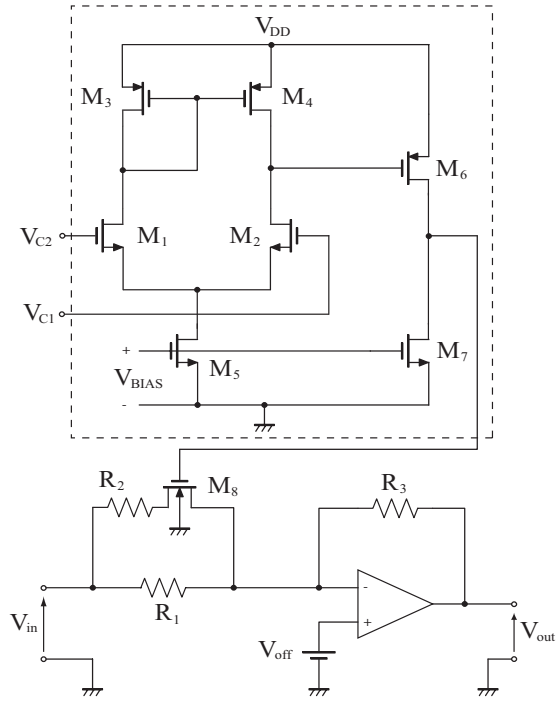

Fig. 8. Variable gain amplifier.

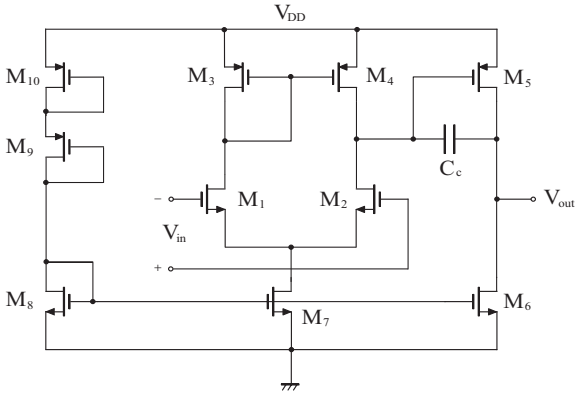

Fig. 9. Operational amplifier.

III. PERFORMANCE EVALUATION OF TCXO

To evaluate the performance of the proposed TCXO, the frequency temperature characteristics has been simulated. A colpitts oscillator is used for the oscillator circuit. Fig. 14 shows the oscillator circuit. Oscillation frequency is designed $26MHz$. Table VI and Table VII show the equivalent parameters of a crystal resonator and the circuit parameters, respec-

TABLE V

PARAMETER OF OPERATIONAL AMPLIFIER.

MOS FET		$W[\mu m]$	$L[\mu m]$
M_1	*nMOS*	10	10
M_2	*nMOS*	10	10
M_3	*pMOS*	10	10
M_4	*pMOS*	10	10
M_5	*pMOS*	200	10
M_6	*nMOS*	100	10
M_7	*nMOS*	10	10
M_8	*nMOS*	10	10
M_9	*pMOS*	1	7
M_{10}	*pMOS*	1	7
C_c		$1.2pF$	

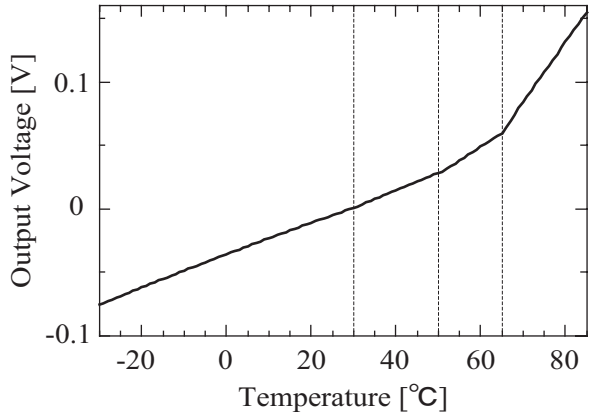

Fig. 10. Modified linear function of temperature.

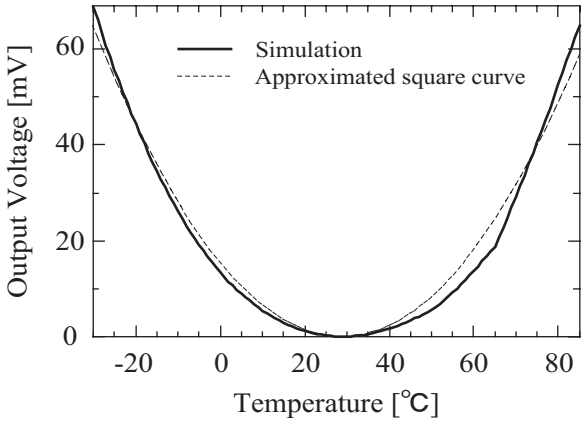

Fig. 11. Output voltage of modified square function generator.

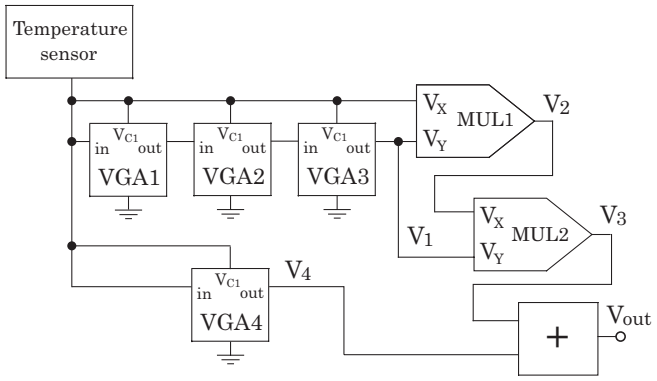

Fig. 12. Modified compensation function generator.

tively. Fig. 15 shows the simulated result. The compensated frequency deviation is within $\pm 0.5ppm$ for the temperature range between -30℃ and 80℃. The uncompensated frequency deviation is $-11ppm \sim +7ppm$. The DC current of the compensation function generator and *VCXO* is about $0.5mA$ and $0.5mA$, respectively. The total power consumption is about $1mA$.

TABLE VI

EQUIVALENT PARAMETER OF CRYSTAL RESONATOR.

Parameter	Value
f_s	$26MHz$
R_1	20.29Ω
L_1	$11.38mH$
C_1	$3.295fF$
C_0	$1.42pF$

IV. CONCLUSION

We have proposed a new MOS temperature compensated crystal oscillator. A new temperature sensor and compensation function generator are introduced. The proposed TCXO has been designed for $3.3V$ power supply voltage and its performance is evaluated by simulation. The temperature sensor uses the temperature dependence of threshold voltage of MOS FET. Sensitivity of $1.17mV/$℃ has been obtained and nonlinearity has been less than 0.4% for the temperature range -30℃ $\sim$ 80℃. Obtained performance is sufficient for the application to TCXO. The compensation function generator makes the cubic function of temperature by multiplying the sensor output. Reducing the effect of the temperature dependence of the multiplier, the temperature range is divided into a few sections and the linear functions of temperature with different temperature coefficients are generated and the cubic function of temperature is composed by these linear functions. The generated function approximates a cubic function with a constant coefficient for the whole temperature range. The total performance of TCXO has been evaluated by simulation. The compensated frequency deviation has been within $\pm 0.5ppm$

TABLE VII

PARAMETER OF VOLTAGE CONTROLLED CRYSTAL OSCILLATOR.

Parameter	Value
L	1μ
W	160μ
C_A, C_B	$20pF$
R_A	$30k\Omega$
R_B	$80k\Omega$
R_D	$1k\Omega$
R_E	$10k\Omega$

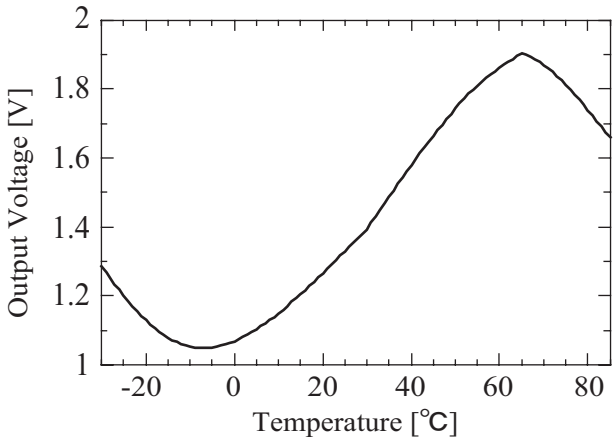

Fig. 13. Characteristics of compensation function.

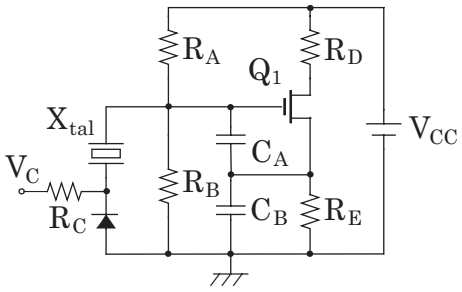

Fig. 14. Voltage controlled crystal oscillator.

for the temperature range between $-30℃$ and $80℃$, at the oscillation frequency $26MHz$. The total power consumption has been about $1mA$. The obtained result is thought to be almost sufficient for practical use. More sophisticated method to reduce the effect of the temperature dependence of multipliers and the improvement for low power operation are thought to be necessary.

REFERENCES

[1] S. Okano; "Direct-Temperature Compensated Crystal Oscillator for Advanced VHF/UHF Radio Communication Systems," Proc. 34th Annual Frequency Control Symposium, pp.488-493,1980 May

[2] M. E. Frerking ; " Crystal Oscillator Design and Temperature Compensation", Van Nostrand Reinhold Company, 1978.

[3] S. Kurogo; "Analog TCXO Using Cubic Functional Voltage Generator", Proc. 50th Annual Frequency Control Symposium, pp.484-492, 1996 May

[4] S. Kubo and S. Shibuya ; " Analog TCXO Using One Chip LSI for Mobile Communication", Proc. of IEEE 1996 International Frequency Control Symposium, pp.728-734, 1996 May.

[5] T. Hara, T. Kudo, S. Uriya, H. SAita, S. Ogura, and Y. Katsuya; "A Digitally Compensated TCXO Using a Single Chip LSI", Proc. of 41st Frequency Control Symposium, pp.435-438, 1987 May

[6] T. Miyayama;"A New Digitally Temperature Compensated Crystal Oscillator for Mobile Tlephone Systems", Proc. 42nd Annual Frequency Control Symposium, pp.327-333, 1988 May

[7] N. S. Deno, C. L. Hahnlen, and D. L. Landis; "A Low Cost High Stability Microcontroller Compensated Crystal Oscillator", Proc. of IEEE 1998 InternationalAnnual Frequency Control Symposium, pp.353-360, 1998 May.

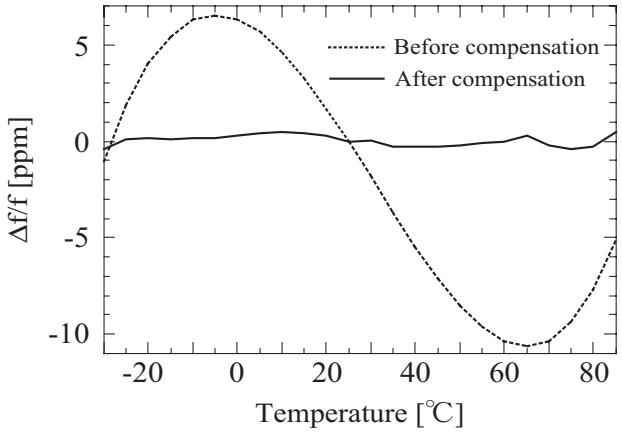

Fig. 15. Frequency Temperature Characteristics of TCXO.

[8] E. Jacquet and J. P. Bardon, and O. Bignon; "Digitally Compensated TCXO with a Low Phase Noise Characteristics", Proc. of 1999 Joint Meeting EFTF-IEEE IFCS, pp.370-375, 1999 May.

[9] E. Jackson, H. Phillips, and B. E. Rose; "The Microcomputer Compensated Crystal Oscillator - A Progress Report", Proc. of IEEE 1996 InternationalAnnual Frequency Control Symposium, pp.687-692, 1996 May.

[10] T. Shioda, Y. Sekine, and H. Otsuka; "High Precision TCXO for Rapid Enviromental Temperature Change", Proc. of 2003 IEEE International Frequency Control Symposium Jointly with the 17th European Frequency and Time Forum, pp.440-449, 2003 May.

[11] K. Nemoto and K. Sato ; " A 2.5ppm Fully Integrated CMOS Analog TCXO", Proc. of IEEE 2001 International Frequency Control Symposium, pp.740-743, 2001 May.

[12] H. Takakubo, H. Ikeda, and K. Takakubo ;"On-Chip Temperature Sensor based on Drain Current Temperature Dependence of MOSFET", The papers of Technical Meeting on Electronic Circuits, IEE Japan, ECT-03-16, pp.25-28, 2003 Jan.

[13] H. Ikeda, K. Takakubo, and H. Takakubo ;"CMOS Temperature-Voltage Converter provided with Reference", The papers of Technical Meeting on Electronic Circuits, IEE Japan, ECT-04-06, pp.26-30, 2004 Jan.

[14] P. Allen and D. Holberg ; "CMOS Analog Circuit Design", Oxford Univesity Press, 2002.

A Low Phase Noise and Wide Tuning Voltage-Controlled SAW Oscillator with Surface Transverse Wave Resonator for SONET Applications

Yao-Huang Kao[1], *Member, IEEE* and Jon-Hong Lin[2], *Student Member, IEEE*

[1]Dep. of Communication Engineering, Chung Hua University and [2]Institute of Communication Engineering, National Chiao-Tung University, Hsin-Chu, Taiwan R. O. C. 30050

Tel: 886-3-5186036, Fax 886-3-5186031, Email: yhkao@chu.edu.tw

ABSTRACT —**A surface transverse wave (STW) resonator based oscillator was developed in response to SONET OC-48 application. The residual noise measurement techniques are used to evaluate the noise contributions in feedback loop components, such as loop amplifier, STW resonator and electronic phase shifter, which can play important roles in determining the oscillator's output phase noise spectrum. The oscillator's phase noise floor is -170 dBc/Hz for carrier-offset frequency greater than 1 MHz. The oscillator's phase noise level of -67 dBc/Hz at 100 Hz carrier offset. Both low close-in phase noise and low white phase noise floor makes the oscillator meet low jitter requirement. The electronic frequency tuning range exceeds ±200 ppm. The oscillator provide 13.5dBm of output power and consume 325mW from +5Volts power supply.**

Index Terms **— Ceramics, coaxial resonators, delay filters, delay-lines, power amplifiers.**

I. INTRODUCTION

Clock recovery circuits are used for data integrity in high-speed digital transmission system. It is actually a phase-locked loop with a low jitter voltage-controlled oscillator (VCO). The VCO is mostly fabricated with a stable resonator. Due to the fabrication process, the most used oscillator at 622MHz for SONET or SDH applications is either by the fourth harmonic of 155MHz crystal or directly 622MHz saw resonator. [1, 2] Both suffer from the degradation factor of 20log (N) =12dB on the phase noise as applications to OC-48 at 2488.32MHz. Recently, the oscillators on 2488MHz have been investigated by using high quality STW resonators. [3, 4, 5] Owing to the higher velocity and lower propagation loss for STW, the photolithography process is relaxed with acceptable yield. In this work, the focus is on the evaluation of phase noise of a highly stable VCSO working directly at 2488.32MHz. The performance of residual noise in each module in the loop is especially examined to get the insight of phase noise performance. The phase noise at 100 Hz offset is about -67dBc/Hz. Both low close-in phase noise and low white phase noise floor make the oscillator meet low jitter requirement. The frequency tuning range exceeds ±200 ppm.

II. OSCILLATOR DESIGN

The architecture of the oscillator is shown in Fig.1. It consists of a loop amplifier, an electronic phase shifter, a lump element reactive Wilkinson power splitter, a lumped element reactive phase adjusting, and a two-port STW resonator. The oscillation starts as the closed loop gain satisfies Barkausen's criteria with total loop gain larger than unity and the phase shift equal to $2n\pi$. The open loop gain is easily evaluated by breaking the loop at the appropriate plane with equal input and output impedance, such as line AB indicated in Fig. 1. Here, the impedances seen are 50ohm as was required by network analyzer. This approach has the advantage that the noise characteristics of the individual component as measured in an open-loop configuration have a direct bearing on the closed-loop phase noise of the oscillator.

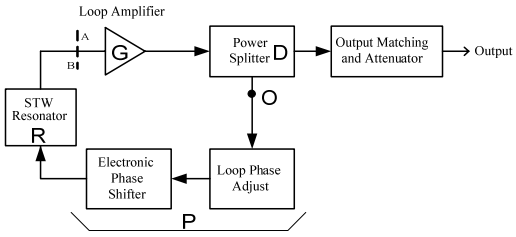

Fig. 1 Block diagram of a feedback loop oscillator.

The STW resonator has the advantages of shear wave with very high velocity and energy trapping so that the diffraction effect of the shallow bulk wave into the substrate is minimized and quality factor is increased. The width of the transducer is approximately 0.5μm. The overlap aperture is about 250μm. The 90° rotated ST-cut quartz is employed to have the turnover temperature approximately at 45°C. The die size of the STW resonator is 1.8mm x 1.2mm. The input and output IDT have 100 fingers are placed between two

shorted reflectors, which has 90 fingers, and are separated by a shorted grating with 3 fingers. Two coupled modes formed by input and output IDTs are coupled just as two coupled parallel LC resonators. The coupling is carefully tuned by the central grating. The frequency response is shown in Fig. 2a. Due to the grounding grating the insertion loss is reduced to 4~5dB, which is much smaller than that of 10~15dB in conventional SAW or STW delay line. The resonator acts as a short circuit with zero phase-shift at the desired frequency. The approximately linear phase change with slope equal to 1.713rad/MHz is obtained within the 3dB frequency band. The up and down limits of the phase change are above ±90°. The loaded Q factor $Q_L = \omega_o (d\phi / d\omega)/2$ is estimated equal to 2124. The group delay is about 1.713×10^{-6}rad/Hz. The spurious are suppressed under 30dB.

The residual phase noise measurement techniques [7] are employed to evaluate the components of loop amplifier, STW resonator and electronic phase shifter. The noise floor of the measurement system is about -170dBc/Hz with 1/f flicker noise corner at 17kHz offset. The residual phase noise of the resonator is revealed in Fig. 2b with drive power approximately equal to that in steady state oscillation.

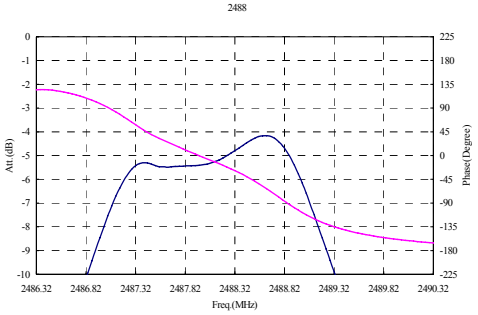

(a)

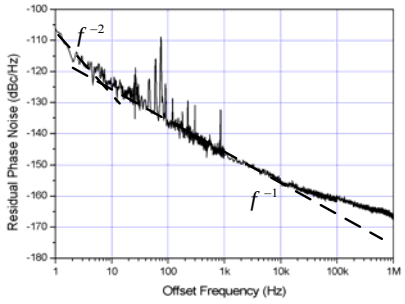

(b)

Fig. 2 (a) Gain and Transmission Phase Responses 2486.32-2490.32MHz, and (b) Residual Phase Noise of STW Resonator

The HBT monolithic amplifier is selected as the loop amplifier because of low noise figure and high dynamic range. The P1dB is at +17dBm and the bandwidth is about 4GHz to prevent high 2nd harmonics. The nominal gain is 17dB to overcome the total loop losses to insure the stable oscillation. The residual phase noise is shown in fig.3.

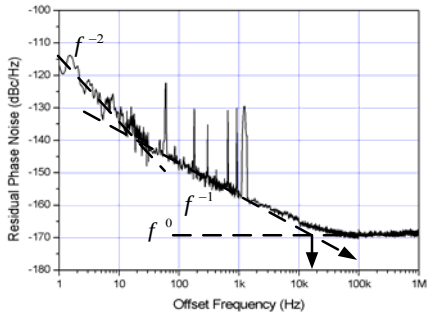

Fig. 3 Residual Phase Noise of Loop Amplifier

An unequal Wilkinson power splitter is employed to adjust the excess small signal loop gain instead of resistive attenuator. [8] The oscillation frequency is trimmed by the electronic phase shifter. Both phase noise and tuning linearity are affected by the varactors. With proper selection of varactor diodes, the high tuning linearity and low residual phase noise are achieved at the same time. The residual phase noise performance is shown as Fig. 4.

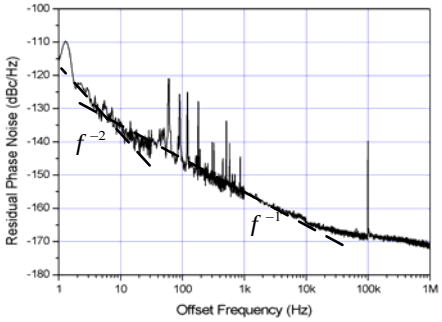

Fig. 4 Residual Phase Noise for the Electronic Phase Shifter

The frequency dependences of total phase shifter and open loop gain seen from the reference plane A-B indicated in the fig.1 are shown in Fig. 5. Curve X and Curve Y are the phase shift with V_{tune}=0Volts and V_{tune}=5Volts, respectively. Curve M and curve N are the open loop gain with V_{tune}=0Volt and 5Volt, respectively. The group delay is about 1.74×10^{-6}rad/Hz. As compared to Fig. 2b, we see that the phase shift is dominated by the saw resonator. The slight increase may be from the tunable phase shifter. The oscillation frequency is predicted from the phase shift at the zero-crossing point with enough gain margin about 2dB. This gives us the benefit of low flicker noise from the amplifier without deep gain compression. To prevent the AM to PM effect, the

tuning bandwidth is approximately equal to the resonator's 1dB bandwidth. It is approximately from 2487.85MHz to 2488.85MHz.

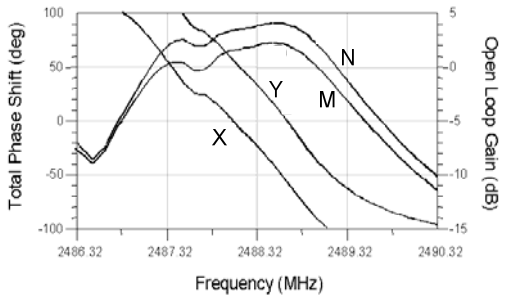

Fig. 5 The open loop gain and phase shift at the oscillation frequency.

III. OSCILLATOR PERFORMANCES

The performances of the oscillator are measured. The second harmonics is suppressed below 58 dB without using output low pass filter. This is attributed to the linear amplifier. The tuning characteristic is shown in Fig. 6 with ±200ppm range and good linearity. The turnover temperature is approximately 45°C, which is mainly determined by the STW resonator. The phase noise of the oscillator is measured as shown in Fig. 8. The spectral shape in curve 1 indeed arrears $1/f^3$ near the carrier. The intersection point with 1/f curve is around 50 kHz offset. The magnitude at 100 kHz offset is -153dBc/Hz, which is lower than those indicated in Table I. The measured parameters of the STW oscillator and the specifications of the other commercial products are summarized in Table I.

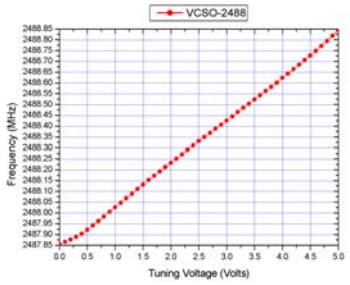

Fig. 6 Oscillation frequency vs. tuning voltage.

IV. PREDICTION OF PHASE NOISE

To analyze the shaping behavior of the close loop, the residual phase noises are examined as shown in Fig. 8. It reveals that the noise n_r from STW resonator (Curve 2) is dominant about 10dB above those from amplifier n_g (curve 3) and varactor n_p (curve 4). The phase shifter has the same order as that in amplifier. The system's floor is also indicated as in curve 5, which is much lower than these measured items. As referred to Fig. 5, the magnitude of the loop gain under steady state is assumed to one with a rather wide bandwidth, at least ±500kHz at 2488.32MHz. The STW resonator looks like a pure resister not an inductor at the oscillator frequency. In the Lesson's model the filter transfer function is considered to be a symmetrical one on each side of the carrier frequency. As shown in Fig.9, the basic open loop circuit is divided to four components, phase shifter, STW resonator, amplifier, and power splitter, whose transfer functions are P(ω), R(ω), G(ω), and D(ω), respectively. The power spectral density (PSD) at output point o is as follows:

$$\Phi_o = (n_g + n_r \cdot |G(\omega)| + n_p \cdot |R(\omega)| \cdot |G(\omega)|) \cdot |D(\omega)|$$

Because of n_r is greater than n_g and n_p, the output noise is further simplified as

$$\Phi_o = n_r \cdot |G(\omega)| \cdot |D(\omega)|$$

The product $|G(\omega)| \cdot |D(\omega)|$ is approximately 8~9dB in this work. The phase shift as a function of frequency is assumed linear with slope or group delay τ_g, which is roughly equal to 1.74×10^{-6} rad/Hz in our case, within the limited bandwidth. Hence, the normalized open loop gain is written as $e^{-j\Delta\omega\tau_g}$, where $\Delta\omega$ is the offset frequency from the center frequency. Then the closed loop gain is obtained as

$$Closed\ Loop\ gain = \frac{1}{1-e^{-j\tau_g\Delta\omega}}$$

According to [8], the PSD of phase noise can be shaped by multiplying the square of closed-loop gain to the residual phase noise. Here, the shaping factor for the PSD is shown as Fig.7.

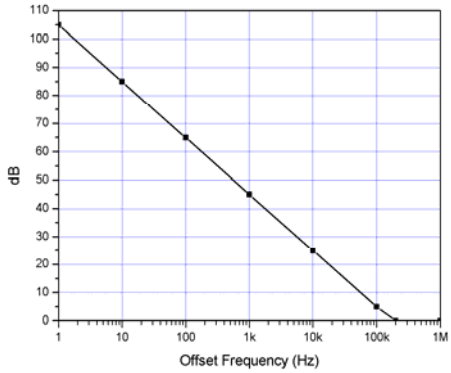

Fig.7 Shaping factor for the PSD.

For the close-in noise with $\Delta\omega$ which is smaller than π/4, the shaping appears as $(\Delta\omega\tau_g)^{-2}$. It is concluded that the phase noise is indeed shaped

from the residual noise by the $(\Delta\omega)^{-2}$ term, which is originated from the high Q resonator.

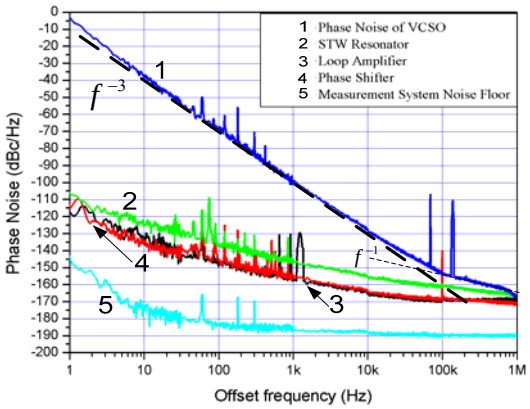

Fig.8 Measured phase noise for the 2488.32MHz STW oscillator.

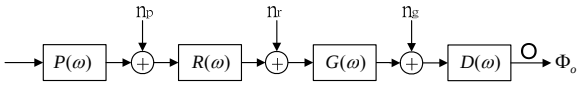

Fig.9 Transfer functions in open loop circuit

Table I: Measured Result for the voltage controlled STW oscillator and Comparison with the other Commercial Products

Item	Value			
	This Work	Synergy	M-tron	SAWTEK
Supply Voltage (Volts)	+5	+5	+5	+5
Supply Current (mA)	65	60	100	55
Output Power (dBm)	+13	+3	+7	+10
Tuning voltage (Volts)	0-5	1-4	0-5	N/A
Tuning Ramge (ppm)	±200	250	±50	80
Sub Harmonic (dBc)	-58	-30	-26	N/A
Phase Noise @ offset 100kHz (dBc/Hz)	-153	-142	-145	-145

V. CONCLUSIONS

A surface transverse wave based oscillator was designed and fabricated in this study. The resonator is operated directly at the specific frequency 2.48GHz to avoid the degradation of phase noise due to frequency multiplication. The resonator with two coupled modes is designed to achieve wide tuning. The tuning bandwidth of resonator is enhanced by trimming the central grating while keeping the steep phase change. The tuning capability achieves ±200ppm. In comparison with the other commercial products, the phase noise performance of this work is better than about 8dB at the offset frequency 100 kHz. The phase noise near the carrier is confirmed to follow the Leeson' prediction. It is concluded that the behavior of phase noise is dominated by the residual noise of SAW resonator and is shaped by the important factor of group delay.

ACKNOWLEDGMENT

This work was supported by the ftech Co. and Southern Taiwan Science Park Administration under the contract 92-1001-B062-001. The authors would like to thank Dr. Long Wu at ftech Co. for fabricating the STW resonator and Dr. Bob Temple at Agilent Co. for the measurement of phase noise.

REFERENCES

[1] O. Ishii, H. Iwata, M. Sugano, and T. Ohshima, UHF AT-CUT crystal resonators operating in the fundamental mode, IEEE Int. Frequency Control Symposium, pp. 975-980, 1998.

[2] N. Nomura, M. Itagaki, and Y. Aoyagi, Small packaged VCSO for 10Gbit Ethernet application, IEEE UFFC-2004, pp.418-421.

[3] B. Fleischmann, A. Roth, P. Russer, R. Weigel, A 2.5GHz Low Noise Phase Locked Surface Transverse Wave VCO, IEEE UFFC-1989, pp.65-69.

[4] I. D. Avramov, Very Wide Tuning Range, Low-Noise Voltage Controlled Oscillators using Ladder Type Leaky Surface Acoustic Wave Filters, IEEE UF*FC-1998*, pp.489-496.

[5] C. E. Hay, M. E. Harrell, and R. J. Kansy, "2.4 and 2.5 GHz Miniature, Low-Noise Oscillators Using Surface Transverse Wave Resonators and a SiGe Sustaining Amplifier," IEEE UFFC-2004, pp. 174-179.

[6] T. L. Bagwell and R. C. Bray, "Novel Surface Transverse Wave Resonators with Low Loss and High Q," *IEEE Proc. Ultrasonics Symp.*, 1987, pp.319-324.

[7] G. K. Montress, T. E. Parker, and M. J. Loboda, "Residual Phase Noise Measurements of VHF, UHF, and Microwave Components," *IEEE Transactions on Ultrasonics, Ferroelectrics, and Frequency Control*, vol.UFFC-41, no. 5, pp.664-679, Sep. 1994.

[8]T. E. Parker and G. K. Montress, "Precision Surface Acoustic Wave (SAW) Oscillator," *IEEE Transactions on Ultrasonics, Ferroelectrics, and Frequency Control*, vol.UFFC-35, no. 3, pp.342-364, May 1988.

[9] D. B. Leeson, "A simple model of feedback oscillator noise spectrum," *Proc. IEEE*, vol. 54, no. 2, pp. 329-330, Feb. 1966.

[10] M. Hikita, A. Sumioka and T. Tabuchi, "A Wideband SAW Resonator and Its Application to a VCO for Mobile Radio Transceivers," *IEEE Transactions on Vehicular Technology*, vol. 43, no. 4, pp.863-869, Nov. 1994.

[11] J.H. Lin and Y.H. Kao "A Low Phase Noise Voltage Controlled SAW Oscillator with Surface Transverse Wave Resonator for SONET Application" *APMC 2005*

Characteristic Improvement of a Colpitts-Type Oscillator for Gigahertz Frequency

Wan-Hsiung WANG†, Keita ASANO††, and Yoshifumi SEKINE††
†Graduate School of Science and Technology, Nihon University, 1-8-14 Surugadai Kanda, Chiyoda-ku, Tokyo 101-8308, JAPAN
††College of Science and Technology, Nihon University,
7-24-1 Narashinodai, Funabashi-shi, Chiba 274-8501, JAPAN

***Abstract*—Recent research has showed that stable frequency is necessary to improve efficiency in the high frequency band. However, it is very difficult to use a Colpitts-type crystal oscillator in the high frequency band.**

Previously, we have reported that a negative resistance is obtained by the Colpitts-type crystal oscillator circuit in the Gigahertz (GHz) frequency band. However, it is necessary to reduce the external capacity in order to obtain negative resistance in the GHz frequency band. The temperature characteristic of the oscillator gets worse due to change in the internal capacity.

In this paper, we show how to stabilize the characteristics of Colpitts-type crystal/SAW oscillators in the GHz frequency band by using PSpice simulation. Next, we show a new Colpitts-type crystal/SAW oscillator, which can obtain a stable negative resistance value with a change of temperature in the GHz frequency band. Furthermore, we propose an effective circuit for reducing the temperature dependency of a transistor.

Keywords: Temperature compensation, Colpitts-type crystal oscillator, Negative resistance, High frequency band

I. INTRODUCTION

The development of radio communication, measurement equipment and so on, higher frequency oscillators have been required more and more. Generally, since the crystal oscillators had high short-term frequency stability, they have been applied to communication technology and information technology. Quartz resonators, which have been developed for the high frequency band, are aimed for application with systems for the next generation [1-2]. Quartz resonators with the high frequency band require a steady oscillator to oscillate in the high frequency band.

Previously, we reported that a sufficient negative resistance was obtained by the Colpitts-type crystal oscillator circuit in the Gigahertz (GHz) frequency band [3-4]. However, it is necessary to reduce the external capacity in order to obtain negative resistance in the GHz frequency band. The temperature characteristic of the oscillator gets worse due to change in the internal capacity.

It is extremely important to understand the temperature factor for the stable oscillation circuit. In order to realize a more stable oscillation frequency, the oscillation circuit must be compensated to be as stable as possible before creating the compensation circuit. At the same time, in regard to the stable
temperature this paper will examine:

1) the temperature characteristics of the quartz resonator and the transistor,

2) the temperature parameters such as the input current and negative resistance, and

3) the current level characteristics of equivalent capacitance according to the impedance change derived from the temperature influence on the circuit.

In addition, this paper will also discuss the results of stable negative resistance.

II. THE HIGH FREQUENCY COLPITTS-TYPE OSCILLATOR WITH A COMMON BASE CIRCUIT

Figure 1 shows a GHz frequency band Colpitts-type oscillator with common base circuit [3-4], which was proposed in our previous paper. The Colpitts-type crystal

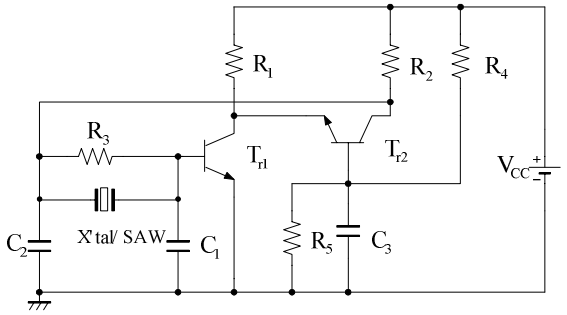

Fig. 1. A high frequency Colpitts-type oscillator with a common base circuit.

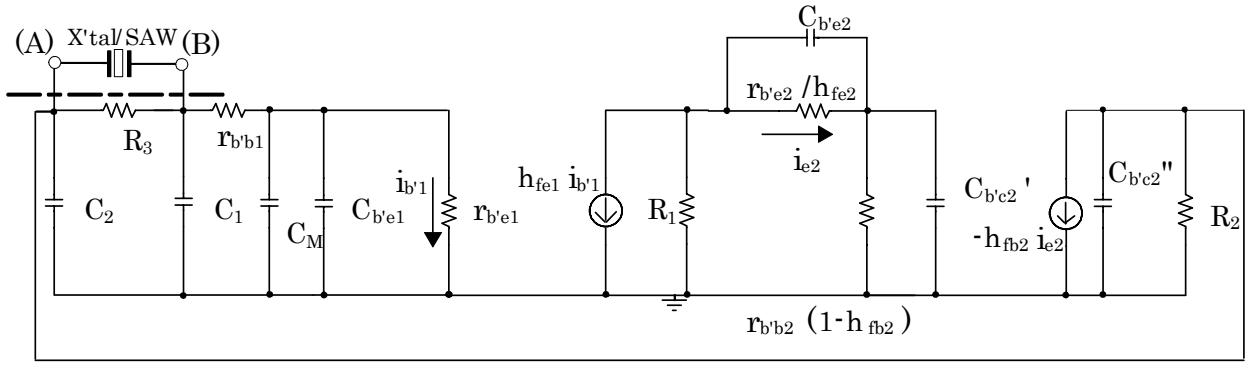

Fig. 2. The equivalent circuit of Fig.1.

oscillator consists of a common emitter T_{r1} and a common base circuit T_{r2} as a cascade amplifier, and has a feedback circuit from the collector of T_{r2} to C_2.

Figure 2 shows the simplified high frequency small signal equivalent circuit in Fig.1. The Miller capacitance C_M is a function of $C_{b'c1}$, which is the transistor's capacitance between the base and collector. The $r_{b'b2}$ is used as impedance reflection to change $r_{b'b2}(1-h_{fb2})$.

In this case, the equation for the equivalent input impedance of the common base circuit is as follows:

$$Z_{i2} = \frac{(r_{b'e2}/h_{fe2})}{1+j\omega C_{b'e2}(r_{b'e2}/h_{fe2})} + \frac{r_{b'b2}(1-h_{fb2})}{1+j\omega C'_{b'c2} r_{b'b2}(1-h_{fb2})} \quad . \tag{1}$$

Where $r_{b'e2}$ is the base-emitter junction resistance, $C_{b'e2}$ is the base-emitter junction capacitance, $r_{b'b2}$ is the base ohmic resistance, and $C'_{b'c2}$ is changed from the base-collector junction capacitance $C_{b'c2}$, which does not have an effect on the Miller capacitance of T_{r2}.

Then, the Miller capacitance of T_{r1} can be calculated by using $h_{fe1} i_{b'1} = g_{m1} v_{b'e1}$. Therefore, C_M is as follows:

$$C_M = (1+\frac{R_1}{1+R_1/Z_{i2}} \cdot \frac{h_{fe1}}{r_{b'e1}}) C_{b'c1} \quad . \tag{2}$$

Next, the equation is readjusted to substitute Eq. (2) for Eq. (1) in the case of $R_1 >> Z_{i2}$. The equation can be approximated as follows:

$$\frac{r_{b'e1}}{h_{fe1}} \cong \frac{(r_{b'e2}/h_{fe2})}{1+j\omega C_{b'e2}(r_{b'e2}/h_{fe2})} + \frac{r_{b'b2}(1-h_{fb2})}{1+j\omega C'_{b'c2} r_{b'b2}(1-h_{fb2})} \quad . \tag{3}$$

Generally, since $r_{b'b2}$ of the transistor is a small value, the second term in Eq. (3) can be ignored. Furthermore, the cutoff frequency f_2 of T_{r2}, which is the common base circuit, is higher than the cutoff frequency of the common emitter circuit. f_2 is described as follows:

$$f_2 = \frac{1}{2\pi C_{b'e2}(r_{b'e2}/h_{fe2})} \quad . \tag{4}$$

In this case, if f_2 is satisfied by Eq. (4) in a high frequency band, T_{r2} can obtain the frequency characteristic in the high frequency band. Therefore, in the high frequency band, T_{r2} can be approximately shown:

$$r_{b'e1}/h_{fe1} \cong r_{b'e2}/h_{fe2} \, . \tag{5}$$

The Miller capacitance of T_{r1} is readjusted by substituting Eq. (5) for Eq. (2). The C_M in Fig.2 is smaller than the Miller capacitance which is calculated from the conventional Colpitts-type crystal oscillator without the common base circuit. Then, the cutoff frequency of T_{r1} is as follows:

$$f_1 = \frac{1}{2\pi(C_{b'e1}+C_M)(r_{b'e1} // r_{b'b1})} \quad . \tag{6}$$

Where $r_{b'e1}$ is the base-emitter junction resistance and $r_{b'b1}$ is the base ohmic resistance.

When C_M is reduced, f_1 will be high. In summary, if the Miller capacitance of T_{r1} is reduced, the cutoff frequency of T_{r1} is increased, and the high frequency characteristic will be improved. That is to say, in the circuit in Fig. 1, it is assumed that $r_{b'b1}$ and $r_{b'b2}$ are small enough to ignore, and the cutoff frequency of T_{r2} is satisfied by Eq. (4) in the high

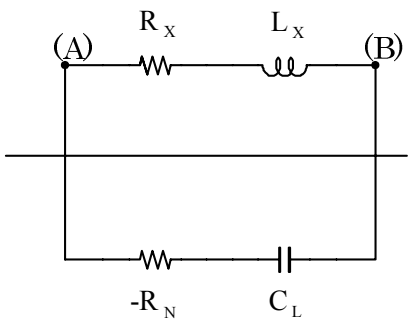

Fig. 3. A simplified diagram of a universal crystal/SAW oscillator.

frequency. It can improve the frequency characteristic in the GHz frequency band. Furthermore, according to this method when the load of T_{r1} and the input impedance of T_{r2} have been matched as satisfied in Eq. (5), the Miller capacitance of the Colpitts-type crystal oscillator with a common base circuit is decreased. The effect of R_1 is disregarded in the Miller capacitance. As a result, there should be an improvement of T_{r1} in the frequency characteristic in the GHz frequency band.

Figure 3 shows the simplified diagram of a universal crystal/SAW oscillator. In this figure, terminals (A) and (B) illustrate the terminals of the crystal/SAW resonator in Fig. 2. In Fig. 3, $-R_N$ and C_L show the impedance values without the crystal/SAW resonator shown in Fig. 2. When the crystal/SAW resonator is not included, the circuit becomes a negative resistance element in series with capacitance. In Fig. 2, we can see how the crystal resonator acts as the resistance element in series with inductance. In this simplified diagram, the negative resistance $-R_N$ is approximated as follows:

$$-R_N \approx -\frac{g_m^{'}}{\omega^2 C_1^{'} C_2^{'}} \quad . \tag{7}$$

Then, $C_1^{'}$ and $C_2^{'}$ are as follows:

$$C_1^{'} = C_1 + C_{b^{'}e1} + C_M \tag{8}$$

$$C_2^{'} = C_2 + C_{b^{'}c2}^{''} \quad . \tag{9}$$

The Colpitts-type crystal oscillator with a common base circuit can obtain the negative resistance characteristic in the high frequency band. Since $C_1^{'}$ and $C_2^{'}$ in Eq. (7) are reduced, the negative resistance reaches a higher frequency. Then, C_M can be reduced. As a result, since Eq. (8) can be changed to a smaller capacitance, the negative resistance of Eq. (7) can be improved in the GHz frequency band.

Therefore, the Miller capacitance of the Colpitts-type crystal oscillator with a common base circuit is decreased. The circuit of Fig. 2 can obtain the negative resistance characteristic in the GHz frequency band.

III. Fluctuation of Negative Resistance

A. Temperature Effect

Figure 4 shows an example of the influence of external capacities C_1 and C_2 for negative resistance characteristics of frequency in terms of temperature parameters. The circuit parameters are set to be 2SC5095, R_1=1[kΩ], R_2=100[Ω], R_3=6[kΩ], R_4=5[kΩ], R_5=15[kΩ], and C_3=1[μF]. Figure 4 (a) shows the negative resistance characteristics under the condition of C_1=C_2=0 and V_{CC}=5[V]. Temperature changes can cause large changes in the frequency band, which ensures obtaining negative resistance. Moreover, the frequency band, which ensures obtaining negative resistance, is narrow and also the negative resistance is small, when the temperature range is between -55~85[℃]. Under the consideration of obtaining the necessary negative resistance, which is 3-5 times that of crystal impedance, it is difficult to obtain sufficient negative resistance in the GHz frequency band in the temperature range of -55~85[℃]. Figure 4(b) stands for the negative resistance characteristics with C_1=3[pF] and shows no differences with those characteristics in (a), where the frequency band, that can provide negative resistance, changes significantly. Figure 4(c) shows the negative resistance characteristics under an additional condition of C_2=3 [pF]. Comparing to (a) and (b) to (c) in the frequency range, that yields negative resistance, lies in a narrower band. However, if the temperature influence is decreased, then sufficient enough negative resistance is obtained over the whole range of -55~85[℃].

Figure 5 shows an example of the influence of power supply voltage V_{CC} for negative resistance characteristics in terms of temperature parameters. It shows the negative resistance characteristics under the condition of C_1=0, C_2=3[pF], and the V_{CC}=3[V], enough negative resistance is obtained over the whole temperature ranges of -55~85[℃].

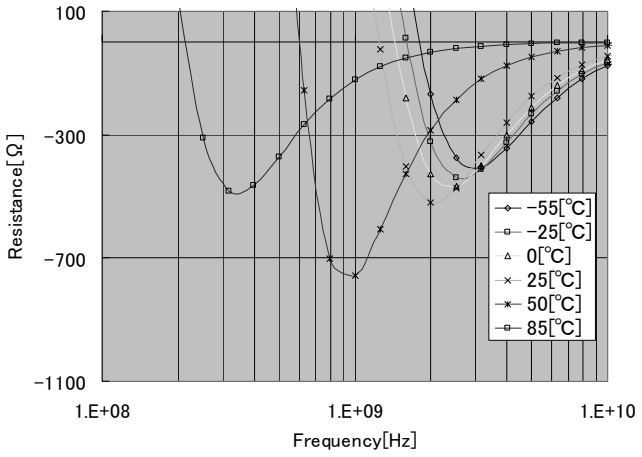

(a) C_1=C_2=0

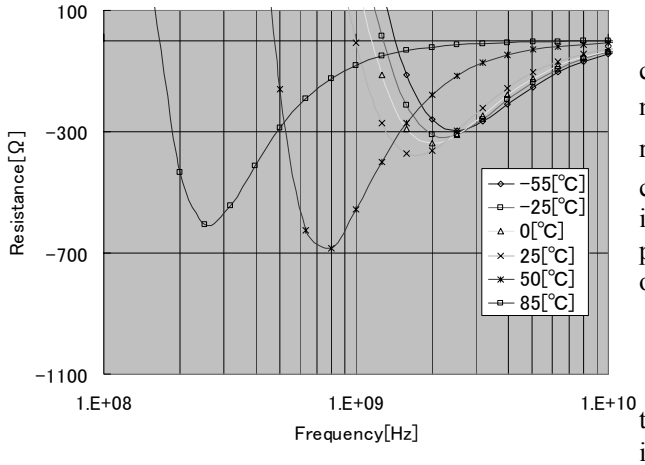

(b) C_1=3[pF], C_2=0

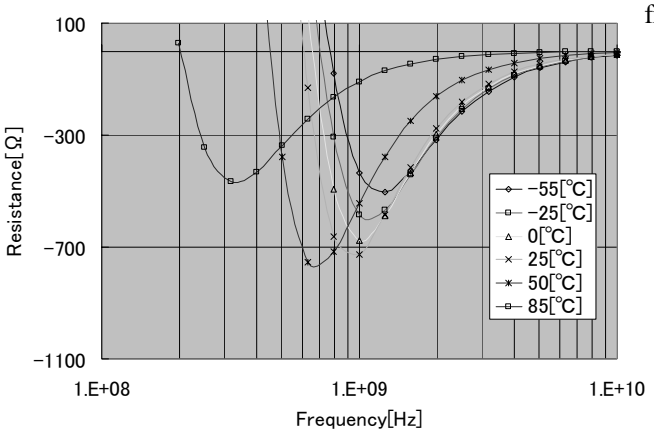

(c) C_1=0, C_2=3[pF]

Fig. 4. Negative resistance values vs. frequency characteristics at Vcc=5[V].

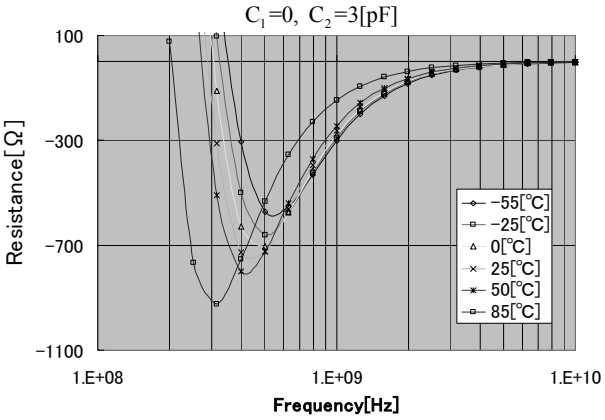

Fig. 5. Negative resistance values vs. frequency characteristics at Vcc=3[V].

B. Current Level Characteristic

Figure 6 shows an example of the current level characteristics of the circuit as shown in Fig.1. When the negative resistance $|R_L|$ on the circuit is greater than resistance R_X at the minimum current level, oscillation can be started. In this figure, when a current level increases, the negative resistance value decreases. When power supply voltage is 1.4[V] or more, it is shown that oscillation may be maintained at a fixed current level.

IV. Negative Resistance Stabilization Method

As described above, the temperature characteristics and the current level characteristics of a Colpitts-type oscillator in the GHz frequency band were clarified.

Next, we propose a Colpitts-type oscillator in the GHz frequency band with a temperature compensating circuit in

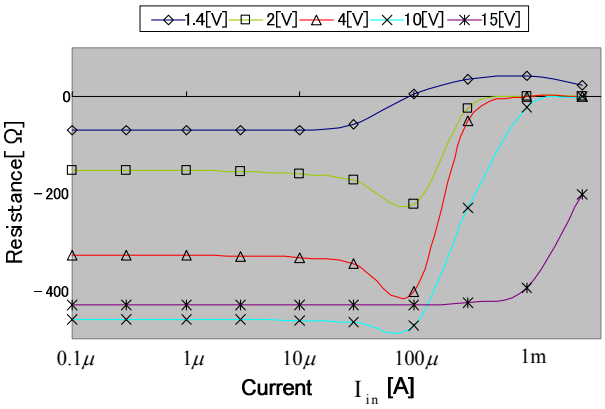

Fig. 6. Negative resistance values vs. current level characteristics in Fig. 1.

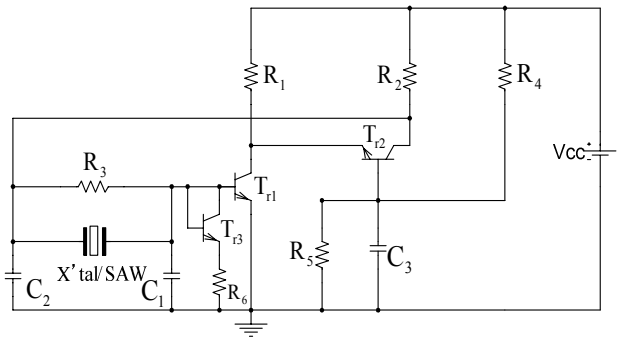

Fig. 7. A proposed Colpitts-type oscillator.

Fig. 7. By adding the Tr3/ R6 to this circuit stable negative resistance can be achieved, even if the temperature ranges are changed in the GHz frequency band.

Figure 8 is an example of the simulated results on the circuit in Fig. 7. These results show the negative resistance to temperature ranges from -55 to 85[℃], where, R_1=1[kΩ], R_2=220[Ω], R_3=6[kΩ], R_4=5[kΩ], R_5=15[kΩ], R_6=250[Ω], C_1=0, C_2=0, C_3=1[μF], T_{r1}/ T_{r2}/ T_{r3}: 2SC5095.

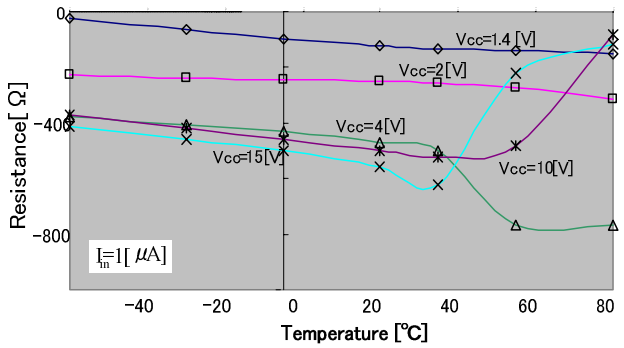

(a) In the case of the circuit in Fig. 1.

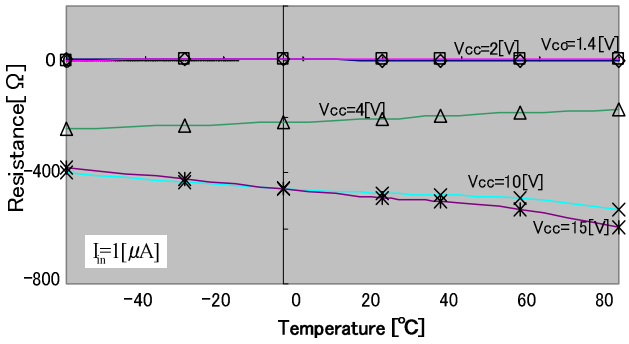

(b) In the case of the circuit in Fig. 7.

Fig. 8. Negative resistance values vs. temperature characteristics.

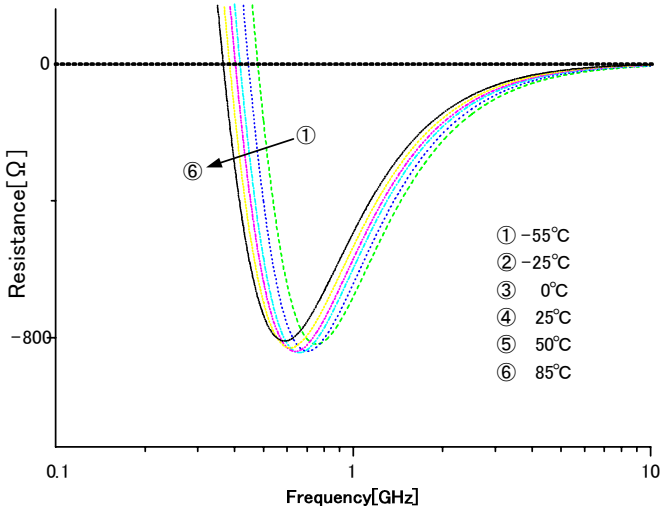

Fig. 9. Negative resistance values vs. frequency characteristics.

The simulated results show that the addition of T_{r3}/ R_6 can reduce the temperature influence.

Figure 9 shows an example of the negative resistance values vs. the frequency characteristics in the circuit in Fig. 7. When the temperature changes over the whole temperature ranges of -55~85[℃], the negative resistance characteristic shows that it is a stable characteristic as compared to the characteristic in Fig.4.

V. CONCLUSIONS

In this paper, we suggest a method to stabilize the oscillating frequency of a Colpitts-type crystal oscillator, which is connected to a common base circuit in the GHz frequency band.

As a result, the findings are shown below:

1. The Colpitts-type crystal/SAW oscillator with a common base circuit can obtain sufficient negative resistance values in the GHz frequency band.

2. Temperature characteristics of the GHz frequency band are clarified.

3. We propose on effective circuit for reducing the temperature dependency of a transistor, and the circuit is a oscillating circuit, which can stabilize the temperature characteristics of negative resistance in the GHz frequency band.

The authors would be gratified if this report can help to develop the piezoelectric.

In the future, we will design a lower power supply

voltage, and an integrated circuit using a Colpitts-type crystal oscillator with a common base circuit.

ACKNOWLEDGMENT

We thanks to Mr. K. KATAYAMA and Mr. K. SAITO of Nihon Univ. for helping us prepare this manuscript.

REFERENCES

[1] J. Matsuoka, T. Sato and T. Ohshima, “A Circuit for High Frequency Crystal Oscillator,” IEEE-FCS, pp. 569-574, 2003

[2] J. Matsuoka, T. Sato and T. Ohshima, “600MHz Crystal Oscillator Circuit Realizing the High Negative Resistance and Low Drive Level,” IEEJ EM Symposium, pp. 45-48, 2003

[3] C. Chang, K. Saeki, and Y. Sekine, “A Colpitts-type Crystal Oscillator with a Common-base Circuit for gigahertz frequency band,” IEE Japan, AVLSIWS, 37.France (2005-10).

[4] C. Chang, K. Nomura, Y. Aoyagi, Y. Sekine, “A Colpitts-Type Crystal Oscillator for GHz Band,” IEICE Trans. Electron., Vol. J89-C, No. 10, pp661-662, (2006)(in Japan)

A Protein Sensor Based on Frequency Controlled Devices

C.-K. Chen[1], Y.-C. Yang[2], H.-C. Chen[2], C.-Y. Wu[1], S.-M. Lin[3], W.-J. Wu[4], C.-K. Lee[1], and S.-S. Lu[2]

[1]Institute of Applied Mechanics

[2]Graduate Institute of Electronics Engineering and Department of Electrical Engineering

[3]Laser Medical Research Center

[4]Department of Engineering Science and Ocean Engineering

National Taiwan University, Taipei, Taiwan

Email: sslu@ntu.edu.tw

Abstract

The protein detection based on a fully integrated phase loop circuit is demonstrated for the first time. The crystal oscillator used in the PLL circuit is reused as the quartz crystal microbalance (QCM) and the division ratio provided by the PLL is used to enhance the sensitivity (200X) of QCM. The size of the proposed protein sensor including QCM, PLL and reaction chamber is smaller than that of USD 1 cent. Immunoglobulin G (IgG) protein concentrations ranging from 60 to 120 ug/mL were measured.

Keywords: QCM, phase-locked loop (PLL), bio, protein, and sensor.

Introduction

Recently bio-chips for sensing biological molecules have been extensively studied [1]-[8]. Up to now, fluorescence-based bio-sensing technology is the most popular method [1]. This technique, however, requires a complicated process of labeling the target bio-molecules with dye and expensive equipments for fluorescence analysis [2]. While label-free sensors have been developed [3]-[8] to overcome these problems, these sensors still require either complex optical setups [3]-[8] and/or extra MEMS processing steps [6]-[8], which inevitably increase the cost, power consumption and system form factor. It is therefore most desirable that integrated circuits can be adopted for biological molecule detection with minimum modification. In this paper, we demonstrate, for the first time, protein detection based on an integrated phase-locked loop (PLL) circuit, in which the crystal oscillator is reused as a quartz crystal microbalance (QCM) for the probing proteins and thus no extra processing steps/optical setups are needed. Consequently, the sensor size, cost and power consumption are greatly reduced.

QCM is a well known biosensor and becoming popular because of its label-free and high-sensitivity characteristics [3]-[5]. The quartz resonance frequency decreases as the bio-molecular was bound on the quartz surface. Sauerbrey [9] has derived a theoretic model to describe the relationship between mass loading and frequency shift. Since quartz crystal oscillator is a must in a traditional phase-locked loop circuit as frequency reference, it can function as QCM and be reused as a protein sensor. The reason for using a PLL is that the frequency shift due to the mass loading of proteins on the quartz crystal is very small and hence a large division ratio provided by the divider in a PLL can amplify the very small frequency shift as illustrated in Fig. 1. In this study, Immunoglobulin G (IgG) was employed as the bio-molecules sample because IgG can provide humoral immunity and plays an essential role in the recognition of foreign proteins.

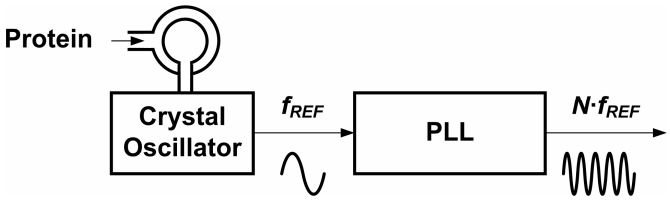

Fig. 1 Protein detection based on an integrated phase-locked loop

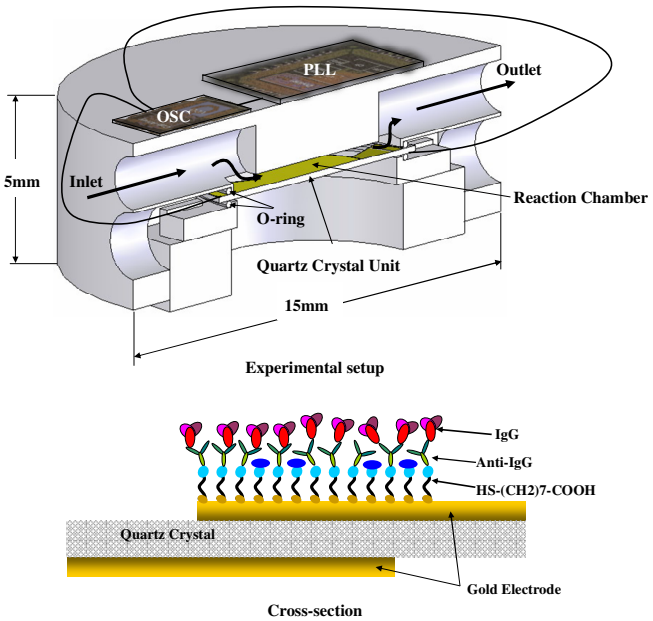

Fig. 2 Experimental setup and cross-section of the QCM

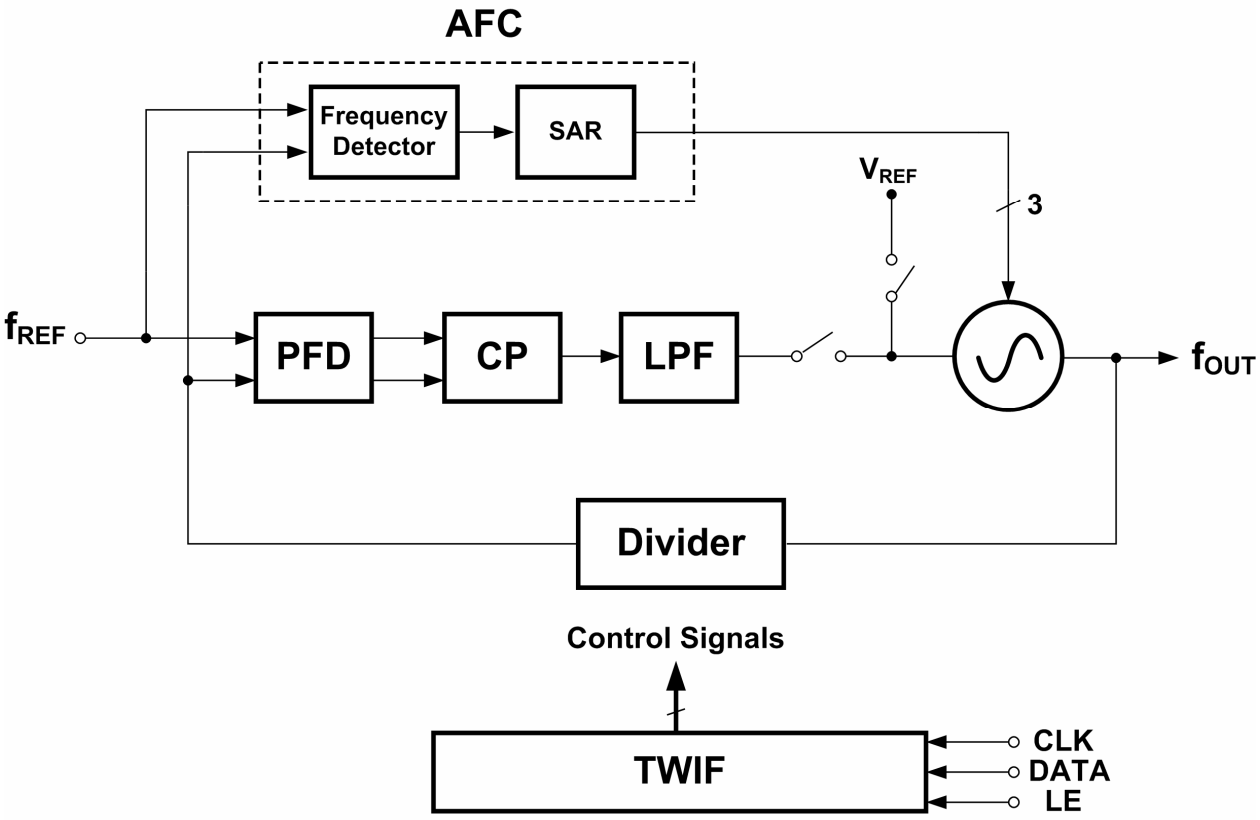

Fig. 3 Block diagram of the fully integrated PLL frequency synthesizer.

In healthy adults, the content of IgG in the whole immunoglobulin serum is approximately 75%. Therefore, IgG molecules are widely used to recognize or identify foreign antigens in the application of bio-analytical sensor. [10].

Experimental Setup

The experimental setup is shown in Fig.2. The antibody of IgG (anti-IgG) proteins was first immobilized on the top gold electrode of a commercially available 10MHz polished AT-cut disk-shape quartz crystal unit with an 8mm diameter. Then the unit was mounted inside a reaction chamber with 15mm in diameter and 5mm in height and the solution of IgG proteins (antigen) was injected into the reaction chamber. As the IgG was bound with the anti-IgG immobilized on the electrode, the mass loading causes the oscillation frequency of the crystal oscillator to shift. That is, the bio signal of IgG/anti-IgG binding is translated into the frequency shift of the crystal oscillator and the extent of frequency shift is proportional to the concentration of IgG. The shifted oscillating frequency of the crystal oscillator is then fed to a fully integrated PLL with a large division ratio of 282 for frequency multiplication. As a result, the small frequency shift was amplified and measured by a signal source analyzer (Agilent E5052A) and then recorded by a LabVIEW program via the GPIB interface. Note the size of the experimental setup including the QCM oscillator, the PLL and the reaction chamber is smaller than that of USD one cent. Preparation steps for anti-IgG on the quartz crystal are explained briefly as follows. First the HS-$(CH_2)_7$-COOH was used to modify quartz surface and then EDC/NHS was injected to activate the functional group (COOH-) followed by flowing anti-IgG for immobilization. Finally ethanolamine was adopted to block the unbinding site.

Circuits

A. Architecture

The functional block diagram of the fully integrated PLL frequency synthesizer is shown in Fig. 3. It consists of a PFD, a charge pump (CP), an on-chip loop filter (LPF), a VCO with a 3-bit binary weighted capacitors array, and a programmable divider. All the control signals are sent into the on-chip registers through a three-wire interface control circuit (TWIF). Since we use a capacitors array to widen the tuning range of the VCO, an auto-frequency calibration (AFC) loop, which consists of a frequency detector and a successive approximation register (SAR), is used in this circuit to choose the proper coarse tuning code of the capacitors array automatically.

B.VCO

Fig. 4 depicts the schematic of the LC-VCO. The core of the differential oscillator is formed by two complementary nMOS and pMOS devices for generating the negative

transconductance and attached to the LC tank of the VCO. The tank consists of a differential high-Q inductor, which is a fully symmetric spiral inductor designed for differential excitation, and two pMOS varactors. To have a wide tuning range and a small VCO gain, a 3-bit binary weighted capacitors array is connected to the LC tank for coarse tuning. Because of their high quality factors, metal-insulator-metal (MIM) capacitors are chosen to form the capacitors array and the capacitances are C_0=180 fF, C_1=360 fF, and C_2=720 fF, respectively. To have the same quality factor for each branch in the array, the sizes of the nMOS switches are also scaled as M_0:M_1:M_2=1:2:4.

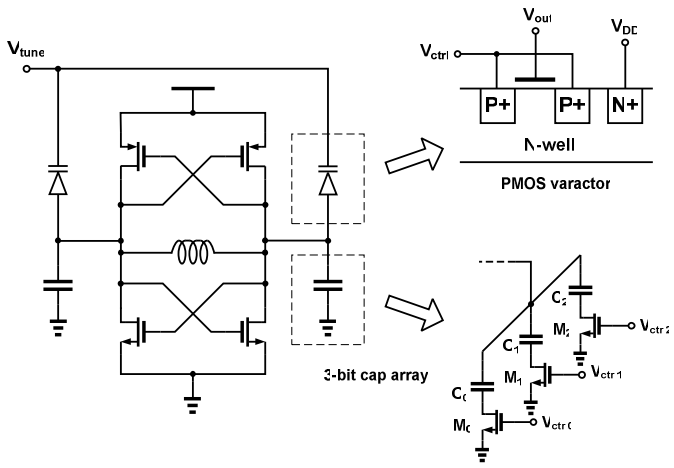

Fig. 4 The schematic of VCO

C. Auto-Frequency Calibration Loop

Since the VCO has a 3-bit capacitors array, an auto-selecting circuit is required to automatically choose the capacitors array setting whenever the output frequency of the synthesizer is changed. We utilize two counters and a comparator as a frequency detector. The two counters counts the input pulses of the reference signal and the divided VCO signal in a specified time period (T_{AFC}). By comparing the pulse numbers in these two counters, the frequency difference can be easily told, and accordingly the finite state machine can decide to increase or decrease the frequency of the VCO. The finite state machine uses the binary search algorithm to determine the final coarse setting of the VCO. Therefore, the same procedure repeats K times, where K is the bit number of the capacitors array, and thus the total time for the AFC is $K \cdot T_{AFC}$.

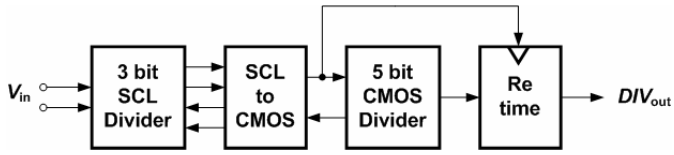

Fig. 5 Block diagram of the programmable divider.

D. Programmable Frequency Divider

The programmable frequency divider is a truly modular programmable divider, whose block diagram is shown in Fig. 5. The frequency divider consists of a three-bit source-coupled logic (SCL) divider, an SCL to CMOS converter, a 5-bit CMOS logic divider and a retiming circuit. A modulus extension circuit is also used in the CMOS divider so that the modulus can range from 32 to 511 [11].

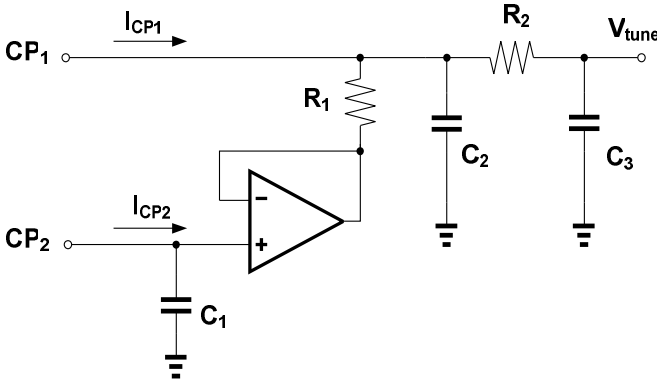

Fig. 6 Schematic of the dual-path loop filter.

To reduce the jitter accumulated in the divider cells, a retiming circuit, which is formed by a D Flip-Flop, is required to re-synchronize the divider output signal. We use the output signal of the converter rather than the VCO signal to retime the divider output so that the power consumption can be reduced (the retiming circuit need not to operate at f_{VCO}) and lots of simulation time can be saved. The tradeoff is that the jitter accumulated in the first two cells can not be removed.

E. PFD, CP and Loop Filter

The PFD employed in this frequency synthesizer is a typical tri-state structure, which consists of two DFFs, a NOR gate, and a delay cell to get rid of the dead zone.

An on-chip dual-path loop filter is adopted in this frequency synthesizer [12]. The schematic of the loop filter is shown in Fig. 6. Since the zero frequency of the PLL is so low that it is impossible to implement the passive resistors and capacitors on the chip, an active amplifier is used to effectively amplify the time constant of this zero. With the two different charge pump currents I_{CP1} and I_{CP2}, the zero frequency can be rewritten as:

$$\omega_z = \frac{I_{CP2}}{C_1 R_1 I_{CP1}} \quad (1)$$

Hence the zero frequency is amplified by a ratio I_{CP2}/I_{CP1}. Choosing that I_{CP2} 20 uA and I_{CP1} 400 uA, C_1 can be effectively amplified by a factor of 20 and then it can be integrated on chip. The design parameters of the loop filter

are as follows: C_1=40 pF, C_2=40 pF, C_3=15 pF, R_2=4.6 kΩ, and R_3=9.1 kΩ. Given that the VCO gain is 100 MHz/V, the reference frequency used to test this PLL is 33 MHz, the divider modulus is around 85, and the charge pump current is 400 uA, the resulting PLL bandwidth is approximately 200 kHz.

The schematic of the charge pump is illustrated in Fig. 7. Switches are put at the sources of current mirrors to improve the switching speed and keep the switching noise low [13]. Since we use capacitors array to widen the VCO tuning range and keep VCO gain K_{VCO} small, the operating voltage range of the VCO control voltage V_{tune} is kept in a linear and small range around half value of V_{DD}. Therefore, the output swing of the charge pump needs not to be large, and thus we may use the cascaded transistors to form the current sources to increase the output impedance.

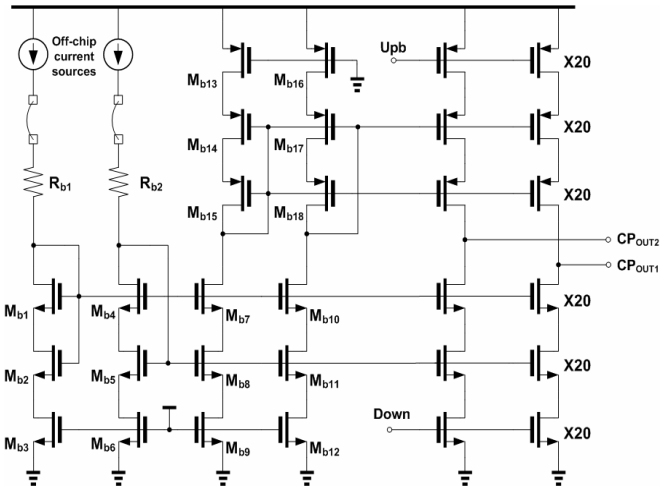

Fig. 7 Schematic of the CP.

Measurement Results

The PLL frequency synthesizer was fabricated in a standard 0.18um CMOS process. The die area is 1 mm^2 (1.23mm×0.83mm) excluding the measurement pads and ESD protection circuits. This PLL frequency synthesizer draws 24 mA from a 2 V voltage supply and thus the total power consumption is 48 mW. The reference frequency used to test this frequency synthesizer is 33 MHz.

The measured phase noise of the frequency synthesizer is shown in Fig. 8 where the measured phase noise is -96/-96/-120/-146 dBc/Hz at a frequency offset of 10k/100k/1M/10M Hz. Fig. 9 shows the measured switching time of the frequency synthesizer including the AFC process, where the total switching time is about 22 us. The AFC process takes 12 us to settle while the phase-locked loop takes about 10 us. There are four time period in the AFC process including one idle period for the control node of the VCO to be switched back to PLL. The total switching time including the AFC process is measured to be less than 40 us in all frequency bands.

The measured frequency shift of the PLL as a function of time (t) with various IgG concentrations is plotted in Fig. 10.

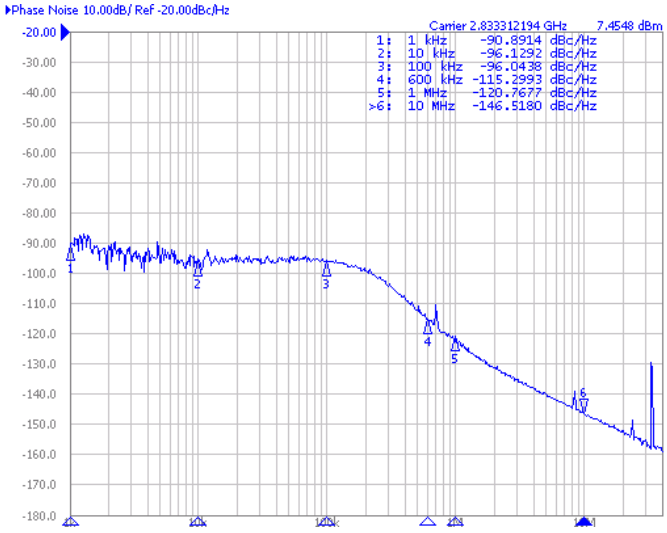

Fig. 8 Measured synthesizer phase noise.

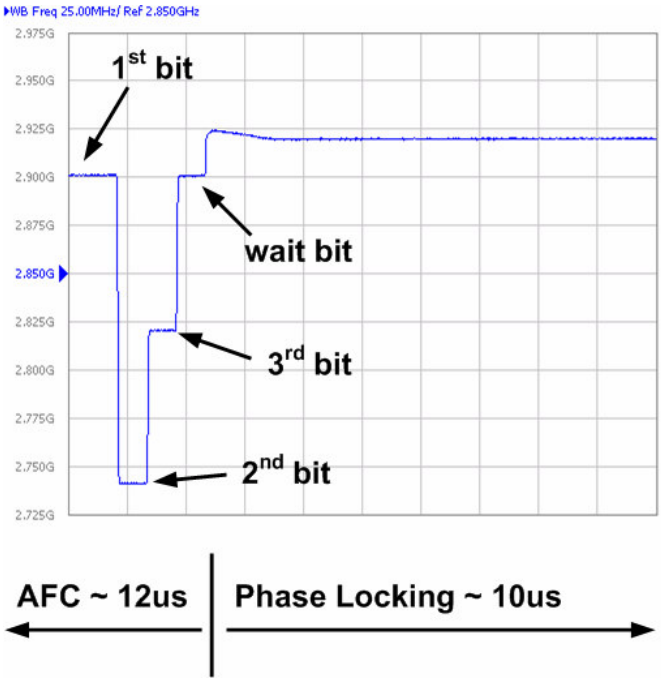

Fig. 9 Measured AFC Process

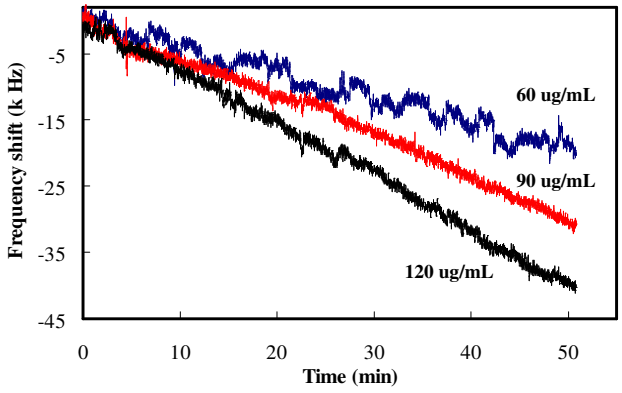

Fig. 10 Measured frequency shift versus time with various IgG concentrations

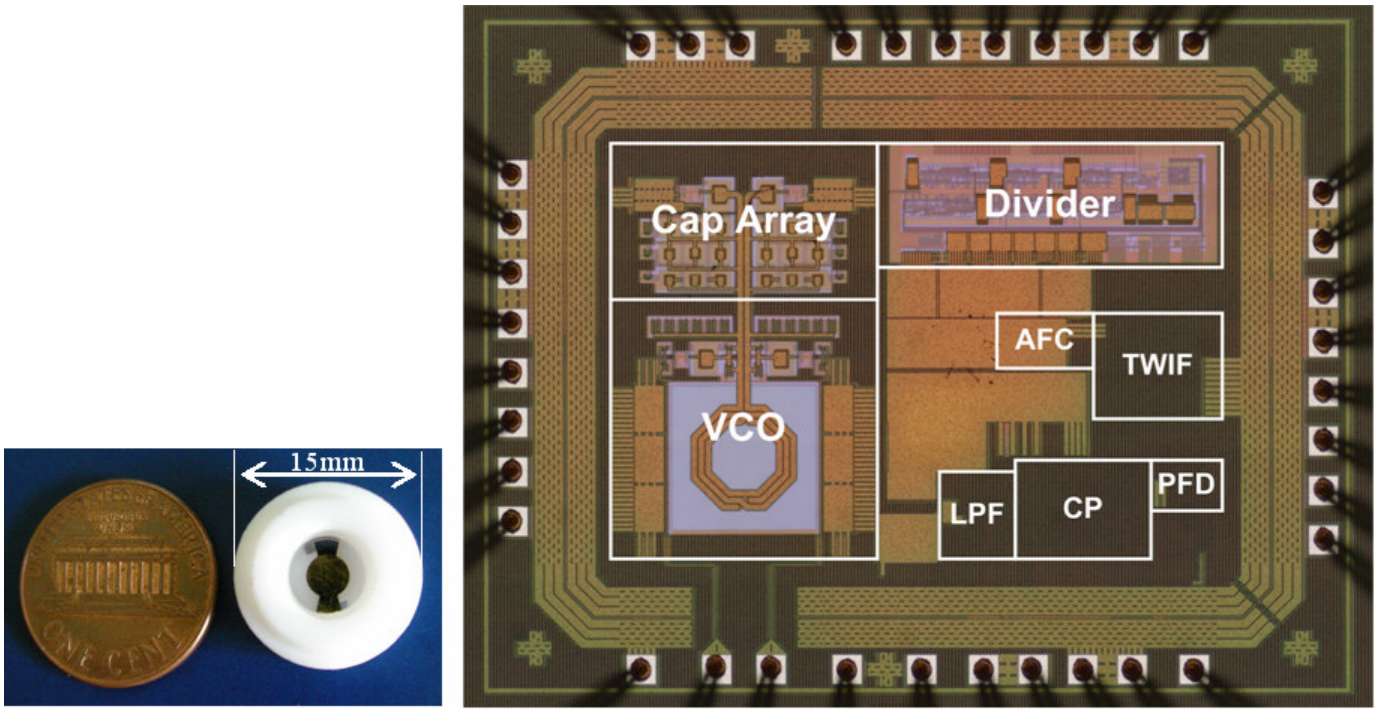

Fig. 12 Microphotographs of USD one cent, QCM in reaction chamber and PLL

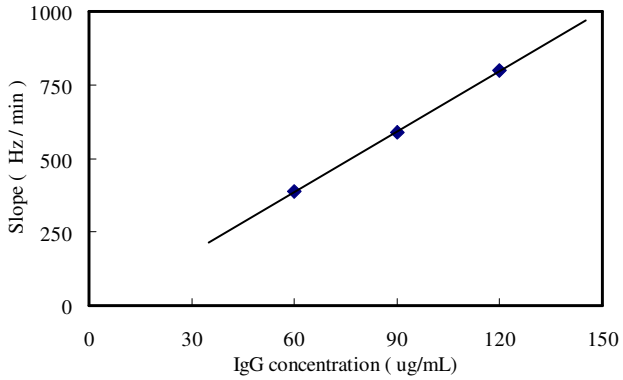

Fig. 11 The slope of frequency shift with respect to time versus IgG concentration

Clearly, frequency shift due to specific IgG-antiIgG binding can be detected for IgG concentrations from 60ug/mL to 120ug/mL. For a given time, the frequency shift (|df|) increases with increasing concentration. The dependence of slope (=|df/dt|) on concentration is shown in Fig. 11 where a linear relationship is observed. In summary, the sensitivity of a traditional QCM biosensor is enhanced with the help of PLL because of the multiplication factor provided by the divider in the loop. Moreover, no extra optical setup or additional processing steps are required since the quartz crystal oscillator needed in a PLL is reused a microbalance for protein detection. Table I is the performance summary of the proposed protein bio-signal PLL. The microphotographs of USD one cent, QCM in reaction chamber and PLL are shown in Fig. 12.

TABLE I
PERFORMANCE SUMMARY

Technology	**0.18 um CMOS**
Measured IgG Range	**60 ug/mL ~ 120 ug/mL**
Power Consumption	**48 mW**
Supply Voltage	**2V**
Reference Frequency	**10 MHz**
Frequency Range	**2.6 GHz~3.2 GHz**
Frequency Step Size	**< 1 Hz**
Synthesizer Phase Noise	**-96 dBc/Hz @ 10kHz** **-96 dBc/Hz @ 100kHz** **-120 dBc/Hz @ 1MHz** **-146 dBc/Hz @ 10MHz**
Bandwidth	**200 kHz**
Lock Time **(including AFC)**	**< 40 us**
Chip Size	**1.23 mm X 0.83 mm (1mm^2)**
Reference Spur	**-77 dBc @ 10MHz**

Acknowledgments

Financial support from the Ministry of Economic Affairs of the R.O.C. under contract no. 94-EC-17-A-05-S1-0017, chip fabrication from CIC are appreciated. implementation.

References

[1] G. Hardiman, "Microarray Platforms- Comparisons and Contrasts," *Pharmacogenomics*, vol. 5, p. 487, 2004

[2] N. Gemma, S. O'uchi, H. Funaki, J. Okada, and S. Hongo, "CMOS Integrated DNA Chip for Quantitative DNA Analysis," *ISSCC Dig. Tech. Papers*, pp.560-561, Feb., 2006.

[3] X.-L. Su and Y. Li, "Surface Plasmon Resonance and Quartz Crystal Microbalance Immunosensors for Detection of Escherichia coli O157:H7," *Transactions of the ASABE.*, vol. 48, pp. 405-413, 2005.

[4] Spangler, B.D., Wilkinson, E. A., Murphy, J. T., Tyler, B. J., "Comparison of the Spreeta® surface plasmon resonance sensor and a quartz crystal microbalance for detection of Escherichia coli heat-labile enterotoxin," *Analytica Chimica Acta*, vol. 444, pp. 149-161, 2001.

[5] X.D. Su, Y. J. Wu, W. Knoll, "Comparison of surface plasmon resonance spectroscopy and quartz crystal microbalance techniques for studying DNA assembly and hybridization," *Biosensors and Bioelectronics,* vol. 21, pp. 719–726, 2005.

[6] J. Fritz, M. K. Baller, H. P. Lang, H. Rothuizen, P. Vettiger, E. Meyer, H.-J. Güntherodt, Ch. Gerber, J. K. Gimzewski, "Translating Biomolecular Recognition into Nanomechanics," *Science*, vol. 288, pp. 316-318, Apr., 2000.

[7] G. Wu, R. H. Datar, K. M. Hansen, T. Thundat, R. J. Cote, and A. Majumdar, "Bioassay of Prostate-Specific Antigen (PSA) Using Microcantilevers," *Nature Biotechnology*, vol.19, pp.856-860, Sept., 2001.

[8] C.-H Chen et al, "A wireless Bio-MEMS for C-Reactive Protein Detection Based on Nanomechanics," *ISSCC*, 2006.

[9] G. Sauerbrey, "Verwendung von Schwingquarzen zur Wägung dünner Schichten und zur Mikrowägung," *Zeitschrift für Physik*, vol. 155,pp. 206, 1959.

[10] R. G. Hamiiton, "Human IgG subclass measurement in the clinical laboratory," *Clinical Chemistry*, vol. 33, pp. 1707-1725, 1987.

[11] Y. –C. Yang, S. –A. Yu, Y. –H. Liu, T. Wang, and S. –S. Lu, "A Quantization Noise Suppression Techniqure for Delta-Sigma Fractional-N Frequency Synthesizers, " *J. Solid-State Circuits*, vol. 41, pp.2500-2511, Dec. 2006.

[12] Y. Koo, et al, "A Fully Integrated CMOS Frequency Synthesizer With Charge-Averaging Charge Pump and Dual-Path Loop Filter for PCS- and Cellular-CDMA Wireless System," *J. Solid-State Circuits*, vol. 37, pp.536-542, May 2002.

[13] W. Rhee, B. Song, and A. Ali, "A 1.1-GHz CMOS fractional-*N* frequency synthesizer with a 3-b third-order ΔΣ modulator," *IEEE J. Solid-State Circuits,* vol. 35, pp. 1453—1460, Oct. 2000.

Waveguide-Type Acoustooptic Modulator Driven by Surface Acoustic Waves

Shoji Kakio*, Motoki Kitamura*, Yasuhiko Nakagawa*, Takefumi Hara†, Hiromasa Ito†,
Tetsuya Kobayashi‡ and Masayuki Watanabe‡
*Interdisciplinary Graduate School of Medicine and Engineering, University of Yamanashi, Takeda-4, Kofu 400–8511, Japan
Email: kakio@yamanashi.ac.jp
†Research Institute of Electrical Communication, Tohoku University, Katahira-2, Aobaku, Sendai 980-8577, Japan
‡Optoquest Corporation, Haraichi–1335, Ageo-shi 362–0021, Japan

***Abstract*— A waveguide-type acoustooptic modulator (AOM) using coplanar AO coupling due to a surface acoustic wave (SAW) in a crossed-channel optical waveguide is proposed for an optical wavelength of 1.55 μm. A novel tapered device was designed to increase the length of the interaction region and thus the driving surface acoustic wave (SAW) power lower. The dependences of the diffraction properties on the SAW beam width were simulated using a beam-propagation method (BPM). The device was fabricated by the proton-exchange method and post-annealing in a 128° rotated Y-cut $LiNbO_3$ substrate and the diffraction properties were measured at an optical wavelength of 1.55 μm. An 84% diffraction efficiency was obtained at the driving voltage of 17 V_{rms} for a SAW beam width of 2 mm and a driving frequency of 200 MHz. An optical frequency domain range using the frequency shifted-feedback (FSF) fiber laser with the waveguide-type AOM was demonstrated. The FSF fiber laser with the waveguide-type AOM can be applied to optical frequency domain ranging equally as well as one with the conventional bulk-type AOM. Furthermore, to obtain a wide frequency-shift range, a monolithically integrated tandem waveguide-type AOM was designed and fabricated. The optical frequency shifts for the sum of two driving frequencies and the difference frequency ranging from DC to 5 MHz were observed.**

I. Introduction

A new type of laser which is called frequency shifted-feedback (FSF) laser with unique spectral properties has been developed and noticed for its potential applications[1]. The FSF laser output consists of periodically generated chirped frequency components whose chirp rate is faster than 100 PHz/s, and the FSF operation is achieved by feedback of the first-order diffracted light of an intracavity acoustooptic modulator (AOM), which is also called the AO frequency shifter (AOFS)[2]. Furthermore, with erbium-doped fiber as the gain medium, an FSF fiber laser is set up. With its unique spectral features, the FSF laser has been demonstrated to be a very useful light source in the optical frequency-domain reflectometry (OFDR) technique[2], and has been effectively applied to hydraulic pressure measurement[3], atmospheric temperature measurement[4], high accuracy optical three-dimensional shape measurement[5], as well as to group velocity dispersion (GVD) and polarization mode dispersion (PMD) measurements for optical fibers[6][7].

In all these applications, a compact and stable FSF fiber laser is required. However, in the present FSF laser system, there is a difficulty in realizing the integration and stabilization of the AOM because the bulk acoustic wave and the spatial lights in the bulk-type AOM are used for obtaining the first-order diffracted light, that is the frequency shifted light. To solve this problem, the waveguide-type AOM driven by surface acoustic waves (SAWs) using guided-optical waves in channel optical waveguides is suitable. In fact, Tsai $et\ al.$ fabricated such a waveguide-type AOM in a crossed-channel waveguide on a $LiNbO_3$ substrate fabricated by the Ti-diffusion method and demonstrated at an optical wavelength of 0.633 μm[8][9]. However, there have been no reports of success at an optical wavelength of 1.55 μm due to both the uneasy realization of AO interaction over the small action length and the high SAW drive power required in the long optical wavelength range.

In this study, we have proposed a waveguide-type AOM in a tapered crossed-channel proton-exchanged (PE) optical waveguide on a 128°-rotated Y-cut $LiNbO_3$ substrate for an optical wavelength of 1.55 μm[10][11]. First, the waveguide-type AOM configuration is described and guided-optical waves in the waveguide-type AOM were simulated using a beam-propagation method (BPM). The dependences of the diffraction properties on the SAW beam width were investigated[12]. Next, the fabrication method of the waveguide-type AOM is described and the diffraction properties were measured at an optical wavelength of 1.55 μm. An 84% diffraction efficiency was obtained at the driving voltage of 17 V_{rms} for a SAW beam width of 2 mm and a driving frequency of 200 MHz[12].

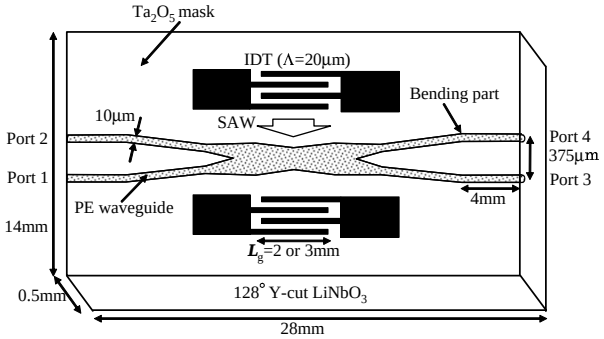

Fig. 1. Configuration of waveguide-type AOM.

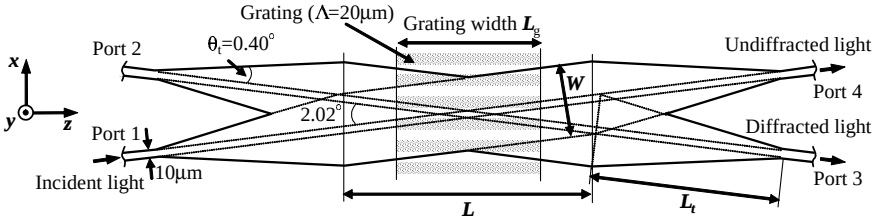

Fig. 2. Waveguide shape in diffraction region of waveguide-type AOM (analytical model for BPM).

Then, an optical frequency domain range using the FSF fiber laser with the waveguide-type AOM was demonstrated. The FSF fiber laser with the waveguide-type AOM can be applied to optical frequency domain ranging equally as well as one with the conventional bulk-type AOM[13]. Furthermore, to obtain a wide frequency-shift range, a monolithically integrated tandem waveguide-type AOM was designed and fabricated. The optical frequency shifts for the sum of two driving frequencies and the difference frequency ranging from DC to 5 MHz were observed[14].

II. Configuration and Design of Waveguide-Type AOM

The configuration of the waveguide-type AOM is shown in Fig. 1. The waveguide was fabricated in the $LiNbO_3$ substrate using the proton-exchange (PE) method and post-annealing, which is more easily realized because of the low-temperature process. Moreover, the PE waveguide can maintain only TM-modes because only the extraordinary refractive index increases after the PE process. This is especially useful for OFDR which needs a laser source with a high linear polarization. We chose a 128° rotated Y-cut $LiNbO_3$ as the substrate because as is well known, it has the highest electromechanical coupling coefficient, K^2=5.5 % for the X-propagation Rayleigh-type SAW and its optical and AO properties such as the change in the extraordinary refractive index (Δn_e) and photo-elastic constants after the PE process and post-annealing have already been investigated[15]. The SAW is launched from the interdigital transducer (IDT) fabricated on the substrate to the diffraction region.

A. Waveguide shape in diffraction region

Figure 2 shows the waveguide shape in the diffraction region of the waveguide-type AOM. The SAW power required for 100% diffraction (P_{100}) can be estimated by using a coupled mode theory[16]. Figure 3 shows the calculated P_{100} of TM_0-mode as a function of the optical wavelength, which was calculated under the assumption that the guided waves propagate in the planar waveguide. From this result, the P_{100} increases with the optical wavelength. Furthermore, the P_{100} is in inverse proportion to the length of the interaction region[16]. Therefore, if a simple crossed-channel waveguide such as that reported at an optical wavelength of 0.633 μm[8] is applied to that at an optical wavelength of 1.55 μm, the SAW drive power becomes huge due to the short interaction region. According to the above, we propose a waveguide shape, in which the diffraction region is as shown in Fig. 2. To increase the length of the interaction region, 10 μm width of the input and output waveguides is increased to a width W of 120∼150 μm using the tapered waveguides with a length of L_t of 7.5∼10 mm. The incident light from Port 1 is diffracted by a SAW in the area of SAW propagation and guided to Port 3, with a Bragg angle of 1.01°, given by:

$$\theta_B = \sin^{-1} \frac{\lambda}{2N\Lambda} \tag{1}$$

where λ is the optical wavelength in free space, N is the effective refractive index, and Λ is the wavelength of the SAW. The diffracted light is corrected by a tapered waveguide and guided to the waveguide of Port 3. Using this novel shape, the AO interaction region is longer than that in a simple crossed-channel waveguide.

B. Beam-Propagation Analysis of Waveguide-Type AOM

OptiBPM 6.0 of Optiwave Co., Ltd. was used as the analytical software. The optical waveguides of the waveguide-type AOM shown in Fig. 1 are in a three-dimensional structure. However, in this analysis, a two-dimensional structure with uniform refractive index distribution in the depth direction along the y-axis was assumed to reduce the calculation time. The analytical model has the same waveguide shape shown in Fig. 2, $i.e.$, n_e (2.167) and Δn_e (0.02), as the fabricated

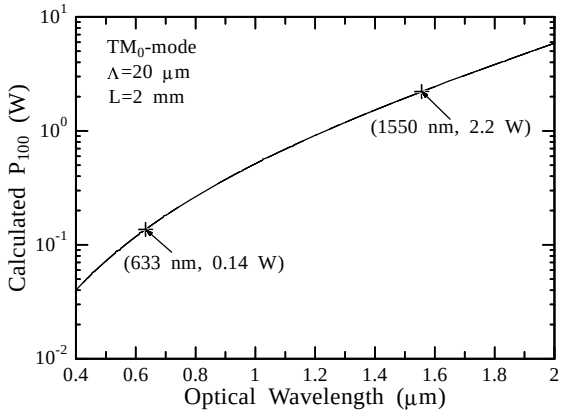

Fig. 3. Calculated SAW power required for 100% diffraction (P_{100}) as a function of the optical wavelenth.

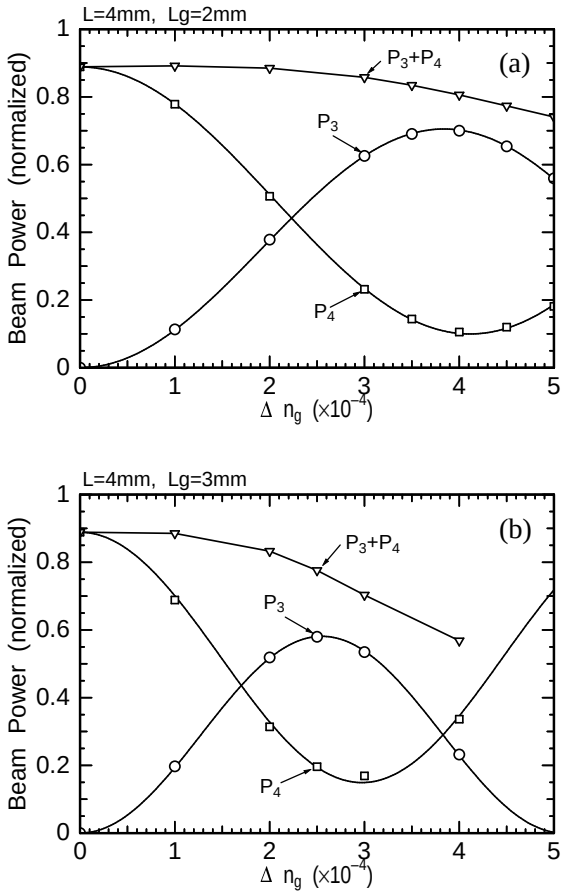

Fig. 4. Calculated diffraction properties for (a) L=4 mm and L_g=2 mm, and (b) L=4 mm and L_g=3 mm.

waveguide-type AOM as described in Section III. Ports 1, 3, and 4 were defined as the input port, diffracted output port, and undiffracted output port, respectively. A Gaussian beam with an optical wavelength of 1.55 μm and a beam waist diameter of 5 μm was assumed as the incident light. The analysis of the diffraction properties resulting from the SAW was performed by setting the refractive index grating expressed as $\Delta n_g \sin(2\pi x/\Lambda)$ in the diffraction region. The period of the grating Λ and the width of the grating L_g were equal to the SAW wavelength of 20 μm and the overlap length of IDT, respectively. The parameters of the length of the diffraction region on the waveguide L are 3, 3.4, and 4 mm, which are used in the experiments as described in Section III. Diffraction property as a function of L_g (0.5 mm$<L_g<L$) was simulated for TM-mode propagation.

C. Simulated diffraction properties

As examples of the simulated diffraction properties, Figs. 4(a) and 4(b) show the light powers of Ports 3 and 4 normalized by incident light power as a function of Δn_g, in the cases of L=4 mm and L_g=2 mm, and L=4 mm and L_g=3 mm, respectively. These parameters are the same as those in the experiment described in Section III. The solid lines in Fig. 4 show the fitted curve in the form of sin^2.

As is evident on comparing these figures, the diffraction properties are improved by decreasing L_g. As concrete improvements, it was found that the minimum power P_4^{min} in Port 4 decreases, the maximum power P_3^{max} in Port 3 increases, and the undesirable difference in Δn_g between both peaks decreases. Theoretically, the light powers in Ports 3 and 4, P_3 and P_4 should satisfy the energy conservation law, that is, $P_3+P_4=1$. However, in all cases, the sum of P_3 and P_4 is smaller than 1 because the leakage of light occurs at the output tapered waveguides. As can be seen in Fig. 4, with a decrease in L_g, the sum of P_3 and P_4 increases and approaches P_4 without the grating.

Figure 5 shows the simulated P_4^{min} and P_3^{max} as functions of L_g for L=3, 3.4, and 4 mm. It was found that the properties are improved with a decrease in L_g and that the improvements in the diffraction properties do not depend on L. The diffraction properties showed an optimum value at approximately L_g=0.8 mm.

On the other hand, the Δn_g required for the maximum diffraction efficiency increases with a decrease in L_g. This means that the input voltage to obtain the maximum diffraction efficiency increases.

D. Simulated optical field distribution

To clarify the reason for the improvements in the diffraction properties, the optical field distribution was also simulated. Figures 6(a)-6(c) show the three-dimensional display in the waveguide with L=4 mm in the cases of L_g=0 (without grating), 2, and 3 mm, respectively, for the maximum diffraction efficiency.

The fundamental mode from the normal waveguide propagates with a curved wave front in the input tapered waveguide. In the case without the grating [Fig. 6(a)], the optical mode propagates through the diffraction region to Port 3 without leakage, and is corrected by the output tapered waveguide. Because of this correction, the local concentration of the field

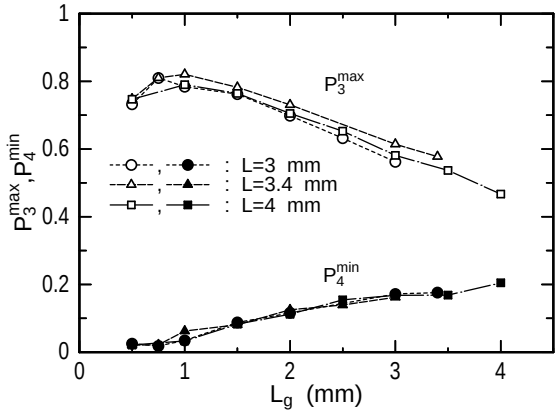

Fig. 5. Calculated beam powers P_3^{max} and P_4^{min} as functions of grating width L_g.

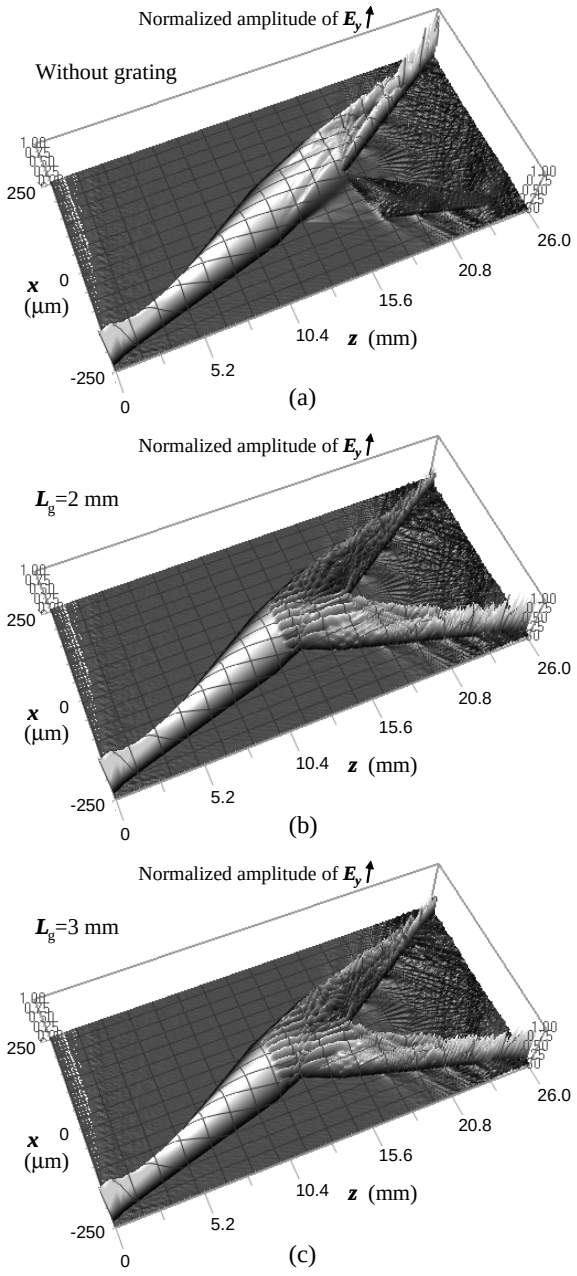

Fig. 6. Amplitude distribution of E_y on waveguide-type AOM with L=4 mm simulated by BPM for (a) without grating, (b) L_g=2 mm, and (c) L_g=3 mm.

distribution is observed around the oblique side of the output tapered waveguide.

On the other hand, the optical mode in the case with the grating [Figs. 6(b) and 6(c)] shows a complicated interference after dividing in the grating and part of this interference leaks to the undiffraction port. As can be seen from Figs. 6(b) and 6(c), by decreasing L_g, the degree of leakage to the undiffraction port can be reduced and the diffracted light power can be improved.

III. Experimental Methods

To confirm the above analytical results, a waveguide-type AOM was fabricated with several parameters of the SAW beam width L_g and the length of the diffraction region on the waveguide, L, and its diffraction properties were evaluated experimentally.

A. Fabrication of waveguide-type AOM

The channel waveguide was fabricated by first forming an RF-sputtered Ta_2O_5 mask with a film thickness of 0.08 μm by the lift-off method on 128° rotated Y-cut $LiNbO_3$, and then by the PE process and post-annealing. The fabrication conditions and the channel waveguide width of 10 μm were designed to obtain a lower coupling loss for a polarization maintained fiber of 1.55 μm optical wavelength and to maintain only the fundamental mode in the depth direction. As a result, the conditions used were as follows: a PE time of 1 h 15 min in a solution of benzoic acid containing 0.2 mole % lithium benzoate at 240°C, an annealing time of 1 h 40 min at 400°C. A Gaussian index profile with a change in extraordinary refractive index (Δn_e) of 0.021 and a waveguide depth of 4.1 μm at $\Delta n_e/e$ was obtained. After polishing and AR-coating the end face of the waveguide, a pair of normal IDT with a period length Λ of 20 μm, N finger pairs and an overlap length of L_g were formed on the substrate by an aluminum thin film using a photo-etching process. The overall dimensions of the fabricated waveguide-type AOM were 28×14 mm^2 as is shown in Fig. 1.

The parameters of the tapered crossed-channel waveguide shape and the IDTs of the five types of fabricated waveguide-type AOM are shown in Table I. As parameters of the sample, a length of the diffraction region on the waveguide L of 3.0, 3.4 or 4.0 mm and a SAW beam width (an overlap length of IDT), L_g, of 2.0 or 3.0 mm were chosen. The fabrication of a sample with L_g less than 2.0 mm was not attempted because it is difficult to observe a peak diffraction due to a large input voltage. The 10 μm width of the channel waveguide of each port was increased to 120, 130 or 152 μm in the diffraction region using a tapered waveguide with a length of 7.5, 8.4 or 10.0 mm. The angle of the tapered waveguide, θ_t, for all types was set to be 0.40°.

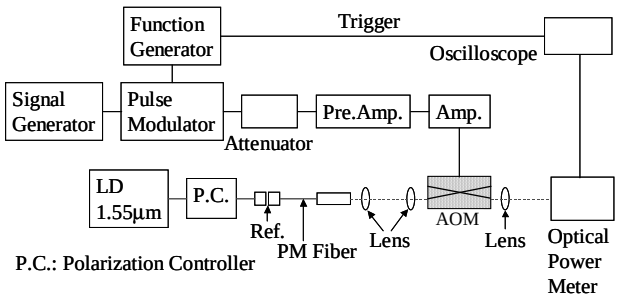

Fig. 7. Diffraction properties measurement setup.

TABLE I

FABRICATION CONDITIONS AND EXPERIMENTAL RESULTS FOR WAVEGUIDE-TYPE AOM.

Sample	Parameters of waveguide shape			Parameters of IDTs		Max. diffraction efficiency (P_3^{max})	Min. undiffraction efficiency (P_4^{min})
	L (mm)	L_t (mm)	W (μm)	L_g (mm)	N		
A	3.4	8.4	130	2	30	76% at 16.1 V_{rms}	8.5% at 17.6 V_{rms}
B	4.0	10.0	152	2	30	84% at 16.7 V_{rms}	9.9% at 17.7 V_{rms}
C	3.4	8.4	130	3	20	63% at 12.6 V_{rms}	15% at 14.6 V_{rms}
D	4.0	10.0	152	3	20	64% at 12.9 V_{rms}	20% at 14.4 V_{rms}
E	3.0	7.5	120	3	20	65% at 13.8 V_{rms}	11% at 16.6 V_{rms}

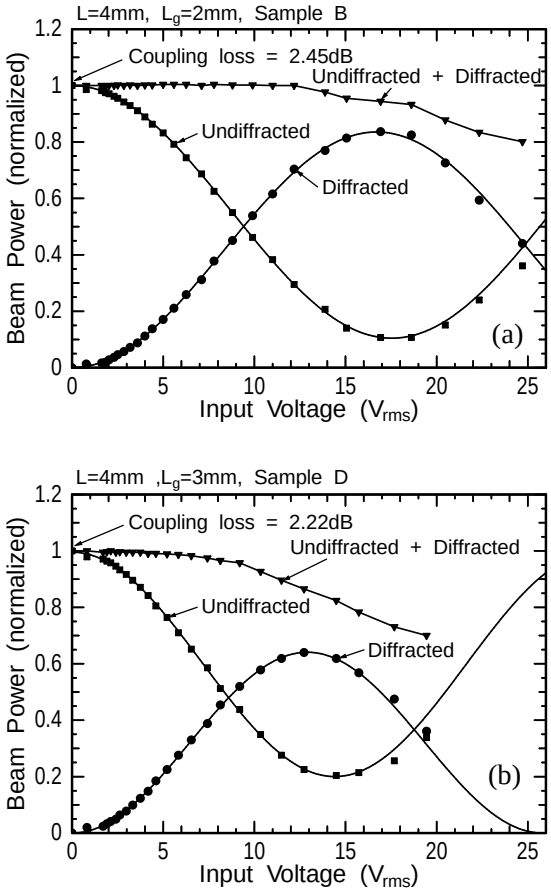

Fig. 8. Measured diffraction efficiency for samples with (a) L=4 mm and L_g=2 mm, and (b) L=4 mm and L_g=3 mm.

B. Diffraction properties

The diffraction properties of the waveguide-type AOM were measured using a 1.55 μm laser diode. Figure 7 shows the measurement setup for the diffraction properties. In order to prevent the generation of heat due to the SAW power, a pulse-modulated RF voltage was supplied to the input IDT. The pulse period and duty ratio were 20 ms and 1/20, respectively, that is, the pulse width was 1 ms.

The measured maximum diffraction and minimum undiffraction efficiencies for each sample are shown in Table I. Figures 8(a) and 8(b) show the diffraction properties as functions of input voltage for sample B of L=4 mm and L_g=2 mm, and sample D of L=4 mm and L_g=3 mm, respectively. According to the simulated results in Fig. 4, by decreasing SAW beam width, the diffraction properties were improved.

The maximum diffraction efficiencies for samples A and B with L_g=2 mm were 76 and 84%, respectively, and these values are larger than those of other samples with L_g=3 mm. Furthermore, for samples A and B, the minimum undiffraction efficiency slightly improved compared with other values. However, a small L_g means that the driving voltage required to obtain the maximum diffraction efficiency increase. Moreover, as can be seen from Fig. 8 and Table I, the undesirable voltage difference between the maximum diffraction efficiency and the minimum undiffraction efficiency was improved to 1$\sim$1.5 V_{rms} from 1.5$\sim$3 V_{rms} by decreasing SAW beam width according to the simulated diffraction properties.

On the other hand, for the parameter L, no major change in the diffraction properties was observed. Therefore, it is clear that the improvements in the diffraction properties are achieved by decreasing SAW beam width, and that no dependence is observed between the diffraction properties and the length of the diffraction region L.

C. Optical frequency domain ranging using FSF fiber laser

An optical frequency domain range using the FSF fiber laser with the waveguide-type AOM was demonstrated. To fabricate a fiber-to-fiber device, the waveguide-type AOM was incorporated into a module and optically connected to the input and output polarization-maintained (PM) fiber arrays, which are constructed by the twin-core ferrule with a pitch of 375 μm, through the collimating and condensing lenses.

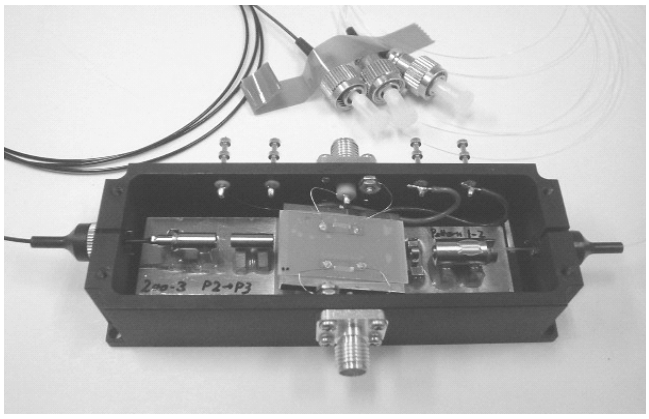

Fig. 9. Photograph of waveguide-type AOM module.

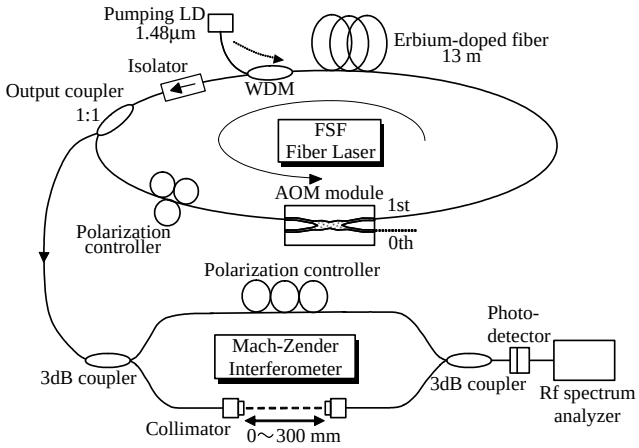

Fig. 10. Experimental setup of optical frequency domain ranging using FSF fiber laser with waveguide-type AOM.

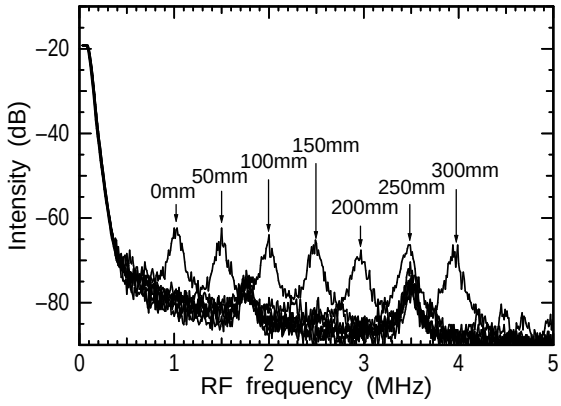

Fig. 11. RF spectrum of beat signal.

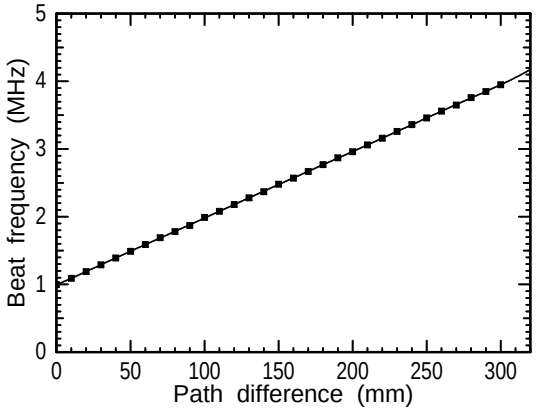

Fig. 12. Beat frequency vs. path difference of interferometer.

Figure 9 shows a photograph of the module of the waveguide-type AOM. A FC type connector was used for optical input and output.

The experimental setup of optical frequency domain ranging using the FSF fiber laser with the waveguide-type AOM is shown in Fig. 10. The erbium-doped fiber (EDF) with the fiber length of 13 m was used as a gain medium. The waveguide-type AOM was driven at a frequency of approximately 200 MHz. The optical frequency of laser light diffracted by an elastic wave through an acoustooptic effect is Doppler shifted by the acoustical frequency. Therefore, the light in the cavity is frequency shifted every round trip by feeding the diffracted light of the waveguide-type AOM back into the EDF.

The FSF fiber laser output with periodically generated chirped frequency components was split into the two arms of the Mach-Zender interferometer. The adjustable path difference was obtained by including the propagation length of spatial light to one arm. The beat signal was detected with a photodetector and the beat spectrum was analyzed using an RF spectrum analyzer. Figure 11 shows the observed RF spectrum. The beat frequency is shifted with path length. The fixed signals at 1.75 MHz and 3.5 MHz are generated by undesirable reflection in the cavity. A linear relationship is observed between the beat frequency and the path length, as shown in Fig. 12[17].

On the basis of the above results, it is apparent that the FSF fiber laser with the waveguide-type AOM can be applied to optical frequency domain ranging equally as well as one with the conventional bulk-type AOM.

IV. Monolithically Integrated Tandem AOM

A wide frequency-shift range makes it attractive for various applications in optical measurements. For instance, using an AOM with a lower frequency shift to realize the FSF fiber laser, longer-distance optical frequency-domain ranging is possible without the determination of the beat order[18]. Using a simple AOM, the frequency shift is almost fixed at around the center frequency of the transducer. On the other hand, using several AOMs and combining upward and downward frequency shifts, a FSF laser oscillation with a small frequency shift was obtained[19][20]. However, it is difficult to realize a compact and stable FSF laser system. Therefore, a structure in which several waveguide-type AOMs are connected in tandem on the same substrate can be considered to be suitable. Moreover, by improving driving power and extinction ratio in this structure, the tandem AOM can be applied to matrix optical switches in photonic networks.

In this section, the monolithically integrated tandem waveguide-type AOM, hereafter abbreviated as the tandem AOM, is investigated.

A. Design and Fabrication of Tandem AOM

The overall configuration of the tandem AOM is shown in Fig. 13. The structure considered is a 2×4 optical switch consisting of one 2×2 and two 1×2 switches. The input ports of the two second-stage 1×2 switches are connected to the two output ports of the first-stage 2×2 switch on the same substrate. Similar to the single waveguide-type AOM, to increase the length of the diffraction region, the 10 μm width of the single-input four-output waveguide is increased to 100

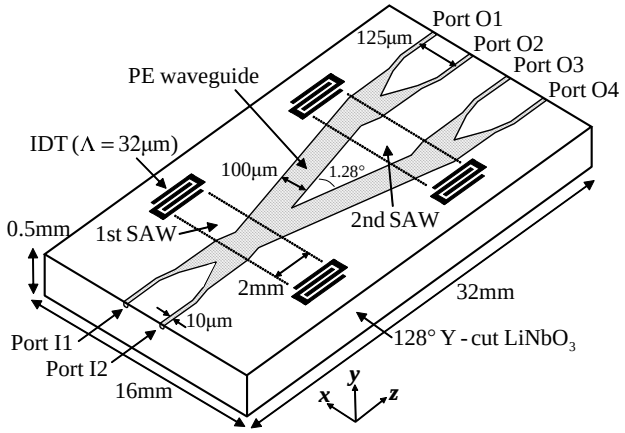

Fig. 13. Configuration of monolithically integrated tandem waveguide-type AOM.

μm using a tapered waveguide 3.3 mm long. The first- and second-stage switches were connected together by the 100-μm-wide straight waveguide according to the waveguide shape designed using BPM as described later. Two pairs of IDTs with a wavelength Λ of 32 μm and an overlap length of 2 mm are used to propagate the SAW with a center frequency of approximately 120 MHz in the first and second stages of the diffraction regions.

Using this structure of the tandem AOM, the optical frequency shifts for the sum of two driving frequencies and the difference between two driving frequencies can be obtained by combining the upward and downward frequency shifts in the first and second SAWs. Moreover, the tandem AOM has a function in which the input beam from Port I1 or I2 can be switched to any of the output ports from Port O1 to O4 by combining the propagations of the first and second SAWs.

In the connection part between the first- and second-stage switches, two types of waveguide shapes, namely, the 3.3-mm-long tapered waveguide and with the 100-μm-wide straight waveguide, were designed. The optical field distribution and diffraction property in these waveguide shapes were simulated using BPM for TM-mode propagation.

Figures 14(a) and 14(b) show three-dimensional displays for the tapered and straight waveguides, respectively, when the refractive index grating required to achieve the maximum diffraction efficiency was set in the first and second diffraction regions. As can be seen from these figures, the amplitude of the optical field in the undiffracted port, which corresponds to the leakage loss, for the tapered waveguide is almost the same as that for the straight waveguide. However, the leakage of the latter which is scattered from connection points between the first and second stages is smaller than that of the former. The calculated values of the beam power in each output port are also shown in Figs. 14(a) and 14(b) when the input power to Port I1 is 1.0. The maximum doubly diffracted power in Port O3 for the tapered and straight waveguides were 0.25 and 0.48, respectively. Therefore, the straight waveguide was adopted for the tandem AOM.

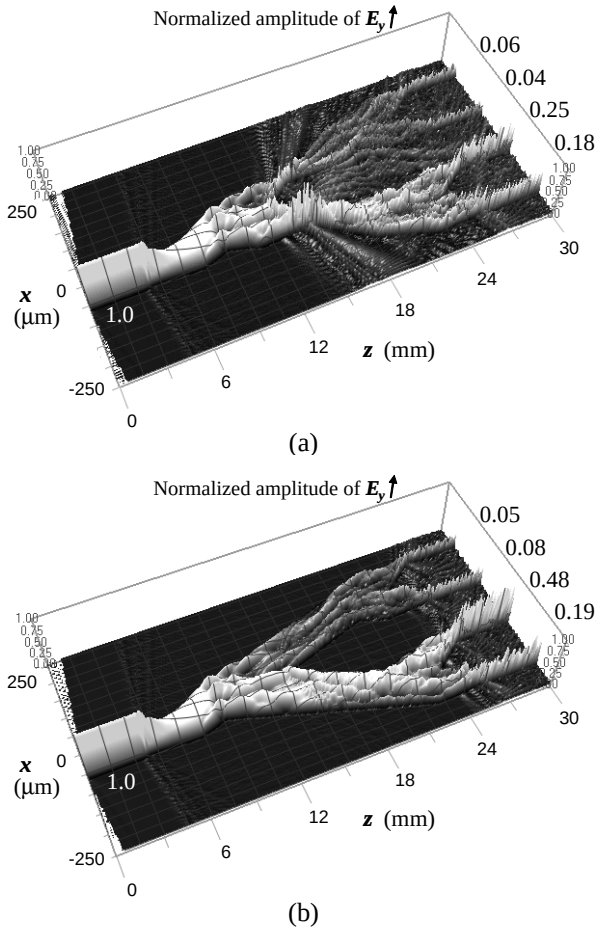

Fig. 14. Amplitude distribution of E_y on tandem AOM with (a) 3.3-mm-long tapered waveguide and (b) with 100-μm-wide straight waveguide. Values at each output port show beam power normalized by input power.

B. Experimental Setup and Results

The fabrication conditions of the waveguide were the same as mentioned in Section III. After polishing and AR-coating the end face of the waveguide, a pair of normal IDTs with Λ=32 μm, 20 finger pairs and an overlap length of 2 mm was formed in the first and second stages. The substrate size after polishing the end face was 32 $\times$16 mm^2.

Diffraction properties were measured using a 1.55 μm laser diode at a driving frequency of approximately 120 MHz. Maximum diffraction efficiencies of 92% and 83% were obtained using the first and second SAWs, respectively. The diffraction properties on the input voltage supplied to the second SAW at the maximum diffraction efficiency by the first SAW is shown in Fig. 15. A peak diffraction efficiency of 63% was obtained by driving both stages at the same frequency. This diffraction efficiency is considered to be sufficient for FSF fiber oscillation.

On the other hand, the minimum undiffraction efficiencies were approximately 20% in every case of first and second SAWs. It is necessary to improve this extinction ratio to apply the tandem AOM to the optical matrix switch.

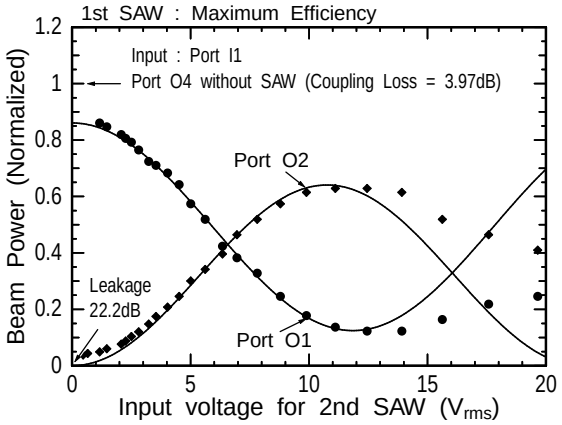

Fig. 15. Diffraction properties of tandem AOM as function of input voltage supplied to second SAW at maximum diffraction efficiency by first SAW.

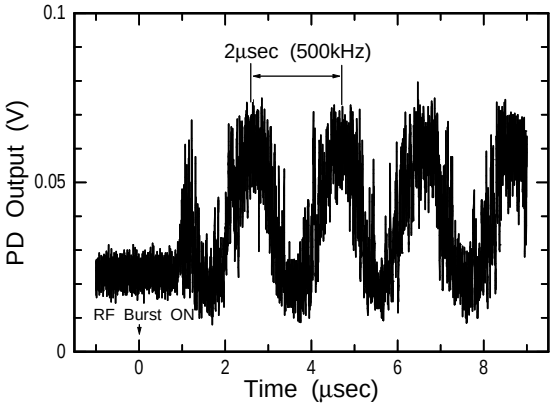

Fig. 17. Example of observed beat signal in oscilloscope for difference frequency $f_1 - f_2$ of 500 kHz.

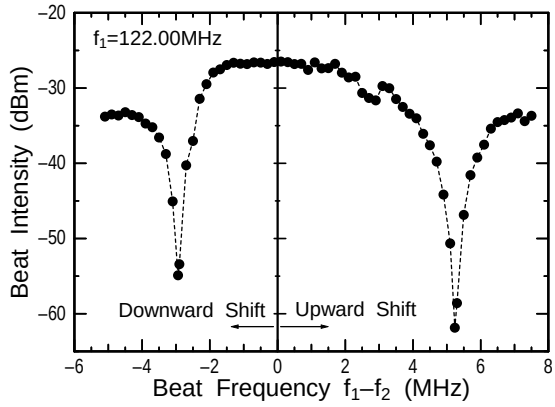

Fig. 18. Beat intensity as function of corresponding difference frequency $f_1 - f_2$ for upward or downward optical frequency shift.

Similar to the single AOM, the tandem AOM was incorporated into a module using the input and output PM fiber arrays, which are constructed by the twin-core or four-core ferrule with a pitch of 125 μm. Using this module, the optical frequency shift was demonstrated by combining the upward and downward frequency shifts in the first and second SAWs. An optical heterodyne detection setup, shown in Fig. 16, was used to measure the frequency shift. The 1.55 μm laser diode output was split into the two arms of the Mach-Zender interferometer. The tandem AOM module, which was driven by both stages at frequencies f_1 and f_2 of approximately 120 MHz, was inserted in one arm, and caused the tested beam to undergo a frequency shift of $f_1 - f_2$ or $f_1 + f_2$. The beam produced by combining the tested and reference beams was coupled with a photodetector to realize heterodyne detection. The beat signal was observed using an oscilloscope and the beat spectrum was measured using an RF spectrum analyzer.

Figure 17 shows an example of the observed beat signal when the difference frequency $f_1 - f_2$ was 500 kHz. Since the period of the beat signal was observed to be 2 μs, it is confirmed that the output beam from the tandem AOM has an optical frequency shift corresponding to the difference frequency of 500 kHz. The optical frequency shift for the sum of two frequencies $f_1 + f_2$ was also observed.

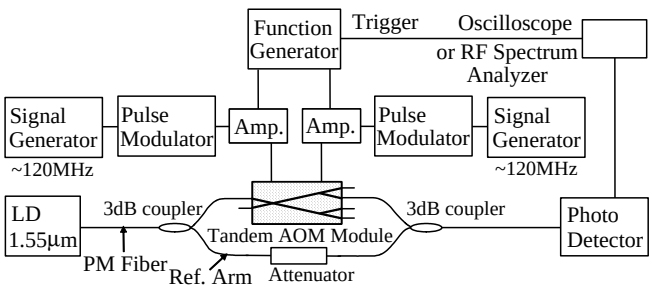

Fig. 16. Optical heterodyne detection setup for measuring frequency shift.

The beat intensity as a function of the difference frequency $f_1 - f_2$ is shown in Fig. 18. In this case, the driving frequency f_2 was changed while f_1 was fixed at 122 MHz. A low-frequency shift ranging from DC to approximately 5 MHz which can be hardly be obtained by a single AOM was obtained. This bandwidth corresponds to that of the IDT used for exciting SAWs. Therefore, an optical frequency shift with a wider bandwidth can be obtained by decreasing the number of IDT pairs.

V. Conclusion

A waveguide-type AOM in a tapered crossed-channel proton-exchanged (PE) optical waveguide on a 128°-rotated Y-cut $LiNbO_3$ substrate was proposed for an optical wavelength of 1.55 μm. The following results were obtained in this study.

1) An analysis using BPM showed that the diffraction properties can be improved by decreasing the SAW beam width.

2) According to the simulated diffraction properties, for the fabricated waveguide-type AOM with an IDT width of 2 mm, an 84% diffraction efficiency was obtained at the driving voltage of 17 V_{rms} and a driving frequency of 200 MHz.
3) An optical frequency domain range using the FSF fiber laser with the waveguide-type AOM was demonstrated. The FSF fiber laser with the waveguide-type AOM can be applied to optical frequency domain ranging equally as well as one with the conventional bulk-type AOM.
4) A monolithically integrated tandem waveguide-type AOM was designed and fabricated. The optical frequency shifts for the sum of two driving frequencies and the difference frequency ranging from DC to 5 MHz were observed.

On the other hand, the minimum undiffraction efficiencies were approximately 10∼20% in every case. To obtain a higher extinction ratio, an optimization of the waveguide shape is needed.

In the future, FSF fiber laser oscillation will be demonstrated using the tandem AOM, and the improvement of the extinction ratio will be investigated for application to an optical matrix switch. Furthermore, a waveguide-type AOM with a lower driving voltage will be achieved by utilizing a unidirectional transducer.

ACKNOWLEDGMENT

This work was supported by the Cooperative Research Project of the Research Institute of Electrical Communication, Tohoku University and the Strategic Information and Communications R&D Promotion Program of the Ministry of Public Management, Japan.

REFERENCES

[1] K. Nakamura, F. Abe, K. Kasahara, T. Hara, M. Sato, and H. Ito, "Interferometric studies on a diode-pumped Nd: YVO_4 laser with frequency-shifted feedback," Opt. Commun, vol.120, p.134, 1995.
[2] K. Nakamura, F. Abe, K. Kasahara, T. Hara, M. Sato, and H. Ito, "Spectral characteristics of an all solid-state frequency-shifted feedback laser," IEEE J. Quantum Electronics, vol.33, p.103, 1997.
[3] T. Hara, K. Nakamura, H. Ito, F. Imamura, R. Hino, and T. Matsuzawa, "Hydraulic pressure measurement by frequency-shifted feedback laser and its application to tsunami measurement," Tech. Dig. Int. Laser Sensing Symp. S7-3, p.285, 1999.
[4] N. Kibayashi, T. Hara, M. Yoshida, K. Nakamura, and Hiromasa Ito, "Average atmosphere temperature measurement by a frequency-shifted feedback laser," Remote Sensing of the Atmosphere, Environment, and Space, Proc. of SPIE, vol.4150, p.45, Sendai 2000.
[5] C. Ndiaye, T. Hara, N. Hamada and H. Ito, "High accuracy optical 3-D shape measurement using a frequency-shifted feedback laser", 23rd International Laser Radar Conference (ILRC23) 80-1, Nara, Japan, 24-28 July, 2006.
[6] M. Yoshida, K. Nakamura, and H. Ito, "A new method for measurement of group velocity dispersion of optical fibers by using a frequency-shifted feedback fiber laser," IEEE J. Photonics Technol. Lett., vol.13, p.227, 2001.
[7] N. Zou, M. Yoshida, Y. Namihira, and H. Ito, "PMD measurement based on delayed self-heterodyne OFDR and experimental comparison with ITU-T round robin measurements," Electron. Lett., vol.38, no.3, pp.115, 2002.
[8] C. S. Tsai, C. T. Lee and C. C. Lee, "Efficient acoustooptic diffraction in crossed channel waveguides and resultant integrated optic module," IEEE Proc. Ultrasonics Symp. p.422, 1982.
[9] C. T. Lee, "Optical-gyroscope application of efficient crossed-channel acoustooptic devices," Appl. Phys., vol.B35, p.113, 1984.
[10] S. Kakio, N. Zou, M. Kitamura, H. Ito, and Y. Nakagawa, "An integrated acoustooptic frequency shifter driven by surface acoustic wave for 1.55 μm optical wavelength," Jpn. J. Appl. Phys., vol.42, no.5B, p.3063, 2003.
[11] S. Kakio, M. Kitamura, Y. Nakagawa, N. Zou, T. Hara, H. Ito, T. Iizuka, T. Kobayashi, and M. Watanabe: "Waveguide-type acoustooptic frequency shifter driven by surface acoustic wave and its application to frequency-shifted feedback fiber laser," IEICE Trans., vol.J86-C, no.12, p.1263, 2003. [in Japanese].
[12] S. Kakio, S. Uotani, Y. Nakagawa, T. Hara, H. Ito, T. Kobayashi, and M. Watanabe, "Improvement of diffraction properties in waveguide-type acoustooptic modulator driven by surface acoustic wave," to be published in Jpn. J. Appl. Phys., vol.46, no.2, 2007.
[13] S. Kakio, S. Uotani, Y. Nakagawa, T. Hara, H. Ito, T. Kobayashi, and M. Watanabe, "Diffraction properties and beam-propagation analysis of waveguide-type acoustooptic modulator driven by surface acoustic wave," Jpn. J. Appl. Phys., vol.44, no.6B, p.4472, 2005.
[14] S. Kakio, M. Kitamura, Y. Nakagawa, N. Zou, T. Hara, H. Ito, T. Iizuka, T. Kobayashi, and M. Watanabe, "Monolithically integrated tandem waveguide-type acoustooptic frequency shifter driven by surface acoustic waves," Proc. of IEEE Ultrasonics Symp., p.240, 2006.
[15] S. Kakio and Y. Nakagawa, "Photo-elastic constants of proton-exchanged $LiNbO_3$," Jpn. J. Appl. Phys., vol.34, no.5B, p.2917, 1995.
[16] K. W. Loh, W. S. C. Chang, W. R. Smith and T. Grudkowski, "Bragg coupling efficiency for guided acoustooptic interaction in GaAs," Appl. Opt., vol.15, p.156, 1976.
[17] K. Nakamura, T. Miyahara, M. Yoshida, T. Hara and H. Ito, "A new technique of optical ranging by a frequency-shifted feedback laser," IEEE J. Photonics Technol. Lett., vol.10, p.1772, 1998.
[18] M. Yoshida, K. Nakamura, and H. Ito, "Frequency-shifted feedback fiber laser," Laser Original, vol.27, no.7, p.490, 1999. [in Japanese]
[19] G. Couquin, K. W. Cheung, M. M. Choy, "Single- and Multiple-wavelength operation of acoustooptically tuned semiconductor lasers at 1.3 μm," IEEE J. Quantum Electronics, vol.25, no.6, p.1575, 1989.
[20] S. Balle, I. C. M. Littler, and K. Bergmann, "Frequency shifted feedback dye laser operating at a small shift frequency," Opt. Commun, vol.102, p.166, 1993.

Surface Acoustic Wave Sensors for Gas Detection

Chi-Yen Shen, Chun-Pu Huang, Kuo-Chien Hsu, and Jin-Shing Jeng
Department of Electrical Engineering, I- Shou University
1, Section 1, Hsueh-Cheng Rd., Ta-Hsu Hsiang, Kaohsiung County, TAIWAN

***Abstract*-This work has investigated the detecting properties of surface acoustic wave (SAW) gas sensors based on L-glutamic acid hydrochloride to ammonia. This sensor exhibited the properties of excellent reversibility, sensitivity, and repeatability to ammonia detection. The sensitivity of the SH-SAW ammonia sensor was 4.6 ppm/ppm and the mass loading dominated the perturbation in dry nitrogen at 50°C. The interference of the humidity on the ammonia sensors was also studied in this work. As the humidity rose in the environment, the perturbation was primarily from the elastic effect. This work would estimate the cross-sensitivity of the interference of the humidity. Finally, the neural network technique was used to identify ammonia in the environment.**

I. INTRODUCTION

Ammonia is an important species for the refrigeration and fertilizer industries and its toxic nature introduces a need to monitor it quantitatively at its low concentration. Ammonia can also be found in the breath of a patient who got gastric adenocarcinoma. So the detection of ammonia concentrations becomes a considerable interest in clinical diagnosis. Some ammonia gas sensors based on different chemical interfaces have been developed. These chemical interfaces include metal-oxides [1-6] and polymer films [7-12]. Most of metal-oxides must be operated at an appropriately high temperature, such as a SnO_2 sensor was operated at 350^{o}C [1]. Recently, Varghese et al. [6] employed Al_2O_3 as sensitive layer to successfully detect ammonia at room temperature. From the earlier investigations [1-6], metal-oxides are suitable for detecting middle-high concentrations of ammonia. Polymer films are superior to metal-oxides, given their low detection limit and selective detection at room temperature. The investigations on the use of polymer films proved to polymer films can detect ammonia effectively. The lowest limit of detection (LOD) reported in the previous investigation was 1ppm to ammonia [11].

In recent years, we have investigated and published the sensing properties of SAW sensors with coating L-glutamic acid hydrochloride to detect ammonia gas from 0.9 to 45100ppm [13,14], in which the L-glutamic acid hydrochloride exhibited fairly reliable, sensitive, reversible, and repeatable gas sensing properties at room temperature. The selectivity of L-glutamic acid hydrochloride to ammonia was also good and the long-term stability of the SAW response exhibited a good performance at room temperature. Meanwhile, the detection limit of L-glutamic acid hydrochloride for airborne ammonia had been estimated to be 0.56ppm at room temperature. However, the response of L-glutamic acid hydrochloride to ammonia less than 100ppm was not linear at room temperature. We have further investigated the sensing properties of lower ammonia concentration (below 23ppm). The linearity of response was especially studied. The frequency shift versus ammonia concentration above 40^{o}C was a monotonic-function and linear [15]. Consequently, we kept focusing on investigating the ammonia detection in ppb level at 50^{o}C. It makes possible to be applied in clinical diagnosis.

The interference of the humidity is often a serious problem of ammonia sensors. All previous studies, which investigated the interference of the humidity so far, made the discussions when the concentration of ammonia was more than 1 ppm. In fact, it is necessary to realize the interference of the humidity on the detection of ppb concentration of ammonia for the application of the biosensor.

The shear horizontal surface acoustic wave (SH-SAW) device fabricated on $LiTaO_3$ substrate is a well known liquid sensor, because it does not present severely attenuation when the surface is loaded with a liquid. In addition, the advantages of SH-SAW device, such as a high electromechanical coupling coefficient, relative small size, fabrication reproducibility, and fast output, are attractive to be the gas and liquid sensors. So this work investigated the SH-SAW sensor coated with L-glutamic acid hydrochloride to demonstrate the interference of the humidity on the detection of ppb concentration of ammonia. Finally, this work applied the neural network technique to identify ammonia in humidity to prove the possibility of the application of the sensors.

II. EXPERIMENTAL

The SH-SAW sensor designed as two-port resonators were fabricated on a 36^{o}YX-$LiTaO_3$ substrate by lift-off methods, using aluminum 1200 Å metallization. A metal layer was deposited on the cavity for good adhesion of the chemical interface. The structure of the SH-SAW sensor in this work is illustrated in Fig. 1. The characteristics of the SH-SAW resonators were measured by network analyzer (E5071A, Agilent, USA). L-glutamic acid hydrochloride was the chemical interface. A known quantity of L-glutamic acid hydrochloride (Aldrich, USA) was weighed and dissolved in a known volume of deionized water at 75°C, to a concentration of 0.1 mg/ml. Prior to the coating layer being applied, the surface of the SH-SAW resonators had been cleaned in acetone, and dried in an oven (Rendah, Taiwan) at 80^{o}C. Then, a coating of L-glutamic acid hydrochloride was deposited on the surface of the SH-SAW resonators by air

brushing. The thickness of L-glutamic acid hydrochloride was approximately 2900 Å measured by ellipsometry.

Two SH-SAW resonators were introduced into a SH-SAW sensing system (Nenogram balance, ftech, Taiwan), which applied a dual-device configuration. The RF electronic oscillator circuit generated RF signals in SH-SAW sensing system. The precise temperature-controller ensured temperature stability with ± 0.01°C. The dry nitrogen diluted the ammonia and was also the carrier gas. A gaseous ambience was controlled by the mass flow controller (Sierra, USA) on the flow rate of 110*ml/min*. All detections were preceded at 50°C. Before testing gas exposure, the sensors were exposed in dry nitrogen for 30 min to stabilize the initial SH-SAW signal. Lastly, a frequency counter monitored the frequency shifts in SH-SAW sensing system, which was connected to a computer system via a RS-232 interface board.

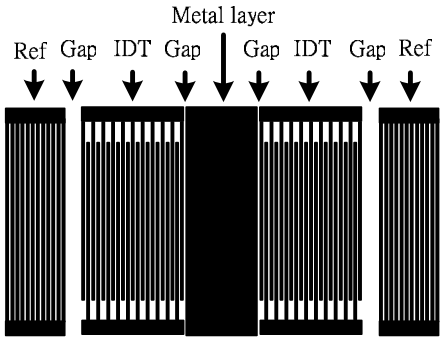

Fig. 1 Two-port SH-SAW resonator used in this study.

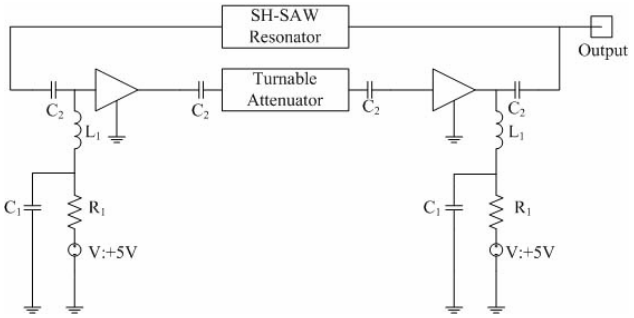

Fig. 2 Circuit of the oscillator applied in this study

III. Results and Discussion

Figure 2 plots the circuit of the oscillator applied in this study. It used two amplifiers and a tunable attenuator to supply enough gain for the oscillation. In general, the sum of amplifiers' gain and SH-SAW resonator's attenuation at well-defined frequency of oscillation is at least 0dB to satisfy Barkhausen's criteria. To ensure oscillation during detection, therefore the sum of amplifiers' gain and SH-SAW resonator's attenuation at well-defined frequency of oscillation was larger than 4dB in this study. Total phase, including the amplifiers, attenuator, resistors, and capacitors in feedback circuit, measured by network analyzer was approximately 360°. Hence, the phase of SH-SAW resonator should be zero or integer times of 360° at well-defined frequency of oscillation to satisfy Barkhausen's criteria. On the other hand, the length of cavity in two-port SH-SAW resonator should be enough to deposit the chemical interface as mentioned above. However, the long length of cavity resulted in a multimode in 3-dB pass band, and it frequently occurred mode hopping during detection. In order to satisfy Barkhausen's criteria for oscillation and avoid the mode hopping simultaneously, the phase of SH-SAW resonator designed in this study was set to be zero at well-defined frequency of oscillation, and the separation between different modes in 3-dB pass band was as large as possible.

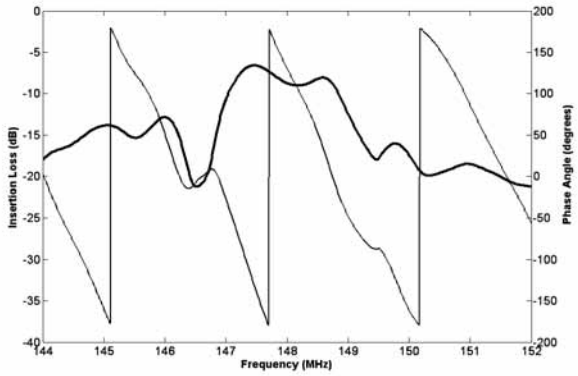

(a)

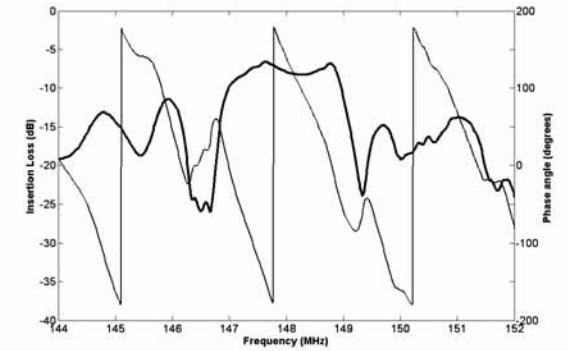

(b)

Fig. 3 Frequency response of two-port SH-SAW resonator: (a) simulation and (b) measurement

The design parameters of the SH-SAW resonator in this study were: the wavelength was 28μm, pairs of IDT were 29, aperture was 750μm, length of reflector was 1400μm, length of cavity was 1148μm, the width of metal layer was1127μm, and the metallization ratio was 0.5. Figure 3 illustrates the frequency response of the SH-SAW resonator designed in this study. By COM simulation, it designed the zero degree of the phase at 148.8MHz. The measurement results were significantly consistent with the simulation. Both exhibited two modes existing in 3-dB pass band and the separation between two modes was approximately 1.4MHz. The

oscillation frequency measured by the spectrum (4395A, Agilent, USA) and shown in Fig. 4 was stably at 148.86MHz after SH-SAW resonator being connected with the oscillator shown in Fig. 2.

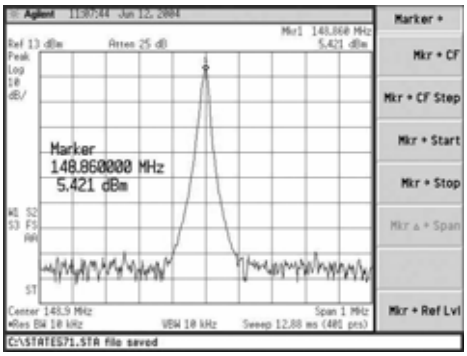

Fig. 4 Oscillation of two-port SH-SAW resonator in measurement.

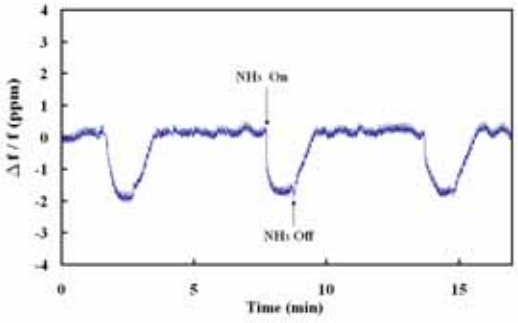

Fig. 5 Response of the SH-SAW gas sensor to 300 ppb ammonia in dry nitrogen at 50°C.

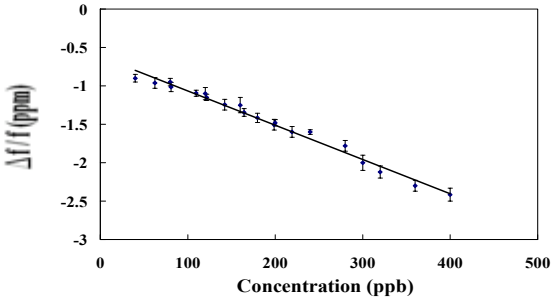

Fig. 6 Responses of the SH-SAW sensor to the concentration of ammonia in dry nitrogen at 50°C.

Figure 5 displays the response of the SH-SAW gas sensor to 300 ppb ammonia in dry nitrogen at 50°C. The response time was in seconds of exposure to ammonia in dry air and the response quickly returned to the base line when ammonia was turned off. Three gases on/off cycles performed a similar response, revealing repeatable detection properties. The responses were almost identical. This meant that the L-glutamic acid hydrochloride film was reversible. The responses of the SH-SAW sensors to 40-400 ppb ammonia were measured in dry nitrogen at 50°C and shown as Fig. 6. It shows that the negative frequency shift linearly increased as the ammonia concentration increased from 40 ppb to 400 ppb. The sensitivity, which is the slope of the curve, of the SH-SAW sensor was 4.6 ppm/ppm in dry nitrogen at 50°C. Fig. 7(a) indicates the frequency shift due to the absorption of humidity. The positive frequency shift rapidly increased as humidity increased until 40%RH. Then the frequency shift gradually increased and saturated at 60%RH. Fig. 7(b) shows the responses to 40 ppb ammonia gas as a function of humidity. It illustrates the similar results to Fig. 7(a).

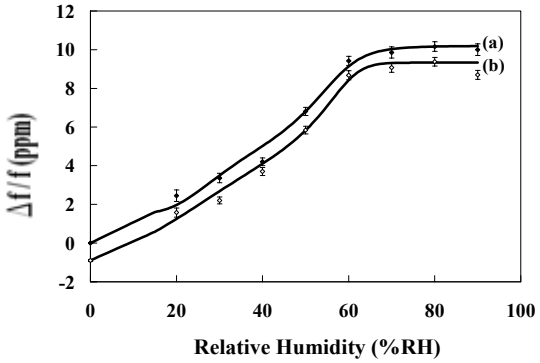

Fig. 7 (a) Responses of the SH-SAW sensor to the relative humidity at 50°C.
(b) Responses of the SH-SAW sensor to 40 ppb ammonia in humidity at 50°C.

The L-glutamic acid hydrochloride deposited on the surface of the SH-SAW sensor acts as a selective sink. The responses of the sensor depend on the changes of properties of the L-glutamic acid hydrochloride to the absorption of target. L-glutamic acid hydrochloride is a stiff and non-conductive material, so the perturbation after absorption can be described as follows [16]

$$\Delta f = (k_1 + k_2) f_0^2 h \rho_f - k_2 f_0^2 h \left\{ \frac{4\mu(\lambda + \mu)}{v_0^2(\lambda + 2\mu)} \right\}, \quad (1)$$

where k_1 and k_2 are negative constants of the substrate material, h is the thickness of the chemical interface, λ, μ are the bulk and shear moduli of the chemical interface, and ρ_f is the density of the chemical interface. The two terms on the right of Eq. (1) indicate the contributions of change in mass loading and elastic effect, respectively, to total changes in frequency shift of the SH-SAW sensor. The frequency response is negative when the change in the elastic effect is negligible or smaller than the change in the mass loading, whereas a positive frequency response occurs as the elastic effect significantly increases and exceeds the change in mass.

The negative frequency shift shown in Fig. 6 presents that the elastic effect was negligible or small during detecting ammonia in dry nitrogen at 50°C. Fig. 7(a) illustrates that the absorption of water molecules could change the modulus of L-glutamic acid hydrochloride and made the elastic effect to significantly increase and exceed the effect in mass loading. The further increasing humidity above 60%RH did not significantly change the modulus and resulted in the saturation of the response. Fig. 7(b) also indicates that the

contribution resulted from humidity was evident.

Therefore, the responses of the sensor can not be described by a simple linear combination of the individual sensitivities for dry ammonia and humidity. A mathematical relation of the response characteristics to dry ammonia and to humidity can be described as [17]

$$S_{(NH_3,H_2O)} = S_{(NH_3)} + S_{(H_2O)} + DS_{(NH_3)}S_{(H_2O)}, \qquad (2)$$

where $S_{(NH_3,H_2O)}$ is the frequency shift to ammonia in humid air in Hz, $S_{(NH_3)}$ the frequency shift to ammonia in dry nitrogen in Hz, $S_{(H_2O)}$ the frequency shift to humidity in Hz, and D is the cross-sensitivity. The third term on the right of Eq. (2) is a cross-term that describes the mutual dependence of the response on ammonia and humidity. To explain the interference from humidity, $S_{(NH_3,H_2O)}$, $S_{(NH_3)}$, and $S_{(H_2O)}$ were separately measured and substituted into Eq. (2). The cross-sensitivity, shown as Fig. 8, to ammonia nonlinearly varied between $\pm 9\times10^{-4}$ Hz^{-1}. For typical values of relative humidity in room ambient air (35to 60%), the cross-sensitivity, D, in this work is smaller than that (=0.018) of 4,4′,4″-[benzene-1,3,5-triyl- tri(ethin-2,1-diyl)tribenzoic acid] (SPCA) coated thickness shear mode (TSM) ammonia sensors [17]. It demonstrates that L-glutamic acid hydrochloride takes less interference of the humidity than SPCA.

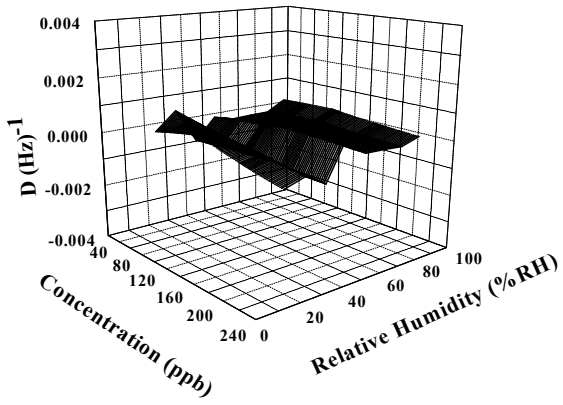

Fig. 8 Dependence of the cross-sensitivity of the SH-SAW sensor on ammonia concentration and relative humidity at 50°C.

In order to identify ammonia in humidity, a fully connected feed-forward neural network with size 2-10-1, i.e., 2 nodes in the input layer, 10 nodes in the hidden layer, and 1 node in the output layer, was used in this work. Each node in a layer was connected to all the nodes in the layer above it. The sigmoid function is used as the signal transfer function for all nodes in the neural model. Its math form can be simply expressed as follows. Suppose we denote the output of node j is X_j, then

$$X_j = \frac{1}{1+\exp(-\sum_i w_{ij}X_i)}, \qquad (3)$$

where w_{ij} is the strength of connection between node j and its input node X_i in the layer below. Training is equivalent to find the proper weights such that a desired output could be generated for a given input. In this work, error back-propagation learning algorithm was used to train the neural model we developed. The inputs of neural model were the frequency shift and the humidity, the output was the concentration of ammonia.

Table I The comparisons between real measurement and identification by neural model.

Inputs of neural model		Output of neural model	Concentration by measurement (ppb)	Absolute error(ppb)
Relative humidity(%RH)	Δf/f (ppm)	Concentration (ppb)		
20	1.20	133.82	142.20	8.38
20	1.22	115.74	121.60	5.86
20	1.47	51.15	62.30	11.15
30	1.98	205.91	219.20	13.29
30	2.01	189.47	179.60	9.87
30	2.02	177.85	164.40	13.45
30	2.14	100.71	109.60	8.89
40	3.31	188.46	179.60	8.86
40	3.50	105.46	109.60	4.14
50	4.21	177.92	179.60	1.68
50	4.25	163.62	164.40	0.78
50	5.12	127.26	121.60	5.66
50	5.56	84.92	81.00	3.92
60	7.85	200.45	198.70	1.75
60	8.02	137.07	142.20	5.13
60	8.11	120.60	121.60	1.00
70	8.30	211.34	219.20	7.86
70	8.39	168.08	164.40	3.68
70	8.45	137.47	142.20	4.73
70	9.08	43.65	40.00	3.65
80	8.82	157.93	164.40	6.47
80	8.86	140.94	142.20	1.26
80	8.88	126.37	121.60	4.77
80	9.38	45.41	40.00	5.41
90	8.04	212.92	219.20	6.28
90	8.13	184.14	179.60	4.54
90	8.26	117.14	109.60	7.54
90	8.44	72.85	81.00	8.15
90	8.56	62.08	62.30	0.22

Mean absolute error = 5.80 ppb

Table I shows the comparisons between real measurement and identification performed by neural network. It shows that the results of identification quite approximated to the measurement data. The mean absolute error (MAE) between the identified concentrations of ammonia and the actual ones was 5.80 ppb. Hence, we conclude that the concentrations of ammonia in humidity were predicated effectively. The application of the SH-SAW ammonia sensors coated with L-glutamic acid hydrochloride can continuously be developed.

IV. Conclusion

In this work, the interference of the humidity on the SH-SAW ammonia sensors coated with L-glutamic acid hydrochloride was studied when the concentration of ammonia was less than 1 ppm. The sensitivity of the sensor was 4.6 ppm/ppm and the mass loading primarily dominated the perturbation in dry nitrogen at 50°C. However, in humidity environment, the frequency shift of the sensor had positive responses and the contribution of the elastic effect was significant. The cross-sensitivity from humidity nonlinearly varied with a range of 9×10^{-4} Hz^{-1}. In our study, the neural network technique was used to overcome the interference of the humidity caused. The neural model could effectively perform the identification of ammonia in a common ambience. The mean absolute error after identification performed by neural model was 5.80 ppb. In future, based on the good performance of the SH-SAW ammonia sensors coated with L-glutamic acid hydrochloride, our lab will keep studying this sensor for practical application.

References

[1] A. Teeramongjonrasmee and M. Sriyudthsak, Methanol and ammonia sensing characteristics of sol-gel derived thin film gas sensors, Sensors and Actuators B, 66 (2000) 256-259.

[2] Y. D. Wang, X. H. Wu, Q. Su, Y. F. Li, and Z. L. Zhou, Ammonia-sensing characteristics of Pt and SiO_2 doped SnO_2 materials, Solid-State Electron., 45 (2001) 347-350.

[3] T. Zhang, Y. Shen, R. Zhang, and X. Liu, Ammonia-sensing characteristics of Pt-doped $CdSnO_3$ semiconducting ceramic sensor, Mater. Lett., 27 (1996) 161-164.

[4] H. Nanto, T. Minami, S. Takada, Zinc-oxide thin-film ammonia gas sensors with high sensitivity and excellent selectivity, J. Appl. Phys., 60 (1986) 482-484.

[5] F. Winquist, A. Spetz, M. Armgarth, C. Nylander, I. Lundstorm, Modified palladium metal-oxide-semconductor structures with increased ammonia gas sensitivity, Appl. Phys. Lett., 43 (1983) 839-841.

[6] O. K. Varghese, D. Gong, W. R. Dreschel, K. G. Ong, and C. A. Grimes, Ammonia detection using nanoporous alumina resistive and surface acoustic wave sensors, Sensors and Actuators B, 94 (2003) 27-35.

[7] M. Penza, E. Milella, M. B. Alba, A. Quirini, and L. Vasanelli, Selective NH_3 gas sensor based on Langmuir-Blodgett polypyrrole film, Sensors and Actuators B, 40 (1997) 205-209.

[8] M. Penza, E. Milella, and V. I. Anisimkin, Gas sensing properties of Langmuir-Blodgett polypyrrole film investigated by surface acoustic waves, IEEE Trans. Ultrason., Ferroelect., Freq. Contr., 45 (1998) 1125-1131.

[9] M. Penza, E. Milella, and V. I. Anisimkin, Monitoring of NH_3 gas by LB polypyrrole-based SAW sensor, Sensors and Actuators B, 47 (1998) 218-224.

[10] M. E. Nicho, M. Trejo, A. Garcia-Valenzuela, J. M. Saniger, J. Palacios, and H. Hu, Polyaniline composite coatings interrogated by a nulling optical-transmittance bridge for sensing low concentrations of ammonia gas, Sensors and Actuators B, 76 (2001) 18-24.

[11] V. V. Chabukawar, S. Pethkar, and A. A. Athawale, Acrylic acid doped polyaniline as an ammonia sensor, Sensors and Actuators B, 77 (2001) 657-663.

[12] I. M. Raimundo and R. Narayanaswamy, Simultaneous determination of relative humidity and ammonia in air employing an optical fibre sensor and artificial neural network, Sensors and Actuators B, 74 (2001)60-68.

[13] C. Y. Shen, C. P. Huang, and H. C. Chuo, The improved ammonia gas sensors constructed by L-glutamic acid hydrochloride on surface acoustic wave devices, Sensors and Actuators B, 50 (2002) 231-236.

[14] C. Y. Shen, C. P. Huang, and W. T. Huang, Gas-detecting properties of surface acoustic wave ammonia sensors, Sensors and Actuators B, 101 (2004) 1-7.

[15] C. Y. Shen, C. P. Huang, and W. T. Huang, The detection properties of ammonia SAW gas sensors based on L-glutamic acid hydrochloride, revised by IEEE Trans. Ultrason., Ferroelect., Freq. Contr. (2004).

[16] H. Wohltjen, Mechanism of operation and design consideration for surface acoustic wave device vapor sensor, Sens. Actuators 5 (1984) 307-325.

[17] U. Schramm, D. Meinhold, S. Winter, C. Heil, J. Muller-Albrecht, L. Wachter, H. Hoff, C.E.O. Roesky, T. Rechenbach, P. Boeker, P. Schulze Lammers, E. Weber, and J. Bargon, A QMB-based temperature-modulated ammonia sensor for humid air, Sens. Actuators B 67 (2000) 219–226

Piezoelectrical and Electrical Properties of Epitaxial Grown Ta_2O_5 Thin Film by RF Magnetron Sputtering

Shih-jeh Wu and Boen Houng*
Department of Mechanical Engineering, Material Science and Engineering*,
I-Shou University
1 Section 1, Hsueh-Cheng Rd.; Ta-Hsu, Kaohsiung 84008, Taiwan
email: wsj007@isu.edu.tw

Abstract-Tantalum pentoxide (Ta_2O_5) thin film has high dielectric constant and stable chemical properties. It is a good solution for tunneling effect due to the reduction of gate length in semiconductors. In addition, it has high refraction coefficient and band gap, thus has potential application on solar cells. From literatures, as grown in preferred (2 0 0) axis crystalline structure it also has good piezoelectric property (high k_{33}) and could be used in MEMS, resonator, filters (FBAR, surface acoustic wave devices). In previous studies, the growth of preferred oriented Ta_2O_5 thin film was performed at elevated temperatures (>850°C) with metal Tantalum target. This causes difficulties for IC manufacturing process. We deposited preferred oriented Ta_2O_5 piezoelectric thin film by RF magnetron sputtering process with sintered Ta_2O_5 target at reduced temperature (400°C). The piezoelectricity and referred (2 0 0) axis crystalline structure are demonstrated.

I. INTRODUCTION

Tantalum pentoxide (Ta_2O_5) thin film has high dielectric constant and stable chemical properties. It is a good solution for tunneling effect due to the reduction of gate length in semiconductors. In addition, it has high refraction coefficient (n=2.18 at λ=550nm) and band gap at 4.2eV, thus has potential application on solar cells. Ta_2O_5 thin film was not widely studied for piezoelectric applications. From limited literatures, as grown in preferred (2 0 0) axis crystalline structure it also has good piezoelectric property (high k_{33}) and could be used in MEMS, resonator, filters (FBAR, surface acoustic wave devices). The comparison of material properties are listed in Table 1 and 2. Compared to ZnO and AlN, Ta_2O_5 thin film has higher electrical mechanical coupling coefficient and medium acoustic speed. In previous studies, the growth of preferred oriented Ta_2O_5 thin film was performed at elevated temperatures (>850°C) with metal tantalum target and oxide atmosphere [2]. This causes difficulties for IC manufacturing process. In this paper we successfully deposited preferred oriented Ta_2O_5 piezoelectric thin film by RF magnetron sputtering process with sintered Ta_2O_5 target at reduced temperature (400°C).

II. MATERIAL SYNTHESIS

Following previous studies [3], pure metal Ta target was used first at different oxygen concentrations and the XRD results show that no significant crystalline structure was found. Annealing process was then taken and the results are shown in Figure 1 and 2. It was found that pure O_2 is favorable to the growth of crystalline. In addition, as the annealing temperature rises above 800°C the crystalline starts to grow. However, the preferred orientation is not significant as the spurious peaks shown. Thus, ceramic target and pure O_2 condition was adopted. 26g tantalum oxide powders (99.993%, Density 8.2, Alfa Aesar) were pressed in 2.5" dia. mould. The target was then sintered at 1250°C for 6 hrs and shrunk to 2" dia. The target was then placed at 5.0cm distance from silicone (p-type [1 0 0]) substrate. The effect of sputtering pressure and power are shown in the XRD results in Figure 2 and 3 respectively. Based on Sherrer formula from FWHM the grain size at different sputtering pressure is shown in Figure 4. The grain size decreases as the sputtering pressure increases. For piezoelectricity measurement the upper and lower aluminum electrodes were sputtered as shown in Figure 5. After the base vacuum pressure less than 10^{-6} torr was reached the carrying Ar gas was mixed with O_2 before entering the chamber. The substrate was heated and controlled at designated temperatures during the sputtering process. RF magnetron sputtering was applied for the deposition process and the sputtering parameters are as shown in Table 3.

III. RESULTS AND DISCUSSIONS

X-ray diffraction diagram of the Ta_2O_5 sample is shown in Figure 6. The dominating peak occurs at 27.45°. From the only JCPD card for Ta_2O_5 (JCPD250922) the peak is at 28.3° ([1 1 1 0] orthorhombic) while in Yasuhiko et al. [2] the preferred [2 0 0] axis is at 28.4° and in β-Ta_2O_5 monoclinic structure. Only the (2; m) in monoclinical and (mm2; 222) in orthorhombic point groups have piezoelectric property as shown in Figure 7. The FWHM calculated is 1.127° and from Scherrer formula the grain size is about 7.948 nm. The identification of the crystalline structure will be determined from the d value from TEM (Transmission Electronic Microscope). The preferred orientation of the deposited film in this study is self-evident and believed to be in [2 0 0] axis while the crystalline structure has to be further identified since there is no previous record can

be found.

The one port impedance measurement result is as shown in Figure 8. For the sample under measurement the major resonant frequency is at about 4.8 GHz and the piezoelectric characteristic is well demonstrated. The effective K^2_{33} calculated is about 5.14%. This is higher than the previous data and may be regarded as caused by different substrates. The SEM picture is as shown in Figure 9. The grain size estimated is very close to the value obtained from Scherrer formula. The surface roughness was measured by AFM and the result was shown in Figure 10. The RMS value of roughness is about 4nm which is good enough for later SAW applications. In reviewing the material properties of Ta_2O_5 thin film, the density is about twice of AlN and ZnO which means it contribute twice of acoustic impedance. For stacked FBAR structure the Ta_2O_5 thin film may be combined with other material to obtain higher resonating performance.

IV. CONCLUSIONS

Piezoelectric Ta_2O_5 thin film was synthesized at low temperature (400°C) by RF-magnetron sputtering. The preferred [2 0 0] axis oriented crystalline structure is examined from XRD although the exact point group has to be identified later. The piezoelectric property is demonstrated from impedance measurement and the exact value of electrical / mechanical coupling coefficients for SAW will be analyzed later.

REFERENCES

[1] Y. Chen, N. W. Emanetoglu, G. Saraf, Pan Wu, Y. Lu, A. Parekh, V. Merai, E. Udovich, D. Long,D. S. Lee, E. A.Armour, M. Pophristic, "Analysis of SAW properties in ZnO/Al[x]Ga[1-x]N/C-Al[2]O[3] structures," IEEE Trans. UFFC, vol. 52, no. 7, 2005, pp. 1161-1169.

[2] Y. Nakagawa and Y. Gomi, "New Piezoelectric Ta_2O_5 Thin Film," Appl. Phys. Lett. 46, 1985, pp. 139-40.

[3] Y. Nakagawa, Y. Gomi, and T. Okada, "Deposition of new piezoelectric Ta2O5 thin films and their surface acoustic-wave properties," J. Appl. Phys. vol. 61, June 1, 1987, p. 5012-5017.

[4] I. T. Tang, H. J. Chen, W. C. Hwang, Y. C. Wang, M. P. Houng, and Y. H. Wang, "Applications of piezoelectric ZnO film deposited on diamond-like carbon coated onto Si substrate under fabricated diamond SAW filter," Jounal of Crystal Growth vol. 262, 2004, pp.461-466.

[5] B. R. Jooste and H. J. Viljoen, "A study of piezoelectric orthorhombic Ta2O5", J. Mater. Res., Vol. 13, No. 2, 1998, pp. 475-82.

[6] W. G. Cady, *Piezoelectricity*, McGraw-Hill, New York, 1946.

[7] Y. Nakagawa and T. Igarashi, "Fabrication of Ta2O5 Piezoelectric Thin Film by the Linear Rapid Thermal Annealing Method and Measurement of Piezoelectricity," Jpn. J. Appl. Phys. Vol. 41 (2002) pp. 3285–3289

ACKNOWLEDGEMENTS

The authors would like to acknowledge the support from NSC Taiwan ROC under NSC # 95-2221-E-214-010.

Table 1 Comparison of piezoelectric properties of different thin films.

	ZnO/sapphire [1]	AlN/sapphire [1]	Ta_2O_5/quartz [2]	ZnO/quartz [3]
Acoustic speed (m/s)	5500	5910	3000	2800
Electrical / mech. coupling coeff. (k_{33} %)	4.5	1	1.54	1
Density(kg/m^3)	5720	3255	8015	5610

Table 2 material properties of Ta_2O_5 thin film from [2].

Constant		Value	Standard error
Elastic constants in 10^{11} N/m^2	c^E_{11}	1.662	…
	c^E_{12}	1.227	0.168
	c^E_{22}	2.148	0.214
	c^E_{55}	0.569	0.085
Piezoelectric constants in C/m^2	e_{11}	-1.814	…
	e_{12}	-0.354	0.226
	e_{26}	1.27	0.068
Dielectric constants	e^T_{11}/e_0	41	…
	e^T_{22}/e_0	19.5	…
	e^S_{11}/e_0	39.1	…
	e^S_{22}/e_0	16.3	…
Density (kg/m^3)		8015	…

Table 3 Sputtering condition of the film structure.

	RF power	Sputtering pressure	Sputtering time	Substrate temperature
Ta_2O_5	230 W	3 mTorr	1.5 hours	400 °C
Al	150 W	3 mTorr	10 min	25 °C

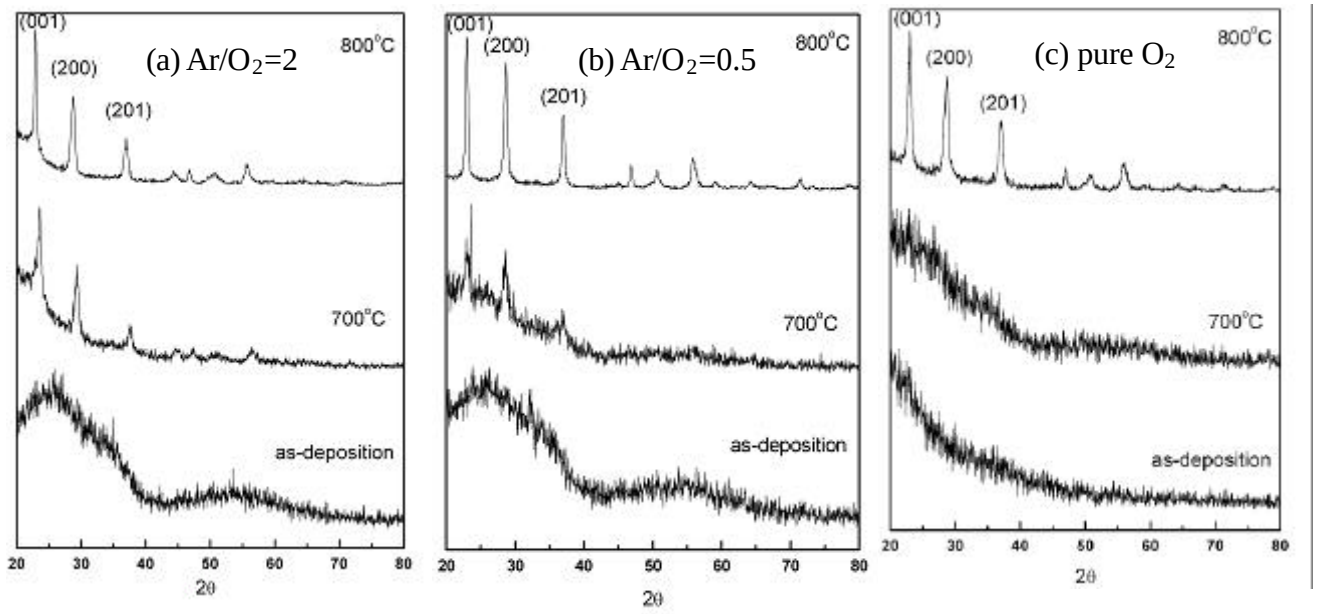

Figure 1 XRD results of different annealing temperatures for pure Ta metal target at different O_2 concentrations (a) $Ar/O_2=2$ (b) $Ar/O_2=0.5$ and (c) pure O_2.

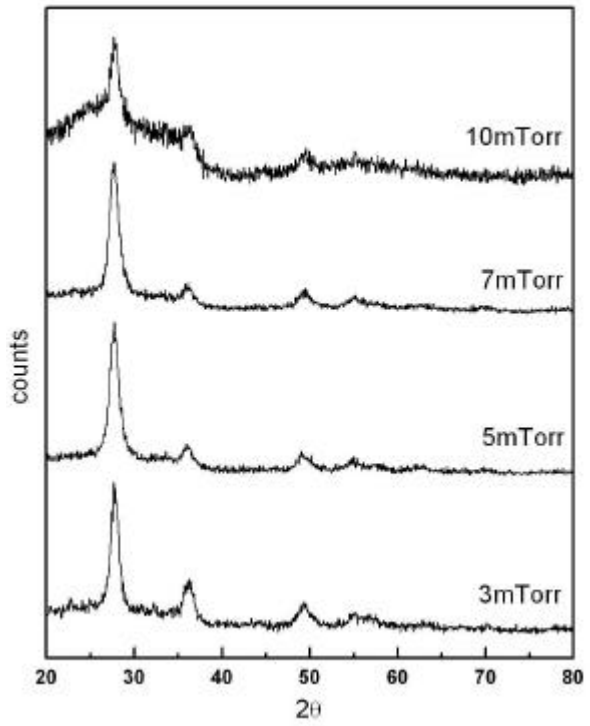

Figure 2 XRD results at different sputtering pressures.

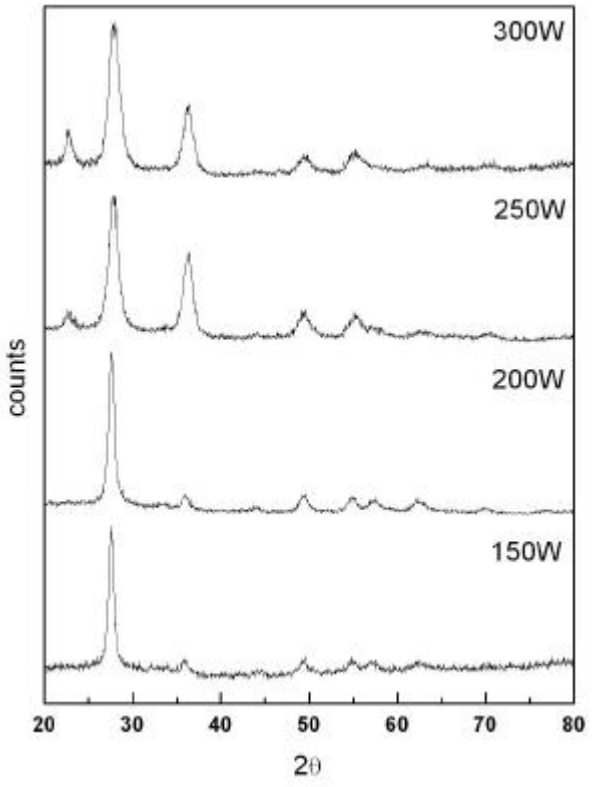

Figure 3 XRD results at different sputtering power.

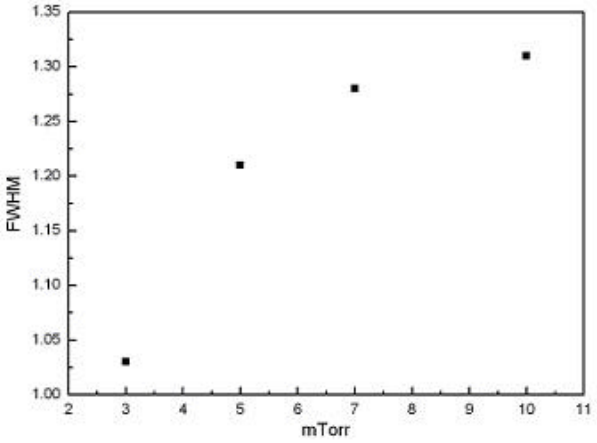

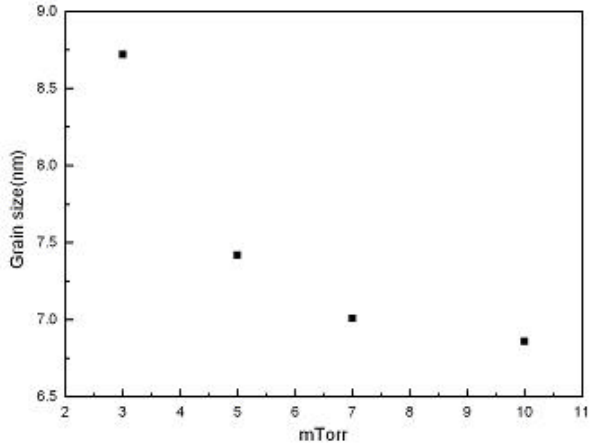

Figure 4 Effect of sputtering pressure on (a) FWHM and (b) grain size from Sherrer formula.

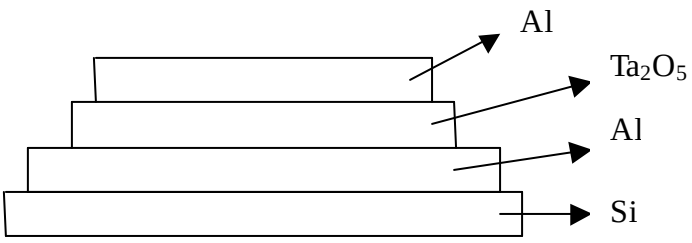

Figure 5 Schematics of the Ta_2O_5 thin film structure for the measurement.

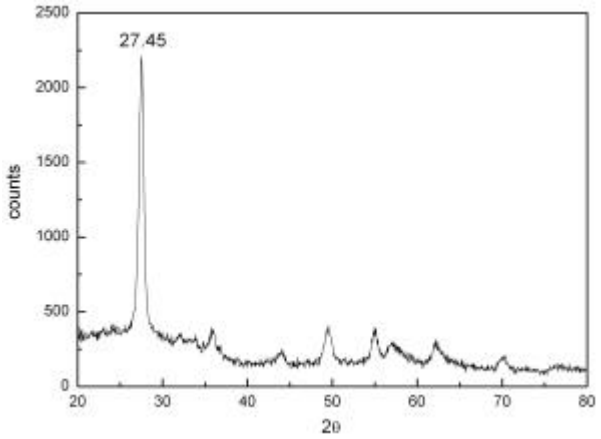

Figure 6 XRD of the deposited Ta_2O_5 thin film at 4.5 hours deposition.

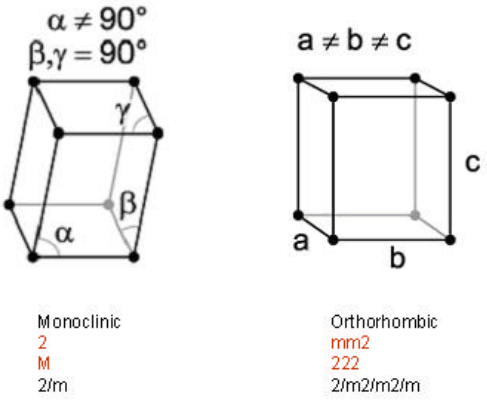

Figure 7 Schematic diagrams of momoclinic and orthorhombic point groups [6].

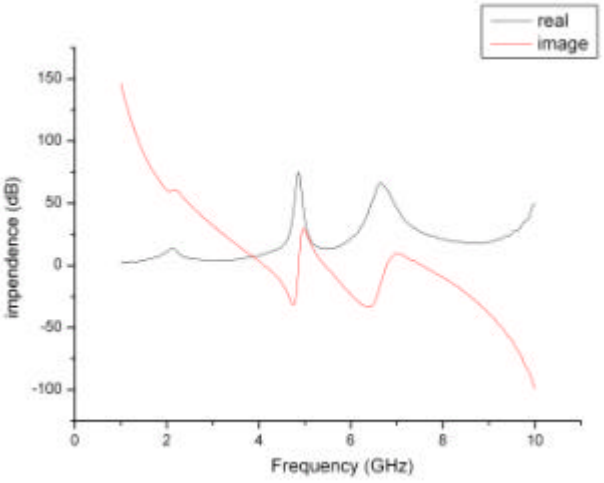

Figure 8 One port impedance of the Ta_2O_5 thin film.

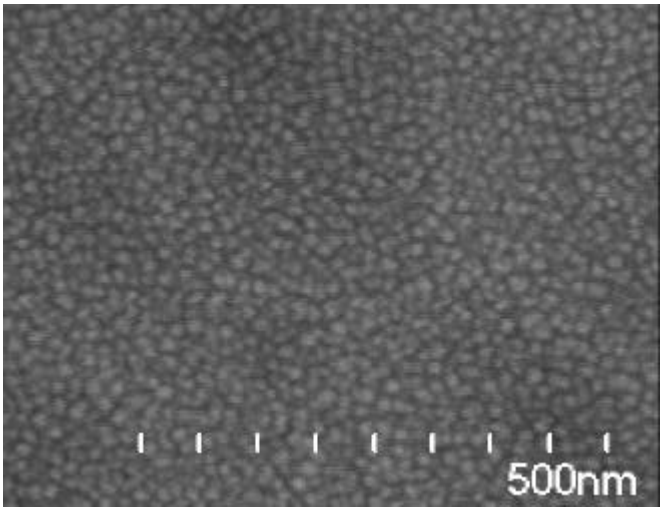

Figure 9 SEM picture of the sputtered Ta_2O_5 film.

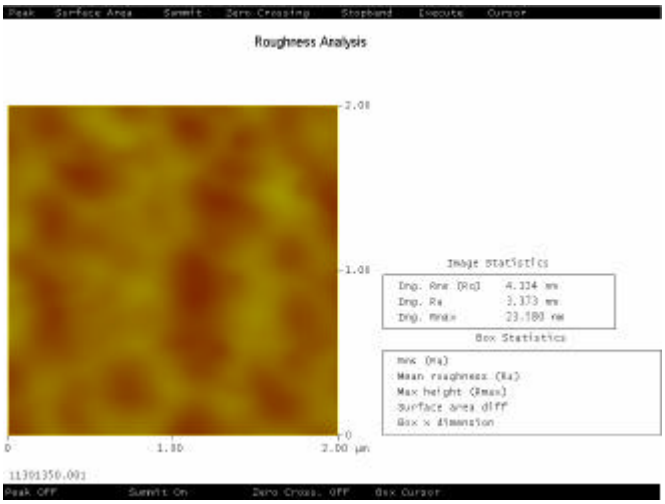

Figure 10 AFM roughness distribution of the Ta_2O_5 thin film.

Crystal Growth and Investigation of Acoustic Properties of $LiAlO_2$ Single Crystal

Mitch M.C. Chou[1], Shu-Ming Wang[2] and Yi-Jen Chiu[3]

[1]Department of Materials Science & Opto-electronic Engineering ,National Sun Yat-Sen University, Kaohsiung, Taiwan

[2]Department of Electrical Engineering, I-Shou University, Kaohsiung, Taiwan.

[3]Institute of Electro-Optical Engineering, National Sun Yat-Sen University, Kaohsiung, Taiwan.

Abstract

A potential piezoelectric crystal $LiAlO_2$ with (100) orientation is grown by means of the Czochralski pulling method. The as-grown crystal is identified as a single phase with good uniformity by X-ray diffraction pattern. (001) TEM image showed an unique cross-hatched pattern which reveals a superlattice structure. Several cubic $LiAlO_2$ specimen, 10.0mm × 10.0mm × 10.0mm were manufactured to characterize its elastic properties. The time-based pulse-echo transmission technique was employed to measure the acoustic velocities of longitudinal and transverse modes. The elastic constants of $LiAlO_2$ were extracted from the acoustic velocity measurements at different propagation directions. It was found that the acoustic velocities of $LiAlO_2$ are much higher than the current piezoelectric crystals, including quartz, $LiNbO_3$ and Langasite family materials.

1. Introduction

$LiAlO_2$ crystal belongs to the space group symmetry $P4_12_12$ in which each lithium and aluminum atom is coordinated at the center of tetrahedron, with four oxygen atoms.[1] It was found to be piezoelectric by J.P. Remeika [2] in 1964. Recently, $LiAlO_2$ attracted more attention as a potential substrate for growing III-nitride semiconductor. It has certain unique properties. The *c* lattice parameter of $LiAlO_2$ is close to two times of the *a* lattice constant(0.6378nm) of GaN, while the *a* lattice constant of $LiAlO_2$ matches the *c* lattice constant (0.5165nm) of GaN. The corresponding lattice mismatch between $LiAlO_2$ and wurtzite GaN is 1.7% for [001] $LiAlO_2$ parallel to [11$\bar{2}$0] GaN and 0.3% for [010] $LiAlO_2$ parallel to [0001] GaN. Secondly, after GaN epitaxial growth, $LiAlO_2$ substrate can be removed by chemical etching. The total area for device manufacturing is enlarged. GaN grown on (100) $LiAlO_2$ substrate is along M-plane (10-10), which places the polar c-axis in the wafer's plane. In this orientation, quantum confined stark effect (QCSE) which causes a red-shift in emission can be eliminated.[3,4,5] However, there is a lack of the information of its growth defect and acoustical properties in the previous reports.

The motivation to do this research is based on the scientific curiosity and the possible acoustic applications of $LiAlO_2$. At present, the largest application of the piezoelectric materials is to make surface acoustic wave devices (SAW) as frequency filters in the wireless communication. Current commercial crystals are quartz, and $LiNbO_3$. Quartz has low acoustic loss and temperature stability, but due to its narrow bandwidth, and small piezoelectric constant, it has limitation in the fabrication of certain filters. Quartz is also limited by its tendency to form twin domains under pressure at temperature above 350°C. $LiNbO_3$ has a high coupling constant, make it a proper material for acoustic transducer, but the temperature shift is large which is not suitable for band pass filter in wireless communication system. Since $LiAlO_2$ shows it piezoelectric properties, and high acoustic velocities, it might be a potential candidate for these acoustic applications.

In this manuscript, a single $LiAlO_2$ crystal was grown by Czochralski pulling technique, and its growth defect was evaluated by using electron microscope. The measurements of acoustic velocities of longitudinal and transverse modes were done by means of the time-based pulse-echo transmission technique. This approach is found efficient and accurate over the frequency interest, and can be fully automated using computer control. The elastic constants of $LiAlO_2$ were then extracted from the acoustic velocities at different propagation directions.

2. Crystal Growth

A stoichiometric mixture of Li_2CO_3 powders and Al_2O_3 grains, both with 99.99% purity, was prepared for the Czochralski pulling method. Since Li_2O is easy to volatilize in both cooling and growth process, 5~10% excess of Li_2CO_3 in weight fraction was added. In order to reduce the material's volume, the raw materials were compressed into tablets and then heated at 1200°C for 10hrs to decompose CO_2. The raw materials were then placed in an iridium crucible. An iridium lid was used to cover the crucible to decrease the temperature gradient and avoid Li evaporation. If the crucible was uncovered,

the melt would deviate from stoichiometric ratio because of Li evaporation.

The crucible was then heated to approximately 1750°C to melt the raw materials. During the growth, nitrogen gas was continuously supplied to prevent the oxidation of the Ir crucible. The seed used had a (100) a-axis. A pulling rate of 3~5mm/hr, and a rotation rate of 20~30rpm were used to control the growth conditions. The crystal growth atmosphere was pure nitrogen with the pressure 1×10^3 Pa. The phase of the as-grown $LiAlO_2$ crystals was identified by X-ray diffraction spectrometer.

3. Result and Discussion

Fig. 1 shows the first $LiAlO_2$ crystal grown in this study. The bottom of the crystal is opaque and milky due to the strong chemical decomposition and had lots of inclusions precipitated and cracks inside. Green laser was used to evaluate the crystal's overall quality. Laser beam was scattered by the voids and inclusions slightly. The voids was caused by the high oxygen concentration. When the oxygen concentration continues increasing and reaches its solubility limit, it will diffuse into the crystal and then form the voids. The inclusions result from the off-stoichiometry of the melt.[6] In addition, the crystal surface is not very smooth. This is because the surface was etched by Li_2O evaporation during the crystal growth.[7] A suitable thermal gradient for $LiAlO_2$ growth was achieved by adding a ZrO_2 after-heater tube to the top of the crucible which was wrapped with two layers of ZrO_2 felts (ZYF-166, Zicar Zirconia). This decreased the vertical temperature gradient and eliminated the chemical decomposition. Al_2O_3 felt (Kaowool 3000) was also tried as an after heater wrapping. Unfortunately, it had a strong reaction with the escaping Li_2O vapor. In addition, the crystal has a very rough surface which might be due to the chemical etching associated with a high temperature reaction with the Li_2O vapor.

Fig. 2 shows the second 2" $LiAlO_2$ crystal grown. The crystal is clear without any visible bubbles, inclusions and cracks. The crystal's surface became smooth and shinny. No chemical decomposition was found especially at the cone area. Compared with Fig. 1, apparently some improvements have been made. At the second run, two layers of ZrO_2 felt were wrapped around a bare ZrO_2 after-heater tube. The vertical temperature gradient was lowered tremendously, and much less Li_2O vapor loss. This setup of the ZrO_2 insulators was proved to be reproducible for the following experiments. In the beginning of the growth, a high rotation rate 30rpm was used to eliminate the voids i.e. enhance forced convection. Then the rotation rate was ramped down to 20rpm gradually to relieve the turbulence of the melt. A higher N_2 pressure was used in the second run and this partly prevented the surface from a high temperature reaction with Li_2O vapor. From a preliminary X-ray scan, the reflection peaks of the $LiAlO_2$ crystal were identified as the ?-phase which has the tetragonal structure and the lattice parameters are a = 5.1698Å, c = 6.2779Å. The X-ray rocking curve showed the FWHM was 0.0452° at (200) $LiAlO_2$.[8] From a preliminary X-ray scan, the reflections on the $LiAlO_2$ specimen appears like a single crystal.

M. Chou et al. [9,10] had measured the thermal expansion coefficients $a_a=7.1\times10^{-6}K^{-1}$ and $a_c=15.0\times10^{-6}K^{-1}$ and also demonstrated no phase transition in $LiAlO_2$ crystal. However, $LiAlO_2$ still has the following disadvantages: it is difficult to get the good single crystals, it reacts with most acids.

TEM specimens oriented in the different directions were prepared to identify the microstructures and defects. It needs to be very careful to work with $LiAlO_2$ TEM sample since if the electron beam is kept stationary on the material more than a few seconds, the material will be vaporized. Fig. 3(a) is the view in (001) direction and its square diffraction pattern. A clear grain boundary was observed. Since the specimen has a certain thickness, double diffraction pattern was found. Fig 3(b) is the other (001) TEM image which showed an unique cross-hatched pattern. This grid pattern reveals a superlattice structure. The possible reason is because Li and Al atoms have the very different atomic diameters and bonding length, they might exchange their lattice sites in this organized way to relieve the stress. These site exchanges will cause the phase shift which results in the interference pattern. These hatched patterns are only seen when preparing specimen looking in the (001) direction. When viewed in the other directions, these patterns are not visible.

In order to investigate the acoustic properties, including the acoustic velocities and stiffness constants, of $LiAlO_2$ crystal, appropriate crystallographic orientations must be determined. Several principal X-, Z-cut and ±45° rotated Y-cut (rotating a Y-cut specimen around the X-axis) specimen are prepared from the as-grown (100) $LiAlO_2$ crystal. The rotated Y-cut specimens were selected from the crystalline planes specified in IEEE standard.[11] Since the acoustic velocity is a function of the propagation direction, the propagation direction must be very accurate for the determination of the acoustical physical constants.

Precisely cut and measured 10.0mm $LiAlO_2$ cubes were manufactured to evaluate its acoustical properties. The time-based pulse-echo transmission technique was employed to measure the acoustic velocities of $LiAlO_2$ material. Two ultrasonic transducers were used to generate the acoustic waves, one (Panametrics V1091, 5 MHz, 1/4 inch) is for the longitudinal mode and the other one (Ultran SWC18-5, 5 MHz, 1/4 inch) is for the shear mode. The ultrasonic source and receiver are mounted on the opposite sides of the specimen. Honey serves as a couplant between the longitudinal transducer and the specimen. And Panametric SWC is the couplant for the shear wave transducer. The couplant is very thin so it does not affect the velocity measurements.[12] If the mounting is bad, some air might stay in the couplant. This affects how much acoustic energy is transferred into the sample and make the acoustic signal weaker. The experimental

setup is shown in Fig. 4. The orientation of the shear mode transducer would allow the maximizing or minimizing of various shear modes depending on the mounting angle with respect to the axis of the specimen.

Acoustic velocities measured in a temperature control environment, 26±0.5°C are summarized in Table I. Fig. 5 showed that the propagation directions, and particle motions of the acoustic waves in the $LiAlO_2$ crystal. Fig.6 is the time domain responses of the acoustic signals propagating along the different directions. The measurement errors are given by the measurement accuracy of the specimen thickness, and temperature fluctuation. Based on the Bar Cohen's estimate [13], the maximum error of velocity estimation induced by the temperature fluctuation is about 0.15%. It was found that the acoustic velocities of $LiAlO_2$ are much higher than the current piezoelectric crystals, including quartz [14], $LiNbO_3$ [15] and Langasite [16] family materials.

As $LiAlO_2$ belongs to the tetragonal structure, it can be characterized by 6×6 symmetrical matrix with six stiffness constants, C_{11}, C_{33}, C_{55}, C_{66}, C_{12} and C_{13}.[17] By using Brown [18] and Cheadle [19] methods, the elastic constants can be extracted from the longitudinal and shear waves velocities at the symmetry axes, and the longitudinal wave velocities at $\pm 45^{\circ}$ to the symmetry axes. Table II is the stiffness constant C_{ij} ($\times 10^9$ N/m^2) of $LiAlO_2$ crystal at room temperature.

4. Conclusion

In summary, Czochralski growth of $LiAlO_2$ single crystal were investigated. An organized cross-hatched pattern which reveals the superlattice structure was found in c-axis TEM specimen. This pattern might be related to Li and Al atoms exchange their lattice sites and cause the phase shift in the TEM image. The exact formation mechanism is still under investigation. It was reported that the determination of the acoustic velocities and stiffness constant of $LiAlO_2$ crystal. We consider carefully the proper propagation directions and modes to accurately determine the material constants. Several principal X-, Z-cut and $\pm 45^{o}$ rotated Y-cut specimen for determining the constants are prepared from the as-grown (100) $LiAlO_2$ crystal. Our work forms the basis for studying the applications of the $LiAlO_2$ material to ultrasonic devices, such as surface acoustic wave devices, resonator, bulk wave filter, sensors, and transducers. Further work is required to maximize accuracy in measuring the arrival time of the signal and start to fabricate the SAW IDT structure on $LiAlO_2$ substrate.

Acknowledgments

This work is supported by NSC of Taiwan, NSC94-2218-E-110-008, ACORC, Aim for the Top University Plan and Center for Nanoscience & Nanotechnology of National Sun Yat-Sen University, Kaohsiung, Taiwan.

References

1. M. Marezio, Acta Cryst., **19**, 396 (1965).
2. J.P. Remeika, A.A. Ballman, Appl. Phys. Lett., **5**, 180 (1964).
3. B. Rau, P. Waltereit, O. Brandt, M. Ramsteiner, K.H. Ploog, J. Puls, F. Henneberger, Appl. Phys. Lett., **77**, 3343 (2000).
4. E. Kuokstis, C.Q. Chen, M.E. Gaevski, W.H. Sun, J.W. Yang, G. Simin, M. Asif Khan, H.P. Maruska, D.W. Hill, M.C. Chou, J.J. Gallagher, B. Chai, Appl. Phys. Lett., **81**, 4130 (2002).
5. P. Lefebvre, B. Gil, J. Allegre, H. Mathieu, N. Grandjean, M. Leroux, J. Massies, P. Bigenwald, MRS Internet J. Nitride Semic. Res., **4S1**, G3.69 (1999).
6. K. Xu, P. Deng, J. Xu, G. Zhou, W. Liu, Y. Tian, J. Cryst. Growth. **216**, 343 (2000).
7. T. Ishii, Y. Tazoh, S. Miyazawa, Jpn. J. Appl. Phys., **36**, L139 (1997).
8. M. M.C. Chou, H.C. Huang, D.S. Gan, W.C. Hsu, J. Cryst. Growth. **291**, 485 (2006).
9. M. M.C. Chou, P.C. Tsao, H.C. Huang, J. Cryst. Growth. **292,** 542 (2006).
10. M. M.C. Chou, H.C. Huang, Y.F. Chang, Appl. Phys. Lett., **88** 161906 (2006).
11. IEEE Standard on Piezoelectricity, **Std 176**, (1987).
12. Blitz, J., and G. Simpson, *Ultrasonic Methods of Nondestructive Testing*. (Chapman & Hall, London, 1996).
13. Y. Bar-Cohen, *Ultrasonic pulse echo immersion technique: Nondestructive testing handbook*. (American society for nondestructive testing, Ohio, 1991).
14. B.J. James, Proc. 42nd Annu. Freq. Contr. Symp., 146 (1998).
15. I. Takanaga, J. Hirohashi, J.I. Kushibiki, Jpn. J. Appl. Phys., **38**, 3202 (1999).
16. Y.V. Pisarevsky, P.A. Senushencov, P.A. Popov, B.V. Mill, Proc. 39nd Annu. Freq. Contr. Symp., 653 (1995).
17. Klaus Helbig, *Foundations of Anisotropy for Exploration Seismics* (Oxford, England, 1994).
18. R.J. Brown, D.C. Lawton, S.P. Cheadle, Geophys. J. Int., **107**, 693 (1991).
19. S.P. Cheadle, R.J. Brown, D.C. Lawton, Geophysics, **56**, 1603 (1991).

Table I. Acoustic velocities of $LiAlO_2$ crystal at the different directions.

Direction of Propagation	Types of waves	m/sec	Resolution (%)
X-axis	Longitudinal (V_{11})	8155	±0.2
	Shear (V_{12})	3693	±0.1
Z-axis	Longitudinal (V_{33})	8225	±0.2
	Shear (V_{13})	4967	±0.1
+45° rotated Y-cut	Longitudinal (V_{44})	8221	±0.2
–45° rotated Y-cut	Longitudinal (V_{66})	7204	±0.2

Table II. Stiffness constant C_{ij} ($\times 10^9$ N/m^2) of $LiAlO_2$ crystal at 26°C.

C_{11}	C_{33}	C_{44}	C_{66}	C_{12}	C_{13}
173.24±0.70	176.23±0.70	64.27±0.26	35.53±0.07	26.08±0.1	48.83±0.20

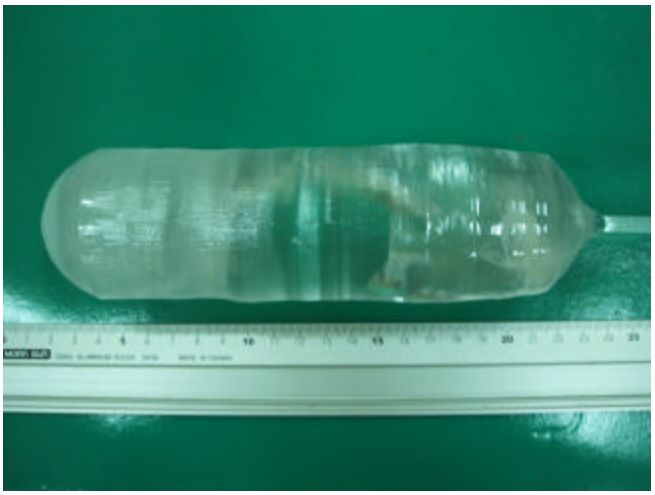

Fig. 1. $LiAlO_2$ single crystals with the (100) growth orientation. A ZrO_2 after-heater tube was added to the top of the crucible. One huge crack and inclusions are found.

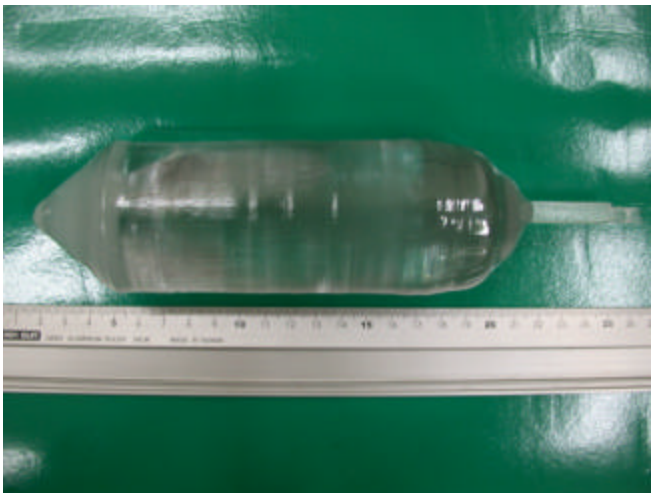

Fig. 2. $LiAlO_2$ single crystals with the (100) growth orientation. Two layers of ZrO_2 felts were wrapped around ZrO_2 after-heater tube.

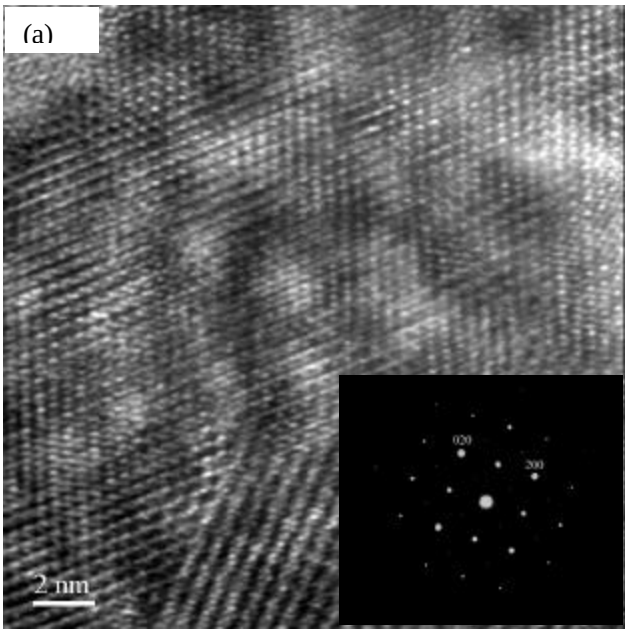

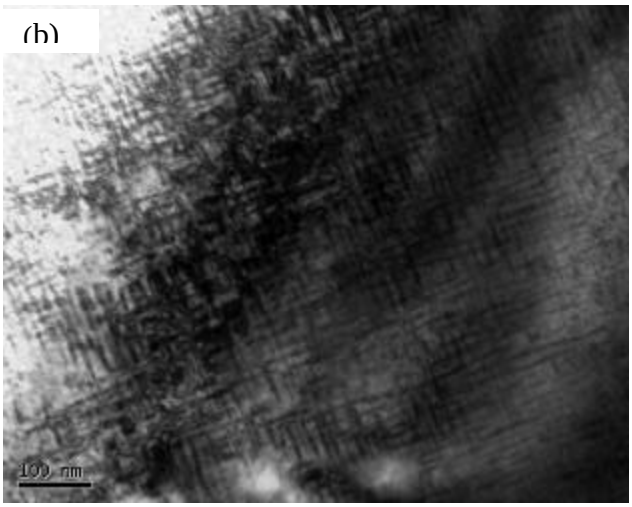

Fig. 3. TEM analysis of (001) $LiAlO_2$ sample, (a) the bright field image and its square diffraction pattern, (b) the unique cross-hatched patterns reveal a superlattice structure.

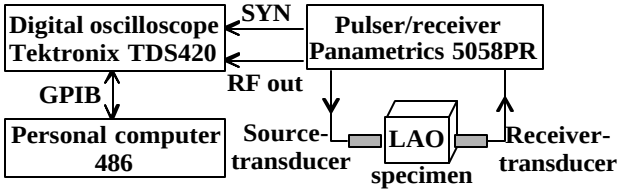

Fig. 4 Experimental setup to measure the acoustic properties of $LiAlO_2$ crystal.

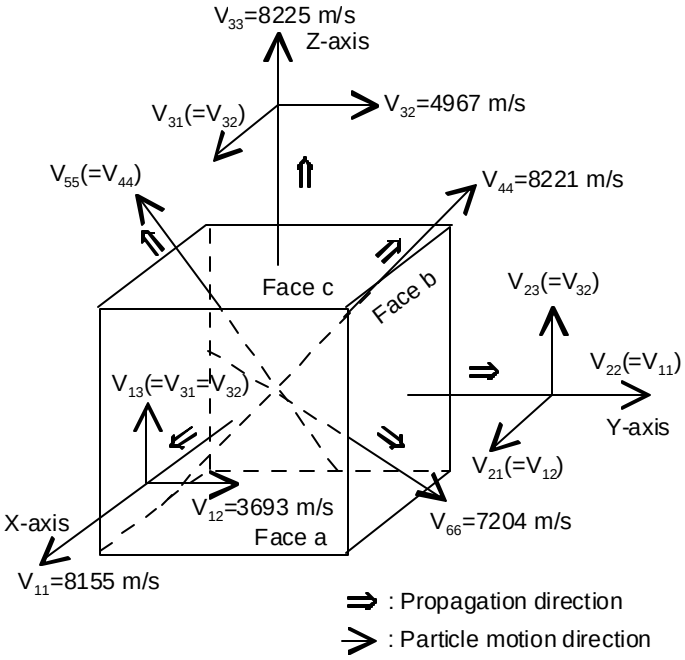

Fig. 5 The propagation directions, and particle motions of the acoustic waves in the $LiAlO_2$ crystal.

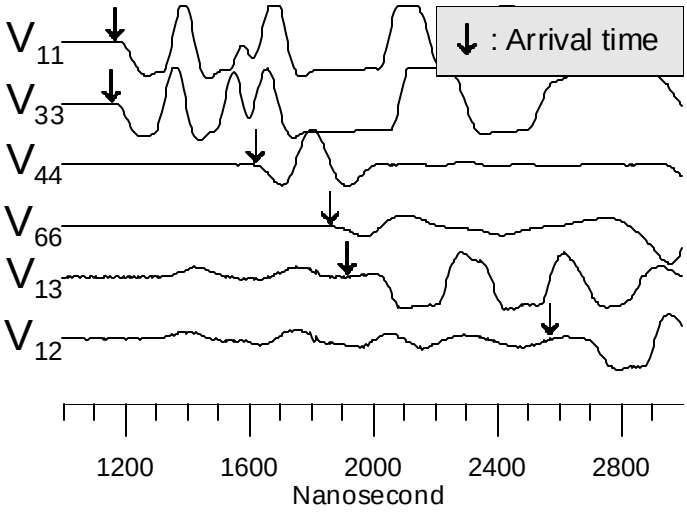

Fig. 6 Time domain response of the acoustic signals of $LiAlO_2$ crystal.

A Super-Precise Method of Evaluating and Selecting EUVL-Grade TiO_2-SiO_2 Ultra-Low-Expansion Glasses Using the Line-Focus-Beam Ultrasonic Material Characterization System

Jun-ichi Kushibiki, Mototaka Arakawa, and Yuji Ohashi
Graduate School of Eng., Tohoku University
Sendai, 980-8579 Japan
{kushi, arakawa, ohashi}@ecei.tohoku.ac.jp

Abstract—**Evaluation method for TiO_2-doped SiO_2 ultra-low-expansion glass having periodic striae associated with its fabrication process was investigated using the line-focus-beam ultrasonic material characterization (LFB-UMC) system, measuring the velocity of leaky surface acoustic wave (LSAW) on a water-loaded specimen surface. We obtained a proper standard specimen of the glass with an LSAW velocity of 3308.18 m/s within ±0.35 m/s for system calibration and determined the relationship between the TiO_2 concentrations and LSAW velocities, resulting in the TiO_2 concentration of 7.09 wt% for the standard specimen. Then, we investigated evaluation procedures for photomasks and optical mirrors of practical size used as reflective optics in extreme ultraviolet lithography (EUVL) systems. Two specimens were prepared with their surfaces parallel to the striae plane from commercial TiO_2-SiO_2 ultra-low expansion glass ingots. The homogeneities / inhomogeneities of each specimen were evaluated at 225 MHz. Evaluation procedures with sufficient accuracy were established for analysis of striae parameters such as striae periodicity and variations. Our ultrasonic method should be standardized as a new evaluation method not only for the development of EUVL-grade glasses and the evaluation of the production processes, but also for the quality control and selection of the production lots.**

Keywords- line-focus-beam ultrasonic material characterization system; velocity measurement; leaky surface acoustic waves; TiO_2-SiO_2 ultra-low expansion glasses; coefficient of thermal expansion; extreme ultraviolet lithography system

I. INTRODUCTION

Ultra-low-expansion glasses, having a CTE within ±5 ppb/K at a desired operating temperature (for example, 22±3°C for photomask blanks), are required for the basic substrate material suitable for reflective optics and photomask blanks in the EUVL system [1]. TiO_2-doped SiO_2 (TiO_2-SiO_2) glass [2, 3] is one of the candidate materials. Ultra-low CTE of the glass is achieved by adjusting the TiO_2 concentration around 7 wt%.

To develop ultra-low expansion glasses with satisfactory CTE characteristics, it is important the fabricated glasses be evaluated so that the obtained information can be used to improve the glass fabrication processes. Methods to evaluate CTE include a direct method [4, 5], in which CTE is measured by a dilatometer with an interferometric system, and indirect methods [1, 6-8], in which CTE is determined by measuring ultrasonic longitudinal velocities, chemical compositions, or refractive indices, which are closely related to the thermal properties of CTE. With the direct method, the Association of Super-Advanced Electronics Technologies (ASET) has succeeded in achieving a resolution of ±2 ppb/K (±2σ, σ: standard deviation) [5]. Among the indirect measurement methods, a method using refractive indices has a higher resolution of ±0.038 ppb/K (±2σ) [1, 6]. However, both of these methods are only capable of measuring the average characteristics of specimens of 100 mm in length, and therefore they cannot be applied to the characterization of the substrate surfaces, which is essential in evaluation of ultra-low expansion glasses for EUVL. Especially for TiO_2-SiO_2 glass, evaluation of periodic TiO_2 concentration distributions, i.e. striae formed during the fabrication process [8], is necessary.

We have proposed an evaluation method for ultra-low expansion glasses using the line-focus-beam ultrasonic material characterization (LFB-UMC) system [9, 10][11-19]. This method allows nondestructive, noncontact analyses of properties of a specimen surface through highly accurate measurement of the phase velocity of leaky surface acoustic waves (LSAWs) excited and propagated on a water-loaded specimen surface. We have applied the present system to evaluate commercial TiO_2-SiO_2 glass and have verified that a very high resolution of LSAW velocity for CTE can be achieved [11, 12]. For this system is also capable of measuring two-dimensional LSAW velocity distributions on the substrate surfaces, striae, which are caused by the periodic distributions of TiO_2 concentration, have been clearly detected [11, 12].

In this paper, we discuss an appropriate measurement method and procedures to employ the LFB-UMC system for evaluations of commercial TiO_2-SiO_2 ultra-low expansion glass for the EUVL system both in the glass development process and in the process where the glass has been sufficiently homogenized, as well as for the quality control and selection in its mass production process.

II. SPECIMENS

Commercial TiO_2-SiO_2 ultra-low expansion glasses with different premium- and mirror-grade (C-7972, Corning Inc.) were used to prepare several specimens to obtain a standard specimen for system calibration and relationship between TiO_2 concentrations and LSAW velocities and to discuss evaluation procedures of glasses for EUVL systems. The glass was produced by deposition in a rotating refractory container with many burners by the direct method, using a flame hydrolysis process, and in the form of a large circular plate glass ingot of 1500 mm in diameter and 150 mm in thickness. It was reported that periodic striae with an interval of about 0.16 mm are formed perpendicularly to the glass deposition direction due to the condition of the production process [8]. The specifications for CTE are provided in the catalog that the absolute value is 0±30 ppb/K at 5-35°C and the homogeneities are within 10 ppb/K for the premium-grade ingot and 15 ppb/K for the mirror-grade ingot [20].

We prepared two types of specimen substrates cut from the ingot with the striae plane perpendicular to the *z* axis as illustrated in Fig. 1(a): the substrate surfaces were parallel (Fig. 1(b)) and perpendicular (Fig. 1(c)) to the striae plane.

We prepared a total of seven perpendicular specimens from four different ingots to obtain a standard specimen and to determine an accurate relationship between LSAW velocities and TiO_2 concentrations. Dimensions of the specimens were 50 mm × 50 mm × 4.8 mm^t.

To investigate three-dimensional structure of striae, a specimen parallel to the striae plane as shown in Fig. 1(b) was prepared with dimensions of 100 mm × 50 mm × 7.96 mm^t from a glass ingot with the premium grade.

In order to discuss evaluation procedures of TiO_2-SiO_2 glasses for photomasks and optical mirrors of the EUVL systems, two parallel specimens, as shown in Fig. 1(b), were prepared with dimensions of 136 mm × 134 mm × 9.98 mm^t for premium-grade specimen (specimen A) and 229 mm × 149 mm × 6.75 mm^t for mirror-grade specimen (specimen B).

All specimens were optically polished on both sides with parallelisms within 10".

III. LFB-UMC SYSTEM AND MEASUREMENT REGION

LSAW velocities were measured with the LFB-UMC system [10] at an ultrasonic frequency *f* of 225 MHz. The measurement principle of the LSAW velocity is described in detail in the literature [9]. Fig. 2 (a) is a cross section of the LFB lens and a specimen with periodic striae, illustrating the measurement principle of the V(*z*) curve. Fig. 2 (b) shows the measurement region *W*×*D* on the specimen surface. A typical V(*z*) curve measured for C-7972 is given in Fig. 3 (a). A spectrum distribution as shown in Fig. 3 (b) is obtained from this waveform by the V(*z*) curve analysis. The oscillation interval Δ*z* obtained from the result of this analysis is substituted into Eq. (1) to obtain the LSAW velocity V_{LSAW}.

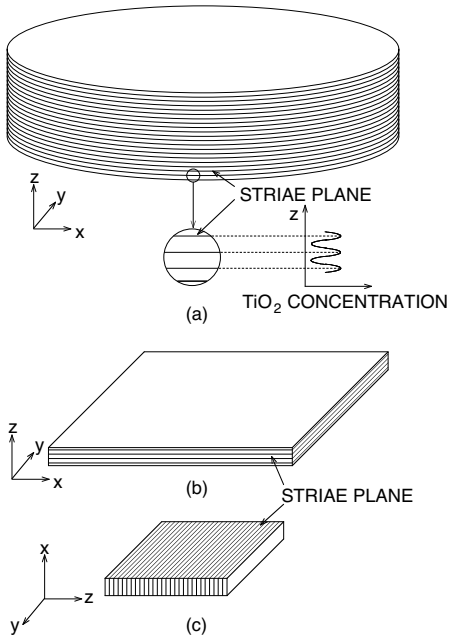

Fig. 1. Specimen preparation. (a) Glass ingot. (b) Specimen with the substrate surface prepared parallel to the striae plane (parallel specimen). (c) Specimen with the substrate surface prepared perpendicular to the striae plane (perpendicular specimen).

$$V_{LSAW} = \frac{V_W}{\sqrt{1-\left(1-\frac{V_W}{2f\Delta z}\right)^2}} \qquad (1)$$

where V_W is the velocity of the longitudinal waves in water. Absolute calibration was performed using a C-7972 standard specimen [13] to obtain the absolute value of the LSAW velocity [21] as shown in Section IV-A. The measurement reproducibility of the LSAW velocity was ±0.17 m/s (±2σ) and the resolution for CTE was ±0.74 (ppb/K) at 225 MHz [19].

When the ultrasonic measurement region *W*×*D* was larger than the periodicity of the striae on the specimen surface, the measured values of the LSAW velocity were averaged within the region [13]. The maximum value of the propagation distance of LSAWs in the focused direction *W* on the specimen surface was 280 μm in the measurement for C-7972 at 225 MHz. The measurement region in the unfocused direction *D* depends on the operating parameters of the ultrasonic device, and the value used in this experiment was approximately 900 μm. As 70 % of Rayleigh-type LSAWs' energy is confined within 0.4 wavelength below the surface as they propagate, the resolution in the depth direction is approximately 6 μm at 225 MHz. The effect of averaging LSAW velocities on specimens with periodic striae was investigated through the numerical calculations, and it was concluded that the true value could be obtained when the periodicity of the striae was larger than 1.6 mm [22] in the measurements at 225 MHz.

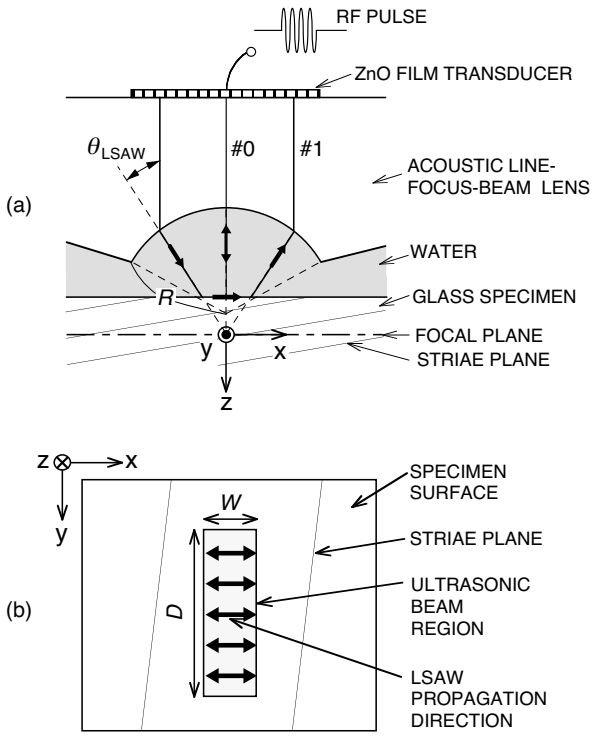

Fig. 2. (a) Cross-sectional geometry of the LFB ultrasonic device describing the principle of V(z) curve measurements. The focal length F in water is equal to 1.15R, where R is the curvature radius of cylindrical sapphire acoustic lens. (b) Measurement region of the LFB at a specific defocus distance formed on the specimen.

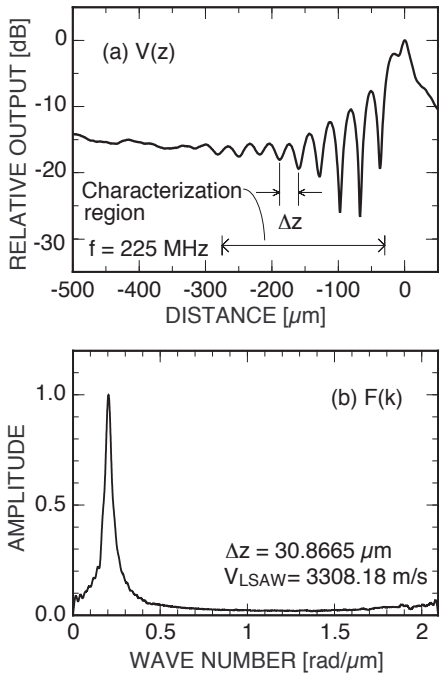

Fig. 3. Typical V(z) curve measured for C-7972 specimen at 225 MHz (a) and spectral distribution analyzed by FFT for the V(z) curve shown above (b).

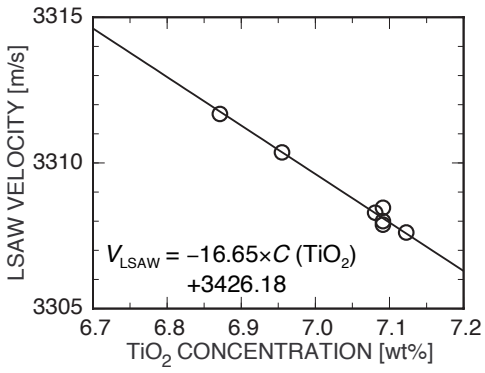

Fig. 4. Relationships between LSAW velocities and TiO_2 concentrations.

IV. Experiments and Discussions

A. Standard Specimen

LSAW velocity values measured with the LFB-UMC system vary according to the systems and ultrasonic devices used for measurements and their operating ultrasonic frequencies [21]. Therefore, the absolute values of the LSAW velocity are obtained by correcting the measured values through a system calibration method that uses a standard specimen whose acoustical physical constants (elastic constants and density for nonpiezoelectric materials) have been accurately measured [21]. The calibration is made by comparing the actual measured LSAW velocity on the standard specimen with the calculated one obtained through numerical calculation using its measured bulk properties, viz., elastic constants and density. So it is necessary for accurate calibration to measure corresponding LSAW velocities at positions where the bulk properties of the standard specimen are measured.

As a standard specimen, homogeneous specimen would be ideal. However, TiO_2-SiO_2 glasses have more or less elastic imhomogeneities due to periodic striae, so we prepared perpendicular specimens from several C-7972 ingots, and investigated the inhomogeneities. We select a specimen with relatively less velocity variations as a proper substrate for the standard specimen. We measured bulk longitudinal and shear wave velocities and density for the standard specimen around 23°C. A standard value of an LSAW velocity of 3308.18±0.35 m/s at 23°C was determined for the standard specimen.

B. Calibration Line for Chemical Composition

The LSAW velocity measurements were carried out at 169 positions in 2-mm steps along both the y- and z-axis directions for an area of 24 mm × 24 mm around the center of seven perpendicular specimens. The area corresponds to that for measuring chemical compositions by X-ray fluorescence analysis. The LSAWs propagated on the surface of the perpendicular specimens in the y-axis direction in Fig. 1(c). The measured velocities were calibrated using the standard specimen obtained in Section IV-A. The maximum difference in the averaged LSAW velocities among the seven specimens

TABLE I. SENSITIVITIES AND RESOLUTIONS FOR CTE, TiO_2 CONCENTRATION, AND DENSITY FOR C-7972 GLASS BY LSAW VELOCITY MEASUREMENTS.

	Sensitivity	Resolution ($\pm 2\sigma$)	
		225 MHz	75 MHz
LSAW velocity	———	±0.17 (m/s)	±0.07 (m/s)
CTE	4.41 (ppb/K)/(m/s)	±0.74 ppb/K	±0.29 ppb/K
TiO_2 concentration	-0.0601 wt%/(m/s)	±0.010 wt%	±0.004 wt%
Density	0.0176 (kg/m^3)/(m/s)	±0.0029 (kg/m^3)	±0.0011 (kg/m^3)

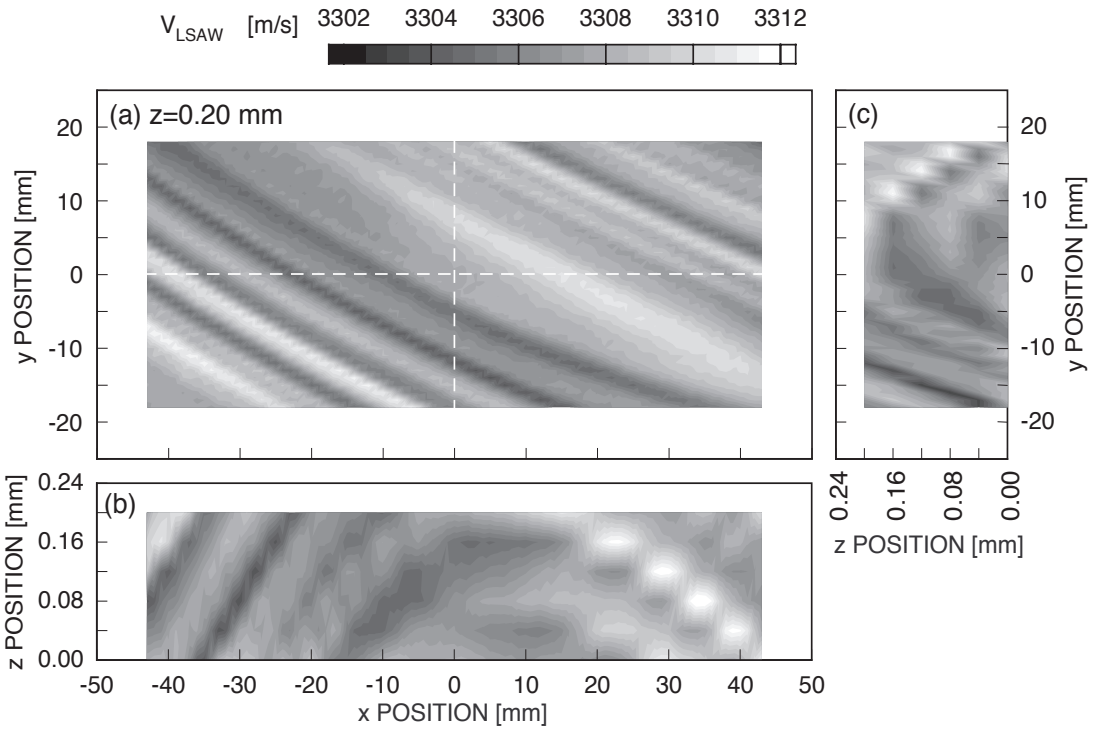

Fig. 5. Three dimensional LSAW velocity distributions for a C-7972 specimen at 225 MHz. The scale along the *z* axis is enlarged one hundred times. (a) *x*-*y* plane. (b) *x*-*z* plane. (c) *y*-*z* plane.

was 4.07 m/s, and the maximum value in the maximum velocity variations on the surface for the seven specimens was 1.87 m/s.

We analyzed chemical compositions of the seven specimens using an X-ray fluorescence analysis (XRF) system. Measurements were made for an area of 25 mm$^\phi$ around the center of each specimen. The main elements were found to be SiO_2 and TiO_2, TiO_2 concentrations of 6.56-6.80 wt% were obtained. The reproducibility of the TiO_2 concentration was estimated to be within 0.02 wt% from 20 repeated measurements for one specimen. The values measured by XRF analysis were calibrated by values measured by an inductively coupled plasma - optical emission spectrometry (ICP-OES) system. In order to obtain an accurate gradient, we added the LSAW velocity of 3426.18 m/s for the standard specimen of synthetic silica glass of C-7980 (Corning Inc.) with 100-percent SiO_2 [23]. The result of a relationship between the LSAW velocities and calibrated TiO_2 concentrations can be obtained as shown in Fig. 4. From this result, we can determine the sensitivity and resolution of the LSAW velocity to the TiO_2 concentration as –0.0601 wt%/(m/s) and ±0.010 wt% for ±2σ at 225 MHz. Furthermore the TiO_2 concentration for the standard specimen with a LSAW velocity of 3308.18 m/s was determined to be 7.09 wt%.

The densities were 2197.74 kg/m^3 for the C-7972 standard specimen and 2199.82 kg/m^3 for the C7980 standard specimen [23]. The CTE for the C-7980 standard specimen is typically 520 ppb/K around 23°C [24], and that for the C-7972 standard specimen is assumed to be 0 ppb/K. The sensitivities and resolutions of LSAW velocity to the CTE, TiO_2 concentration, and density were presented in Table I.

C. Three-Dimensional Striae Structure

Two-dimensional LSAW velocity distributions were measured for the specimen described in Section II. Then, the specimen surface was optically polished to reduce the thickness by about 40 μm, viz., a quater period of striae, and the LSAW velocities were measured along *x*-, and *y*-axes. This procedure was repeated five times. The results were shown in Fig. 5. From the results, we can easily understand the three-dimensional configuration of striae that was not clear in the two-dimensional data of Fig. 5(a). The measurement results revealed that the striae plane curved gently down in the radial direction, having a slightly convex cross section layered with a striae periodicity of 0.16 mm and a curvature radius of 440 mm, and also existed in a circular form with a curvature radius of 450 mm. The maximum LSAW velocity change obtained over the entire measurement region of the specimen was 11.66 m/s, corresponding to a TiO_2 concentration of 0.70 wt% and a CTE of 51.4 ppb/K from the calibration line obtained in Section IV-B. These results reflect the glass production-process conditions such as the arrangement of the multiple burners, the rotation speed of refractory container, the glass liquid flow, and the temperature distributions on the glass deposit surfaces and within the container. Results provided by this ultrasonic method could be fed back to optimize the conditions of the glass manufacturing process in order to realize homogeneous glass ingots for EUVL use.

D. Evaluation and Selection of EUVL-Grade TiO_2-SiO_2 Ultra-Low-Expansion Glasses

Two-dimensional LSAW velocity distributions were measured for specimens A and B described in Section II. The results are presented in Fig. 6, together with the line-scanning measurements along *x*- and *y*-axes. For specimen A, the averaged LSAW velocities were 3308.10 m/s and 3308.23 m/s for two-dimensional and line-scanning measurements, with maximum velocity differences of 12.98 m/s and 11.84 m/s. For specimen B, the averaged LSAW velocities were 3307.33 m/s and 3307.22 m/s for two-dimensional and line-scanning measurements, with maximum velocity differences of 7.68 m/s and 7.28 m/s. We can obtain that the averaged TiO_2 concentrations correspond to 7.09 wt% and 7.14 wt% for specimens A and B, with the maximum differences of 0.78 wt% and 0.46 wt%, from the calibration line obtained in Section IV-B. And, the maximum velocity differences correspond to the CTE variations of 57.2 ppb/K and 33.8 ppb/K for specimens A and B. The estimated CTE variations were 5.7 and 2.3 times larger than the specifications. This is considered to be due to the fact that the manufacturer evaluates the CTE of the glass ingots by measuring the velocities of longitudinal waves propagating in the thickness direction of the ingots and their distributions [1, 7]. Therefore, CTE variations caused by striae on the specimen surface or in the glass ingots could not be detected accurately [13].

Based on the measurement results, we discuss evaluation methods of the EUVL-grade TiO_2-SiO_2 glasses in the developmental stage and in the stage that more homogeneous glass ingots can be obtained, and for the quality control and selection. The flowchart for evaluation, quality control, and selection of EUVL-grade TiO_2-SiO_2 glasses using the LFB-UMC system is shown in Fig. 7.

In the development of the glasses, it is important to evaluate the absolute CTE and the parameters of periodic striae such as the periodicity, variations, and distributions. It is very useful to understand the striae structures by the two-dimensional measurements, as shown in Fig. 6. However, the number of measurements was too many. On the other hand, the number for line-scanning measurements was much less, and it is possible to obtain almost the same averaged velocities and maximum velocity variations as those of the two-dimensional measurements. The CTE characteristics of TiO_2-SiO_2 ultra-low-expansion glasses are adjusted by controlling the concentration of TiO_2. Therefore, TiO_2 concentrations are calculated from the averaged LSAW velocities using the calibration line, and it should be fed back to the glass fabrication conditions. The CTE within ±5 ppb/K needed for EUVL-grade ultra-low-expansion glass substrates are satisfied when LSAW velocity variations are within ±1.13 m/s, calculated from the sensitivity of 4.41 (ppb/K)/(m/s).

In the stage that the glass production processes are improved to reduce striae and more homogenous ingots are produced, it is not necessary to measure LSAW velocities with fine steps. For example, we can obtain averaged TiO_2 concentrations from the averaged LSAW velocities by line-scanning measurements with steps from several millimeters to several tens millimeters using the calibration line.

In the stage for mass production of the EUVL-grade ultra-low-expansion glass, it is necessary to conduct quality control and selection of the substrates suitable for different parts of the reflective optics in the EUVL system, having differently required CTE specifications, viz., temperatures at which CTE becomes zero (zero-CTE temperature). In the mass-production stage, it is possible to measure the LSAW velocities at several sampling points, such as 9 points, 5 points, ultimately only 1 point at center of the substrate and to select the substrates for the desired use, if problems concerned with striae are already solved, and the CTE distributions are smaller than ±5 ppb/K. It is possible to obtain higher CTE resolution if the operating frequency is changed to the lower frequencies, such as 75 MHz, although it was 225 MHz in this paper [14].

V. Conclusion

In this paper, we discussed a method of evaluating and selecting EUVL-grade TiO_2-SiO_2 ultra-low-expansion glasses using the LFB-UMC system, based on two-dimensional and line-scanning LSAW velocity measurement results. It was clarified that the line-scanning measurements were much more useful than the two-dimensional measurements to obtain information of maximum differences and averaged values of the LSAW velocities on the surface of substrates, corresponding to the CTE information, needed for EUVL systems, that could not be obtained in the conventional CTE measurement techniques. This ultrasonic method with much higher accuracy is very useful not only for evaluation to develop more homogeneous ultra-low expansion glasses on the developmental stage, but also for quality control and selection of the glass on the mass-production stage at which

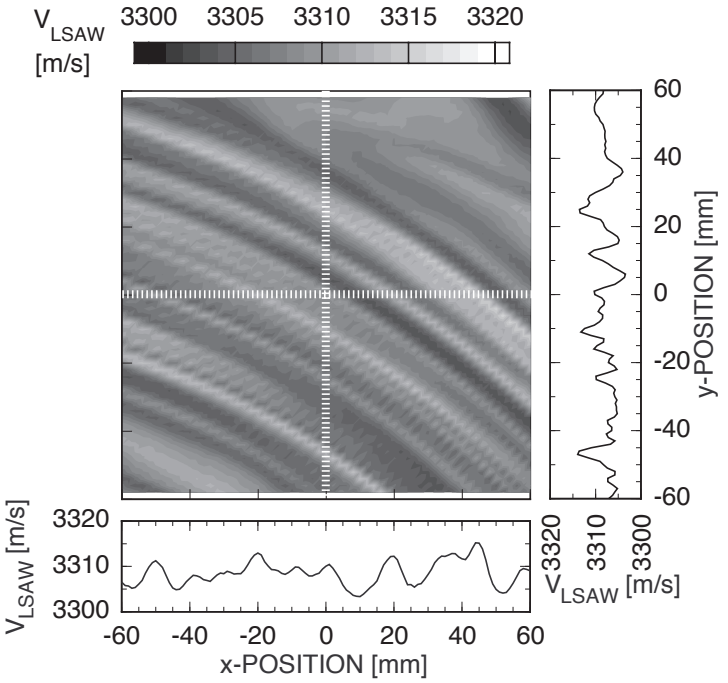

(a) Specimen A

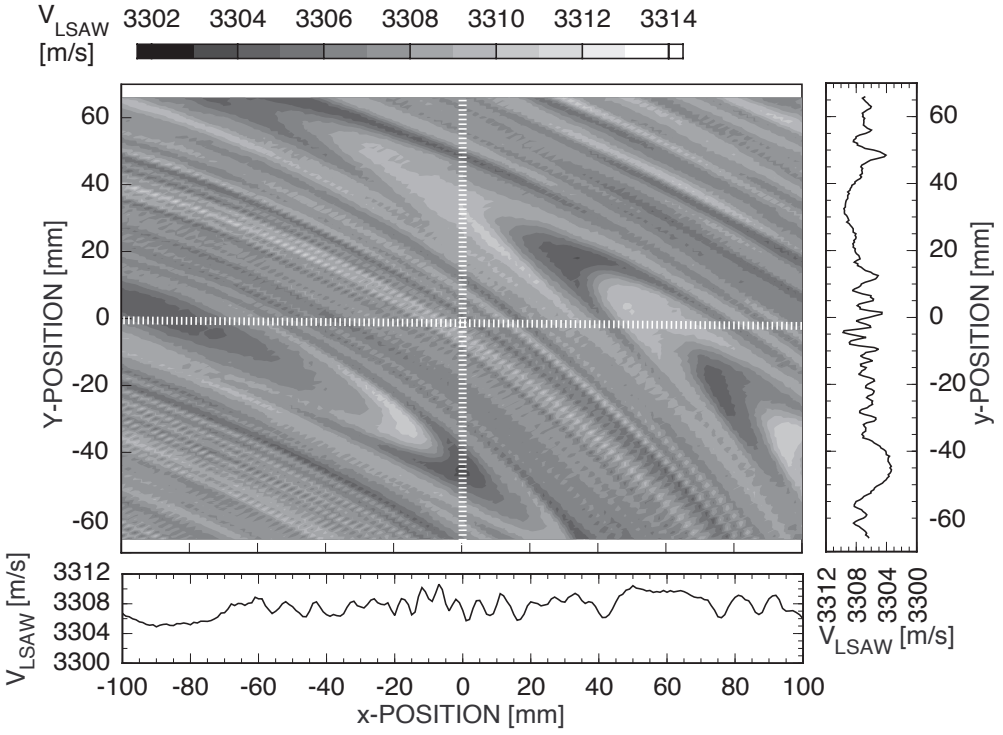

(b) Specimen B

Fig. 6. LSAW velocity distributions for two-dimensional scanning and line-scanning for specimens A and B at 225 MHz. White dotted lines show the measurement positions of line-scanning.

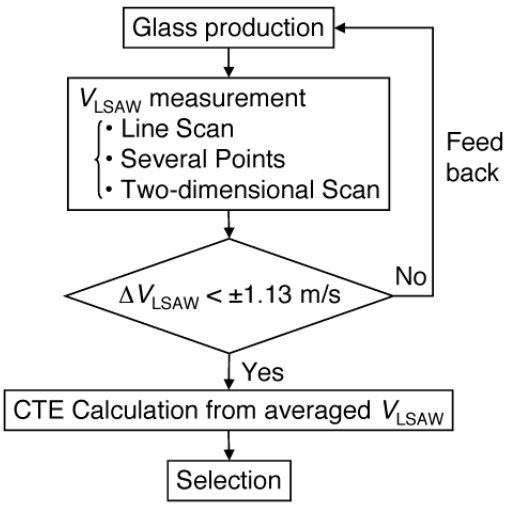

Fig. 7. Flowchart for evaluation, quality control, and selection of EUVL-grade TiO_2-SiO_2 glasses using the LFB-UMC system.

inspection of all substrates is required. Our ultrasonic method should be standardized for an evaluation method of the EUVL-grade ultra-low-expansion glasses.

ACKNOWLEDGMENTS

The authors are very grateful to K. Suzuki and S. Sannohe for their experimental assistance. This work was supported in part by a Research Grant-in-Aid for the 21st COE (Center of Excellence) Program funded by the Japanese Ministry of Education, Culture, Sports, Science, and Technology.

REFERENCES

[1] K. E. Hrdina, B. G. Ackerman, A. W. Fanning, C. E. Heckle, D. C. Jenne and W. D. Navan, "Measuring and tailoring CTE within ULE® glass," Proc. SPIE, vol. 5037, pp. 227-235 (2003).

[2] P. C. Schultz and H. T. Smyth, "Ultra-low-expansion glasses and their structure in the SiO_2-TiO_2 system," in *Amorphous Materials*, eds. R. W. Douglas and B. Ellis (Willey-Interscience, New York, 1970) pp. 453-461.

[3] R. B. Greegor, F. W. Lytle, D. R. Sandstrom, J. Wong, and P. Schultz, "Investigation of TiO_2-SiO_2 glasses by X-ray absorption spectroscopy," J. Non-Cryst. Solid., vol. 55, pp. 27-43 (1980).

[4] V. G. Badami and M. Linder, "Ultra-high accuracy measurement of the coefficient of thermal expansion for ultra-low expansion materials," Proc. SPIE, vol. 4688, pp. 469-480 (2002).

[5] Y. Takeichi, I. Nishiyama, and N. Yamada, "High-precision (<1 ppb/°C) optical heterodyne interferometric dilatometer for determining absolute CTE of EUVL materials," Proc. SPIE, vol. 6151, 61511Z (2006).

[6] B. L. Harper, K. E. Hrdina, W. D. Navan, J. Ellison, and A. Fanning, "Measuring thermal expansion variations in ULE® glass with interferometry," Proc. SPIE, vol. 5374, pp. 847-853 (2004).

[7] M. J. Edwards, E. H. Bullock, and D. E. Morton, "Improved precision of absolute thermal expansion measurements for ULE™ glass," Proc. SPIE, vol. 2857, pp. 58-63 (1996).

[8] K. E. Hrdina, B. Z. Hanson, P. M. Fenn, and R. Sabia, "Characterization and characteristics of a ULE® glass tailored for the EUVL needs," Proc. SPIE, vol. 4688, pp. 454-461 (2002).

[9] J. Kushibiki and N. Chubachi, "Material characterization by line-focus-beam acoustic microscope," IEEE Trans. Sonics Ultrason., vol. SU-32, pp. 189-212 (1985).

[10] J. Kushibiki, Y. Ono, Y. Ohashi, and M. Arakawa, "Development of the line-focus-beam ultrasonic material characterization system," IEEE Trans. Ultrason., Ferroelect., Freq. Contr., vol. 49, pp. 99-113 (2002).

[11] J. Kushibiki, M. Arakawa, Y. Ohashi, K. Suzuki, and T. Maruyama, "A promising evaluation method of ultra-low-expansion glasses for the extreme ultra-violet lithography system by the line-focus-beam ultrasonic material characterization system," Jpn. J. Appl. Phys., vol. 43, pp. L1455-L1457 (2004).

[12] J. Kushibiki, M. Arakawa, Y. Ohashi, K. Suzuki, and T. Maruyama, "A super-precise CTE evaluation method for ultra-low-expansion glasses using the LFB ultrasonic material characterization system," Jpn. J. Appl. Phys., vol. 44, pp. 4374-4380 (2005).

[13] J. Kushibiki, M. Arakawa, Y. Ohashi, and K. Suzuki, "Evaluation method of TiO_2-SiO_2 ultra-low-expansion glasses with periodic striae using the LFB ultrasonic material characterization system," IEEE Trans. Ultrason., Ferroelect., Freq. Contr., vol. 53, pp. 1627-1636 (2006).

[14] M. Arakawa, J. Kushibiki, Y. Ohashi, and K. Suzuki, "Accurate calibration line for super-precise coefficient of thermal expansion evaluation technology of TiO_2-doped SiO_2 ultra-low-expansion glass using the line-focus-beam ultrasonic material characterization system," Jpn. J. Appl. Phys., vol. 45, pp. 4511-4515 (2006).

[15] Y. Ohashi, M. Arakawa, and J. Kushibiki, "Super-accurate velocity measurement for evaluating TiO_2-SiO_2 ultra-low-expansion glass using the line-focus-beam ultrasonic material characterization system," Jpn. J. Appl. Phys., vol. 44, pp. L1313-L1315 (2005).

[16] Y. Ohashi, M. Arakawa, and J. Kushibiki, "Improvement of velocity measurement accuracy of leaky surface acoustic waves for materials with highly attenuated waveform of the V(z) curve by the line-focus-beam ultrasonic material characterization system," Jpn. J. Appl. Phys., vol. 45, pp. 4505-4510 (2006).

[17] Y. Ohashi, J. Kushibiki, M. Arakawa, and K. Suzuki, "Experimental study for evaluating striae structure of TiO_2-SiO_2 glasses using the line-focus-beam ultrasonic material characterization system," Jpn. J. Appl. Phys., vol. 45, pp. 6445-6451 (2006).

[18] M. Arakawa, J. Kushibiki, Y. Ohashi, and K. Suzuki, "Accurate velocity measurement of periodic striae of TiO_2-SiO_2 glasses by the line-focus-beam ultrasonic material-characterization system," Jpn. J. Appl. Phys., vol. 45, pp. 8925-8927 (2006).

[19] M. Arakawa, J. Kushibiki, and Y. Ohashi, "Striae evaluation of TiO_2-SiO_2 ultra-low expansion glasses using the line-focus-beam ultrasonic material characterization system," Proc. SPIE, vol. 6151, 615123 (2006).

[20] Technical data of C-7972 glass from Corning Inc.

[21] J. Kushibiki and M. Arakawa, "A method for calibrating the line-focus-beam acoustic microscopy system," IEEE Trans. Ultrason., Ferroelect., Freq. Contr., vol. 45, pp. 421-430 (1998).

[22] M. Arakawa, Y. Ohashi, and J. Kushibiki, "Evaluation method for striae of TiO_2-SiO_2 glasses using the LFB ultrasonic material characterization system-Accurate measurement of leaky surface acoustic wave velocity," *Tech. Rep. IEICE*, vol. US2005-85, pp. 19-24 (2005).

[23] J. Kushibiki, M. Arakawa, and R. Okabe, "High-accuracy standard specimens for the line-focus-beam ultrasonic material characterization system," IEEE Trans. Ultrason., Ferroelect., Freq. Contr., vol. 49, pp. 827-835 (2002).

[24] Technical data of C-7980 glass from Corning Inc.

Phase Linear・Flat Wide Band・Low Loss Filters Using Unidirectional Dispersive Inter Digital Transducers

Kazuhiko Yamanouchi and Yusuke Satoh
Tohoku Institute of Technology, Sendai 982-8577, Japan

Abstract- Dispersive transducers have sharp cut-off and flat wide band frequency characteristics. Also phase linear and the very low loss characteristics are obtained by combining down-chirp and up-chirp unidirectional dispersive transducers (DUDIDT and UUDIDT).

In this paper, DUDIDT and UUDIDT were investigated using TeO_2 thin film gratings with the large impedance ratios. The impedance ratio of r=Ze/Zg (Ze: with shorted thin film and Zg: without open thin film) were investigated using TeO_2 thin films. The results showed the large impedance ratio, r=0.96 at the thickness of H/λ =0.01 on TeO_2/128 ° Y-X $LiNbO_3$. These grating are applied for DUDIDT and UUDIDT. The very low insertion loss of 0.2dB and flat wide band of 10% and the very sharp cut-off characteristics were theoretically obtained and the experimental results showed the insertion loss of 0.6 dB at 400MHz.

1. Introduction

The success of practical applications of SAW devices in the field of filters, signal process and others depends on the choice of substrate materials. The important properties to be taken into consideration for SAW devices would be the electromechanical coupling coefficient, k^2 (should be as high as possible), the temperature coefficient of frequency, TCF (should be as small as possible), spurious response for high performance. Also the unidirectional transducer and SAW resonators using the internal reflections and the bulk acoustic resonators with multi-layers require the high reflectivity with the large impedance ratio gratings of low propagation loss under the very thin film conditions. Especially, the flat wide band and the very low insertion loss filters using unidirectional transducers with gratings of large impedance ratios are required.

Dispersive unidirectional transducers have the above properties. Also phase linear characteristics are obtained by combining the down-chirp and up-chirp unidirectional dispersive transducers (DUDIDT and UUDIDT) with thin film gratings. The SiO_2 thin film gratings have good properties as dielectric reflectors. Unfortunately, the SAW velocities of the SiO_2 are almost the same as substrate velocities, for examples, as 128 ° Y-X $LiNbO_3$. Therefore the thick films for large impedance ratios with some propagation attenuations are needed. The grating substrates of the very low velocity thin films below 1000m/s have the large reflectivity with low propagation attenuations for SAW and bulk waves because of decreasing the grating film thickness. The velocity of Y-X TeO_2 has the lowest velocity of 850m/s for Rayleigh waves. Therefore, the TeO_2 thin films are used as the gratings with the large impedance ratios at the very thin thickness. Also, these grating films are easily fabricated on piezoelectric substrates.

In this paper, the large impedance ratios of TeO_2 grating/128 ° Y-X $LiNbO_3$, 36 ° Y-X $LiTaO_3$ and 5 ° Y-X $LiNbO_3$ are investigated theoretically and experimentally, and applied to dispersive unidirectional transducers. The theoretical and experimental results of unidirectional dispersive SAW transducers and filters using large impedance ratios are described.

2. Phase linear・Sharp Cut Off・ Flat Wide Band and Low Loss Filters using Dispersive Unidirectional Transducers and New Reflecting Materials of TeO_2 Thin Film

Dispersive Interdigital Transducers (DIDT) on Y-Z $LiNbO_3$ have the unidirectionality toward down-chirp direction [1], as shown in Fig.1. Also, the unidirectional DIDT (UDIDT) shows flat wide band and sharp cut-off frequency characteristics without amplitude weighting of sinX/X. Therefore, phase linear, flat wide band and low loss filters by combining the down-chirp and up-chirp unidirectional dispersive transducers (DUDIDT and UUDIDT) are obtained as shown in Fig.2. The very thin grating films with low propagation attenuations and large impedance ratios are very important for unidirectional DIDT. Therefore, the new grating TeO_2 films with the very low SAW velocities are investigated.

Figure 3 shows the configuration of the super low velocity film/piezoelectric substrate, where SAW

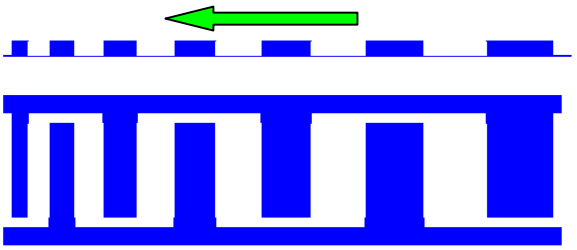

Fig.1 Unidirectional dispersive interdigital transducers

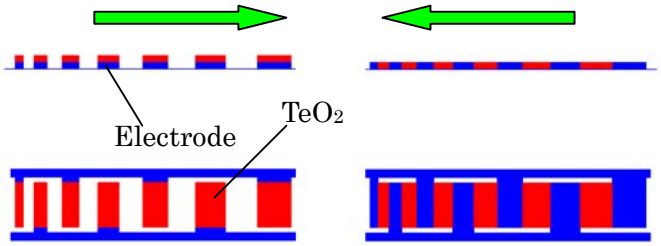

Fig.2 Phase linear filters combined DUDIDT and UUDIDT

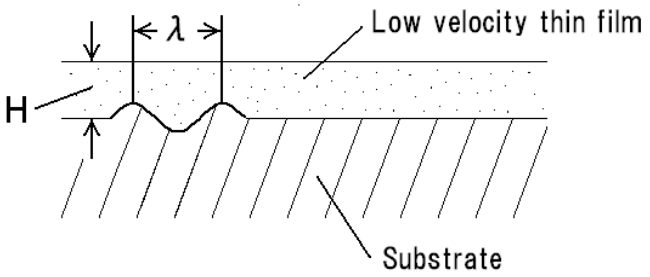

Fig.3 Configuration of super low velocity film/piezo-electric substrate

wavelength is λ and the film thickness is H. From the piezoelectric equations, the equation of motion and Laplace's equation, we can obtain the wave equation. Also the mechanical and electrical boundary conditions for the boundary surface and for the thin film surface give the boundary condition equations. We can obtain the Rayleigh wave[2] and the leaky surface wave[3] solutions from the two equations.

The electromechanical coefficients of SAW, k^2 are given by

$$k^2 = 2(v_f - v_m)/v_f \quad (1)$$

where v_f: velocity of open boundary, v_m: velocity of short boundary.

The propagation characteristics of TeO_2 single crystals are calculated by A.J.Slobodnik[4]. The velocity of Y-X TeO_2 has the lowest velocity of 850m/s for Rayleigh waves. Therefore, the TeO_2 thin films with super low velocities are used as the large impedance ratio gratings. Experimental results showed the TeO_2 films are amorphous from X-ray diffraction measurements. The density of TeO_2 thin film is measured by the thickness and the weigh of TeO_2 thin films sputtered on $LiNbO_3$ substrate under the conditions shown in session 3 and elastic constants are determined by the measured velocities and the impedance ratio of TeO_2 film/$LiNbO_3$ substrates shown in session 3. These values are as follows, density of $\rho=4880kg/m^3$ and elastic constants of $c_{11}=0.16\times10^{11}N/m^2$ and $c_{44}=0.07\times10^{11}N/m^2$. The propagation characteristics of SAW and leaky SAW on amorphous TeO_2/128°Y-X, TeO_2/5°Y-X $LiNbO_3$ and TeO_2/36° Y-X $LiTaO_3$ using above values are investigated.

2.1 Calculation results of TeO_2/128°Y-X $LiNbO_3$

Figure 4 shows the calculation results of velocity and k^2 vs H/λ for TeO_2/128°Y-X $LiNbO_3$[5]. The results show the large velocity change of 150m/s for H/λ=0.02, compared with the SiO_2 thickness of H/λ=0.1. The above values are almost the same as those of TeO_2/$LiNbO_3$.

Figure 5 shows the impedance change of r=Ze/Zg (Ze: with shorted thin film and Zg: without open thin film). The ratio of 128° Y-X $LiNbO_3$ with TeO_2 thin film gratings gives the impedance ratio of r=0.96 at the thickness of H/λ=0.01, compared with the same ratio for SiO_2 grating of H/λ=0.03.

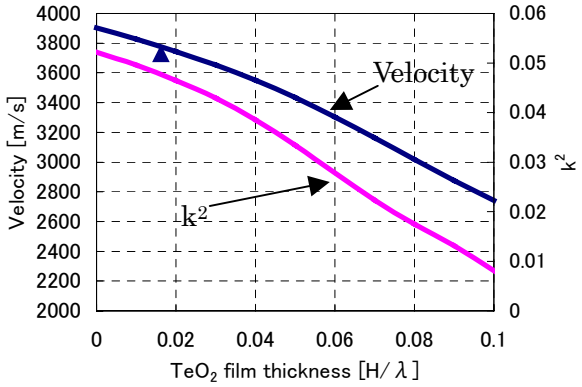

Fig.4 Calculation results of velocity and k^2 vs H/λ for TeO_2 /128 °Y-X $LiNbO_3$(▲;Experimental)

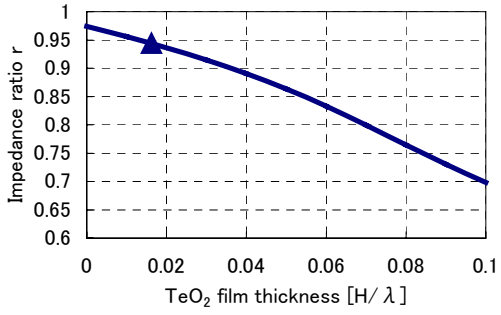

Fig.5 Impedance ratio of r=Ze/Zg (Ze: with shorted thin film and Zg: without open thin film).

2.2 Calculation results of TeO_2/36° Y-X $LiTaO_3$

Figure 6 shows the calculation results of velocity and k^2 vs thickness of TeO_2 /36 °Y-X $LiTaO_3$[6] vs H/λ. The results show the large velocity change of 80m/s for H/λ=0.02. Also the k^2 increases for H/λ (k^2=0.075 for H/λ=0.04, compared with k^2=0.045 for H/λ=0).

Figure 7 shows the impedance change of r=Ze/Zg. The ratio of 36 ° Y-X $LiTaO_3$ with TeO_2 thin film gratings gives the large impedance ratio of r=0.95 at the thickness of H/λ=0.02.

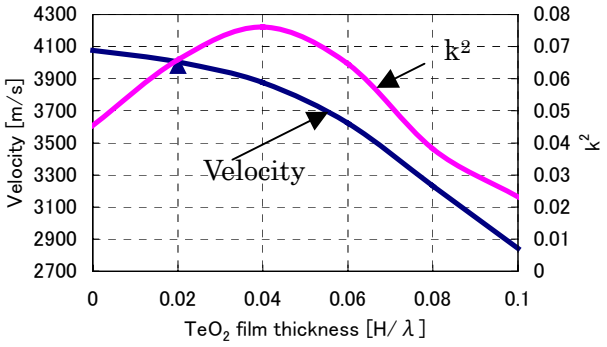

Fig.6 Calculation results of velocity and k^2 vs H/λ for TeO_2 /36 °Y-X $LiTaO_3$ (▲;Experimental)

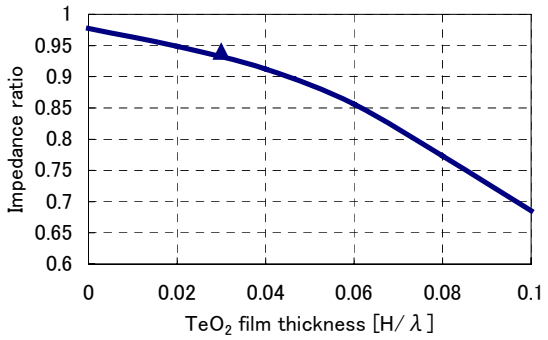

Fig.7 Impedance ratio of r=Ze/Zg

2.3 Calculation results of TeO_2/5° Y-X $LiNbO_3$

Figure 8 shows the calculation results of velocity and k^2 vs thickness of TeO_2 /5 °Y-X $LiNbO_3$[3,7] vs H/λ. The results show the large velocity change of 200m/s for H/λ=0.02. Also the k^2 increases for H/λ (k^2=0.29 for H/λ=0.02, compared with k^2=0.24 for H/λ=0.0).

Figure 9 shows the impedance change of r=Ze/Zg. The ratio of 5 ° Y-X $LiNbO_3$ with TeO_2 thin film gratings gives the large impedance ratio of r=0.81 at the thickness of H/λ=0.02.

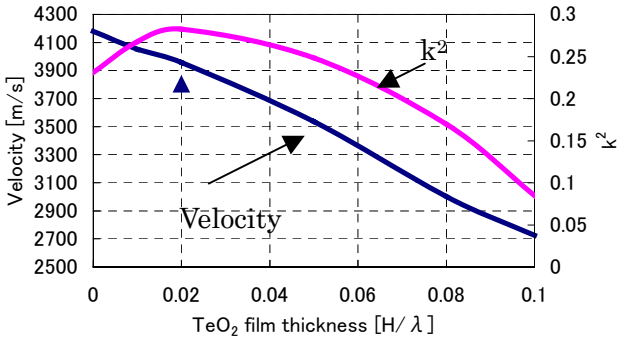

Fig.8 Calculation results of velocity and k^2 vs H/λ for TeO_2 /5 °Y-X $LiNbO_3$ (▲;Experimental)

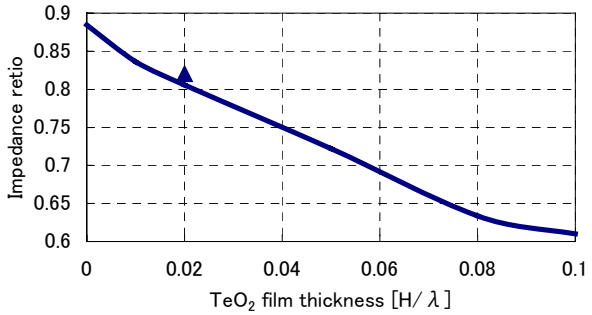

Fig.9 Impedance change of r=Ze/Zg for Y-X TeO_2 /5 °Y-X $LiNbO_3$

2.4 Caluculation Results of Phase linear・Sharp Cut Off・ Flat Wide Band and Low Loss Filters using Dispersive Unidirectional Transducers

The frequency characteristics of phase linear, flat wide band and low loss filters by combining the down-chirp and up-chirp unidirectional dispersive transducers (DUDIDT and UUDIDT) shown in Fig.2 are calculated.

Figure 10 shows the results of phase linear filters using TeO_2 grating/128°Y-X $LiNbO_3$, where N=100, electrode thickness(Al) H/λ=0.03, TeO_2 thickness H/λ=0.02, W=20λ, respectively. Also, in order to obtain sharper cut off frequency characteristics, soft distance weighting [8] are applied. The very low insertion loss of 0.2dB and flat wide band of 10% and the very sharp cut-off characteristics are obtained.

The insertion loss for long DUIDT with wide band characteristics will be increased due to the propagation attenuation on IDT. These are improved by dividing the inline DUDIDT and UUDIDT into the M-parallel line UDIDT as shown in Fig.11. In this case, propagation attenuation are reduced to 1/M. Figure 12(a) and (b) show the calculation results of in-line and 3-parallel filters using DUDIDT and UUDIDT at the propagation attenuation of 0.01dB/λ. Insertion loss are improved from 3.5 dB to 1.5 dB, at Nt=300.

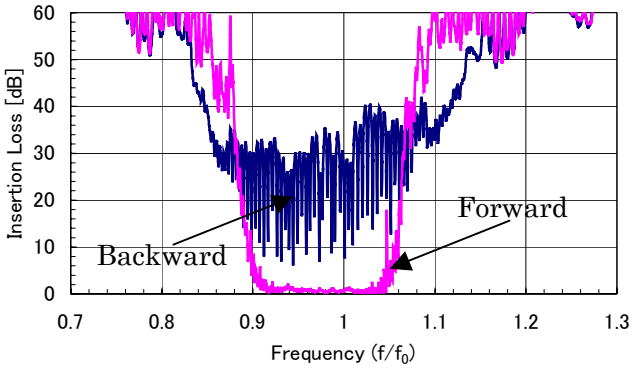

Fig.10 Calculation results of phase linear filters using TeO_2/128°Y-X $LiNbO_3$, where N=100, electrode thickness(Al) H/λ=0.03, TeO_2 thickness H/λ=0.02, W=20λ with distance weighting[8]

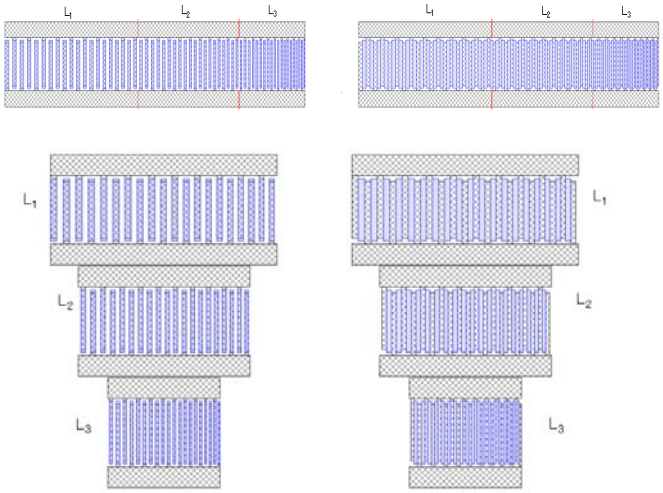

Fig.11 Configuration of dividing the inline DUDIDT and UUDIDT into the M-parallel line UDIDT

3. Experimental Results of Unidirectional Dispersive Filters

TeO_2 thin films are fabricated using RF-Magnetron Sputtering Equipment. Sputtering conditions are as follows, Target:Te-metal, Gas Composition by weight ratio: Ar:O_2 (1:1), Sputtering Pressure: 1.0 Pa., RF power: 60W+60W, Substrate Temp.: Without heating, Growth Rate: 1μm/h.
The measured velocities of TeO_2/128° Y-X $LiNbO_3$ are shown in Fig.4 by mark ▲ from the measured velocity. The elastic constants of amorphous thin TeO_2 films are estimated from the measured velocity.

Figure 13 shows the experimental results of phase linear filters using TeO_2 grating/128°Y-X $LiNbO_3$, where N=50, electrode thickness(Al) H/λ=0.03, TeO2 thickness H/λ=0.03, W=20λ, respectively. The minimum insertion loss of about 0.6dB are obtained.

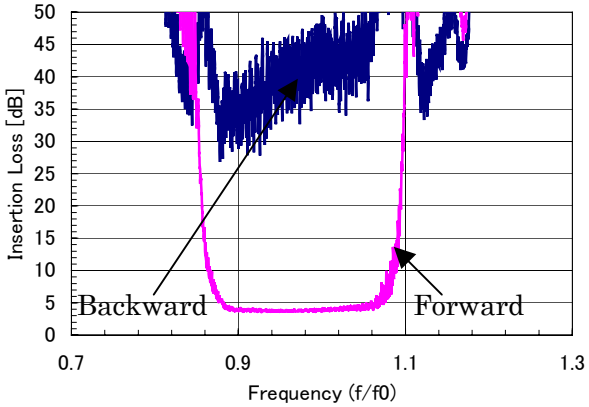

Fig.12(a) Calculation results of in-line phase linear filters using TeO_2/128°Y-X $LiNbO_3$, where Nt=300, electrode thickness(Al) H/λ=0.03, TeO_2 thickness H/λ=0.02, W=25λ, propagation atenuation =0.01dB/λ with distance weighting[8]

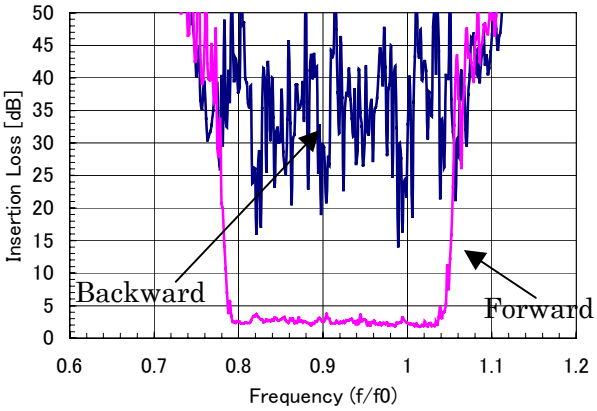

Fig.12(b) Calculation results of 3-parallel phase linear filters using TeO_2/128°Y-X $LiNbO_3$, where Nt=300($N_{1,2,3}$=100), electrode thickness(Al) H/λ=0.03, TeO_2 thickness H/λ=0.02, W=25λ, propagation atenuation =0.01dB/λ with distance weighting[8]

Figure 14 shows the experimental results of phase linear filters using TeO_2 grating/128°Y-X LiNbO3, where N=100, electrode thickness(Al) H/λ=0.03, TeO_2 thickness H/λ=0.03, W=20λ, respectively. The minimum insertion loss of about 2.0 dB are obtained.
Figure 15 shows the experimental results of phase linear filters using TeO_2 grating/128°Y-X $LiNbO_3$, where N=150, electrode thickness(Al) H/λ=0.03, TeO_2 thickness H/λ=0.03, W=20λ, respectively. The minimum insertion loss of about 2.8 dB are obtained.

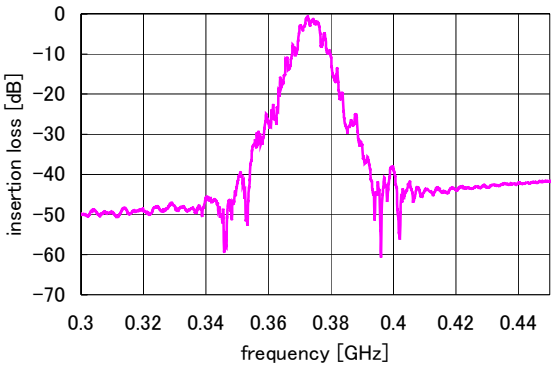

Fig.13 Experimental result of UDIDT filter with phase linear. Insertion loss of about 0.6dB at N=50.

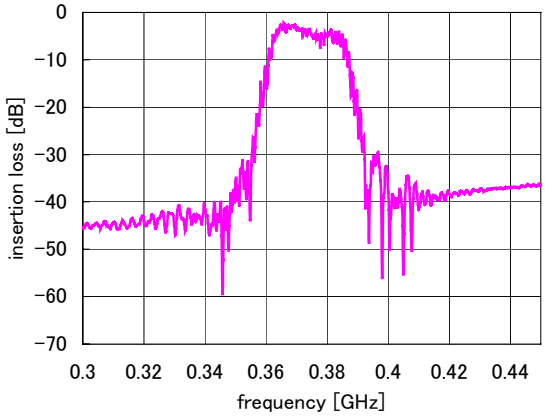

Fig.14 Experimental result of UDIDT filter with phase linear, Insertion loss of about 2.1dB at N=100.

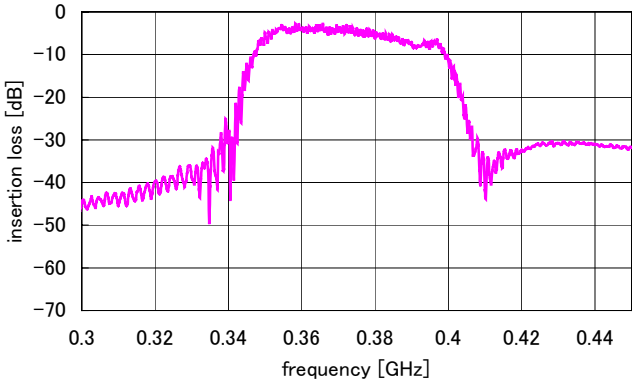

Fig.15 Experimental result of UDIDT filter with phase linear, Insertion loss of about 2.8dB at N=150.

5. Conclusion

The propagation characteristics of TeO_2 grating/Rotated Y-cut, X-propagating $LiNbO_3$,$LiTaO_3$ substrates with large k2 and impedance ratio are theoretically investigated. The large reflectivities are obtained by using the very low velocity thin films of TeO_2. The grating films are applied to unidirectional dispersive transducers and filters. Theoretical results showed the minimum insertion loss of 0.4dB.Experimental results showed the minimum insertion loss of 0.6dB. We are now investigating higher frequency filters and wide band filters with parallel connection UIDT.

Refernces

[1]K.Yamanouchi, J.Ogata, N.Mihota and S.Kato,“Unidirectional Transducer and Application to High Efficient Elastic Convolvers",1991 IEEE Ultrasonics Symposium Proceedings, Vo.1,pp.251-254

[2]J.J.Campbell and W.R.Jones:“A method for estimating optimal cuts and propagation directions for excitation and propagation directions for excitation of piezoelectric surface waves", IEEE Trans. Sonics and Ultrason.,Vol.SU-15,1988,pp.209-217

[3] K.Yamanouchi and K.Shibayama,“Propagation and Amplification of Rayleigh Waves and Piezoelectric Leaky Surface Waves in LiNbO3", Journal of Applied Physics, Vol.43, No.3, March 1972, pp.856-862

[4]A.J.Slobodonik,Jr, “The Temperature Coefficient of Acoustic Surface Wave Velocity on Delay on Lithiume Niobate 、 Lithiume and Tellurium Dioxide, 〃 AFCRL-72-0082(NTIS AD-742287)

[5]K.Shibayama,K.Yamanouchi,H Sato and T.Meguro、 “Optimum Cut for Rotated Y-Cut $LiNbO_3$ Crystal Used as the Substrate and Acoustic Surface Wave Filters," Proc. of the IEEE, Vol.64, No.5, May 1976, pp.595-597

[6] K.Iwahashi, K.Yamanouchi and K. Shibayama, “Temperature dependence of leaky surface wave velocity in $SiO_2/LiTaO_3$ structure with high coupling", Proc. Ultrason. Comm. in Inst. electron. Comm. Eng, Japn. US77-43, (Sept. 1977), pp.37-42 and K.Yamanoyuchi, K.Iwahashi and K.Shibayam,Wave Electronics, 3(1979), pp.319-333、and K. Nakamura, F. Kazumi and H. Shimizu, “SH-type and Rayleigh-type surface wave in rotated Y-cut $LiTaO_3$", Proc. Ultrason. Comm. in Inst. Electron. Comm. Eng. Japn., US77-42, (Sept. 1977), pp. 31-36 and K.Nakamura, M.Kazumi and H.Shimizu,Proc. of IEEE Ultrason. Symp., pp.819-822, (1977)

[7]K.Yamanouchi and H.Satoh, “ Theoretical and Experimental Results of Unidirectional Interdigital Transducers Using Grating SAW Substrates and Zero TCF Ladder Type Filters at 2GHz一Ranges"、 2004

IEEE Ultrason. Symp. Proc., Vol.2,pp.1335-1338
[8] K.Yamanouchi, T.Meguro and K.Shibayama, “Acoustic Surface Wave Filters Using New Distance Weighting Techniques",1980 IEEE Ultrasonics Symposium Proceedings, pp.313-316

→

Sputtering (103) Oriented AlN Films and its Acoustic Wave Mode Analysis

* Sean Wu[1], Ruyen Ro[2], Maw-Shung Lee[3], Zhi-Xun Lin[4]

[1]Department of Electronics Engineering and Computer Sciences, Tung-Fang Institute of Technology, 110 Tung-Fung Road, Hunei Shiang, Kaohsiung 829, Taiwan, R.O.C. E-mail：wusean@giga.net.tw

[2]Department Of Communication Engineering, I-Shou University, 1, Section 1, Hsueh-Cheng Rd., Ta-Hsu Hsiang, Kaohsiung County, Taiwan 840, R.O.C. E-mail：ryro@isu.edu.tw

[3]Department of Electronics Engineering, National c University of Applied Sciences, 415 Chien Kung Road, Kaohsiung 807, Taiwan, R.O.C. E-mail：mslee@cc.kuas.edu.tw

[4]Department of Electrical Engineering, National Kaohsiung University of Applied Sciences, 415 Chien Kung Road, Kaohsiung 807, Taiwan, R.O.C. E-mail：f880310211@hotmail.com

Abstract

Highly (103) oriented AlN films were successfully sputtered in different nitrogen concentrations [$N_2/(N_2+Ar)$ *100%] in this research. The dependence of the nitrogen concentrations and the material characteristics of the films (crystalline structure and micro morphology) were investigated. The results showed that the X-ray diffraction (XRD) intensity of the (103) peak increased as the nitrogen concentrations decreased. The columnar grains of the (103) oriented AlN films grew perpendicular to the substrate surface and the surface morphology exhibited small (about 30-50 nm) dense uniform grains. The (103) AlN films at 50 % had the strongest diffraction intensity at the (103) peak, a small full width at half maximum (FWHM) value (0.252°), and a good N/Al atom composition ratio (0.92). The theoretical bulk acoustic wave properties of (103) oriented AlN films were also studied by solving the Christoffel equation. The result showed that the (103) oriented AlN films will excite two bulk acoustic wave modes. One is a quasi longitudinal mode and the other is a quasi fast shear mode. For the quasi longitudinal mode, the phase velocity is 10717 m/s and the piezoelectric coupling constant (K^2) is 4 %. For the quasi fast shear mode, the phase velocity is 5957 m/s and the K^2 is 3.8%. The quasi fast shear acoustic mode of the (103) oriented AlN films is suitable for application on the FBAR liquid sensor.

KEYWORDS：sputtering, AlN, (103) oriented, FBAR

I. INTRODUCTION

Recently, important efforts have been made in the development of electro-acoustic resonators for sensing in liquid media. Traditionally a film bulk acoustic wave (FBAW) device based on AlN, films grown with perfect c-axis orientation are sought in order to optimally excite a longitudinal thickness mode [1]-[8]. It is not suitable to be applied on liquid sensors. That is because a longitudinally polarized wave resonator operated in a liquid medium exhibits a significant acoustic leakage into the liquid and hence results in a substantial loss of resolution [9]. For the liquid sensor application, a resonator with a shear mode does not produce any compressional motion into the liquid and thus no energy leakage [10]-[13]. Different oriented piezoelectric films will form the different vibration modes and acoustic properties. Thus, a FBAW resonator can excited a shear mode becomes very important.

Bjurstrom et al used a two-stage sputtering process to deposit tilted AlN films to form a quasi (103) AlN texture [14], [15]. The resulting film had a distinct tilted texture with the mean tilt of the c-axis varying roughly in the interval 28 to 32 degrees over the wafer. Then they used the tilted AlN films to make FBAR devices which successfully excited two bulk acoustic wave modes (a quasi-longitudinal mode and a quasi-shear mode simultaneously). The quasi-shear mode was successfully applied to the FBAR liquid sensor. Film uniformity is a main issue in the mass production yield and lowing cost for FBAR devices. Unfortunately, the titled sputtering method above seems to form non-uniformity films on a wafer. Thus depositing the (103) oriented AlN films is very important.

In this research, we successfully deposited highly (103) oriented AlN films by the sputtering method and the theoretical bulk acoustic wave (BAW) properties of (103) oriented AlN films were also studied in detail.

II. EXPERIMENTAL PROCESS

AlN films were deposited by r.f. magnetron sputtering from a water-cooled 3-inch diameter aluminum target (99.99%) in argon/nitrogen gas mixtures. The purity of the nitrogen gas was 99.9995% and that of the argon gas was 99.99%. The sputtering parameters are shown in Table I. The crystalline structure and the crystallographic orientation of the films were determined using a glancing incident angle X-ray diffraction (XRD) instrument (PANalytical X'PERT PRO). The power of the XRD (Cukα radiation) was fixed at 45 kV and 40 mA. The incident angle of the X-ray was fixed at 0.5° and the XRD diffraction angles (2θ) ranged from 30° to 80°. The crystal quality of the films was obtained from the full width at half maximum (FWHM) of the XRD spectrum. A scanning electron microscope (SEM) instrument (Hitachi-4700) was used to observe the surface morphology and cross section of the AlN films. The atom composition ratio (N/Al) of the AlN films was determined by the energy dispersive the X-ray spectroscopy (EDS) instrument (HORIBA). At a low $N_2/(N_2+Ar)$ ratio, the nitrogen deficiency occurred in AlN, which was therefore sub-stoichiometric and lost long-range order domains [16]. Therefore, the high nitrogen concentrations (75%, 67%, 58% and 50%) are used to depositing AlN films in this experiment.

III. RESULTS AND DISCUSSION

A. Structure analysis of (103) oriented AlN films

The X-ray examination of piezoelectric films has been a major tool for determining the uniformity of crystalline structure [17].The higher the degree of orientation of a piezoelectric, the higher the electromechanical coupling coefficient of the piezoelectric [18]. Fig. 1 shows the XRD patterns of the AlN films as a function of the nitrogen concentrations. Fig.1 shows the XRD patterns of the films prepared at 75%, 67%, 58% and 50%. Those films all exhibit only the (103) peak. The (103) AlN films prepared at 50% has the strongest diffraction intensity of the (103) peak. However, as the $N_2/(N_2+Ar)$ ratio increased further, the excessive nitrogen partial pressure made the sputtered atoms less energetic, which in turn reduced the crystallinity and the degree of (103) orientation. We further determines the FWHM values of the (103) XRD peak at the different nitrogen concentrations. The results are shown in Table II. It is found the FWHM values of the (103) XRD peak decreased (from 0.72° to 0.252°) as the nitrogen concentration decreased (from 75% to 50%). Small FWHM value indicates the highly oriented crystallites. Therefore, those films at 50 % are the best highly (103) oriented AlN crystalline structures in this research.

One of the early indicators of a good piezoelectric film is the quality of its color and its transparency. Optical "eyeing" is an indicator of good or poor piezoelectric properties but it is not a quantitative measure. Those (103) AlN films prepared in this research are all transparent. The SEM analysis gives a more quantitative "eyeing" picture for surface and sidewall microstructures. We further do the SEM analysis of those films. Fig. 2 shows the surface morphology of the films. In the nitrogen concentration region (75%-50%), the surface morphology of the (103) AlN films look very alike. The photographs exhibited the grains are small (about 30-50 nm) dense uniform grains. We also analyze the composition of the films by EDS. The results are shown in Table III. As the nitrogen concentrations decrease (from 75% to 50%), the N/Al atom ratio increase (from 0.72 to 0.92). It is found the higher the degree of (103) orientation, the smaller FWHM value and the higher N/Al atom ratio. The degree of the preferred orientation was a key material parameter and the other material parameters, the FWHM value and the atom composition ratio, were related to the degrees of preferred orientation. The (103) AlN films at 50 % have the strongest diffraction intensity of the (103) peak, the smallest FWHM value (0.252°) and the best N/Al atom composition ratio (0.92). The SEM cross sections of the (103) AlN films are shown in Fig. 3. It is found the columnar grains of the (103) AlN films are perpendicular to the substrate surface. The film thicknesses at the nitrogen concentrations (75%-50%) are almost the same (about 1.25 μm). As the nitrogen concentrations decrease, the film thicknesses increase slightly.

B. Bulk acoustic wave properties of (002) and (103) oriented AlN films

The three-dimensional wave equation was generally referred to as the Christoffel equation [19]. It admitted three solutions, the properties of which were determined by the relation of the propagation direction to the stiffness matrix. The Christoffel equation and Christoffel matrix (Γ) were

$$k^2\Gamma_{ij}v_j = \rho\omega^2 v_i \tag{1}$$

$$\Gamma_{ij} = l_{iK}c_{KL}l_{Lj} \tag{2}$$

The Christoffel matrix for a piezoelectrically stiffened crystal (Γ') was

$$\Gamma'_{ij} = l_{iK}\left(c_{KL} + \frac{[e_{Kl}l_j][l_i e_{iL}]}{l_i\varepsilon^S_{ij}l_j}\right)l_{Lj} \tag{3}$$

Where v_j and v_i were the particle velocity; l_{iK} and l_{Lj} were the propagation direction matrix; l_i and l_j were the propagation direction; e_{Kl} and e_{iL} were the piezoelectric matrix; c_{KL}, ε^S_{ij}, k, ω, and ρ were the stiffness matrix, the permittivity matrix, the wave number, the angle frequency, and the mass density, respectively.

Christoffel matrix was 3×3 with elements that depend only on the propagation direction of the wave and stiffness constants of the crystal. The material constants [20] of the AlN are shown in Table IV. Using the AlN material constants and the propagation direction, we could get the Christoffel matrix by (3). Solving the Christoffel matrix involved solving an eigenvalue problem; the eigenvalues were three real positive numbers that were simply the three phase velocities of the possible propagating waves.

A piezoelectric coupling constant (K^2) can be derived by this equation [19].

$$v'_a = v_a(1+K^2)^{1/2} \tag{4}$$

Where v'_a and v_a were stiffened and unstiffened phase velocity.

For an (002) oriented AlN films, the wave propagation direction is $\hat{l} = \hat{a}_x l_x + \hat{a}_y l_y + \hat{a}_z l_z = \hat{a}_z l_z$, and the Christoffel matrix of (002) oriented AlN films (Γ'_{002}) was given by (3).

$$\Gamma'_{002} = \begin{bmatrix} c_{44} & 0 & 0 \\ 0 & c_{44} & 0 \\ 0 & 0 & c_{33} + \dfrac{e_{33}^2}{\varepsilon_{33}} \end{bmatrix}$$

From solving the Christoffel matrix of (002) oriented, we obtain the eigenvalues: $\{c_{44}, c_{44}, c_{33} + \frac{e_{33}^2}{\varepsilon_{33}}\}$ and the corresponding eigenvectors: $\{[1\,0\,0],[0\,1\,0],[0\,0\,1]\}$. Therefore, the pure longitudinal mode correspond to the eigenvalue ($c_{33} + \frac{e_{33}^2}{\varepsilon_{33}}$) thus has the phase velocity ($\sqrt{\frac{c_{33} + \frac{e_{33}^2}{\varepsilon_{33}}}{\rho}}$). There are two pure shear modes with the same velocities ($\sqrt{\frac{c_{44}}{\rho}}$). The K^2 value is given by (4). The K^2 value of the pure longitudinal mode is $\frac{e_{33}^2}{c_{33}\varepsilon_{33}}$ and the K^2 values of the two pure shear modes is zero. We further use the material constants of the AlN in Table IV and get the following results.

The phase velocities and piezoelectric coupling constant (K^2) of the (002) oriented AlN films are:

pure longitudinal mode:

velocity: 10931 (m/s)

K^2 : 6.245%

pure shear mode:

velocity: 5796 (m/s)

K^2 : 0%

The K^2 value of the pure shear mode is zero. Therefore, the (002) oriented AlN only provide a pure longitudinal mode, where the velocity is 10931 m/s and the K^2 is 6.245%.

For the (103) oriented AlN films, the wave propagation direction is $\hat{l} = \frac{1}{\sqrt{10}}\hat{a}_x l_x + \frac{3}{\sqrt{10}}\hat{a}_z l_z$. The Christoffel matrix of (103) oriented AlN films (Γ'_{103}) is given by (3).

$$\Gamma'_{103} = \begin{bmatrix} \Gamma'_{103(11)} & 0 & \Gamma'_{103(13)} \\ 0 & \Gamma'_{103(22)} & 0 \\ \Gamma'_{103(31)} & 0 & \Gamma'_{103(33)} \end{bmatrix}$$

$$\Gamma'_{103(11)} = \frac{9(e_{15}+e_{31})^2 + (c_{11}+9c_{44})(\varepsilon_{11}+9\varepsilon_{33})}{10(\varepsilon_{11}+9\varepsilon_{33})}$$

$$\Gamma'_{103(13)} = \frac{3((e_{15}+e_{31})(e_{15}+9e_{33}) + (c_{13}+c_{44})(\varepsilon_{11}+9\varepsilon_{33})}{10(\varepsilon_{11}+9\varepsilon_{33})}$$

$$\Gamma'_{103(22)} = \frac{9c_{44}+c_{66}}{10}$$

$$\Gamma'_{103(31)} = \frac{3((e_{15}+e_{31})(e_{15}+9e_{33}) + (c_{13}+c_{44})(\varepsilon_{11}+9\varepsilon_{33})}{10(\varepsilon_{11}+9\varepsilon_{33})}$$

$$\Gamma'_{103(33)} = \frac{(e_{15}+9e_{33})^2 + (9c_{33}+c_{44})(\varepsilon_{11}+9\varepsilon_{33})}{10(\varepsilon_{11}+9\varepsilon_{33})}$$

From solving the Christoffel matrix of (103) oriented, we obtain the eigenvalues: $\{E_1, E_2, E_3\}$, and the corresponding eigenvectors: $\{[0.2\,0\,1],[0\,1\,0],[1\,0\,0.2]\}$. Therefore, the quasi longitudinal mode correspond to the eigenvalue E_1 has the phase velocity $\sqrt{\frac{E_1}{\rho}}$. The phase velocities of the pure slow shear mode and the quasi fast shear mode are $\sqrt{\frac{E_2}{\rho}}$ and $\sqrt{\frac{E_3}{\rho}}$ respectively.

$$\begin{aligned} E_1 = {} & \frac{1}{20(\varepsilon_{11}+9\varepsilon_{33})}(10e_{15}^2 + 9e_{31}^2 + 81e_{33}^2 + 18e_{15}(e_{31}+e_{33}) \\ & + (c_{11}+9c_{33}+10c_{44})(\varepsilon_{11}+9\varepsilon_{33}) \\ & + ((10e_{15}^2 + 18e_{15}(e_{31}+e_{33}) + 9(e_{31}^2+9e_{33}^2) \\ & + (c_{11}+9c_{33}+10c_{44})(\varepsilon_{11}+9\varepsilon_{33}))^2 \\ & - 4(\varepsilon_{11}+9\varepsilon_{33})(c_{11}((e_{15}+9e_{33})^2 + (9c_{33}+c_{44})(\varepsilon_{11}+9\varepsilon_{33})) \\ & + 9(c_{44}(e_{31}-9e_{33})^2 - c_{13}^2(\varepsilon_{11}+9\varepsilon_{33}) \\ & + 9c_{33}((e_{15}+e_{31})^2 + c_{44}(\varepsilon_{11}+9\varepsilon_{33})) \\ & - 2c_{13}((e_{15}+e_{31})(e_{15}+9e_{33}) + c_{44}(\varepsilon_{11}+9\varepsilon_{33})))))^{0.5}) \end{aligned}$$

$$E_2 = \frac{9c_{44}+c_{66}}{10}$$

$$\begin{aligned} E_3 = {} & \frac{1}{20(\varepsilon_{11}+9\varepsilon_{33})}(10e_{15}^2 + 9e_{31}^2 + 81e_{33}^2 + 18e_{15}(e_{31}+e_{33}) \\ & + (c_{11}+9c_{33}+10c_{44})(\varepsilon_{11}+9\varepsilon_{33}) \\ & - ((10e_{15}^2 + 18e_{15}(e_{31}+e_{33}) + 9(e_{31}^2+9e_{33}^2) \\ & + (c_{11}+9c_{33}+10c_{44})(\varepsilon_{11}+9\varepsilon_{33}))^2 \\ & - 4(\varepsilon_{11}+9\varepsilon_{33})(c_{11}((e_{15}+9e_{33})^2 + (9c_{33}+c_{44})(\varepsilon_{11}+9\varepsilon_{33})) \\ & + 9(c_{44}(e_{31}-9e_{33})^2 - c_{13}^2(\varepsilon_{11}+9\varepsilon_{33}) \\ & + 9c_{33}((e_{15}+e_{31})^2 + c_{44}(\varepsilon_{11}+9\varepsilon_{33})) \\ & - 2c_{13}((e_{15}+e_{31})(e_{15}+9e_{33}) + c_{44}(\varepsilon_{11}+9\varepsilon_{33})))))^{0.5}) \end{aligned}$$

The K^2 value is derived by (4). We further use the material constants of the AlN in Table IV and get the following results.

The velocities and piezoelectric coupling constant (K^2) of the (103) oriented AlN films are:

quasi longitudinal mode:

velocity: 10717 (m/s)

K^2 : 4%

pure slow shear mode :

velocity : 5777 (m/s)

K^2 : 0%

quasi fast shear mode :

velocity : 5957 (m/s)

K^2 : 3.8%

The K^2 of the pure slow shear mode is zero. Therefore, the (103) oriented AlN films provide a quasi longitudinal mode and a quasi fast shear mode. The acoustic properties of the quasi longitudinal mode are the velocity (10717 m/s) and the K^2 value (4 %). The acoustic properties of the quasi fast shear mode are the velocity (5957 m/s) and the K^2 value (3.8%).

IV. CONCLUSIONS

The (103) oriented AlN films are successfully prepared on the silicon substrate by r.f. magnetron sputtering. It exhibits the XRD intensity of the (103) peak increase as the nitrogen concentrations decrease. The columnar grains of the (103) oriented AlN films grow perpendicular to the substrate surface and the surface morphology exhibited the small (about 30-50 nm) dense uniform grains. It is found the higher the degree of (103) orientation, the smaller FWHM value and the higher N/Al atom ratio. These material parameters are all inter-related. The (103) AlN films at 50 % has the strongest diffraction intensity of the (103) peak, the smallest FWHM value (0.252°) and the best N/Al atom composition ratio (0.92).

The theoretical bulk acoustic wave properties of (103) oriented AlN films are also studied in this research. It is found the (103) oriented AlN films could provide a quasi longitudinal mode and a quasi fast shear mode. The acoustic properties of the quasi longitudinal mode are the velocity (10717 m/s) and the K^2 value (4 %). The acoustic properties of the quasi fast shear mode are the velocity (5957 m/s) and the K^2 value (3.8%).

V. ACKNOWLEDGMENTS

This research was supported by the National Science Council of Republic of China, under grant No.NSC-95-2221-E-272-001.

VI. REFERENCES

[1] K. M. Lakin, J. S. Wang, G. R. Kline, A. R. Landin, Y. Y. Chen, and J. D. Hunt, "Thin Film Resonators and Filters," IEEE Ultrasonics Symposium, pp. 466-475, 1982.

[2] K. M. Lakin, G. R. Kline, R. S. Ketcham, A. R. Landin, W. A. Burkland, K. T. McCarron, S. D. Braymen, and S. G. Burns, "Thin Film Resonator Technology," IEEE 41st Annual Symposium on Frequency Control, pp. 371-381,1987.

[3] K. M. Lakin, G. R. Kline, R. S. Ketcham, J. T. Martin, and K. T. McCarron, "Stacked crystal filters implemented with thin films," IEEE Proceedings of the 43rd Annual Symposium on Frequency Control, pp. 536-543,1989.

[4] R. Jakkaraju, G. Henn, C. Shearer, M. Harris, N. Rimmer and P. Rich, "Integrated approach to electrode and AlN depositions for bulk acoustic wave (BAW) devices," Microelectronic Engineering, vol. 70, pp. 566-570, 2003.

[5] T. Nishihara, T. Yokoyama, T. Miyashita and Y. Satoh, "High performance and miniature thin film bulk acoustic wave filters for 5 GHz," IEEE Ultrasonics Symposium Proceedings, vol.1 pp.969 – 972, 2002.

[6] R. Lanz and P. Muralt, "Bandpass filters for 8 GHz using solidly mounted bulk acoustic wave resonators," IEEE Trans. Ultrason., Ferroelectr., Freq. Control, vol. 52, pp. 936–946, 2005.

[7] H. P. Lobl, M. Klee, R. Milsom, R. Dekker, C. Metzmacher, W. Brand, and P. Lok, "Materials for bulk acoustic wave (BAW) resonators and filters," J. Eur. Ceram. Soc., vol. 21, pp. 2633–2640, 2001.

[8] V. Mortet, M. Nesladek, J. M'Dhaen, G. Vanhoyland, O. Elmazria, M. B. Assouar, P. Alnot, and M. B. D'Olieslaeger, "Deposition of aluminium nitride film by magnetron sputtering for diamond-based surface acoustic wave applications," Phys. Stat. Sol. A, vol. 193, pp. 482–488, 2002.

[9] Hao Zhang and Eun Sok Kim, Journal of Microelectromechanical Systems, vol. 14, pp.699-706, 2005.

[10] D. S. Ballantine, R. M. White, S. J. Martin, A. J. Ricco, E. T. Zellers, G. C. Frye, and H. Wohltjen, *Acoustic wave sensors; theory, design, and physico-chemical applications*: Academic Press, 1996.

[11] S. M. Reddy, J. P. Jones, and T. J. L. Lewis, "The coexistence of pressure waves in the operation of quartz-crystal shear-wave sensors," J. Appl. Phys., vol. 83, pp. 2524–2532, 1998.

[12] L. McKenna, M. I. Newton, G. McHale, R. Lucklum, and J. Schroeder, "Compressional acoustic wave generation in micro-droplets of water in contact with quartz crystal resonators," J. Appl. Phys., vol. 89, pp. 676–680, 2001.

[13] G. Kovacs and A. Venema, "Theoretical comparison of sensitivities of acoustic shear-wave modes for (bio)chemical sensing in liquids," Appl. Phys. Lett., vol. 61, pp. 639–641, 1992.

[14] G. Wingqvist, J. Bjurstrom, L. Liljeholm, I. Katardjiev and A. Lloyd Spetz, "Shear mode AlN thin film electroacoustic resonator for biosensor applications," IEEE Sensors, pp. 492-495, 2005.

[15] J. Bjurstrom, G. Wingqvist, and I. Katardjiev, "Synthesis of textured thin piezoelectric A1N films with a nonzero c-axis mean tilt for the fabrication of shear mode resonators", IEEE Ultrasonics Symposium, vol. 1, pp. 321-324 ,2005.

[16] M. Ohring, *The Materials Science of Thin Films*: Academic Press, 1992.

[17] Fred S. Hickernell, "Measurement techniques for evaluating piezoelectric thin films," IEEE Proceedings of Ultrasonics Symposium, vol. 1, pp. 235-242, 1996.

[18] Mortio Akiyama, Hamid Reza Kokabi, Kazuhiro Nonaka, Kazuhisa Shobu and Tadahiko Watanabe, "Influence of Substrate Temperature on Physical Structure of AlN Thin Films Prepared on Polycrystalline $MoSi_2$ by rf Magnetron Sputtering," J. Am. Ceram. Soc., vol. 78, pp. 3304-3308, 1995.

[19] Joel F Rosenbaum, *Bulk Acoustic Wave Theory and Devices*: Artech House Boston London, 1998.

[20] John G. Gualtieri, John A. Kosinski, Arthur Ballato, "Piezoelectric materials for acoustic wave applications," IEEE Trans. Ultrason., Ferroelectr., Freq. Control, vol. 41, pp. 53-59, 1994.

Table I Sputtering conditions in the experiment

Target	**Aluminum (99.99%)**
Substrate	**Silicon**
Gas 1	**N_2 (99.9995%)**
Gas 2	**Ar (99.99%)**
Target-substrate distance	**5-10 cm**
Base pressure	**10^{-6} Torr**
Sputtering pressure	**3~7 m Torr**
RF power	**150~350 W**
Substrate temperature	**100~300 ℃**
Nitrogen concentration $(N_2/N_2+A_r)*100\%$	**50%, 58 %, 67 %, 75 %**
Total flow rate	**12 sccm**
Sputtering time	**120 min**

Table II The full width at half maximum of the AlN thin films deposited in different nitrogen concentrations

nitrogen concentrations	FWHM (degrees)
75%	0.72
67%	0.443
58%	0.288
50%	0.252

Table III The atom composition ratio (N/Al) of the AlN thin films deposited in different nitrogen concentrations

nitrogen concentrations	N/Al (%)
75%	0.72
67%	0.81
58%	0.87
50%	0.92

Table IV Material constants of the AlN

Density (kg/m^3)	ρ	3512
Elastic stiffness (G Pa)	c_{11}	345
	c_{12}	125
	c_{13}	120
	c_{33}	395
	c_{44}	118
	c_{66}	110
Piezoelectric stress constant (C/m^2)	e_{15}	-0.48
	e_{31}	-0.45
	e_{33}	1.55
Dielectric permittivity (ε_0)	ε_{11}	9
	ε_{33}	11

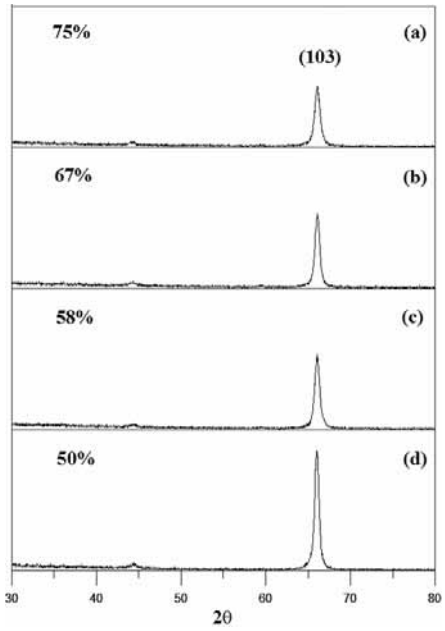

Fig.1 The XRD patterns of the AlN thin films deposited in different nitrogen concentrations (a) 75% (b) 67% (c) 58% (d) 50%

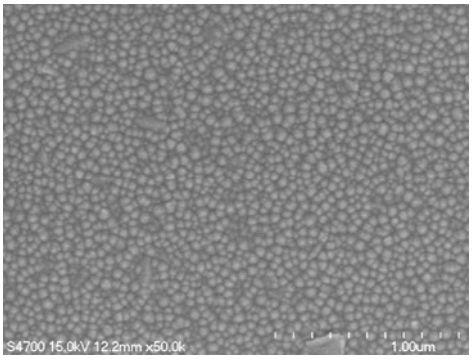

(a)

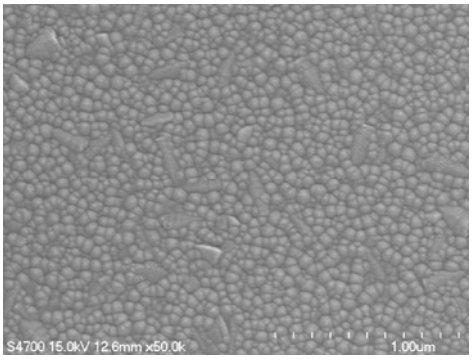

(b)

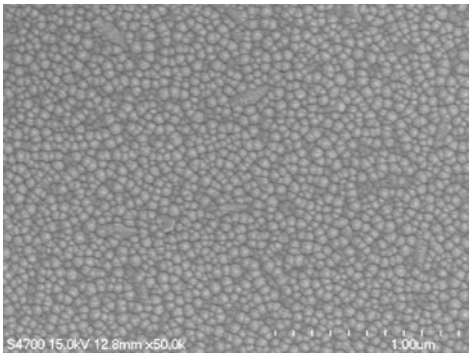

(c)

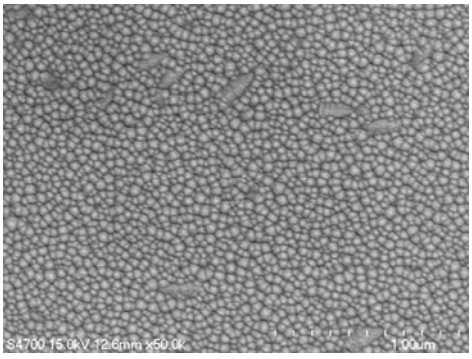

(d)

Fig.2 The SEM surface morphology of the AlN thin films deposited in different nitrogen concentrations (a) 75% (b) 67% (c) 58% (d) 50%

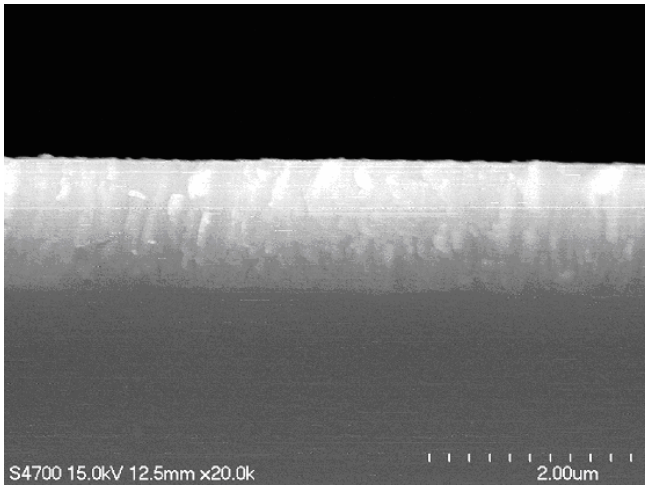

Fig.3 The SEM cross section of the (103) oriented AlN films

Ultra-Nanocrystalline Diamond Films for surface Acoustic Wave Device Application

I-Nan Lin[a*], Yen-Chih Lee[b], Su-Jien Lin[b], Nyan-Hwa Tai[b], Chi-Young Lee[b], and Hsiu-Fung Cheng[c]
[a] *Department of Physics, Tam-Kang University, Taipei, Taiwan 251, R.O.C.*
[b] *Department of Material Science and Engineering, National Tsing-Hua University, Hsin-Chu, Taiwan 300, R.O.C.*
[c] *Department of Physics, National Taiwan Normal University, Taipei, Taiwan 106, R.O.C.*

Abstract UNCD thin films possess very fine grains (~5-10 nm) and smooth surface (rms~10 nm) characteristics, which makes these films very promising for the applications in a device requiring smooth surface, such as surface acoustic wave devices. However, in order to deposit uniform and continuous diamond films at low substrate temperature, creation of nucleation centers is foremost step. In this study, various substrate pretreatment methods are employed for enhancing the formation of continuous and high nucleation density ultra-nano-crystalline diamond (UNCD) films. How the deposition parameters modify the growth behavior of the films will also be investigated. The results showed that the surface morphologies and other properties of these UNCD films are correlated intimately with pretreatment methods, although all the UNCD films have shown almost similar grain size and Raman spectra. Nucleation density as high as ~10^{11} cm^{-2} is grown from these applied pretreatment techniques. Moreover, maintaining ultra small grains size during the growth stage of diamond films is crucial in order to achieve very smooth surface for the films. For this purpose, Ar-plasma was utilized instead of commonly used H_2-plasma, to induce the C_2-radicals from the methane. All the processing parameters markedly affect the growth rate for the UNCD films. This investigation indicates that the key parameters are ratio of C_2^+ and H^+ radicals and substrate temperature.

I. Introduction

The unique combination of physical and chemical properties of diamond film has drawn more attention among researcher to use diamond in many applications. However, the high roughness of microcrystalline diamond films made them inapplicable in specific applications. In the recent past, very smooth ultrananocrystalline diamond (UNCD) films deposited by CH_4/Ar mixture have been established. The detail mechanism for the formation of UNCD from CH_4/Ar plasma has been reported [1, 2]. Recent application of nano-diamond films in bio-sensors [3], filed emission [4, 5] and bio-medical application [6] have shown the promising future of this nano-material. The adhesion of thin film to the substrates is very critical for the performance of MEMS and IC devices. Smooth and good adhesion properties are especially important to grow thick diamond films normally required for application like SAW[7] and MEMS devices[8].

The substrate pretreatment process strongly affects the nucleation and growth process of diamond films, which determines the deposition rate, crystal quality, surface roughness, and film-to-substrate adhesion. There are many methods for effectively forming the diamond nuclei on smooth Si substrates, including ultrasonication[9], carbide-metal addition[10], pre-carburized[11], and bias-enhanced-nucleation (BEN) method[12,13]. However, how does these processes alter the film-to-substrate adhesion is still not well understood. The main objective of the present work is to systematically investigate the relationship between nucleation pretreatment methods and growth condition with UNCD film characteristics, such as smoothness, film to substrate adhesion, bonding structure and deposition rate.

II. Experimental

In this study, four pre-nucleation techniques were used for forming diamond nuclei, which, in turn, is used for growing UNCD films. The Si-substrates were either (i) ultrasonicated with diamond powder solution, designated as *U-substrates*; (ii) ultrasonicated with diamond-&-Ti mixed powder solution, designated as *U-m substrates*; (iii) pre-carburized with CH_4/Ar plasma and then ultrasonicated with diamond powder solution, designated as *PC-U-substrates*; (iv) bias-enhanced nucleation process, designated as *BEN-substrates*. The UNCD films were grown in a IPLAS CRYNNUS 2.45 GHz microwave plasma enhanced chemical vapor deposition (MPECVD) system with the same deposition parameters.

Table I presents the detail experimental deposition conditions used for UNCD growth for investigating the growth stage behavior. The chamber pressure, CH_4/Ar ratio, temperature and microwave power were varied in series -P, -C, -T and -MW, respectively, keeping rest of the parameters constant. Surface morphology of samples was examined with a field emission scanning electron microscope (JEOL 6010). Surface topography and roughness was measured with atomic force microscope (PARK).The adhesion between UNCD and Si substrate was determined by a ramping-load scratch test using nanoindenter instrument equipped with a nanoscratch capability (MTS, USA). Crystal quality of UNCD films was investigated by Raman spectroscope using 514 nm argon laser beam (Renishaw).

III. Results and discussion

Figure 1 shows the surface morphology of UNCD films deposited after different nucleation methods, indicating that all the UNCD films grown on the U, U-m, PC-U and BEN substrates are rather uniform. Nucleation density of UNCD, which is determined by density of UNCD clusters, varies with pre-treatment methods, and is ~$5x10^8$/cm^2 for U-substrates, ~$5x10^9$ grains/cm^2 for U-m substrates, ~$1x10^{11}$ grains/cm^2 for PC-U substrates, and ~$1x10^{10}$ grains/cm^2 for BEN-substrates. The PC-U and BEN substrates are fully covered by UNCD, forming a continuous film, whereas the U- and U-m substrates are not fully covered by the UNCD. There are still some uncovered regions. The surface roughness for UNCD/U-Si films (57.75 nm-rms) is one order of magnitude larger than other UNCD films, which is, presumably due to lower nucleation density and incomplete substrate coverage of diamond grains for the U-Si substrates. As to the two films grown on high nucleation density substrates and were fully covered by diamond grains, the UNCD/PC-U and UNCD/BEN films, the surface roughness is 6.61 nm (rms) and 10.65 nm (rms), respectively. The rougher surface for UNCD/BEN-Si films is closely correlated with the smaller nucleation density and the formation of cauliflower morphology of the UNCD/BEN-Si films. All the UNCD films possess similar granular structure, containing grains with a size less than 10 nm, regardless of the pre-nucleation techniques used.

The diamond-to-substrate adhesion also changes pronouncedly due to these pre-nucleation processes, which will be discussed shortly. Figure 2(a) represents the typical sliding wear tracks on UNCD films resulted by nano-scratching testing procedures. It shows a clear critical point, where the UNCD films start to delaminate from substrate. Figure 2(b) shows the penetration profiles of ramping load nano-scratch surface for UNCD films grown on substrates pretreated by different nucleation methods, where the surface penetration is plotted as a function of the applied load. During the nano-scratching test, the Berkovich tip gradually penetrated through the UNCD films due to the linearly increasing load. The profile drops suddenly when the films delaminate from the substrate. The load at which the Berkovich tip suddenly drops is designated as critical loads (L_C).

The UNCD/U substrate films show poor film-to-substrate adhesion, which is apparently due to the low nucleation density and incomplete coverage of the UNCD films over the substrate. The UNCD/BEN-substrate films (67 mN) show the best film-to-substrate adhesion, with the critical loads about 3 times as large as that for UNCD/U-m (24 mN) and UNCD/PC-U (22 mN) films. The main factor influencing the adhesion behavior of the UNCD films is apparently the bonding strength between UNCD and Si substrate. In BEN process, the carbon species were accelerated, possessing high kinetic energy and easily form covalent bonding, SiC, when bombarding the Si-substrates, which has been proved in many literatures [14, 15]. The UNCD-to-Si substrate adhesion is thus greatly enhanced. In contrast, in all the other ultrasonication process, the kinetic energy of the powders is relatively low and the bombardment damage on the Si-substrate is relatively mild. An amorphous carbon film was formed prior to the formation of diamond nuclei. The UNCD-to-Si substrate adhesion is thus inherently low.

Figure 3 (a) shows the effect of various parameters on the deposition rate of UNCD. The growth rate of UNCD film was found to depend on microwave power (series-MW), chamber pressure (series-P), CH_4-Ar ratio (series-C) and substrate temperature (series-T). Optical emission spectroscopy (OES) is used to investigate the relationship between deposition parameters and plasma conditions, and use the ratio of the strongest C2 peak (516.5 nm) and H_α peak (656.3 nm) as a probe to monitor the plasma condition, shown in Fig. 3 (b). Both of deposition rate and C2/H_α ratio keep constant at low microwave region and decrease at high microwave region, and also increase with chamber pressure and CH_4-Ar ratio. The primary correlation between plasma condition and deposition rate is C2 species ratio which could be controlled by deposition parameters.

UNCD film was grown at a deposition rate of ~1 μm/h with following combination of parameters: 780 W microwave power, 150 torr pressure, 850°C temperature and 1 % methane to argon ratio. Figure 4 shows typical SEM image of thus obtained UNCD films and diamond grains of size less than 10 nm had been grown under above described deposition conditions. The surface roughness of UNCD films was similar under varied deposition conditions. Figure 5 shows Raman spectra of UNCD films which were deposited on silicon at different experimental conditions. These Raman spectra were found very similar to previously reported literatures [9, 16]. There are four main peaks normally observed at around 1140 cm^{-1}, 1350 cm^{-1}, 1480 cm^{-1} and 1580 cm^{-1} in visible Raman spectra of UNCD films. The broad peak at 1350 cm^{-1} and 1580 cm^{-1} are commonly termed as D-band and G band, respectively. The peaks at 1140 cm^{-1} and 1480 cm^{-1} were assigned to trans-polyacetylene segments [17, 18] presented at the grain boundaries and surfaces of nano-diamond films. In our study, the peak height of 1140 cm^{-1} and 1480 cm^{-1} suggested the increase in trans-polyacetylne percentage with substrate temperature (series-T). Raman spectra of series-P, -C and -MW samples were almost the same indicating not much changed in crystallinity of UNCD films by varying pressure, CH_4/Ar ratio and microwave power.

IV. Conclusion

UNCD films with grain size less than 10 nm was grown on Si-substrate pretreated by four different techniques. Nucleation density between 10^8~10^{11} grains/cm^2 was obtained, which depend on different pre-treated process. AFM study revealed that the PC-U process results in the best surface smoothness for UNCD films (rms 6.61 nm) due to high nucleation

density. The nano-scratch examination indicates that the high as 67 mN, which is about 3 times larger than other UNCD films grown on ultrasonication pretreated Si-substrates. Naturally smooth UNCD films with similar surface morphology and bonding structure could be prepared with wide deposition window. UNCD deposition rate and quality could be controlled by plasma conditions, especially C2 ratio and substrate temperature.

References

[1] D. Zhou, T.G. McCauley, L.C. Qin, A.R. Krauss, and D.M. Gruen, J. Appl. Phys. 83 (1998) 540.

[2] D.M. Gruen, Annu. Rev. Mater. Sci. 29 (1999) 211.

[3] A. Hartl, E. Schmich, J.A. Garrido, J. Hernando, S.C.R. Catharino, S. Walter, P. Feulner, A. Kromka, D. Sreinmuller, M. Stutzmann, Nature Materials, 3 (2004) 736.

[4] W. Zhu, G.P. Kochanski, S. Jin, Science 282 (1998) 1471.

[5] K. Wu, E.G. Wang, Z.X. Cao, Z.L. Wang, X. Jiang, J. Appl. Phys. 88 (2000) 2967.

[6] M.D. Fries, Y.K. Vohra, Diam. Rel. Mater. 13 (2004) 1740.

[7] F. Benedic, M.B. Assouar, F. Mohasseb, O. Elmazria , P. Alnot , A. Gicquel, Diam. Rel. Mater. 13 (2004) 347.

[8] L. Sekaric, J.M. Parpia, H.G. Craighead, T. Feygelson, B.H. Houston, J.E. Butler, Appl. Phys. Lett. 81 (2002) 4455.

[9] X. Xiao, J. Birrell, J. E. Gerbi, O. Auciello, J. A. Carlisle, J. Appl. Phys. **96** (2004) 2232

[10] W. L. Wang, K. J. Liao, L. Fang, J. Esteve, M. C. Polo, Diam. Rel. Mater., **10** (2001) 383

[11] L. Sekaric, J. M. Parpia, H. G. Craighead, T. Feygelson, B. H. Houston, J. E. Butler, Appl. Phys. Lett. **81** (2002) 4455

[12] S. Yugo, T. Kanai, T. Kimura, T. Muto, Appl. Phys. Lett. **58** (1991) 1036.

[13] Q. Chen, Z. Lin, Appl. Phys. Lett. **68** (1996) 2450.

[14] J. Gerber, S. Sattel, H. Ehrhardt, J. Robertson, P. Wurzinger, P. Pongratz, J. Appl. Phys., **79** (1996) 4388

[15] P. Reinke and P. Oelhafen, Phys. Rev. B, **56** (1997) 2183

[16] Y. Hayashi, T. Soga, Tribology International 37 (2004) 965.

[17] A.C. Ferrari, J. Robertson, Phys. Rev. B, 63 (2001) 121405.

[18] H. Kuzmany, R. Pfeiffer, N. Salk, B. Gunther, Carbon 42 (2004) 911.

Table I: Experimental deposition conditions for UNCD growth on BEN silicon surface.

Materials	Pressure (Torr)	CH_4/Ar Ratio (%)	Temperature (^oC)	MW Power (W)
Series-P	**100~150**	**1 %**	**400**	**1200**
Series-C	**150**	**0.5 ~ 2 %**	**400**	**1200**
Series-T	**150**	**1 %**	**400 ~ 600**	**750**
Series-MW	**150**	**1 %**	**600**	**600 ~ 1200**

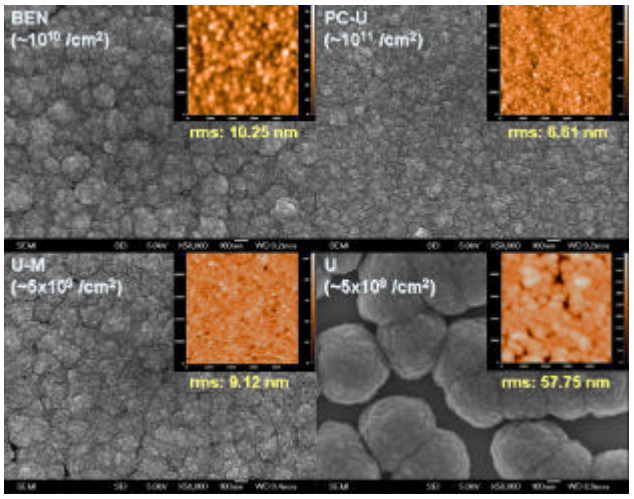

Fig 1. SEM and AFM micrographs of UNCD films grown on silicon substrates, which were pretreated by four different nucleation techniques; (a) *U:* ultrasonicated with diamond powder solution, rms ~ 57.75 nm; (b) *U-m:* ultrasonicated with diamond/Ti mixed powder solution, rms ~ 9.12 nm; (c) *PC-U:* pre-carburized and then ultrasonicated with diamond powder solution, rms ~ 6.61 nm; (d) *BEN:* bias-enhanced nucleation process, rms ~ 10.25 nm.

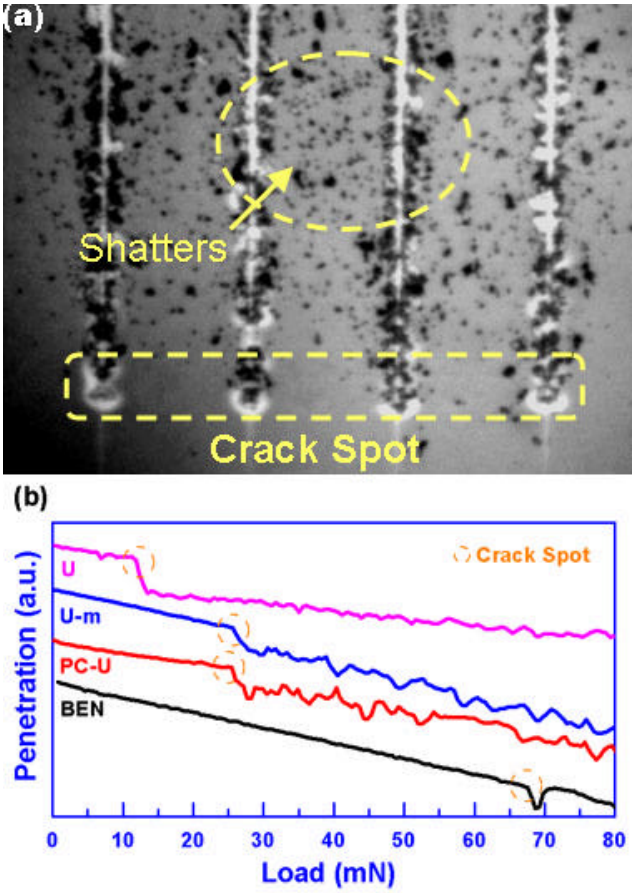

Fig. 2. (a) The micrograph showing the typical damaged image after nano-indentor tip scratching of UNCD films grown on silicon substrate and (b) the penetration curves of the nano-indentor tip scratching along UNCD films, where (i) *U:* ultrasonicated with diamond powder solution; (ii) *U-m:* ultrasonicated with diamond-&-Ti mixed powder solution; (iii) *PC-U:* pre-carburized and then ultrasonicated with diamond powder solution; (iv) *BEN:* bias-enhanced nucleation process).

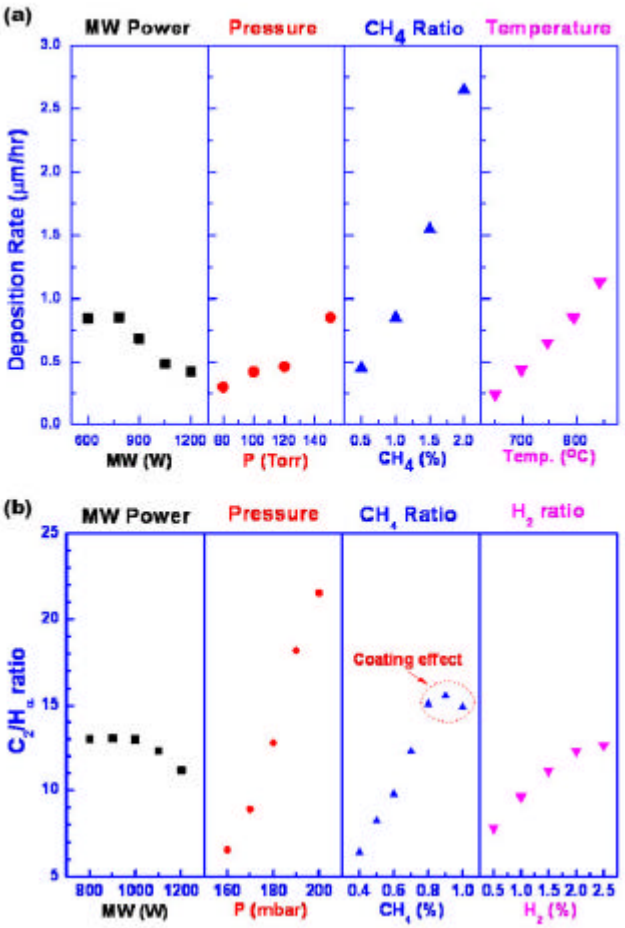

Fig. 3. Effect of total pressure (P), CH_4 to Ar ratio (C), substrate temperature (T) and microwave power (MW) on (a) the deposition rate and (b) optical emission spectra (OES) of UNCD

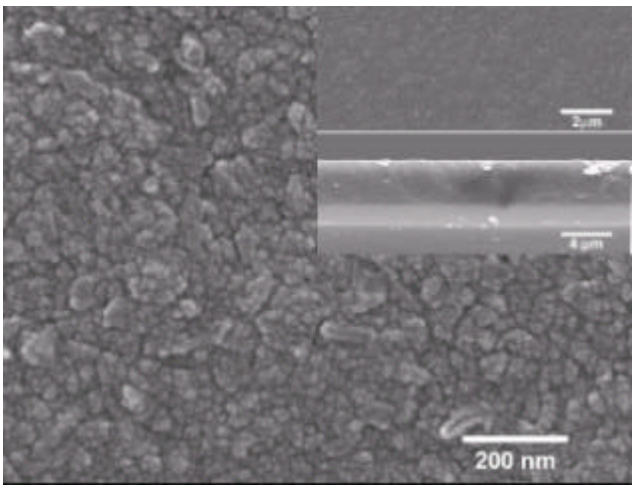

Fig. 4. FE-SEM image of UNCD grown under deposition condition of 750 W microwave power, 150 torr total pressure, total flow of 200 sccm Ar-CH_4 (CH_4-1 %) and substrate temperature 850 ^{o}C in 3 h deposition period. Inset shows a cross-sectional view.

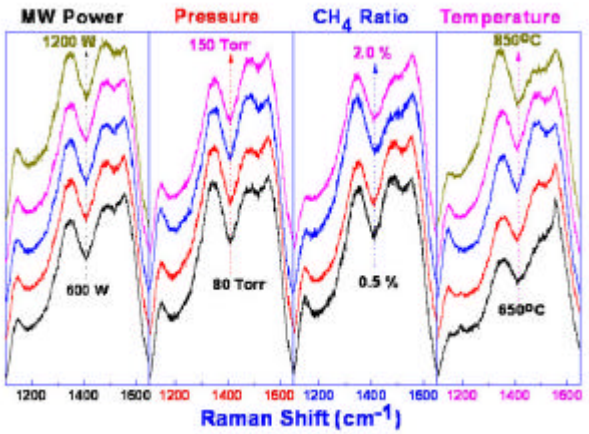

Fig. 5. Visible Raman spectra for UNCD films obtained under different experimental conditions.

A MEMS Vacuum Tube Resonator with Field-Emission Type Pick-up Mechanism

Winston Sun, Kiyotaka Yamashita, Benoit Charlot, Hiroyuki Fujita, and Hiroshi Toshiyoshi

***Abstract*—In this paper we propose a new method for detecting nanometric oscillation that is compatible with RF-MEMS (radio frequency-micro electro mechanical system) band-pass filter applications. A silicon microfabricated oscillator (resonator) has been designed to have a pair of sharp tips made of single crystalline silicon located with a few microns gap. A DC voltage (~ 240 V) was applied to the gap to cause the field-emission (FE) current (~ 100 nA) through the vacuum (2 x 10^{-8} Torr) between the tip. The FE current through the vacuum is electrostatically modulated by the mechanical oscillation of the electrically biased modulator, such that the amplitude o of oscillation can be known by the modulation of the sensed FE current.**

***Index Terms*—MEMS, resonator, oscillator, field emission**

I. Introduction

Conventional radio-frequency microelectromechanical system (RF-MEMS) mechanical filters and recently developed devices utilize capacitive coupling for both excitation and detection of nanometric oscillation [1-4]. However, the capacitance diminishes fast when the device size decreases from several hundreds micron scale to a micron, which makes signal detection difficult. Besides, direct capacitive coupling often associates with mismatching issues and stray capacitance of electrical interconnection, and it also suffers from small fan out.

Recent vacuum microelectronics achievements [5,6] have opened up the room for more application opportunities based on the field-emission (FE) effect. Micro- or nanomechanical resonators have the advantages of generally high quality factor (Q-factor), compatibility with batch fabrication capability, and well-established semiconductor microfabrication processes. As device dimensions such as tip radii and anode-cathode gap decrease, the field-emission current increases even with a given constant bias voltages. This work investigates the possibilities of signal detection by integrating the field-emission tips in a MEMS resonator device by using only one photolithography step for simple fabrication processes.

Winston SUN is with the Institute of Industrial Science (IIS), the University of Tokyo, 4-6-1 Komaba, Meguro-ku, Tokyo, Japan (e-mail: winston@iis.u-tokyo.ac.jp)

Kiyotaka Yamashita is also with IIS, the University of Tokyo. (e-mail: kiyo@iis.u-tokyo.ac.jp)

Benoit Charlot is currently with LIMMS / CNRS – IIS (UMI 2820), Laboratory for Integrated Micro Mechatronic Systems, a Japan-France international collaboration lab located at the IIS, the University of Tokyo, Tokyo, Japan (e-mail: benoit@iis.u-tokyo.ac.jp)

Hiroyuki Fujita is the Director of Center for International Research on Micro Mechatronics (CIRMM) at the IIS, the University of Tokyo, Tokyo, Japan (e-mail: fujita@iis.u-tokyo.ac.jp)

Hiroshi Toshiyoshi is also with the CIRMM, IIS, the University of Tokyo (e-mail: hiro@iis.u-tokyo.ac.jp)

II. Field Emission Modulator Mechanism

The conceptual operation principle for the field-emission resonator MEMS is illustrated in Figure 1 (a). In between the sharp tips, an electrically biased silicon micromachined resonator is located along the field-emission current path, which is intervened by the resonator; the FE current in vacuum is transmitted straight to the opposing tip when no electromechanical interference exists. On the other hand, the current is spatially modulated when the electrically biased oscillator is brought into close vicinity to the path.

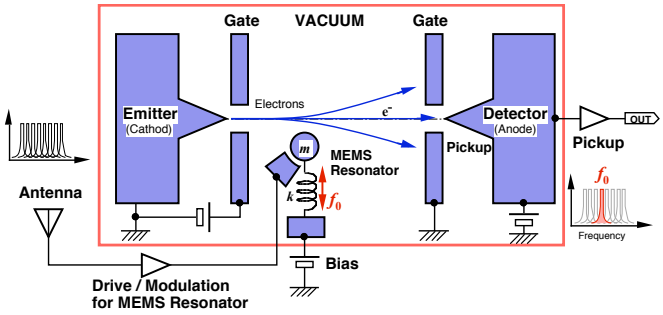

(a)

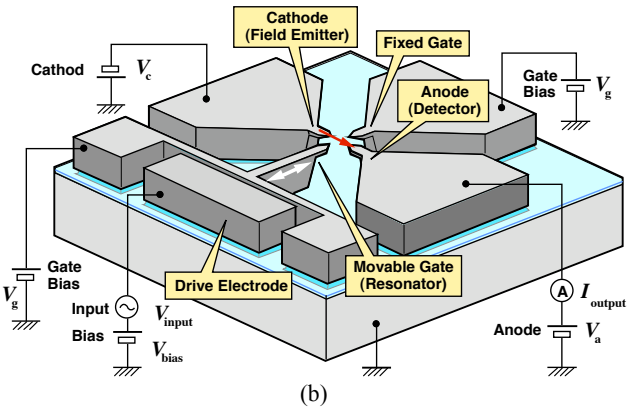

(b)

Figure 1 Conceptual drawing of the proposed MEMS resonator with field emission oscillation mechanism that works as a band-pass filter. (a) Parameters m, f_0, and k are the resonator mass, modulation frequency (= resonant frequency), and elastic constant of the resonator suspension, respectively. (b) Illustration of the electrical wiring for the MEMS resonator

device. Parameters v_c, v_a, and v_g are the voltages applied to the cathode, anode, and the gate, respectively. Parameters v_{in}, v_b are the sinusoidal input and constant bias voltages for the resonator, respectively. Parameters i_{FE}, is the output field-emission current.

The electrons that pass the fixed screening aperture gates are finally detected by the anode, by which a signal component of a particular frequency is band-pass filtered. The higher the level of vacuum we would make, the easier it is for the field emission to be excited. Thanks to the reduced air damping effect, the micro resonator can be oscillated at a larger Q factor.

For a wireless application, for instance, frequency signal picked up by the antenna is pre-processed and fed into the driving electrode for the micromechanical resonator. The objective of this work is to correlate the information carried by the FE current and the dynamic characteristics of the MEMS resonator. The electrical connections needed to operate the MEMS resonator are illustrated in Figure 1 (b); the MEMS resonator is implemented as a micromechanical bridge with a movable tip driven by the electrostatic coupling. The four tips are arranged in a cross that is different from the conceptual drawing in Figure 1 (a); such tips and small gap could be made by the silicon micromachining technique, as discussed in the following section.

III. MEMS Fabrication

The fabrication process for the MEMS resonator is illustrated in Figure 2. In Fig. 2 (a), we started the process with a silicon-on-insulator (SOI) wafer with an active silicon layer of 10 microns, buried oxide of 2 microns, and a silicon handle wafer of 625 microns. After oxidizing the silicon surface and patterning the oxide mask, the mask patterns were transferred to the device layer by using the silicon deep reactive ion etching (DRIE) process as shown in Fig. 2 (b). In Fig. 2 (c), the tips were sharpened by the anisotropic wet etching of silicon in a 15% tetramethyl ammonium hydroxide (TMAH) solution at 60 degree C. Under the protection of the oxide mask, the THAM anisotropic etching from the silicon sidewalls caused the beam cross sections to be come trapezoidal or even triangular shape. Once TMAH etching was adequate to separate these narrow connecting beams, the oxide mask could be removed in a buffered hydrofluoric (BHF) acid solution. More timed THAM etching to further sharpen the tips might be necessary.

As the electrical leakage current was related to the surface conditions at the interface between the BOX layer and the handle layer, the timed partial BOX removal in Fig. 2 (d) sometimes was a critical step. At the current stage, the exact mechanism of the leakage remains unclear to us. For the MEMS resonator device that contains a resonator, we used vapor-phase hydrofluoric acid (VHF) etching to prevent the movable components from sticking to the substrate by the surface tension force of liquid [8]. The etching time must be adequate to sacrificially release the MEMS resonator but must not too long to completely remove the exposed BOX layer [7].

The processed chips were then placed under the optical microscope on a probe station. The microactuators were mechanically displaced by using a micromanipulated probe to determine if the movable parts were fully released without stiction. Once successful release was observed, the chip was then wire-bonded onto a ceramic chip holder. After connecting a device to a function generator, mechanically oscillation at the resonator tip was visually observed. In our current prototype devices, the resonators were designed to be large enough for visual observation to make it easy for us to correlate the mechanical motion with the FE current modulation.

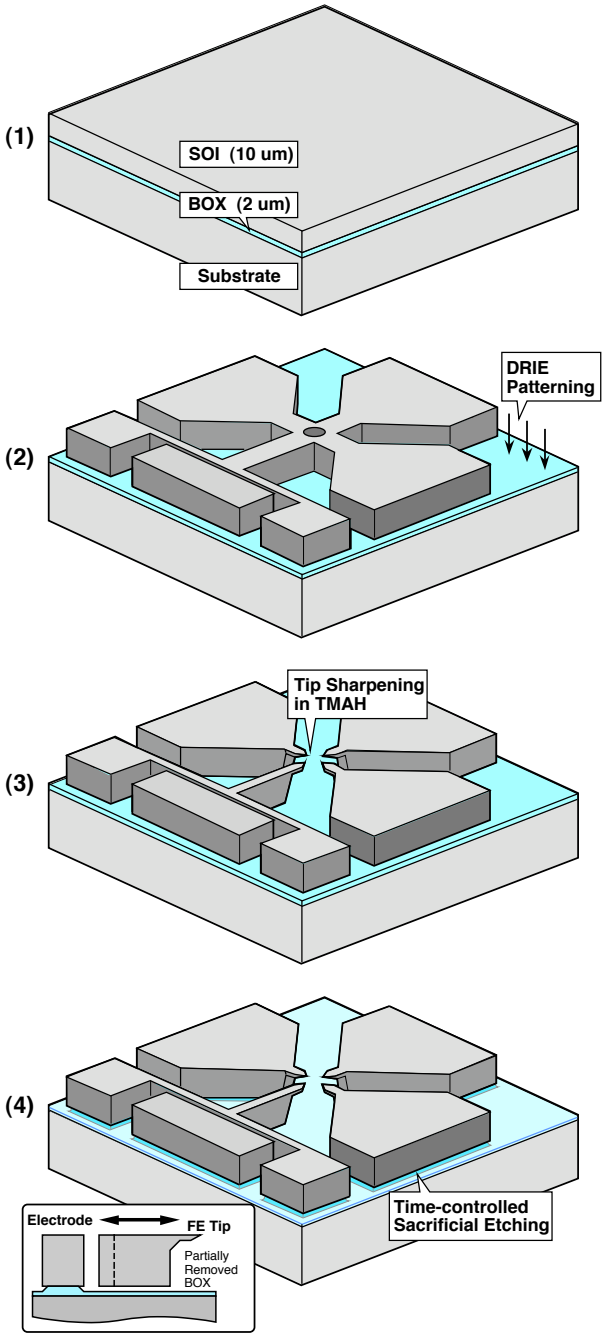

Figure 2. The fabrication process illustrates how the sharp anode-cathode tips of the RE device are formed. The same process can also be used on the SR device except that the vapor HF etching is optional. (a) The process begins with transferring the mask pattern to the front-side of an oxidized SOI wafer. (b) With the protection of an oxide mask, TMAH etching shapes the precursor tips. (c) Oxide mask removal and further TMAH etch separate and sharpen the tips. (d) Partial vapor HF etch appears to help reduce leakage current. Exact reason for such behavior is not fully understood

IV. Field-Emission Detection Experiment

The experimental setup includes a semiconductor parameter analyzer (SPA, Agilent E5263A) and the vacuum chamber that provides the $2\text{x}10^{-8}$ Torr ($2.7\text{x}10^{-6}$ Pa) vacuum environment. The current flow through the anode channel i_a and the cathode channel i_c can be measured simultaneously by the SPA. A multichannel electrical interface is used to provide the vacuum chamber. In our experiment, one output channel of the SPA provides a constant positive anode voltage v_a, which is equipoential to the gate voltage v_g, and the other output channel sweeps a negative cathode voltage v_c, while the SPA simultaneously captures the electrical current variation along the circuit in the nano Ampere range. The general purpose interface bus (GPIB) input/output (I/O) interface of the SPA is connected througha GPIB-universal serious bus (USB) conversion module to a personal computer (PC) with the LabView software. An interface program was written for control and data acquisition.

V. Results and Discussion

The field-emission phenomenon can be mathematically described by the governing Fowler-Nordheim (FN) equation show in Equation (1). It expresses the FE current density J as a function of the external electric field F and the material work function ϕ (~4.5 eV for bare silicon) [5, 9],

$$J = 1.54\times10^{-6}\frac{F^2}{1.1\phi}\exp\left[-6.83\times10^{7}\frac{\phi^{3/2}}{F}\left\{0.95-\left(\frac{3.79\times10^{-4}\sqrt{F}}{\phi}\right)^2\right\}\right]. \quad (1)$$

In Equation (1), the units of the FE current density J and the external electric field F are A cm^{-2} and V cm^{-1}, respectively. The FE current i_{FE} can be expressed in terms of J and the effective FE tip area α as follows:

$$i_{FE} = \alpha J. \quad (2)$$

The relation between F and the electric field coefficient β and the anode-cathode potential difference v_{ac} is shown as follows:

$$F = \beta |v_a - v_c| = \beta v_{ac} \quad (3)$$

For our MEMS resonator, the values of α and β are estimated to be $8.9\text{x}10^{-14}$ cm^2 and $6.4\text{x}10^{5}$ cm^{-1}, respectively. By combining and rearranging Equations (1), (2), and (3), the field-emission current can be written in terms of the anode-cathode potential difference v_{ac}, effective tip area of α, electric field coeffcient β, and work function ϕ as follows:

$$J = \left\{1.42\times10^{-6}\frac{\alpha\beta^2}{\phi}\exp\left(\frac{10.4}{\sqrt{\phi}}-\frac{6.44\times10^{7}\phi^{3/2}}{\beta v_{ac}}\right)\right\}v_{ac}^2. \quad (4)$$

After tailoring the MEMS resonator design and fabrication conditions, the anode-cathode gap was reduced to 3 microns, and the FE current was measured to be over 90 nA at a bias voltage of 240 V, as shown in Fig. 4 (a). The values of α and β were estimated by using a fitting curve to Equation (4), and we found α and β to be $1.1\text{x}10^{-13}$ cm^2 and $5.8\text{x}10^{5}$ cm^{-1}, respectively. A corresponding FN plot is shown in Fig. 4 (b). Our recent experiment (now shown in this paper) shows further improvement of FE current after coating the silicon tips with metal of lower work functions, such as molybdenum and yttrium.

VI. Conclusion and Outlook

MEMS resonator with field-emission current detection mechanism has been designed and developed. The FE current was clearly observed in high vacuum. MEMS resonators of higher resonant frequencies (MHz range) are under development by using the Lame resonator design. Devices working with lower bias voltages (~10 V) are developed separately by using a shorter cathode-anode gap. To our interest, FE current at low vacuum level was also observed thanks to the small anode-cathode distance compared with the mean free path of the electrons. This suggests a potential of device-level vacuum packaging rather than using a bulky vacuum system, leading to a compatibility with mobile electronics.

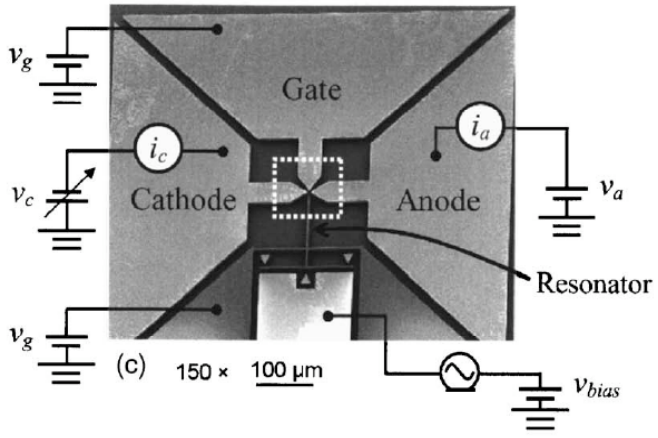

(a)

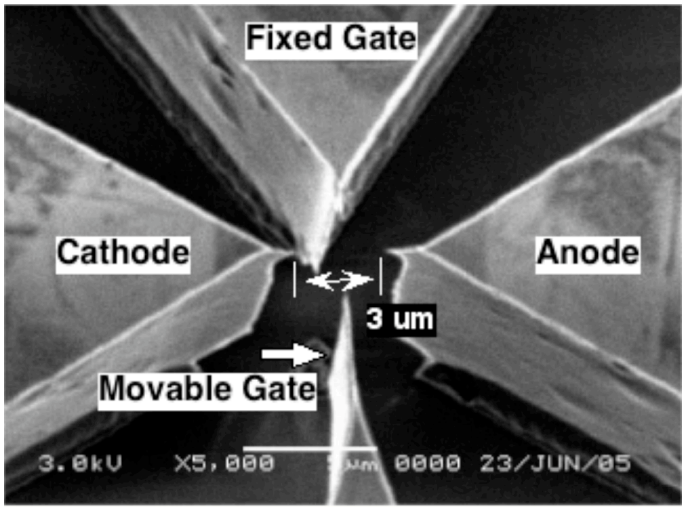

Figure 3 SEM picture of the MEMS resonator. (a) The entire view of the resonator and the field-emission tips. The actuator tip is electrostatically modulated by using the mechanism of parallel-plate electrodes. (b) A close up view of the field emission tips.

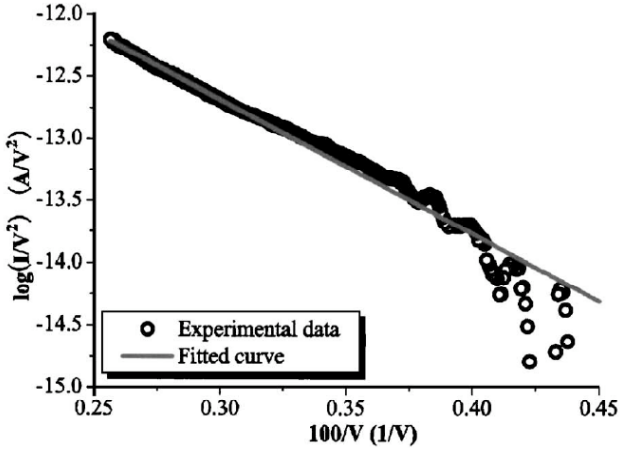

(b)

Figure 4 I-V curve of the FE current from the MEMS resonator device. Slightly varied TMAH etching time produces closer gap of 3 microns and sharper tips, which result in larger FE current. At a 240 V anode-cathode potential difference, FE current is measured to be about 94.03 nA. (b) FN plot of the RE device.

ACKNOWLEDGMENT

This research is supported in part by the 21st Century COE (Center of Excellence) program of the Electrical Engineering Department, the University of Tokyo. A part of this work was supported by the Grant-in-Aid Program for Scientific Research provided by the Japan Society for Promotion of Science (JSPS). Photolithography masks used in this work were developed by using the Electron Beam facility of the VLSI Design and Education Center (VDEC), the University of Tokyo.

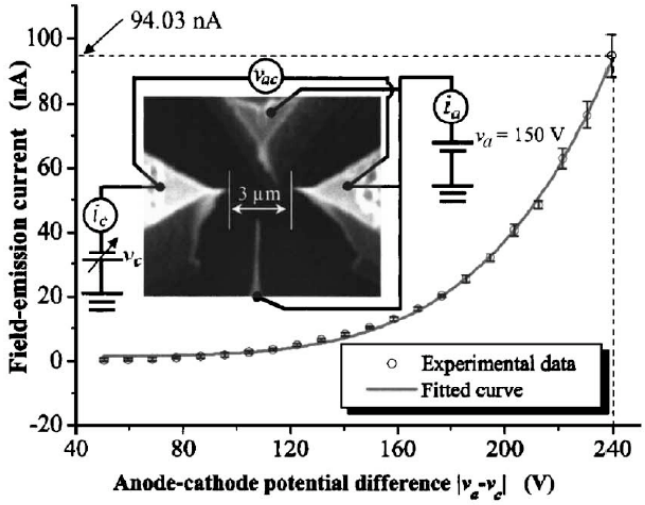

(a)

REFERENCES

[1] L. Lin, R. T. Howe, and A. P. Pisano, J. Microelectromech. Syst. Vol. 7, p. 286, 1998.
[2] K. Wang and C. T.-C. Nguyen, J. Microelectromech. Syst. Vol. 8, p 534, 1999.
[3] M. U. Demirci and .C. T.-C. Nguyen, Proc. 18th IEEE Int. Conf. on Microelectromech. Syst. (MEMS 2005), Miami, FL, Jan. 30 – Feb. 3, 2005 (IEEE, New York, 2005), p. 207.
[4] Y. Xie. S. S. Li, Y. W. Lin, Z. Ren, and C. T.-C. Nguyen, Proc. 18th IEEE Int. Conf. on Microelectromech. Syst. (MEMS 2005), Miami, FL, Jan. 30 – Feb. 3, 2005 (IEEE, New York, 2005), p. 219.
[5] D. Temple, Mater. Sci. Eng., R. 24, 185, 1999.
[6] Y. Takiguchi, et al., IEICE Trans. Electron. E85-C, p. 1916, 2002.
[7] N. Nozawa, K. Kakushima, G. Hashiguchi , and H. Fujita, Proc. 3rd Workshop on Physical Chemistry of Wet Etching of Silicon, Nara, Japan, 4-6 June 2002, pp. 52-53.
[8] Y. Fukuta, H. Fujita, and H. Toshiyoshi, Jpn. J. Appl. Phys., Part. 1, Vol. 42, p. 3690, 2003.
[9] R. H. Fowler and D. L. Nordheim, Proc. R. Soc. London, Ser. A. vol. 19, p. 173, 1928.

Chip-scale Atomic Clock Based on Coherent Population Trapping

Shigeyoshi GOKA and Yasuaki WATANABE
Graduate School of Sciences and Engineering,
Tokyo Metropolitan University
Minamiosawa Hachioji-shi, Tokyo, 192-0397 Japan
goka@eei.metro-u.ac.jp

I. INTRODUCTION

Miniaturized atomic frequency-references that use lamp-pumped alkali-vapor cells and external microwave fields to probe clock transitions while retaining stability at long-term frequency that is typical of atomic standards (~ 10-11 @ 1 second for 1 day) have recently become commercially available. However, their size (>100 cm^3) and power dissipation (>5 W) are insufficient to fulfill the demands of applications such as global-positioning system receivers and in-field telecommunication devices. They require compactness, low cost, low power consumption, high-frequency stability, and robustness, none of which can be met with atomic beams or fountains.

Coherent population trapping (CPT), which was discovered more than thirty years ago by Alzetta et al. [1], is a resonance phenomenon due to the quantum mechanical interference effect in atomic systems that cancels the absorption of a bichromatic light field [2]. These narrow features were recognized as possible microwave-frequency references, such as laser cooling below the one photon recoil limit and high-sensitivity magnetometry [3,4]. CPT resonances for alkali atoms can be probed between long-lived ground states in an all-optical way using two different laser wavelengths.

A vertical-cavity surface-emitting laser diode (VCSEL) fundamentally only operates on one specific longitudinal laser-mode and can easily be fabricated as part of a whole array of emitters [5,6]. Recent progress with VCSEL has obtained high modulation bandwidths of several gigahertz and near-infrared wavelengths where cesium and rubidium have their strongest D1 and D2 resonance lines (894, 852, 794 and 780 nm). These characteristics can provide a bichromatic light field, which is required for the CPT phenomenon, using the direct modulation of a laser current; therefore, VCSELs are very suitable for compact frequency references and magnetometers.

A program for chip-scale atomic clocks (CSACs) using CPT was introduced in 2001 by the National Institute of Standards and Technology (NIST) for portable applications and the program's goals are listed.

- Volume < 1 cm^3
- Power dissipation < 30 mW
- Fractional frequency instability < 10^{-11} @ 1hr

In addition, a cost of a CSAC is aimed at less than US$ 10 by using a method of micro-electro-mechanical system (MEMS) fabrication. Since the NIST program started, much research on CSACs has been done. A summary of CSACs based on CPT is introduced in this paper.

II. Coherent Population Trapping Resonance

CPT can occur in the Λ system shown in Fig. 1. The two ground states (|1> and |2>) are coupled to a common excited state (|3>) via two light fields interacting with two transitions (ω1 and ω2). If the difference frequency, Δ_{hfs}, of the light fields matches the ground-state splitting, the atoms are optically pumped into a coherent superposition of the ground states, which no longer absorbs light (the so-called "dark-resonance"). The listed $\Delta_{hfs}/2\pi$ and wavelengths of the light field between ground and excited states corresponding to ω2 in rubidium and cesium alkali atoms are shown in Table 1.

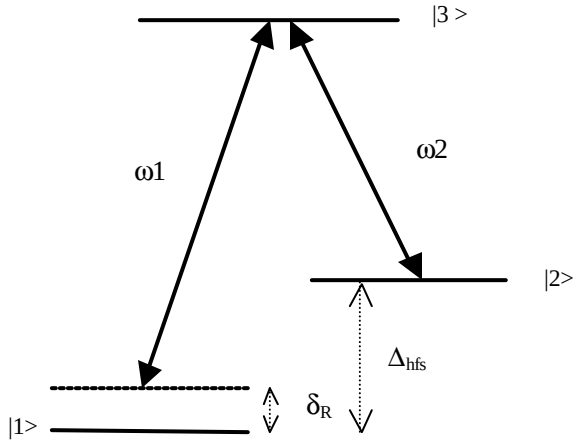

Fig. 1 Three level Λ system in alkali-metal atoms.

Table 1 Wavelengths of light field between ground and excited states and frequency differences between two ground states.

Atom	D1 line	D2 line	$\Delta_{hfs}/2\pi$
Rb^{85}	795 nm	780 nm	3.0 GHz
Rb^{87}			6.8 GHz
Cs	894 nm	852 nm	9.2 GHz

III. Experimental Configuration

A VCSEL's injection current is modulated at half the ground-state hyperfine splitting frequency of an alkali atom to prepare a bichromatic light field. The modulation frequency in Cs is 4.6 GHz and the two first-order sidebands are used to excite the resonance [3]. The temperature of the VCSEL and DC drive current are carefully controlled to keep the output laser frequency constant. The linearly polarized output from the VCSEL is sent through a quarter-wave plate to create circular polarization and is attenuated by natural-density filters [7]. A cell is placed inside a magnetic shield to reduce stray magnetic fields and a longitudinal magnetic field is applied with coils to isolate the m=0 to m=0 transition from the other m=0 transitions [8]. The temperature of the cell is also stabilized to avoid light shifts and power broadening in the dark line. The light transmitted through the cell is detected with a photodiode. Figure 2 outlines the system for measuring an atomic reference using the Cs D2-line (Kitching et al. [7]).

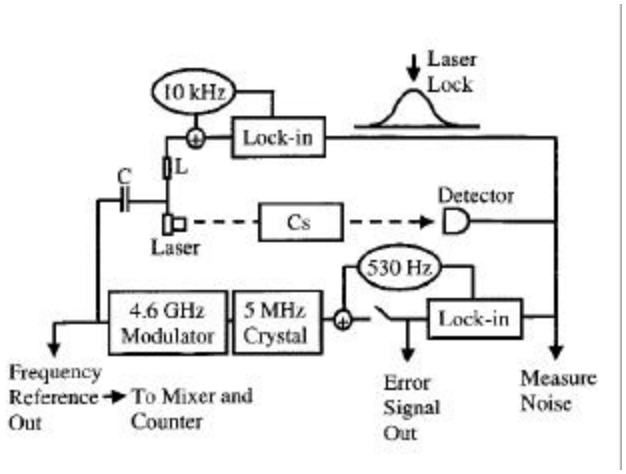

Fig. 2. Electronics and servo systems used to (a) lock laser to absorption profile and (b) lock crystal oscillator to dark-line resonance. (Kitching et al., IEEE Trans. Instrum. Meas., 49, 1313, 2000. [7])

IV. Microfabricated Vapor Cells

Conventional atomic vapor cells have been produced with glass-blowing techniques using gas torches. However, these methods of fabricating cells are not feasible at sizes less than 1 cm. Liew et al. [9] developed methods of fabricating millimeter-sized cesium vapor cells using silicon micromachining instead of glass-blowing technology. There is a photograph of a fabricated micro Cs cell in Fig. 3. Cells were heated and light from a VCSEL (852 nm) was passed through them. The results revealed typical cesium optical absorption consisting of

two resonances separated by 9.2 GHz, corresponding to the two ground-state hyperfine levels. Cells fabricated with this method have been applied to a state-of–the-art micro-atomic-clock physics package [10].

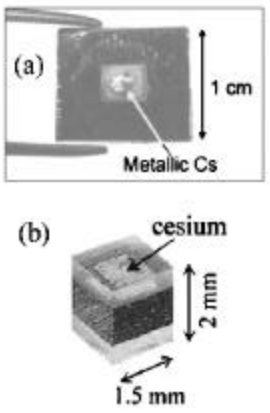

Fig. 3. (a) Photograph of top cell showing cesium inside. (b) Photograph of smaller cesium cell. (Liew et al., Appl. Phys. Lett., 84, 2694, 2003. [9])

V. HIGH CONTRAST CPT RESONANCE

It is important that the CPT resonance line for atomic-frequency references has large amplitude is narrow to gain the signal-to-noise ratio of the resonance. Experiments with the D2 line of Cs have shown that the signal contrast is roughly 1%. The amplitude of CPT resonance is inversely proportional to the number of the excited-state hyperfine levels. According to Stahler et. al [11], the excitation of ^{85}Rb D1 transition results in both narrower resonance and more resonance contrast than with D2 transition, as plotted in Fig. 4 This method of improving CPT contrast was applied to the ^{87}Rb-based CSAC [12-13] to improve its long-term frequency stability. The results obtained by Knappe et al. [13] are plotted in Fig. 5. Long-term frequency stability was significantly improved with a novel method of filling chip-scale alkali vapor cells and ^{87}Rb D1 transition.

An other method of increasing CPT contrast was reported by Kargapoltsev et al. [14]. The amplitude of nonlinear dark resonance excited on the D1 line with a counter-propagating bichromatic $\sigma+$ - $\sigma-$ field can be

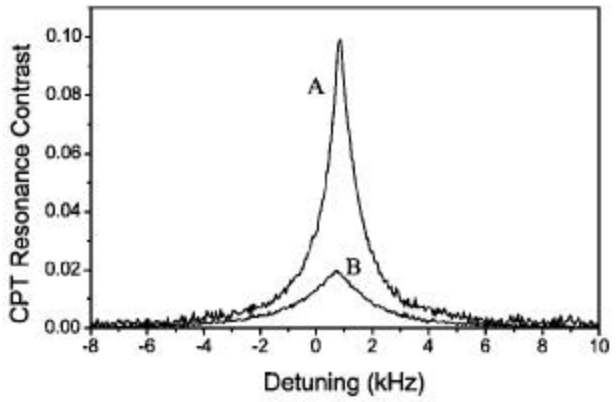

Fig. 4. CPT resonance for excitation on A, D1 transition and B, D2 transition with resonant laser intensity of 160 $\mu W/cm^2$. (Stahler et. al, Opt. Lett., 27, 1472, 2002.[10])

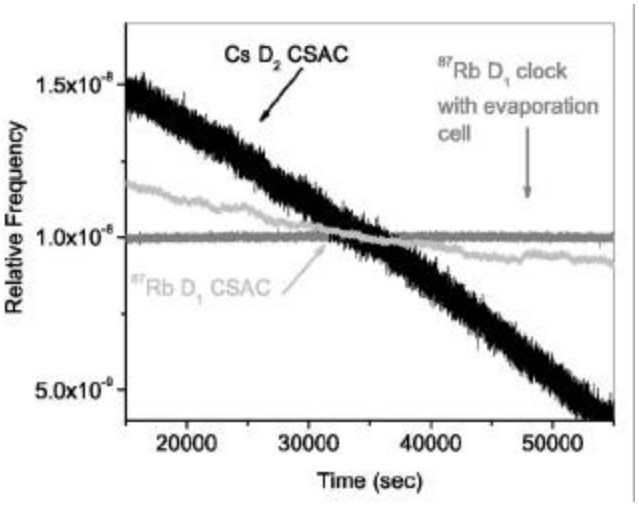

Fig. 5. Output frequency of CPT clock, normalized to frequency of ground-state hyperfine splitting of alkali atom, for Cs atoms excited on D_2 line CSAC (black), ^{87}Rb atoms excited on D_1 line CSAC (light gray) and ^{87}Rb D_1 line frequency reference based on cell fabricated with new evaporative filling method (gray). (Knappe et al., Opt. Lett., 30, 2351, 2005. [13])

improved over the usual scheme of co-propagating circularly polarized laser beams in small Cs cells having a diameter of 2mm and a length 4mm. These results may be important in applications such as highly miniaturized atomic frequency references or magnetometers. Their initial experiments confirm the theoretical predictions.

VI. CONCLUSION

CSACs based on CPT were briefly introduced. Prototype state-of–the-art ultra-small chip CSACs were fabricated using MEMS technology and their characteristics were improved. However, many problems remain to be solved in commercial products, such as power dissipation, down sizing, long lifetime, and the accuracy and stability of frequency.

REFERENCES

[1] G. Alzetta, A. Gozzini, L. Moi, and G. Orriols, "An experimental method for the observation of the RF transitions and laser beat resonances in oriented Na vapor," Nuovo Cimento, vol. B 36, pp. 5–20, 1976.

[2] R. Wynands and A. Nagel, "Precision spectroscopy with coherent dark states", Appl.Phys. B, Vol. 68, 1, 1999

[3] C. Affolderbach, A. Nagel, S. Knappe, C. Jung, D. Wiedenmann and R. Wynands "Nonlinear spectroscopy with a vertical-cavity surface-emitting laser" Appl. Phys. B 70, 407-413, 2000

[4] P. D. D. Schwindt, S. Knappe, V. Shah, L. Hollberg, J. Kitching, L. Liew and J. Moreland, "Chip-scale atomic magnetometer," Appl. Phys. Lett., 85, 6409, 2004.

[5] K. Iga, F. Koyama, and S. Kinoshita, "Surface-emitting semiconductor lasers," IEEE J. Quantum Electron., vol. 24, pp. 1845–1855, 1988.

[6] M. Grabherr et al., "Efficient single-mode oxide-confined GaAs VCSEL's emitting in the 850-nm wavelength regime," IEEE Photon. Technol. Lett., vol. 9, pp. 1304–1306, 1997.

[7] J. Kitching, S. Knappe, N. Vukicevic, L. Hollberg, R. Wynands, and W. Weidemann, "A microwave frequency reference based on VCSEL-driven dark line resonances in Cs vapor," IEEE Trans. Instrum. Meas., 49, 1313, 2000.

[8] S. Knappe, V. Velichansky, H.G. Robinson, J. Kitching, and L. Hollberg, "Compact atomic vapor cells fabricated by laser-induced heating of hollow-core glass fibers," Rev. Sci. Instrum., 74, 3142, 2003.

[9] L. Liew, S. Knappe, J. Moreland, H. Robinson, L. Hollberg and J. Kitching, "Microfabricated alkali atom vapor cells," Appl. Phys. Lett., 84, 2694, 2003.

[10] J. Kitching, S. Knappe, L. Liew, J. Moreland, P. Schwindt, V. Shah, V. Gerginov, and L. Hollberg "Microfabricated atomic frequency references," Metrologia, 42, S100, 2005.

[11] M. Stahler, R. Wynands, S. Knappe, J. Kitching, L. Hollberg, A. Taichenachev, and V. Yudin, "Coherent population trapping resonances in a thermal 85Rb vapor: D1 versus D2 excitation," Opt. Lett., 27, 1472, 2002.

[12] S. Knappe, P. Schwindt, V. Shah, L. Hollberg, J. Kitching, L. Liew, and J. Moreland, "A chip-scale atomic clock based on 87Rb with improved frequency stability," Opt. Exp., 13, 1249, 2005.

[13] S. Knappe, V. Gerginov, P. D. D. Schwindt, V. Shah, H. G. Robinson, L. Hollberg, and J. Kitching, "Atomic vapor cells for chip-scale atomic clocks with improved long-term frequency stability," Opt. Lett., 30, 2351, 2005.

[14] S. Kargapoltsev, J. Kitching, L. Hollberg, A.V. Taichenachev, V.L. Velichanski, and V.I. Yudin, "High-contrast dark resonances in s_+-s_- optical field," Laser Phys. Lett., 1, 495, 2004.

[15] S. Knappe, J. Kitching, L. Hollberg, and R. Wynands, "Temperature Dependence of Coherent Population Trapping Resonances," Appl. Phys. B., 74, 317, 2002.

AN ASSESSMENT OF THE RECENT DEVELOPMENT OF MEMS OSCILLATORS AS COMPARED WITH CRYSTAL OSCILLATORS

C.S. LAM

TXC Corporation, Ping Cheng City, Taoyuan County, Taiwan

Abstract- Due to its high Q and temperature stable properties, for many years, quartz crystal based oscillators are important clock sources in consumer, commercial, industrial, and military digital sub-modules and modules. The demand for quartz crystal resonators and oscillators continues to rise. The unique fabrication and encapsulation requirements though render quartz crystal resonators and oscillators difficult or close to impossible to be integrated onto the mature silicon based IC platforms. The recent technical breakthroughs of MEMS (Micro Electro Mechanical Systems) based resonators and oscillators seem to re-ignite the interest in displacing/replacing the quartz crystal technology and to open up again the prospect in clock source integration.

This paper discusses and assesses, from the viewpoint of a quartz crystal manufacturer, such development and its possible impact on the quartz crystal industry which also experiences major progresses in miniaturization, performance enhancement, cost reduction, etc., in the past few years. This paper is not to discredit the MEMS oscillator efforts but to help the quartz crystal manufacturers to understand more about the efforts and advise them what they need to prepare for.

Keywords: MEMS, quartz, resonator, crystal oscillator

1. Introduction

Due to its high Q and temperature stable properties, for many years, quartz crystal based oscillators are important clock sources in consumer, commercial, industrial, and military digital sub-modules and modules.[1] The demand for quartz crystal resonators and oscillators continues to rise. The unique fabrication and encapsulation requirements though render quartz crystal resonators and oscillators difficult or close to impossible to be integrated onto the mature silicon based IC platforms.

For a typical handset, four different piezoelectric components are needed- RF SAW filter (~900 MHz to 2 GHz using $LiTaO_3$ or $LiNbO_3$), IF SAW filter (~50 to 400 MHz using maintly quartz), and TCXO (temperature-compensated crystal oscillator, ~10 to 30 MHz and quartz-based) in the RF section; and tuning fork (32.768 KHz and quartz-based) for standby clocking in the baseband section (Fig. 1).

Quite a few years ago the successful development of direct conversion technology in transceiver chipsets rendered IF SAW filter obsolete in many GSM handsets (as in Fig. 1). Some GSM transceiver chipsets now have the digitally-compensated crystal oscillator (DCXO) circuit of the TCXO integrated on-chip.[2] However, a quartz crystal is still needed off-chip (Fig. 2). As the handset market continues to grow, developing Micro Electro Mechanical Systems (MEMS) components as switches, filters, resonators/oscillators, etc. in the RF section of handsets seems to be the logical route of the final solution- integration (Fig. 3).

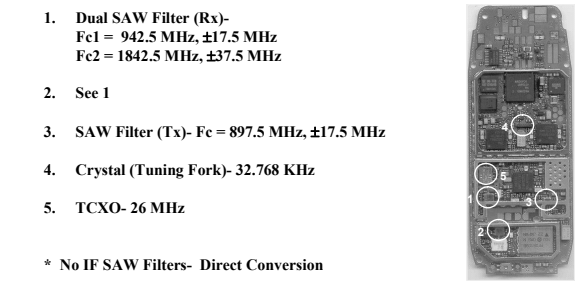

Fig. 1 Piezoelectric Components in a Typical Dual Band GSM Handset (GSM900 and DCS1800)

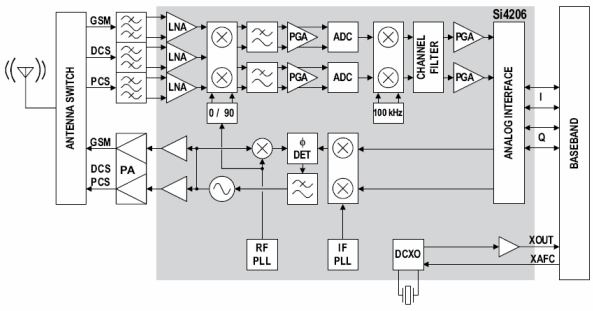

Fig. 2 GSM Transceiver Chipset with On-chip DCXO[2]

About 15 to 25 years ago, thin film resonators (TFRs) were vigorously discussed and researched as they could

possibly be integrated onto the mature silicon based IC platforms.[3] After that it came 5 years of a quiet period. In 1994, HP research personnel presented the first report on film bulk acoustic resonator (FBAR)[4] and in 2001 Agilent announced the production of FBAR-based duplexers. FBAR (also coined BAWR nowadays by some), with its small size, silicon etching process and sacrificial layer removal step, can be considered as a MEMS component. As of now, FBAR-based duplexers and filters have successfully replaced a small portion of the rooted RF SAW duplexer/filter market but they still have to be individually packaged- like the RF SAW devices. Discrete RF SAW filter (and/or FBAR), TCXO (or quartz crystal) and quartz tuning fork are still the key off-chip piezoelectric components in handsets. FBAR integration and the full scale MEMS integration as in Fig. 3 are not likely to happen in the foreseeable future.[5]

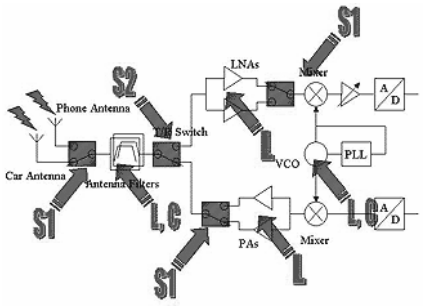

Fig. 3 Applications of MEMS in RF Section of Handsets[5]

The recent technical breakthroughs of MEMS based resonators and oscillators seem to re-ignite the interest in displacing/replacing the quartz crystal technology and to open up again the prospect in clock source integration. This paper discusses and assesses, from the viewpoint of a quartz crystal manufacturer, such development and its possible impact on the quartz crystal industry which also experiences major progresses in miniaturization, performance enhancement, cost reduction, etc., in the past few years. This paper is not to discredit the MEMS oscillator efforts but to help the quartz crystal manufacturers to understand more about the efforts and advise them what they need to prepare for.

2. Silicon Solutions

Silicon clock oscillators are CMOS integrated circuits without using ceramic resonators, quartz crystals or other external components for frequency determination. The author commented in 2003[6] on such solution based on the Maxim's EconOscillator/Divider and Micro Oscillator's MOI-2000 Oscillator (Fig. 4).[7] One can easily note that the frequency stability of these oscillators is 5,000 to 15,000 ppm and so their applications are somewhat limited.

Linear Technology also offers a family of silicon oscillators with stability ranging from 2,500 to 15,000 ppm.[8] Recently, Mobius Microsystems announced the offering of the "All-silicon Copernicus Clock with 2,500 ppm frequency stability over process, voltage, and temperature."[9]

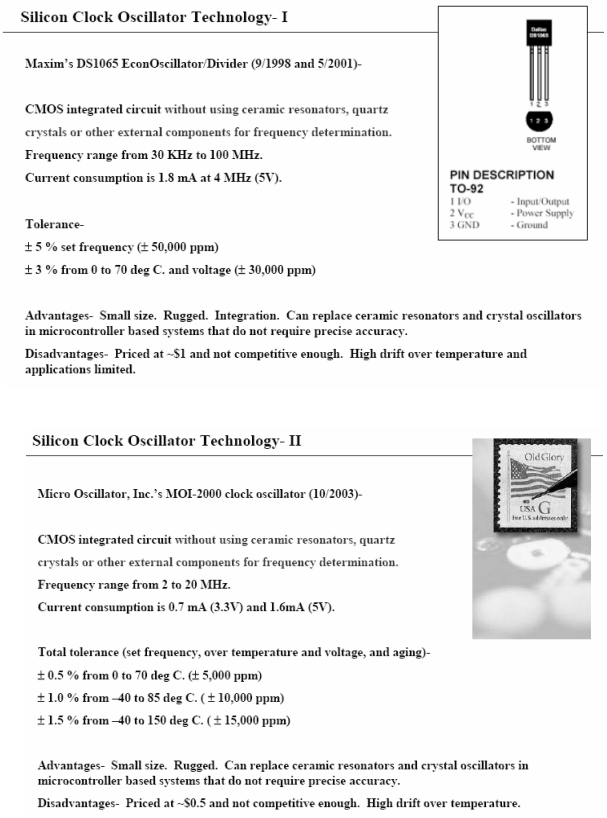

Fig. 4 Silicon Clock Oscillator Technology, I- Maxim's EconOscillator/Divider and II- Micro Oscillator's MOI-2000[7]

Silicon clock oscillators can be integrated onto other silicon based IC platforms. One big advantage is their ruggedness (suitable for high shock and vibration applications) as there is no discrete mechanical resonant element. Their biggest disadvantage is clearly their poor frequency stability.

3. Quartz Solutions

It is almost 80 years since the applications of quartz crystals in telecommunication equipment first appeared.[1] Due to its high Q, unchallenged frequency-temperature stability, low cost, technical maturity, and widely commercial availability, quartz

crystal continues to be the choice, and sometimes the only choice, in providing stable frequency sources in the ever expanding digital world.

BAW-based (<MHz ~ 200 MHz)	*SAW-based (<50 MHz ~ 3 GHz)*
Passives-	
Tuning Fork and Resonator	**SAWR**
MCF	**SAWF**
Oscillators-	
CXO	**CSO**
PCXO	
VCXO (Voltage-Controlled)	**VCSO**
TCXO (Temp. Compensated)	**TCSO?**
OCXO (Oven-Controlled)	**OCSO?**
Timing Modules-	
Clock Data Recovery (CDR)	**Clock Data Recovery (CDR)**
Clock Smoother (CS)	**Clock Smoother (CS)**
Frequency Translator (FX)	**Frequency Translator (FX)**
STM	**STM**
….	**….**

Table 1 BAW (Crystal)- and SAW-based Passives, Oscillators and Timing Modules

Powered by the fierce growth in wired and wireless equipment, quartz crystal (Bulk Acoustic Wave based = BAW-based) and its high frequency version SAW device (Surface Acoustic Wave based) are being used widely ranging from a simple passive resonator to a complex synchronous timing module (STM) as show in Table 1.

Though unthinkable a few years ago, AT-cut quartz crystal (resonator) as small as 2.5x2mm^2 is now being shipped in volume (Fig. 5).[10] Applications which need even smaller quartz crystals (2x1.6 and 1.6x1mm^2) are expected to appear and quartz crystal manufacturers are getting ready for them. Smaller than 5x3.2mm^2 quartz crystals need to be sealed in vacuum to retain impedance integrity. Low MHz small size quartz crystal blanks also need to be beveled (contoured) to sustain efficient energy trapping.

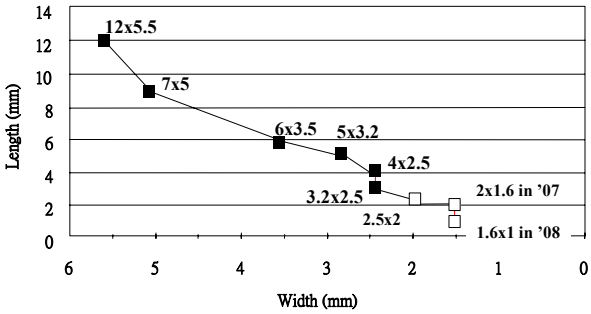

Fig. 5 Development of Quartz Crystals

As for the crystal oscillators, delivery of 2.5x2mm^2 CMOS fixed frequency clock crystal oscillators (XOs/CXOs) is ramping up (Fig. 6) and quartz crystal manufacturers are preparing the yet smaller 2x1.6mm^2 version.[10] Oscillator IC suppliers also continue to shrink the IC sizes and for the 2.5x2mm^2 CXO one can still use wirebonding instead of flipchipping (Fig. 7).

CMOS programmable clock crystal oscillators (PCXOs) are widely available in 7x5, 5x3.2 and 3.2x2mm^2 sizes.[11] These oscillators have on-chip phase lock loops (PLLs) with at least two dividers to allow programming to almost any frequency within a working frequency range (e.g. 2 to 200 MHz) based on a single low frequency quartz crystal (e.g. 25 MHz). These oscillators are attractive to designers as they can be quickly programmed to the frequencies desired for development purpose but they suffer from higher jitter which is inherent to all PLL-based oscillators. CXOs with differential LVPECL/LVDS output are also available in 14x9 and 7x5mm^2 platforms. Recently, one supplier began to offer programmable LVPECL CXO.[12] The frequency stability of the above quartz crystal, CXO and PCXO is usually specified at less than 100, 50, 25 and 10 ppm dependent on the temperature range of operation- significantly better than the all silicon solutions.

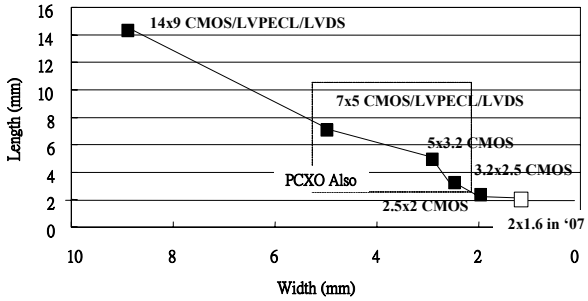

Fig. 6 Development of Crystal Oscillators

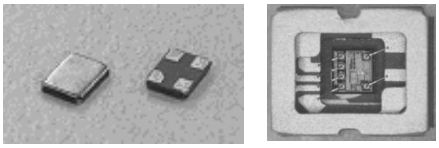

Fig. 7 2.5x2 mm^2 CMOS Crystal Oscillators[10]

To provide even better frequency stability, temperature-compensated crystal oscillator (TCXO) is available. AT-cut quartz crystal's frequency-temperature stability is cubic in nature. The oscillator IC can have added voltage-frequency pulling function to analogously or digitally compensate the cubic frequency-temperature as depicted in Fig. 8. For nowadays handset applications, a frequency stability of better than 2.5 ppm TCXO is usually needed to provide the accurate reference clock of frequency synthesizing within the RF transceiver IC. For GPS equipment, TCXO of less than 1 or 0.5 ppm is needed. In 2004, the smallest TCXO available was 3.2x2.5mm^2 (Fig. 9).[13]

Now it is 2.5x2mm^2.

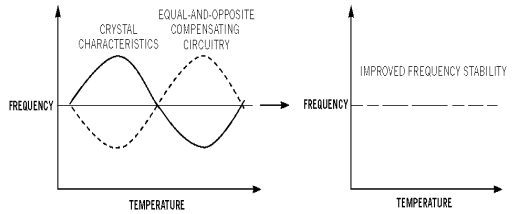

Fig. 8 Temperature Compensation of Quartz Crystal for TCXO Applications.

Overall, in the past few years, quartz crystal manufacturers have done the what once thought was impossible in shrinking the sizes of quartz crystal, CXO, PCXO and TCXO to where we are and most important of all, without sacrifying performance and cost.[14,15] Claims and threats to displace/replace quartz crystal devices come and go. More and more quartz crystal devices are shipped yearly and the average selling price continues to drop.

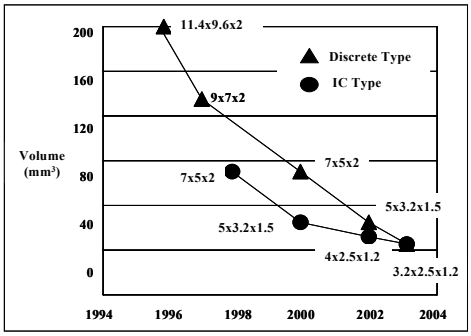

Fig. 9 Development of TCXO for Handset Applications till 2004

4. MEMS Solutions

Suggesting to use MEMS techniques to build the resonant elements for oscillator applications is not something new. The MEMS resonant elements are usually micromachined on silicon and they come in the shapes of combs, beams, discs, etc. For quartz crystal resonators, the vibration is based on piezoelectric excitation. For MEMS resonant element, it's based on electrostatic dynamics with "transducer gap" typical less than 1 μm (Fig. 10).[16,17] Similar to the silicon clocks discussed in Section 2, MEMS resonators are rugged as they are small and integration is possible.

In 1998, Sandia National Laboratories announced "Microscopic machines may replace quartz crystals, Pollen-grain-sized parts soon in watches, TVs, computers."[18] Based on the earlier MEMS works funded by DARPA[19], Discera was established in 2001 with the mission "to become a global leader in CMOS MEMS resonator technology and to offer a broad portfolio of patented PureSilicon™ resonators whose breakthrough technology is proven reliable and used to create the industry's most advanced and economical Frequency Control and RF Circuits ….. Discera is the trend setter in today's multi-billion dollar timing industry, displacing quartz crystal solutions with systems-on-a-chip alternatives."[20]

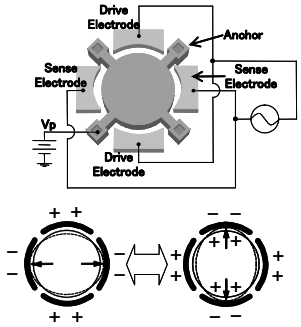

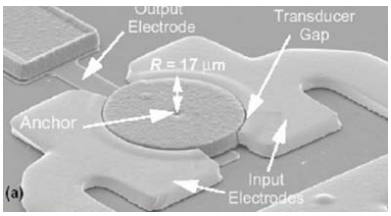

Fig. 10 Electrostatic Dynamics of Disc-Like MEMS Resonator[16,17]

In 2003, Discera offered the first MEMS oscillator MRO-100 (3x3mm^2) in 19.2 MHz for multiband wireless transceiver application (Fig. 11). The resonant element was a 30μm x8μm^2 MEMS beam.

1. A packaged MRO-100 micro-oscillator is almost lost on the face of a US penny.

Fig. 11 3x3mm^2 MEMS Oscillator[20]

In 2003, Forman[21] commented "the challenge for Discera is in convincing customers to abandon an entrenched, known technology (quartz crystal technology) in favor of something new- convincing them to go with the devil they don't know." In 2004, Discera also demonstrated the first integrated 1.6 GHz tunable oscillator, likely for the VCO (usually discrete LC-based) of the local oscillator in wireless transceiver applications.

As of today, no detailed specifications of the above two oscillators are available in the public domain and it's difficult to assess their acceptability in the commercial market.

Based on the IP licensed through Bosch, SiTime was established couple of years ago with the mission to become "a fabless integrated circuit company developing silicon timing, clock, and RF chips, which incorporate MEMS timing reference devices inside standard silicon electronic chips, eliminating the need for quartz crystals."[22] The first products introduced were the SiT8002 series programmable oscillators and the SiT1 series fixed frequency oscillators (likley programmed from the SiT8002 series). The CMOS oscillators are available in 7x5, 5x3.2, 3.2 and 2.5x2mm^2 (Fig. 12)- clearly targeting at the pin-to-pin compatible quartz crystal oscillator market (Fig. 6).

Fig. 12 SiTime's MEMS Oscillator[22]

The key success by SiTime over previous MEMS efforts was that "the clean and high vacuum sealing technology developed was able to minimize contamination and to support low aging of the MEMS resonator."[23,24] The SiT8002 and SiT1 series oscillators started out with a packaged 4-beam MEMS resonator (Fig. 13) wirebonded onto a leadframe-supported oscillator IC, and the whole assembly was then plastic-molded.

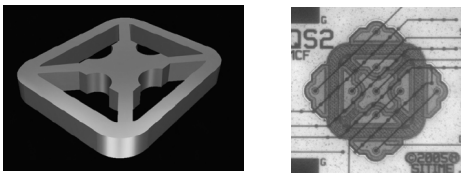

Fig. 13 MEMS Resonator based on 4-Beam Structure[22]

Little information was available on the MEMS resonator until SiTime announced the offering of it as a SiT0100 part (Fig. 14). The MEMS resonator operates at 5.1 MHz with 6-pad connection which is different from the familiar 2-pad connection of a quartz crystal resonator. The know-how in driving the MEMS resonator, Q and resistance values of the resonator, programming methodology of the oscillator, etc. are only available under a non-disclosure fees-associated agreement. No commercial available oscllator ICs are known to be available yet in pairing with this MEMS resonator.

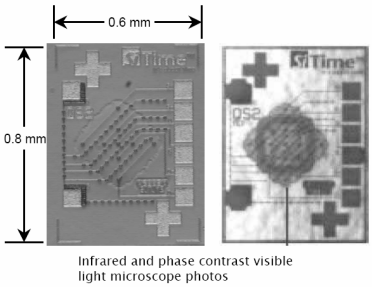

Fig. 14 Packaged 0.8x0.6x0.15mm3 MEMS Resonators[22]

Based on the public information available, one can say the SiT8002 series MEMS oscillators have a 5.1 MHz MEMS resonator inside and the oscillator output frequency is programmed (PLL'ed) from this MEMS resonator- similar to the PCXOs mentioned in Section 3. It is of interest to mention the series number SiT8002 is remarkably similar to that of the SG-8002 series PCXO from a major crystal oscillator manufacturer.[11] Recalling silicon-based MEMS resonator in general exhibits an inherent ~-30 ppm/°C frequency stability. To achieve the frequency stability claimed by the MEMS oscillators (say 50 to 100 ppm), temperature compensation is needed- similar to the TCXOs mentioned in Section 3 except likely a simpler linear compensation is performed. In summary, the current MEMS oscillators need to be-

programmed to frequency (like PCXO) and
programmed to compensate frequency stability (like TCXO).

A PCXO needs to go through the following steps after encapsulation- tested, programmed, and tested (all done at room temperature). A TCXO needs to go through the following elaborate and costly steps after encapsulation- frequency-temperature test over the temperature range of operation, compensation, and frequency-temperature verification test over the temperature range of operation. Since the silicon-based MEMS resonator exhibits a linear frequency-temperature stability, compensation over the entire temperature of operation might not be needed to achieve a few tens of ppm stability. To get better stability, compensation based on frequencies measured at several temperatures close to the room temperature might be needed. Based on the information available so far, several questions with regard to the cuurent generation off MEMS oscillators can be posted-

Higher current drain than regular CXO to power the PLL circuits?

Poorer jitter performance as it's inherent to PLL-based oscillators?

Digital compensation often creates frequency perturbations within small temperature increments. Would that present problems for many applications?

Plastic molding is not hermetic- limitation in applications?

Programming and compensation can be costly?

As for integration, Johnson[25] commented "Though Discera's MEMS is cast into a CMOS chip, neither its nor SiTime's MEMS chips hold circuitry. Today, adding MEMS to a CMOS chip with circuitry would risk turning the circuitry to soup by virtue of the high temperatures needed to sculpt MEMS structures from silicon. Consequently, like quartz crystals, MEMS resonators today require a separate CMOS chip, containing a feedback path to maintain oscillation, a PLL to stabilize frequency and other conditioning circuitry to optimize performance. In the case of quartz crystals, the CMOS chip is wired to the crystal inside the package. By contrast, the MEMS resonator, as a planar CMOS chip itself, can be directly bonded to the chip holding the circuitry." As said in the introduction, FBAR integration is not likely to happen in the foreseeable future. The author believes it applies to MEMS oscillators also.

5. Quartz Plus MEMS Solutions

As said in the introuction, "FBAR, with its small size, silicon etching process and sacrificial layer removal step, can be considered as a MEMS component."

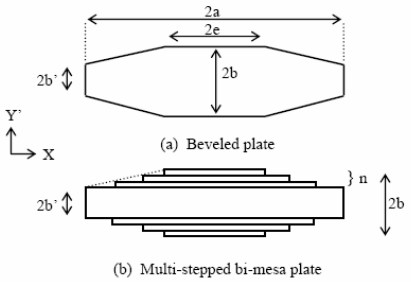

Fig. 15 (a) Beveled Quartz Crystal and (b) Bi-Mesa Quartz Crystal[26]

Nowadays many quartz crystal components are miniaturized and some sorts of MEMS processing steps are involved- like the double-side photolithography, etch through, Au etch protection, etc. of miniature quartz tuning forks; etching steps of bi-mesa type quartz crystals (Fig. 15)[26], Lamé mode quartz crystal[27]; etc. A major crystal oscillator manufacturer already coined the term "QMEMS" in recognizing the importance of linking the quartz and MEMS technologies for the next generations of quartz crystal devices.[28] Recently both Discera and SiTime announced their alliances with two individual quartz crystal manufacturers.[29,30] It seems instead of pushing pure MEMS-based solutions, some MEMS companies consider the best route is to link up with the quartz crystal manufacturers to identify markets which can best use both the quartz and MEMS techniques.

6. Discussions

This paper discusses and assesses, from the viewpoint of a quartz crystal manufacturer, the performances of silicon clocks and MEMS oscillators as compared with quartz crystal oscillators. This paper is not to discredit the MEMS oscillator efforts but to help the quartz crystal manufacturers to understand more about these products. The author believes MEMS oscillator technology has yet many issues (technical, cost, acceptance, etc.) to overcome in order to compete with the rooted quartz crystal oscillator technology.[31] The quartz crystal industry, though experiences major progresses in miniaturization, performance enhancement, cost reduction, etc. in the past few years, shall have to continue to retain its competitiveness through further

miniaturization,
cost reduction,
performance improvement,
ease of use improvement,
reliability improvement,
development of new applications,
investigation of Quartz + MEMS techniques,
etc.

References

1. *"A History of the Quartz Crystal Industry in the USA,"* Virgil E. Bottom. Proc. 1981 Annual Frequency Control Symposium, pp. 3-12, http://www.ieee-uffc.org/fc_history/bottom.html.
2. *AERO™ I+ Tranceiver for GSM and GPRS Wireless Communications*, Silicon Laboratories, http://www2.silabs.com/public/documents/tpub_doc/dsheet/Wireless/Aero_RF_Transceivers/en/aeroI+.pdf.
3. *"Sputtered AlN Films for Bulk-Acoustic-Wave Devices,"* J.S. Wang and K.M. Lakin, Proc. 1981 Ultrasonics Symposium, pp. 502-505.
4. *"Micromachined Thin Film Bulk Acoustic Wave Resonators,"* R. Ruby and P. Merchant, Proc. 1994

IEEE Int'l Frequency Control Symposium, pp. 135-138.
5. *"MEMS in CMOS- 21st Century RF and Microwave Applications,"* Patrick Albert, John Costello and Patrick Salomon, RFdesign, July 2000.
6. *"Applications of Frequency Control Products for Telecommunication & Handset and Their Development Trends,"* IT Market Conference, Dec. 19, 2003, Beijing, http://www.txc.com.tw/download/TECH_PAPER/2003-ITMarket-1-English.pdf.
7. *"Microcontroller Clock- Crystal, Resonator, RC Oscillator, or Silicon Oscillator?"* Maxim's Application Note 2154 http://www.maxim-ic.com/appnotes.cfm/appnote_number/2154 and *"MOI-2000 CMOS Clock Oscillator,"* Micro Oscillator, http://www.micro-oscillator.com/MOI2000_Data%20Sheet4-04.pdf.
8. *Linear Technology Silicon Oscillators,* http://www.linear.com/pc/viewCategory.do?navId=H0,C1,C1010,C1096.
9. *"Mobius Microsystems Introduces the All-silicon Copernicus Clock,"* May 10, 2005, http://www.us.design-reuse.com/news/news10402.html.
10. *TXC Corporation's* 2006 Products Roadmap.
11. *Epson-Toyocom SG-8002 Series Programmable Crystal Oscillators,* http://www.epsontoyocom.co.jp/english/product/OSC/programmable.html.
12. *"Versatile OTP Oscillator Delivers Differential LVPECL for Data Designers with Deadlines,"* C-MAC MicroTechnology, September 1, 2005, http://news.thomasnet.com/fullstory/467366.
13. *"Development of Miniaturized Analog and Digital Temperature Compensated Crystal Oscillators,"* C.S. Lam and C.W. Chiang, Proc. Second Symposium on Acoustic Devices for Future Mobile Communication Systems, March 3~5, 2004, Chiba, Japan.
14. *"Why oscillators are the best frequency sources for wireless designs,"* Roger Burns, RFdesign, August 1, 2003, http://rfdesign.com/mag/radio_why_oscillators_best/index.html.
15. *"It's Crystal Clear: Quartz Still Resonates with Designers,"* Jon Titus, ECN, October 1, 2006, http://www.ecnmag.com/article/CA6380016.html?filename=ECN20061001ec6ocs100_.xml.
16. *"Current Activities of Japanese Quartz Industries,"* Masanobu Okazaki, Proc. 100th Meeting of the No. 150th Committee on Acoustic Wave Devices, Japanese Society for the Promotion of Science, Dec. 4~5, 2006, Taipei, Taiwan.
17. *"Design and Fabrication Procedure for High Q MEMS Resonators,"* Wan-Thai Hsu, Microwave Journal, February 1, 2004, pp. 60-74.
18. *"Microscopic machines may replace quartz crystals, Pollen-grain-sized parts soon in watches, TVs, computers,"* Sandia National Laboratories, News Release, July 7, 1998, http://www.sandia.gov/media/memquar.htm.
19. *"Transceiver Front-end Architectures using High-Q Micromechanical Resonators,"* C. T.-C. Nguyen, Proc. IEEE European MIDAS Workshop, University of Surrey, United Kingdom, July 17-18, 2000.
20. *Discera,* http://www.discera.com.
21. *"Discera's dilemma: Making enough noise to merit mobile's attention,"* David Forman, Small Times, June 23, 2003, http://www.smalltimes.com/document_display.cfm?document_id=6261
22. *Sitime,* http://www.sitime.com.
23. *"Silicon MEMS Oscillators to Replace Quartz Crystals,"* Aaron Partridge and John McDonald, SiTime Corporation's 2006 Promotion Materials.
24. *"A New Paradigm in Time: Silicon MEMS Resonators vs. Quartz Crystals,"* Thomson Dialog NewsEdge, May 1, 2006, http://www.tmcnet.com/usubmit/2006/05/01/1627534.htm.
25. *"MEMS Eyes Quartz Crystal Apps,"* R. Colin Johnson, EE Times, October 23, 2006 http://www.embedded.com/rss/showArticle.jhtml?articleID=193401321&cid=RSSfeed_embedded_news
26. *"Decoupling Effect of Multi-Stepped Bi-Mesa AT-Cut Quartz Resonator,"* S. Goka et al., Proc. 2003 IEEE International Frequency Control Symposium, pp. 694-697.
27. *"Quasi–Lamé–Mode Quartz–Crystal Resonators,"* Yasutaka Shimizu, et al., Japan. J. Appl. Phys. Vol.39 (2000), Part 1, No. 5B, 30 May 2000, pp. 3010-3013.
28. *"What is QMEMS?"* Epson-Toyocom, http://www.epsontoyocom.co.jp/english/info/2006/qmems.html.
29. *"Vectron and Discera to Drive New Era of MEMS Timing Devices,"* November 14, 2006, http://www.discera.com/03b_zp111406.shtml.
30. *"SiTime and Micro Crystal Enter MEMS Oscillator Joint Development Agreement,"* November 13, 2006, http://www.sitime.com/news/releases/micro111306.htm.
31. *"MEMS oscillators, has their time come?"* Jérémie Bouchaud and Bernardo Knoblich, Wicht Technologie Consulting, http://www.memsinvestorjournal.com/2006/10/mems_oscillator.html#more.

Surface Waves in Micro-machined Phononic Crystals

Tsung-Tsong Wu
Institute of Applied Mechanics,
National Taiwan University,
Taipei 106, TAIWAN
wutt@ndt.iam.ntu.edu.tw

Zi-Gui Huang
Institute of Applied Mechanics,
National Taiwan University,
Taipei 106, TAIWAN
huang@ndt.iam.ntu.edu.tw

Bing-Giun Liang
Institute of Applied Mechanics,
National Taiwan University,
Taipei 106, TAIWAN
lbg@ndt.iam.ntu.edu.tw

***Abstract*—The existence of elastic band gaps in phononic crystals (PCs) may lead to development of various acoustic devices, such as filters and transducers. In this paper, we demonstrate the existence of the frequency band gaps of surface acoustic waves (SAW) in micro-machined air/silicon phononic band structures using layered normal and slanted finger interdigital transducers (IDT and SFIT). The frequency band gap width and total band gap of SAW in micro-machined air/silicon phononic crystals are studied experimentally.**

Keywords-phononic crystal*; *SAW; BAW*; *Band gap*; *MEMS

I. INTRODUCTION

Existence of complete band gaps of electromagnetic waves in photonic band structures extending throughout the Brillouin zone has demonstrated a variety of fundamental and practical interests [1, 2]. This has led to rapid growing interests in the analogous acoustic effects in periodic elastic structures called the phononic crystals (PCs). Phononic crystals that are made up of different elastic materials can prevent acoustic waves of certain frequencies from passing by, and thus, form the frequency band gap features [3].

On the study of bulk acoustic waves (BAW) in phononic band structures, the plane-wave expansion (PWE) method was adopted to calculate band gap features of two-dimensional periodic composites [4, 5]. Except for the PWE method, the layered multiple scattering theory was applied to study the frequency band gaps of BAW in three-dimensional periodic acoustic composites and the band structure of a phononic crystal consisting of complex and frequency-dependent Lame´ coefficients [6, 7]. In addition, the finite-difference time-domain (FDTD) method was applied to predict exactly the transmission properties of slabs of phononic crystals and to interpret the experimental data of two-dimensional systems [8-10]. The FDTD method was also used to calculate the periodic solid-solid, solid-liquid, and solid-vacuum composites [11]. The coupling characteristics of localized phonons in photonic crystal fibers were investigated theoretically [12]. Recently, Sun and Wu [13] investigated and analyzed the mode coupling in joined parallel phononic crystal waveguides using the FDTD method with periodic boundary condition. Also, Wu *et al*. [14] discussed the design of a highly magnified directional acoustic source based on the resonant cavity of two-dimensional phononic crystals.

The frequency band gap features of surface acoustic waves (SAW) are studied mainly using the PWE and variational methods [15-20]. Tanaka *et al*. [15-17] presented the theory of surface waves propagating in two-dimensional phononic crystals consisting of two cubic materials in square lattice, and also explained the stop band distribution of the surface, pseudosurface, and bulk waves using the PWE method. Recently, Wu *et al*. [18, 19] extended the theory to describe the phononic crystals consisting of materials with general anisotropy, and discussed the level repulsion of BAW in periodic composite materials. In addition, Huang and Wu [20] also investigated the temperature effect on frequency band gaps of SAW and BAW in phononic crystals. Except for the PWE method, Sun and Wu [21] adopted the FDTD method to analyze the SAW propagating in two-dimensional phononic waveguides.

On the experimental side, the detection and control of the high frequency sound were investigated in a dual-core square-lattice photonic crystal fibre perform using the interferometric set up [22]. Vines *et al*. [23, 24] conducted experimental study on surface waves generated by a line-focus acoustic lens at the water-loaded surfaces of two-dimensional superlattices that intersect the surface normally. Propagation of Scholte-like acoustic waves at the liquid-loaded surfaces of periodic structures has also been studied [25]. Rayleigh wave attenuation in a semi-infinite two-dimensional elastic-band-gap crystal, and surface state phenomena in linear and point defects were reported and discussed [26, 27].

Experimental studies on the band gap features of phononic crystals existed in the literature are mostly with the dimension in the order of mm and frequency in the kHz range. Toward the application of phononic crystals to the silicon based MEMS components, such as low insertion loss filter, micro acoustic channel etc., it is necessary to reduce the size to micrometer (or even further in the nanometer) scale and the frequency in the ranges from couple hundred MHz to couple GHz. Recently, Wu *et al*. [28, 29] investigated the frequency band gap features of surface waves in micro-machined air/silicon phononic band structures. The experimental setups were designed to demonstrate the frequency band gap of SAW propagating along the [100] direction of air/silicon phononic band structures using layered interdigital transducers (IDT) and slanted finger interdigital transducers (SFIT) for single and wideband frequencies, respectively.

In this paper, we summarized the recent study on the measurements of SAW band gaps in air/silicon phononic band structures. The theory of SAW in phononic crystal is briefly introduced first. Then, calculated results of band gaps in air/silicon phononic crystals with different filling fractions are presented and discussed. To measure the band gaps of the micro-fabricated phononic crystals, both of the normal IDT and slanted IDT are introduced. Finally, previous results on the SAW band gap measurements for SAW propagates along the [100] direction of silicon are summarized. Finally, a series of experiments designed for testing the total band gap of the air/silicon phononic crystals are conducted and discussed.

II. Surface Acoustic Waves in Phononic Crystals

In the following, formulation for calculating SAW band gap of phononic crystal is summarized [18]. In an inhomogeneous linear elastic medium with no body force, the equation of motion of the displacement vector $\mathbf{u}(\mathbf{r},t)$ can be written as

$$\rho(\mathbf{r})\ddot{u}_i(\mathbf{r},t) = \partial_j[C_{ijmn}(\mathbf{r})\partial_n u_m(\mathbf{r},t)], \tag{1}$$

where $\mathbf{r} = (\mathbf{x},z) = (x,y,z)$ is the position vector; $\rho(\mathbf{r})$ and $C_{ijmn}(\mathbf{r})$ are the position-dependent mass density and elastic stiffness tensor respectively. A phononic crystal composed of a two-dimensional periodic array (x-y plane) of material *A* embedded in a background material *B* is considered. Due to the spatial periodicity, the material constants, $\rho(\mathbf{x})$ and $C_{ijmn}(\mathbf{x})$ can be expanded in Fourier series with respect to the two-dimensional reciprocal lattice vectors (RLV), $\mathbf{G}=(G_1,G_2)$, as

$$\rho(\mathbf{x}) = \sum_{\mathbf{G}} e^{i\mathbf{G}\cdot\mathbf{x}}\rho_{\mathbf{G}}, \tag{2}$$

$$C_{ijmn}(\mathbf{x}) = \sum_{\mathbf{G}} e^{i\mathbf{G}\cdot\mathbf{x}}C_{\mathbf{G}}^{ijmn}, \tag{3}$$

where $\rho_{\mathbf{G}}$ and $C_{\mathbf{G}}^{ijmn}$ are the corresponding Fourier coefficients.

On utilizing the Bloch's theorem and expanding the displacement vector $\mathbf{u}(\mathbf{r},t)$ in Fourier series for the analyses of surface and bulk waves, we arrive

$$\mathbf{u}(\mathbf{r},t) = \sum_{\mathbf{G}} e^{i\mathbf{k}\cdot\mathbf{x}-i\omega t}(e^{i\mathbf{G}\cdot\mathbf{x}}\mathbf{A}_{\mathbf{G}}e^{ik_z z}), \tag{4}$$

where $\mathbf{k} = (k_1,k_2)$ is the Bloch wave vector, ω is the circular frequency, k_z is the wave number along the z direction, and $\mathbf{A}_{\mathbf{G}}$ is the amplitude of the displacement vector. It is noted that as the component of the wave vector k_z equal to zero, Eq. (4) degenerates into the displacement vector of a bulk acoustic wave. On substituting Eqs. (2), (3) and (4) into Eq. (1), and after collecting terms systematically, we obtain

$$(\mathbf{A}k_z^2 + \mathbf{B}k_z + \mathbf{C})\mathbf{U} = 0, \tag{5}$$

where **A**, **B**, and **C** are $3n\times3n$ matrices, and are functions of the Bloch wave vector **k**, components of the two-dimensional RLV, circular frequency ω, the Fourier coefficients of mass density $\rho_{\mathbf{G}}$ and components of elastic stiffness tensor $C_{\mathbf{G}}^{ijmn}$. n is the total number of RLV used in the Fourier expansion, and **U** is the eigenvector. The expressions of the matrices **A**, **B**, and **C** were listed in [18].

By applying the traction free boundary conditions on the surface, the dispersion relation for surface waves propagating in the two-dimensional phononic crystals, with both of the filling and background materials belonging to the triclinic system can be obtained. When k_z in Eq. (5) is equal to zero, the equation degenerates into

$$\mathbf{C}\mathbf{U} = 0. \tag{6}$$

Eq. (6) can be utilized to calculate the dispersion relations of bulk waves propagating in the two-dimensional phononic crystals.

III. Band Gap Calculations of Air/Silicon Phononic Crystals

In the following, two-dimensional phononic crystal with square lattice consisting of circular cylinder (*A*) embedded in a background material (*B*) with lattice spacing *a* is considered and shown in Fig. 1(a). Figure 1(b) is the surface Brillouin region of a square lattice in which the reciprocal lattice vector is $\mathbf{G} = (2\pi N_1/a, 2\pi N_2/a)$, where $N_1, N_2 = 0,\pm1,\pm2,\cdots$ and the filling fraction is ff= $\pi r^2/a^2$. The irreducible part of the surface Brillouin zone of a square lattice is shown in Fig. 1(b), which is a triangle with vertices $\overline{\Gamma}$, $\overline{X}$, and $\overline{M}$.

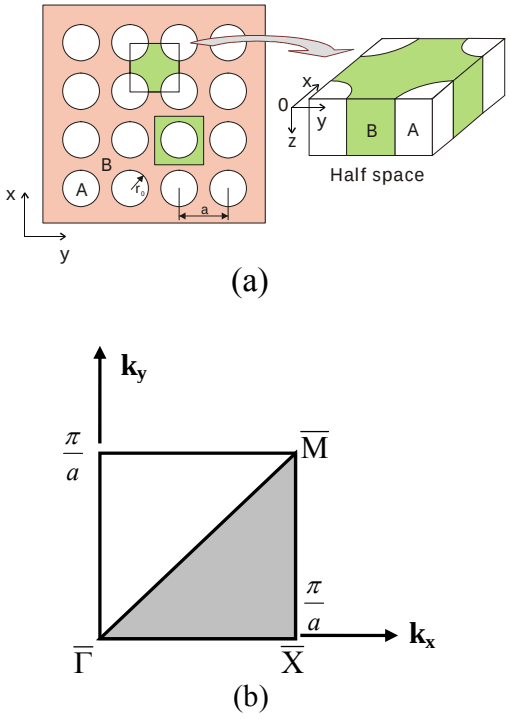

Figure 1. (a) Two-dimension phononic crystals with square lattice; (b) Surface Brillouin zone of a square lattice. (adopted from [29])

Figure 2 shows the results of SAW and BAW modes propagating on the surface of a two-dimensional air/silicon phononic band structure. The vertical axis is the normalized frequency ($\omega^* = \omega a / C_t$) and the horizontal axis is the reduced wave vector ($k^* = ka/\pi$). C_t and k are the shear velocity of Si and the wave vector along the Brillouin zone, respectively. In the calculations, the x-y plane is parallel to the (001) plane and the x axis is parallel to the [100] direction of the silicon. As shown in Fig. 2, along the $\overline{\Gamma}$ - $\overline{X}$ boundary of the irreducible Brillouin zone, the fundamental and the higher surface wave modes are belonging to the normal SAW modes (solid circles). For comparison, the dispersion relations of the bulk modes are also shown in Fig. 2. The thin solid lines represent the fundamental (SV_0) and the higher shear vertical modes (SV_1). The square symbols are those for the fundamental modes (L_0). The bold solid lines represent the fundamental shear horizontal modes (SH_0), while the lines with "×" symbols represent the higher shear horizontal modes (SH_1).

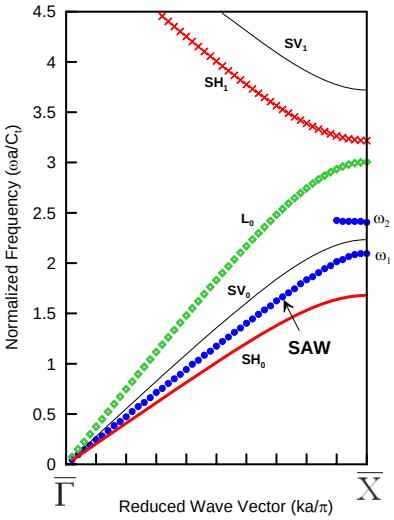

Figure 2. The dispersion relations of the SAW and BAW modes along the $\overline{\Gamma}$ - $\overline{X}$ boundary of the irreducible part of the Brillouin zone.

The frequencies ω_1, ω_2 and the SAW band gap width ($\Delta\omega = \omega_2 - \omega_1$) as a function of the filling fraction are calculated and shown in Fig. 3. The left vertical axis is the normalized frequency, the right vertical axis is the band gap width, and the horizontal axis is the filling fractions. The solid circles represent the fundamental and higher SAW modes while the open circles with dash lines represent the band gap widths of SAW modes at the $\overline{X}$ point. We note that the frequencies ω_1 and ω_2 decrease as the filling fraction of the band structure increases. The SAW band gap widths $\Delta\omega$ increase as the filling fraction increase and reach the maximum value at about ff= 0.48. In Fig. 3, the vertical dash line indicates the locations of the frequencies ω_1, ω_2 and the frequency band gap widths of SAW modes at ff= 0.385.

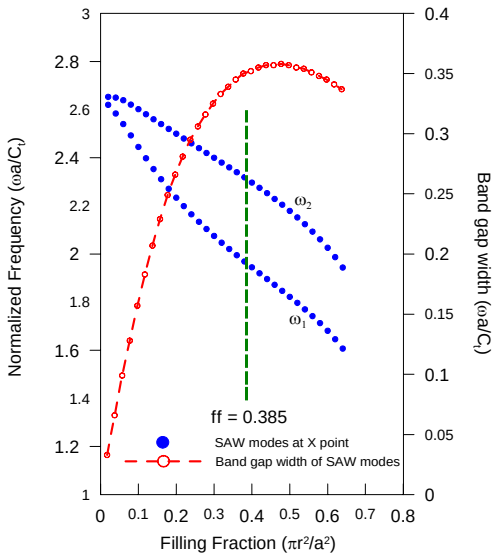

Figure 3. The variations of the frequencies ω_1, ω_2 and the band gap widths due to the filling fraction. The band gap width is defined as $\Delta\omega = \omega_2 - \omega_1$. The left vertical axis is the normalized frequency, the right vertical axis is the band gap width, and the horizontal axis is the filling fractions.

On the other hand, the existence of a total band gap in a phononic crystal means that waves within the band gap frequency are forbidden along any propagating direction. For the case of two-dimensional air/silicon phononic crystals, the calculated results showed that total band gap exist only when the filling fraction is high enough. Shown in Fig. 4 is the dispersion of SAW and BAW modes in the phononic crystal with filling fraction equal to 0.608 and a= 20 μm. The total band gap frequencies of the two-dimensional air/silicon phononic crystals are located from 126 MHz to 181 MHz.

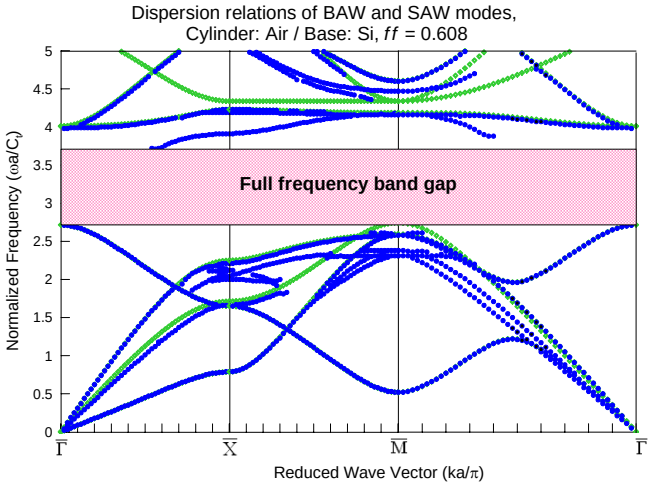

Figure 4. The dispersion of SAW and BAW modes in the phononic crystal with filling fraction equal to 0.608.

IV. Layered IDT/ZnO/Silicon SAW Devices

In order to measure the band gaps of SAW in the air/silicon phononic crystal, SAW delay line was introduced to generate high frequency acoustic waves. Since silicon is not a piezoelectric material, thin piezoelectric film has to be coated

on top of the silicon. A schema of the layered SAW delay line with slanted finger interdigital transducer (SFIT/ZnO/Si) is shown in Fig. 5.

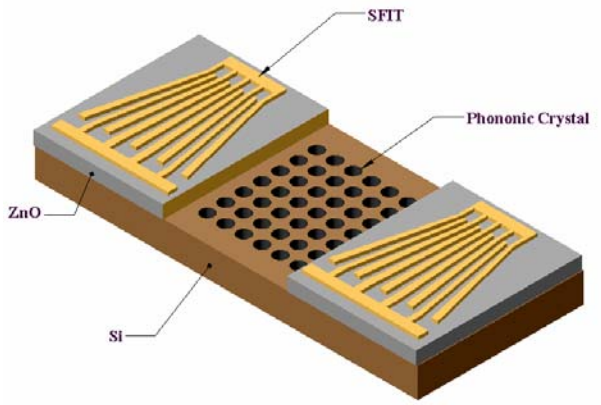

Figure 5. A schema of the layered SAW delay line with slanted finger interdigital transducer (SFIT/ZnO/Si).

Unlike the half-space SAW filter, the phase velocity of a layered SAW device is dispersive. Consequently, the dispersion has to be considered in the design of a layered SAW device [30]. The main difference between layered and half space structures is that the phase velocity and electromechanical coupling coefficient are dispersive and therefore function of frequency. So when we employ the coupling of mode (COM) model [31] to analyze a layered SAW device, some of the COM parameters become frequency-dependent and have to be considered in the analysis [32]. The dispersive COM parameters in layered structures include phase velocity shift, reflection coefficient, transduction coefficient, IDT capacitance, and propagation loss. In this study, the dispersion of the COM parameters was included in the calculation of the frequency response of the layered SAW device utilized in the band gap measurements.

V. Measurement Results and Discussion

In the following, fabrication processes of the two-dimensional phononic band structures are introduced briefly. Firstly, the layered SAW devices are fabricated by the lift-off method. Then the square regions of ZnO film between the input and output IDT (or SFIT) are etched out by wet-etching process in order to fabricate the air/silicon phononic crystal on the silicon substrate. At last, after the conventional lithography process, the periodic cylinders of two-dimensional air/silicon phononic crystal can be carried out by ICP etching (Inductively Coupled Plasma-reactive ion etching) process. In this paper, depths of the two-dimensional periodic cylinders are at least 80 μm. Since the energy of SAW modes is mostly confined to a depth of one to two wavelengths of the SAW, the finite slab is suitable for discussing the frequency band gap features of SAW modes.

(1). Measurement of SAW band gap width along [100] direction using layered SFIT

In [29], the experimental setup (Fig. 5) was designed to demonstrate the frequency band gap width of SAW propagating along the [100] direction of air/silicon phononic band structures using the layered SFIT for wideband frequencies. In Fig. 5, silicon based phononic crystals consisting of six rows of air cylinders and the layered SAW systems (two SFITs and one delay line) were fabricated. In the experiment, the lattice constant a=10 μm, the radius of the circular cylinder r_0=3.5 μm, and the filling fraction ff=0.385. The predicted frequency band gap along the x axis was located between 183 MHz and 215 MHz.

In Fig. 6, the frequency band gaps of the air/silicon phononic crystals were revealed by the layered SFIT in the range of pass-band frequency. The vertical axis is the insertion loss in units of dB and the horizontal axis is the frequency in units of MHz. The S_{21} parameter was measured from the network analyzer as the insertion loss. The rectangular region represents the frequency band gap of fabricated phononic crystals with six rows of air cylinders. The dashed line and solid lines denotes the measurements with and without phononic crystals respectively. The two dashed lines are the results of different sets with the same design. We found that the insertion loss that is measured with phononic crystals in the range of pass-band frequency is clearly lower than those without phononic crystals. Most of the SAW energy was blocked by phononic band structures. The result showed good agreement with the theoretical evaluation by the PWE method.

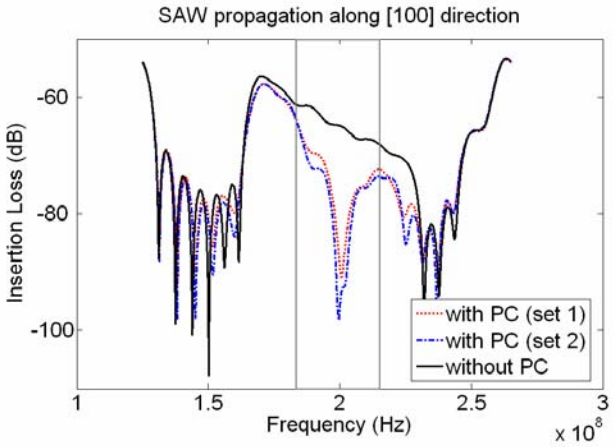

Figure 6. The frequency band gaps of the phononic crystals are revealed by the layered SFIT in the range of pass-band frequency. The rectangular region represents the frequency band gap of fabricated phononic crystals with six rows of air cylinders.

(2). Measurement of SAW total band gap using layered IDT

In this paper, to verify the total band gap of SAW in two-dimensional air/silicon phononic crystals, a series of band gap measurements using the layered IDT were conducted. In the design, the lattice constant was chosen as 20 μm, and the radius of the circular cylinder was equal to 8.8 μm. The calculated total band gap frequencies are located between 126 MHz and 181 MHz. According to the band gap frequencies, the corresponding design propagating frequencies were chosen as 100, 140, and 200 MHz. One was located in the total frequency band gap (140 MHz) and the other two were not (100 and 200

MHz). Five different propagation angles of SAW devices in this experimental setup were selected as 0°, 26.565°, 45°, 63.435° and 90°.

Figures 7-9 show the frequency responses of SAW passing through phononic crystals. In the figures, there are three diagrams which indicate the results of SAW propagating along the three different angles, i.e., 0°, 26.565°, and 45°. Due to the symmetry, the frequency responses at angles 63.435° and 90° are similar to those at 26.565° and 0°, respectively and therefore are not shown in this paper. In each diagram, the dashed and solid lines represent the measurements with and without phononic band structures. The results shown in Figs. 7 and 9 are those for the designed frequencies located in the pass-band frequencies, one is below the total frequency band gap and the other one is above the total frequency band gap. The results showed that rather severe attenuations are found in the results, nevertheless, transmission of the high frequency waves through the phononic band structures still can be identified clearly.

The results shown in Fig. 8 are those for the designed frequency located in the total frequency band gap. In contrast to those shown in Figs. 7 and 9, the frequency responses showed a total vanishing of the incident SAW. This shows that the incident SAW has been completely blocked by the phononic band structures.

From the series of experiments shown in this subsection, we have demonstrated the transmission of high frequency SAW through a phononic band gap structure so far if the frequency is not located in the total band gap frequencies. However, we note that big attenuation due to the scattering and material damping has been found in the present cases of air/silicon phononic band structures. On the contrary, the results also showed that there is almost no energy can penetrate through the phononic band structure even for the small number of rows of the air cylinders (six in this paper). This means that air/silicon phononic band gap structure can serve as a very good wave isolator.

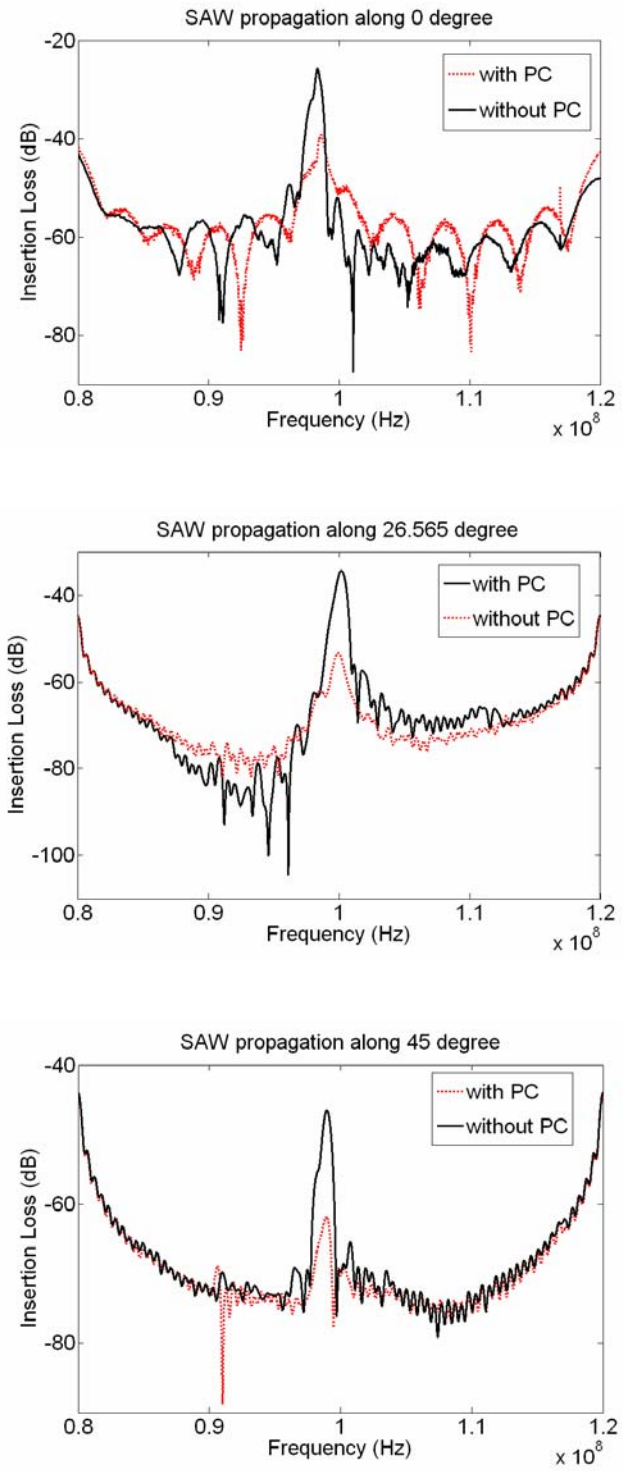

Figure 7. Frequency responses with/without phononic crystals. (below the total frequency band gap)

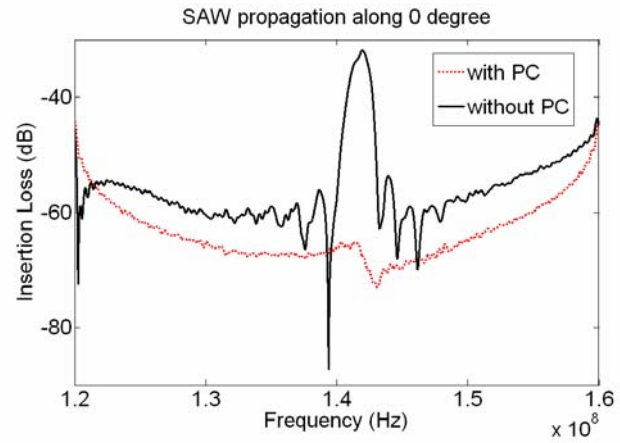

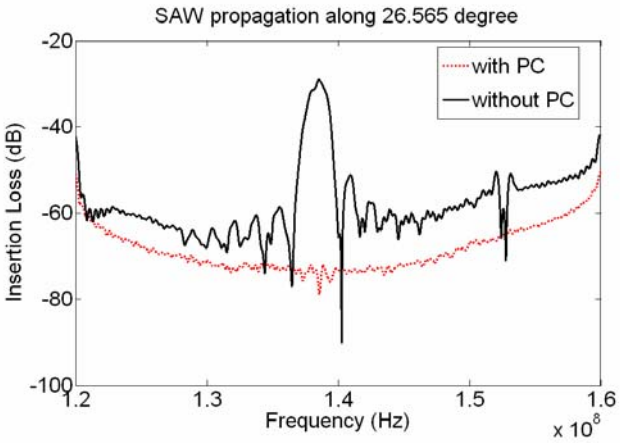

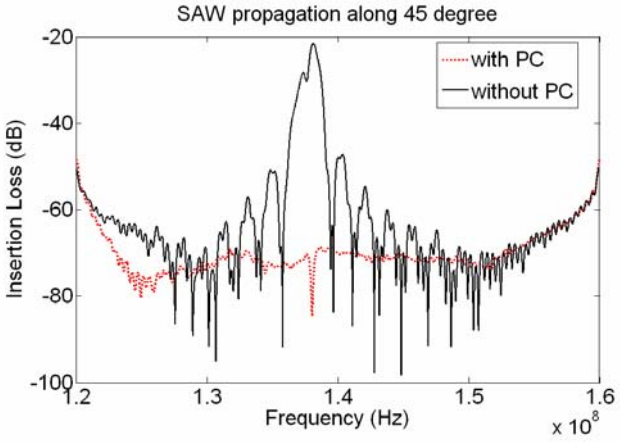

Figure 8. Frequency responses with/without phononic crystals. (within the total frequency band gap)

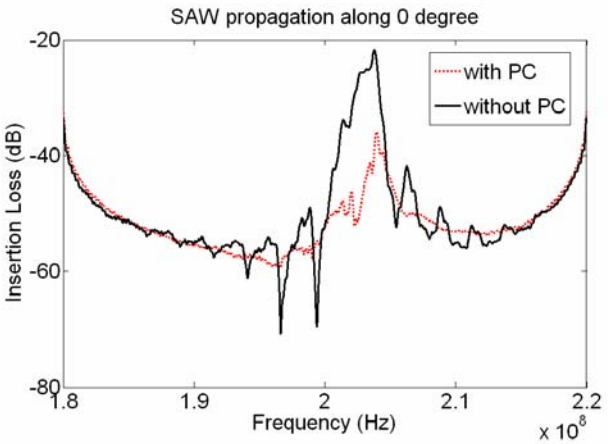

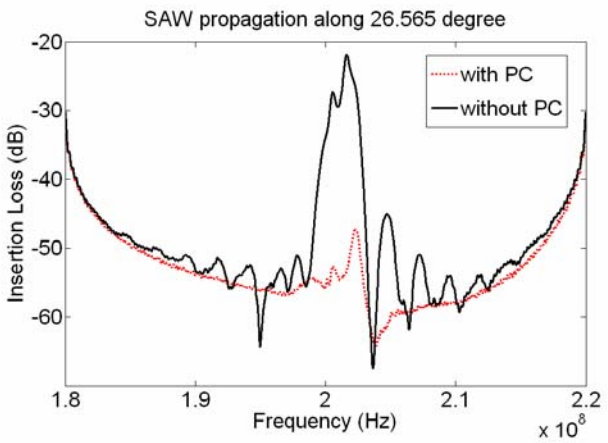

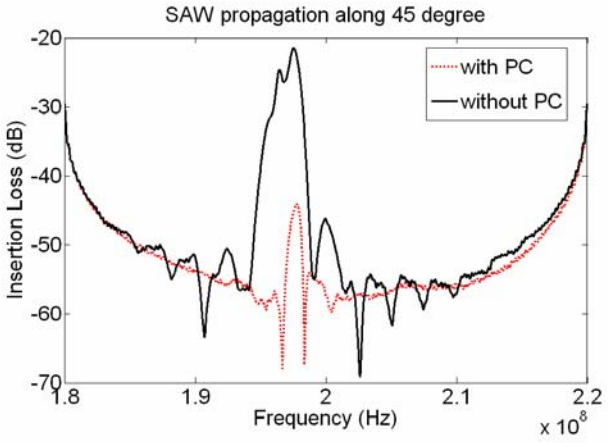

Figure 9. Frequency responses with/without phononic crystals. (above the total frequency band gap)

VI. CONCLUSION

In this paper, we summarized the recent study on the measurements of SAW band gaps in air/silicon phononic band structures. Layered SAW devices were employed to generate high frequency SAW in the micro-fabricated phononic band structures. Normal IDT was used to demonstrating the transmission and blocking of SAW in the phononic band structures. The slanted IDT was utilized to measure the bandwidth of the band gap. The experimental results demonstrated the transmission characteristics of high frequency SAW in the micro-fabricated phononic band structures. In the stop band, the transmission of SAW is completely blocked by the phononic band structure, even for the small number of air cylinder rows was used. The results of this study may serve as an important basis for the study of micro-acoustic waveguides.

ACKNOWLEDGMENTS

The authors thank the National Science Council (NSC94-2811-E-002-039) of Taiwan for financial support.

REFERENCES

[1] S. G. Johnson and J. D. Joannopoulos, "PHOTONIC CRYSTALS: The road from theory to practice," Kluwer academic publishers, Boston, 2003.

[2] J. D. Joannopoulos, R. D. Meade, and J. N. Winn, "Photonic Crystals: Molding the flow of light," Princeton University Press, Princeton, NJ, 1995.

[3] A. Modinos, N. Stefanou, I. E. Psarobas, V. Yannopapas, "On wave propagation in inhomogeneous systems," Physica B 296, pp. 167, 2001.

[4] M. Sigalas and E. N. Economou, "Elastic and acoustic wave band structure," J. Sound Vib. 158, pp. 377, 1992.

[5] M. S. Kushwaha, P. Halevi, L. Dobrzynski, and B. Djafari-Rouhani, "Acoustic Band Structure of Periodic Elastic Composites," Phys. Rev. Lett. 71, pp. 2022, 1993.

[6] I. E. Psarobas, N. Stefanou, and A. Modinos, "Scattering of elastic waves by periodic arrays of spherical bodies," Phys. Rev. B 62, pp. 278, 2000.

[7] Z. Liu, C. T. Chen, P. Sheng, A. L. Goetzen, and J. H. Page, "Elastic wave scattering by periodic structures of spherical objects: Theory and experiment," Phys. Rev. B 62, pp. 2446, 2000.

[8] D. Garcia-Pablos, M. Sigalas, F. R. Montero de Espinoza, M. Torres, M. Kafesaki, N. Garcia, "Theory and Experiments on Elastic Band gaps," Phys. Rev. Lett. 84, pp. 4349, 2000.

[9] M. Sigalas and N. Garcia, "Theoretical study of three dimensional elastic band gaps with the finite-difference time-domain method," J. Appl. Phys. 87, pp. 3122, 2000.

[10] M. Sigalas and N. Garcia, "Importance of coupling between longitudinal and transverse components for the creation of acoustic band gaps: The aluminum in mercury case," Appl. Phys. Lett. 76, pp. 2307, 2000.

[11] Y. Tanaka, Y. Tomoyasu, and S. Tamura, "Band structure of acoustic waves in phononic lattices: Two-dimensional composites with large acoustic mismatch," Phys. Rev. B 62, pp. 7387, 2000.

[12] A. Khelif, B. Djafari-Rouhani, V. Laude, and M. Solal, "Coupling characteristics of localized phonons in photonic crystal fibers," J. Appl. Phys. 94, pp. 7944-7946, 2003.

[13] J. H. Sun and T.-T. Wu, "Analyses of mode coupling in joined parallel phononic crystal waveguides," Phys. Rev. B 71, article no. 174303, 2005.

[14] T.-T. Wu, C. H. Hsu, and J. H. Sun, "Design of a highly magnified directional acoustic source based on the resonant cavity of two-dimensional phononic crystals," Appl Phys. Lett. 89 (17), article no. 171912, 2006.

[15] Y. Tanaka and S. Tamura, "Surface acoustic waves in two-dimensional periodic elastic structures," Phys. Rev. B 58, pp. 7958, 1998.

[16] Y. Tanaka and S. Tamura, "Acoustic stop bands of surface and bulk modes in two-dimensional phononic lattices consisting of aluminum and a polymer," Phys. Rev. B 60, pp. 13294, 1999.

[17] Y. Tanaka, Y. Tomoyasu, and S. Tamura, "Band structure of acoustic waves in phononic lattices: Two-dimensional composites with large acoustic mismatch," Phys. Rev. B 62, pp. 7387, 2000.

[18] T.-T. Wu, Z. G. Huang, and S. Lin, "Surface and bulk acoustic waves in two-dimensional phononic crystals consisting of materials with general anisotropy," Phys. Rev. B 69, article no. 094301, 2004.

[19] T.-T. Wu and Z. G. Huang, "Level repulsion of bulk acoustic waves in composite materials," Phys. Rev. B 70, article no. 214304, 2004.

[20] Z. G. Huang and T.-T. Wu, "Temperature effects on bandgaps of surface and bulk acoustic waves in two-dimensional phononic crystals," IEEE Trans. Ultrason. Ferroelectr. Freq. Control 52(3), pp. 365, 2005.

[21] J. H. Sun and T.-T. Wu, "Propagation of surface acoustic waves through sharply bent two-dimensional phononic crystal waveguides using a finite-difference time-domain method," Phys. Rev. B 74, article no. 174305, 2006.

[22] P. St. J. Russell, E. Marin, and A. Díez, "Sonic band gaps in PCF preforms: enhancing the interaction of sound and light," Optics Express 11, pp. 2555, 2003.

[23] R. E. Vines, J. P. Wolfe, and A. G. Every, "Scanning phononic lattices with ultrasound," Phys. Rev. B 60, pp. 11871, 1999.

[24] R. E. Vines and J. P. Wolfe, "Scanning phononic lattices with surface acoustic waves," Physica B 263-264, pp. 567, 1999.

[25] A. G. Every, R. E. Vines, and J. P. Wolfe, "Line-focus probe excitation of Scholte acoustic waves at the liquid-loaded surfaces of periodic structures," Phys. Rev. B 60, pp. 11755, 1999.

[26] F. Meseguer, M. Holgado, D. Caballero, N. Benaches, J. Sa'nchez-Dehesa, C. Lo´pez, and J. Llinares, "Rayleigh-wave attenuation by a semi-infinite two-dimensional elastic-band-gap crystal," Phys. Rev. B 59, pp. 12 169, 1999.

[27] M. Torres, F. R. Montero de Espinosa, D. Garica-Pablos, and N. Garcia, "Sonic Band Gaps in Finite Elastic Media Surface States and Localization Phenomena in Linear and Point Defects," Phys. Rev. Lett. 82, pp. 4282, 1999.

[28] T.-T. Wu, Z. G. Huang, and S. Y. Liu, "Surface acoustic wave band gaps in micro-machined air/silicon phononic structures – theoretical calculation and experiment," Zeitschrift für Kristallographie 220, pp. 841, 2005.

[29] T.-T. Wu, L. C. Wu, and Z. G. Huang, "Frequency band-gap measurement of two-dimensional air/silicon phononic crystals using layered slanted finger interdigital transducers," J. Appl. Phys. 97, article no. 094916, 2005.

[30] T.-T. Wu and Y. Y. Chen, "Exact Analysis of Dispersive SAW Devices on ZnO/Diamond/Si Layered Structures," IEEE Trans. Ultrason. Ferroelectr. Freq. Control, 49(1), pp. 142, 2002.

[31] B. P. Abbott, "A Derivation of the Coupling-of-Modes Parameters Based on the Scattering Analysis of SAW Transducers and Gratings," Proc. IEEE Ultra. Symposium, 5, 1991.

[32] Y. Y. Chen, T.-T. Wu, and T. T. Chou, "Analysis of the frequency response of a dispersive IDT/ZnO/sapphire SAW filter using effectivity and coupling of modes model," J. Phys. D: Appl. Phys. 37, pp. 120, 2004.